ADVANCES IN QUANTUM CHEMISTRY

Volume 46

John R. Sabin &
Erkki Brändas

ADVANCES IN

QUANTUM CHEMISTRY

VOLUME 46

ADVANCES IN
QUANTUM CHEMISTRY

THEORY OF THE INTERACTION OF SWIFT IONS WITH MATTER. PART 2

EDITORS

JOHN R. SABIN
QUANTUM THEORY PROJECT
UNIVERSITY OF FLORIDA
GAINESVILLE, FLORIDA

ERKKI BRÄNDAS
DEPARTMENT OF QUANTUM CHEMISTRY
UPPSALA UNIVERSITY
UPPSALA, SWEDEN

FOUNDING EDITOR

PER-OLOV LÖWDIN
1916–2000

GUEST EDITORS

REMIGIO CABRERA-TRUJILLO
QUANTUM THEORY PROJECT
UNIVERSITY OF FLORIDA
GAINESVILLE, FLORIDA

JOHN R. SABIN
QUANTUM THEORY PROJECT
UNIVERSITY OF FLORIDA
GAINESVILLE, FLORIDA

VOLUME 46

ELSEVIER
ACADEMIC
PRESS

Amsterdam · Boston · Heidelberg · London · New York · Oxford
Paris · San Diego · San Francisco · Singapore · Sydney · Tokyo

ELSEVIER B.V.
Sara Burgerhartstraat 25
P.O. Box 211, 1000 AE Amsterdam
The Netherlands

ELSEVIER Inc.
525 B Street, Suite 1900
San Diego, CA 92101-4495
USA

ELSEVIER Ltd
The Boulevard, Langford Lane
Kidlington, Oxford OX5 1GB
UK

ELSEVIER Ltd
84 Theobalds Road
London WC1X 8RR
UK

First edition 2004

ISBN: 0-12-034846-2
ISSN: 0065-3276

♾ The paper used in this publication meets the requirements of ANSI/NISO Z39.48-1992 (Permanence of Paper). Printed and bound in Great Britain.

Contents

Contributors

Numbers in parentheses indicate the pages where the authors' contributions can be found.

Barnabás Apagyi (267), Department of Theoretical Physics, Institute of Physics, Technical University of Budapest, H-1521 Budapest, Hungary

Peter Bauer (153), Institut fuer Experimental Physik, Johannes Kepler Universitaet Linz, A-4040 Linz, Austria

Hans Bichsel (329), Nuclear Physics Laboratory 354290, University of Washington, Seattle, WA 98195-4290, USA

Robert J. Buenker (165), Bergische Universitaet Wuppertal, Fachbereich C, Theoretische Chemie Gaussstr. 20, D-42119 Wuppertal, Germany

J. Burgdörfer (29), Institute for Theoretical Physics, Vienna University of Technology, Wiedner Hauptstr. 8-10, A-1040 Vienna, Austria

Remigio Cabrera-Trujillo (121), Quantum Theory Project, University of Florida, Gainesville, FL, USA

Annette Calisti (293), UMR6633, Université de Provence, Centre Saint Jérôme, 13397 Marseille Cedex 20, France

Scott M. Cohen (241), Department of Physics, Duquesne University, Pittsburgh, PA 15282-0321, USA

Salvador A. Cruz (195), Departamento de Física, Universidad Autónoma Metropolitana-Iztapalapa, Apartado Postal 55 534, 09340 México, D.F., Mexico

James W. Dufty (293), Department of Physics, University of Florida, Gainesville, FL 32611, USA

P. M. Echenique (1), Departamento de Física de Materiales, Facultad de Química, Universidad del País Vasco, Apartado 1072 and Centro Mixto, C.S.I.C.-UPV/EHU, 20080 San Sebastián, Spain; Donostia International Physics Center, Paseo Manuel de Lardizabal, No. 4, 20018 San Sebastián, Spain

F. J. García de Abajo (65), Centro Mixto CSIC-UPV/EHU and Donostia International Physics Center (DIPC), Manuel de Lardizábal 4, 20018 San Sebastián, Spain

Mineo Kimura (165), Graduate School of Science and Engineering, Yamaguchi University, Ube, Yamaguchi 755-8611, Japan

C. Lemell (29), Institute for Theoretical Physics, Vienna University of Technology, Wiedner Hauptstr. 8-10, A-1040 Vienna, Austria

István Nagy (267), Department of Theoretical Physics, Institute of Physics, Technical University of Budapest, H-1521 Budapest, Hungary

Jens Oddershede (121), Quantum Theory Project, University of Florida, Gainesville, FL, USA; Kemisk Institut, Syddansk Universitet, Odense, Denmark

Lukáš Pichl (165), Foundation of Computer Science Laboratory, University of Aizu, Tsuruga, Ikki, Aizuwakamatsu, Fukushima 965-8580, Japan

V. H. Ponce (65), Centro Atómico Bariloche, Comisión Nacional de Energía Atómica, 8400 San Carlos de Bariloche, Argentina

L. E. Porter (91), Washington State University, Pullman, WA 99164-1302, USA

R. H. Ritchie (1), Oak Ridge National Laboratory, P.O. Box 2008, Oak Ridge, TN 37831-6123, USA

John R. Sabin (121), Quantum Theory Project, University of Florida, Gainesville, FL, USA; Kemisk Institut, Syddansk Universitet, Odense, Denmark

A. Sarasola (1), Departamento de Física de Materiales, Facultad de Química, Universidad del País Vasco, Apartado 1072 and Centro Mixto, C.S.I.C.-UPV/EHU, 20080 San Sebastián, Spain

Dieter Semrad (153), Institut fuer Experimental Physik, Johannes Kepler Universitaet Linz, A-4040 Linz, Austria

Jacques Soullard (195), Instituto de Física, Universidad Nacional Autónoma de México, Apartado Postal 20 364, 01000 México, D.F., Mexico

N. Stolterfoht (307), Hahn-Meitner-Institut Berlin, Glienickerstr. 100, D-14109 Berlin, Germany

B. Sulik (307), Institute of Nuclear Research (ATOMKI), H-4001 Debrecen, Hungary

Bernard Talin (293), UMR6633, Université de Provence, Centre Saint Jérôme, 13397 Marseille Cedex 20, France

K. Tőkési (29), Institute of Nuclear Research of the Hungarian Academy of Sciences (ATOMKI), P. O. Box 51, H-4001 Debrecen, Hungary; Institute for Theoretical Physics, Vienna University of Technology, Wiedner Hauptstr. 8-10, A-1040 Vienna, Austria

X.-M. Tong (29), Department of Physics, Kansas State University, Manhattan, KS 66506-2601, USA

E. Zaremba (1), Department of Physics, Queen's University, Kingston, Ont., Canada K7L 3N6

Preface

It will soon be a century since Niels Bohr developed the first theory of energy deposition of α-particles colliding with a material target. Although his approach was based on a harmonically bound electron and was purely classical, it provided the basis for the study of several processes which would later become important in fields such as radiotherapy, dosimetry, material modification, surface analysis, aerology, astrophysics, plasma physics, etc. Personalities as Hans Bethe, Enrico Fermi, and Jens Lindhard, among others, laid the foundations to what now has become the study of energy deposition and energy loss in atomic and molecular collisions.

From the technological point of view, there is a quantum leap between the materials developed and equipment used today and what was available to the original pioneers of this field.

It is not only the technological applications that have taken advantage of the study of energy deposition of ions and atoms in materials, but it has also led to greater theoretical understanding among the interaction of ions, atoms, and molecules. The introduction of new methods into the analysis of energy deposition, charge transfer and phase effects has spawned new lines of research. Of the newer methods presently used are density functional theory, montecarlo methods, and various *ab initio* methods (close-coupling, electron-nuclear dynamics, etc…), among others. Some of these methods require extensive computational resources, however the details and the understanding that such computations lead to is unprecedented. This is an aspect of the field that will evolve as faster and more powerful computers become available.

The intention of this and the previous volume in the series is to present the latest stage of the field of energy deposition as it is actually viewed by many of the major players in the arena. It is hard to incorporate all of the important players and all of the topics related to energy deposition in a single volume dedicated to this field, however we have tried to present the state of the art as it is now.

We thank all the contributors that have spent time and dedication in the preparation of their contributions, and hope this volume will serve as a starting point to new researchers in the field, as a reference, and serve as a guide to the direction which energy deposition is taking.

Remigio Cabrera-Trujillo, John R. Sabin

Gainesville, January, 2004

This Page Intentionally Left Blank

Density Functional Theory-based Stopping Power for 3D and 2D Systems

A. Sarasola,[1] R. H. Ritchie,[2] E. Zaremba[3] and P. M. Echenique[1,4]

[1] *Departamento de Física de Materiales, Facultad de Química, Universidad del País Vasco, Apartado 1072 and Centro Mixto, C.S.I.C.-UPV/EHU, 20080 San Sebastián, Spain*
[2] *Oak Ridge National Laboratory, P.O. Box 2008, Oak Ridge, TN 37831-6123, USA*
[3] *Department of Physics, Queen's University, Kingston, Ont., Canada K7L 3N6*
[4] *Donostia International Physics Center, Paseo Manuel de Lardizabal, No. 4, 20018 San Sebastián, Spain*

Abstract

We have reviewed the theoretical and experimental results on linear and non-linear screening and stopping power for 3D and 2D systems. In the linear case ($Z_1/v \ll 1$), dielectric formalism has been used to characterize such systems, while the non-linear aspects are described within the density functional theory (DFT) framework. Differences between proton and antiproton probe particles are discussed, both in the quadratic response function theory and in the DFT. For heavy ions, the main results on Z_1 oscillations are revised.

Contents

ADVANCES IN QUANTUM CHEMISTRY, VOLUME 46
ISSN: 0065-3276 DOI 10.1016/S0065-3276(04)46001-8

1. INTRODUCTION

The interaction of particles of charge Z_1 entering a solid medium with velocity v has been extensively studied for nearly a century. Understanding of the dynamical properties of microscopic matter must come from measurements at the macroscopic level. It is the task of theory to interpret these results to yield information about the complex microworld. Physicists approach this task by building models. Here we review various models of energy loss for 2D and 3D electron gases, including the state-of-art density functional theory (DFT).

The simplest but widely used model for the description of the valence band electrons of a metal is the homogeneous electron gas. A useful parameter characterizing it is the average electronic density n_0, or equivalently, the average electron radius r_s (in units of the Bohr radius), where

$$\frac{1}{n_0} = \frac{4}{3}\pi r_s^3.$$

An n-dimensional electron gas is defined by the number of spatial coordinates (n) in which electrons can move freely. The 3D case has been studied extensively since Drude constructed his theory of electrical and thermal conduction by applying the kinetic theory of gases to a metal. In the late 1970s, the 2D electron systems began to be studied. Among the properties of the 2D systems that have attracted active theoretical and experimental interest are phase-transitions and long-range order or transport and percolation properties of disordered 2D systems. A 2D Coulomb gas, where electrons are restricted to move in a 2D space, can be applied as an approximation to metal–insulator semiconductor structures or on the surface of liquid helium [1].

Lindhard [2] used linear response theory to calculate the stopping power of charged particles within a 3D electron gas model. He used quantum perturbation theory, treating the perturbing potential to the lowest order. The self-consistent response of the electrons to this perturbation was considered within a mean-field theory, each electron moving in a field determined by all others. At the same time, Bohm and Pines [3] constructed a quantum theory of the electron gas, describing (1) the long-range part of the Coulomb interaction in terms of collective fields that gives rise to plasma oscillations and, (2) individual electron interaction with the other ones and with collective fields *via* a screened short-range interaction.

In the 2D case, Stern [4] studied the polarizability of a 2D electron gas (2DEG) within the random phase approximation (RPA). Later on, exchange and correlation effects [5] were included providing a 2D equivalence of the Thomas–Fermi–Dirac method. Horing *et al.* [6] calculated the energy loss of a fast charged particle moving parallel to a 2D electron gas. This was extended by including the effect of finite temperature [7], local field corrections [8] and recoil [9].

Although the dielectric function formalism provides a qualitative description of dynamic screening over the whole range of projectile velocities, it is not quantitatively accurate, especially at low velocities where at metallic densities the charged particle represents a strong perturbation to the system even for the smallest charge $Z_1 = 1$. In general, linear response theory will remain valid as long as $Z_1/v \ll 1$ condition is satisfied, whereas non-linear effects will become significant when it is not.

Different approximations have been tried in order to go beyond the linear description of screening and stopping power. A systematic expansion in powers of the projectile charge Z_1 is the basis for a natural extension of linear theory. This first option is based on the calculation of the induced density to second order in Z_1 and thus, of the induced potential at the Hartree level. It is done using the quadratic response function within the RPA. As in the linear case, it essentially describes the mean field of all electronic interactions. However, being an expansion in Z_1, the theory is limited to those situations in which the corrections to the linear results are relatively small. In practice, for low projectile velocities, the theory is limited to the lowest possible value of Z_1 ($Z_1 = 1$) and high electron densities. Applied to the stopping power, this theory provides a Z_1^3 correction, the well-known Barkas term. Since the work of Ashley *et al.* [10] on the classical oscillator model (an extension of Bohr's classic treatment) many groups have used quadratic response approaches [11–14], but is worthwhile to mention the application of this concept to the full range of velocities done by Pitarke *et al.* [15,16] and the complement to that work done by Arbó *et al.* [17] for the electron gas model.

A second alternative to describe the non-linear effects is to use a hydrodynamic description of the electron gas. In this approach, the electron gas is considered as a charged fluid that interacts with the external particle [18–20] and is essentially described by the electronic charge density and the velocity of the fluid. In the static limit, a Thomas–Fermi–von Weizsäcker [21] description of electronic screening is obtained whereas, for higher velocities a numerical solution of coupled hydrodynamic equations is needed.

The third possible approximation to calculate the non-linear screening of a static external impurity, particularly useful at low ion velocities, can be achieved by using the DFT. The theory is based on the theorems of Hohenberg and Kohn [22]. Its practical implementation, based on the standard orbital picture, results in the so-called Kohn–Sham equations [23]

providing a tool to calculate a self-consistent potential to all orders in Z_1. Popovic and Stott [24] and Almbladh and von Barth used the DFT to study the problem of non-linear screening of a static proton in a 3D electron gas. The KS method, by construction, gives stationary-state phase shifted one-particle states. These phase shifts, at the Fermi level, are natural inputs in the scattering formulation of the retarding force, the stopping power of an electron gas for slow intruders.

An important self-consistency condition on the scattering potential is provided by the Friedel sum rule (FSR) [25]. Often one-parameter model potentials have been used to determine the screening parameter in a consistent way applying this rule [26–30].

But as the ion velocity increases the standard DFT method ceases to be valid and some generalization or alternative approach becomes necessary to investigate the importance of non-linearities for velocities up to the Fermi velocity. Lifschitz and Arista [31,32] developed an extension to the FSR to finite velocities and a self-consistent optimization of the scattering potential and related phase shifts. Zaremba *et al.* [33] extended non-linear screening theory making an accurate calculation of dynamic screening, but instead of treating the full cylindrical symmetry of the problem, they made an spherical average in the interaction potential. Salin *et al.* [34] extended this to account for full cylindrical symmetry.

In this review, Section 2 is devoted to the linear theory of 3D and 2D electron gases in the dielectric formalism, and prove the equivalence between linear response formalism and scattering theory in the Born approximation for slowly moving ions. An extensive description of non-linear effects within the DFT is completed in Section 3: relevant results on non-linear static screening and stopping at low ion velocities in 3D and 2D electron gases for proton and antiproton projectiles and the effective charge treatment for heavier ion are discussed. A brief comparison with second-order perturbation theory results and non-linear dynamic screening effects on slowly moving ions is also presented.

Atomic units are used unless otherwise stated.

2. LINEAR THEORY OF STOPPING POWER

2.1. Dielectric formalism in a 3D electron gas

The scalar electric potential created by an external charge density ρ in a polarizable homogeneous medium is obtained from Poisson's Fourier transformed equation

$$\varepsilon(\vec{q}, \omega) q^2 \phi(\vec{q}, \omega) = 4\pi \rho^{\text{ext}}(\vec{q}, \omega), \tag{1}$$

where $\varepsilon(\vec{q}, \omega)$ is the dielectric constant which characterizes the medium and is a function of both the frequency, ω, and the wave vector, $\vec{q}$, of the perturbing potential.

The field produced by this external charge will rearrange the whole electronic system, giving rise to an induced charge density, and therefore, an induced potential. These two magnitudes are related by

$$\phi^{\text{ind}}(\vec{q}, \omega) = \frac{4\pi}{q^2}\rho^{\text{ind}}(\vec{q}, \omega) = \frac{4\pi}{q^2}\chi(\vec{q}, \omega)\phi^{\text{ext}}(\vec{q}, \omega), \tag{2}$$

where $\chi(\vec{q}, \omega)$ is the density–density response function.

In the same way, the electric field induced in each point of space $\vec{r}$ and time t will be given by the gradient of the induced scalar potential.

$$\begin{aligned}\vec{E}^{\text{ind}}(\vec{r}, t) &= -\nabla\phi^{\text{ind}}(\vec{r}, t) \\ &= \int \frac{\mathrm{d}\vec{q}}{(2\pi)^3}\int_{-\infty}^{\infty}\frac{\mathrm{d}\omega}{2\pi}(-\mathrm{i}\vec{q})\mathrm{e}^{\mathrm{i}(\vec{q}\cdot\vec{r}-\omega t)}\frac{4\pi}{q^2}\rho^{\text{ext}}(\vec{q}, \omega)\frac{4\pi}{q^2}\chi(\vec{q}, \omega).\end{aligned} \tag{3}$$

For the case of a point charge Z_1 moving with v constant velocity the charge density is given by $\rho^{\text{ext}}(\vec{r}, t) = Z_1\delta(\vec{r} - \vec{v}t)$ or $\rho^{\text{ext}}(\vec{q}, \omega) = 2\pi Z_1\delta(\omega - \vec{q}\cdot\vec{v})$ in Fourier space. Introducing it in equation (3):

$$\vec{E}^{\text{ind}}(\vec{r}, t) = \frac{Z_1}{2\pi^2}\int \mathrm{d}\vec{q}(-\mathrm{i}\vec{q})\frac{\mathrm{e}^{\mathrm{i}\vec{q}(\vec{r}-\vec{v}t)}}{q^2}\frac{4\pi}{q^2}\chi(\vec{q}, \vec{q}\cdot\vec{v}). \tag{4}$$

The mean energy loss of the particle per unit path or stopping power can be obtained from the stopping force exerted by the medium in the direction of motion and evaluated at the particle position

$$\begin{aligned}\frac{\mathrm{d}E}{\mathrm{d}x} &= Z_1\hat{v}\vec{E}(\vec{r}, t)\Big|_{\vec{r}=\vec{v}t} = \frac{Z_1^2}{2\pi^2 v}\int\frac{\mathrm{d}\vec{q}}{q^2}(-\mathrm{i}\vec{q}\cdot\vec{v})\frac{4\pi}{q^2}\chi(\vec{q}, \vec{q}\cdot\vec{v}) \\ &= -\mathrm{i}\frac{4Z_1^2}{v^2}\int_0^{\infty}\frac{\mathrm{d}q}{q^3}\int_{-qv}^{qv}\mathrm{d}\omega\ \omega\chi(\vec{q}, \omega) \\ &= \frac{4Z_1^2}{v^2}\int_0^{\infty}\frac{\mathrm{d}q}{q^3}\int_{-qv}^{qv}\mathrm{d}\omega\ \omega\ \mathrm{Im}[\chi(\vec{q}, \omega)].\end{aligned} \tag{5}$$

Making use of the relation between the dielectric function $\varepsilon(\vec{q}, \omega)$ and the density–density response function, $\chi(\vec{q}, \omega)$, within the RPA [35]

$$\mathrm{Im}\left(\frac{-1}{\varepsilon(\vec{q}, \omega)}\right) = \frac{4\pi}{q^2}\mathrm{Im}[\chi(\vec{q}, \omega)], \tag{6}$$

we obtain the well-known expression for the stopping power:

$$\frac{\mathrm{d}E}{\mathrm{d}x} = \frac{2Z_1^2}{\pi v^2}\int_0^\infty \frac{\mathrm{d}q}{q}\int_0^{qv} \mathrm{d}\omega\,\omega\,\mathrm{Im}\left(\frac{-1}{\varepsilon(\vec{q},\omega)}\right). \tag{7}$$

This equation can be interpreted in terms of the probability of creating an excitation of momentum $\vec{q}$ and frequency ω:

$$P(\vec{q},\omega) = \frac{16\pi^2 Z_1^2\,\delta(\omega - \vec{q}\cdot\vec{v})}{q^2\cdot v}\,\mathrm{Im}\left(\frac{-1}{\varepsilon(\vec{q},\omega)}\right). \tag{8}$$

The values of the plane (q,ω) that satisfy $\mathrm{Im}(-1/\varepsilon) \neq 0$ will contribute to the stopping of the particle, creating both electron–hole pairs ($\mathrm{Im}(-\varepsilon) \neq 0$) and collective excitations or plasmons ($\varepsilon = 0$).

A mean inelastic collision time τ can also be defined

$$\tau^{-1} = \int \frac{\mathrm{d}\vec{q}}{(2\pi)^3}\int_0^\infty \frac{\mathrm{d}\omega}{(2\pi)} P(\vec{q},\omega) \tag{9}$$

or equivalently, an energy width of the particle state, $\Gamma = 1/\tau$. The energy width of the particle state corresponds to the imaginary part of the energy of the particle that leads to a temporal decay of the probability density of the incident particle flux $\mathrm{e}^{-\Gamma t}$. The energy straggling parameter W can also be defined from the second energy moment of this probability. In summary, the energy width Γ, the energy loss per unit path length or stopping power $\mathrm{d}E/\mathrm{d}x$ and the energy loss straggling parameter W can be written [36]

$$\Gamma = \int \frac{\mathrm{d}\vec{q}}{(2\pi)^3}\int_0^\infty \frac{\mathrm{d}\omega}{(2\pi)} P(\vec{q},\omega), \tag{10}$$

$$\frac{\mathrm{d}E}{\mathrm{d}x} = \frac{1}{v}\int \frac{\mathrm{d}\vec{q}}{(2\pi)^3}\int_0^\infty \frac{\mathrm{d}\omega}{(2\pi)}\,\omega P(\vec{q},\omega), \tag{11}$$

$$W = \frac{1}{n_0 v}\int \frac{\mathrm{d}\vec{q}}{(2\pi)^3}\int_0^\infty \frac{\mathrm{d}\omega}{(2\pi)}\,\omega^2 P(\vec{q},\omega), \tag{12}$$

where n_0 is the homogeneous electron gas density.

2.2. Dielectric formalism in a 2D electron gas

Making an equivalence with the 3D case, Bret and Deutsch [7] developed the 2D response function formalism within the RPA at any finite temperature. Our procedure will be parallel to the 3D case and will restrict to the zero temperature case. Thus, if an ion of charge magnitude Z_1 travels within

the confined 2D gas with $\vec{v}$ velocity parallel to the plane, its charge density will be given by

$$\sigma(\vec{r},t) = Z_1\delta(\vec{r}-\vec{v}t), \tag{13}$$

and its Fourier transform

$$\sigma(\vec{Q},\omega) = Z_1\delta(\omega-\vec{Q}\cdot\vec{v}), \tag{14}$$

so, the induced electric field

$$\begin{aligned}\vec{E}^{\mathrm{ind}}(\vec{r},t) &= \int\frac{\mathrm{d}^2Q}{(2\pi)^2}\int\frac{\mathrm{d}\omega}{2\pi}(-\mathrm{i}\vec{q})\mathrm{e}^{\mathrm{i}(\vec{Q}\vec{r}-\omega t)}\frac{2\pi}{Q}\sigma(\vec{Q},\omega)\frac{2\pi}{Q}\chi(\vec{Q},\omega)\\ &= \frac{Z_1}{2\pi}\int\frac{\mathrm{d}Q}{Q}\int\mathrm{d}\omega(-\mathrm{i}\vec{Q})\exp\left[\mathrm{i}\left(Qy\sqrt{1-\frac{\omega^2}{Q^2v^2}}\right)\right]\chi(\vec{Q},\omega),\end{aligned} \tag{15}$$

and thus, the electric force acting on the ion

$$F = \frac{\mathrm{d}E}{\mathrm{d}x} = Z_1\vec{E}^{\mathrm{ind}}\cdot\hat{v}\Big|_{\vec{r}=\vec{v}t} = \frac{Z_1^2\mathrm{i}}{v}\int\frac{\mathrm{d}Q}{Q}\int\frac{\omega\,\mathrm{d}\omega}{\sqrt{Q^2v^2-\omega^2}}\chi(Q,\omega), \tag{16}$$

and as in the RPA the relation between the loss function and the imaginary part of polarizability is given by

$$\mathrm{Im}\left(\frac{-1}{\varepsilon(\vec{Q},\omega)}\right) = \frac{2\pi}{Q}\mathrm{Im}\,\chi(\vec{Q},\omega), \tag{17}$$

the stopping power resulted to be

$$\frac{\mathrm{d}E}{\mathrm{d}x} = \frac{Z_1^2}{2\pi v}\int_0^\infty\mathrm{d}Q\int\frac{\omega\,\mathrm{d}\omega}{\sqrt{Q^2v^2-\omega^2}}\mathrm{Im}\left(\frac{-1}{\varepsilon(\vec{Q},\omega)}\right). \tag{18}$$

2.3. From response function formalism to scattering theory

In scattering theory, the stopping power of an external impurity due to its interaction with an electron gas is understood from a different point of view. The frame of reference is set on the external ion and a flux of independent electrons with velocity $-\vec{v}$ approaches it. The electrons scatter off the effective potential created by the presence of the ion. In general, the calculation of the scattering potential is a rather complicated task, but in low-velocity conditions, screening can be considered in the static limit ($\omega\rightarrow 0$), providing an easy way to calculate the energy loss.

Although the relation between the response function formalism and the scattering theory is not obvious [37], Hu and Zaremba [13] demonstrated

that, in the low-velocity limit, linear response theory in the RPA is equivalent to calculating the scattering amplitude for the statically screened RPA potential in the Born approximation. The aim of Section 3 will be to illustrate the previous assesment.

Considering low-energy ions implies that low-energy exchanges between the projectile and the electron gas will be allowed. So, in the low-frequency limit:

$$\begin{aligned}\text{Im } \chi(\vec{q},\omega) &= \frac{\text{Im } \chi^0(\vec{q},\omega)}{\left(1+\frac{4\pi}{q^2}\text{Re } \chi^0(\vec{q},\omega)\right)^2+\left(\frac{4\pi}{q^2}\text{Im } \chi^0(\vec{q},\omega)\right)^2} \\ &= \frac{\text{Im } \chi^0(\vec{q},\omega)}{\varepsilon(\vec{q})^2}, \end{aligned} \tag{19}$$

where the limits of Re $\varepsilon(\vec{q},\omega)$ and Im $\varepsilon(\vec{q},\omega)$ are taken from Ref. [13] and $\chi^0(\vec{q},\omega)$ is the Lindhard function [2] and represents the density response function of a system of non-interacting electrons. Its imaginary part

$$\begin{aligned}\text{Im } \chi^0(\vec{r},\vec{r}',\omega) = 2\pi\sum_{\vec{k},\vec{k}'} n_k(1-n_{k'})\varphi_k^*(\vec{r})\varphi_k(\vec{r}')\varphi_{k'}(\vec{r})\varphi_{k'}^*(\vec{r}') \\ \times\,\delta(\varepsilon_{k'}-\varepsilon_k-\omega), \end{aligned} \tag{20}$$

where $\vec{k}$, $\vec{k}'$ are the initial and final state wave vectors, n_k, $n_k{}'$ are the Fermi occupation numbers which at $T = 0$ K are

$$n_k = \theta(k_\text{F} - |\vec{k}|), \tag{21}$$

and $\varphi_k(\vec{r}) = (1/\sqrt{V})\text{e}^{\text{i}\vec{k}\vec{r}}$ are the electronic wave functions.

Transforming to Fourier space, we get

$$\begin{aligned}\text{Im } \chi^0(q,\omega) &= \int \text{d}(\vec{r}-\vec{r}')\text{e}^{-\text{i}\vec{q}(\vec{r}-\vec{r}')}\,\text{Im } \chi^0(\vec{r},\vec{r}',\omega) \\ &= \int \text{d}(\vec{r}-\vec{r}')\text{e}^{-\text{i}\vec{q}(\vec{r}-\vec{r}')}2\pi\sum_{\vec{k},\vec{k}'} n_k(1-n_{k'}) \\ &\quad\times\frac{1}{V^2}\text{e}^{-\text{i}\vec{k}(\vec{r}-\vec{r}')}\text{e}^{\text{i}\vec{k}'(\vec{r}-\vec{r}')}\delta(\varepsilon_{k'}-\varepsilon_k-\omega) \\ &= \frac{2\pi}{V^2}\sum_{\vec{k},\vec{k}'} n_k(1-n_{k'})V\delta_{\vec{k}',\vec{k}+\vec{q}}\,\delta(\varepsilon_{k'}-\varepsilon_k-\omega). \end{aligned} \tag{22}$$

On the other hand, the statically screened external potential is

$$v_{\mathrm{sc}}(q) = \frac{v^{\mathrm{ext}}(q)}{\varepsilon(q)} = \frac{4\pi Z_1/q^2}{\varepsilon(q)}. \tag{23}$$

Returning to the linear expression of stopping power equation (5), introducing the low-frequency limits equations (19) and (23), and replacing the integral $\int \mathrm{d}\vec{q}/(2\pi)^3$ by the sum $(1/V)\sum_{\vec{q}}$ an expression for the stopping force is obtained:

$$F = -\frac{1}{2v^2}\frac{2\pi}{V^2}\sum_{\vec{k},\vec{k}'} n_k(1-n_{k'})\frac{1}{|\vec{k}-\vec{k}'|}v_{\mathrm{sc}}^2(|\vec{k}-\vec{k}'|) \times \int_{-|\vec{k}-\vec{k}'|v}^{|\vec{k}-\vec{k}'|v} \mathrm{d}\omega\, \omega\delta(E_{k'}-E_k-\omega). \tag{24}$$

The sum over all possible initial states with momentum $\vec{k}$ and final momentum $\vec{k}'$, where

$$\frac{k'^2}{2} = \frac{k^2}{2} + \omega$$

gives

$$\sum_{\vec{k}} n_k(1-n_k') = \frac{V}{(2\pi)^3}\int \mathrm{d}\hat{k}\int_0^\infty k^2\,\mathrm{d}k n(E_k)[1-n(E_k+\omega)]$$

$$= \frac{V}{(2\pi)^3}\int \mathrm{d}\hat{k}\int_{E_{\mathrm{F}}-\omega}^{E_{\mathrm{F}}}\sqrt{2E}\,\mathrm{d}E = \frac{V}{(2\pi)^3}\sqrt{2E_{\mathrm{F}}}\omega\int \mathrm{d}\hat{k}, \tag{25}$$

i.e., $n(E_k)[1-n(E_k+\omega)]$ acts like an ω delta function at E_{F} for small ω. And thus, the force acting over the ion is

$$F = -\frac{\sqrt{2E_{\mathrm{F}}}v}{3(2\pi)^5}\int \mathrm{d}\hat{k}\int \mathrm{d}\hat{k}'\sqrt{2E_{\mathrm{F}}}|\vec{k}-\vec{k}'|^2 v_{\mathrm{sc}}^2(|\vec{k}-\vec{k}'|)$$

$$= -\frac{4vE_{\mathrm{F}}^2}{3(2\pi)^5}\int \mathrm{d}\hat{k}\int \mathrm{d}\hat{k}'(1-\cos\theta)v_{\mathrm{sc}}^2(|\vec{k}-\vec{k}'|), \tag{26}$$

taking into account that

$$|\vec{k}-\vec{k}'| = q = 2k_{\mathrm{F}}\sin(\theta/2) = \sqrt{k^2+k'^2-2kk'\cos\theta} = k_{\mathrm{F}}\sqrt{1-\cos\theta}.$$

As in the Born approximation $f(\theta) = -(1/2\pi)v_{\mathrm{sc}}(|\vec{k}-\vec{k}'|)$ [38], a general result for the stopping force as a function of the scattering amplitude is

obtained:

$$F = \frac{-8v}{3\pi} E_F^2 \int_0^\pi d\theta \sin\theta(1 - \cos\theta)|f(\theta)|^2. \tag{27}$$

Following the expansion for a perturbative scattering potential (Born approximation) the low-frequency limit in the dielectric formulation is obtained:

$$\frac{dE}{dx} = \frac{v}{3\pi} \int_0^{2k_F} dq\, q^3 \left[v_{sc}^2(q) \frac{1}{(2\pi)^2} \right] = v \frac{4Z_1^2}{3\pi} \int_0^{2k_F} \frac{dq}{q|\varepsilon(q)|^2}. \tag{28}$$

3. DENSITY FUNCTIONAL THEORY

The central statement of DFT was proven by Hohenberg and Kohn [22] in 1964: the exact ground-state of an interacting system of electrons is expressed as a unique functional of the electronic density $n(\vec{r})$.

Kohn and Sham [23] demonstrated that the electronic density of the system can be obtained by solving N monoelectronic self-consistent Schrödinger equations

$$-\tfrac{1}{2}\nabla^2\phi(\vec{r}) + V_{eff}(\vec{r})\phi(\vec{r}) = \varepsilon_i\phi(\vec{r}), \tag{29}$$

where $V_{eff}(\vec{r})$ denotes the effective potential suffered by each electron

$$V_{eff}(\vec{r}) = V_{ext}(\vec{r}) + \int d\vec{r}' \frac{n(\vec{r}')}{|\vec{r} - \vec{r}'|} + V_{xc}[n(\vec{r})]. \tag{30}$$

Here, the first term represents the external potential, and in the case of a metallic system formed by the ions and valence electrons, represents the Coulomb potential due to positive ions. The second corresponds to the Hartree potential, which accounts for the electron–electron interaction and finally, $V_{xc}[n(\vec{r})]$ is the exchange and correlation potential.

$\phi_i(\vec{r})$ represent the one-electron states, and the electronic density of the system then is

$$n(\vec{r}) = \sum_{i \in occ.} |\phi_i(\vec{r})|^2. \tag{31}$$

The sum over occupied states includes both bound electronic states and scattering states.

The simplicity of the theory has to do with the local character of the effective potential, although the complexity of handling a many-body problem has been translated to the exact description of exchange and correlation. In practice, an approximation must be used for $V_{xc}[n(\vec{r})]$. A widely used one is the local density approximation (LDA) in which

the exchange and correlation potential is taken to be

$$V_{\mathrm{xc}}[n(\vec{r})] = \left[\frac{\mathrm{d}n\varepsilon_{\mathrm{xc}}(n)}{\mathrm{d}n} \right]_{n=n(\vec{r})}, \tag{32}$$

where $\varepsilon_{\mathrm{xc}}(n)$ is the exchange-correlation energy per particle of a homogeneous electron gas. Although, in principle, this approximation should only be valid for systems in which the electronic density varies slowly, it has given good results in many different systems, showing that DFT is a useful tool for describing the structure of solids [39,40].

3.1. Static screening

3.1.1. 3D electron gas

As stated before, in the case of a static proton in a jellium metal non-linear screening plays an important role. Almbladh *et al.* [41] and Zaremba *et al.* [42] studied the problem in a self-consistent way, using the Kohn and Sham scheme for the whole range of metallic densities. Charge neutrality requires the FSR [25] to be satisfied: if an impurity with Z_1 charge, including n_{b} bound states, is located in a 3D electron gas, a self-consistent potential will ensure that the induced charge exactly cancels the effective impurity charge, $Z = Z_1 - n_{\mathrm{b}}$. When the phase shifts do not depend on the azimuthal quantum numbers, m_{l} and m_{s}, and depend strongly on the l the orbital quantum number, the FSR is given by

$$Z = \frac{2}{\pi} \sum_{l} (2l+1)[\delta_l(E_{\mathrm{F}}) - \delta_l(0)], \tag{33}$$

and by Levinson's theorem [43]

$$n_{\mathrm{b}} = \frac{2}{\pi} \sum_{l} (2l+1)\delta_l(0), \tag{34}$$

so, the FSR relation may be written

$$Z_1 = \frac{2}{\pi} \sum_{l} (2l+1)\delta_l(E_{\mathrm{F}}). \tag{35}$$

The spherical symmetry of the problem makes easier the resolution of Schrödinger equation. The density of electrons in the system is given by

$$n(\vec{r}) = \sum_{i \in \mathrm{occ.}} |\phi_i(\vec{r})|^2 = \sum_{i \in \mathrm{occ.}} R_{il}^2(r) Y_{lm}^2(\theta, \varphi), \tag{36}$$

where $Y_{lm}(\theta, \varphi)$ is a spherical harmonic and $R_{il}(r)$ is a solution of the radial Schrödinger equation for energy E_i. As in the absence of the proton the radial solution can be written in terms of the spherical Bessel function of the first

kind, $j_l(kr)$, the total screening charge can be written as

$$\Delta n(r) = 2\sum_{b=1}^{B} |\phi_b(\vec{r})|^2 + \frac{1}{\pi^2}\sum_l (2l+1)\int_0^{k_F} \mathrm{d}k\, k^2[R_{kl}^2(kr) - j_{kl}^2(kr)]$$
$$\equiv \Delta n_b(r) + \Delta n_s(r), \tag{37}$$

where Δn_b is the screening charge due to B bound states and $\Delta n_s(r)$ represents the screening charge from scattering or continuum states.

This screening density at the proton site as a function of r_s is plotted in Fig. 1. This figure shows that (1) linear theory underestimates notoriously the charge pile-up at the proton and (2) in the limit of dilute gas the induced density becomes similar to that of the hydrogen atom.

To illustrate the range of the polarization cloud a screening length (r_0) can also be defined:

$$\frac{Z_1}{r_0} - V(r_0) = \frac{1}{e}\frac{Z_1}{r_0}. \tag{38}$$

Contrary to linear calculations, Almbladh *et al.* [41] show that the screening length and the induced potential at the proton site remain almost constant for all the metallic densities. Density functional results provide $r_0 \sim 0.6$ a.u. and $V_H(0) \sim 1.2$ a.u. values for r_s from 1 to 6, whereas linear theory predicts variations from 0.9 to 1.5 a.u. for the screening length and from 0.8 to 0.5 a.u. for the induced density at the origin.

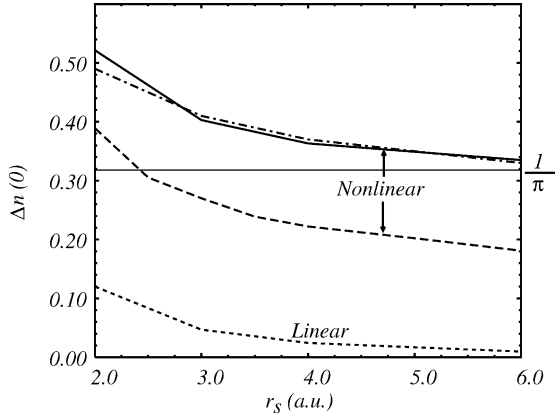

Fig. 1. Induced electron density at the proton position as a function of r_s. The non-linear results are obtained in the DFT: Hartree level calculation (long dashed line), Hartree + exchange and correlation potential (solid line [44] and dot-dashed line [41]). The linear result (short dashed line) is obtained with an RPA dielectric function. The horizontal solid line corresponds to the H atom value.

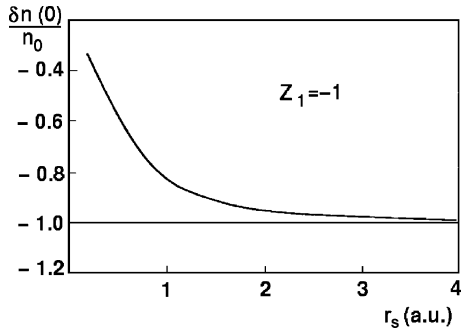

Fig. 2. Ratio of the depletion hole density $\Delta n(r)$, at the antiparticle site, to the background density n_0, as a function of the density parameter r_s.

For a negative charge, such as an antiproton, the electrons of the medium would be repelled from the neighbourhood of the impurity. The hole in the electronic density created around the antiparticle would extend to at least r_s. In Fig. 2 the ratio of the induced density at the antiproton to the background density as a function of r_s is plotted. In the low-density limit, the electron density around the antiproton is reduced by an amount equal to n_0. This calculation was done by Nagy *et al.* [45] within the density functional framework and was complemented with two subsequent papers. One uses a parametric dielectric function [46] while the other considers an explicit version of DFT, based on the Thomas–Fermi–Weizsäcker approximation [47].

3.1.2. 2D electron gas

As in 3D, in 2D linear theory has been shown not to be accurate for a realistic description of screening. However, it is worth mentioning the work done by Stern and Howard [48] to describe the screening and bound state formation by the use of analytical expressions based on Thomas–Fermi approach for the screened potential. Wang and Ma [49] described the non-linear effects using a Fermi–Thomas type potential as model potential and included the FSR to calculate a consistent screening length. In a 2D electron gas the FSR is formulated as [48]

$$Z_1 = \frac{2}{\pi} \sum_{m=-\infty}^{\infty} \eta_m(E_F). \tag{39}$$

Zaremba *et al.* [50] presented a DFT calculation in a 2D electron gas. They considered a static point charge Z_1, a distance d from the 2D electron gas

plane. The potential created by this charge in the 2D gas plane is

$$V_{\text{ext}} = \frac{-Z_1}{\sqrt{d^2 + r^2}}. \tag{40}$$

The exchange and correlation potential is defined in the LDA and it is used in the parametrization of Tanatar and Ceperley [51]. Solving self-consistently the Kohn–Sham equations (equation (29)), the electronic screening charge obtained is composed of two contributions: bound electrons and continuum electrons. The electronic wave functions expressed in this cylindrical coordinates are of the form

$$\psi_i(\vec{r}) \equiv \mathrm{e}^{im\phi} R_{nm}(r), \tag{41}$$

where m is the angular momentum quantum number and n distinguishes the different radial solutions [48].

In Fig. 3 the screening density at a proton site as a function of r_s and the spatial dependence of the screening density is presented. Solid lines represent full calculations, i.e., exchange and correlation included, and the dashed line corresponds to results from Hartree level calculations.

The induced density at the origin is practically independent of the density of the electron gas, which reflects the similar character of the screening due to bound states in the whole metallic range. As we will see in Section 3.1.3, what changes from a low value of r_s to a high one is the behavior of continuum states.

When the impurity is moved a distance d from the 2D electron gas sheet, the amplitude of the induced density decreases rapidly as d increases. If the impurity is far enough away, non-linear effects on the screening density become insignificant.

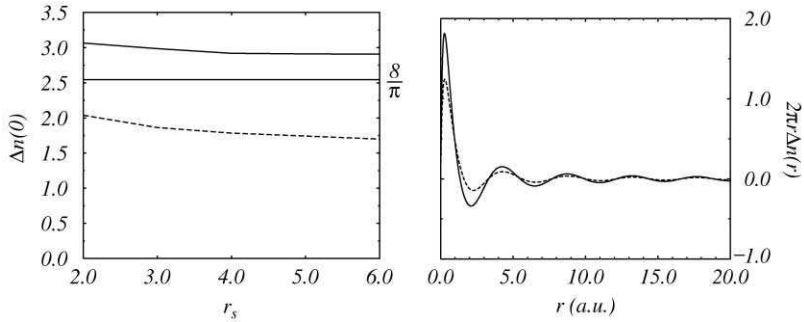

Fig. 3. On the left hand side, induced electronic density at the proton site as a function of the density parameter r_s. On the right, the spatial distribution of screening density for $r_s = 2$. Dashed line: Hartree level calculations, solid line: inclusion of exchange and correlation potential. Horizontal solid line: 2D hydrogen atom.

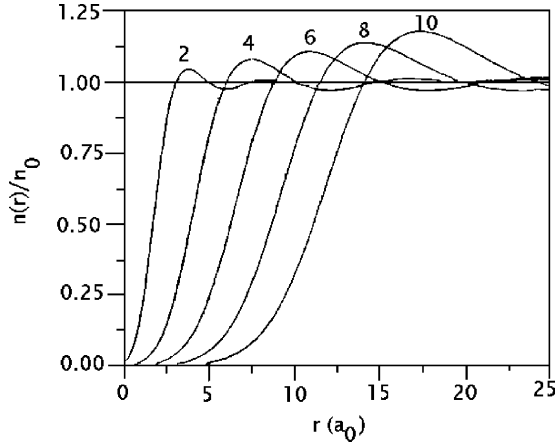

Fig. 4. Normalized density as a function of distance for an antiproton. The different curves are labelled by the r_s value.

Screening in the case of an antiproton in 2DEG is quite similar to that in the 3D case. As can be seen in Fig. 4 the antiproton is surrounded by a deficiency of electronic density, or a hole. The radius of that hole is equal to r_s as was the case for 3D electron gas. When comparing antiproton screening with that of a proton, Zaremba *et al.* [50] showed that for a large value of r_s and at large distances, the screening cloud surrounding both particles are equal.

3.1.3. Bound states and scattering states

The contribution to the screening density by bound and scattering electrons is of great relevance to the nature of screening. One of the most important results regarding this section is that in a 2D electron gas, bound states exist for all values of the density parameter, whereas in a 3D electron gas, a minimum value of r_s is needed to bind electron states.

3D electron gas. As explained in Section 3.1.1, the value of r_s at which a bound state appears for a static proton in this formalism, was found to be ~ 2. For larger values of r_s, the bound state has increasing importance to the screening charge density at the position of the proton. It can be clearly seen in Fig. 5. The dominant role of bound states at low densities is accompanied by the fact that the value of the bound state energy increases with r_s, making the bound state more stable. The spatial distribution of bound and scattering electrons is of notably distinct nature. Contrary to the local character of bound states, the screening charge of continuum states oscillate about a mean value below zero, showing long-range Friedel oscillations.

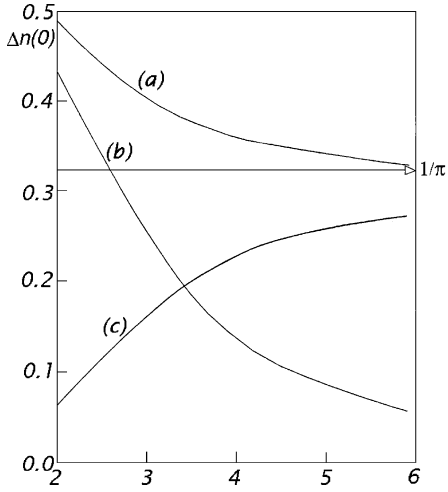

Fig. 5. Induced electron density at the proton position, obtained in the DFT, as a function of r_s. The bound (c) and scattering (b) parts of the total density (a) are shown separately. From Ref. [52].

2D electron gas. In the 2D case, the local and non-local characters of bound and continuum states can also be considered. As can be seen in Fig. 6, the bound screening density is partially compensated in the close neighbourhood of the impurity by that due to the continuum electrons.

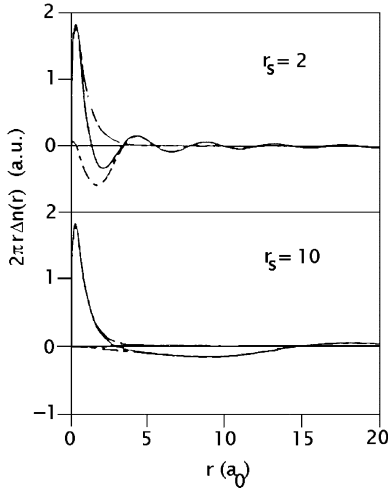

Fig. 6. Screening density as a function of position for two r_s values. The dashed curve shows the bound state contribution, the chain curve, the continuum state contribution and the solid curve, the total.

However, the nature of the bound state distribution is very similar despite the very different background densities ($r_s = 2$ and $r_s = 10$), while the continuum state distribution varies significantly. If these two contributions are integrated over all space, the bound state contributes two electrons whereas the continuum states must themselves support a total charge of $+1$, since the FSR must be satisfied. The extension of the scattering state is directly related with the r_s value, i.e., the $Z = 1$ impurity can be interpreted as H^- ion surrounded by a positive charge density of $r \sim r_s$ extension.

3.2. Dynamic screening

3.2.1. 3D electron gas

When an ion moves in an electron gas the potential and the charge distribution induced will be asymmetric in the axis of movement. If the speed is sufficiently high to generate collective excitations, a trailing wake potential will be created and linear response theory would be adequate to describe the dynamic screening involved [53]. Within the DFT various approximations have been considered to describe the scattering potential for a slow ion. Bönig and Schönhammer [54,55] used a hard sphere potential to evaluate exactly the scattering phase shifts. Zaremba *et al.* [33] considered that the electrons of the metal occupy a shifted Fermi sphere which leads to an asymmetry of the screening charge density and scattering potential along the line of motion of the projectile. To obtain an approximate self-consistent solution of this dynamic screening problem, they used the spherically averaged density to define an averaged scattering potential (spherical potential approximation). In a subsequent paper Salin *et al.* [34] developed the shifted Fermi sphere approach to take into account the full cylindrical symmetry of the system. They could solve the radial coupled Schrödinger equations and obtain the induced density due to continuum and bound states. In Fig. 7 the comparison of the induced density with the static calculation is exhibited. In both cases, proton (left image) and antiproton (right image), the forward–backward asymmetry is revealed when comparing with the static case. The asymmetry in this calculation has two sources: the asymmetrical self-consistent potential and the summation over the states on the shifted Fermi sphere.

The dynamic approach allows an investigation on the velocity-dependence of the Kohn–Sham bound state energy. It is found that the faster the ion travels in the electron gas, the more bound the electron is. A detailed investigation must address the question of comparing capture-loss rates, i.e. processes, which are not included in the adiabatic (laminar flow) picture. This may be an interesting field for future investigations.

Similarly, motivated by the increasing interest in the physics of 2D systems, calculations for finite ion velocities would be desirable and useful.

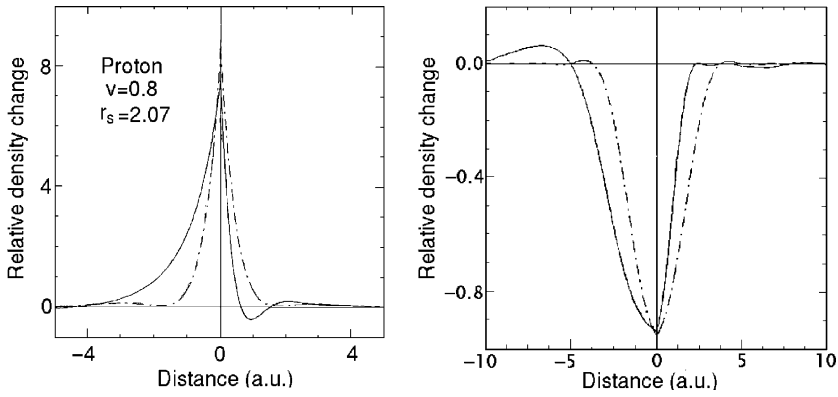

Fig. 7. Screening charge density for proton (left hand side) and an antiproton (right hand side) plotted in the direction of movement. The velocity $v = 0.8$ a.u. and the density parameter $r_s = 2.07$. The full DFT calculations (full line) are compared with the static case (dashed-dotted line).

3.3. Stopping at low ion velocities

3.3.1. 3D electron gas

For a slow ion with velocity v smaller than the Fermi velocity the stopping power can be formulated in terms of the scattering phase shifts at the Fermi energy. These are calculated by solving the radial part of Schrödinger equation for a statically screened spherically symmetric potential and must fulfill the FSR.

In Section 2.3, we deduced a general formula for the stopping force acting on the impurity as a function of scattering amplitude. Taking up again equation (27) and applying it to the case of a strong potential, such as a slowly moving ion:

$$f(\theta) = \frac{1}{k} \sum_l (2l+1) \mathrm{e}^{\mathrm{i}\delta_l} \sin \delta_l P_l(\cos \theta), \tag{42}$$

so that

$$\int_0^\pi \mathrm{d}\theta \sin\theta (1 - \cos\theta)(f(\theta))^2 = \frac{2}{k_\mathrm{F}^2} \sum_{l=0}^{\infty} (l+1) \sin^2(\delta_l(E_\mathrm{F}) - \delta_{l+1}(E_\mathrm{F})), \tag{43}$$

and thus, the stopping power

$$S = \frac{8E_\mathrm{F}v}{3\pi} \sum_l (l+1) \sin^2(\delta_l(E_\mathrm{F}) - \delta_{l+1}(E_\mathrm{F})). \tag{44}$$

If we define the transport cross-section as

$$\sigma_{\mathrm{tr}}(E_{\mathrm{F}}) = \frac{4\pi}{k_{\mathrm{F}}^2} \sum_l (l+1)\sin^2(\delta_l(E_{\mathrm{F}}) - \delta_{l+1}(E_{\mathrm{F}})), \tag{45}$$

the well-known stopping power expression in scattering theory is obtained

$$S = n_0 v v_{\mathrm{F}} \sigma_{\mathrm{tr}}(E_{\mathrm{F}}), \tag{46}$$

where

$$n_0 = \frac{3}{4\pi r_{\mathrm{s}}^3}, \tag{47}$$

and

$$v_{\mathrm{F}} = (3\pi^2 n_0)^{1/3}. \tag{48}$$

This result was applied by Echenique, Nieminen and Ritchie (ENR) [56] to calculate the stopping power of H^+ and He^+ ions in a 3D electron gas.

In the work of ENR self-consistent DFT was used to obtain the scattering phase shifts. A comparison of both calculations together with the ones from linear response can be seen in Fig. 8. They found significant differences in the low-density region while convergence of linear and non-linear theories is achieved when $r_{\mathrm{s}} \to 0$. The formation of bound states (for $r_{\mathrm{s}} > 1.9$ in the case of a H^+ as estimated by Zaremba *et al.* [42] and Almbladh *et al.* [41]), explains the fast decay of energy loss values compared with those of linear theory, since those bounded electrons screen out the ion in electron gas. The crossing of the curves for H^+ and He^+ is explained, in the original paper, by means of atomic scattering cross-sections for zero-energy electrons on the respective atoms.

Mann and Brandt [57] did a systematic study of proton stopping power in 20 different materials using the ENR theory. A much better agreement with experiment than the one provided by linear theory was obtained.

In the case of a slow antiproton in a 3D electron gas, Nagy *et al.* [45] calculated the stopping power using DFT to compute the scattering potential. In Fig. 9 the friction coefficient as a function of the density parameter is plotted. The values for the proton and antiproton converge in the high-density limit, in which linear theory is valid and the result must not depend on the charge sign. For higher values of r_{s} the stopping of the proton is twice that of the antiproton, as can be seen in the inset of the figure. In a later work, Krakovsky and Percus [58] compared their results of stopping for antiprotons, based on Sjölander and Stott (SS) non-linearly screened scattering potential, with those of Nagy *et al.* and found that both results have 3% agreement.

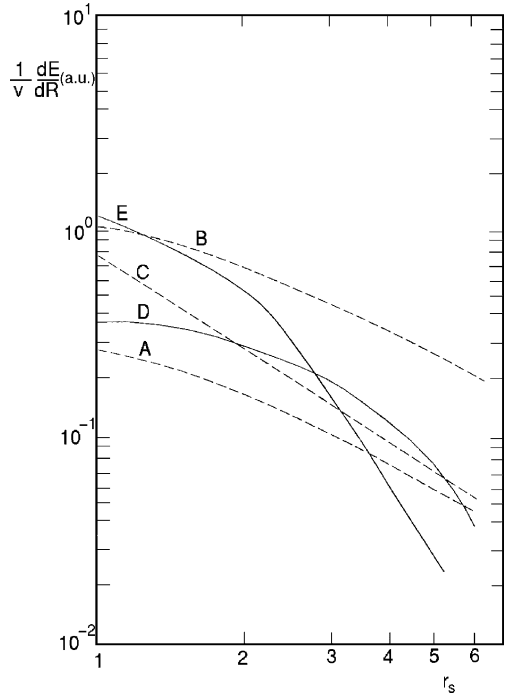

Fig. 8. Low-velocity stopping power as a function of r_s. Curves A and B are calculated in linear-response theory for $Z_1 = 1$ and 2, respectively. Curve C is from Ref. [26] for a slow, singly ionized He atom. Curves D and E are the density functional results for a proton and a helium nucleus, respectively.

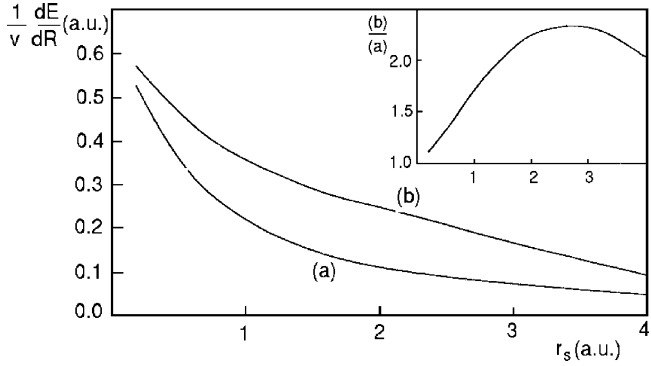

Fig. 9. Stopping power of a homogeneous electron gas for slow antiprotons (curve a) and protons (curve b) as a function of the density parameter r_s. Both results are obtained with the same density functional description. The curve in the inset shows the ratio (b)/(a) as a function of r_s.

3.3.2. 2D electron gas

The problem of stopping in 2D electron gases is not only of academic interest. It could have some applicability in systems such as semiconductor heterostructures, the surface of liquid helium or in electrons in image states on metal surfaces. As in the 3D case, for a slow ion with velocity v smaller than the Fermi velocity v_F of the 2D electron gas, the stopping power of the ion is due to the scattering at the Fermi surface expressed as a function of scattering phase shifts. The stopping power has a similar [54,59] expression as in the 3D case

$$S = n_0 v v_F \sigma_{tr}(E_F), \tag{49}$$

but now

$$n_0 = \frac{1}{(\pi r_s)^{1/2}} \tag{50}$$

$$v_F = (2\pi n_0)^{1/2}, \tag{51}$$

and

$$\sigma_{tr}(E_F) = \frac{4}{v_F} \sum_{m=0}^{\infty} \sin^2[\delta_m(E_F) - \delta_{m+1}(E_F)]. \tag{52}$$

The behavior of the stopping power in a 2D electron gas is qualitatively similar to the situation in 3D. As can be seen in Fig. 10, the DFT results (full line, including V_{xc} and dashed-line without V_{xc}) approach the linear one

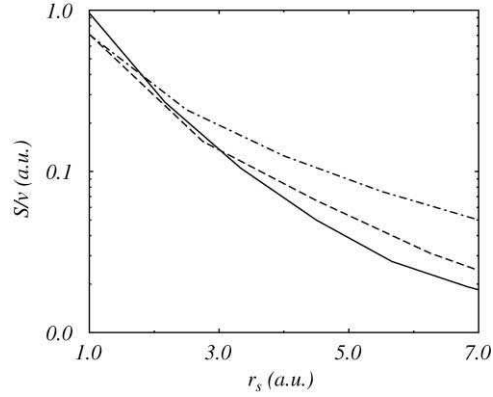

Fig. 10. Stopping power as a function of density parameter r_s for $Z = 1$. The solid curve presents the full non-linear calculation, including exchange and correlation, while the dashed curve shows the result in the Hartree approximation. The dot-dashed curve corresponds to linear screening taken from Ref. [49].

(dash-dotted line) in the high-density limit. Besides, the full non-linear calculation is larger than the linear one at high densities while the opposite occurs in the low-density region, as was the case in the 3D situation.

Non-linear stopping of antiprotons in a 2DEG has also been calculated by several groups, introducing the non-linearity in diverse ways. Wang and Ma [49] used a model potential (linearized Thomas–Fermi potential) as scattering potential and calculate the stopping consistently. Krakovsky and Percus [58] used, as in the 3D case, the non-linear effective potential deduced from SS theory. The Z_1^3 term or Barkas term of stopping power was calculated by Bergara *et al.* [60] using dynamical quadratic response function and fully self-consistent DFT calculation was done by Zaremba *et al.* [50].

3.3.3. Z_1 oscillations

For positive ions heavier than the proton ($Z_1 > 1$), an effective charge can be defined in an operational manner:

$$Z_1^* = \left(\frac{(\mathrm{d}E/\mathrm{d}x)_{Z=Z_1}}{(\mathrm{d}E/\mathrm{d}x)_{Z=1}} \right)^{1/2}. \tag{53}$$

In Fig. 11 we show the effective charge for several incident bare ions and for three electron-gas densities. The Z_1 oscillations appear naturally since they are related to the appearance of new bound states which are taken into account in a natural way in our self-consistent calculation. A qualitative understanding of the main features of the oscillation can easily be achieved in terms of scattering theory and resonance levels in solids, since the problem is analogous to the residual resistivity due to nonmagnetic impurities in solids. For small charges, doubly occupied bound states are found in the density functional calculation. For $Z_1 = 5-8$ the 2p electrons form an unbound, resonant state in the conduction band. That this will produce a maximum in the scattering cross-section can be easily understood by taking into account the resonant phase shifts, approximating them from the FSR as

$$\delta_1 \cong \frac{\pi(Z_1 - 4)}{6}. \tag{54}$$

This will predict a maximum in the stopping power when $\delta_1 = \pi/2$ thus at $Z_1 = 7$. Similar arguments explain qualitatively the oscillating structure of the curves as maxima due to 3p, 3d and 4p resonances, while minima are related to the formation of closed shells. For a dilute electron gas the screening cloud approaches the free-atom electron structure, and the minima appear at the formation of closed atomic shells as the screening increases due

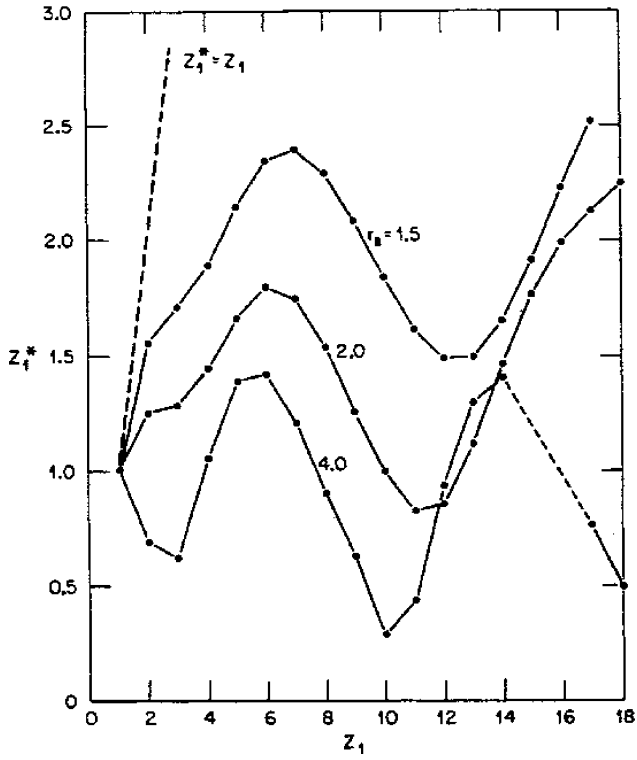

Fig. 11. Effective charge Z_1^* as a function of Z_1 for $r_s = 1.5$, 2 and 4.

to increasing electronic density. This minimum shifts to higher ionic charges since a stronger ionic potential is necessary to compensate the electronic screening and so have the strength to bind an extra electron. This is clearly shown in the graph as displacement of the minimum from the atomic value ($Z_1 = 10$) as the electron density increases (r_s decreases). For very small r_s no bound states are formed and linear-response theory should be valid, and Z_1^* approaches Z_1. Comparison of experimental data with the theoretical predictions for stopping power of carbon, aluminum and silicon can be found in the literature [62–64]. In Fig. 12 we show the comparison between experimental data and theory on the energy loss of 'best channeled' ions in the $\langle 110 \rangle$ axial channel in Si. The electron density in a channel increases from a small value along the axis to values an order of magnitude larger near the string of atoms defining the channel. In the figure, the overall trend is closely reproduced by the theoretical calculation. More recently, Winter *et al.* [65,66] have studied the energy loss of ions in the density profile of the electron selvage in front of a metal surface.

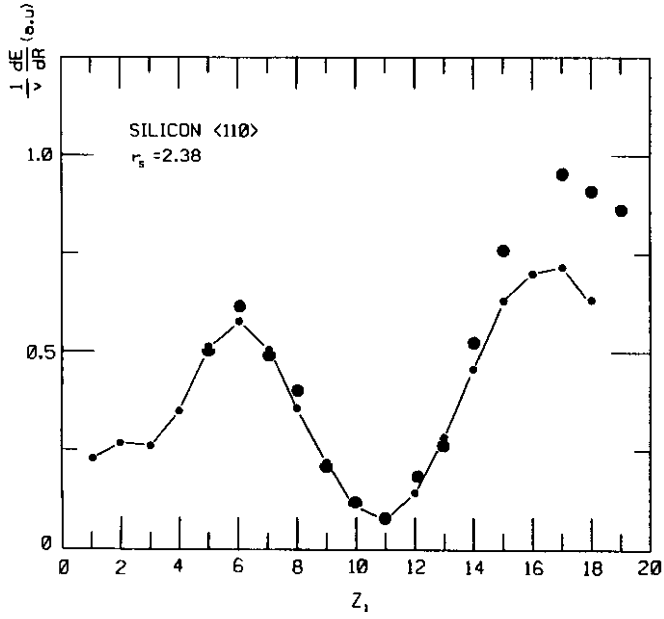

Fig. 12. Stopping power for 'well-channeled' ions in the 110 axial channel of silicon as a function of Z_1. The chained curve gives the theoretical prediction for $r_s = 2.38$. The experimental points are from Ref. [61].

3.3.4. Quadratic response function

Perturbation theory up to linear order gives satisfactory results in the prediction of the stopping power of swift particles. But at lower velocities, as Barkas [67] pointed out with his experiments, the description of stopping power needs higher terms in the Z_1 expansion in order to explain the charge sign dependence. A few years ago, complete many-body perturbative calculations of Z_1^3 correction in the RPA for an electron gas were provided [15,16,68].

Figure 13 shows the comparison between density functional and second-order perturbative calculations as a function of the density parameter. In the high-density limit, the Z_1^3 calculation for a proton coincides with DFT proton stopping and antiproton stopping values multiplied by -1 as was expected, since the ion potential is a small perturbation compared to the kinetic energy of electrons. As r_s increases, the potential energy becomes more important relatively and a separation between DFT and Z_1^3 calculations occur. On the other hand, as the perturbative method does not account for the bound states, the Z_1^3 result is farther from that for the proton than from the antiproton one.

Analogously, one can calculate the next term in the Z_1 expansion of the potential for a particle travelling parallel to a 2D electron gas with a fixed

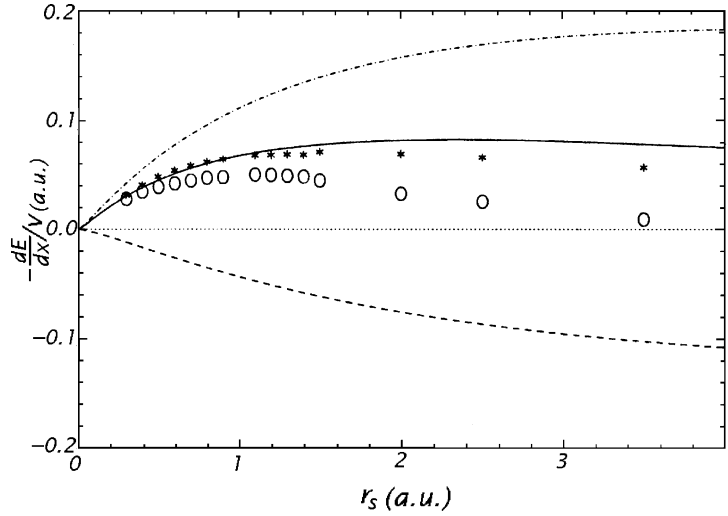

Fig. 13. Friction coefficient as a function of the density parameter. Solid curve corresponds to quadratic response calculation, the dashed and dashed-dotted curves are contributions due to f_1^L and f_2^L to the solid curve explained in Ref. [16]; stars represent a fully self-consistent DFT calculation for an antiproton multiplied by -1 and circles are DFT calculations for a proton.

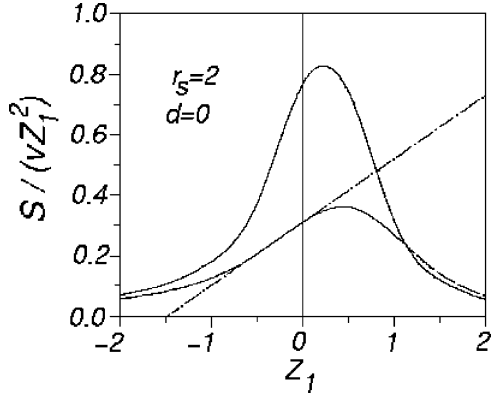

Fig. 14. Normalized stopping power as a function of the projectile charge Z_1, for $r_s = 2$ and $d = 0$. The solid curve is obtained from the non-linear screening result including exchange-correlation; the dashed curve shows the corresponding result in the Hartree approximation (no exchange-correlation); the straight chain curve is the quadratic response result [60].

distance of d from it. The linear contribution to the stopping power was calculated by Horing *et al.* [6] and the first non-linear term was obtained in a paper by Bergara *et al.* [60].

In Fig. 14, we show the stopping power of an impurity moving on a 2D electron gas ($d = 0$) as a function of projectile charge for quadratic response correction [60] (dot-dashed line) and self-consistent DFT calculation with (solid line) and without (dashed line) the inclusion of exchange and correlation term [50] in the effective potential. What one can easily deduce is that the range of validity of quadratic response agrees with what one can expect, since it is valid for small values of Z_1, even though it is somewhat better for small negative charges than for positive ones.

4. FINAL REMARKS AND CONCLUSIONS

In summary, in this review we have shown the main results on static and low-energy ion screening and stopping power due to the interaction with 3D and 2D electron gases. A proof of the equivalence between scattering theory and response function formalism in the low-energy limit is also included in this part.

The second and principal part of the review focuses on the DFT calculations that different groups have done. The detailed study of the screening in the static case settles the basis for the more complex treatment of finite velocity ions. The distinct character of bound and scattering states or the consequences of going from a 3D system to a 2D one are key features of the dynamic screening and of the stopping power of slow ions. A comparison between DFT and the quadratic response approach for positive and negative probe charges and the oscillatory behavior of the magnitudes related to stopping with the particle charge for heavier ions are also reviewed and updated.

ACKNOWLEDGEMENTS

We wish to thank A. Arnau, A. Bergara, I. Campillo, R. Díez Muiño, J. I. Juaristi, I. Nagy, M. Peñalba, J. M. Pitarke, V. H. Ponce and A. Salin. A. S. and P. M. E. acknowledge the financial support by Eusko Jaurlaritza, Max Planck Research Award, Spanish MCYT under Contract No. BFM2001-0076 and Basque Departamento de Educación, Universidades e Investigación, the University of the Basque Country UPV/EHU (Grant No. 9/UPV 00206.215-13639/2001).

REFERENCES

[1] T. Ando, A. B. Fowler and F. Stern, *Rev. Mod. Phys.*, 1982, **54**, 437.
[2] J. Lindhard, *Kgl. Dan. Videns. K. Selsk. Mat. Fys. Medd.*, 1954, **28**, 8.
[3] D. Bohm and D. Pines, *Phys. Rev.*, 1953, **92**, 609.
[4] F. Stern, *Phys. Rev. Lett.*, 1967, **18**, 546.
[5] A. A. Grinberg and S. Luryi, *Phys. Rev. B*, 1987, **36**, 7638.
[6] N. J. M. Horing, H. C. Tso and G. Gumbs, *Phys. Rev. B*, 1987, **36**, 1588.
[7] A. Bret and C. Deutsch, *Phys. Rev. E*, 1993, **48**, 2994.
[8] Y.-N. Wang and T.-C. Ma, *Phys. Lett. A*, 1995, **200**, 319.
[9] A. Bergara, I. Nagy and P. M. Echenique, *Phys. Rev. B*, 1997, **55**, 12864.
[10] C. Ashley, R. H. Ritchie and W. Brandt, *Phys. Rev. B*, 1972, **5**, 2393.
[11] J. D. Jackson and R. L. McCarthy, *Phys. Rev. B*, 1972, **6**, 4131.
[12] C. C. Sung and R. H. Ritchie, *Phys. Rev. A*, 1983, **28**, 674.
[13] C. D. Hu and E. Zaremba, *Phys. Rev. B*, 1988, **37**, 9268.
[14] H. Esbensen and P. Sigmund, *Ann. Phys., NY*, 1990, **201**, 152.
[15] J. M. Pitarke, R. H. Ritchie and P. M. Echenique, *Nucl. Instrum. Methods Phys. Res. B*, 1993, **79**, 209.
[16] J. M. Pitarke, R. H. Ritchie and P. M. Echenique, *Phys. Rev. B*, 1995, **52**, 13883.
[17] D. Arbó, M. S. Gravielle and J. E. Miraglia, *Phys. Rev. A*, 2001, **64**, 022902.
[18] A. Arnau and E. Zaremba, *Nucl. Instrum. Methods Phys. Res. B*, 1994, **90**, 32.
[19] J. J. Dorado, O. H. Crawford and F. Flores, *Nucl. Instrum. Methods Phys. Res. B*, 1994, **93**, 175.
[20] J. J. Dorado, O. H. Crawford and F. Flores, *Nucl. Instrum. Methods Phys. Res. B*, 1995, **95**, 144.
[21] C. F. Weizsäcker, *Z. Phys.*, 1935, **96**, 431.
[22] P. Hohenberg and W. Kohn, *Phys. Rev.*, 1964, **136**, B864.
[23] W. Kohn and L. J. Sham, *Phys. Rev.*, 1965, **140**, A1133.
[24] Z. D. Popovic and M. J. Stott, *Phys. Rev. Lett.*, 1974, **33**, 1164.
[25] J. Friedel, *Phil. Mag.*, 1952, **43**, 153.
[26] T. L. Ferrell and R. H. Ritchie, *Phys. Rev. B*, 1977, **16**, 115.
[27] P. F. Meier, *Helv. Phys. Acta*, 1975, **48**, 227.
[28] A. Cherubini and A. Ventura, *Lett. Nuovo Cimento*, 1985, **44**, 503.
[29] B. Apagyi and I. Nagy, *J. Phys. C*, 1985, **20**, 1465.
[30] B. Apagyi and I. Nagy, *J. Phys. C*, 1988, **21**, 3845.
[31] A. F. Lifschitz and N. R. Arista, *Phys. Rev. A*, 1998, **57**, 200.
[32] N. R. Arista and A. F. Lifschitz, *Phys. Rev. A*, 1999, **59**, 2719.
[33] E. Zaremba, A. Arnau and P. M. Echenique, *Nucl. Instrum. Methods B*, 1995, **96**, 619.
[34] A. Salin, A. Arnau, P. M. Echenique and E. Zaremba, *Phys. Rev. B*, 1999, **59**, 2537.
[35] D. Pines, *Elementary Excitations in Solids*, Addison-Wesley, New York, 1963.
[36] P. M. Echenique, F. Flores and R. H. Ritchie, *Solid State Physics*, 1990, **43**, 229.
[37] P. Sigmund, *Phys. Rev A*, 1982, **26**, 2497.
[38] L. I. Schiff, *Quantum Mechanics*, 3rd edn, McGraw-Hill, New York, 1985.
[39] O. Gunnarson and B. I. Lundqvist, *Phys. Rev. B*, 1976, **13**, 4274.
[40] M. Nekovee and J. M. Pitarke, *Comput. Phys. Commun.*, 2001, **137**, 123.
[41] C. O. Almbladh, U. Barth, Z. D. Popovic and M. J. Stott, *Phys. Rev. B*, 1976, **14**, 2250.
[42] E. Zaremba, L. M. Sander, H. B. Shore and J. H. Rose, *J. Phys. F*, 1977, **7**, 1763.
[43] N. Levinson, *Kgl. Dan. Videns. K. Selsk. Mat. Fys. Medd.*, 1949, **25** (9).
[44] P. M. Echenique, I. Nagy and A. Arnau, *Int. J. Quantum Chem.*, 1989, **23**, 521.
[45] I. Nagy, A. Arnau, P. M. Echenique and E. Zaremba, *Phys. Rev. B*, 1989, **40**, 11983.
[46] I. Nagy, B. Apagyi and K. Ladányi, *Phys. Rev. A*, 1990, **42**, 1806.
[47] K. Ladányi, I. Nagy and B. Apagyi, *Phys. Rev. A*, 1992, **45**, 2989.

[48] F. Stern and W. E. Howard, *Phys. Rev.*, 1967, **163**, 816.
[49] Y.-N. Wang and T.-C. Ma, *Phys. Rev. A*, 1997, **55**, 2087.
[50] E. Zaremba, I. Nagy and P. M. Echenique, *Phys. Rev. Lett.*, 2003, **90**, 046801.
[51] B. Tanatar and D. M. Ceperley, *Phys. Rev. B*, 1989, **39**, 5005.
[52] N. Barberan and P. M. Echenique, *J. Phys. B*, 1986, **19**, L81.
[53] A. Mazarro, P. M. Echenique and R. H. Ritchie, *Phys. Rev. B*, 1983, **27**, 4117.
[54] L. Bönig and K. Schönhammer, *Phys. Rev. B*, 1989, **39**, 7413.
[55] W. Zwerger, L. Bönig and K. Schönhammer, *Phys. Rev. B*, 1991, **43**, 6434.
[56] P. M. Echenique, R. M. Nieminen and R. H. Ritchie, *Solid State Commun.*, 1981, **37**, 779.
[57] A. Mann and W. Brandt, *Phys. Rev. B*, 1981, **24**, 4999.
[58] A. Krakovsky and J. Percus, *Phys. Rev. B*, 1995, **52**, R2305.
[59] I. Nagy, *Phys. Rev. B*, 1995, **51**, 77.
[60] A. Bergara, J. M. Pitarke and P. M. Echenique, *Phys. Rev. B*, 1999, **59**, 10145.
[61] F. H. Eisen, *Can. J. Phys.*, 1968, **46**, 561.
[62] J. C. Ashley, R. H. Ritchie, P. M. Echenique and R. M. Nieminen, *Nucl. Instrum. Methods B*, 1986, **15**, 11.
[63] P. M. Echenique, R. M. Nieminen, J. C. Ashley and R. H. Ritchie, *Phys. Rev. A*, 1986, **33**, 897.
[64] P. M. Echenique, *Nucl. Instrum. Methods B*, 1987, **27**, 256.
[65] H. Winter, C. Auth, A. Mertens, A. Kirste and M. J. Steiner, *Europhys. Lett.*, 1998, **41**, 437.
[66] H. Winter, J. I. Juaristi, I. Nagy, A. Arnav and P. M. Echenique, *Phys. Rev. B*, 2003, **67**, 245401.
[67] W. H. Barkas, N. J. Dyer and H. H. Heckman, *Phys. Rev. Lett.*, 1963, **11**, 26.
[68] J. M. Pitarke, R. H. Ritchie and P. M. Echenique, *Europhys. Lett.*, 1993, **24**, 613.

Friction Force for Charged Particles at Large Distances from Metal Surfaces

K. Tőkési,[1,2] X.-M. Tong,[3] C. Lemell[2] and J. Burgdörfer[2]

[1] *Institute of Nuclear Research of the Hungarian Academy of Sciences (ATOMKI), P. O. Box 51, H-4001 Debrecen, Hungary*
[2] *Institute for Theoretical Physics, Vienna University of Technology, Wiedner Hauptstr. 8-10, A-1040 Vienna, Austria*
[3] *Department of Physics, Kansas State University, Manhattan, KS 66506-2601, USA*

Abstract

We present a theoretical study of the dissipative component of the force acting on a highly charged ion moving in front of a solid surface at large distances. The friction force (stopping power) of the surface is analyzed employing both the specular-reflection model and time-dependent density functional theory (TDDFT). Contributions from particle–hole and plasmon excitations are discussed. A simple method to include corrections due to the finite width of the plasmon resonance at large wavelength into the TDDFT description of stopping power is suggested.

Contents

1. INTRODUCTION

The study of multiply charged ion–solid interactions is of considerable technological importance for the understanding of material damage, surface modification, and plasma–wall interactions. The recent availability of

ADVANCES IN QUANTUM CHEMISTRY, VOLUME 46
ISSN: 0065-3276 DOI 10.1016/S0065-3276(04)46002-X

sources for slow highly charged ions (HCI), namely electron cyclotron resonance (ECR) and electron beam ion sources (EBIS) has led to a flurry of research activities, both experimental and theoretical, in the field of HCI–solid interactions [1–7]. On the most fundamental level, its importance is derived from the complex many-body response of surface electrons to the strong Coulomb perturbation characterized by a large Sommerfeld parameter $\eta_S = Z/v \gg 1$ (Z is the charge and v the velocity of the incident HCI).

From numerous experimental as well as theoretical studies the following scenario of the HCI–surface interaction has emerged: when an HCI approaches a solid surface, one or more electrons are resonantly captured at large distances (d_c) into high Rydberg states of the projectile. As a result, so-called hollow atoms (ions) are formed where the atomic charge cloud transiently resides in shells with large diameters while the core is virtually empty [8–17]. Direct observation of this short-lived state is complicated by the fact that the ion is always attracted towards the surface by its self-image potential. Consequently it will suffer close collisions upon impact on the surface and the memory of the hollow atom is all but erased. This problem has motivated the study of interactions of HCIs with internal surfaces of microcapillaries and nanocapillaries as an alternative technique to study the above surface processes [18–22]. Metal and insulating capillaries have become available at the NEC Laboratory at Yokohama [23,24], Japan and at the Hahn-Meitner-Institut Berlin, Germany [25,26]. The use of capillary targets allows the extraction of hollow atoms in vacuum. Observation of photons or Auger electrons emitted from them in flight becomes possible. Ions traveling approximately parallel to the capillary axis (Fig. 1a) will be attracted by image forces toward the cylindrically shaped internal wall of the capillary [27–32]. When the distance of the ion to the wall reaches a critical value $|\rho_0 - \rho| \leq |\rho_0 - \rho_c| = d_c$, resonant charge transfer according to the classical over-the-barrier (COB) model can take place [3,4]. Trajectories of type 2 (Fig. 1a) will undergo close collisions with the surface as discussed above leading to (almost) complete relaxation to the neutral ground state and the loss of memory on the original charge and excitation state. Trajectories of type 3 will undergo only large-distance 'above surface' collisions near the exit edge of the capillary and form hollow atoms/ions due to the electron capture from the surface. These ions can escape prior to hitting the wall and, hence, preserve the memory of the above surface hollow atom formation.

In this contribution we focus on the third class of trajectories that will exit without experiencing charge transfer (trajectories of type 1 in Fig. 1a) and presents the dominant fraction of projectiles. The point of departure of the following analysis is the fact that these ions cruise over a large distance ≥ 1 μm parallel to the surface in its close proximity ($\lesssim 100$ nm). They may provide a sensitive probe of energy loss at microscopically large distances. Heavy particles as opposed to electrons feature well-defined classical

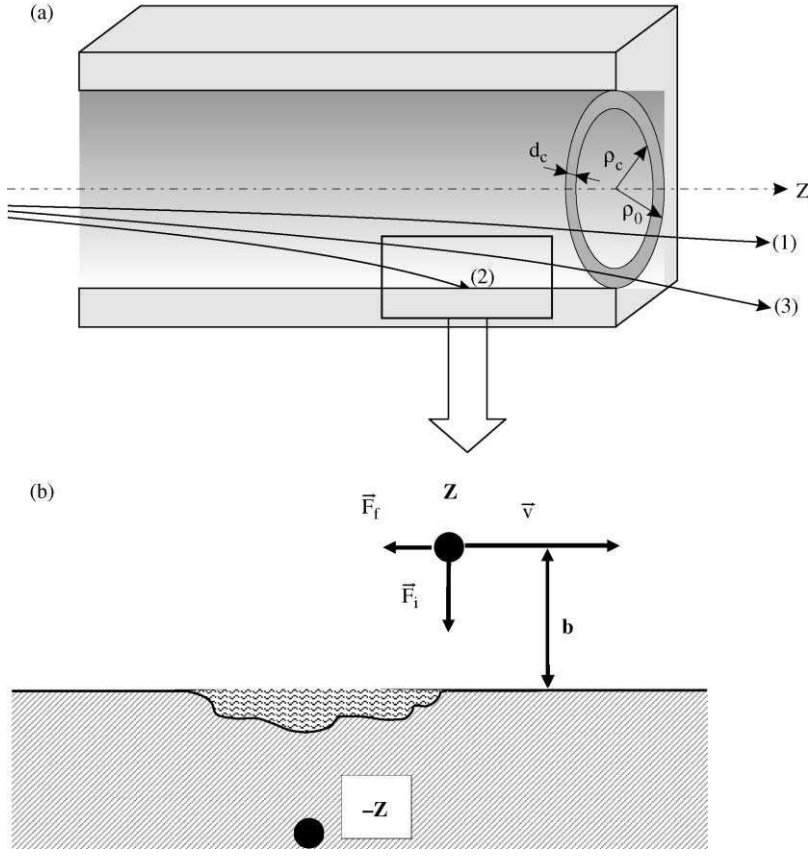

Fig. 1. (a) Sketch of a microcapillary or nanotube with typical ion trajectories. ρ_c is the critical capture radius and d_c is the critical capture distance. (b) Illustration of image ($\vec{F}_i$) and friction force ($\vec{F}_f$) at a distance b from the surface of the projectile moving with velocity $\vec{v}$ parallel to the metal surface.

trajectories that allow the determination of the local distance-dependent dielectric response of the surface.

When charged particles are placed in front of the metal surface, electrons in the surface and the bulk will be polarized and build up an induced charge density. This induced charge density can be visualized as image charge of opposite sign (Fig. 1b). Therefore, the interaction between the charged particle and its image charge is attractive and the particle will be accelerated towards the surface. Due to the image force, ($\vec{F}_i$ in Fig. 1b), charged particles will eventually always undergo close collisions with the surface even if the initial component of the velocity normal to the surface $v_\perp$ was zero. When a charged particle is moving with finite parallel velocity $v_\parallel$ the induced charge

density will lag behind the ion leading to an additional force in the direction opposite to that of the ion velocity ($\vec{F}_{\mathrm{f}}$ in Fig. 1b). This force represents the so-called friction force or stopping power, $S = -\mathrm{d}E/\mathrm{d}x$. Friction or dissipative forces can thus be visualized in terms of the lateral displacement of the response charge in the direction $-\hat{v}$. In turn, the latter can be associated with microscopic energy-dissipative processes, the creation of electron–hole pairs and collective excitations, i.e., surface and bulk plasmons. Energy loss and stopping power near surfaces poses several interesting problems, among them the separation of surface from bulk effects [33–42].

One of the first pioneering treatments of friction forces near surfaces invoked the specular reflection model (SRM) [43–45]. In many applications of ion–surface scattering this simplified classical dielectric response picture has proven to be a very powerful tool. Within the SRM the dielectric response is described by the bulk dielectric function (ε_{b}) below the surface, while above the surface ε is assumed to be given by its vacuum value 1. The presence of the surface is thus represented by a discontinuous ε. The key point of the SRM is that the induced charge density is highly localized on the surface represented by a δ-shaped charge density on the interface. This assumption may lead to the correct representation for the long-range image potential but fails to account the realistic potential distribution in the vicinity of the surface due to the crude description of the induced charge density. Meanwhile, linear-response calculations based on time dependent density functional theory (TDDFT) [46–50] have been performed for the stopping power in the bulk [51–52] and, more recently, near jellium surfaces [53,54]. Cazalilla and Garcia de Abajo [55] have shown that at low velocities and in the vicinity of the surface the stopping power data are significantly larger calculated within the framework of TDDFT than SRM. So far, an investigation of the stopping power at large distances within the framework of TDDFT is not available.

In this chapter we provide a comparative analysis of the friction force for charged particles within the framework of SRM and TDDFT with the emphasis on large distances from the surface. We will treat the problem in TDDFT at the level of the local-density approximation (LDA) and the random phase approximation (RPA). The contributions of particle–hole and plasmon excitations are considered separately. Moreover, we will suggest an improved description of the stopping power based on our density functional calculations that includes plasmon decay and is applicable at large distances from the surface. Atomic units are used unless stated otherwise.

2. THEORETICAL BACKGROUND

We briefly review the theoretical framework for the dielectric response of surfaces which provides the starting point for our investigations of energy loss and stopping at large distances.

2.1. Surface response function

The response of a many-body system to an external perturbation is one of the key quantities of interest in many-body physics. When the response is treated within perturbation theory to first order (linear response) the corresponding response function can be determined quite accurately for a large class of systems. For many-body systems of charged particles such as quasi-free electrons of a metal interacting with an electric field set up by an external charge, the response function is usually expressed in terms of the (bulk) dielectric constant $\varepsilon_{\mathrm{b}}(\vec{q}, \omega)$

$$\varepsilon_{\mathrm{b}}(\vec{q}, \omega) = \frac{\rho_{\mathrm{ext}}(\vec{q}, \omega)}{\rho(\vec{q}, \omega)}, \tag{1}$$

where ρ_{ext} is the external charge causing the dielectric displacement while ρ includes both ρ_{ext} and the induced displacement charge ρ_{ind} in the medium. This definition taken from classical electrodynamics turns out to be the inverse of the dielectric response function for charged particle systems whose exact expression can be found in books on many-body theory [56]

$$\frac{1}{\varepsilon(\vec{q}, \omega)} - 1 = \frac{4\pi}{q^2} \chi(\vec{q}, \omega). \tag{2}$$

The right-hand side of equation (2) is denoted by $\chi(\vec{q}, \omega)$, the response function. Equation (2) represents the dynamic (i.e., frequency ω and wavenumber $\vec{q}$ dependent) polarizability of the medium. This expression as functions of $\vec{q}$ and ω is valid for systems which are translationally invariant with respect to both position $\vec{r}$ and time t. The charge density fluctuation is space- and time dependent with Fourier components $\rho(\vec{q}, \omega)$. For isotropic systems, ε will depend only on the magnitude of $|\vec{q}| = q$ and ω. Equation (2) is directly applicable only for homogeneous systems such as bulk solids when the lattice structure can be neglected (e.g., 'jellium').

Due to the breaking of translational symmetry in the direction of the surface normal ($\hat{z}$), the response function becomes non-local in z while retaining its dependence on the wave vector in the plane of the surface. The dielectric response theory for the bulk requires, therefore, modifications near surfaces. In order to motivate the non-local generalization of χ we express χ in terms of the induced density ρ_{ind} as

$$\rho_{\mathrm{ind}}(q, \omega) = \chi(q, \omega) \Phi_{\mathrm{ext}}(q, \omega), \tag{3}$$

where $\Phi_{\mathrm{ext}}(q, \omega)$ is the three-dimensional (3D) Fourier transform of a Coulomb potential. The extension of equation (3) to the case of broken translational invariance along the surface normal can now be easily guessed as

$$\rho_{\mathrm{ind}}(Q, \omega, z, b) = \int \mathrm{d}z' \, \chi(Q, \omega, z, z') \Phi_{\mathrm{ext}}(Q, \omega, z', b), \tag{4}$$

where b is the z-coordinate of the external point charge. In the following 3D vectors are denoted by lower case, ($\vec{p} = (\vec{P}, p_z)$ with $p^2 = P^2 + p_z^2$) while 2D vectors in the surface plane are denoted by capital letters. In the 2D Fourier representation, the Coulomb potential of an external unit point charge is given by

$$\Phi_{\text{ext}}(Q, \omega, z, b) = \frac{2\pi}{Q} \mathrm{e}^{-Q|z-b|}. \tag{5}$$

The response function χ is still local in the Fourier variables (Q, ω) but non-local in the coordinate z in which the translational symmetry is broken. In the special case that χ depends only on the coordinate difference $(z - z')$ translational symmetry is restored, and equation (4) reduces to equation (3).

In order to simplify the notation and clarify the underlying general structure of the method we introduce here a convenient Dirac bracket type matrix notation with respect to the non-local coordinates. Accordingly, ρ_{ind} of equation (4) will be identified as a matrix element of the operator $\underline{\underline{\rho}}_{\text{ind}}(Q, \omega)$,

$$\rho_{\text{ind}}(Q, \omega, z, z') = \langle z|\underline{\underline{\rho}}_{\text{ind}}(Q, \omega)|z'\rangle, \tag{6}$$

where the induced charge density at the coordinate z is generated by a source located at z'. Analogously, the external potential can be viewed as matrix elements of the operator $\underline{\underline{\Phi}}_{\text{ext}}(Q, \omega)$,

$$\Phi_{\text{ext}}(Q, \omega, z, z') = \langle z|\underline{\underline{\Phi}}_{\text{ext}}(Q, \omega)|z'\rangle = \frac{2\pi}{Q} \exp(-Q|z - z'|). \tag{7}$$

In this matrix notation equation (4) simplifies to

$$\underline{\underline{\rho}}_{\text{ind}}(Q, \omega) = \underline{\underline{\chi}}(Q, \omega)\underline{\underline{\Phi}}_{\text{ext}}(Q, \omega) \tag{8}$$

in complete analogy to equation (3).

Within the framework of the self-consistent field (SCF) method or RPA we can replace equation (8) by

$$\underline{\underline{\rho}}_{\text{ind}}(Q, \omega) = \underline{\underline{\chi}}_0(Q, \omega)\underline{\underline{\Phi}}_{\text{SCF}}(Q, \omega), \tag{9}$$

where χ_0 is the independent particle susceptibility, and the self-consistent potential is given by

$$\underline{\underline{\Phi}}_{\text{SCF}}(Q, \omega) = \underline{\underline{\Phi}}_{\text{ind}}(Q, \omega) + \underline{\underline{\Phi}}_{\text{ext}}(Q, \omega). \tag{10}$$

The SCF method takes into account the collective screening by a many-body system. The self-consistency is imposed by requiring ρ_{ind} to satisfy Poisson's equation which takes the form

$$\underline{\underline{\Phi}}_{\text{ind}}(Q, \omega) = \underline{\underline{\Phi}}_{\text{SCF}}(Q, \omega) - \underline{\underline{\Phi}}_{\text{ext}}(Q, \omega) = \underline{\underline{K}}(Q, \omega)\underline{\underline{\rho}}_{\text{ind}}(Q, \omega), \tag{11}$$

where the kernel $\underline{\underline{K}}(Q, \omega)$ in the SCF or RPA is given by the matrix element of the bare Coulomb interaction between electrons

$$\langle z|\underline{\underline{K}}_{\mathrm{RPA}}(Q, \omega)|z'\rangle = \frac{2\pi}{Q} \mathrm{e}^{-Q|z-z'|}. \tag{12}$$

Improvements beyond the RPA can be accomplished, for example, by including exchange-correlation corrections of density functional theory into the kernel

$$\langle z|\underline{\underline{K}}_{\mathrm{LDA}}(Q, \omega)|z'\rangle = \frac{2\pi}{Q} \mathrm{e}^{-Q|z-z'|} + \Phi'_{\mathrm{xc}}(n_0(z))\delta(z - z'), \tag{13}$$

where

$$\Phi_{\mathrm{xc}}{}'(n_0) = \left.\frac{\delta \Phi_{\mathrm{xc}}(n)}{\delta n}\right|_{n=n_0} \tag{14}$$

is the functional derivative taken at the unperturbed, but z dependent, density $n_0(z)$. Equation (13) corresponds to the LDA. It should be noted that LDA refers here to the kernel of the SCF equation and not to the exchange-correlation potential in the Kohn–Sham equations for the single-particle orbitals generating χ_0. Combining equations (8) and (9) with equation (11) we find an operator (integral) equation for the response function $\underline{\underline{\chi}}$

$$\underline{\underline{\chi}}(Q, \omega) = [1 - \underline{\underline{\chi}}_0(Q, \omega)\underline{\underline{K}}(Q, \omega)]^{-1}\underline{\underline{\chi}}_0(Q, \omega) \tag{15}$$

and the corresponding equation for the induced potential

$$\underline{\underline{\Phi}}_{\mathrm{ind}}(Q, \omega) = \underline{\underline{K}}(Q, \omega)\underline{\underline{\chi}}(Q, \omega)\underline{\underline{\Phi}}_{\mathrm{ext}}(Q, \omega). \tag{16}$$

Equation (16) provides the starting point for the calculation of the friction force. The key quantity is the surface loss function $g(Q, \omega)$ related to $\underline{\underline{\Phi}}_{\mathrm{ind}}(Q, \omega)$ as

$$g(Q, \omega) = \frac{Q}{2\pi} \mathrm{e}^{2Qb}\langle b|\underline{\underline{\Phi}}_{\mathrm{ind}}(Q, \omega)|b\rangle. \tag{17}$$

The imaginary part of $g(Q, \omega)$ provides the key input to the stopping power calculation.

2.2. Friction force for particles moving parallel to the surfaces

We are interested in calculating the dissipative component of the force acting on the charged projectile with charge Z moving with a velocity parallel to the solid surface ($\vec{v} = V\hat{x}$). We assume that the trajectory is not modified due to the interaction. We also assume that the surface is located in the (x, y) plane.

Within the linear-response theory all calculations for the stopping power S can be performed for unit charge $Z = 1$ using the scaling

$$S(Z, b, v) = Z^2 S(Z = 1, b, v) = Z^2 S(b, v). \tag{18}$$

In our numerical calculations the velocity of the projectile is 0.29 a.u., and we consider Al as target. From the matrix element of the induced potential, i.e., the surface loss function, the position-dependent friction force or stopping power can be written as

$$S(b, V) = -\frac{1}{V} \int \frac{\mathrm{d}^2 \vec{Q}}{(2\pi)^2} \vec{Q}\vec{V} \, \mathrm{Im}[\langle b | \underline{\underline{\Phi}}_{\mathrm{ind}}(Q, \omega = \vec{Q}\vec{V}) | b \rangle], \tag{19}$$

with $Q^2 = Q_y^2 + \omega^2/V^2$. Equivalently, equation (19) can be written in cylindrical coordinates as

$$S(b, V) = -\int_0^{+\infty} \mathrm{d}Q \, \mathrm{e}^{-2Qb} \int_0^{2\pi} \mathrm{d}\phi \cos\phi \frac{Q}{2\pi} \mathrm{Im}[g(Q, QV\cos\phi)]. \tag{20}$$

3. SPECULAR REFLECTION MODEL

The SRM pioneered by Ritchie and co-workers [43–45] provides a simplified intuitive model of the surface response while retaining many of the essential physics features of ion–surface scattering. In the following, we discuss the surface loss function $g(Q, \omega)$ within the framework of the SRM. We consider an external unit charge with coordinates $\vec{r}(t) = (\vec{V}t, v_z|t|)$, approaching and specularly reflected from a surface

$$\rho_{\mathrm{ext}}(\vec{r}, t) = \delta(\vec{r} - \vec{V}t - v_z|t|), \tag{21}$$

where the dependence on the time through $|t|$ expresses the specular reflection condition. Its space–time Fourier transform is

$$\rho_{\mathrm{ext}}(\vec{q}, \omega) = -\mathrm{i}[(q_z v_z - (\omega - \vec{Q}\vec{V}) - \mathrm{i}\gamma)^{-1} + (q_z v_z + \omega - \vec{Q}\vec{V})^{-1}]. \tag{22}$$

The dielectric response in the half-space below the surface ($z < 0$) is described by the bulk dielectric function, $\varepsilon_{\mathrm{b}}(\vec{q}, \omega)$ while above the surface ($z > 0$) ε is given by its vacuum value 1. This discontinuous change of the dielectric response at the interface models the symmetry breaking due to the presence of a surface within the SRM. Assuming that the parallel (V) and perpendicular (v_z) velocity components of the particle satisfy the relation $V \gg v_z$, the induced potential per unit charge at position $\vec{r}$ is given by [57,58]

$$\Phi_{\mathrm{ind}}(\vec{R}, r_z, b, \omega) = \frac{1}{2\pi} \int \frac{\mathrm{d}\vec{Q}}{Q} \mathrm{e}^{\mathrm{i}\vec{Q}\vec{R}} [\Phi^{(1)} + \Phi^{(2)}], \tag{23}$$

with

$$\Phi^{(1)} = \Theta(b)\Theta(r_z)\frac{\varepsilon_s(Q,\omega)-1}{\varepsilon_s(Q,\omega)+1}e^{-Q(r_z+b)}, \tag{24}$$

$$\Phi^{(2)} = \Theta(b)\Theta(-r_z)\frac{2\varepsilon_s(Q,r_z,\omega)}{\varepsilon_s(Q,\omega)+1}e^{-Qb}, \tag{25}$$

where $\vec{r} = (\vec{R}, r_z)$, $\omega = \vec{V}\vec{Q}$, and $\Theta(x)$ is the Heaviside step function. The terms $\Phi^{(1)}$ and $\Phi^{(2)}$ refer to the region of the electronic coordinate above and below the surface. The projectile is assumed to be above the surface ($b > 0$). The induced potential can be expressed in terms of the surface dielectric function [45,59]

$$\varepsilon_s(Q,z,\omega) = \frac{Q}{\pi}\eta(Q,z,\omega), \tag{26}$$

where

$$\eta(Q,z,\omega) = \int_{-\infty}^{\infty}\frac{dq_z\, e^{iq_z z}}{(Q^2+q_z^2)\varepsilon_b(q,\omega)}. \tag{27}$$

In the following, we will use the simplified notation $\eta(Q,\omega) = \eta(Q, z = 0, \omega)$ for its value at $z = 0$. From equation (23) we can directly identify the Fourier component of the induced potential

$$\langle r_z|\underline{\underline{\Phi}}_{ind}(Q,\omega)|b\rangle = \Phi_{ind}(Q,r_z,b,\omega) = \frac{2\pi}{Q}[\Phi^{(1)}+\Phi^{(2)}], \tag{28}$$

with diagonal elements

$$\langle b|\underline{\underline{\Phi}}_{ind}(Q,\omega)|b\rangle = \frac{2\pi}{Q}\frac{\varepsilon_s(Q,\omega)-1}{\varepsilon_s(Q,\omega)+1}e^{-2Qb}. \tag{29}$$

Consequently, the surface loss function in the SRM reduces to

$$g_{SRM}(Q,\omega) = \frac{\varepsilon_s(Q,\omega)-1}{\varepsilon_s(Q,\omega)+1}. \tag{30}$$

For later reference we introduce here another response function, $\bar{\varepsilon}$, not to be confused with ε_s, as

$$\frac{1}{\bar{\varepsilon}(Q,\omega)} - 1 = \frac{2\pi}{Q}\int_{-\infty}^{+\infty}dz\int_{-\infty}^{+\infty}dz'\chi(Q,z,z'\omega). \tag{31}$$

Its significance is derived from the fact that it contains both bulk- and surface-specific contributions to the dielectric response. Within the SRM,

when including also bulk excitations, equation (31) becomes

$$\frac{1}{\bar{\varepsilon}(Q,\omega)} = \frac{\varepsilon_{\mathrm{s}}(Q,\omega)-1}{\varepsilon_{\mathrm{s}}(Q,\omega)+1} - \frac{1}{\varepsilon_{\mathrm{b}}(Q,q_z=0,\omega)}. \tag{32}$$

Figure 2 displays schematically the excitation spectrum represented by $\bar{\varepsilon}$ in the (ω, q) plane. The accessible continuum of energies for electron–hole pair excitation correspond to the region between the lines L_ℓ and L_{u}, where

$$L_\ell = qq_{\mathrm{F}} + \frac{q^2}{2}, \tag{33a}$$

$$L_{\mathrm{u}} = -qq_{\mathrm{F}} + \frac{q^2}{2}, \tag{33b}$$

and q_{F} is the Fermi wave vector, while the plasmon lines at low q lie to the left of L_ℓ. We also display the lower (q_ℓ) and upper (q_{u}) cut-off at energy transfer ω. These values are

$$q_\ell(\omega) = \sqrt{q_{\mathrm{F}}^2 + 2\omega} - q_{\mathrm{F}}, \tag{34a}$$

$$q_{\mathrm{u}}(\omega) = \sqrt{q_{\mathrm{F}}^2 + 2\omega} + q_{\mathrm{F}}. \tag{34b}$$

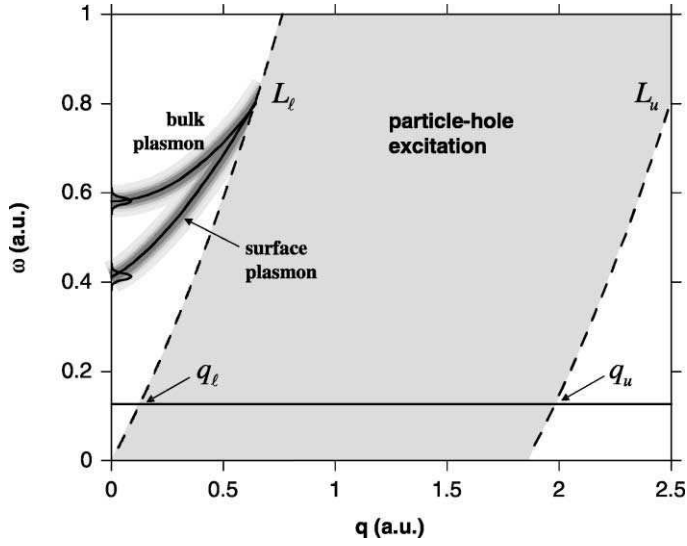

Fig. 2. Schematic representation of the excitation spectrum as a function of momentum transfer. The allowed energies for electron–hole pair excitation correspond to the region between the lines L_ℓ and L_{u}. Also shown are the broadened bulk and surface plasmon lines.

There is a wide variety of models of bulk dielectric functions available that can be used to determine $g_{\mathrm{SRM}}(Q,\omega)$ via equations (26)–(30). Benchmarks of a numerically satisfactory description are (a) the correct optical photoabsorption limit ($\sim \mathrm{Im}\{\varepsilon_{\mathrm{b}}^{-1}(q=0,\omega)\}$), (b) the correct asymptotic free-particle dispersion $\sim q^2/2$ for $q \gg 1$, (c) the correct dispersion relation for bulk plasmons at small q, and (d) the correct width (or damping) of the plasmon peak.

Ferell *et al.* [60] suggested an approximate form

$$\varepsilon_{\mathrm{b}}(q,\omega) = 1 + \frac{\omega_{\mathrm{p}}^2}{s^2q^2 - \mathrm{i}\pi\omega s^2 q\theta(2q_{\mathrm{F}}-q)/2q_{\mathrm{F}} - \omega(\omega+\mathrm{i}\gamma)}, \quad (35)$$

where $\omega_{\mathrm{p}} = \sqrt{(3/r_{\mathrm{s}}^3)}$ is the classical bulk plasmon frequency, r_{s} is the Wigner–Seitz radius, and γ is the damping of collective excitation. In equation (35), s denotes the group velocity of the plasmons at small wavenumbers. From the Lindhard dielectric function [61] we expect

$$s_1 = q_{\mathrm{F}}/\sqrt{3}, \quad (36a)$$

while the hydrodynamical model gives

$$s_2 = \sqrt{3/5}q_{\mathrm{F}}. \quad (36b)$$

Brandt and Reinheimer [62] recommended a mixed description for s, namely

$$s_3 = \begin{cases} q_{\mathrm{F}}/\sqrt{3}, & \text{when } \omega < qq_{\mathrm{F}} \\ \sqrt{3/5}q_{\mathrm{F},} & \text{when } \omega > qq_{\mathrm{F}.} \end{cases} \quad (36c)$$

Further improvements can be built into equation (35) by choosing

$$\varepsilon_{\mathrm{b}}(q,\omega) = 1 + \frac{\omega_{\mathrm{p}}^2}{s^2q^2 + q^4/4 - \mathrm{i}\pi\omega s^2 q\theta(x_1)\theta(x_2)/2q_{\mathrm{F}} - \omega(\omega+\mathrm{i}\gamma(q))}, \quad (37)$$

where $x_1 = \omega - q^2/2 + q_{\mathrm{F}}q$ and $x_2 = q^2/2 + q_{\mathrm{F}}q - \omega$. These cut-offs conform with the energy–momentum dispersion of a free particle $\sim q^2/2$. Moreover, we allow for a momentum dependent damping, $\gamma(q)$ [63,64]. Explicit expressions for $\gamma(q)$ can be obtained from fits to experimental data. For the case of Al, measurements for the broadening of the bulk plasmon loss peak as a function of q have been reported [65,66] and can be represented by

$$\gamma(q) = \gamma_0 + \gamma_2 q^2 + \gamma_4 q^4, \quad (38)$$

with $\gamma_2 = 0.0148$ a.u. and $\gamma_4 = 0.765$ a.u. [65]. In our numerical studies we will use $r_{\mathrm{s}} = 2.07$ and $\gamma_0 = 0.03$ a.u. for Al.

Figure 3 displays the density plot of the excitation spectrum, i.e., $\mathrm{Im}\{-\bar{\varepsilon}(Q,\omega)^{-1}\}$ (see equation (32)) using ε_b as given by equation (37) for Al. The bulk and surface plasmon dispersion can be clearly seen. The solid line L_l in Fig. 3 indicates the onset of the continuum. In Fig. 4 we display cuts through $\mathrm{Im}\{-1/\bar{\varepsilon}\}$ calculated within SRM for various values of Q for the three choices of s (see equations (36a)–(36c)). The region of small ω predominantly contributes to the stopping power at large distances from the surface. With increasing momentum transfer Q, both the surface and bulk plasmon peaks shift to higher energies. The dispersion of plasmon peaks is controlled by s_i. Overall, the spectrum is only weakly dependent on s_i. The largest variation is seen for small ω. A negative dispersion as discussed in Ref. [53] is not reproduced in the SRM for Al. Using the abbreviations

$$a = s^2q^2 - \omega^2 + q^4/4, \tag{39}$$

$$d = \frac{\pi s^2 q\,\theta(x_1)\theta(x_2)}{2q_F}. \tag{40}$$

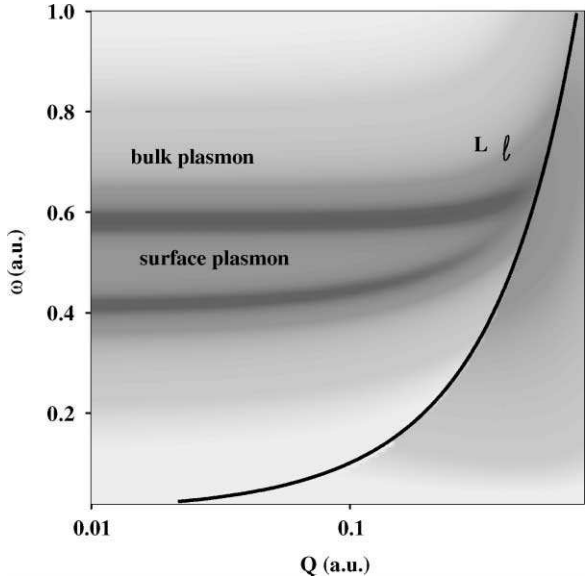

Fig. 3. Gray scale plot (white: minimum intensity, black: maximum intensity) of the energy loss function, $\mathrm{Im}[-1/\bar{\varepsilon}(Q,\omega)]$ (equation (32)) for Al based on SRM calculation using the hydrodynamic model for s. The line indicates the border $L_\ell = qq_F + q^2/2$ where the channel for particle–hole excitation opens. (Color online.)

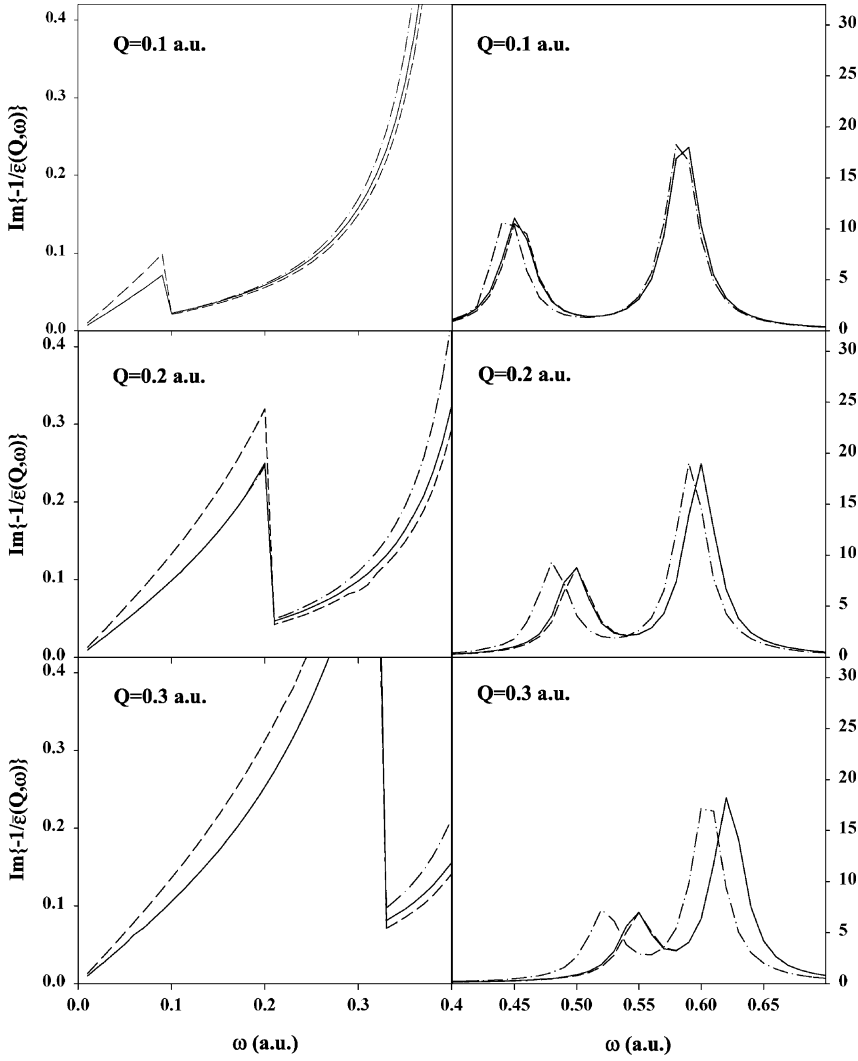

Fig. 4. Energy loss function, i.e., the inverse dielectric function, $\mathrm{Im}[-1/\bar{\varepsilon}(Q,\omega)]$, calculated within SRM for various values of Q. Dash-dotted line: dispersion of Lindhard model (equation (36a)), dashed line: hydrodynamic model (equation (36b)), solid line: Brandt–Reinheimer model (equation (36c)).

the surface dielectric function can be expressed as

$$\eta(Q,\omega) = A - \mathrm{i}(B + C), \tag{41}$$

where

$$A = \int_{-\infty}^{\infty} \mathrm{d}q_z \left\{ \frac{a(a+\omega_\mathrm{p}^2) + \omega^2(\gamma+d)^2}{q^2[(a+\omega_\mathrm{p}^2)^2 + \omega^2(\gamma+d)^2]} \right\}, \tag{42a}$$

$$B = \int_{-\infty}^{\infty} \mathrm{d}q_z \left\{ \frac{\omega\omega_\mathrm{p}^2\gamma}{q^2[(a+\omega_\mathrm{p}^2)^2 + \omega^2(\gamma+d)^2]} \right\}, \tag{42b}$$

$$C = \int_{-\infty}^{\infty} \mathrm{d}q_z \left\{ \frac{\omega\omega_\mathrm{p}^2 d}{q^2[(a+\omega_\mathrm{p}^2)^2 + \omega^2(\gamma+d)^2]} \right\}, \tag{42c}$$

which leads to a surface loss function

$$\mathrm{Im}\{g_{\mathrm{SRM}}(Q,\omega)\} = -\frac{2\tilde{B}}{(\tilde{A}+1)^2 + (\tilde{B}+\tilde{C})^2} - \frac{2\tilde{C}}{(\tilde{A}+1)^2 + (\tilde{B}+\tilde{C})^2}, \tag{43}$$

with $\tilde{A} = QA/\pi$, $\tilde{B} = QB/\pi$, and $\tilde{C} = QC/\pi$. The terms $\tilde{B}$ and $\tilde{C}$ are associated with the plasmon and particle–hole damping, respectively. Ignoring for the moment the fact that in the denominator both $\tilde{B}$ and $\tilde{C}$ appear and thus these contributions are mixed, we can write equation (43) as

$$\mathrm{Im}\{g_{\mathrm{SRM}}(Q,\omega)\} = \mathrm{Im}\{g_{\mathrm{SRM}}^{\mathrm{pl}}(Q,\omega)\} + \mathrm{Im}\{g_{\mathrm{SRM}}^{\mathrm{ph}}(Q,\omega)\}. \tag{44}$$

We refer to $\mathrm{Im}\{g_{\mathrm{SRM}}^{\mathrm{pl}}(Q,\omega)\}$ and $\mathrm{Im}\{g_{\mathrm{SRM}}^{\mathrm{ph}}(Q,\omega)\}$ as the surface loss functions due to the collective plasmon excitations and due to the particle–hole excitations, respectively. At large distances from the surface, the dominant contribution to the loss arises from small momentum ($Q \ll 1$) and energy transfers ($\omega \ll 1$). Therefore, we can determine the asymptotic form of equation (44) by neglecting all terms in first order in ω^2 [44]. In this case an unambiguous separation can be achieved between the plasmon and particle–hole excitations

$$\mathrm{Im}\{g_{\mathrm{SRM}}^{\mathrm{pl}}(Q,\omega)\} = -\frac{2\tilde{B}}{(\tilde{A}+1)^2}, \tag{45}$$

$$\mathrm{Im}\{g_{\mathrm{SRM}}^{\mathrm{ph}}(Q,\omega)\} = -\frac{2\tilde{C}}{(\tilde{A}+1)^2}. \tag{46}$$

In this limit analytic expressions can be derived for the stopping power [44]. By contrast we refer in the following to equation (43) as the numerical solution of the SRM model.

3.1. Plasmon excitation

In the long-wave limit of plasmon excitations we find

$$\mathrm{Im}\{g^{\mathrm{pl}}_{\mathrm{SRM}}(Q,\omega)\} = -\frac{2\tilde{B}}{(\tilde{A}+1)^2} = -2\frac{Q}{\pi}\frac{1}{(\tilde{A}+1)^2}\frac{\omega\gamma_0 q^4_{\mathrm{TF}}}{\omega^2_{\mathrm{p}}}\delta, \quad (47)$$

with $q_{\mathrm{TF}} = (12/\pi)^{1/3}/\sqrt{r_{\mathrm{s}}}$ being the Thomas–Fermi wave vector and

$$\delta = \int_{-\infty}^{\infty}\frac{\mathrm{d}q_z}{(q_z^2+Q^2)(q_z^2+Q^2+q^2_{\mathrm{TF}})^2}$$

$$= \pi\left[\frac{1}{q^4_{\mathrm{TF}}Q} - \frac{2Q^2+3q^2_{\mathrm{TF}}}{2q^4_{\mathrm{TF}}(Q^2+q^2_{\mathrm{TF}})^{3/2}}\right]. \quad (48)$$

The stopping power is, in the limit of large distances $b \gg 1$, determined by the $Q \to 0$ limit

$$\lim_{Q\to 0}\left[-\mathrm{Im}\left\{g^{\mathrm{pl}}_{\mathrm{SRM}}(Q,\omega)\right\}\right] = \omega\frac{2\gamma_0}{\omega^2_{\mathrm{p}}}. \quad (49)$$

Inserting equation (49) into equation (19) leads to

$$S^{\mathrm{pl}}_{\mathrm{SRM}} = \frac{2\gamma_0}{\pi V^2\omega^2_{\mathrm{s}}}\int_0^{\infty}\mathrm{d}\omega\,\omega^2\int_0^{\infty}\mathrm{d}Q_y\frac{\exp\left(-2b\sqrt{Q_y^2+\omega^2/V^2}\right)}{\sqrt{Q_y^2+\omega^2/V^2}}, \quad (50)$$

where $\omega_{\mathrm{s}} = \omega_{\mathrm{p}}/\sqrt{2}$ is the classical surface plasmon frequency. This double integral can be calculated analytically to yield

$$S^{\mathrm{pl}}_{\mathrm{SRM}} = \frac{2\gamma_0}{\pi V^2\omega^2_{\mathrm{s}}}\int_0^{\infty}\mathrm{d}\omega\,\omega^2 K_0(2b\omega/V) = \frac{\gamma_0 V}{8\omega^2_{\mathrm{s}}}\frac{1}{b^3}, \quad (51)$$

where K_0 is the modified Bessel function of second kind.

Generalizing the observation that at small Q and ω values the term of the loss function associated with plasmon excitation is linearly dependent on the frequency (see equation (49)) we can write

$$\mathrm{Im}\{-g^{\mathrm{pl}}_{\mathrm{SRM}}(Q,\omega)\} = \omega\,F^{\mathrm{pl}}_{\mathrm{SRM}}(Q,V). \quad (52)$$

Figure 5 shows the surface loss function given by the numerical solution of the SRM model. The linear dependence is fulfilled approximately for $\omega \lesssim 0.01$ a.u. However, if $\omega > 0.01$ a.u. higher order contributions in the dielectric function become non-negligible and the linear dependence ceases to be valid. We have calculated $F^{\mathrm{pl}}_{\mathrm{SRM}}(Q,V)$ for different dielectric functions. Figure 5 presents data for different choices of the plasmon group velocity s (see equations (36a)–(36c)), the hydrodynamic model (s_2) and

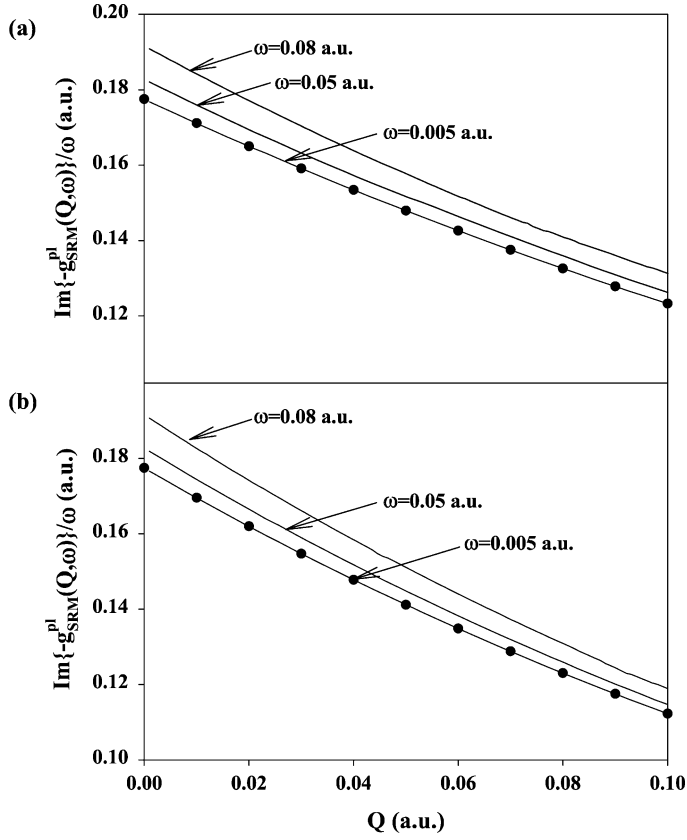

Fig. 5. Surface loss function divided by the frequency for plasmon excitation as a function of momentum transfer, Q, for various ω within the SRM. Solid line: direct numerical integration of equation (43). Circle: fit with $F^{\mathrm{pl}}_{\mathrm{SRM}}(Q) = a^{\mathrm{pl}}_{\mathrm{SRM}} \times \exp(-c^{\mathrm{pl}}_{\mathrm{SRM}}Q)$. (a) The bulk dielectric function is described by equation (37) with Brandt–Reinheimer dispersion s_3 (equation (36c)), (b) the bulk dielectric function is described by equation (37) with hydrodynamical dispersion s_2 (equation (36b)).

the Brandt–Reinheimer model (s_3). In both cases, $F^{\mathrm{pl}}_{\mathrm{SRM}}(Q, V)$ can be fitted to the form

$$F^{\mathrm{pl}}_{\mathrm{SRM}}(Q, V) = a^{\mathrm{pl}}_{\mathrm{SRM}}(V)\mathrm{e}^{-c^{\mathrm{pl}}_{\mathrm{SRM}}(V)Q}. \tag{53}$$

with

$$a^{\mathrm{pl}}_{\mathrm{SRM}}(V) = 2\gamma_0 V/\omega_{\mathrm{p}}^2. \tag{54}$$

The decay constant $c^{\mathrm{pl}}_{\mathrm{SRM}}(V)$ was fitted to the data calculated at $\omega = 0.005$ a.u. Using s_3 we find $c^{\mathrm{pl}}_{\mathrm{SRM}} = 3.65$, while for the hydrodynamical model for s_2, $c^{\mathrm{pl}}_{\mathrm{SRM}} = 4.58$. Using the functional form equation (53)

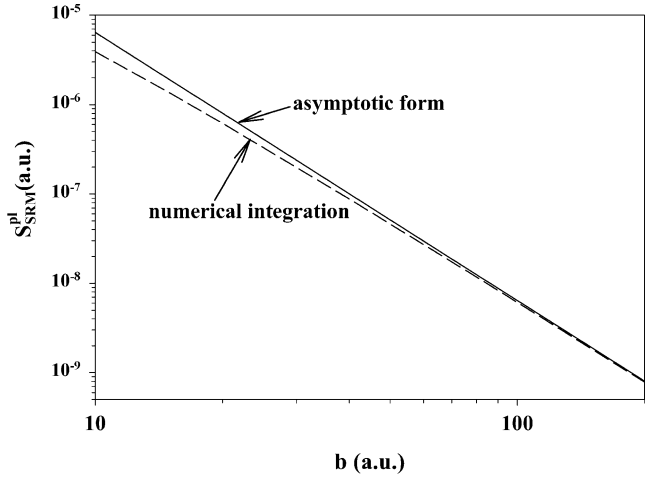

Fig. 6. Stopping power contribution due to the plasmon excitation, $S^{\mathrm{pl}}_{\mathrm{SRM}}$. Dashed line: direct integration using the surface loss function equation (43) with Brandt–Reinheimer dispersion s_3 (equation (36c)), solid line: long wavelength limit given by equation (45).

the integrals in equation (19) can still be calculated analytically and the stopping power follows as

$$S^{\mathrm{pl}}_{\mathrm{SRM}} = \frac{\gamma_0 V}{8\omega_{\mathrm{s}}^2} \frac{1}{(b + c^{\mathrm{pl}}_{\mathrm{SRM}})^3}. \tag{55}$$

We note for later reference that a similar asymptotic form can be derived from a Taylor expansion of the loss function $g(Q, \omega)$ keeping only the leading order terms in Q. Figure 6 displays the stopping power contribution originating from plasmon excitation. About 100 a.u. from the surface the asymptotic form (equation (51)) agrees very well with the numerical solution of the SRM and describes the stopping power very accurately. However, at smaller distances discrepancies indicate that contributions from shorter wavelengths become important.

3.2. Particle–hole excitation

In the long-wave limit, the contribution from particle–hole excitation can be written as

$$\mathrm{Im}\{g^{\mathrm{ph}}_{\mathrm{SRM}}(Q, \omega)\} = -\frac{2\tilde{C}}{(\tilde{A}+1)^2} = -2\frac{Q}{\pi}\frac{1}{(\tilde{A}+1)^2} 2\omega\alpha, \tag{56}$$

with

$$\alpha = \int_{-\sqrt{4k_F^2-Q^2}}^{\sqrt{4k_F^2-Q^2}} \frac{\mathrm{d}q_z}{\sqrt{q_z^2+Q^2}(q_z^2+Q^2+q_{TF}^2)^2}. \tag{57}$$

The integral (equation (57)) yields

$$\alpha = \frac{Q^2+2q_{TF}^2}{2q_{TF}^3(Q^2+q_{TF}^2)^{3/2}} \ln\left(\frac{u_m\sqrt{u^2+1}+\sqrt{u_m^2-u^2}}{u_m\sqrt{u^2+1}-\sqrt{u_m^2-u^2}}\right) - \frac{u_m\sqrt{u_m^2-u^2}}{q_{TF}^4(u^2+1)(u_m^2+1)}, \tag{58}$$

with $u = Q/q_{TF}$, $u_m = 2k_F/q_{TF}$.

In the long-wave limit $Q \to 0$, equation (56) reduces to

$$\lim_{Q\to 0}\left[-\mathrm{Im}\{g_{SRM}^{ph}(Q,\omega)\}\right] = \omega\frac{4Q}{\pi q_{TF}^4}\ln\left[\frac{1}{u^2}\frac{4u_m^2}{u_m^2+1}\right]. \tag{59}$$

Inserting equation (59) into equation (19) the particle–hole contribution to stopping follows as

$$S_{SRM}^{ph} = \frac{8}{\pi^2 V^2 q_{TF}^4}\int_0^\infty \mathrm{d}Q_y \int_0^\infty \mathrm{d}\omega\, \omega^2\, \mathrm{e}^{-2Qb} \ln\left[\frac{1}{u^2}\frac{4u_m^2}{u_m^2+1}\right]. \tag{60}$$

Performing the integrals analytically and after some algebra the stopping power can be written in the following form

$$S_{SRM}^{ph} = \frac{3V\ln(0.983 q_{TF} b)}{2\pi q_{TF}^4}\frac{1}{b^4}. \tag{61}$$

In general, the particle–hole contribution to the surface loss function, $\mathrm{Im}\{-g_{SRM}^{ph}(Q,\omega)\}$, can be written in analogy to equation (52) as

$$\mathrm{Im}\{-g_{SRM}^{ph}(Q,\omega)\} = \omega F_{SRM}^{ph}(Q,V). \tag{62}$$

Figure 7 shows the surface loss function for particle–hole excitation. The linear dependence implied by equation (62) is fulfilled for $\omega \lesssim 0.01$ a.u. For larger ω, $\omega > 0.01$ a.u., higher order contributions in the bulk dielectric function become important. Our numerical calculations can be fitted to the functional form

$$F_{SRM}^{ph}(Q,V) = a_{SRM}^{ph}(V) Q \ln(c_{SRM}^{ph}/Q)\theta[Q - Q_1(\omega)], \tag{63}$$

suggested by the analytic structure of $g_{SRM}^{ph}(Q,\omega)$. The constants were fitted to the numerical data calculated at $\omega = 0.005$ a.u. and within a narrow range of Q, $0 < Q < 0.05$ a.u. For the Brandt–Reinheimer model (s_3) we find $a_{SRM}^{ph} = 2.08$, $c_{SRM}^{ph} = 0.72$, while for the hydrodynamical model (s_2)

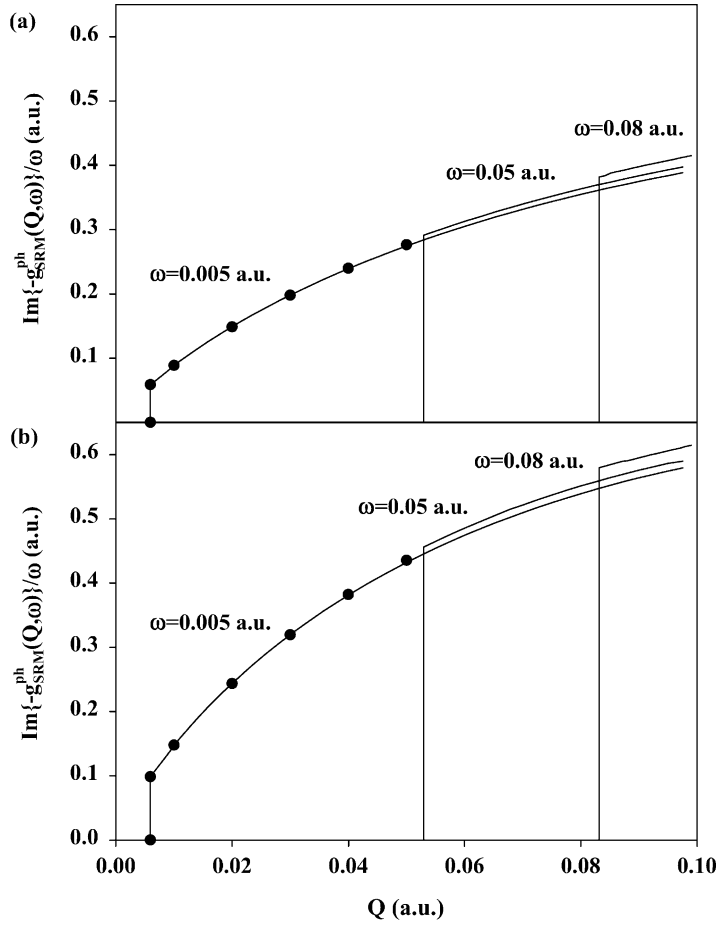

Fig. 7. Surface loss function divided by the frequency for particle–hole excitation as a function of momentum transfer, Q, for various ω within the SRM. Solid line: direct numerical integration with equation (43). Circle: fit with $F^{\mathrm{ph}}_{\mathrm{SRM}}(Q) = a^{\mathrm{ph}}_{\mathrm{SRM}} Q \ln(c^{\mathrm{ph}}_{\mathrm{SRM}}/Q)\theta[Q - Q_1(\omega)]$. (a) The bulk dielectric function is described by equation (37) with Brandt–Reinheimer dispersion s_3 (equation (36c)), (b) the bulk dielectric function is described by equation (37) with hydrodynamical dispersion s_2 (equation (36b)).

we have $a^{\mathrm{ph}}_{\mathrm{SRM}} = 3.8$, $c^{\mathrm{ph}}_{\mathrm{SRM}} = 0.50$. Also for the particle–hole excitations the asymptotic form can alternatively be found using a Taylor expansion of the loss function, $g(Q, \omega)$, and keeping only the leading order terms in Q. Figure 8 shows the stopping power contribution due to the particle–hole excitation. Above 100 a.u. from the surface the asymptotic form describes

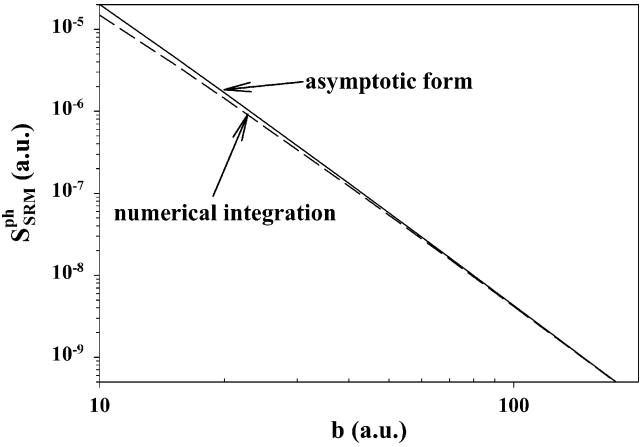

Fig. 8. Stopping power contribution due to the particle–hole excitation, $S^{\mathrm{ph}}_{\mathrm{SRM}}$. Dashed line: direct integration using the surface loss function described by equation (43) with Brandt–Reinheimer dispersion s_3 (equation (36c)), solid line: long wavelength limit given by equation (46).

the stopping power very accurately while discrepancies arise at smaller distances.

4. TIME DEPENDENT DENSITY FUNCTIONAL THEORY

TDDFT has developed in recent years into an attractive alternative to the SRM for calculating the surface response. In this section we investigate its predictions for the surface response and stopping power at large distances. The coordinate space representation of the matrix element for the induced potential equation (16) reads

$$\Phi_{\mathrm{ind}}(Q,z,b,\omega)=\int_{-\infty}^{+\infty}\mathrm{d}z' K(Q,z,z')\int_{-\infty}^{+\infty}\mathrm{d}z''\chi(Q,z',z'',\omega)\Phi_{\mathrm{ext}}(Q,z'',b,\omega), \tag{64}$$

where $\chi(Q,z,z',\omega)$ is the first-order many-body response function, and

$$K(Q,z,z')=\frac{2\pi}{Q}\exp(-Q|z-z'|)+\delta(z-z')\frac{\partial\Phi_{\mathrm{xc}}}{\partial n}\bigg|_{n=n_0(z)}, \tag{65}$$

in LDA. The first term in equation (65) describes the bare Coulomb interaction between electrons and the second term is the exchange-correlation correction. The scalar electric potential Φ_{ext} due to a charged particle moving parallel to the surface with velocity $\vec{V}$ and at a distance b can

be expressed as

$$\Phi_{\rm ext}(Q,z,b,\omega) = \frac{2\pi}{Q} Z\delta(\omega - \vec{Q}\vec{V}) {\rm e}^{-Q|z-b|}. \tag{66}$$

The 2D density plot of the energy loss function, $\mathrm{Im}(-1/\bar{\varepsilon})$ (equation (31)), of Al within the framework of the LDA (Fig. 9) resembles the 2D distribution given by the SRM (Fig. 3). Cuts through the distribution $\mathrm{Im}[-1/\bar{\varepsilon}(Q,\omega)]$ at different Q (Fig. 10) indicate that the RPA and LDA approximations to the kernel (equations (12) and (13)) agree with each other. Based on this observation we perform the analytical investigation of the large-distance behavior of the TDDFT stopping power employing the RPA kernel. Equation (64) can thus be written as

$$\Phi_{\rm ind}^{\rm RPA}(Q,b,b,\omega) = \frac{(2\pi)^2}{Q^2} \int_{-\infty}^{+\infty} {\rm d}z \int_{-\infty}^{+\infty} {\rm d}z'\, {\rm e}^{-Q|b-z|} \mathrm{Im}[\chi(Q,z,z',\omega)] {\rm e}^{-Q|z'-b|}. \tag{67}$$

With b approaching infinity, i.e., when b is large compared to z (z') we can write

$$\Phi_{\rm ind}^{\rm RPA}(Q,b,b,\omega) = \frac{(2\pi)^2}{Q^2} {\rm e}^{-2Qb} \int_{-\infty}^{a} {\rm d}z \int_{-\infty}^{a} {\rm d}z'\, {\rm e}^{Q(z+z')}\, \mathrm{Im}\,[\chi(Q,z,z',\omega)]. \tag{68}$$

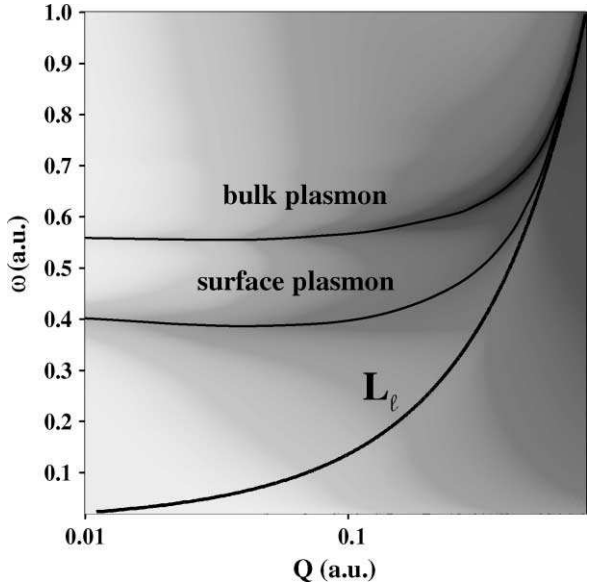

Fig. 9. Gray scale plot (white: minimum intensity, black: maximum intensity) of the energy loss function, $\mathrm{Im}[-1/\bar{\varepsilon}(Q,\omega)]$ (equation (31)), of Al using TDDFT with LDA kernel. The line indicates the border $L_\ell = qq_{\rm F} + q^2/2$ where the channel for particle–hole excitation opens. (Color online.)

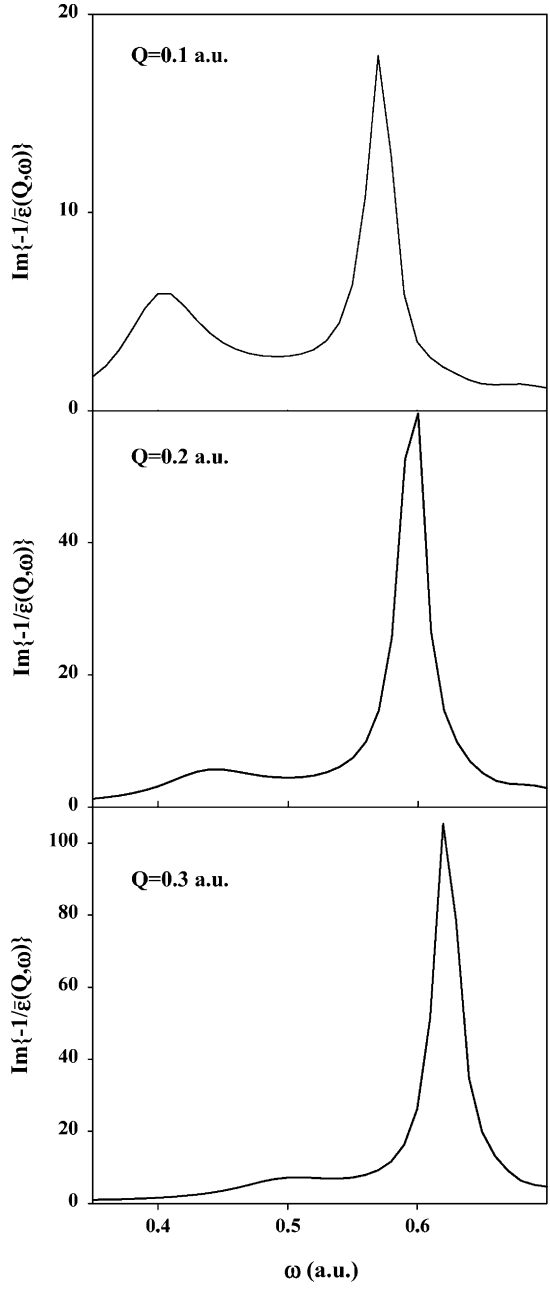

Fig. 10. Energy loss function, i.e., $\mathrm{Im}[-1/\bar{\varepsilon}(Q,\omega)]$, calculated within TDDFT with RPA kernel. (Results with LDA kernel are identical within the graphical resolution.)

In practice the integration is performed from deep inside the solid to a sufficiently large distance a far from the surface until convergence is achieved. Substituting equation (68) into equation (17), the surface loss function in RPA within the framework of TDDFT reads,

$$g_{\mathrm{RPA}}(Q,\omega) = \frac{2\pi}{Q}\zeta(Q,\omega), \tag{69}$$

where

$$\zeta(Q,\omega) = \int_{-\infty}^{a}\int_{-\infty}^{a} \mathrm{d}z\,\mathrm{d}z'\,\mathrm{e}^{Q(z+z')}\,\mathrm{Im}\,[\chi(Q,z,z',\omega)]. \tag{70}$$

The large b behavior can be determined by means of power series expansion in Q around $Q=0$. We note that because of the relation $\omega = \vec{V}\vec{Q}$, the frequency simultaneously approaches zero which requires some care. In order to determine the leading term of equation (70), the functions $\mathrm{e}^{Q(z+z')}$ and $\chi(Q,z,z',\omega)$ are expanded in Taylor series

$$\mathrm{e}^{Q(z+z')} = 1 + Q(z+z') + \frac{Q^2}{2}(z+z')^2 + \frac{Q^3}{6}(z+z')^3 + \cdots, \tag{71}$$

$$\chi_i(Q) = \chi_i(0) + Q\chi_i^{(1)}(0) + \frac{Q^2}{2}\chi_i^{(2)}(0) + \frac{Q^3}{6}\chi_i^{(3)}(0) + \cdots, \tag{72}$$

where $\mathrm{Im}[\chi(Q,z,z',\omega)] = \mathrm{Im}[\chi(Q,z,z',QV\cos\phi)]$ is denoted by $\chi_i(Q,\omega)$ and

$$\left.\frac{\mathrm{d}^k\chi_i(Q,\omega)}{\mathrm{d}^kQ}\right|_{Q=0}$$

is denoted by $\chi_i^{(k)}(0)$. To third order in Q equation (70) becomes

$$\begin{aligned}\zeta(Q,\omega) &= \zeta(Q,V,\phi)\\ &\approx \zeta_0(Q,V,\phi) + \zeta_1(Q,V,\phi) + \zeta_2(Q,V,\phi) + \zeta_3(Q,V,\phi),\end{aligned} \tag{73}$$

where

$$\zeta_0(Q,V,\phi) = \int_{-\infty}^{+\infty}\mathrm{d}z\int_{-\infty}^{+\infty}\mathrm{d}z'\,\chi_i(0), \tag{74a}$$

$$\zeta_1(Q,V,\phi) = \int_{-\infty}^{+\infty}\mathrm{d}z\int_{-\infty}^{+\infty}\mathrm{d}z'\,Q[(z+z')\chi_i(0) + \chi_i^{(1)}(0)], \tag{74b}$$

$$\zeta_2(Q,V,\phi) = \int_{-\infty}^{+\infty}\mathrm{d}z\int_{-\infty}^{+\infty}\mathrm{d}z'\frac{Q^2}{2}[(z+z')^2\chi_i(0) + 2(z+z')\chi_i^{(1)}(0) + \chi_i^{(2)}(0)], \tag{74c}$$

$$\zeta_3(Q,V,\phi)=\int_{-\infty}^{+\infty}\mathrm{d}z\int_{-\infty}^{+\infty}\mathrm{d}z'\frac{Q^3}{6}[(z+z')^3\chi_i(0)+3(z+z')^2\chi_i^{(1)}(0) + 3(z+z')\chi_i^{(2)}(0)+\chi_i^{(3)}(0)]. \tag{74d}$$

The derivatives of $\chi_i(Q,\omega)$ are given by

$$\chi_i^1(0)=\frac{\partial\chi_i(Q,0)}{\partial Q}\bigg|_{Q=0}+V\cos\phi\frac{\partial\chi_i(0,\omega)}{\partial\omega}\bigg|_{\omega=0}, \tag{75a}$$

$$\chi_i^2(0)=\frac{\partial^2\chi_i(Q,0)}{\partial^2 Q}\bigg|_{Q=0}+2V\cos\phi\frac{\partial^2\chi_i(Q,\omega)}{\partial Q\partial\omega}\bigg|_{Q,\omega=0}+V^2\cos^2\phi\frac{\partial^2\chi_i(0,\omega)}{\partial^2\omega}\bigg|_{\omega=0}, \tag{75b}$$

$$\chi_i^3(0)=\frac{\partial^3\chi_i(Q,0)}{\partial^3 Q}\bigg|_{Q=0}+3V\cos\phi\frac{\partial^3\chi_i(Q,\omega)}{\partial Q^2\partial\omega}\bigg|_{Q,\omega=0}+3V^2\cos^2\phi \times\frac{\partial^3\chi_i(Q,\omega)}{\partial Q\partial^2\omega}\bigg|_{Q,\omega=0}+V^3\cos^3\phi\frac{\partial^3\chi_i(0,\omega)}{\partial^3\omega}\bigg|_{\omega=0}. \tag{75c}$$

Inserting equations (74a)–(74d) and (75a)–(75c) into equations (73) and (20) leads to

$$S_{\mathrm{RPA}}(b,V)=S_{\mathrm{RPA}}^{\mathrm{pl}}(b,V)+S_{\mathrm{RPA}}^{\mathrm{ph}}(b,V), \tag{76}$$

where

$$S_{\mathrm{RPA}}^{\mathrm{pl}}(b,V)=\frac{\pi V}{2}c_{\mathrm{pl}}\int_0^{+\infty}\mathrm{d}Q\,Q^2\,\mathrm{e}^{-2Qb}, \tag{77}$$

$$S_{\mathrm{RPA}}^{\mathrm{ph}}(b,V)=\left[\frac{\pi V}{2}c_{\mathrm{ph}}^{(1)}+\frac{3\pi V^3}{24}c_{\mathrm{ph}}^{(2)}\right]\int_0^{+\infty}\mathrm{d}Q\,Q^3\,\mathrm{e}^{-2Qb}, \tag{78}$$

and

$$c_{\mathrm{pl}}=\int_{-\infty}^{+\infty}\mathrm{d}z\int_{-\infty}^{+\infty}\mathrm{d}z'\left[(z+z')\frac{\partial\chi_i(0,\omega)}{\partial\omega}\bigg|_{\omega=0}+2\frac{\partial^2\chi_i(Q,\omega)}{\partial Q\partial\omega}\bigg|_{Q,\omega=0}\right], \tag{79}$$

$$c_{\mathrm{ph}}^{(1)}=\int_{-\infty}^{+\infty}\mathrm{d}z\int_{-\infty}^{+\infty}\mathrm{d}z'\left[(z+z')\frac{\partial\chi_i(0,\omega)}{\partial\omega}\bigg|_{\omega=0}+2(z+z')^2\frac{\partial^2\chi_i(Q,\omega)}{\partial Q\partial\omega}\bigg|_{Q,\omega=0} + \frac{\partial^3\chi_i(Q,\omega)}{\partial^3\omega}\bigg|_{\omega=0}\right], \tag{80a}$$

$$c_{\mathrm{ph}}^{(2)}=\int_{-\infty}^{+\infty}\mathrm{d}z\int_{-\infty}^{+\infty}\mathrm{d}z'\left[\frac{\partial^3\chi_i(0,\omega)}{\partial^3\omega}\bigg|_{\omega=0}\right]. \tag{80b}$$

In deriving the RPA expression for the stopping power we made use of the fact that because of charge neutrality $\chi_i^{(1)}(0)$ vanishes and that the first non-vanishing contribution to the stopping power arises from ζ_2. The integrations in equations (77) and (78) can be performed analytically resulting in the stopping power at large distances

$$S_{\mathrm{RPA}}^{\mathrm{pl}}(b,V)=\frac{\pi V}{8}c_{\mathrm{p}}\frac{1}{b^3}, \tag{81}$$

$$S_{\mathrm{RPA}}^{\mathrm{ph}}(b,V)=\left[\frac{3\pi V}{16}c_{\mathrm{ph}}^{(1)}+\frac{3\pi V^3}{64}c_{\mathrm{ph}}^{(2)}\right]\frac{1}{b^4}. \tag{82}$$

In analogy with SRM, we have identified $S_{\mathrm{RPA}}^{\mathrm{pl}}$ and $S_{\mathrm{RPA}}^{\mathrm{ph}}$ as the stopping power due to the plasmon and particle–hole excitations, respectively. This assignment originates from the small Q expansion where terms to the same order in Q can be identified. Its physical justification hinges on the explicit calculation of c_{pl}, $c_{\mathrm{ph}}^{(1)}$, and $c_{\mathrm{ph}}^{(2)}$.

Starting point for the calculations of the many-body response function, $\chi(Q,z,z',\omega)$ is the noninteracting particle density–density correlation function $\chi_0(Q,z,z',\omega)$. An explicit expression for $\chi_0(Q,\omega,z,z')$ can be easily determined within the independent-particle model for the semi-infinite jellium [53]. For later reference we point out that lattice effects and thus coupling to phonons are neglected. Using the Fermi function at zero temperature for the occupation numbers, $f(\vec{p})=\theta(k_{\mathrm{f}}-p)$, $\chi_0(Q,z,z',\omega)$ can be written in terms of the one-electron wave functions and eigen-energies as

$$\chi_0(Q,\omega,z,z')=\sum_{p_z,p_z',\vec{P}}(f(\vec{p}_z)-f(\vec{p}_z'))\times\left(\frac{\phi_{p_z}^*(z)\phi_{p_z}(z')\phi_{p_z'}(z)\phi_{p_z'}^*(z')}{\omega+\varepsilon_{p_z}-\varepsilon_{p_z'}-\vec{Q}\vec{P}-\frac{1}{2}Q^2+\mathrm{i}\gamma}\right) \tag{83}$$

with

$$f(\vec{p}_z)=f(\vec{P},p_z),\qquad f(\vec{p}_z')=f(\vec{P}+\vec{Q},p_z'). \tag{84}$$

Within the framework of DFT $\chi_0(Q,\omega,z,z')$ is constructed from Kohn–Sham orbitals $\phi_{p_z}(z)$ [46] with energies ε_{p_z} in the degree of freedom along the surface normal. They are self-consistent solutions of

$$[-\tfrac{1}{2}\nabla^2+V_{\mathrm{eff}}(z)]\phi_{p_z}(z)=\varepsilon_{p_z}\phi_{p_z}(z), \tag{85}$$

where V_{eff} is the effective potential which depends only on the z-coordinate because of translational invariance along the jellium surface and can be

written in the LDA as

$$V_{\text{eff}}(z) = \Phi(z) + \Phi_{\text{xc}}(n[z]), \tag{86}$$

where $\Phi(z)$ is the electrostatic potential which satisfies the Poisson equation and $\Phi_{\text{xc}}(n[z])$ is the exchange-correlation potential for which we use the Wigner formula [67]

$$\Phi_{\text{xc}}(n) = -\frac{0.611}{r_{\text{s}}(n)} - \frac{0.587}{(r_{\text{s}} + 7.8)^2}(r_{\text{s}} + 5.85). \tag{87}$$

χ_0 can be rewritten with the help of Green's functions in the form

$$\chi_0(Q, \omega, z, z') = \sum_{\vec{p}} f(\vec{p})\phi^*_{p_z}(z)\phi_{p_z}(z')[G(z, z', \varepsilon_+) + G^*(z, z', \varepsilon_-)], \tag{88}$$

with

$$\varepsilon_+ = \varepsilon_k + \omega - \vec{P}\vec{Q} - Q^2/2 + \mathrm{i}\Gamma, \tag{89a}$$

$$\varepsilon_- = \varepsilon_k - \omega - \vec{P}\vec{Q} - Q^2/2 + \mathrm{i}\Gamma. \tag{89b}$$

In principle, Γ should be an infinitesimally small positive number. In practice, we use in our numerical calculations $\Gamma = 0.01$ a.u. for reasons of numerical stability. Finally, the integral equation (15) for χ and thus the induced potential are solved by discretization on a grid in z-space. The inevitable discretization errors pose problems when investigating the small Q limit numerically as Fourier reprocity requires a very wide slab size ($L \approx 2\pi/Q$). In fact, this difficulty may have caused spurious results in previous numerical investigations of the surface response function [68]. We, therefore, combine numerical with analytic techniques in order to explore the small Q (and large b) behavior. Starting point is the observation (Fig. 11) that the surface loss function $\mathrm{Im}[-g(Q, \omega)]$ divided by the frequency using both RPA and LDA kernel becomes nearly frequency independent at small values of Q and ω. This linear frequency dependence is fulfilled for both RPA and LDA when $\omega \lesssim 0.01$ a.u. In analogy to our treatment of the SRM model we assume that the loss function can be written as

$$-\mathrm{Im}\{g_{\text{DFT}}(Q, \omega)\} = \omega F_{\text{DFT}}(Q, V). \tag{90}$$

In principle, the DFT calculation using either RPA or LDA kernel, contains all excitations, i.e., particle–hole, surface and bulk plasmon excitations. However, the present jellium calculation predicts that the surface plasmon width decreases linearly with Q as $Q \to 0$ [69–72]. This is due to the fact that the plasmon coupling to the lattice and the plasmon decay into a double electron–hole pair is neglected from the outset. The significance of corrections of the unphysically long lifetimes for long-wave plasmon excitations becomes obvious when realizing that the asymptotic plasmon contribution within the SRM depends linearly on the $Q \to 0$ value of $\gamma(Q)$.

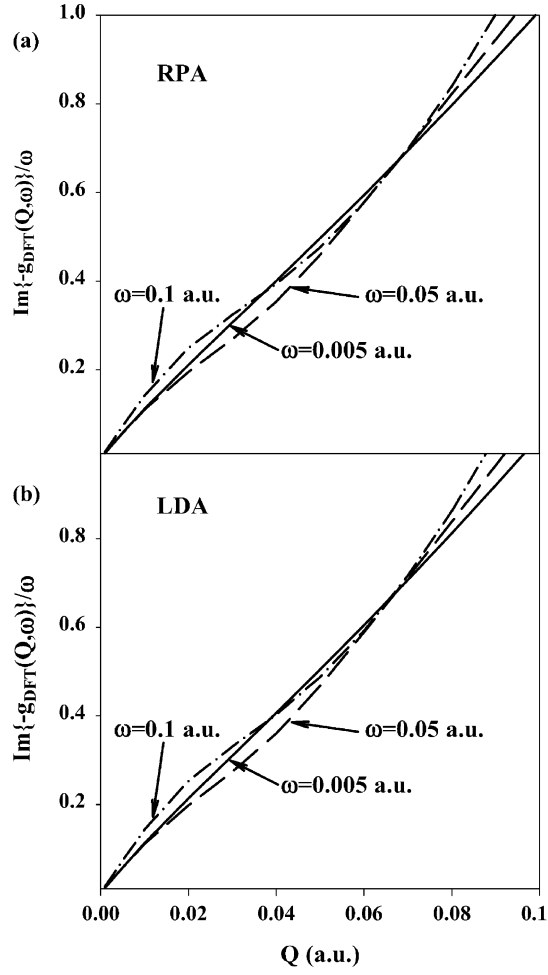

Fig. 11. Surface loss function divided by the frequency as a function of momentum transfer, Q, with (a) RPA and (b) LDA kernel.

Consequently, the plasmon contribution ($\sim b^{-3}$) to stopping vanishes in the asymptotic limit $b \to 0$ of DFT for a structureless jellium. Numerically the coefficient $c_{\rm pl}$ is found to be either negligibly small or equal to zero. Corrections of this deficiency will be discussed below.

Since the asymptotic contribution to stopping comes from particle–hole excitations we fit the numerical data at $\omega = 0.005$ a.u. and $0 < Q < 0.05$ a.u. (Fig. 12) to the functional form (see equation (63))

$$F_{\rm DFT}(Q, V) = a_{\rm DFT}(V) Q \ln(c_{\rm DFT}/Q), \tag{91}$$

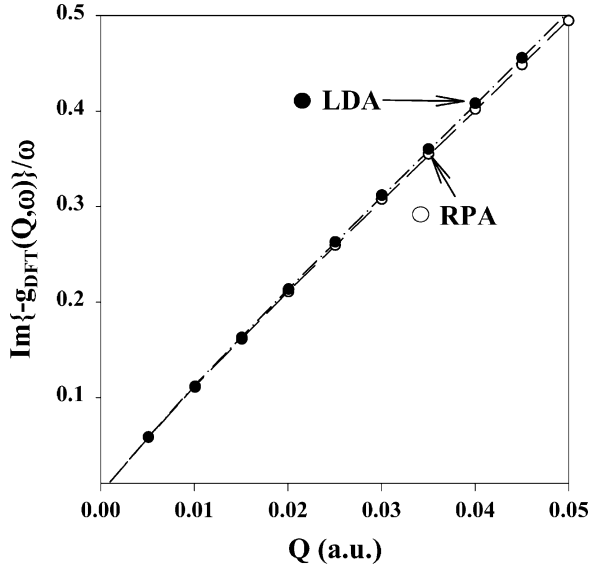

Fig. 12. Surface loss function divided by the frequency as a function of momentum transfer, Q. The calculations are performed for $\omega = 0.005$ a.u. Dashed line: RPA, dash-dotted line: LDA, Circles: fit with $F_{\mathrm{DFT}}(Q) = a_{\mathrm{DFT}} Q \ln(c_{\mathrm{DFT}}/Q)$.

As coefficients we find for RPA $a_{\mathrm{DFT}}^{\mathrm{RPA}} = 0.676$, $c_{\mathrm{DFT}}^{\mathrm{RPA}} = 1.1 \times 10^5$, and for LDA, $a_{\mathrm{DFT}}^{\mathrm{LDA}} = 0.640$, $c_{\mathrm{DFT}}^{\mathrm{LDA}} = 3.3 \times 10^5$. Inserting equations (90) and (91) into equation (19) the integration with respect to Q can again be done analytically leading to the stopping power in the form

$$S_{\mathrm{DFT}} = \frac{3 a_{\mathrm{DFT}} V}{16 b^4} [H_{\mathrm{DFT}} + \ln(b)], \tag{92}$$

where H_{DFT} is equal to $H_{\mathrm{DFT}}^{\mathrm{RPA}} = 11.08$ a.u. for RPA and $H_{\mathrm{DFT}}^{\mathrm{LDA}} = 12.16$ for LDA. This power law closely mirrors the one we found for particle–hole excitation in SRM.

5. COMPARISON BETWEEN SRM AND TDDFT

Figure 13 shows the surface loss function as a function of the momentum transfer Q for $\omega = 0.0037$ a.u. calculated in the framework of the SRM and TDDFT. Almost over the whole range of Q the loss function is significantly larger in DFT than in the SRM (Fig. 13a). Moreover, the loss function is smaller for the RPA kernel than the LDA kernel. This is due to the fact that the effective interaction potential is stronger in RPA than in LDA. The exchange correlation term in LDA reduces the repulsive interaction

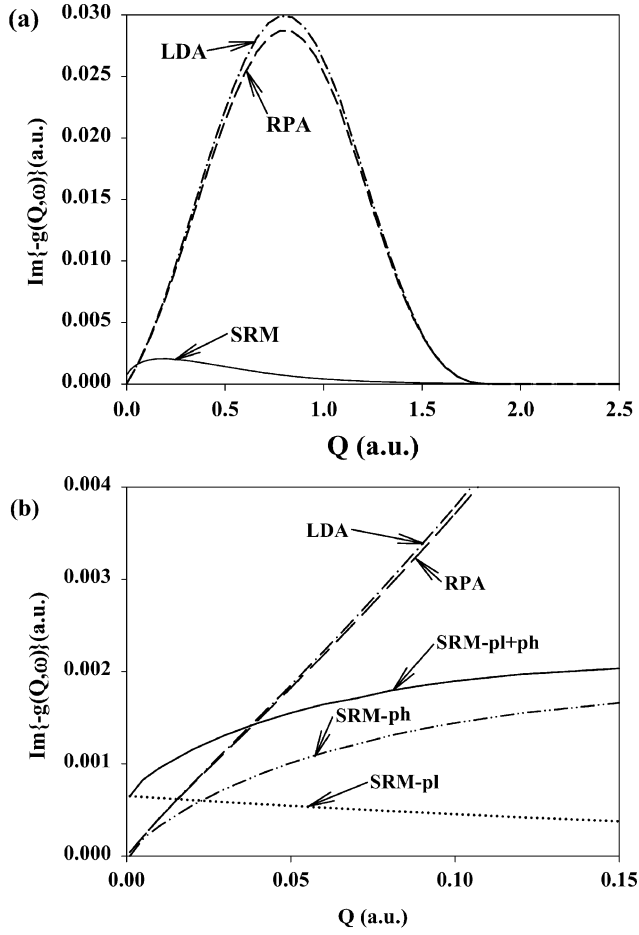

Fig. 13. Surface loss function as a function of momentum transfer Q at $\omega = 0.0037$ a.u. (a) for a wide range of Q, (b) enlarged for the case of small momentum transfers. Dash-dotted line: LDA, dashed line: RPA, solid line: SRM, SRM contributions due to plasmon excitation (dotted line) and particle–hole excitation (double-dotted dashed line).

potential, thereby increasing the polarizability of the surface electron density. The enhancement in LDA is only about 5% compared to RPA. We note here that this is in contradiction with the observation of Liebsch [68] where the difference between the LDA and RPA calculation at the peak position is about 60%.

For very small values of Q, however, (Fig. 13b) the order is reversed: below the critical value of Q ($Q_c \approx 0.04$ a.u.) the loss function within DFT drops below the SRM value. Decomposing the SRM loss function into its

plasmon and particle–hole contributions clearly indicates that the underestimate of width of the plasmon spectrum at $Q = 0$ in TDDFT is the main source for the smaller TDDFT values for $\mathrm{Im}[-g(Q, \omega)]$. The discrepancy is highlighted in detail in Fig. 14 where the surface loss functions as a function of frequency for various values of parallel momentum transfer are shown. The transition from the $Q \approx 0$ regime (Fig. 14a) where the SRM exceeds the TDDFT value to the regime where particle–hole excitation dominates and thus $\mathrm{Im}[-g(Q, \omega)]$ calculated in TDDFT is larger near $Q \gtrsim 0.04$ (Fig. 14b and c) is clearly seen.

Finally, the distance-dependent stopping power equation (20) near an Al surface with parallel velocity $v = 0.29$ a.u. is presented both for small to intermediate distances (Fig. 15a) and large distances (Fig. 15b). Our present calculations confirm the observation by Cazalilla and Garcia de Abajo [55] that at low velocities and in the vicinity of the surface large differences between the stopping power calculated within the framework of TDDFT and the one calculated with the SRM exist. The latter decreases faster with increasing distance than the former. This behavior directly mirrors the surface loss function at intermediate to large values of Q (see Fig. 14b and c). Also the results for the RPA and LDA kernels reflect corresponding differences between $\mathrm{Im}[-g_{\mathrm{DFT}}^{\mathrm{RPA}}]$ and $\mathrm{Im}[-g_{\mathrm{DFT}}^{\mathrm{LDA}}]$. At large distances (Fig. 15b) a completely different situation emerges. The stopping powers for RPA and LDA kernels are virtually indistinguishable (labeled as DFT) and fall below the value of the SRM at about ≈ 40 a.u. Obviously, this transition is related to the dominance of the plasmon contribution near $Q = 0$ missing in TDDFT because of the incorrect width of the plasmon resonance at small Q.

6. IMPROVEMENT OF TDDFT AT LARGE DISTANCES

The asymptotic analysis of the large-distance behavior of the stopping power immediately suggests remedies for the TDDFT. The underestimate of the width $\gamma(Q)$ of the plasmon line near $\omega_s(Q \approx 0)$ leads to an underestimate of the surface loss function near $\mathrm{Im}\, g(Q \approx 0, \omega \approx 0)$. With Q approaching zero, the energy and momentum conservation cannot be satisfied for decay of a plasmon in a single particle–hole excitation. At long-wavelengths $Q < Q_{\mathrm{ph}}$, where Q_{ph} is the wave number where the plasmon dispersion merges into the continuum of particle–hole excitations, plasmons do not suffer Landau damping. The energy conservation for the single particle–hole decay reads

$$\omega(Q) = \varepsilon_{\vec{P}+\vec{Q}} - \varepsilon_{\vec{P}} = \frac{Q^2}{2} + \vec{P}\vec{Q}, \tag{93}$$

and, therefore,

$$\lim_{Q \to 0} \omega(Q) = 0. \tag{94}$$

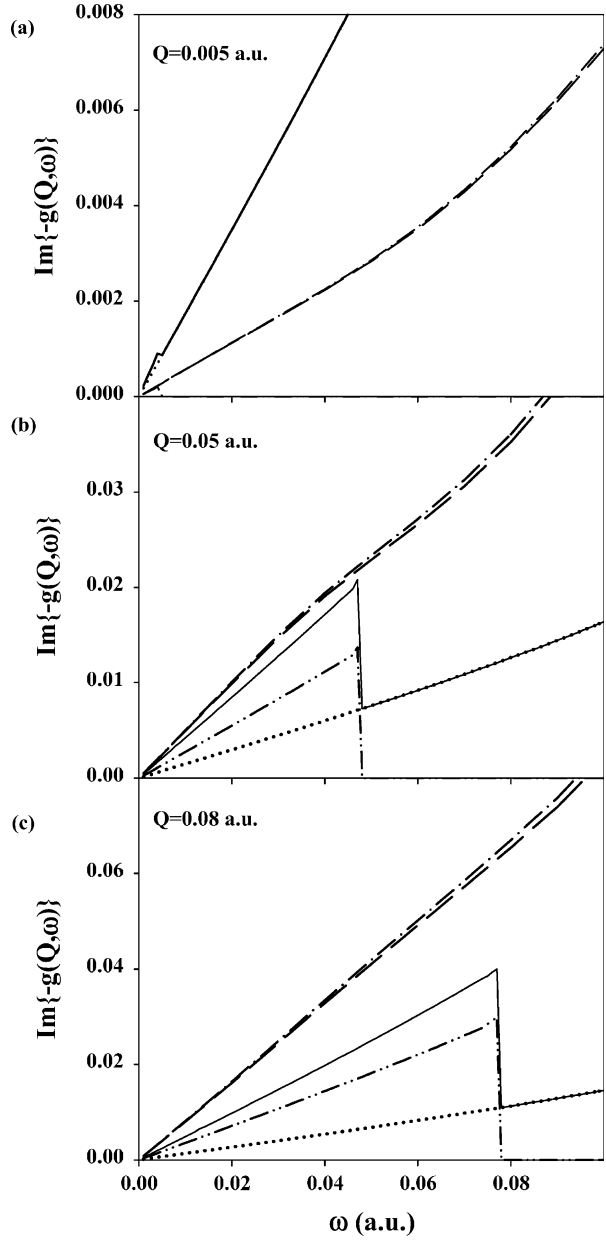

Fig. 14. Surface loss function as a function of frequency for various values of parallel momentum transfer. Dash-dotted line: LDA, dashed line RPA, solid line: SRM with dispersion s_3 (equation (36c)), SRM contributions due to plasmon excitation (dotted line) and particle–hole excitation (double-dotted dashed line).

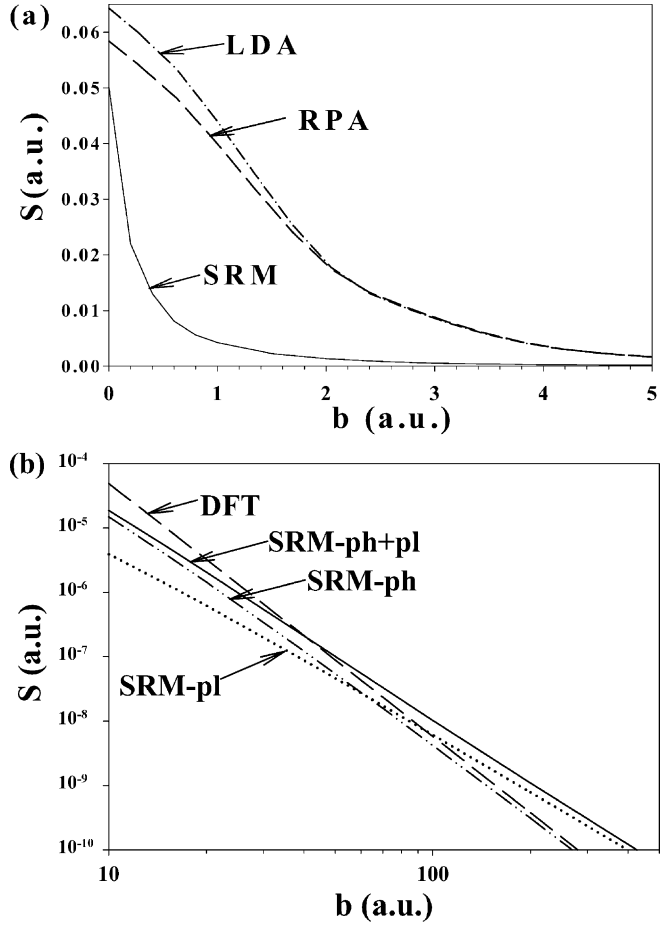

Fig. 15. Distance-dependent stopping power for a unit charge moving on a parallel trajectory with velocity $V = 0.29$ a.u. in front of an Al surface. Dash-dotted line: LDA, dashed line RPA, solid line: SRM. (a) Small to intermediate distances (linear scale), (b) large distances (log scale).

It is clear that at small values of Q the decay of plasmons with energy $\omega_s(Q = 0) > 0$ is suppressed. Ichimaru [73] has shown that the decay rate of the plasmon is proportional to Q^2. Therefore, it vanishes in the long-wavelength limit. The width at $\gamma(Q \approx 0)$ near $Q = 0$ is governed primarily by two processes: decay of the plasmon into a particle–hole excitation accompanied by momentum transfer to the lattice (phonons) and emission of pairs of particle–hole excitations [56]. These processes can be taken into account by shifting the plasmon pole in the complex plane near $Q = 0$ by an amount given by first-order perturbation theory, i.e., by Fermi's golden rule for these

processes. A simplified method to accomplish such a correction is suggested by the behavior of the surface loss function at small Q (see Fig. 13b). Below Q_c the surface loss function calculated within DFT, $\mathrm{Im}[-g_{\mathrm{DFT}}(Q,\omega)]$ crosses the line $\mathrm{Im}[-g_{\mathrm{SRM}}(Q,\omega)]$, because of the missing plasmon decay channels. We can simply correct for this deficiency by setting

$$\mathrm{Im}[-g^{\mathrm{pl}}_{\mathrm{DFT}}(Q,\omega)] = \mathrm{Im}[-g_{\mathrm{DFT}}(Q,\omega)] + \mathrm{Im}[-g^{\mathrm{pl}}_{\mathrm{SRM}}(Q,\omega)] \times\left[1+\exp\left(\frac{Q-Q_c}{Q_w}\right)\right]^{-1}. \quad (95)$$

In equation (95) $\mathrm{Im}[-g^{\mathrm{pl}}_{\mathrm{SRM}}]$ is the plasmon contribution (equation (45)) to the SRM, $\mathrm{Im}[-g_{\mathrm{DFT}}]$ stands for the TDDFT calculations using either the RPA or LDA kernels which give virtually identical results at small Q where the correction applies. The parameters entering equations (95) and (45) can be taken from perturbation theory for interband transitions and correlated two-electron processes. For Al, the critical point for the transition Q_c is at $Q_c \approx 0.04$ a.u. and the transition width is set to $Q_w \approx 0.01$ a.u. Figure 16 displays the position-dependent DFT stopping power, corrected for plasmon decay, $\mathrm{Im}[-g^{\mathrm{pl}}_{\mathrm{DFT}}]$, for a unit charge moving along a parallel trajectory with velocity $V = 0.29$ a.u. in front of an Al surface. This improved form of stopping power including plasmon decay (TDDFT-pl) significantly exceeds the SRM in the vicinity of the surface while approaching the SRM at large distances.

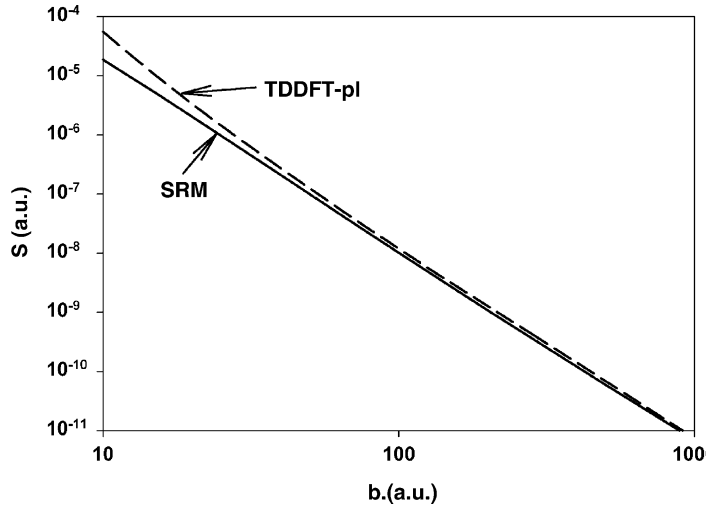

Fig. 16. Distance-dependent stopping power for a unit charge moving in a parallel trajectory with velocity $V = 0.29$ a.u. in front of an Al surface. dashed line: DFT-pl, solid line: SRM.

7. CONCLUSIONS

In summary, we have presented a detailed investigation of the asymptotic form of the stopping power for charged particles moving parallel to a metal surface at large distances. A comparative study of the linear response employing the SRM and TDDFT shows dramatic differences: in the vicinity of the surface the SRM underestimates the stopping power since it underestimates the local electron density that provides the drag force. At large distances, the roles are reversed: the TDDFT calculation for a jellium surface neglecting lattice effects and coupling to phonons underestimates the stopping power. The latter originates from the vanishing (surface) plasmon line width in the long-wavelength limit. Since the SRM contains the experimental line width on a phenomenological level, its asymptotic stopping power results in the correct power law $\sim(\text{distance})^{-3}$ and dominates over the TDDFT result $\sim(\text{distance})^{-4}$. We have proposed a simple extension of the TDDFT description that remedies this deficiency. While in the vicinity of the surface this new stopping power calculation gives values significantly larger than obtained by SRM, it converges to the SRM in the asymptotic region above the surface. We hope our results will stimulate experimental investigations of the surface dielectric response function at large distances probed by transmission of HCIs through microcapillaries or nanotubes [74]. It is worth noting that such a proposal resembles the measurement of electron energy loss of electrons transmitted through cylindrical microchannels [75, 76]. Higher charges and better defined classical trajectories of HCI should provide a favorable setting for probing the stopping power at large distances.

ACKNOWLEDGEMENTS

We gratefully acknowledge invaluable inspiration and guidance over many years by our friend and pioneer of this field, Rufus Ritchie. The work was supported by the Hungarian Scientific Research Found: OTKA No. T032306, the Austrian Fonds zur Förderung der wissenschaftlichen Forschung, FWF (Austria), the grant 'Bolyai' from the Hungarian Academy of Sciences, TéT A-19/2001, and EU under contract no. HPRI-CT-2001-50036.

REFERENCES

[1] A. Arnau, F. Aumayr, P. M. Echenique, M. Grether, W. Heiland, J. Limburg, R. Morgenstern, P. Roncin, S. Schippers, R. Schuch, N. Stolterfoht, P. Varga, T. J. M. Zouros and H. P. Winter, *Surf. Sci. Rep.*, 1997, **27**, 113.

[2] R. Morgenstern, in *Review paper at the X'96 International Conference on X-Ray and Inner-Shell Processes, Hamburg, 1996* (ed. B. Sonntag), AIP Proceedings, 1997.

[3] J. Burgdörfer, P. Lerner and F. W. Meyer, *Phys. Rev. A*, 1991, **44**, 5674.
[4] J. Burgdörfer, in *Review of Fundamental Processes and Applications of Atoms and Ions* (ed. C. D. Lin), World Scientific, Singapore, 1993, p. 517.
[5] T. Schenkel, *et al.*, *Prog. Surf. Sci.*, 1999, **61**, 23.
[6] F. Aumayr, J. Burgdörfer, P. Varga and H. P. Winter, *Comments At. Mol. Phys.*, 1999, **34**, 201.
[7] J. Burgdörfer, in *Scattering and Inverse Scattering in Pure and Applied Science* (eds E. R. Pike and P. C. Sabatier), Academic Press, London, 2001, p. 1081.
[8] H. Winter, C. Auth, R. Schuch and E. Beebe, *Phys. Rev. Lett.*, 1993, **71**, 1939.
[9] F. W. Meyer, L. Folkerts, I. G. Hughes, S. H. Overbury, D. M. Zehner, P. A. Zeijlmans van Emmichoven and J. Burgdörfer, *Phys. Rev. A*, 1993, **48**, 4479.
[10] J. Das and R. Morgenstern, *Comments At. Mol. Phys.*, 1993, **29**, 205.
[11] A. Arnau, R. Köhrbrück, M. Grether, A. Spieler and N. Stolterfoht, *Phys. Rev. A*, 1995, **51**, R3399.
[12] J. P. Briand, G. Giardino, G. Borsoni, M. Froment, M. Eddrief, C. Sébenne, S. Bardin, D. Schneider, J. Jin, H. Khemliche, Z. Xie and M. Prior, *Phys. Rev. A*, 1996, **54**, 4136.
[13] C. Lemell, H. P. Winter, F. Aumayr, J. Burgdörfer and F. W. Meyer, *Phys. Rev. A*, 1996, **53**, 880.
[14] Q. Yan, D. M. Zehner and F. W. Meyer, *Phys. Rev. A*, 1996, **54**, 641.
[15] C. Lemell, J. Stöckl, J. Burgdörfer, G. Betz, H. P. Winter and F. Aumayr, *Phys. Rev. Lett.*, 1998, **81**, 1965.
[16] J. J. Ducrée, F. Casali and U. Thumm, *Phys. Rev. A*, 1998, **57**, 338.
[17] X. M. Tong, D. Kato, T. Watanaba, H. Shimizu, C. Yamada and S. Ohtani, *Phys. Rev. A*, 2001, **63**, 052505.
[18] Y. Yamazaki, S. Ninomiya, F. Koike, H. Masuda, T. Azuma, K. Komaki, K. Kuroki and M. Sekiguchi, *J. Phys. Soc. Jpn*, 1996, **65**, 1199.
[19] Y. Yamazaki, *Phys. Scr. T*, 1997, **73**, 293.
[20] S. Ninomiya, Y. Yamazaki, F. Koike, H. Masuda, T. Azuma, K. Komaki, K. Kuroki and M. Sekiguchi, *Phys. Scr. T*, 1997, **73**, 316.
[21] S. Ninomiya, Y. Yamazaki, F. Koike, H. Masuda, T. Azuma, K. Komaki, K. Kuroki and M. Sekiguchi, *Phys. Rev. Lett.*, 1997, **78**, 4557.
[22] Y. Yamazaki, Invited papers of XXth ICPEAC, Vienna, 1997. in *Photonic, Electronic and Atomic Collisions* (eds F. Aumayr and H. P. Winter), World Scientific, Singapore, 1998, p. 693.
[23] H. Masuda and K. Fukuda, *Science*, 1995, **268**, 1466.
[24] H. Masuda and M. Satoh, *Jpn. J. Appl. Phys.*, 1996, **35**, L126.
[25] N. Stolterfoht, J. H. Bremer, V. Hoffmann, R. Hellhammer, D. Fink, A. Petrov and B. Sulik, *Phys. Rev. Lett.*, 2002, **88**, 133201.
[26] N. Stolterfoht, J. H. Bremer, V. Hoffmann, R. Hellhammer, Z. D. Pesic, D. Fink, A. Petrov and B. Sulik, *Nucl. Instrum. Methods B*, 2003, **203**, 246.
[27] K. Tőkési, L. Wirtz and J. Burgdörfer, *Nucl. Instrum. Methods B*, 1999, **154**, 307.
[28] K. Tőkési, L. Wirtz, C. Lemell and J. Burgdörfer, *Phys. Rev. A*, 2000, **61**, 020901(R).
[29] K. Tőkési, L. Wirtz, C. Lemell and J. Burgdörfer, *Nucl. Instrum. Methods B*, 2000, **164/165**, 504.
[30] N. R. Arista and M. A. Fuentes, *Phys. Rev. A*, 2001, **63**, 165401.
[31] N. R. Arista, *Phys. Rev. A*, 2001, **64**, 032901.
[32] K. Tőkési, L. Wirtz, C. Lemell and J. Burgdörfer, *Phys. Rev. A*, 2001, **64**, 042902.
[33] A. Selloni and R. Del Sole, *Surf. Sci.*, 1986, **168**, 35.
[34] K. Tőkési, D. Varga, L. Köver and T. Mukoyama, *J. Electron. Spectr. Relat. Phenom.*, 1995, **76**, 427.
[35] F. Yubero, S. J. M. Sanz, B. Ramskov and S. Tougaard, *Phys. Rev. B*, 1996, **53**, 9719.
[36] K. Tőkési, L. Köver, D. Varga and J. Tóth, *Surf. Rev. Lett.*, 1997, **4**, 955.

[37] M. Vicanek, *Surf. Interf. Anal.*, 1999, **440**, 1.
[38] C. M. Kwei, C. Y. Wang and C. J. Tung, *Surf. Interf. Anal.*, 1998, **26**, 682.
[39] S. Tanuma, S. Ichimura and K. Goto, *Surf. Interf. Anal.*, 2000, **30**, 212.
[40] W. S. M. Werner, *Surf. Interf. Anal.*, 2001, **31**, 141.
[41] K. Tőkési, X.-M. Tong, C. Lemell and J. Burgdörfer, *Phys. Scr. T*, 2001, **92**, 27.
[42] G. Gergely, *et al.*, *Surf. Interf. Anal.*, 2002, **33**, 410.
[43] R. H. Ritchie and A. L. Marusak, *Surf. Sci.*, 1966, **4**, 234.
[44] R. Núñez, P. M. Echenique and R. H. Ritchie, *J. Phys. C*, 1980, **13**, 4229.
[45] P. M. Echenique, R. H. Ritchie, N. Barberan and J. Inkson, *Phys. Rev. B*, 1981, **23**, 6486.
[46] W. Kohn and L. J. Sham, *Phys. Rev.*, 1965, **140**, 1133.
[47] E. K. U. Gross and W. Kohn, *Adv. Quantum Chem.*, 1990, **21**, 255.
[48] A. E. Eguiluz, *Phys. Rev. Lett.*, 1983, **51**, 1907.
[49] A. Liebsch, *Phys. Rev. B*, 1987, **36**, 7378.
[50] X.-M. Tong and S.-I. Chu, *Phys. Rev. A*, 1997, **55**, 3406.
[51] P. M. Echenique, R. M. Nieminen and R. H. Ritchie, *Solid State Commun.*, 1981, **37**, 779.
[52] I. Campillo, J. M. Pitarke and A. G. Eguiluz, *Phys. Rev. B*, 1998, **58**, 10307.
[53] A. Liebsch, *Electronic Excitations at Metal Surfaces*, Plenum Press, New York, 1997, and references in it.
[54] A. Garcia-Lekue and J. M. Pitarke, *Phys. Rev. B*, 2001, **64**, 035423.
[55] M. A. Cazalilla and F. J. Garcia de Abajo, *Nucl. Instrum. Methods B*, 1997, **125**, 106.
[56] P. Nozieres and D. Pines, *The Theory of Quantum Liquids*, Addision-Wesley, New York, 1990.
[57] F. J. Garcia de Abajo and P. M. Echinique, *Phys. Rev. B*, 1992, **46**, 2663.
[58] C. O. Reinhold and J. Burgdörfer, *Phys. Rev. A*, 1997, **55**, 450.
[59] D. M. Newns, *Phys. Rev. B*, 1970, **1**, 3304.
[60] T. L. Ferell, P. M. Echenique and R. H. Ritchie, *Solid State Commun.*, 1979, **32**, 419.
[61] J. Lindhard, *Kgl. Dan. Videns. K. Selsk. Mat. Fys. Medd.*, 1954, **28**, 8.
[62] W. Brandt and J. Reinheimer, *Phys. Rev. B*, 1970, **2**, 3104.
[63] R. H. Ritchie and A. Howie, *Phil. Mag.*, 1977, **36**, 463.
[64] R. H. Ritchie, R. N. Hamm, J. E. Turner, H. A. Wright and W. E. Bloch, *Basic Life Sci.*, 1992, **58**, 99.
[65] B. W. Ninham, C. J. Powell and N. Swanson, *Phys. Rev.*, 1966, **145**, 209.
[66] P. Zacharias, *J. Phys. F*, 1975, **5**, 645.
[67] E. P. Wigner, *Phys. Rev.*, 1934, **46**, 1002.
[68] A. Liebsch, *Phys. Rev. B*, 1997, **55**, 13263.
[69] J. Harris and A. Griffin, *Phys. Lett.*, 1971, **34A**, 51.
[70] P. J. Feibelman, *Phys. Rev. Lett.*, 1973, **30**, 975.
[71] P. J. Feibelman, *Phys. Rev. B*, 1974, **9**, 5077.
[72] P. J. Feibelman, *Prog. Surf. Sci.*, 1982, **12**, 287.
[73] S. Ichimaru, *Rev. Mod. Phys.*, 1997, **54**, 13263.
[74] K. Tőkési and J. Burgdörfer, *Surf. Sci.*, 2000, **454–456**, 1038.
[75] R. J. Warmack, R. S. Becker, V. E. Anderson, R. H. Ritchie, Y. T. Chu, J. Little and T. L. Ferell, *Phys. Rev. B*, 1984, **29**, 4375.
[76] K. C. Mamola, R. J. Warmack and T. L. Ferell, *Phys. Rev. B*, 1987, **35**, 2682.

Resonant-Coherent Excitation of Channeled Ions

F. J. García de Abajo[1] and V. H. Ponce[2]

[1] *Centro Mixto CSIC-UPV/EHU and Donostia International Physics Center (DIPC), Manuel de Lardizábal 4, 20018 San Sebastián, Spain*
[2] *Centro Atómico Bariloche, Comisión Nacional de Energía Atómica, 8400 San Carlos de Bariloche, Argentina*

Abstract

A theoretical description of charge transfer processes during ion channeling is presented, with special emphasis on coherent transitions originating in the periodicity of the crystal lattice. The interplay between coherent interaction with the periodic crystal lattice potential and inelastic electron–electron collisions is shown to be crucial in both intra-ionic transitions and electron loss from the ion. The mixing and energy shifting of the electronic states of the projectile is introduced *via* both the crystal potential, averaged over the ion trajectory, and the induced wake potential. A full calculation of the various electronic transitions occurring during ion channeling is offered and comparison with measured survival charge fractions is shown to result in excellent agreement when a detailed account of the necessary ingredients is incorporated, including the time evolution of the ion trajectory along the channel. One of these ingredients is electron loss from the projectile due to coherent interaction with the crystal lattice. It is shown, in particular, that the angular distribution of coherently emitted electrons is directed along preferential directions determined by the reciprocal crystal lattice.

Contents

ADVANCES IN QUANTUM CHEMISTRY, VOLUME 46
ISSN: 0065-3276 DOI 10.1016/S0065-3276(04)46003-1

1. INTRODUCTION

An ion moving under channeling conditions inside a crystal or near its surface is subject to the perturbation of both the static potential set up by the ordered atoms of the crystal and the induced potential originating in the charge density fluctuations produced by the presence of the ion. The periodic components of the crystal potential may induce transitions in the internal electronic state of the ion (coherent electron excitation [1–4] and electron capture and loss [5,6]) while leaving the state of the target unchanged. However, the induced potential produces changes in the electronic state of the target itself, like the creation of electron–hole pairs and collective plasmon modes, and this can occur either without modifying the internal electronic state of the projectile or accompanying simultaneous changes in the latter. The inelastic nature of the induced potential results in a retarding force acting back on the ion and producing stopping.

A theory suitable to deal with all of these mechanisms of charge transfer between projectile and target will be derived from first principles in this chapter, and will be illustrated with examples of numerical calculation and comparison with experiments. Special emphasis will be placed on the so-called resonant-coherent excitation (RCE), i.e., the excitation of the internal electronic state of the ion caused by the spatial periodicity of the lattice, which is experienced by the moving ion as a periodicity in time, enabling transitions of frequency corresponding to different harmonics contributing to the crystal potential. Okorokov [7] predicted this effect and later reported on experimental evidence for He^+ ions axially channeled in Ag [8,9]. Unsuccessful attempts to reproduce this result [10–12] led Datz *et al.* [1–4] to obtain the first solid experimental evidence of RCE for heavier ions, attributing previous negative results to the short lifetime of excited states of channeled He^+ ions, whose size is comparable to the channel width. In a set of elegant experiments, these authors observed the reduction in the transmission of fixed charge state hydrogenic ions of atomic number $Z_1 = 5–9$, axially channeled in Au and Ag crystals, when one of the harmonics of the crystal potential matches the energy difference between the electron ground state and some excited state, the latter being more easily ionizable than the former due to stronger interaction with the solid.

A large deal of work has been devoted to experimentally study charge state fractions of ions traversing solids under axial [13] and planar [13,14] channeling conditions, or scattered after surface channeling [15,16]. Most of these studies share in common the use of large velocities $v = 2–100$ a.u., which entail a comparatively weak interaction with the solid, thereby ensuring that the electronic states of the ions live long enough to exhibit well-defined resonances. However, long-lived states are also possible at lower ion velocities when the electronic states of the projectile lie inside a band gap of the crystal [17]. Some of the most relevant experimental work in

connection to charge transfer and RCE during ion channeling is reviewed in Table 1.

In order to study the charge state of channeled ions, it is convenient to separate the interaction between the moving ion and the crystal into two distinct contributions to the total potential: the static crystal potential, consisting of the interaction with all electrons and nuclei in the unperturbed medium, and the induced potential resulting from the distortion produced in the medium by the projectile. Notice that the so-called wake potential [48–51] corresponds to the part of the induced potential related to the perturbation of valence band electrons.

Under axial, planar, or surface channeling conditions, the trajectory forms a glancing angle with respect to the channel, and thus, the ion motion perpendicular to the crystal axis, plane, or surface, in each case, can be decoupled from the fast motion along the remaining direction *parallel* to the channel, leading to the concept of the so-called continuous axial, planar, or surface potential, respectively [52]. These are nothing but the average of the crystal potential over trajectories parallel to the channel with fixed impact parameter [32,52,53].

1.1. Ingredients needed to describe charge exchange during channeling

To be more specific, the following ingredients need to be incorporated to the theory: intra-ionic transitions connecting electronic bound states of the ion *via* frequency components of the crystal potential (Section 1.1.1); splitting and mixing of electronic states, originating in the net electric field created by both the induced wake potential and the continuous axial, planar, or surface potential, in each case [54,55] (Section 1.1.2); electron loss due to coherent excitation to the continuum (Section 1.1.3); non-coherent electron–electron collisions leading to (de-)excitation and electron loss (Section 1.1.4); electron capture from occupied states of the target (Section 1.1.5); and the ion trajectory, which accompanies the dynamical evolution of the electronic state of the ion (Section 1.1.6).

1.1.1. Resonant-coherent excitation

RCE can be regarded as an elastic process in the laboratory frame, in which the lattice acts like a source of momentum. RCE, in order to take place, requires that the energy difference between bound states lies near some of the harmonic energies of the crystal potential. The effect of the rest of the harmonics is negligible. RCE has been observed under both axial [1–3] and planar [4,43] channeling conditions, and more recently also in surface channeling conditions [17,19,27,29,35]. Experimental corroboration exists that some harmonics can be suppressed due to destructive interference

Table 1. Experimental studies of resonant-coherent excitation and charge state fractions of ions channeled through thin films and surfaces, ordered by projectile atomic number

Authors	Projectile → Target	Energy, MeV (Velocity, a.u.)	Trajectory
Gaillard *et al.* (1976) [13]	$H^+ \rightarrow$ Au, Ni	0.5–2 (4.5–8.9)	(111) plane[a–d]
			(110) plane[b–d]
			⟨110⟩ axis[c–e]
Winter *et al.* (1991) [18]	$H^+ \rightarrow$ Al	0.1–1.2 (2–6.9)	(111) surface[c,d]
Auth *et al.* (1997) [17–20]	H → LiF	(0.35–0.57)	(100) surface[f,g]
Hecht *et al.*(1998) [21,20]	H → LiF	(0.28–0.6)	(100) surface[g,h]
Berry *et al.* (1974) [11]	$He^+ \rightarrow$ Au	0.26–0.34 (1.6–1.8)	⟨110⟩ axis[d]
Kimura *et al.* (1988) [22]	$He^+ \rightarrow$ SnTe	0.5–1.9 (2.2–4.4)	(100) surface[d,i]
Fujii *et al.* (1989–1990) [23,24]	$He^+ \rightarrow$ Au	0.5–1.9 (2.2–4.4)	(100) plane[a,d,j]
	$He^+ \rightarrow$ SnTe		(100) plane[a,d,j]
Fujii *et al.* (1991) [25]	$He^+ \rightarrow$ SnTe	0.5–1.9 (2.2–4.4)	(100) surface[d]
Kimura *et al.* (1992) [16]	$He^{+,2+} \rightarrow$ SnTe	0.5 (2.2)	(100) surface[d,k]
Narumi *et al.* (1995) [26]	Li^+–$Li^{3+} \rightarrow$ SnTe	3.2 (4.3)	(100) surface[d,k]
Kimura *et al.* (1996–1998) [27–30]	$B^{4+} \rightarrow$ SnTe	4.5–6.5 (4.1–4.9)	(100) surface[h,l–o]
Datz *et al.* (1978–1979) [1–3]	$C^{5+} \rightarrow$ Au	16.5–24.7 (7.4–9.1)	⟨100⟩ axis[h,m]
Krause *et al.* (1993) [31]	$C^{5+} \rightarrow$ Si	5–35 (4.1–10.8)	⟨111⟩ axis[h,p]
Krause *et al.* (1994) [32]	C^{3+}–$C^{6+} \rightarrow$ Si	10–30 (5.8–10)	⟨100⟩ axis[l]
Datz *et al.* (1996) [33]	$C^{6+} \rightarrow$ Si	26 (9.3)	(100) plane[q]
Datz *et al.* (1978–1979) [1–3]	$N^{6+} \rightarrow$ Au	34.5–42 (9.9–11)	⟨100⟩ axis[h,m]
	$N^{6+} \rightarrow$ Au	16–35 (6.8–10)	⟨111⟩ axis[h,m]
Datz *et al.* (1979–1980) [3,4]	$N^{6+} \rightarrow$ Au	15–27 (6.5–8.8)	(100) plane[h]
	$N^{5+} \rightarrow$ Au	15–20 (6.5–7.6)	(100) plane[h]
Krause *et al.* (1993) [31]	$N^{6+} \rightarrow$ Si	13–42 (6.1–10.9)	⟨111⟩ axis[h,p]
Datz *et al.*(1995) [34]	$N^{6+} \rightarrow$ Au	45.5 (11.4)	(100) plane[h,r]
Hatke *et al.* (1997–1998) [35,36]	$N^{6+} \rightarrow$ Pt	21.8–23 (7.9–8.1)	(110) surface[h,r]
Datz *et al.* (1978–1979) [1–3]	$O^{7+} \rightarrow$ Au	38–45 (9.7–10.6)	⟨110⟩ axis[h,m]
Datz (1979) [3]	O^{5+}–$O^{8+} \rightarrow$ Au	40 (10)	⟨110⟩ axis[h]
Azuma *et al.* (1996) [14]	O^{6+}–$O^{8+} \rightarrow$ Si	103.5 (16.1)	(110) plane[d,q]
Datz *et al.* (1978–1979) [1–3]	$F^{8+} \rightarrow$ Au	34.6–45 (8.5–9.7)	⟨100⟩ axis[h,m]
	$F^{7+} \rightarrow$ Au	31–39.5 (8.1–9.1)	⟨100⟩ axis[h,m]
Fujimoto *et al.* (1988) [37]	$Ne^{9+} \rightarrow$ Au	75–100 (12.2–14.1)	⟨111⟩ axis[a,f]

Datz *et al.* (1991) [38]	$Mg^{11+} \rightarrow Au$	150–167 (15.7–16.6)	$\langle 100 \rangle$ axis[h,s]
Datz *et al.* (1995) [34]	$Mg^{11+} \rightarrow Ni$	607.8 (31.6)	$\langle 100 \rangle$ axis[h]
Datz *et al.* (1996) [33]	$Mg^{11+} \rightarrow Au$	157–178 (5.6–6.0)	$\langle 111 \rangle$ axis[f,h]
Forster *et al.* (1996) [39]	$Si^{13+} \rightarrow Si$	20–24 (5.3–5.8)	$\langle 112 \rangle$ axis [h]
		20–26 (5.3–6.1)	$\langle 111 \rangle$ axis[h]
Azuma *et al.* (1998–1999) [40–43]	$Ar^{17+} \rightarrow Si$	15580 (97)	(100) plane[g,h,l,m,q,t]
			(110) plane
			(111) plane
Azuma *et al.* (2003) [44]	$Ar^{17+} \rightarrow Si$	15580 (97)	(110) plane[f,t,u]
Ito *et al.* (2000–2003) [45,46]	$Ar^{17+} \rightarrow Si$	15580 (97)	(110) plane[f,g,t]
Nakai *et al.* (2003) [47]	$Ar^{17+} \rightarrow Si$	3755 (57.1)	(100) plane[g,h,l,t]
Datz *et al.* (1996) [33]	$Ti^{21+} \rightarrow Si$	225–375 (13.7–17.8)	$\langle 111 \rangle$ axis[r,v]

[a] Comparison with random orientation is offered.
[b] The variation of $[H^0]$ with angle of incidence is also analyzed.
[c] $[H^0]$ charge fractions of the order of 10^{-3}.
[d] RCE not detected.
[e] Amorphous target.
[f] RCE observed through X-ray yield.
[g] Dependence of RCE with respect to the azimuthal angle of incidence.
[h] RCE observed through charge state fractions.
[i] Comparison with transmission data.
[j] Dependence of charge fractions with incidence angle normal to the channel.
[k] Dependence on the angle of incidence.
[l] Analysis of the trajectories included.
[m] Dependence of the RCE and charge state fractions on a slight angular tilt with respect to the channel direction.
[n] Axially channeled ions along the [100] direction in the (001) surface. $B^{4+,5+}$ are detected, since the first electron is rapidly lost.
[o] Effect of surface steps analyzed *via* dependence on angles of incidence/scattering.
[p] Interference effects of the crystal potential in RCE.
[q] 2D maps of the dependence of ion transmission on the direction of emergence.
[r] Dependence of charge fractions on azimutal angle of incidence.
[s] Charge state fractions measured with different angles of acceptance.
[t] Outstanding identification of sublevel contributions to RCE and charge fractions.
[u] RCE detected *via* changes in convoy electron emission yield.

effects [31]. Moreover, both an increase in ionized charge state fractions [1–4,27] and an enhancement in the convoy electron yield on resonance have been reported [56].

When ions of large atomic number are considered (e.g., Mg^{11+}), they have chances to leave the crystal in an excited state after suffering RCE without further ionization, thus leading to the emission of X-rays by radiative de-excitation. This light emission has been experimentally observed [34,37,38, 57] and proved to be polarized in a way related to the channel geometry and the ion trajectory [34].

In a recent experiment, Auth *et al.* [17,19] have combined the detection of this type of light emission with the use of low-velocity ($v \sim 0.5$ a.u.) light projectiles such as H atoms reflected on a LiF surface, taking advantage of the large band gap of this material to minimize charge transfer between surface and projectile, a situation that increases the lifetime of the electronic states involved in the RCE, which is a necessary condition to have a sufficiently sharp resonance.

The theoretical development of RCE started with first-order perturbation treatments [9] and continued by solving a set of coupled-channel equations involving only the bound states relevant to the process [58] (i.e., K and L shells of hydrogenic ions). The observed energy shift and splitting of atomic levels bound to the channeled ions were satisfactorily explained by Crawford and Ritchie [54] in terms of the wake potential [48,49]. Early attempts to describe RCE at surfaces were also reported [59–61]. The shape of the resonance is well understood as originating in the dependence of the splitting along the ion trajectory [34,62,63]. Further analysis has shown a complex dynamical evolution of the electronic states under discussions along the trajectory of the ion [62,64].

1.1.2. Energy mixing and splitting of electronic states

The electronic states of the ion are mixed and energy split by interaction with the target. The resulting new basis of adiabatic states, among which RCE processes can occur, depends on the impact parameter of the ion in the channel, which varies along the trajectory [62]. This may modify the conditions for which RCE takes place, and in particular, this can depend strongly on the ion impact parameter across the channel (see Fig. 1).

1.1.3. Resonant-coherent excitation to the continuum: coherent loss

RCE can take place in such a way that the excited state lies in the continuum, leading to electron coherent loss (CL) [6]. This is similar to what happens in low-energy electron diffraction, where a plane wave is reflected on a surface along directions dictated by both energy conservation and a change in parallel momentum equal to a reciprocal surface lattice vector. Instead, the incoming electron is attached to the ion in the present context, and it

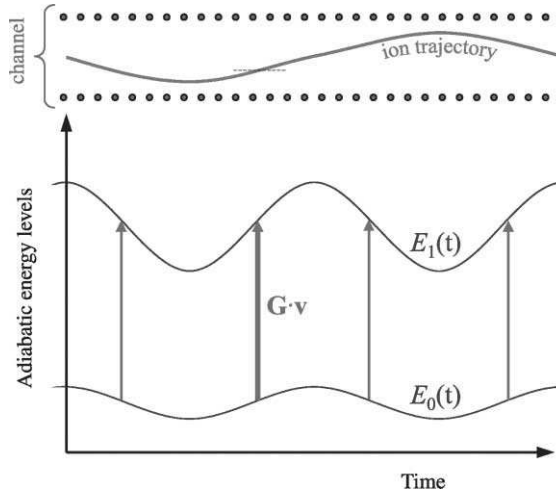

Fig. 1. Schematic representation of the trajectory of the ion as it moves along a channel defined by atomic walls in a crystal (upper part) and evolution of the adiabatic electronic states of the ion (lower part). The energy of the latter depends on the distance of the ion to the atomic walls, and there are certain positions along the trajectory for which the energy difference between two such states are in resonance with some harmonic **G** of the crystal potential (vertical arrows).

represents a finite-size distribution in momentum space centered around the ion velocity [5,65,66]. The bound states of the ion can be de-populated *via* this effect, introducing a width in the electronic adiabatic levels. It has been speculated for the case of surface channeling that coherently emitted electrons should travel with well-defined energy around preferential directions [66]. Experimental evidence of this type of electron emission is still missing. Also, for planar or axial channeling in the bulk, when very thin films and large projectile velocities are considered, the ejected electron may have a mean free path in the solid comparable to the film thickness, so that it may leave the target carrying direct information on the excitation process.

1.1.4. Inelastic processes

The creation of electron–hole pairs and plasmon excitations in the target needs to be considered as well in connection to the simultaneous promotion of a moving ion-bound electron, which can occur by absorbing energy out of the fast ion motion. The theory of this kind of two-electron Auger transitions was developed by Guinea *et al.* [67] to study charge state fractions of ions moving in an electron gas. Their model was extended later by Sols and Flores [65] to include capture from inner shells of target atoms and coherent processes of the sort discussed in Section 1.1.3. In the context of the present work, the importance of two-electron Auger processes in

the resulting charge state of fast-channeled ions was conclusively demonstrated by Datz *et al.* [38].

1.1.5. Electron capture

The ion may capture electrons from the target. In particular, electron capture from inner shells of target atoms may be important when the ion finds itself traveling very close to any plane or string of atoms of the crystal.

There is a fundamental difference between electron capture and two-electron Auger processes on one hand and the RCE and loss discussed in Sections 1.1.1 and 1.1.3 on the other. The latter are produced by periodic components of the static crystal-lattice potential, and hence they are elastic processes from the point of view of the target (i.e., the target does not change its internal state, since it only acts like a reservoir of momentum, while the projectile changes both its internal state and the momentum of its center of mass). Thus, RCE and CL are indeed coherent processes for which keeping track of the phase of the probability amplitudes is important. Quite differently, electron–electron collisions and electron capture are incoherent in the sense that they involve changes of the target state. In practice, the loss of a projectile electron *via* CL is inelastic, since the probability that the electron comes back to its original state is negligible and it will eventually interact inelastically with the solid. The same goes for the hole left behind during electron capture.

1.1.6. The ion trajectory

Finally, the ion moves following a nearly classical trajectory, which is governed by the continuous axial, planar, or surface potential, together with the image potential in the case of surface channeling [66], provided the ion energy is large enough to ensure a relatively negligible stopping.

We will present a formal derivation of the theory needed to deal with charge transfer processes during channeling in Section 2 and calculated results for RCE will be shown and compared with experiments later on in this chapter. Atomic units (a.u., $e = \hbar = m = 1$) will be used from now on, unless otherwise specified.

2. THEORETICAL FRAMEWORK

A semi-classical formalism will be followed to describe the time evolution of the projectile electronic state. The ion trajectory will be governed by the continuous channel potential and considered to be unaffected by charge transfer processes, while the electronic state itself will be described by the Schrödinger equation.

Let us focus, for simplicity, on a hydrogenic ion of atomic number Z_1 moving under planar or surface channeling conditions, so that the position of the projectile nucleus evolves according to $\mathbf{r}_p(t) = (\mathbf{R}_p + \mathbf{v}t, z_p(t))$, where $\mathbf{v}$ stands for the ion velocity parallel to the channel plane or surface. The generalization of this situation to multi-electron ions or axial channeling adds no conceptual difficulty. In what follows, upper case vectors will denote components parallel to the channel or surface, respectively, and z will represent the perpendicular direction. In practice, the time of interaction with the target will be sufficiently small to guarantee that the parallel velocity $\mathbf{v}$ remains nearly constant and the effect of ion energy loss on the trajectory is negligible.

Channeling conditions require that the trajectory forms small angles at any point with the channel direction, and therefore, $z_p(t)$ is a slowly varying function of the time. This permits distinguishing two different time scales: the fast motion along the channel and the slow modulations of the trajectory in the normal direction.

The quantum states of the entire system (ion–target) can be safely separated into two different parts corresponding to the state of the electron bound to the ion and the state of the target, respectively. The state of this composite can be written as

$$|\Phi\rangle = \sum_{\mu n} a_{\mu n}\, \mathrm{e}^{-\mathrm{i}\varepsilon_{\mu n} t} |\mu n\rangle, \tag{1}$$

where $a_{\mu n}$ is the amplitude of stationary state $|\mu n\rangle$ of energy $\varepsilon_{\mu n}$, and μ and n denote electronic and target quantum numbers, respectively. In particular $n = 0$ will refer to the ground state of the target.

The evolution of the composite wave function is described by the Schrödinger equation,

$$(\hat{H}_0 + \hat{U})|\Phi\rangle = \mathrm{i}\frac{\partial}{\partial t}|\Phi\rangle, \tag{2}$$

where $\hat{H}_0$ is the non-interacting part, i.e., $\hat{H}_0|\mu n\rangle = \varepsilon_{\mu n}|\mu n\rangle$, and $\hat{U}$ describes the ion–target interaction. The latter can be written as

$$\hat{U} = Z_1 \hat{V}(\mathbf{r}_p) - \hat{V}(\mathbf{r}_p + \mathbf{r}), \tag{3}$$

where both the target nuclear potential and the electronic degrees of freedom of the target are incorporated in $\hat{V}$, and the dependence on the projectile-electron coordinate $\mathbf{r}$ relative to the ion center of mass comes exclusively *via* the second term.

Part of this interaction is represented by the static crystal potential, which corresponds to the average of $\hat{V}$ in the target ground state $|n = 0\rangle$. Owing to

the periodicity of the crystal in its ground state, one can write

$$V^{\mathrm{C}}(\mathbf{r}_{\mathrm{p}}+\mathbf{r}) = \langle 0|\hat{V}(\mathbf{r}_{\mathrm{p}}+\mathbf{r})|0\rangle = \sum_{\mathbf{G}} V^{\mathrm{C}}_{\mathbf{G},z_{\mathrm{p}}(t)+z}\, \mathrm{e}^{\mathrm{i}\mathbf{G}\cdot(\mathbf{R}_{\mathrm{p}}+\mathbf{R}+\mathbf{v}t)}, \tag{4}$$

where the sum is extended over reciprocal lattice vectors parallel to the surface or channel, $\mathbf{G}$.

The local average value of V^{C} along the trajectory for a given impact parameter z_{p},

$$\bar{V}^{\mathrm{C}}(\mathbf{R}_{\mathrm{p}}+\mathbf{R}, z_{\mathrm{p}}+z) = \sum_{\mathbf{G}\cdot\mathbf{v}=0} V^{\mathrm{C}}_{\mathbf{G},z_{\mathrm{p}}+z}\, \mathrm{e}^{\mathrm{i}\mathbf{G}\cdot(\mathbf{R}_{\mathrm{p}}+\mathbf{R})}, \tag{5}$$

plays an important role in mixing and splitting bound energy levels, and also in determining the ion trajectory.

Projecting equation (2) on the basis of stationary states introduced above, one finds the following infinite set of coupled-channel equations:

$$\mathrm{i}\frac{\mathrm{d}a_{\mu n}}{\mathrm{d}t} = \sum_{\mu' n'} \langle \mu n|\hat{U}|\mu' n'\rangle \exp[\mathrm{i}(\varepsilon_{\mu n} - \varepsilon_{\mu' n'})t] a_{\mu' n'}. \tag{6}$$

It is convenient to define a finite subspace P consisting of the target ground state together with a selected set of relevant bound states of the projectile electron (e.g., K and L shells). The remaining orthogonal subspace Q contains all kinds of excited states of the target and projectile electron states. This separation permits one to reduce equation (6) to a finite set of relevant coupled equations limited to subspace P, which can be solved numerically. This is described in detail in Appendix A, where the following two steps have been followed:

(a) First, the amplitude of each Q state is calculated within first-order perturbation theory, assuming that the P-state amplitudes remain constant during a sufficiently long time interval. This is a reasonable assumption far from resonance, which is the situation discussed in Appendix A. However, when two P states are on resonance, their amplitudes exhibit rapid Rabi oscillations and one has to follow a different procedure: during a short period of time, they can be calculated from equation (6) by neglecting all transitions to Q states; when the resulting oscillating amplitudes are used in the right-hand side of equation (6) to calculate Q-state amplitudes, one obtains the same expressions as in the off-resonance situation (this analysis is a straightforward generalization of Appendix A and it will not be given here).

(b) The Q-state amplitudes calculated in this way are inserted back into equation (6) for $|\mu n\rangle \in P$. Then, the right-hand side of the equation can be rearranged in order to be expressed in terms of the amplitudes of P

states and some coupling rates representing the leakage of electron probability from P due to transitions to Q states. A finite set of equations is obtained for the amplitudes of P states.

The final result, derived in Appendix A, reads

$$\mathrm{i}\frac{\mathrm{d}a_\alpha}{\mathrm{d}t} = \sum_\beta \Sigma_{\alpha\beta}\, \mathrm{e}^{\mathrm{i}(\varepsilon_\alpha-\varepsilon_\beta)t} a_\beta + \sum_{\beta,\mathbf{G}} V^{\mathrm{C}}_{\alpha\beta,\mathbf{G}}\, \mathrm{e}^{\mathrm{i}(\varepsilon_\alpha-\varepsilon_\beta-\mathbf{G}\cdot\mathbf{v})t} a_\beta, \tag{7}$$

where α and β denote the electronic part of P states, and

$$\Sigma_{\alpha\beta} = V_{\alpha\beta} - \frac{\mathrm{i}}{2}(\Gamma^{\mathrm{CL}}_{\alpha\beta} + \Gamma^{\mathrm{Auger}}_{\alpha\beta}) \tag{8}$$

represents complex self-energy matrix elements. Here, the resonant term

$$V^{\mathrm{C}}_{\alpha\beta,\mathbf{G}} = -\langle\alpha|V^{\mathrm{C}}_{-\mathbf{G},z_\mathrm{p}+z}\, \mathrm{e}^{-\mathrm{i}\mathbf{G}\cdot(\mathbf{R}+\mathbf{R}_\mathrm{p})}|\beta\rangle$$

connects states $|\alpha\rangle$ and $|\beta\rangle$ *via* the harmonic $\mathbf{G}$ of the crystal potential; the rates $\Gamma_{\alpha\beta}$ account for the leakage of electron probability due to both coherent excitation to the continuum (i.e., CL),

$$\Gamma^{\mathrm{CL}}_{\alpha\beta} = 2\pi \sum_{k\in Q}\sum_{\mathbf{G}} \langle\alpha|V^{\mathrm{C}}_{\mathbf{G},z_\mathrm{p}+z}\, \mathrm{e}^{\mathrm{i}\mathbf{G}\cdot\mathbf{R}}|k\rangle\langle k|V^{\mathrm{C}}_{-\mathbf{G},z_\mathrm{p}+z}\, \mathrm{e}^{-\mathrm{i}\mathbf{G}\cdot\mathbf{R}}|\beta\rangle\delta(\varepsilon_k - \varepsilon_\beta - \mathbf{G}\cdot\mathbf{v}), \tag{9}$$

and incoherent electron–electron Auger processes,

$$\Gamma^{\mathrm{Auger}}_{\alpha\beta} = \sum_\mu \int_0^\infty \frac{\mathrm{d}\omega}{2\pi} \int \frac{\mathrm{d}\mathbf{q}}{(2\pi)^3} \frac{16\pi^2}{q^2} \mathrm{Im}\left\{\frac{-1}{\varepsilon(q,\omega)}\right\} \times \langle\alpha|\mathrm{e}^{\mathrm{i}\mathbf{q}\cdot\mathbf{r}}|\mu\rangle\langle\mu|\mathrm{e}^{-\mathrm{i}\mathbf{q}\cdot\mathbf{r}}|\beta\rangle\delta(\varepsilon_\mu - \varepsilon_\beta + \omega - \mathbf{q}\cdot\mathbf{v}); \tag{10}$$

and

$$V_{\alpha\beta} = -\langle\alpha|\bar{V}^{\mathrm{C}} + (Z_1 - 1/2)\phi_{\mathrm{wake}}|\beta\rangle, \tag{11}$$

where ϕ_{wake} is the wake potential induced by a unit charge [5,68,69]. The 1/2 term stands for the electron self-interaction. In the case of surface channeling, ϕ_{wake} may have a smooth dependence on the time, introduced through the surface-atom separation, but even in planar channeling it will contain a z_p dependence due to the different charge density of valence electrons for different positions across the channel, since deeply bound target electrons will also give a small contribution to the induced potential.

3. DYNAMICAL MIXING OF ELECTRONIC STATES

RCE is produced by the second term in the right-hand side of equation (7). In our picture, the energies ε_α are time independent. However, we can define an adiabatic basis set obtained by diagonalizing the first term in the right-hand side of equation (7)

$$\sum_\beta V_{\alpha\beta} a_\beta^\lambda = (E_\lambda - \varepsilon_\alpha) a_\alpha^\lambda, \tag{12}$$

where a_α^λ is the projection of perturbed state $|\phi_\lambda\rangle$ (of energy E_λ) on to unperturbed state $|\alpha\rangle$ (of energy ε_α). Then, the energies of this adiabatic basis set of states depend on the position of the ion relative to the channel, and therefore, they evolve with time as the ion moves along the channel. This is schematically depicted in Fig. 1, where one can see that the condition for RCE occurs at specific values of the position of the ion with respect to the crystal atomic walls.

The dependence of the adiabatic states on the ion position is due to both the crystal potential and the induced wake potential (equation (11)). The crystal potential has been calculated by summing up the contributions coming from all target atoms in the Ziegler, Biersack, and Littmark approximation [70,71]. This neglects many-body effects in the crystal potential that are not so important in this context because of the electron-transition energies under consideration.

For the wake potential, a dielectric formalism has been followed [5,68] (also to obtain Auger matrix elements [5,69]). Use has been made of the random-phase-approximation dielectric function [72] for a homogeneous electron gas of density corresponding to the average over the ion trajectory along several target atom spacings. For surface channeling, the situation is more complicated due to the role played by collective surface excitations (surface plasmons) in the induced potential. This is clearly observed in the induced wake potential produced by a point charge moving parallel to an aluminum surface for different impact parameters of the charge relative to the surface, as shown in Fig. 2. Oscillations of frequency $\omega_s = \omega_p/\sqrt{2}$ (surface plasma frequency) are observed outside the metal ($z > 0$), whereas bulk plasma oscillations of frequency ω_p show up as well when the charge is moving inside the medium.

A specific example of adiabatic-state energies that will become useful later on is shown in Fig. 3 for Mg^{11+} hydrogen-like ions moving with a velocity of 31.6 a.u. in a (100) channel of a Ni crystal. The relevant states within the P subspace are those of the K and L shells of the ion. In particular, L states are degenerate outside the crystal and they are mixed and energy shifted due to the noted interaction. Figure 3 represents the energy difference between the 1s state and the adiabatic states of the L shell. The p state

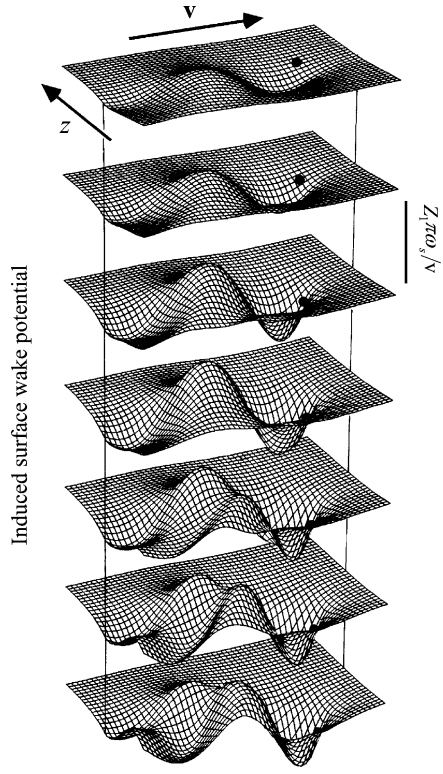

Fig. 2. Induced surface wake potential created by a charged particle of charge Z_1 moving with constant velocity $v = 2$ a.u. parallel to an aluminum surface for various impact parameters: $z/L = 0.4$, 0.2, 0, -0.2, -0.4, -0.6, and -0.8 (from top to bottom), where $L = \pi v/2\omega_s$ (4.04 Å) and ω_s is the surface plasmon energy. The surface, represented by vertical lines, is placed at $z = 0$. Each grid extends from $z = -L$ to L along the surface normal, and from $x = -4L$ to L along the direction of motion. The subdivisions in the grids correspond to squares of side $L/10$. The particle (black circles) is located at $x = 0$ and is moving from left to right.

perpendicular to the paper does not mix with the other L states. However, a complex pattern of evolution is observed for the mixing of the latter. The actual shape of the four adiabatic states of the L shell is shown in the insets. Notice that the state $\lambda = 1$ is oriented towards the channel wall, and consequently, it can be more easily populated by RCE than the rest [34].

Under the same conditions as in Fig. 3 the impact-parameter dependence of transition rates (9) and (10), are represented in Fig. 4 in order to illustrate the interplay between coherent (Γ^{CL}, solid curves) and Auger (Γ^{AL}, dashed curves) electron-loss mechanisms: incoherent Auger processes are dominant near the channel mid-planes, whereas coherent ionization dominates in

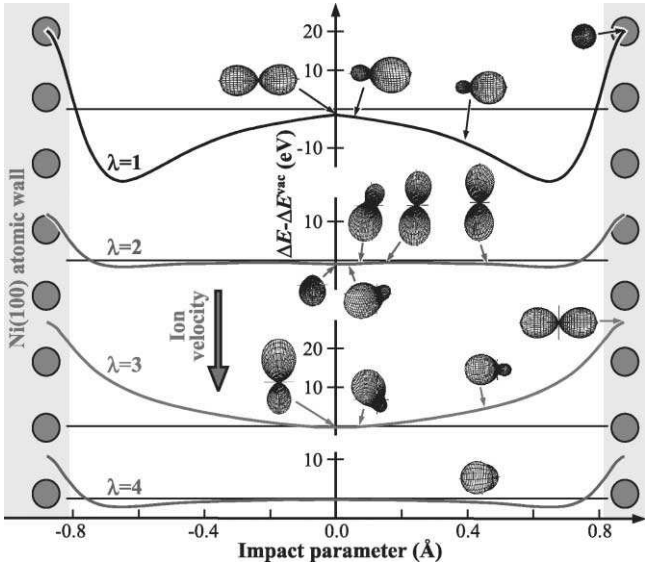

Fig. 3. Transition energies between the 1s state and the hybrid adiabatic states of the L shell of a 25 MeV/amu Mg^{11+} ion moving parallel to a (100) planar channel of a Ni crystal as a function of distance from the channel mid-plane (impact parameter). The energy differences ΔE are given relative to the vacuum value, ΔE^{vac}. The shape of the electronic wave function of the different excited states is shown for various positions in the channel by means of the accompanying insets. They represent the radial integral of the squared electron wave function. The ion moves from top to bottom.

the vicinity of the atomic walls. The rate of Auger excitation is also shown for completeness (Γ^{AE}, dot-dashed curves). The latter can be in turn divided into Auger loss (AL) and Auger (de-)excitation (AE) to different bound states: $\Gamma_{\alpha\beta}^{\mathrm{Auger}} = \Gamma_{\alpha\beta}^{\mathrm{AL}} + \Gamma_{\alpha\beta}^{\mathrm{AE}}$, depending whether the state k lies in the continuum of the ion or in any of its excited states. These two contributions are of the same order of magnitude.

4. RESONANT-COHERENT EXCITATION TO THE CONTINUUM

Let us analyze in more detail the CL processes described by equation (9). It is convenient to notice that only some **G** vectors contribute significantly, since form factors like $\langle\alpha|V_{\mathbf{G},z_{\mathrm{p}}+z}\,\mathrm{e}^{\mathrm{i}\mathbf{G}\mathbf{R}}|k\rangle$ take very small values unless $(k_x, k_y) \simeq \mathbf{G}$, and this condition can be made consistent with the conservation of energy, expressed through the δ function, only for specific **G** vectors. This has been taken into account in the calculation of the CL rate shown in Fig. 4.

For planar or surface channeling, the direction of emission of the lost electrons can be obtained from the construction shown in Fig. 5. This is

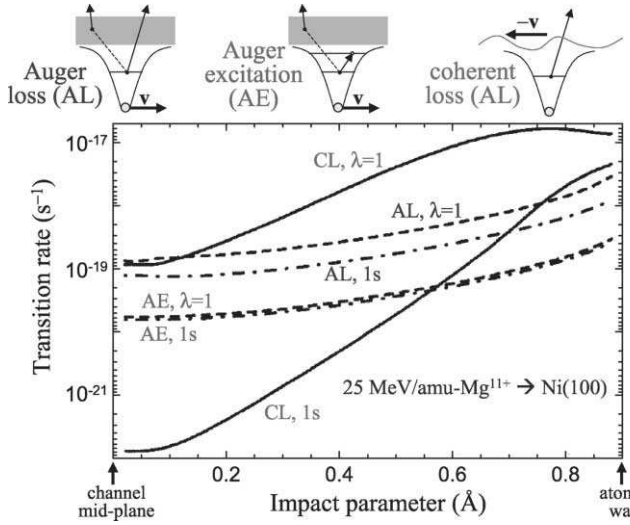

Fig. 4. Impact-parameter dependence of the transition rates involving 1s and $\lambda = 1$ states (see Fig. 3). Γ^{CL} (coherent-loss; solid curves), Γ^{AL} (Auger loss, which is a part of equation (10); dashed curves), and Γ^{AE} (Auger excitation, the remaining part of equation (10); dot-dashed curves) are calculated under the same conditions as in Fig. 3. The insets above the plot are intended to show schematically the processes under consideration.

similar to momentum transfer in low-energy electron diffraction [73], except that the ejected electrons are now represented by a distribution that is centered around the ion velocity in momentum space. The width of such distribution is determined by the Fourier transform of the bound electron initial wave function, and it is of the order of $1/Z_1$, which is typically smaller than the distance between adjacent **G** points.

This means that CL can produce the emission of electrons with well-defined momentum along preferential directions. This is actually the case shown in Fig. 6. A detailed calculation of the trajectory and the corresponding time-evolution of the electronic states of the ion has been performed to obtain the data represented in the figure [66]. This corroborates the idea that CL leads to preferential directions of emission.

5. FULL CALCULATION AND COMPARISON WITH EXPERIMENT

The electron evolves non-adiabatically in part, in the sense that the excited electron wave function retains during long times (of the order of the period

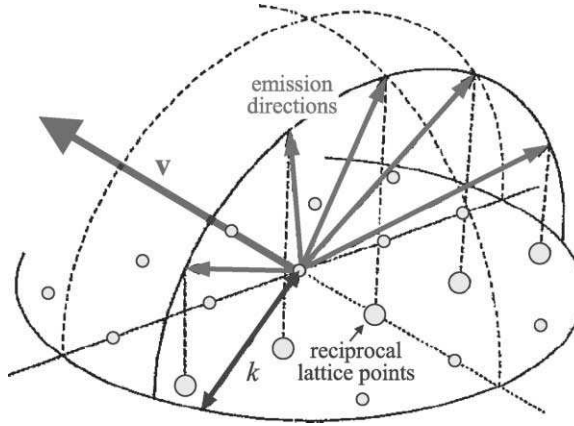

Fig. 5. Schematic construction of the direction of emission in the coherent loss process for surface or planar channeling. The reciprocal lattice vectors of the surface or plane, **G**, are represented by hollow circles (see equation (9)). The construction makes use of the sphere of constant electron momentum k in the rest frame of the ion. Coherently lost electrons are promoted to such sphere and the directions of emission are preferentially given by the points whose projection on the surface or plane coincides with one of the **G** vectors.

of the trajectory oscillations in the channel) the character of the original adiabatic state to which it was promoted [63]. So, the features associated to RCE can only be fully understood through a detailed calculation that incorporates the time evolution of the ion trajectory and its electronic state.

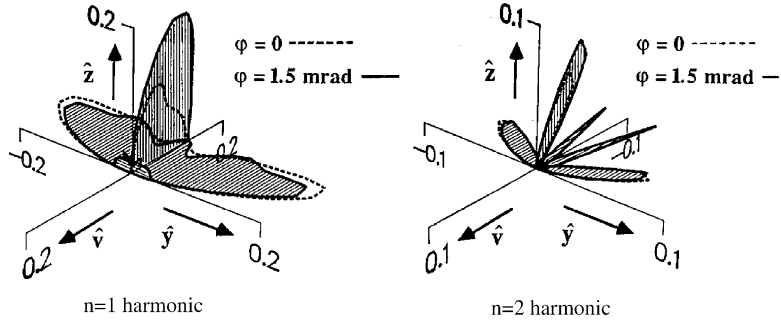

Fig. 6. Angular distribution of coherently emitted electrons after scattering of 2.5 MeV He^+ ions on a W(100) surface with two different grazing angles of incidence (see labels). The ions are directed along a ⟨100⟩ azimuthal direction. The emission is shown for the two first crystal-potential harmonics ($\mathbf{G}\cdot\mathbf{v} = 2\pi n v/a$, where $n = 1-2$ and $a = 3.16$ Å is the lattice constant) along the direction of motion.

The electron transition energy of resonance $\Delta E_{\rm res}$ depends on the orientation of the trajectory *via* $\mathbf{G}\cdot\mathbf{v}$ (see equation (7)). For an ion moving parallel to a (100) surface or planar channel of an fcc crystal, like that considered in Fig. 3, one has

$$\frac{\Delta E_{\rm res} a}{2\pi v\gamma} = k\cos\varphi + l\sin\varphi, \tag{13}$$

where $\gamma = 1/\sqrt{1 - c^2/v^2}$ accounts for the relativistic Lorentz contraction of the lattice constant a, φ is the angle between the ion velocity and a $\langle 100\rangle$ direction, and (k, l) are integers such that $k + l$ is an even number. Equation (13) can be combined with the data displayed in Fig. 3 to obtain the impact parameter at which the resonance condition is fulfilled as a function of the angle φ [62]. For example, for $\varphi = 26.2°$ the $\lambda = 1$ state of Fig. 3 is in resonance with the 1s state at the impact parameter indicated by the dotted lines of Fig. 7.

The Schrödinger equation (7) has been solved numerically for a trajectory corresponding to the dashed line shown in Fig. 7. The Auger and RCL processes have been neglected for simplicity and the ion trajectory has been calculated using the ZBL inter-atomic potential. The electron of the hydrogenic Mg^{11+} ions under consideration was initially prepared in the ground state 1s. The solid line shows the probability of finding the electron in

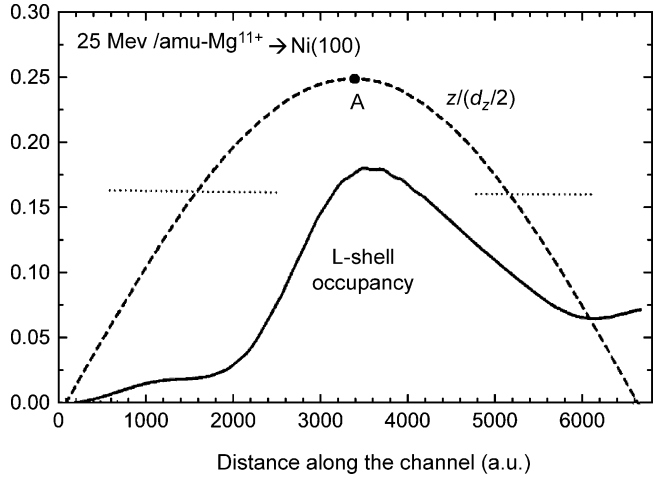

Fig. 7. Under the same conditions as in Fig. 3, the probability of occupancy of the L shell (solid curve) is shown along the trajectory of the ion (dashed curve) when the ion velocity forms an angle $\varphi = 26.2°$ with respect to a $\langle 100\rangle$ direction within the plane. The projectile is prepared in the 1s state initially. The dotted horizontal bars indicate the impact parameter of the resonance with the $\lambda = 1$ state.

an excited state within the L shell as a function of the distance along the direction parallel to the channel. Notice that RCE occurs after the ion has crossed the resonance. A more detailed analysis of this particular example shows that the evolution of the electron as the ion evolves in the channel is not adiabatic [62], and this explains partly why the occupancy does not change suddenly at the resonant impact parameters. On the way back to the channel mid-plane, the resonant-coherent interaction acts in the sense of reducing the population of excited states (resonant-coherent de-excitation).

This reduction can be complete for certain impact parameters z_A, as shown in Fig. 8, where the occupancy of the L shell at the end of the trajectory shown in the inset is shown for an ion initially prepared in the ground state 1s. Each point of the curve corresponds to a different trajectory as a function of the trajectory amplitude z_A. The oscillations observed in the figure are familiar in the study of potential-curve crossing of low-energy ions [74].

Finally, Fig. 9 represents the probability that a Mg^{11+} ion survives after crossing a thin Ni film as shown in the inset (i.e., Mg^{11+} fraction on exit). By changing the angle within the planar channel, one can tune the energy of resonance according to equation (13), giving rise to the structure shown in the figure [63]. In the calculation, the beam has been considered to enter the film parallel to the channel planes with no divergence. An average

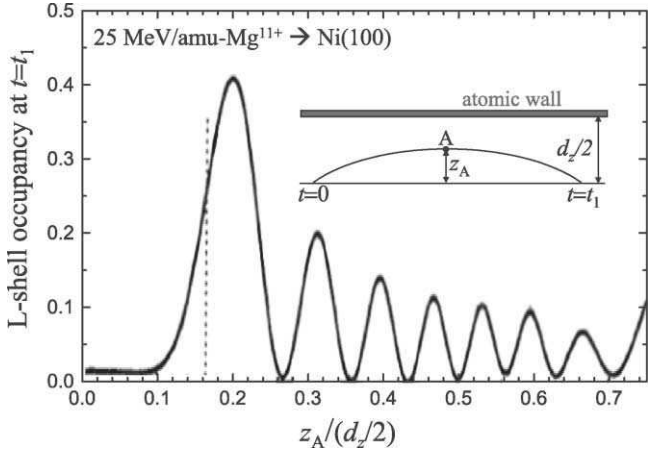

Fig. 8. Probability that an electron prepared in the ground state at time $t = 0$ is in the L shell at time $t = t_1$ due to RCE for different impact parameters z_A, under the same conditions as in Fig. 3. The ion trajectory is schematically shown in the inset. The angle with respect to a $\langle 100 \rangle$ direction within the plane has been taken $\varphi = 26.2°$. The dotted line shows the distance at which the state $\lambda = 1$ in Fig. 3 is in resonance with the (2,0) harmonic (see equation (13)). Finally, d_z represents the channel width.

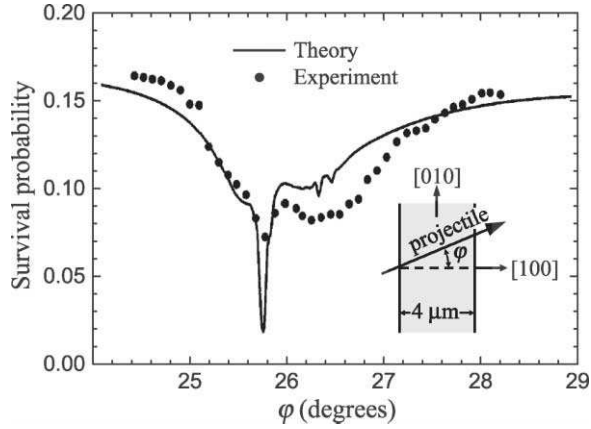

Fig. 9. Survival fraction of 25 MeV/amu Mg^{11+} ions after passing through a (100) planar channel of a 4000 Å thick Ni single crystal. φ is the angle between the velocity and a $\langle 100 \rangle$ direction within the channel plane. The inset represents a top view of the channel. The faces of the crystal are perpendicular to that direction. Solid line: present theory, multiplied by a factor of 0.3 to fit the experimental point corresponding to $\varphi = 28°$. Circles: experiment [34].

over initial impact parameters has been performed. The agreement between theory and experiment is relatively good, and the main features of the survival probability curve are well reproduced.

ACKNOWLEDGEMENTS

This work has been partially supported by the Basque Departamento de Educación, Universidades e Investigación, the University of the Basque Country UPV/EHU (Contract No. 00206.215-13639/2001), and the Spanish Ministerio de Ciencia y Tecnología (Contract No. MAT2001-0946).

APPENDIX A. COUPLED CHANNEL EQUATIONS FOR THE RELEVANT BOUND STATES

This appendix describes the steps required to obtain equation (7). An electron originally bound to the ion will be singled out in what follows, and it is the evolution of this electron that we shall be considering.

Let us start by introducing in the states of the electron–target system an explicit dependence both on the target state n and on the quantum numbers of the relevant electron. The index of the latter will be denoted α for a subset

of electron states bound to the ion, k for the rest of states, and μ for both of them. Then, the matrix elements of the ion–target interaction operator that appears in the coupled-channel set of equations (6) take the form, according to equation (3),

$$\langle \mu n|\hat{U}|\mu' n'\rangle = \frac{1}{A}\sum_{\mathbf{Q}} \mathrm{e}^{\mathrm{i}\mathbf{Q}\cdot(\mathbf{R}_\mathrm{p}+\mathbf{v}t)}[Z_1\delta_{\mu\mu'}\langle n|V_{\mathbf{Q},z_\mathrm{p}}|n'\rangle - \langle \mu n|V_{\mathbf{Q},z_\mathrm{p}+z}\,\mathrm{e}^{\mathrm{i}\mathbf{Q}\cdot\mathbf{R}}|\mu' n'\rangle], \tag{A1}$$

where $V_{\mathbf{Q},z_\mathrm{p}}$ is the interaction potential in momentum space along the directions parallel to the channel plane or surface and A is the area of the entire surface (or plane). In particular, for elastic channels (i.e., $n = n' = 0$) one finds

$$\langle \mu 0|\hat{U}|\mu' 0\rangle = \sum_{\mathbf{G}} \mathrm{e}^{\mathrm{i}\mathbf{G}\cdot(\mathbf{R}_\mathrm{p}+\mathbf{v}t)}[Z_1\delta_{\mu\mu'}V^\mathrm{C}_{\mathbf{G},z_\mathrm{p}} - \langle \mu|V^\mathrm{C}_{\mathbf{G},z_\mathrm{p}+z}\,\mathrm{e}^{\mathrm{i}\mathbf{G}\cdot\mathbf{R}}|\mu'\rangle],$$

where $V^\mathrm{C}_{\mathbf{G},z}$ are Fourier components of the crystal potential (see equation (4)). The lattice symmetry is reflected in the use of 2D reciprocal lattice vectors, $\mathbf{G}$. Notice that $\langle \mu n|\hat{U}|\mu' n'\rangle$ does not possess this symmetry, in general, for excited states of the target $|n\rangle$ and $|n'\rangle$, so that the summation over $\mathbf{Q}$ in equation (A1) is dense.

Now, we proceed to integrate equation (6) for the states of the subset Q considered in Section 2 (i.e., $|\mu n\rangle$, with $n \neq 0$, and $|k0\rangle$ with k belonging to Q) over a time interval $\Delta t = t - t_0$, assuming that only P states $|\alpha 0\rangle$ contribute to the right-hand side of the equation (first-order perturbation theory). In other words, the occupancy of Q states will be considered to be much smaller than that of $|\alpha 0\rangle$, since coherence is quickly lost during the evolution of the electron in the former. Furthermore, it will be assumed that $z_b(t)$, and hence also the crystal potential at the position of the ion, does not change significantly during the time interval Δt. Finally, $a_{\alpha 0}$ will be taken to remain practically constant during that period of time [75]. Then, one finds

$$a_{\mu,n>0} = \frac{-1}{A}\sum_{\alpha,\mathbf{Q}} a_{\alpha 0}[Z_1\delta_{\mu\alpha}\langle n|V_{\mathbf{Q},z_\mathrm{p}}|0\rangle - \langle \mu n|V_{\mathbf{Q},z_\mathrm{p}+z}\,\mathrm{e}^{\mathrm{i}\mathbf{Q}\cdot\mathbf{R}}|\alpha 0\rangle] \times \mathrm{e}^{\mathrm{i}\mathbf{Q}\cdot\mathbf{R}_\mathrm{p}}\,\frac{\mathrm{e}^{\mathrm{i}(\varepsilon_{\mu n}-\varepsilon_{\alpha 0}+\mathbf{Q}\cdot\mathbf{v})t} - \mathrm{e}^{\mathrm{i}(\varepsilon_{\mu n}-\varepsilon_{\alpha 0}+\mathbf{Q}\cdot\mathbf{v})t_0}}{\varepsilon_{\mu n} - \varepsilon_{\alpha 0} + \mathbf{Q}\cdot\mathbf{v}},$$

and

$$a_{k0} = \sum_{\alpha,\mathbf{G}} a_{\alpha 0}\langle k|V^\mathrm{C}_{\mathbf{G},z_\mathrm{p}+z}\,\mathrm{e}^{\mathrm{i}\mathbf{G}\cdot\mathbf{R}}|\alpha\rangle \mathrm{e}^{\mathrm{i}\mathbf{G}\cdot\mathbf{R}_\mathrm{p}}\,\frac{\mathrm{e}^{\mathrm{i}(\varepsilon_{k0}-\varepsilon_{\alpha 0}+\mathbf{G}\cdot\mathbf{v})t} - \mathrm{e}^{\mathrm{i}(\varepsilon_{k0}-\varepsilon_{\alpha 0}+\mathbf{G}\cdot\mathbf{v})t_0}}{\varepsilon_{k0} - \varepsilon_{\alpha 0} + \mathbf{G}\cdot\mathbf{v}}.$$

Substituting these amplitudes back into equation (6) and taking the $\Delta t \to \infty$ limit, consistent with trajectories nearly parallel to the channel,

one obtains

$$\mathrm{i}\frac{\mathrm{d}a_\alpha}{\mathrm{d}t} = \sum_\beta a_\beta (A_{\alpha\beta} + B_{\alpha\beta} + C_{\alpha\beta}), \tag{A2}$$

where $a_{\alpha 0}$ has been abbreviated as a_α,

$$A_{\alpha\beta} = \sum_{\mathbf{G}} \mathrm{e}^{\mathrm{i}(\varepsilon_\alpha - \varepsilon_\beta - \mathbf{G}\cdot\mathbf{v})t}\, \mathrm{e}^{-\mathrm{i}\mathbf{G}\cdot\mathbf{R}_\mathrm{p}} [Z_1 \delta_{\alpha\beta} V^\mathrm{C}_{-\mathbf{G},z_\mathrm{p}} - \langle\alpha| V^\mathrm{C}_{-\mathbf{G},z_\mathrm{p}+z}\, \mathrm{e}^{-\mathrm{i}\mathbf{G}\cdot\mathbf{R}} |\beta\rangle], \tag{A3}$$

$$B_{\alpha\beta} = -\mathrm{i}\pi \sum_{\mathbf{G}\mathbf{G}'} \sum_k \mathrm{e}^{\mathrm{i}(\varepsilon_\alpha - \varepsilon_\beta - \mathbf{G}'\cdot\mathbf{v})t}\, \mathrm{e}^{-\mathrm{i}\mathbf{G}'\cdot\mathbf{R}_\mathrm{p}} \delta(\varepsilon_k - \varepsilon_\beta - \mathbf{G}\cdot\mathbf{v}) \times \langle\alpha| V^\mathrm{C}_{\mathbf{G}-\mathbf{G}',z_\mathrm{p}+z}\, \mathrm{e}^{\mathrm{i}(\mathbf{G}-\mathbf{G}')\cdot\mathbf{R}} |k\rangle\langle k| V^\mathrm{C}_{-\mathbf{G},z_\mathrm{p}+z}\, \mathrm{e}^{-\mathrm{i}\mathbf{G}\cdot\mathbf{R}} |\beta\rangle, \tag{A4}$$

and

$$C_{\alpha\beta} = -\frac{\mathrm{i}\pi}{A^2} \sum_{\mathbf{Q}\mathbf{Q}'} \sum_{\mu,n>0} \mathrm{e}^{\mathrm{i}(\varepsilon_\alpha - \varepsilon_\beta - \mathbf{Q}'\cdot\mathbf{v})t}\, \mathrm{e}^{-\mathrm{i}\mathbf{Q}'\cdot\mathbf{R}_\mathrm{p}} \delta(\varepsilon_{\mu n} - \varepsilon_{\beta 0} - \mathbf{Q}\cdot\mathbf{v}) \times [Z_1 \delta_{\alpha\mu} \langle 0| V_{\mathbf{Q}-\mathbf{Q}',z_\mathrm{p}} |n\rangle - \langle\alpha 0| V_{\mathbf{Q}-\mathbf{Q}',z_\mathrm{p}+z}\, \mathrm{e}^{\mathrm{i}(\mathbf{Q}-\mathbf{Q}')\cdot\mathbf{R}} |\mu n\rangle] \times [Z_1 \delta_{\beta\mu} \langle n| V_{-\mathbf{Q},z_\mathrm{p}} |0\rangle - \langle\mu n| V_{-\mathbf{Q},z_\mathrm{p}+z}\, \mathrm{e}^{-\mathrm{i}\mathbf{Q}\cdot\mathbf{R}} |\beta 0\rangle]. \tag{A5}$$

The identity

$$\lim_{\Delta t\to\infty} \frac{1 - \mathrm{e}^{-\mathrm{i}\Delta E \Delta t}}{\Delta E} = \mathrm{i}\pi\delta(\Delta E),$$

has been used to derive these expressions taking $\Delta E = \varepsilon_{\mu n} - \varepsilon_{\beta 0} - \mathbf{Q}\cdot\mathbf{v}$ in equation (A5) and $\Delta E = \varepsilon_k - \varepsilon_\beta - \mathbf{G}\cdot\mathbf{v}$ in equation (A4).

The terms proportional to Z_1 in equation (A3) and Z_1^2 in equation (A5) are independent of the electron state, and therefore they represent an overall energy shift that can be disregarded in the present analysis. The remaining terms in equations (A3)–(A5) permit us to reduce equation (A2) to the form of equation (7). More precisely,

(1) $A_{\alpha\beta}$. The last summation on the right-hand side of equation (7) comes from the remaining term in equation (A3), which contains the oscillatory perturbation that leads to RCE. The part of that sum over reciprocal lattice vectors such that $\mathbf{G}\cdot\mathbf{v} = 0$ permits defining a continuous channel potential that enters equations (7) and (8) *via* the first term in equation (11).

(2) $B_{\alpha\beta}$. When α and β have very different energy (e.g., if one of them belongs to the K shell and the other to the L shell), $B_{\alpha\beta}$ represents a small contribution to $\alpha \to \beta$ transitions involving non-resonant

intermediate states in the continuum, k. However, when their energy difference is small (i.e., if either $\alpha = \beta$ or they belong to the L shell), $B_{\alpha\beta}$ describes RCE of the electron to the continuum ($\mathbf{G}' = 0$ term), and it can be recast as the self-energy contribution given by equation (9).

(3) $C_{\alpha\beta}$. This term gives rise to non-resonant contributions coming from the excitation and polarization of the target. In particular, the part proportional to Z_1 can be expressed in terms of the so-called wake potential [5,68], whereas the remaining part describes excitations of the electron to the continuum due to the screened interaction with the target. We will approximate the response of the target by that of an infinite electron gas with density equal to the time-averaged local density at the position of the moving ion. Then, the summation over target excitations can be dumped into the dielectric function of such an electron gas, $\varepsilon(\mathbf{q}, \omega)$, using the well-known relation [76]

$$\mathrm{Im}\left\{\frac{-1}{\varepsilon(\mathbf{q},\omega)}\right\} = \frac{4\pi^2}{q^2}\sum_n |\langle 0|\rho(\mathbf{q})|n\rangle|^2 \delta(\omega - \omega_{n0}), \qquad \omega > 0,$$

where ρ is the electron density operator and ω_{n0} are excitation energies. Working in 3D momentum space $\mathbf{q}$ with real space volume ω and retaining only $\mathbf{q}' = 0$ terms (this assumes translational invariance in the response function), one finds from equation (A5)

$$C_{\alpha\beta} = -\frac{\mathrm{i}}{2\Omega}\sum_{\mathbf{q}}\int_0^\infty \frac{\mathrm{d}\omega}{2\pi}\frac{16\pi^2}{q^2}\sum_\mu \mathrm{e}^{\mathrm{i}(\varepsilon_\alpha - \varepsilon_\beta)t}\delta(\varepsilon_\mu - \varepsilon_\beta + \omega - \mathbf{q}\cdot\mathbf{v})$$
$$\times \mathrm{Im}\left\{\frac{-1}{\varepsilon(\mathbf{q},\omega)}\right\}[Z_1\delta_{\alpha\mu} - \langle\alpha|\mathrm{e}^{\mathrm{i}\mathbf{q}\cdot\mathbf{r}}|\mu\rangle][Z_1\delta_{\beta\mu} - \langle\mu|\mathrm{e}^{-\mathrm{i}\mathbf{q}\cdot\mathbf{r}}|\beta\rangle],$$

which yields a real potential proportional to Z_1 acting on the electron, as written in equation (11) in terms of the wave potential, and a contribution to the self-energy *via* Auger transitions (equation (10)).

REFERENCES

[1] S. Datz, C. D. Moak, O. H. Crawford, H. F. Krause, P. F. Dittner, J. G. del Campo, J. A. Biggerstaff, P. D. Miller, P. Hvelplund and H. Knudsen, *Phys. Rev. Lett.*, 1978, **40**, 843.

[2] C. D. Moak, S. Datz, O. H. Crawford, H. F. Krause, P. F. Dittner, J. G. del Campo, J. A. Biggerstaff, P. D. Miller, P. Hvelplund and H. Knudsen, *Phys. Rev. B*, 1979, **19**, 977.

[3] S. Datz, *J. Physique Colloque*, 1979, **40**, C1.

[4] S. Datz, C. D. Moak, O. H. Crawford, H. F. Krause, P. D. Miller, P. F. Dittner, J. G. del Campo, J. A. Biggerstaff, H. Knudsen and P. Hvelplund, *Nucl. Instrum. Methods Phys. Res. B*, 1980, **170**, 15.

[5] P. M. Echenique, F. Flores and R. H. Ritchie, *Solid State Phys.*, 1990, **43**, 229.

[6] F. J. García de Abajo and J. M. Pitarke, *Nucl. Instrum. Methods Phys. Res. B*, 1994, **90**, 222.

[7] V. V. Okorokov, *JETP Lett.*, 1965, **2**, 111.

[8] V. V. Okorokov, D. L. Tolchenkov, I. S. Khizhnyakov, Y. N. Cheblukov, Y. Y. Lapitski, G. A. Iferov and Y. N. Zhukova, *JETP Lett.*, 1972, **16**, 415.
[9] V. V. Okorokov, D. L. Tolchenkov, I. S. Khizhnyakov, Y. N. Cheblukov, Y. Y. Lapitski, G. A. Iferov and Y. N. Zhukova, *Phys. Lett. A*, 1973, **43**, 485.
[10] M. J. Gaillard, J.-C. Poizat, J. Remillieux and M. L. Gaillard, *Phys. Lett. A*, 1973, **45**, 306.
[11] H. G. Berry, D. S. Gemmell, R. E. Holland, J.-C. Poizat, J. Remillieux and J. N. Worthington, *Phys. Lett. A*, 1974, **49**, 123.
[12] M. Mannami, H. Kudo, M. Matsushita and K. Ishii, *Phys. Lett. A*, 1977, **64**, 136.
[13] M. J. Gaillard, J.-C. Poizat, J. Remillieux, A. Chateau-Thierry, A. Gladieux and W. Brandt, *Nucl. Instrum. Methods*, 1976, **132**, 547.
[14] T. Azuma, K. Komaki, M. Yamagata, Y. Yamazaki, M. Sekiguchi, T. Hattori and T. Hasegawa, *Nucl. Instrum. Methods Phys. Res. B*, 1996, **115**, 310.
[15] K. Kimura, Y. Fujii, M. Hasegawa, Y. Susuki and M. Mannami, *Phys. Rev. B*, 1988, **38**, 1052.
[16] K. Kimura, H. Ohtsuka and M. Mannami, *Phys. Rev. Lett.*, 1992, **68**, 3797.
[17] C. Auth, A. Mertens, H. Winter, A. G. Borisov and F. J. García de Abajo, *Phys. Rev. Lett.*, 1997, **79**, 4477.
[18] H. Winter, R. Kirsch and J. C. Poizat, *Phys. Rev. A*, 1991, **67**, R1660.
[19] C. Auth and H. Winter, *Phys. Rev. A*, 2000, **62**, 12903.
[20] H. Winter, C. Auth and T. Hecht, *Vacuum*, 2002, **66**, 137.
[21] T. Hecht and H. Winter, *Phys. Lett. A*, 1998, **243**, 306.
[22] K. Kimura, Y. Fujii, M. Hasegawa, Y. Susuki and M. Mannami, *Phys. Rev. B*, 1988, **38**, 1052.
[23] Y. Fujii, K. Sueoka, K. Kimura and M. Mannami, *J. Phys. Soc. Jpn*, 1989, **58**, 2758.
[24] Y. Fujii, K. Sueoka, K. Kimura and M. Mannami, *Radiat. Effects*, 1990, **114**, 239.
[25] Y. Fujii, S. Fujiwara, K. Kimura and M. Mannami, *Nucl. Instrum. Methods Phys. Res. B*, 1991, **58**, 18.
[26] K. Narumi, Y. Fujii, K. Toba, K. Kimura and M. Mannami, *Nucl. Instrum. Methods Phys. Res. B*, 1995, **100**, 1.
[27] K. Kimura, H. Ida, M. Fritz and M. Mannami, *Phys. Rev. Lett.*, 1996, **76**, 3850.
[28] M. Mannami, K. Kimura, K. Narumi, M. Yamamoto and S. Naito, *Nucl. Instrum. Methods Phys. Res. B*, 1997, **125**, 97.
[29] K. Kimura and M. Mannami, *Phys. Rev. A*, 1998, **57**, 1121.
[30] K. Kimura, S. Ooki, H. Ida and M. Mannami, *Nucl. Instrum. Methods Phys. Res. B*, 1998, **135**, 419.
[31] H. F. Krause, S. Datz, P. F. Dittner, N. L. Jones and C. R. Vane, *Phys. Rev. Lett.*, 1993, **71**, 348.
[32] H. F. Krause, J. H. Barrett, S. Datz, P. F. Dittner, N. L. Jones, J. G. del Campo and C. R. Vane, *Phys. Rev. A*, 1994, **49**, 283.
[33] S. Datz, H. F. Krause and C. R. Vane, *Nucl. Instrum. Methods Phys. Res. B*, 1996, **115**, 363.
[34] S. Datz, P. F. Dittner, H. F. Krause, C. R. Vane, O. H. Crawford, J. S. Forster, G. S. Ball, W. G. Davies and J. S. Geiger, *Nucl. Instrum. Methods Phys. Res. B*, 1995, **100**, 272.
[35] N. Hatke, M. Dirska, M. Grether, E. Luderer, A. Robin, A. Nrmann and W. Heiland, *Phys. Rev. Lett.*, 1997, **79**, 3395.
[36] N. Hatke, M. Dirska, E. Luderer, A. Robin, M. Grether, A. Närmann and W. Heiland, *Nucl. Instrum. Methods Phys. Res. B*, 1998, **135**, 307.
[37] F. Fujimoto, K. Komaki, A. Ootuka, E. Vilalta, Y. Iwata, Y. Hirao, T. Hasegawa, M. Sekiguchi, A. Mizobuchi, T. Hattori and K. Kimura, *Nucl. Instrum. Methods Phys. Res. B*, 1988, **33**, 354.

[38] S. Datz, P. F. Dittner, J. G. del Campo, K. Kimura, K. F. Krause, T. M. Rosseel and C. R. Vane, *Radiat. Effects*, 1991, **117**, 73.
[39] J. S. Forster, G. C. Ball, W. G. Davies, J. S. Geiger, J. U. Andersen, J. A. Davies, H. Geissel and F. Nickel, *Nucl. Instrum. Methods Phys. Res. B*, 1996, **115**, 363.
[40] T. Azuma, T. Ito, Y. Yamazaki, K. Komaki, M. Sano, M. Torikoshi, A. Kitagawa, E. Takada and T. Murakami, *Nucl. Instrum. Methods Phys. Res. B*, 1998, **135**, 61.
[41] K. Komaki, T. Azuma, T. Ito, Y. Takabayashi, Y. Yamazaki, M. Sano, M. Torikoshi, A. Kitagawa, E. Takada and T. Murakami, *Nucl. Instrum. Methods Phys. Res. B*, 1998, **146**, 19.
[42] K. Komaki, *Nucl. Instrum. Methods Phys. Res. B*, 1998, **135**, 16.
[43] T. Azuma, T. Ito, K. Komaki, Y. Yamazaki, M. Sano, M. Torikoshi, A. Kitagawa, E. Takada and T. Murakami, *Phys. Rev. Lett.*, 1999, **83**, 528.
[44] T. Azuma, Y. Takabayashi, T. Ito, K. Komaki, Y. Yamazaki, E. Takada and T. Murakami, *Nucl. Instrum. Methods Phys. Res. B*, 2003, **212**, 397.
[45] T. Ito, Y. Takabayashi, K. Komaki, T. Azuma, Y. Yamazaki, S. Datz, E. Takada and T. Murakamic, *Nucl. Instrum. Methods Phys. Res. B*, 2000, **164/165**, 68.
[46] T. Azuma, T. Muranaka, Y. Takabayashi, T. Ito, C. Kondo, K. Komaki, Y. Yamazaki, S. Datz, E. Takada and T. Murakami, *Nucl. Instrum. Methods Phys. Res. B*, 2003, **205**, 779.
[47] Y. Nakai, T. Ikeda, Y. Kanai, T. Kambara, N. Fukunishi, T. Azuma, K. Komaki, Y. Takabayashi and Y. Yamazaki, *Nucl. Instrum. Methods Phys. Res. B*, 2003, **205**, 784.
[48] J. Neufeld and R. H. Ritchie, *Phys. Rev.*, 1955, **98**, 1632.
[49] P. M. Echenique, R. H. Ritchie and W. Brandt, *Phys. Rev. B*, 1979, **20**, 2567.
[50] F. J. García de Abajo and P. M. Echenique, *Phys. Rev. B*, 1993, **48**, 13399.
[51] P. M. Echenique, F. J. García de Abajo, V. H. Ponce and M. E. Uranga, *Nucl. Instrum. Methods Phys. Res. B*, 1995, **96**, 583.
[52] S. Datz, C. D. Moak, T. S. Noggle, B. R. Appelton and H. O. Lutz, *Phys. Rev.*, 1969, **179**, 315.
[53] F. Abel, G. Amsel, M. Bruneaux, C. Cohen and A. L'Hoir, *Phys. Rev. B*, 1976, **13**, 993.
[54] O. H. Crawford and R. H. Ritchie, *Phys. Rev. A*, 1979, **20**, 1848.
[55] J. P. Rozet, A. Chetioui, P. Bouisset, D. Vernhet, K. Wohrer, A. Touati, C. Stephan and J. P. Grandin, *Phys. Rev. Lett.*, 1987, **58**, 337.
[56] K. Kimura, J. P. Gibbons, S. B. Elston, C. Biedermann, R. DeSerio, N. Keller, J. C. Levin, M. Breinig, J. Burgdörfer and I. A. Sellin, *Phys. Rev. Lett.*, 1991, **66**, 25.
[57] Y. Iwata, K. Komaki, Y. Yamazaki, M. Sekiguchi, T. Hattori, T. Hasegawa and F. Fujimoto, *Nucl. Instrum. Methods Phys. Res. B*, 1990, **48**, 163.
[58] Y. H. Ohtsuki, *Charged Beam Interaction with Solids*, Taylor & Francis, London, 1983.
[59] E. Kupfer, H. Gabriel and J. Burgdörfer, *Z. Phys.*, 1981, **300**, 35.
[60] J. Burgdörfer, H. Gabriel and E. Kupfer, *Nucl. Instrum. Methods*, 1982, **194**, 337.
[61] R. Kawai and M. Kawai, *Surf. Sci.*, 1988, **195**, 535.
[62] F. J. García de Abajo and P. M. Echenique, *Nucl. Instrum. Methods Phys. Res. B*, 1996, **115**, 299.
[63] F. J. García de Abajo and P. M. Echenique, *Phys. Rev. Lett.*, 1996, **76**, 1856.
[64] A. Salin, A. Arnau and P. M. Echenique, *Phys. Rev. B*, 1998, **57**, 2772.
[65] F. Sols and F. Flores, *Phys. Rev. B*, 1984, **30**, 4878.
[66] F. J. García de Abajo, V. H. Ponce and P. M. Echenique, *Phys. Rev. Lett.*, 1992, **69**, 2364.
[67] F. Guinea, F. Flores and P. M. Echenique, *Phys. Rev. Lett.*, 1981, **47**, 604.
[68] F. J. García de Abajo and P. M. Echenique, *Phys. Rev. B*, 1992, **46**, 2663.
[69] M. Rösler and F. J. García de Abajo, *Phys. Rev. B*, 1996, **54**, 17158.
[70] J. F. Ziegler, J. P. Biersack and U. Littmark, in *Proceedings of the International Ion Engineering Congress, ISIAT'83 & IPAT'83* (ed. J. F. Ziegler), Pergamon Press, New York, 1983, p. 1861.

[71] J. O'Connor and J. P. Biersack, *Nucl. Instrum. Methods Phys. Res. B*, 1986, **15**, 14.
[72] J. Lindhard, *K. Dan Vidensk. Selsk. Mat. Fys. Medd.*, 1954, **28** (8).
[73] J. B. Pendry, *Low Energy Electron Diffraction*, Academic Press, London, 1974.
[74] J. B. Delos and W. R. Thorson, *Phys. Rev. A*, 1972, **6**, 728.
[75] When $z_b(t)$ is such that the condition of RCE is fulfilled, the amplitudes $a_{\alpha 0}$ corresponding to states that are in resonance oscillate very rapidly. Under these circumstances, it can be proved that the final expressions derived in Appendix A and given in Section 2 remain valid as well.
[76] D. Pines and P. Nozières, *The Theory of Quantum Liquids*, W.A. Benjamin, New York, 1966.

This Page Intentionally Left Blank

The Barkas-Effect Correction to Bethe–Bloch Stopping Power

L. E. Porter

Washington State University, Pullman, WA 99164-1302, USA

Abstract

A brief history of the discovery of the Barkas-effect correction to the Bethe–Bloch stopping power formula is presented, followed by a recounting of the initial theoretical calculations prepared as a quantitative explanation. A current version of the modified Bethe–Bloch formula is described in detail. An overview of the current capability to assess the validity of several existing formalisms for calculating the Barkas-effect correction term is provided, in the course of which discussion of numerous sources of uncertainty ensues. Finally, an opinion on the significance of this departure from Bethe–Bloch theory is offered, along with a presentation of a few recent developments and of some areas for focus in future exploration in the field of the stopping power of matter for charged particles.

Contents

1. HISTORICAL BACKGROUND

1.1. Experimental evidence

The energy loss of charged particles when traversing matter has been studied extensively during the past century. Mechanisms for energy loss have been

ADVANCES IN QUANTUM CHEMISTRY, VOLUME 46
ISSN: 0065-3276 DOI 10.1016/S0065-3276(04)46004-3

categorized according to the type of projectile and the various projectile velocity regimes in which certain processes dominate in order to formulate theoretical approaches to energy loss calculation. This monograph will treat only the electronic stopping power of amorphous targets for massive projectiles, i.e., projectiles at least as massive as a muon. The velocity regime where the first Born approximation is valid in scattering theory constitutes the region in which Bohr–Bethe–Bloch theory of stopping power had prevailed for some two-thirds of the 20th century. That theory features a direct dependence of stopping power on the square of the projectile atomic number (z). Yet the first clear indication of a deviation from the prediction of Bethe–Bloch theory arose in studies involving the ranges of positive and negative pions in nuclear emulsion [1], studies conducted by the Walter H. Barkas Particle Physics Group. The initial unambiguous evidence that two particles of the same rest mass and energy but of opposite charge do lose energy at different rates arose from a series of further experiments in nuclear emulsion conducted between 1960 and 1963 [2], reported in the latter year [3]. The suggestion that negative particles lose energy at rates lower than those for positive particles of the same rest mass and energy was first articulated by Barkas [2]. The first instance of a theoretical estimate for the stopping power differences of oppositely charged particles consisted of an attempt by Fermi to explain the observed results on the basis of a projectile-charge sign-dependent term in the Mott theory of scattering of electrons (from both positive and negative pions, in the coordinate frame in which the pion is at rest) [2]. The correction thus derived was inadequate to explain the observed range discrepancy, and since the Mott scattering formula is valid for high projectile velocities the proposed correction is not generally applicable to slow (stopping) particles. Barkas investigated the extension of the Bethe–Bloch formula by exploitation of higher-order Born approximations, and found that the second-order Born approximation provides a term proportional to z^3, i.e., a term of the correct nature to account for the observed difference in stopping powers [4]. Barkas shared this observation with the author while the latter served on a postdoctoral appointment in the Particle Physics Group of Professor Barkas at the University of California, Riverside. A summary of earlier experimental evidence from the particle physics measurements in nuclear emulsion was provided in 1969 by a member of the original experimental group, Heckman, as co-author, along with a report of a refined experiment to determine the projectile velocity interval where the stopping power difference was detectable [5]. The magnitude of the relative difference in energy-loss rates was found to vary from slightly more than 1% at $\beta\,(= v/c) = 0.14$ to some 14% at $\beta = 0.05$ in this study [5]. Meanwhile, an experiment successfully conducted to observe the z^3-effect for H and He projectiles of the same velocity traversing thin targets of Al and Ta was reported in 1969 as well [6].

1.2. Advent of theory

Theoretical explanations of the observed experimental results followed soon afterward. In an early review of stopping power knowledge [7] results of the experiments initiated by Barkas and his colleagues [1–3,5,6] were acknowledged. Moreover, Fano speculated that the prospective z^3-correction to the Bethe–Bloch formula might be separated from target shell corrections at projectile velocities comparable to those of inner-shell electrons, yet sufficiently large to avoid electron capture by the positive projectiles [7]. Studies of the z^3-effect prior to 1971 were discussed in a general review [8]. An extensive treatment of the low velocity projectile-z^3 dependence of stopping power appeared soon afterward, wherein stopping power theory was extended to include a correction term proportional to the projectile-z^3 in a classical equivalent of the second Born approximation [9]. This treatment was concerned with distant collisions of projectiles with bound target electrons, in an attempt to explain the observed low velocity projectile-z^3 effect [9]. Some 8 months later another theoretical explanation of the low-velocity projectile-z^3 dependence of stopping power appeared, including a close-collision (relativistic effect) contribution as well [10]. The approach of the latter treatment [10] purportedly followed that of its predecessor [9], but differed therefrom in detail. Elaborations and extensions of the first major formalism [9] followed soon afterward [11–13]. An application [14] of the second formalism [10] was published prior to an application [15] of the first [9]. Definitive tests of the extant theories [9,10] were sought.

Soon after the initial discovery of the effect it appeared feasible to isolate the projectile-z^3 correction term in the Bethe–Bloch stopping power formula [4]. An early suggestion was made to attempt such a measurement with electrons and positrons [8]. The difference in the stopping powers of a given target for those two projectiles is not confined to the z^3-term, however. An alternative approach would be the employment of massive projectiles, such as positive and negative muons [16] or pions [17]. (Muons seemed preferable because of their distinguished record of abstinence from any complicating hadronic interactions.) Eventually, measurements of stopping power ratios for positive and negative pions traversing various target materials were conducted [18], but at energies too high for detectability of the z^3-effect. Shortly afterward positive and negative muon beams were used to evaluate the z^3-correction for stopping powers of aluminum, and for ranges in targets of copper and aluminum [19].

1.3. Further developments

Additional theoretical treatments of the projectile-z^3 effect appeared. In one study the approach of Ref. [9] was altered by treating the target atom by quantum mechanics, using a multipole expansion of the coulomb interaction

for distant collisions, and calculating z^3-contributions to the mean energy loss and excitation probabilities due to the dipole and quadrupole terms of the multipole expansion [20]. This new approach led to formulas identical to those of Ref. [9]. The authors of this study [20] questioned the correctness of excluding close collision contributions to the z^3-correction term, which characterized the initial calculation [9]. In this vein the Bloch version of the stopping power formula [21] was invoked [20], noting that one term contained corrections to the z^2-dependence [21] but only in even powers of z – and hence incapable of providing the z^3-dependence based on observations [1–6]. The Bloch term [21] was restored to the stopping power formula by Lindhard in his reappraisal of the contributions to the z^3-correction [22]. In this study Lindhard concluded [22] that close collision contributions to the z^3-term must be included, resulting in a z^3-correction about twice the magnitude of the low velocity correction term previously obtained by Jackson and McCarthy [10]. Further accurate stopping power measurements with H, He, and Li ions traversing several metal targets [23] proved supportive of the Lindhard proposal [22], as subsequently elaborated by Esbensen [24]. The latter set of new stopping power data [23] was subjected to a fit by Ritchie and Brandt [25] with the Bloch term included in the revised Bethe–Bloch formula in order to re-evaluate the scaled minimum-impact parameter (denoted as b in the original studies [9,11–13]). The value of b thus changed from 1.8 ± 0.2 to 1.4 ± 0.1. A further discussion of the Lindhard suggestion and of the Ritchie–Brandt alternative will appear below. However, an exposition of a specific formalism featuring the projectile-z^3 correction to the Bethe–Bloch formula will next be addressed.

1.4. Modified Bethe–Bloch formula

The presentation in this section will draw freely on portions of Ref. [26]. Stopping power can be calculated from Bohr–Bethe–Bloch theory with the expression,

$$S = \frac{4\pi e^4 N_A z^2 Z L}{m_0 c^2 \beta^2 A}, \tag{1}$$

where e and m_0 are, respectively, the charge and rest mass of the electron, N_A is Avogadro's number, Z and A are, respectively, the target atomic number and atomic weight, z is the projectile atomic number, β is the (laboratory frame) relativistic velocity parameter ($v = \beta c$), and L is a complicated quantity known as the stopping number per target electron. When the (unit-dependent) constant in equation (1) is evaluated one obtains

$$S\ (\text{MeV cm}^2/\text{g}) = \frac{0.30706 Z z^2 L}{A\beta^2}. \tag{2}$$

The dimensionless stopping number consists of three terms

$$L = L_0 + \xi z L_1 + L_2, \tag{3}$$

where L_0 is an extension of the basic quantity derived from the first Born approximation by Bethe [27] and Bloch [21], zL_1 (with amplitude ξ) is the term constituting (effectively) the second-order Born approximation correction known as the projectile-z^3 correction term, and L_2 is the correction term containing even powers of z (commencing with z^2) obtained by Bloch [21]. The basic stopping number

$$L_0 = \ln\left(\frac{2m_0c^2\beta^2}{1-\beta^2}\right) - \beta^2 - \ln I - C_0/Z - \delta/2, \tag{4}$$

contains an explicit function of projectile velocity, the natural logarithm of the target mean excitation energy (I), the velocity-dependent inner shell corrections (C_0), and the velocity-dependent (highly relativistic) density effect correction (δ) [28].

The target mean excitation energy, defined as the sum of dipole oscillator strengths

$$\ln I = \sum_i f_i \ln E_i, \tag{5}$$

for E_i the energy and f_i the dipole oscillator strength for the ith energy level, can be calculated from first principles only if each f_i and E_i pair of values is known. Similarly, the inner shell corrections [7,29]

$$C_0 = \sum_i C_{0i}(\beta^2), \tag{6}$$

where C_{0i} is the correction for the ith shell (i = K, L, M,…), cannot in general be directly calculated for complex atoms. A method that has proved successful [30,31] is to use the shell corrections for the K and L shells as calculated by Walske [32,33] accompanied by scaling parameters with values to be determined through fits to accurate experimental data:

$$C_0 = \sum_i V_i C_{0i}(H_i\beta^2), \tag{7}$$

where V_i and H_i are the scaling parameters for the ith shell (with $V_k = H_k = 1$). Other options for assigning shell corrections will be discussed below.

The projectile-z^3 effect (or, Barkas effect) correction term is itself the sum of two terms, the first of which ($\xi z L_{1l}$) is more significant for low projectile velocities and the second of which ($\xi z L_{1h}$) is more significant for high projectile velocities. The first can be calculated from either one of two formalisms introduced in 1972, one for low velocities [9] and the other for

both low and very high velocities [10]. Additional formalisms will be discussed below. The fully developed formalism [9,11–13,25] based on Ref. [9] has generally been utilized by the author for analyses of stopping power measurements that include low projectile velocities:

$$L_{1l} = \frac{F(b/\sqrt{x})}{\sqrt{Zx^3}}, \tag{8}$$

where the function F has been tabulated in Ref. [13], $x = 18{,}787\beta^2/Z$, and b is the composite free parameter (impact parameter) of the Barkas-effect formalism [9,11–13,25]. The second term ($\xi z L_{1h}$), which also should be included in all analyses of stopping power measurements, can be calculated from the simple expression [10],

$$L_{1h} = \pi\alpha\beta/2, \tag{9}$$

where α denotes the fine structure constant.

The Bloch term [21] is given by

$$L_2 = \Psi(1) - \mathrm{Re}[\Psi(1 + \mathrm{i}y)], \tag{10}$$

where Ψ denotes the digamma function [34] and $y = z\alpha/\beta$.

Finally, the density effect correction (δ) can be obtained from the extensive formalism of Ref. [28] and further references cited therein. This highly relativistic correction, however, which takes into account the reduction of stopping power caused by polarization of the medium by relativistic charged particles [35], would provide a difference in calculated stopping power of less than 0.5% for any plausibly prospective (massive) projectile–target combination encompassed in the current study. Hence further discussion of this term will be deferred to a later section where concerns of a more general nature are articulated.

All of the preceding discussion is predicated on the implicit assumption that the projectile charge remains constant throughout the energy loss process. However, if the projectile energies considered are so low as to allow the gain and loss of electrons at velocities comparable to those of target atomic electrons, some type of projectile effective charge formalism must be invoked in order to simulate the results of gain and loss of electrons. One technique utilized [36] is to represent the projectile charge as ($z^*e = \gamma ze$), called an 'effective charge', rather than the base projectile charge (ze). The factor γ is defined in the author's formalism as

$$\gamma = 1 - \zeta e^{-\lambda v_r}, \tag{11}$$

where v_r denotes the ratio of projectile velocity in the laboratory frame of reference (v) to the Thomas–Fermi velocity $e^2/\hbar z^{2/3}$, so that $v_r = \beta/\alpha z^{2/3}$. The two symbols, λ and ζ, which signify effective charge parameters valid over the entire projectile velocity interval considered, must be evaluated for

any given projectile–target combination [36]. A considerably more extensive treatment of the effective charge topic will appear below.

The formalism thus assembled has provided a technique for analyses of stopping power measurements for the purpose of extracting values of various parameters. Section 2 contains an exposition of concerns over limitations of the formalism presented, even for the case of simple light projectiles and the simplest possible target, i.e., an elemental target of monatomic atoms in the gaseous state.

2. OVERVIEW AND PERSPECTIVE

2.1. Modeling of complicated physical processes

Nearly everyone is gratified by solving correctly a problem designed to embody and illustrate one or more principles of physics. The author has told numerous classes in elementary and intermediate university physics courses that the attractiveness of physics lay chiefly in its simplicity, in that principles were often explained in terms of, or illustrated by, situations devised to exclude numerous predictable complicating factors. Thus physics is by design far simpler than other physical sciences and subjects based on the study of real-world situations such as engineering and applied physics. Advanced physics courses represent preparation for the transition to the understanding and description of more complicated principles, phenomena, and processes in order to expand the base of knowledge in the subject and to furnish a student with the tools needed in research. The process known as modeling is utilized from introductory physics onward, of course.

The field of stopping power constitutes an excellent example of both the advantages and shortcomings of the modeling process. Reduction of enormously complex physical phenomena to a problem amenable to a tractable solution surely represents the salient advantage, whereas concerns over unjustified simplifications, perhaps from neglect of subsidiary physical processes involved, lead to the disadvantage of a need for ongoing refinement and even corrections to the initial solution. The history of developments in the stopping power field over the past century both illuminates and illustrates the implicit saga of achieving new levels of understanding while moving ever onward to reach the next level.

2.2. Calculation of stopping power

The last two terms of L_0 in equation (4) are called correction terms, the first for inner shell corrections, especially important at low projectile velocities, and the second for the density effect correction, especially important at highly relativistic projectile velocities. (Some physicists believe that

the inner shell correction term of equation (4) should not be called a 'correction' at all, because the term represents an integral part of the stopping number.) However, Fano explains the spirit of the use of the 'correction' terminology [7]. Moreover, the density effect term can be considered as always present, but of sufficient magnitude with respect to the other terms in the total stopping number, L of equation (3), to be significant only for highly relativistic projectile velocities.

The contribution of a given term to the sum, L, may be small, but not necessarily negligible with respect to the other terms in the sum. The author has published results of a study [26] to provide a comparison of the relative magnitudes of the low velocity Barkas effect term, the high velocity Barkas effect term, and the Bloch term for five different elemental targets from $Z = 7$ to 79 in order to provide guidance for others in the field [37]. This summary of values for comparison at 24 proton energies from 1 to 350 MeV is shown in Table 1, which varies slightly from Table 1 of Ref. [26] and Table I of Ref. [37]. It should be noted that with increasing proton energy the relative contribution from L_{1h} eventually surpasses that from L_{1l}, the proton energy of equality being about 20 MeV for N_2, 30 MeV for Al, 50 MeV for Cu, 60 MeV for Ag, and 70 MeV for Au. In order to assess the relative contribution of the density effect corrections one should consult the detailed tables of Ref. [28]. For example, according to Table B of Ref. [28] the relative contribution to the stopping power of graphite for 100 MeV protons lies between 5×10^{-4} and 15×10^{-4} and rises to a value between 25×10^{-4} and 35×10^{-4} for 200 MeV protons. However, for Au the value for 100 MeV protons lies below 5×10^{-4}, and for 200 MeV protons lies between 5×10^{-4} and 15×10^{-4}. Thus this contribution may prove quite comparable to the L_{1h} contribution, as is the case for 200 MeV protons impinging on a Au target. Clearly, in a calculation based on all known features of the modified Bethe–Bloch formula no term should be deemed negligible without a specific verification. In the following sections the process of extracting values of parameters appearing in the modified Bethe–Bloch formula from stopping power measurements will be discussed. In that arena, where one seeks the most accurate values permitted by the measurements, it is essential that all known terms in the formula be included.

A further complication in the calculation of stopping power from the modified Bethe–Bloch formula is the difficulty of establishing the contribution from each separate term, some of which difficulty must be attributed to the necessity of ascertaining the values of specific components of a given term independent of contributions from other terms. The latter task may not be feasible because of the need for finding the values of those components through fits to stopping power measurements. The problem lies in the fact that every term of the modified Bethe–Bloch formula possesses dependences on various relevant physical quantities in the problem that differ markedly from those of other terms. Numerous parameters appear in

Table 1. Values of L_1, L_2, and $\pi\alpha\beta/2$, each relative to L_0, for N_2, Al, Cu, Ag, and Au targets for proton energies (E_p) from 1 to 350 MeV

	N_2			Al			Cu			Ag			Au		
E_p (MeV)	L_{1l}/L_0 ($\times 10^4$)	$-L_2/L_0$ ($\times 10^4$)	$\pi\alpha\beta/2L_0$ ($\times 10^4$)	L_{1l}/L_0 ($\times 10^4$)	$-L_2/L_0$ ($\times 10^4$)	$\pi\alpha\beta/2L_0$ ($\times 10^4$)	L_{1l}/L_0 ($\times 10^4$)	$-L_2/L_0$ ($\times 10^4$)	$\pi\alpha\beta/2L_0$ ($\times 10^4$)	L_{1l}/L_0 ($\times 10^4$)	$-L_2/L_0$ ($\times 10^4$)	$\pi\alpha\beta/2L_0$ ($\times 10^4$)	L_{1l}/L_0 ($\times 10^4$)	$-L_2/L_0$ ($\times 10^4$)	$\pi\alpha\beta/2L_0$ ($\times 10^4$)
1	167	100	2	349	122	2	937	176	3	989	216	4	547	255	5
2	80	41	2	164	48	2	424	64	3	504	76	4	352	91	5
5	27	13	3	54	15	3	136	18	4	178	21	4	168	25	5
10	11	6	3	22	6	3	55	8	4	75	8	5	83	10	5
15	7	4	4	13	4	4	32	5	5	44	5	5	52	6	6
20	4	3	4	9	3	4	21	3	5	30	4	5	37	4	6
25	3	2	4	6	2	5	16	2	5	22	3	6	28	3	7
30	3	2	4	5	2	5	12	2	5	18	2	6	23	3	7
40	2	1	5	3	1	5	8	1	6	12	2	6	16	2	7
50	1	1	5	2	1	6	6	1	6	9	1	7	12	1	8
60	1	1	6	2	1	6	5	1	7	7	1	7	9	1	8
70	1	1	6	2	1	6	4	1	7	5	1	7	8	1	8
80	1	1	6	1	1	6	3	1	7	5	1	8	6	1	9
90	1	1	6	1	1	7	3	1	7	4	1	8	5	1	9
100	0	0	6	1	0	7	2	1	8	3	1	8	5	1	9
125	0	0	7	1	0	7	2	0	8	2	0	9	3	1	10
150	0	0	7	1	0	8	1	0	9	2	0	9	3	0	10
175	0	0	8	0	0	8	1	0	9	2	0	10	2	0	11
200	0	0	8	0	0	8	1	0	9	1	0	10	2	0	11
225	0	0	8	0	0	9	1	0	10	1	0	10	2	0	11
250	0	0	8	0	0	9	1	0	10	1	0	10	1	0	11
275	0	0	9	0	0	9	1	0	10	1	0	11	1	0	12
300	0	0	9	0	0	9	0	0	10	1	0	11	1	0	12
350	0	0	10	0	0	10	0	0	11	1	0	11	1	0	12

the formalism. The target mean excitation energy (I) and Barkas-effect parameters (b and ξ) are all independent of projectile energy, as are the scaling parameters associated with the energy-dependent shell corrections. Shell corrections are generally assumed to be independent of projectile, but opinion is not unanimous on this issue. There are no free parameters in the Bloch term, which depends on projectile charge and energy. Although the mean excitation energy (I) and Barkas effect parameter (b) are generally assumed to be independent of bare projectile charge (and hence identity), the author has recently discovered evidence to the contrary [38–42]. Finally, if it is necessary to introduce some effective charge formalism such as that of equation (11), the two parameters were generally expected to hold values independent of both projectile and target identity, as well as of projectile energy. The systematics of the actual behavior of these parameters as functions of z and Z have been studied in some detail [36].

A number of authors have spoken to this point. Sabin and Oddershedde provided an excellent treatise on the interdependence of various parameters while attempting to determine the mean excitation energies of the transition metals from iron to zinc [43]. Porter and Shepard had previously noted the difficulty of fitting the sum, $\ln I + C_0/Z$, when including the Barkas-effect term in the Bethe–Bloch formula, and had resorted to postulating no change in the shell corrections in order to ascertain the shift in values of I (only) under this assumption [15]. (That tactic was justified by the very small shell corrections required for the hydrocarbon targets that were the focus of the study [15].) By 1980 Bichel had commenced a complete revision of previously recommended shell corrections [44] based on the inclusion of the Barkas and Bloch terms in analyses of stopping power measurements [30]. Soon after the appearance of the Lindhard suggestion that a factor of about two should be applied to the Barkas term [10] in order to account for contributions from close collisions, studies were conducted [45] to investigate the efficacy of either this option or the alternative of changing the cut-off value of the minimum impact parameter from 1.8 [9] to 1.4 [25]. (It was in this context that Porter introduced the amplitude of the Barkas term, ξ in equation (3), as a variable parameter [46].) In a comprehensive review of the status of evaluating the contributions of terms of higher order in z than z^2, Basbas accepted the finding by Porter and collaborators [45] that measurements could not distinguish any preference between the two options [47]. The same conclusion was drawn in the case of a proton–antiproton experiment utilizing a Si target [48]. Insofar as additional shell corrections are concerned, say in L_1 and/or L_2, the possible need for shell corrections within the L_1 term was recognized by the architects of the Barkas-effect correction term, but the effect of such shell corrections was considered negligible [9]. Estimates of shell corrections for L_1 and L_2 have been provided [49]. In another attempt to obtain the correct contribution from each term, Bichsel [50] assumed that z^*, C, L_1, and L_2 are independent functions

and proceeded to search for forms for L_1 and z^* that would provide the best fit for the measurements of Refs. [23,48]. The cases cited in this paragraph constitute only a sampling of multitudinous such studies, but the complexity of the problem has been illustrated. To this realization of the complications attendant to establishing values of various parameters in the formalism one must add the awareness that the number of stopping power measurements per unit projectile energy, plus the accuracy and scatter of those data points, usually forbid the concurrent determination of the values of more than two or at most three dominant parameters [51]. In the context of this understanding, other important aspects of stopping power studies will be discussed.

2.3. Complications from aggregation effects

The basic theories developed by Bohr and Bethe originally applied strictly to pure monatomic targets in the gaseous state [7]. Hence a target composed of something as simple as an element in the condensed state, or of a homonuclear diatomic molecule in the gaseous state, will manifest bonding effects. The case of numerous atoms interacting simultaneously with both a projectile and each other was first examined by Fermi, as the 'density effect' [35,52]. However, the connection between the Bethe and Fermi theories was explained by Fano [7,53], who later described how the Bethe theory can be adapted to molecules and condensed matter [7]. Both physical state effects and bonding effects are generally grouped together as aggregation effects. If a target is known to possess aggregation effects, the target will be referred to herein as a composite material. This general category clearly contains compounds, and perhaps mixtures. In order to manage aggregation effects, the first approximation invoked is the assumption of linear additivity of the stopping effects of the constituents. This assumption, originally propounded by Bragg [54], which is known as 'Bragg's rule', or the 'additivity rule', represents a point of departure in studying aggregation effects. In the case of a composite material stopping cross-sections, stopping powers, and parameters of modified Bethe–Bloch theory are characterized by departures from the linear additivity assumption. The comparison procedure for stopping cross-sections and stopping powers should be obvious, but the handling of parameters appearing in modified Bethe–Bloch theory requires some discussion. An average mean excitation energy was carefully defined by Fano [7]. Average values of the ratio (Z/A), the shell corrections (C/Z), and the mean excitation energy (I) were also defined by Barkas and Berger [55]. A brief summary of explanations of these averages will now be included for the sake of clarity.

The proper average mean excitation energy (I_{avg}) can be calculated [7] as

$$\ln I_{\text{avg}} = \sum_j n_j Z_j \ln I_j / \sum_j n_j Z_j, \tag{12}$$

where Z_j, n_j, and I_j are, respectively, the atomic number, atomic concentration, and mean excitation energy of the jth component of the composite material. Similarly, the average value of Z/A should be calculated [55] as

$$(Z/A)_{\text{avg}} = (1/\rho)\sum_j \rho_j Z_j/A_j, \tag{13}$$

with A_j and ρ_j, respectively, denoting the atomic weight and partial (mass) density of the jth component, and with ρ representing the overall target (mass) density. As a consequence of this particular definition [55] of $(Z/A)_{\text{avg}}$, it follows that $(Z/A)_{\text{avg}} = (Z)_{\text{avg}}/(A)_{\text{avg}}$, and that shell corrections can be simply computed. That is, from the proper definition of average shell correction [55], although an obvious typographical error in the defining equation in Ref. [55] must be corrected,

$$(C/Z)_{\text{avg}} = \left(\frac{1}{(Z/A)_{\text{avg}}}\right)\frac{1}{\rho}\sum_j \rho_j Z_j C_j/A_j Z_j, \tag{14}$$

where C_j in the present context represents the total shell correction peculiar to the (entire atom of the) jth component, a simpler version is readily obtained:

$$(C/Z)_{\text{avg}} = \left(\sum_j n_j C_j\right)\Big/\left(\sum_j n_j Z_j\right) = (C)_{\text{avg}}/(Z)_{\text{avg}}. \tag{15}$$

Thus the average shell correction for an electron of the (fictitious) composite atom is calculable in analogy with the average mean excitation energy. That is, the former quantity can be considered as the average shell correction per electron for the given component atoms (C_j/Z_j) where the weight function is the fractional electron population $(n_j Z_j)$:

$$(C/Z)_{\text{avg}} = \left[\sum_j n_j Z_j (C_j/Z_j)\right]\Big/\left(\sum_j n_j Z_j\right). \tag{16}$$

If the shell corrections for each component are known (for any specified projectile velocity), then the average shell correction can be readily obtained.

The Barkas-effect correction [9,11–13,25] must also be calculated for composite targets, whereas the Bloch term [21], a function only of projectile charge and projectile velocity, need not. Actually, only the low-velocity portion of the Barkas-effect correction [9,11–13,25] must be calculated for composite targets (L_{1l} in equation (8)), since the relativistic portion of the correction [10] is a function only of projectile velocity ($L_{1h} = \pi\alpha\beta/2$ in equation (9)). A prescription for this calculation, based on assumed

applicability of Bragg's rule, was published in Ref. [11]. Reports of use of the described method [11] appeared shortly afterward [15,56].

Tabulations of the several parameters used in calculating the density-effect correction for nearly 200 composite materials (as well as some 100 elemental materials) are contained in Ref. [28].

As a consequence of the early formulation of the additivity rule [54] and its general application to composite-material targets ever since, it seems plausible that the rule has been extensively tested. Such is indeed the case, and several reviews on the subject have appeared [58–62].

2.4. Status of calculation of known terms in the Bethe–Bloch formula

The terms of the Bethe–Bloch formula that must be considered when calculating stopping power are the L_0-term (including the shell correction term, the mean excitation energy term, and the density effect term), the Barkas term, the Bloch term, some strategem for simulation of the results of gain and loss of electrons by projectiles at low velocities, and possibly terms of higher odd order in projectile-z than z^3. The latter possibility has been explored extensively by Ahlen [63–65], who discovered that for large velocities ($z/\beta < 100$) a z^7-term arises from the close collision contribution to stopping power. This correction, which is valid for the $\beta > 0.3$ regime [63], is completely negligible for the low energy regime [65]. No other additional terms of odd order in z (above z^3) were found [63–65]. Of course, all terms of even order in z (above z^2) are included in the Bloch term [21]. However, at very high projectile velocities it is necessary to provide corrections for the internal charge structure and the intrinsic magnetic dipole moment of the projectile [62]. Clearly the modified Bethe–Bloch formula is subject to criticism for many reasons, but it is quite remarkable that the multitudinous complicated phenomena associated with the energy loss of charged particles traversing matter should lend themselves so obligingly to descriptions by theories based on the several models such as those employed.

The status of calculation of the Barkas-effect term depends on that of the other terms in the Bethe–Bloch formula because results of measurements are compared with the calculated sum of terms, providing problems with separation of contributions [15,43,50,66]. Those terms are obtained from theory based on models. The initial calculation of the energy loss of a fast charged projectile, based on inelastic collisions with orbiting electrons bound to the nuclei of target atoms, was carried out by Bohr utilizing a semiclassical approach [67]. A subsequent calculation based on a quantum-mechanical formulation featuring the first Born approximation was conducted by Bethe [27]. Subsequently Bloch considered also the perturbations of the wave functions of atomic electrons induced by the projectile [21] and established the connection between the methods of Bohr [67] and Bethe [27]. An electron bound harmonically to the nucleus of

a target atom with angular frequency ω becomes the basis of a model of harmonic oscillators erected with the aid of the Thomas–Fermi statistical model of the atom to provide an approximate description of a many-electron atom [10]. The harmonic oscillator model was employed in deriving an expression for the Barkas-effect term by the early theorists whose work was described in Sections 1.2 and 1.3: Ashley, Ritchie, and Brandt (ARB) [9, 11–13,25], Jackson and McCarthy (JM) [10], and Hill and Merzbacher (HM) [20]. A further interesting investigation employed the harmonic oscillator model and the second-order Born approximation to calculate a new version of Barkas-effect term [68], L_{1l} in equation (8). Results were published for two different values of an adjustable parameter of the formulation by the authors, Morgan and Sung (MS) [68]. The two options given by MS [68] plus one each by ARB [9,11–13,25] and JM [10] afforded four different formalisms for calculation of the Barkas-effect term, L_{1l}. In a pragmatic study to ascertain which formalism furnished the best agreement with an available measurement summary [69] of the stopping powers of 12 elements with Z-values from 1 to 18 for 0.5 to 5.0 MeV protons and alpha particles, the ARB method emerged as that providing the best predicted stopping powers in general [70]. An alternate model that can be used for the analysis of stopping problems is a free electron gas with plasma frequency ω [22]. This simplified electron gas model can be used to study the collective response of electrons to the perturbing projectile potential [71]. The initial detailed treatment of stopping power with this model, published by Lindhard [72], was followed soon thereafter [71] by other similar studies [73–75]. Both this model and the harmonic oscillator model were employed by Lindhard in his investigation of the need to include close-collision contributions in the Barkas-effect term [22]. That study was buttressed soon afterwards by confirmatory calculations [76] utilizing both models [24], the harmonic oscillator model [77], and the electron gas model [71,78–80]. A rigorous many-body, perturbation-theoretic calculation of the Barkas-effect correction over a broad range of projectile velocities in the electron gas model [76] was found to provide good agreement with stopping power measurements for protons and antiprotons traversing Si targets [48,81]. A subsequent related study to investigate the Barkas-effect correction to the stopping power of an electron gas for charged projectiles, using a complete random phase approximation [82], also provided results in agreement with the proton–antiproton measurements with a Si target [48,81]. The electron gas model was used to formulate a completely nonlinear hydrodynamic theory of the electronic stopping power for charged projectiles in matter [83]. Nonlinear effects for the electron-gas model applied to solid targets were also investigated [84]. An interesting alternative, based on an extension of the Friedel sum rule to finite velocities and a self-consistent optimization of the scattering potential and related phase shifts, was used for calculation of nonlinear effects in the relevant range of velocities near the stopping

power maximum in order to obtain energy losses of protons and antiprotons in Al and Si [85]. The foregoing sampling of studies exploiting the electron gas model, and variations thereof, should constitute convincing evidence of the high value of the model to the theory of energy deposition in matter by charged projectiles.

Two additional models have seen service in the continuing struggle to advance the frontier of understanding of the complex phenomenon of electronic stopping power. The first, known as the kinetic theory of stopping [49], rests on the assumption that shell corrections possess an origin predominantly derived from the kinematics of target electrons in the initial state as opposed to the effect of being bound to the nuclei of target atoms or to each other for the collision dynamics [86]. The second, called the hydrogenic model [87], is based on the assumption that each electron bound to a target nucleus can be considered as occupying an hydrogen-like orbit about that nucleus [88]. All reasonable models based on sound physical principles should be utilized in appropriate scenarios in order to improve the theory of energy deposition in electronic stopping power.

Insofar as the calculation of the low velocity Barkas-effect term, L_{1l}, is concerned, the aforementioned comparison of three formalisms (all based on the harmonic oscillator model) for agreement with numerous measurements revealed a general superiority of the ARB [9,11–13,25] apparatus [70]. In a study of the model-based calculated stopping powers of several target materials for light projectiles, wherein all four of the models described above are compared, the harmonic oscillator model apparently emerged as the most valuable [87]. Since the author of this chapter has long adhered to the use of the ARB formalism [9,11–13,25], that practice will continue in the future, and the remainder of this section will be predicated on the assumption that the modified Bethe–Bloch formula will serve as the basis for comparison of theory and measurements.

2.5. Interaction of theory and experiment

The observation near the beginning of Section 2.4 that one must fit a sum of terms to experimental data deserves reiteration in the spirit of exploring further insights. A reminder concerning experimental data is in order. One problem that has long plagued the comparison exercise is the existence of flawed measurements, sometimes flawed for one or more esoteric reasons, sometimes for rather banal reasons, and sometimes because the experimentalists involved insisted on the cosmetic approach known as smoothing the data. The latter measure is both unnecessary and unwarranted, because the smoothing function employed may bias the data in such a manner as to render comparison with theory difficult, and the results thereof misleading. Thus that practice has long been deplored by the author [89]. Even if untarnished measurements are available, the problem of obtaining for

comparison of measurement with theory the best available calculation of the stopping power of a given target for a specified projectile remains. One might look for a trustworthy first principles calculation. If that option is also closed, one can resort to a calculation based on the modified Bethe–Bloch formula, supplemented by subsidiary model-based calculations wherein certain needed parameter-values were determined previously by comparisons with other measurements. The details of this procedure, stemming from a realistic approach to the information available, can be explored in the interest of portraying the often difficult choices to be made enroute to achieving a theory-based calculated value to compare with a reliable measured value. (A quite similar description has been provided by Sabin and Oddershedde [43,66].)

The terms containing parameters of the formulation are the I-term, the C_0-term, the L_{1l}-term and (for the more plausible scenarios) either a δ-term or perhaps an effective charge modification to ze (γ in equation (11)). The δ-term has been discussed at some length above, so that the present case will be that of a required selection of an effective charge factor. The mean excitation energy, defined in terms of dipole oscillator strengths, is difficult to calculate from theory for an arbitrary target. The vast majority of targets are composite targets (i.e., targets possessing aggregation effects), for example. This point will emphasize the virtual impossibility of obtaining a theory-based value for many targets. Hence I remains a parameter of Bethe–Bloch theory, perhaps to be obtained from fits to measurements with equation (2). (Another option is to select a value from one of several extant tabulations [31,69,90], each based on fits to numerous measurements.) In such a case it may be necessary to ascertain the values of other parameters concurrently, parameters such as those characterizing C_0 (the H_i and V_i for the Bichsel–Walske values [30,31]), b and ξ in L_{1l}, and λ and ζ in γ. Rarely if ever will the accuracy, density (number per unit projectile energy), and internal consistency of a set of stopping power measurements support the concurrent extraction of more than three parameter-values. Hence one must select reliable values of some of the several parameters enumerated and proceed to obtain fits to measurements in order to ascertain the values of the few remaining parameters. In this vein one might assign shell correction scaling parameters according to the Bichsel rubric [30,31], or adopt the calculational techniques of Bonderup [91] or of Khandelwal and Merzbacher [92] or of Oddershedde and Sabin [93], for example. Whatever the source of prescribed values for I and C_0, some uncertainties (perhaps sizeable) in those values must be taken into account, thus imposing larger uncertainties on the remaining terms or factors, or on the parameters utilized within each term. The point has been belabored quite enough. However, the γ-factor may well carry with it an additional large uncertainty. The author's version of a summary of some significant developments in effective charge studies will

be set forth in Section 2.6 because of the importance of that feature when applied to the stopping power formula.

2.6. Effective charge

The title of this section, which is a brief summary of some significant events in the evolution of the theory of energy deposition, has long been a topic of considerable discussion, and even of controversy, among physicists. Surely most stopping power physicists agree that at low projectile velocities there are gains and losses of electrons by a given projectile. That is, the existence of charge-changing processes is recognized. However, few if any extant theories of stopping power can encompass those processes, so that artifices must be employed in order to simulate the effects of charge-changing processes. One such artifice is the concept of effective charge. That terminology certainly implies a relationship to the charge carried by the projectile, at least in some sense, perhaps a sort of carefully defined average. A great deal of effort has been expended in order to ascertain that relationship (if any).

Some philosophers of science believe that the concepts which have proved most useful in science are those which possess considerable elasticity. Supportive examples abound. If the idea is valid, then the concept of effective charge deserves a place in the sun. Study of this concept has occupied many of the great talents in the history of stopping power investigations.

Bohr stated [94] in 1940 that "The continual capture and loss of electrons by the high speed fragments is a rather complex phenomenon, but, to a first approximation, we may assume that the fragments will possess an average effective charge…". The concept of an effective charge to characterize the stopping of partially stripped ions was thus born. The Bohr stripping criterion stated [95] that all projectile electrons with orbital velocities less than the translational projectile velocity would be detached; when this criterion was applied to a Thomas–Fermi model of the atom the resulting expression for effective charge was

$$q_{\text{eff}} = z^{1/3} v / v_0, \tag{17}$$

where $v_0 = 2e^2/\hbar$. The concept was based on the point-charge model and on a scenario wherein the majority of collisions occur with impact parameters larger than the radius of the bound electron cloud of the projectile [96]. In fact, Bohr assumed that the ratio of electron capture and loss cross-sections for the projectile reached unity when the aforementioned velocity ratio reached unity. Lamb's calculation of an 'average charge' was, by contrast, based on an assumption about the energy of outermost electrons in the projectile, namely, that ionization energy of those electrons is

(under equilibrium conditions) equal to the kinetic energy of the (practically free) stopping medium electrons relative to the projectile [97]. If a central Coulomb field acted upon each electron of the ion the Bohr and Lamb treatments would lead to identical results; deviations from a Coulomb field of the average field in the ion cause noticeable differences in results, however [98]. The approach of Knipp and Teller was to adopt Bohr's assumption that the 'average charge' depends primarily on the ratio of electronic to ionic velocities and to ascertain from experimental data the value of the ratio, having calculated electronic velocities from the Thomas–Fermi model [98]. The 'average charge' utilized in that study was the root-mean-square charge.

In a heavy ion stopping power investigation by Pierce *et al.* [99], the fractional effective charge, $z^*e = \gamma ze$, of the projectile became a value of ze (z^*e) which provided the experimental stopping power when calculated from (a rather simple form of) Bethe–Bloch theory and the factorization assumption: $S = \gamma^2 z^2 S_p/\gamma_p^2$, where the 'p' subscript refers to proton for measurements of stopping power conducted for the same projectile velocity in the same medium. (This assumption, implicit in the theory of Knipp and Teller, had by then been used by many investigators in the field, including Northcliffe [100].) Results indicated that the effective charge values differed considerably from measured rms charge states, so that effective charge was relegated to the position of another parameter. In a report given some 3 months later, Pierce and Blann [101] found that the effective charge could be expressed in terms of the Thomas–Fermi electron velocity ($v_0 z^{2/3}$) with the function

$$\gamma = 1 - \exp(-0.95v/v_0 z^{2/3}) = 1 - \exp(-0.95\beta/\alpha z^{2/3}), \qquad (18)$$

where α is the fine structure constant and β is the standard velocity parameter of special relativity, $\beta = v/c$. (Indeed, Barkas [102] had previously used an empirical value of $\gamma = 1 - \exp(-125\beta/z^{2/3})$, whereas $0.95/\alpha = 130$). These results were valid for projectile velocities (squared) greater than 0.3 MeV/u. However, although effective charges agreed well with rms charges for gaseous targets, there was no obvious relationship between the two for solid targets.

The effective-charge theory of Knipp and Teller for the electronic stopping power of target materials for heavy ions was reviewed and revised by Sauter and Bloom [103,104] about three decades ago. The primary revision consists of the assumption that the ionization energy of the most weakly bound electron attached to the ion should be equal to the maximum kinetic energy transferable to it by the electrons in the medium traversed [103]. If the medium electrons can be taken as free then the condition becomes $v_f = v$, where v_f is the velocity of the last bound electron [103]. A statistical value of v_f was selected, using Thomas–Fermi–Dirac theory,

so as to remove the effect of large variations near the closure of atomic shells [103].

In the same year that Ref. [104] appeared, the introduction of the projectile-z^3 term into the Bethe–Bloch formula occurred [9–13]. Indeed, the first application of the Ref. [10] formalism [14] included an analysis of stopping power measurements with a Si target and C, N, and O projectiles at energies where gain and loss of electrons were expected. In 1977 Ferrell and Ritchie extended the dielectric-function method (from the electron gas model) of calculating electronic stopping power for a point-charge projectile to apply for the case of a partially stripped ion [105]. In another approach the Bethe–Bloch formula with the Barkas-effect term included was applied directly to the analyses of a number of stopping power measurements with heavy ion projectiles in order to determine the behavior of a single effective-charge parameter (λ in equation (11)) as a function of both z and Z [106]. Brandt and several colleagues studied an effective charge model for heavy ions with intermediate velocities with the goal of summarizing large quantities of stopping cross-section information [107–111]. A semiphenomenological analysis of the different mechanisms participating in the slowing down process for projectiles was used to develop a universal equation for the electronic stopping of ions in solids [112]. Another interesting study involved the dielectric-function method from the electron gas model plus local electron density models to calculate the stopping powers of solid materials for 1 keV/u to 2.5 MeV/u protons and helium ions, with a resulting calculated energy dependence for the effective charge of the helium ions that agreed well with experimental data [113]. Armed with several new data files for heavy ion stopping powers, Porter sought to learn the dependences of the two effective charge parameters (λ and ζ in equation (11)) as functions of z and Z, this time with the Bloch term [21] restored to the modified Bethe–Bloch formula [36]. Bichsel studied both the Barkas term, L_{1l}, and the charge-state correction, z^*, for protons and antiprotons, He ions, and Li ions; in the case of a Au target the form of L_{1l} proved to be inaccurate, and for Li ions the charge-state correction generally used appeared to be too large for Al, Cu, Ag, and Au [50]. In another report on effective charge, one by Sigmund and Schinner, the conclusion was that there is no theoretical basis for the effective charge concept as it is commonly used in heavy-ion stopping [114]. (That conclusion failed to serve as an iconoclastic revelation to the physicists who had arrived at the same opinion some decades ago.)

Meanwhile, other avenues have been explored with the hope of improving available descriptions of the process of colliding atoms, i.e., the case of both target and projectile possessing electronic structure. An excellent investigation of this system appeared in 1997, with numerous pertinent background references cited therein [115]. This sort of approach appears most likely to

bear fruit, although no electron exchange *per se* is considered in the description of the colliding atoms. In the meantime, an effective charge or other form of artifice will be employed to simulate the effects of gain and loss of electrons by a slow projectile. The absence of any interpretation of this effective charge concept in terms of first principles or established model-based calculations will continue to induce uncertainties in values of both the effective charge parameters and other parameters of the modified Bethe–Bloch formula.

2.7. Further exploration and refinement

A continuing, intriguing interest of the author over the past 5 years or so has been the discovery of a projectile-z dependence of two dominant parameters of the modified Bethe–Bloch formula, namely, the mean excitation energy (I) and the Barkas-effect parameter (b), when the values are established through fits to stopping power measurements [38–42]. One observed trend is decreasing I-values with increasing z, whereas the trend for b-values is the opposite. In the preceding sections a great deal of emphasis has been placed on the significance of obtaining a fit to a sum of terms. The author has noted that usually some terms are accepted as correct while values for others are determined through the fitting procedure. For example, the author customarily fixes the values of shell correction scaling parameters and assumes the validity of the Bloch term and the form of L_{1I} while seeking values of I, b, and λ. Thus one can easily question the wisdom of stipulating the correctness of the other constituents of the sum, as noted in Section 2.2 above. In the course of a study undertaken to explain the basis of the observed trends, Cabrera-Trujillo, Sabin, and Oddershedde have noted the expected discrepancy in a parameter-value calculated from a firm definition (e.g., the value of I from equation (5)) compared with a value extracted from measurements [116]. Those authors note that the observed trends [38–42] are the opposite of anticipated trends [116]. It is suggested, also, that the observed trends may have resulted from failure to utilize a proper model for dressed projectiles, and an excellent model of colliding atoms [115] is then used to reproduce the anticipated trends [116]. However, a portion of the evidence cited for the observed trends is based on bare projectiles [38–42]. In fact, some of the most convincing evidence arose from the analyses of the cornerstone measurements [23] discussed above. Results of the analyses of the stopping powers of Al, Cu, and Ag for ^{1}H, ^{4}He, and ^{7}Li projectiles are summarized in Table 2 (of which the Al and Cu results were reported previously [40]) and in Figs 1–9. The symbol σ appearing in Table 2 represents the fitting figure of merit, which is the root-mean-squared relative deviation of calculated (S_c) from measured stopping power (S_m) with

Table 2. Summary of results from analyses of Al, Cu, and Ag measurements from Ref. [23], including the projectile energy interval of measurements (ΔE), number of measurements (N), mean excitation energy (I), Barkas-effect parameter (b), and figure of merit (σ)

Target	Projectile	ΔE (MeV)	N	I (eV)	b	σ
Al	Proton	0.8–6.4	29	166.5	1.37	0.20
Al	Alpha particle	3.2–22.2	25	165.4	1.36	0.25
Al	^{7}Li ion	8.3–23.4	12	156.8	1.79	0.43
Cu	Proton	1.2–7.2	31	329.0	1.30	0.24
Cu	Alpha particle	5.6–19.9	19	328.5	1.41	0.15
Cu	^{7}Li ion	11.0–19.3	7	324.5	1.58	0.31
Ag	Proton	0.8–6.4	29	485.4	1.23	0.91
Ag	Alpha particle	3.2–19.9	22	485.1	1.38	1.19
Ag	^{7}Li ion	8.3–20.6	10	467.3	1.60	0.67

uncertainty (ΔS_{m}) for N measurements:

$$\sigma = \sqrt{\frac{1}{N}\sum_{i=1}^{N}\left(\frac{S_{\mathrm{c}} - S_{\mathrm{m}}}{\Delta S_{\mathrm{m}}}\right)_i^2}. \tag{19}$$

Clearly the trends are quite generally followed, and for projectiles that are bare over the entire energy interval, with the possible exception of the low energy [7] Li ions. Nonetheless, the rather crude model proposed by the author [38] to explain the trends can benefit from attempts to provide a more

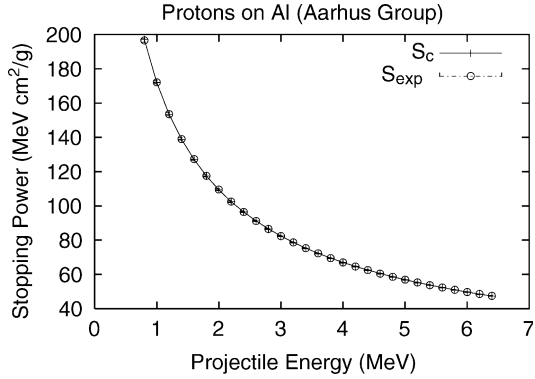

Fig. 1. Comparison of calculated stopping powers (+) with measured (○) stopping powers from Ref. [23] for protons traversing targets of Al, using a two-parameter fit for mean excitation energy (I) and Barkas-effect parameter (b).

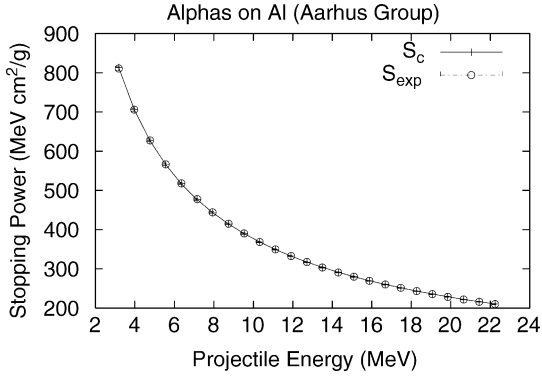

Fig. 2. Comparison of calculated stopping powers (+) with measured (○) stopping powers from Ref. [23] for alpha particles traversing targets of Al, using a two-parameter fit for mean excitation energy (I) and Barkas-effect parameter (b).

complete explanation [116] on the basis of a promising model [115]. Finally, a possible source of the observed trends may lie in the selection of shell corrections [116] – a suggestion with which the author readily agrees. It is possible that shell corrections are indeed projectile-dependent, as purportedly [50] believed by Basbas [47], so that the z-dependence could have been transferred to I and b when the shell corrections were held fixed with no z-dependence. The quest for a complete explanation of the observed trends has opened with an excellent study [116].

The discussion in Section 2.5 of the grave difficulties encountered when seeking to extract the values of parameters from stopping power

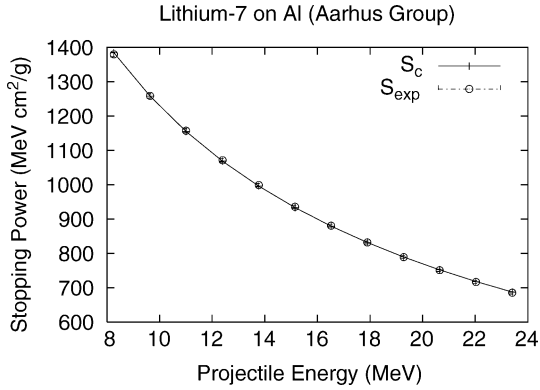

Fig. 3. Comparison of calculated stopping powers (+) with measured (○) stopping powers from Ref. [23] for ^{7}Li ions traversing targets of Al, using a two-parameter fit for mean excitation energy (I) and Barkas-effect parameter (b).

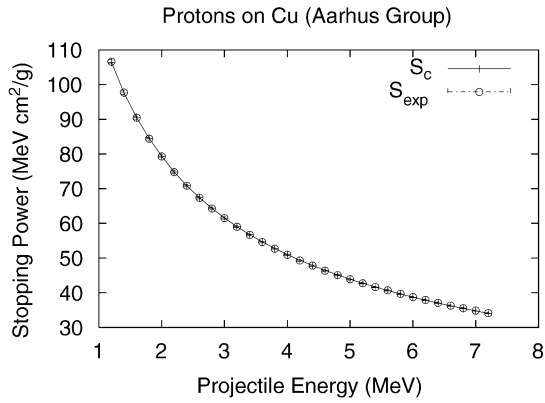

Fig. 4. Comparison of calculated stopping powers (+) with measured (○) stopping powers from Ref. [23] for protons traversing targets of Cu, using a two-parameter fit for mean excitation energy (I) and Barkas-effect parameter (b).

measurements emphasizes the need for research for better understanding of all pertinent terms in the modified Bethe–Bloch formula. There is still a need for improved calculation of mean excitation energies, based on first principles or improved models, or both. Similarly, considerable uncertainties are associated with almost any form of calculated shell corrections, so that improvement of theory represents a challenge. Moreover, there is no guarantee of the correctness of the form of either the L_1- or L_2-term. When the complexity of the problem of describing properly the gain and loss of electrons by a slow projectile is thrown into the mix, one must be impressed

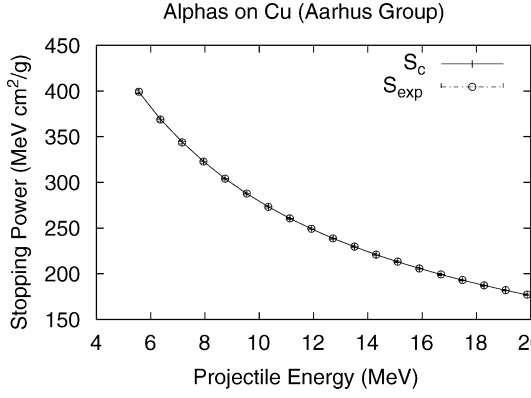

Fig. 5. Comparison of calculated stopping powers (+) with measured (○) stopping powers from Ref. [23] for alpha particles traversing targets of Cu, using a two-parameter fit for mean excitation energy (I) and Barkas-effect parameter (b).

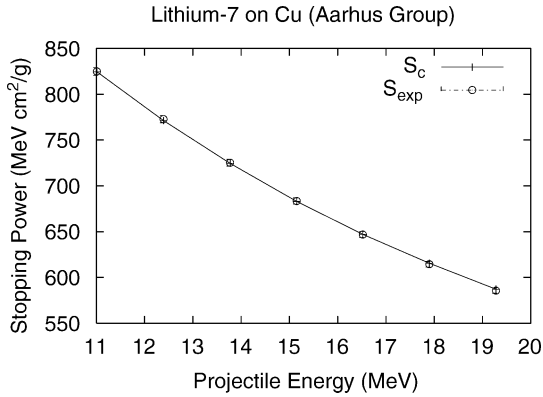

Fig. 6. Comparison of calculated stopping powers (+) with measured (○) stopping powers from Ref. [23] for ^{7}Li ions traversing targets of Cu, using a two-parameter fit for mean excitation energy (I) and Barkas-effect parameter (b).

by the enormous opportunities for further advances in our knowledge of the stopping power of matter for charged projectiles. That is, since all the terms and corrections in the Bethe–Bloch formula are interdependent, one is faced with a series of choices as to which quantities to hold fixed while others are investigated. Barkas was enthused over his discovery that by comparing the stopping powers of a given target material for each member of a particle–antiparticle pair of projectiles, the z^3-term could be isolated [4]. Now, some four decades later, one must cautiously interject the caveat that I, C_0, and L_1 are assumed to be independent of projectile charge in order truly to isolate

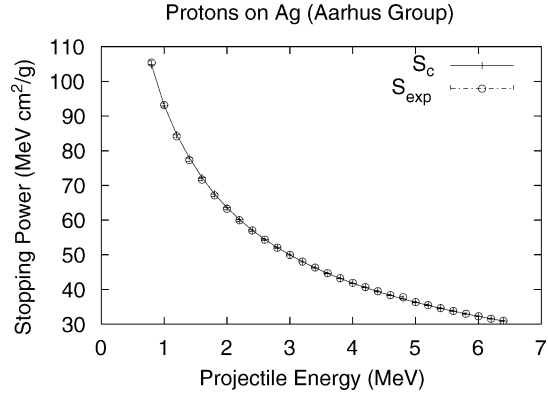

Fig. 7. Comparison of calculated stopping powers (+) with measured (○) stopping powers from Ref. [23] for protons traversing targets of Ag, using a two-parameter fit for mean excitation energy (I) and Barkas-effect parameter (b).

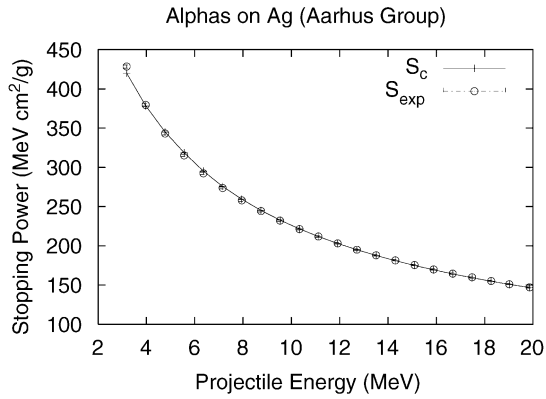

Fig. 8. Comparison of calculated stopping powers (+) with measured (○) stopping powers from Ref. [23] for alpha particles traversing targets of Ag, using a two-parameter fit for mean excitation energy (I) and Barkas-effect parameter (b).

the z^3-term by subtraction of the two stopping powers, even in the absence of some complicating effective charge formalism. Irony reigns. Yet when one reflects on the prolific production of research results, both in theory and in measurement, over those four decades, he cannot but stand in awe of the remarkable progress in the field attained during that period. A sizeable fraction of the burgeoning research effort was stimulated by the discovery of the Barkas-effect correction. In the same vein, although the central topic of this monograph is the projectile-z^3 term, one cannot isolate the impact of that term from the importance of the other terms and corrections in the modified Bethe–Bloch formula. Thus the author hopes to see significant advances in

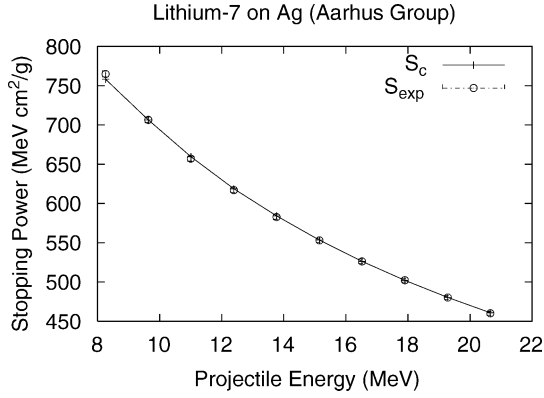

Fig. 9. Comparison of calculated stopping powers (+) with measured (○) stopping powers from Ref. [23] for ^7Li ions traversing targets of Ag, using a two-parameter fit for mean excitation energy (I) and Barkas-effect parameter (b).

assessment of the proper form of the Barkas-effect term in conjunction with improvements in the calculation of each related term or correction in the stopping power formula. A few areas of research in which the author would prefer to see progress are

- development of an effective charge formalism in the context of heavy ion stopping powers;
- further research in theory and measurement of stopping powers of conductors, semiconductors, and insulators;
- encouragement of laboratories capable of sophisticated stopping power experiments to focus on foil thickness uniformity control and determination with a goal of achieving 0.1% measurements.

REFERENCES

[1] F. M. Smith, W. Birnbaum and W. H. Barkas, *Phys. Rev.*, 1953, **91**, 765; W. H. Barkas, W. Birnbaum and F. M. Smith, *Phys. Rev.*, 1956, **101**, 778.
[2] H. H. Heckman, *Stopping Power Differences between Positive and Negative Particles at Low Velocities*, UCRL Report 19211 (Preprint). Lawence Radiation Laboratory, University of California, Berkeley, April 1969.
[3] W. H. Barkas, J. N. Dyer and H. H. Heckman, *Phys. Rev. Lett.*, 1963, **11**, 26; W. H. Barkas, J. N. Dyer and H. H. Heckman, *Phys. Rev. Lett.*, 1963, **11**, 138(E).
[4] W. H. Barkas, private communication, 1966.
[5] H. H. Heckman and P. J. Lindstrom, *Phys. Rev. Lett.*, 1969, **22**, 871.
[6] H. H. Andersen, H. Simonsen and H. Sorensen, *Nucl. Phys.*, 1969, **A125**, 171.
[7] U. Fano, *Annu. Rev. Nucl. Sci.*, 1963, **13**, 1.
[8] M. Inokuti, *Rev. Mod. Phys.*, 1971, **43**, 297.
[9] J. C. Ashley, R. H. Ritchie and W. Brandt, *Phys. Rev. B*, 1972, **5**, 2393.
[10] J. D. Jackson and R. L. McCarthy, *Phys. Rev. B*, 1972, **6**, 4131.
[11] J. C. Ashley, R. H. Ritchie and W. Brandt, *Phys. Rev. A*, 1973, **8**, 2402.
[12] J. C. Ashley, *Phys. Rev. B*, 1974, **9**, 334.
[13] J. C. Ashley, V. E. Anderson and W. Brandt, Z_1^3 *Effect in the Stopping Power of Matter for Charged Particles: Tables of Functions*, NAPS Document No. 02195, ASIS National Auxiliary Publication Service, c/o Microfiche Publications, 305 E. 46th St., New York, NY 10017.
[14] B. Sellers, F. A. Hanser and J. G. Kelley, *Phys. Rev. B*, 1973, **8**, 98; J. G. Kelley, B. Sellers and F. A. Hanser, *Phys. Rev. B*, 1973, **8**, 103.
[15] L. E. Porter and C. L. Shepard, *Nucl. Instrum. Methods*, 1974, **117**, 1.
[16] L. E. Porter, J. E. Brolley and L. C. McIntyre, LASL Office Memorandum of August 16, 1971 to Chairman, LAMPF Program Advisory Committee.
[17] R. D. Edge (private communication); R. D. Edge, C. W. Darden, B. M. Preedom, M. Blecher, K. Gotow and D. A. Jenkins, Proposal No. 372 of November 16, 1977 (revised November 10, 1978) to LAMPF Program Advisory Committee.
[18] J. A. Nordin and R. M. Henkleman, *Phys. Med. Biol.*, 1979, **24**, 781.
[19] W. Wilhelm, H. Daniel and F. J. Hargmann, *Phys. Lett.*, 1981, **B98**, 33.
[20] K. W. Hill and E. Merzbacher, *Phys. Rev. A*, 1974, **9**, 156.
[21] F. Bloch, *Ann. Phys. (Leipzig)*, 1933, **16**, 285.
[22] J. Lindhard, *Nucl. Instrum. Methods*, 1976, **132**, 1.

[23] H. H. Andersen, H. Knudsen, J. F. Bak and B. R. Nielsen, *Phys. Rev. A*, 1977, **16**, 1929.
[24] H. Esbensen, PhD Thesis, University of Aarhus, 1977.
[25] R. H. Ritchie and W. Brandt, *Phys. Rev. A*, 1978, **17**, 2102.
[26] L. E. Porter, *Stopping Power and Penetration Physics*, Chapter 4 of Handbook of Neutral Particle Beam Discrimination, Air Force Weapons Laboratory, Technical Report, 1988, unpublished.
[27] H. A. Bethe, *Ann. Phys.*, 1930, **5**, 325; H. A. Bethe, *Z. Phys*, 1932, **76**, 293.
[28] R. M. Sternheimer, M. J. Berger and S. M. Seltzer, *At. Data Nucl. Data Tables*, 1984, **30**, 261.
[29] M. S. Livingston and H. A. Bethe, *Rev. Mod. Phys.*, 1937, **9**, 245.
[30] H. Bichsel, private communication, 1980.
[31] ICRU Report No. 49, *Stopping Power and Ranges for Protons and Alpha Particles*, International Commission on Radiation Units and Measurements, Bethesda, MD, 1993.
[32] M. C. Walske, *Phys. Rev.*, 1952, **88**, 1283.
[33] M. C. Walske, *Phys. Rev.*, 1956, **101**, 940.
[34] M. Abramowitz and I. A. Stegun, *Handbook of Mathematical Functions*, National Bureau of Standards, Washington, DC, 1964.
[35] E. Fermi, *Phys. Rev.*, 1940, **57**, 485.
[36] L. E. Porter, *Radiat. Res.*, 1987, **110**, 1.
[37] L. E. Porter, *Appl. Phys. Lett.*, 1992, **61** (3), 360.
[38] L. E. Porter, *Int. J. Quantum Chem.*, 2002, **90**, 684.
[39] L. E. Porter, J. Räisänen and F. Munnik, *Int. J. Quantum Chem.*, 2002, **90**, 1368.
[40] L. E. Porter, *J. Electron. Spectrosc.*, 2003, **129**, 273.
[41] J. Räisänen, W. H. Trzaska, T. Alanko, V. Lyapin and L. E. Porter, *J. Appl. Phys.*, 2003, **94**, 2080.
[42] L. E. Porter, *Int. J. Quantum Chem.*, 2003, **95**, 504.
[43] J. R. Sabin and J. Oddershedde, *Phys. Rev. A*, 1989, **39**, 1033.
[44] H. Bichsel, *AIP Handbook*, 3rd edn, 1972, Section 8d.
[45] See, for example, L. E. Porter and R. G. Jeppesen, *Nucl. Instrum. Methods*, 1983, **204**, 605.
[46] L. E. Porter and D. I. Thwaites, *Phys. Rev. A*, 1982, **25**, 3407.
[47] G. Basbas, *Nucl. Instrum. Methods*, 1984, **B4**, 227.
[48] L. H. Andersen, P. Hvelplund, S. P. Müller, J. O. P. Pedersen, E. Uggerhüj, K. Elsener and E. Morenzoni, *Phys. Rev. Lett.*, 1989, **62**, 1731.
[49] P. Sigmund, *Phys. Rev. A*, 1982, **26**, 2497.
[50] H. Bichsel, *Phys. Rev. A*, 1990, **41**, 3642.
[51] L. E. Porter, *Phys. Rev. A*, 1994, **50**, 2397.
[52] E. Uehling, *Annu. Rev. Nucl. Sci.*, 1954, **4**, 315.
[53] U. Fano, *Phys. Rev.*, 1956, **103**, 1202.
[54] W. H. Bragg and R. Kleeman, *Phil. Mag.*, 1905, **10**, 318.
[55] W. H. Barkas and M. J. Berger, *Tables of Energy Losses and Ranges of Heavy Charged Particles*, National Academy of Sciences National Research Council Publication 1133, Washington, DC, 1967.
[56] C. L. Shepard and L. E. Porter, *Phys. Rev. B*, 1975, **12**, 1649.
[57] R. M. Sternheiner, S. M. Seltzer and M. J. Berger, *Phys. Rev. B*, 1982, **26**, 6067.
[58] L. E. Porter, *Additivity Rule*, in Proceedings of the Second New York University Workshop on Penetration Phenomena: Current Stopping Power Problems, New York University, January, 1978, unpublished.
[59] D. I. Thwaites, *Radiat. Res.*, 1983, **95**, 495.
[60] D. I. Thwaites, *Nucl. Instrum. Methods*, 1985, **B12**, 84.
[61] D. I. Thwaites, *Nucl. Instrum. Methods*, 1987, **B27**, 293.
[62] S. P. Ahlen, *Rev. Mod. Phys.*, 1980, **52**, 121.

[63] S. P. Ahlen, *Phys. Rev. A*, 1978, **17**, 1236.
[64] M. H. Salamon, S. P. Ahlen, G. Tarlé and K. C. Crebbin, *Phys. Rev. A*, 1981, **23**, 73.
[65] S. P. Ahlen, *Phys. Rev. A*, 1982, **25**, 1856.
[66] J. R. Sabin and J. Oddershedde, *Nucl. Instrum. Methods*, 1990, **B44**, 253.
[67] N. Bohr, *Phil. Mag.*, 1913, **25**, 10; N. Bohr, *Phil. Mag.*, 1915, **30**, 581.
[68] S. H. Morgan, Jr. and C. C. Sung, *Phys. Rev. A*, 1979, **20**, 818.
[69] J. F. Ziegler, *Handbook of Stopping Cross Sections for Energetic Ions in All Elements*, The Stopping and Ranges of Ions in Matter, Pergamon, New York, 1980, Vol. 5. More recent compilations of SRIM have been issued by J.F. Ziegler.
[70] L. E. Porter and H. Lin, *J. Appl. Phys.*, 1990, **67**, 6613.
[71] C. D. Hu and E. Zaremba, *Phys. Rev. B*, 1988, **37**, 9268.
[72] J. Lindhard, *Kgl. Dan. Videns. K. Selsk. Mat. Fys. Medd.*, 1954, **28** (8).
[73] J. Neufeld and R. H. Ritchie, *Phys. Rev.*, 1955, **98**, 1632.
[74] R. H. Ritchie, *Phys. Rev.*, 1959, **114**, 644.
[75] J. Lindhard and A. Winter, *Kgl. Dan. Videns. K. Selsk. Mat. Fys. Medd.*, 1964, **34** (4).
[76] J. M. Pitarke, R. H. Ritchie, P. M. Echenique and E. Zaremba, *Europhys. Lett.*, 1993, **24**, 613.
[77] H. Mikkelsen and P. Sigmund, *Phys. Rev. A*, 1989, **40**, 101.
[78] C. C. Sung and R. H. Ritchie, *Phys. Rev. A*, 1983, **28**, 674.
[79] H. Esbensen and P. Sigmund, *Ann. Phys.*, 1990, **201**, 152.
[80] J. M. Pitarke, R. H. Ritchie and P. M. Echenique, *Nucl. Instrum. Methods*, 1993, **B79**, 209.
[81] R. Medenwalt, S. P. Müller, E. Uggerhüj, T. Worm, P. Hvelplund, H. Knudsen, K. Elsener and E. Morenzoni, *Nucl. Instrum. Methods*, 1991, **B58**, 1; R. Medenwalt, S. P. Müller, E. Uggerhüj, T. Worm, P. Hvelplund, H. Knudsen, K. Elsener and E. Morenzoni, *Phys. Lett.*, 1991, **A155**, 155.
[82] J. M. Pitarke, R. H. Ritchie and P. M. Echenique, *Phys. Rev. B*, 1995, **52**, 13883.
[83] A. Arnau and E. Zaremba, *Nucl. Instrum. Methods*, 1994, **B90**, 32.
[84] J. J. Dorado, O. H. Crawford and F. Flores, *Nucl. Instrum. Methods*, 1994, **B93**, 175; *erratum*, 1995, **B95**, 144; J. J. Dorado, O. H. Crawford and F. Flores, *Nucl. Instrum. Methods*, 1995, **B96**, 610.
[85] N. R. Arista and A. F. Lifschitz, *Phys. Rev. A*, 1999, **59**, 2719.
[86] P. Sigmund and U. Haagerup, *Phys. Rev. A*, 1986, **34**, 892.
[87] P. Sigmund, *Nucl. Instrum. Methods*, 1994, **B85**, 541.
[88] H. Bichsel, *Phys. Rev. A*, 1992, **46**, 5761.
[89] H. Bichsel and L. E. Porter, *Phys. Rev. A*, 1982, **25**, 2499.
[90] J. F. Janni, *At. Data Nucl. Data Tables*, 1982, **27**, 149.
[91] E. Bonderup, *Kgl. Dan. Videns. K. Selsk. Mat. Fys. Medd.*, 1967, **35** (17).
[92] G. S. Khandelwal and E. Merzbacher, *Phys. Rev.*, 1966, **144**, 349.
[93] J. Oddershedde and J. R. Sabin, *At. Data Nucl. Data Tables*, 1984, **31**, 275.
[94] N. Bohr, *Phys. Rev.*, 1940, **58**, 654.
[95] N. Bohr, *Phys. Rev.*, 1941, **59**, 270.
[96] H. Geissel, in *Semiclassical Description of Atomic and Nuclear Collisions* (eds J. Bang and J. De Boer), North-Holland, Amsterdam, 1985, pp. 431–462.
[97] W. E. Lamb, Jr., *Phys. Rev.*, 1940, **58**, 696.
[98] J. Knipp and E. Teller, *Phys. Rev.*, 1941, **59**, 659.
[99] T. E. Pierce, W. W. Bowman and M. Blann, *Phys. Rev.*, 1968, **172**, 287.
[100] L. C. Northcliffe, *Annu. Rev. Nucl. Sci.*, 1963, **13**, 67.
[101] T. E. Pierce and M. Blann, *Phys. Rev.*, 1968, **173**, 390.
[102] W. H. Barkas, Nuclear Research Emulsions, Academic Press, New York, 1963, Vol. I.
[103] S. D. Bloom and G. D. Sauter, *Phys. Rev. Lett.*, 1971, **26**, 607.
[104] G. D. Sauter and S. D. Bloom, *Phys. Rev. B*, 1972, **6**, 699.

[105] T. L. Ferrell and R. H. Ritchie, *Phys. Rev. B*, 1977, **16**, 115.
[106] L. E. Porter, *Phys. Rev. B*, 1977, **5**, 1812.
[107] B. S. Yarlagadda, J. E. Robinson and W. Brandt, *Phys. Rev. B*, 1978, **17**, 3437.
[108] S. Kreussler, C. Varelas and W. Brandt, *Phys. Rev. B*, 1981, **23**, 82.
[109] A. Mann and W. Brandt, *Phys. Rev. B*, 1981, **24**, 4999.
[110] M. Kitagawa and W. Brandt, *Phys. Rev. B*, 1982, **25**, 5631.
[111] F. Schulz and W. Brandt, *Phys. Rev. B*, 1982, **26**, 4864.
[112] E. C. Montenegro, S. A. Cruz and C. Vargas-Aburto, *Phys. Lett.*, 1982, **92A**, 195.
[113] T. Kaneko, *Phys. Rev. A*, 1986, **33**, 1602.
[114] P. Sigmund and A. Schinner, *Nucl. Instrum. Methods*, 2001, **B174**, 535.
[115] R. Cabrera-Trujillo, S. A. Cruz, J. Oddershedde and J. R. Sabin, *Phys. Rev. A*, 1997, **55**, 2864.
[116] R. Cabrera-Trujillo, J. R. Sabin and J. Oddershedde, *Phys. Rev. A*, 2003, **68**, 042902.

This Page Intentionally Left Blank

Molecular Stopping Powers from the Target Oscillator Strength Distribution

Remigio Cabrera-Trujillo,[1] John R. Sabin[1,2] and Jens Oddershede[1,2]

[1]*Quantum Theory Project, University of Florida, Gainesville, FL, USA*
[2]*Kemisk Institut, Syddansk Universitet, Odense, Denmark*

Abstract

In this contribution we consider the linear energy deposition, or stopping power, of swift ions in materials as obtained from oscillator strength distributions. We consider the first Born approximation and its connection with the generalized oscillator strength distribution (GOSD), and the calculational problems involved in obtaining an accurate GOSD. We then consider the Bethe approximation to the first Born approximation, and the details of the dipole oscillator strength distribution necessary to calculate the stopping power in this approximation. Some examples are given, and the reliability of such calculations is estimated.

Contents

ADVANCES IN QUANTUM CHEMISTRY, VOLUME 46
ISSN: 0065-3276 DOI 10.1016/S0065-3276(04)46005-5

1. INTRODUCTION

The linear energy loss or stopping power [1] of a non-relativistic swift ion as it passes through matter, $-\mathrm{d}E/\mathrm{d}x$, summarizes the energy transfer from the ion to the target atoms or molecules. From simple conservation of energy and momentum, it is clear that at all but the lowest collision energies, the bulk of the energy transfer will be to target electrons as electronic excitation and/or ionization. It is this energy transfer that we wish to consider, and thus restrict our considerations to electronic stopping. It should be noted, however, there are other modes of energy transfer that can be studied, for example energy transfer to target nuclei kinetic energy (known as nuclear stopping, and effective only at low projectile energy), and to vibrational and rotational modes of polyatomic systems.

As the energy transfer in normal stopping experiments is from the kinetic energy of the projectile to the target *via* electronic excitation, it is not unexpected that the strength of the transition, the oscillator strength, should play a major role.

The early classical Bohr treatment of energy deposition [2] considers stopping to be due to electromagnetic excitations of charged harmonic oscillators with circular frequency ω in a uniform electric field, which is generated by the passing projectile. The collision was characterized by an impact parameter rather than by the momentum transfer, and it is the impact parameter that plays the role of oscillator strength in this classical theory. Similarly, an early theory for stopping in solids by Lindhard [3] approached the problem from the point of view of a charged projectile penetrating an electron gas. Here it is the dielectric constant that serves the function of an oscillator strength distribution.

In this review we will only consider the fully quantum mechanical treatment of energy deposition.

The most used approximation in the study of the interaction of swift, massive ions with matter is the first Born approximation, a perturbative treatment where it is assumed that the scattering is sufficiently weak, i.e., the projectile–target interaction is weak enough that one may apply first order perturbation theory in the interaction. The most fundamental quantity describing such an interaction in the first Born approximation is the generalized oscillator strength distribution (GOSD) of the target system [4–6].

The GOSD completely determines the differential cross-section for inelastic scattering of swift projectiles from target atoms or molecules (or any other target, for that matter) at the level of the first Born approximation. Plotting Generalized Oscillator Strength (GOS) as a function of transferred energy and momentum forms the Bethe surface which, according to Inokuti [5] "…embodies all information concerning the inelastic scattering of charged particles by an atom or molecule within the first Born approximation."

Addition of the condition that the projectile velocity is large compared to that of the target electrons leads to the Bethe approximation [4] where the relevant quantity is the mean excitation energy, I_0, defined as the first moment of the dipole oscillator strength distribution (DOSD) for the target (*vide infra*).

Over the past two decades, we have been concerned with the calculation of oscillator strengths in the context of energy deposition by swift ions. In order to calculate the energy loss, or stopping power, of a swift ion in a medium, one needs to integrate over the entire oscillator strength distribution, either for the Generalized (GOSD) or Dipole (DOSD) oscillator strength distribution (*vide infra*), depending on the level of approximation employed. Thus one must have a method that will calculate these distributions reliably. For this purpose, we have used the polarization propagator scheme [7], which is described in Section 4.

The usefulness of the GOSD has stimulated many theoretical studies of its properties [8]. Perhaps most useful for applications are those studies which result in an analytic representation of the GOSD over some region of the Bethe surface, although many investigate specific transitions in specific systems. The point common to these investigations is that, with some exceptions, they treat atomic targets only, due to the complexity of the calculations involved for molecules. Although most molecules are anisotropic, experimental circumstances have been such that samples are prepared in such a way that they exhibit a certain degree of alignment. Thus previous theoretical interest has been in the isotropic or rotationally averaged GOS. New experimental technology has become available in the past decades, however, that makes it possible to prepare samples with a high degree of alignment, such as ultra-thin overlayers on solids, liquid crystals, and the recently reported methods involving pendular states prepared in rotationally cooled molecular beams [9–14]. Thus sample molecules may have a particular orientation with respect to the probe beam, and the tensor or directional properties of the GOSD and related optical quantities become topic of interest [15,16]. In other words, only transitions with proper polarization will be excited when the sample has a fixed orientation with respect to the beam, and rotational averages are no longer the only quantities of interest.

In our case, the motivation for investigation of the GOSD is the calculation of the stopping cross-section, or linear energy deposition cross-section, for energy loss of swift ions traversing material targets. Our goal is, rather

than to produce numbers that agree with experiment better than those produced by other schemes, to calculate stopping cross-sections from first principles physics and knowledge of molecular structure. From this approach, we hope to gain understanding of the details of the energy deposition process. We have tried to develop a general method that can be used to generate directional as well as rotationally averaged, or isotropic, GOSDs for molecular targets of chemically interesting size. We thus need a method which can treat many tens of electrons in an acceptably accurate way. In this contribution, we survey our calculation of GOSDs and their use in calculating stopping cross-sections in specifically and randomly oriented targets.

2. PRÉCIS OF OSCILLATOR STRENGTH BASED STOPPING THEORY

The simplest incarnations of the theory of linear energy transfer, or stopping power, of a material target for a swift ion are based, at all but the lowest energies where nuclear kinetic energy is exchanged, on quantum mechanical coulomb scattering of a structureless projectile with velocity v by the electrons of the target, with resulting excitation and ionization of the target, and loss of projectile kinetic energy [5,17]. The velocity dependent stopping power is generally expressed in terms of a stopping cross-section, $S(v)$, which is related to the stopping power by a scatterer density n and then to the stopping number, $L(v)$, which contains the physics of the process, as

$$-\frac{\Delta E(v)}{\Delta x} \approx -\frac{\mathrm{d}E}{\mathrm{d}x} = nS(v) = \frac{4\pi n e^4 Z_1^2 Z_2}{m_\mathrm{e} v^2} L(v) \tag{1}$$

The negative sign assures that the stopping is positive for decreasing projectile velocity, Z_1 is the projectile charge. We note that unless projectiles are fully stripped and at high energy, some electron capture and loss may be expected [18,19] and that, under the proper conditions, a projectile might even gain energy [20]. It should be noted that the electronic structure of the projectile can also affect the stopping power [19] and, consequently, the interpretation of stopping, a question addressed in Section 5.3.

Going beyond first-order perturbation theory, the stopping number can be expanded in a Born series in the fixed projectile charge Z_1

$$L(v) = \sum_i Z_\mathrm{p}^i L_i(v) \tag{2}$$

where i labels both the power of the projectile charge and the order of perturbation theory in each term. Each of the terms L_i has been developed, typically motivated by an experimental observation. Thus, one refers to the Bethe/Born ($i = 0$), Barkas ($i = 1$), and Bloch ($i = 2$) terms. In addition,

even higher level and relativistic terms [21] can be included. A similar series for the stopping cross-section, can also be written:

$$S(v) = \sum_i Z_1^i S_i(v) \tag{3}$$

We will consider only the lowest level term here, $S_0(v)$, which arises from the first, or plane wave, Born approximation.

For fixed charge structureless projectiles, i.e., when the projectile experiences neither electron gain or loss nor electronic excitation, and at the level of the first Born approximation, the stopping cross-section may be expressed in terms of the GOSs $F_{0n}(\mathbf{q})$, written as [5]:

$$S_0(v) = \frac{4\pi e^4 Z_1^2}{m_e v^2} \sum_{n>0} \int_{q_{\min}(v)}^{q_{\max}(v)} F_{0n}(\mathbf{q}) \frac{\mathrm{d}q}{q} \tag{4}$$

The upper and lower limits to the integral are determined by the kinematically allowed momentum transfer in the collision [5] and are given by

$$q_{\min}(v) = \frac{M_1 v}{\hbar} \left[1 - \sqrt{1 - \frac{2(E_n - E_0)}{M_1 v^2}} \right] \tag{5}$$

and

$$q_{\max}(v) = \frac{M_1 v}{\hbar} \left[1 + \sqrt{1 - \frac{2(E_n - E_0)}{M_1 v^2}} \right] \tag{6}$$

When the approximation that the projectile kinetic energy is much greater than the electron binding energy is made, the approximate limits become by

$$q_{\min} = \frac{E_{0n}}{\hbar v} \tag{7}$$

and

$$q_{\max} = \frac{2m_e v}{\hbar} \tag{8}$$

We note that the situation is somewhat more complicated if the projectile is allowed to exchange charge with the target during collision [19]. The GOSs for discrete transition are written as

$$F_{0n}(\mathbf{q}) = \frac{2m_e E_{0n}}{\hbar^2 q^2} \left| \left\langle 0 \left| \sum_{j=1}^{N} \mathrm{e}^{-\mathrm{i}\mathbf{q}\cdot\mathbf{r}_j} \right| n \right\rangle \right|^2 \tag{9}$$

As usual, $E_{0n} = E_n - E_0$ and $\mathbf{q}$ are the energy and momentum transferred during the collision, and concomitant excitation of the target from the ground state $|0\rangle$ to an excited state $|n\rangle$. The sum is over all electrons.

3. OSCILLATOR STRENGTH DISTRIBUTIONS

3.1. Generalized oscillator strengths

For all practical purposes, one may view energy transfer (E) as a continuous parameter, as the majority of energy transfer is to continuum target states. The GOSs are then labeled $F(\mathbf{q}, E)$ and the GOSD, or distribution of GOS per unit energy, is given by

$$\frac{\mathrm{d}F(\mathbf{q},E)}{\mathrm{d}E} = \sum\!\!\!\!\!\!\int_n \frac{2m_\mathrm{e}E_{0n}}{\hbar^2 q^2}\left|\left\langle 0\left|\sum_{j=1}^{N}\mathrm{e}^{\mathrm{i}\mathbf{q}\cdot\mathbf{r}_j}\right|n\right\rangle\right|^2 \delta(E_{0n}-E) \tag{10}$$

where $\sum\!\!\!\!\!\!\int$ indicates summation over discrete states and integration over continuum states. When $\mathrm{d}F(\mathbf{q},E)/\mathrm{d}E$ is plotted against q^2 and E, one obtains the Bethe surface. The GOSD and Bethe surface embody the characteristics of the excitation (and ionization) in an N-electron target traversed by a swift ion, either bare [5] or dressed [19].

The GOS between individual states is important as it provides information into the absorption process for high-energy radiation, i.e., on the characteristics of the inelastic collision between fast ions or neutrals, and an atomic or molecular target. As is evident from equation (9), the GOS depends on both energy and momentum transfer to the target from the projectile. For small momentum transfer, i.e., long wavelength, the GOS becomes the dipole oscillator strength (DOS). The GOS for a particular transition can be measured directly using methods such as Electron Energy Loss Spectroscopy (EELS) [22]. The properties of oscillator strengths are addressed extensively by Fano and Cooper [23].

3.2. Dipole oscillator strengths

Rather than calculating the GOSD for a particular target atom, molecule or solid, which can be very computationally intensive, one can expand the exponentials in equation (10) as

$$\mathrm{e}^{\mathrm{i}\mathbf{q}\cdot\mathbf{r}} = 1 + \mathrm{i}\mathbf{q}\cdot\mathbf{r} + \frac{(\mathrm{i}\mathbf{q}\cdot\mathbf{r})^2}{2!} + \frac{(\mathrm{i}\mathbf{q}\cdot\mathbf{r})^3}{3!} + \cdots \tag{11}$$

and then make the assumption of small momentum transfer, keeping only the first two terms of the expansion. This is referred to as the dipole, optical, or long-wavelength approximation. When this approximation is inserted into equation (4), a little algebra results in the Bethe formula [4,24,25] for stopping

$$S_0(v) = \frac{4\pi e^4 Z_1^2}{m_\mathrm{e}v^2}\ln\frac{2m_\mathrm{e}v^2}{I_0} \tag{12}$$

Here I_0 is referred to as the mean excitation energy of the target, and is computed as the energy weighted average of the target DOSD

$$\ln I_0 = \frac{\int \mathrm{d}f/\mathrm{d}E \ln E \, \mathrm{d}E}{\int \mathrm{d}f/\mathrm{d}E \, \mathrm{d}E} \tag{13}$$

where the $\mathrm{d}f/\mathrm{d}E$ is now the DOSD, or distribution per unit energy of the DOS from state $|0\rangle$ to $|n\rangle$ (for a rotationally averaged transition)

$$f_{0n} = \frac{2m_e E_{0n}}{3\hbar^2 e} |\langle 0|\mathbf{r}|n\rangle|^2 \tag{14}$$

From the definition of the mean excitation energy, it is clear that it is the fundamental material quantity involved in determining the stopping within the Bethe approximation to the first Born approximation, and that it depends on target properties only (*caveat* – see Section 3.4).

One should note that $S_0(v)$ in the Bethe formulation is only an approximation to the quantity calculated in the full first Born approximation. To get the Bethe value, the additional assumption of projectile speed much greater than that of the scattering electrons has been made. In order to correct for that, so-called shell corrections, $C_k(v)/Z_2$ are frequently added to the Bethe term to correct for the error introduced into the first Born approximation by adding the fast projectile assumption. The shell corrections are normally treated on an orbital-by-orbital basis, and are labeled as k. It should, thus, be possible to calculate shell corrections directly by calculating, using identical basis sets, the difference in L_0 in the first Born approximation, *via* the GOSD, and in the Bethe approximation, *via* the DOSD. As far as we are aware, this has not been done. Several other ways to calculate shell corrections have been published [26–28]. References to various other schemes for calculating shell corrections can be found in Refs. [29,30].

Although the Bethe approximation was developed in terms of a unified target characterized by a single mean excitation energy, I_0, we have shown that better results are obtained if each target electron is treated separately, and the excitation characteristics of each electron determined separately. As the electrons within an atomic or molecular orbital are equivalent, we have determined mean excitation energies on an orbital basis with some success [29]. This is done by determining the DOSs of all transitions out of a single shell and determining a mean excitation energy for them: I_0^k. The total target mean excitation energy is then given by

$$\ln I_0 = \frac{1}{N_2} \sum_k \omega_k \ln I_k \tag{15}$$

where the ω_k are weighting factors related to orbital occupation numbers and N_2 is total number of target electrons.

3.3. Directional characteristics of oscillator strength distributions

Although most molecules are anisotropic, experimental setups generally are contrived so that samples are prepared without regard to alignment of the target with respect to the beam direction. Consequently, most of the experiments determining either oscillator strength distributions or energy deposition have been for the orientationally averaged, or isotropic quantities. Recently, however, several schemes have been developed which allow preparation of gaseous as well as solid samples which have a specific molecular alignment with respect to the beam [9–14]. Thus rotational averages are no longer the only quantities of interest, and the directional characteristics of oscillator strength distributions become relevant.

For an ion beam penetrating non-symmetric matter, the stopping power depends on relative orientations of the ion beam and the direction of the symmetry axes of the target. This dependence can be traced to two separate, but related causes. First, for projectiles with trajectories at sufficiently small angles with respect to a crystal axis or plane, the trajectories are governed by the crystal potential, and this channeling phenomenon may reduce the energy deposited by tens of percent in stopping power as compared to particles traversing the material in a so-called random direction. Second, and the subject of this section, the target may consist of molecules which have directional bonds, and even when channeling effects are insignificant, the efficiency of the projectile in exciting target electrons may depend on the orientation of the molecules with respect to the direction of motion of the projectile.

When comparing calculated oscillator strengths and quantities derived from them to experimental numbers, care needs be taken to use angularly (rotationally) averaged theoretical numbers unless the experiment is done with an aligned sample. For example, for a linear molecule aligned at an angle θ to the beam, one can express $\langle F_{0n}(\mathbf{q})\rangle_{\text{ang.av.}}$ in terms of $F_{0n}(\mathbf{q})$. The angularly averaged GOS is then

$$\langle F_{0n}(q)\rangle_{\text{ang.av.}} = \frac{1}{8\pi^2}\int \mathrm{d}\Omega F_{0n}(\mathbf{q}) \tag{16}$$

where $\mathrm{d}\Omega$ is the element of solid angle for the rotational average. Both the first Born approximate treatment of stopping (equation (4)) and the long wavelength Bethe approximation to it (equation (12)) involve directional quantities in the oscillator strength distributions: namely, $\mathbf{r}$. It is these quantities that we wish to discuss.

3.3.1. The GOSD

From equation (9) it is clear that any particular transition will contribute to the oscillator strength sum only when the polarization of the transition and

momentum transfer in the collision have the correct mutual orientation. One way to view this is to consider the expansion of $e^{i\mathbf{q}\cdot\mathbf{r}}$ in equation (11). If $\langle 0|\mathbf{r}|0\rangle$ is expressed in terms of its Cartesian components, $e^{i\mathbf{q}\cdot\mathbf{r}}$ can be expressed as a sum of terms of the sort $\langle 0|s^p t^q u^r|n\rangle$ where $s, t, u = x, y, z$ and p, q and r are integers. It is thus clear that, for a particular term to contribute to the sum, and thus to the energy deposition, $s^p t^q u^r$ must have the same polarization as $|n\rangle$. Orientational effects in the energy deposition follow [31,32].

3.3.2. The DOSD

At the Bethe [4] level of approximation, the mean excitation energy is the important parameter for energy deposition. The mean excitation energy (see equation (13)) may be explicitly written in terms of the Cartesian components of the moments of the DOSD $L(0)$ and $S(0)$, which are determined by the components of the dipole operator as

$$\ln I_0 = \frac{L(0)}{S(0)} = \frac{\sum_\alpha L^\alpha(0)}{\sum_\alpha S^\alpha(0)} \tag{17}$$

with

$$S^\alpha(0) = \frac{2}{3}\sum_{n\neq 0} E_{0n}\langle 0|\alpha|n\rangle\langle n|\alpha|0\rangle \tag{18}$$

and

$$L^\alpha(0) = \frac{2}{3}\sum_{n\neq 0} E_{0n}\langle 0|\alpha|n\rangle\langle n|\alpha|0\rangle \ln E_{0n} \tag{19}$$

where α represents one of the Cartesian components of the operator and where we, for simplicity, have assumed that there are no mixed components of the oscillator strength. As projectiles can only excite scattering electrons where the polarization of the excitation is perpendicular to the projectile velocity [24,31,32], the subset of excitations with non-zero contributions to the moments of the DOSD (equations (18) and (19)) will vary depending on the orientation of the target molecule with respect to the beam direction. As the moments determine the mean excitation energy which, in the Bethe approximation, also determines the stopping cross-section, a contribution to the stopping cross-section is expected only from those excitations having polarization commensurate with the beam direction. Thus the stopping cross-section will be directionally dependent. We have reported the general

formulation of a Bethe theory for molecules with specific orientation with respect to the beam direction [31], and have reported the directional components of the stopping cross-section and the mean excitation energy for a series of small molecules [32].

For example, consider swift ions impinging on a homonuclear diatomic molecule. If z is the Cartesian direction of the internuclear axis, then the spectrum of allowed excitations with polarization perpendicular to the molecular axis ($\Pi \leftarrow \Sigma$) and with polarization parallel to the molecular axis ($\Sigma \leftarrow \Sigma$) will be quite different, giving a mean excitation energy, and thus Bethe stopping power, which depends on target orientation.

It should also be noted that the mean excitation energies associated with particular polarizations of molecular orientations (I_0^α) add to give the random, or normal, mean excitation energy I_0 as

$$S(0)\ln I_0 = \sum_\alpha S^\alpha(0)\ln I^\alpha \tag{20}$$

3.4. Projectile structure

The energy deposition studies which are based on oscillator strength distributions arise from the first Born approximation, and assume that the projectile is a structureless point mass which, through collisions with the target electrons, can excite the target, but can neither exchange electrons with the target nor itself be excited or ionized. This assumption is physically unrealistic except for high energies where the projectile is completely stripped, but has been extensively used over the years.

At velocities in the range $v_0 < v < v_0 Z_1^2$ where v_0 is the Bohr velocity [17], excitation, capture, and loss of electrons by the projectile happen with high probability, and lead to important contributions to the energy loss. The problem was first considered by Kim and Cheng [18], and later by us [19] and others [33].

3.4.1. Effect of projectile structure in the first Born approximation (GOS)

The crucial point in this case is that a collision between a dressed projectile and a target is symmetric: either of the collision partners can be considered the target (or projectile), and electron excitation, exchange and ionization, commensurate with the collision energy, can occur on either center. In the case of the first Born approximation, the stopping cross-section can be written [19] in terms of the GOSs of the target (t) and of the projectile (p). (We note that the designation of target and projectile is arbitrary.)

The stopping cross-section can then be written as [19]

$$S(v) = \frac{2e^4}{m_e v^2} \sum_{n,m} \left\{ \int_{q_{\min}}^{q_{\max}} |Z_t \delta_{m_0 m} - M^t_{m_0 m}(\mathbf{q})|^2 F^p_{n_0 n}(\mathbf{q}) \frac{d\mathbf{q}}{q^2} + \int_{q_{\min}}^{q_{\max}} |Z_p \delta_{n_0 n} - M^p_{n_0 n}(\mathbf{q})|^2 F^t_{m_0 m}(\mathbf{q}) \frac{d\mathbf{q}}{q^2} \right\} \quad (21)$$

or

$$S(v) = S_p(v) + S_t(v) \quad (22)$$

Here, n denotes states associated with the projectile, m denotes states associated with the target, and $d\mathbf{q} = q\, dq\, d\phi$ is the orientationally averaged momentum transfer. The M values are atomic form factors [34] and have the form

$$M^p_{n_0 n}(\mathbf{q}) = \left\langle n_0 \left| \sum_{j=1}^{N_1} e^{-i\mathbf{q}\cdot\mathbf{r}_j} \right| n \right\rangle \quad (23)$$

for the projectile, and symmetrically for the target.

In the Bethe approximation, the maximum and minimum momentum transferred during the collision are given by

$$q_{\min} = \frac{E_{n_0 n} + E_{m_0 m}}{\hbar v} \quad (24)$$

and

$$q_{\max} = \frac{2m_e v}{\hbar} \quad (25)$$

which apply symmetrically to both the projectile and to the target.

Note that the stopping cross-section has terms involving matrix elements of $e^{\pm i\mathbf{q}\cdot\mathbf{r}}$, and that each term has mixed contributions from both the target and the projectile. In fact, the energy deposition alone can be attributed to neither.

3.4.2. Effect of projectile structure in the Bethe approximation (DOS)

Derivation of a similar equation [19] under the Bethe assumptions leads, again, to a two-term equation containing contributions from both projectile and target. Following the normal derivation of the Bethe formula [4], one introduces the Bethe Sum Rule (see Section 4.2). If in addition to the atomic numbers (Z_i) of the collision partners, we define the number of electrons associated with each as N_i, then the net charge on the collision partner under consideration is $q_i = Z_i - N_i$.

The stopping power can then be written [19] as

$$S(v) = \frac{2e^4}{m_e v^2} \int_{\varepsilon/\hbar v}^{2m_e v/\hbar} \left\{ N_t [Z_p - M^p_{n_0 n_0}(\mathbf{q})]^2 + N_p [Z_t - M^t_{n_0 n_0}(\mathbf{q})]^2 \frac{d\mathbf{q}}{q^2} \right\} \quad (26)$$

The equivalent of a mean excitation energy in this formulation is ε, which is defined as

$$\varepsilon = I_{0,t}^{1/(1+\alpha)} \cdot I_{0,p}^{\alpha/(1+\alpha)} \tag{27}$$

and the quantity that functions as a (dimensionless) charge is

$$\alpha = \frac{(Z_\mathrm{t} - N_\mathrm{t})^2 N_\mathrm{p}}{(Z_\mathrm{p} - N_\mathrm{p})^2 N_\mathrm{t}} \tag{28}$$

Note again, that target and projectile properties are intermingled.

Equation (26) is then the resulting stopping formula in the Bethe approximation for non-relativistic collision energies. It takes into account excitations and ionizations of both the projectile and target through the mean excitation energy, as does the standard Bethe theory. Again, as with standard Bethe theory, the projectile velocity must be large with respect to the electron velocities in both the projectile and the target.

Although excitations and ionizations for both collision partners are taken into account, at least at the level of the Bethe theory, it does not contain an *a priori* scheme for determining the total number of electrons, N_i to be associated with each of the collision partners. For our calculational studies, we thus adopted [19] the Bohr adiabatic criterion [35,36] for use in conjunction with this model.

4. THE POLARIZATION PROPAGATOR

4.1. Introduction

In order to compute oscillator strength distributions, both the GOSD and the DOSD, and evaluate a stopping cross-section from equations (4) and (9) or equations (12)–(14), a method which will produce the entire oscillator strength distribution, in principle for an infinite number of transitions, must be used, as the sums and integrals in equations (4) and (13) are over all possible transitions. The method we have used, the polarization propagator method, is detailed elsewhere [7], but can be summarized as follows.

We consider two operators $\mathcal{A}$ and $\mathcal{B}$ which correspond to two system observables. The spectral representation of the polarization propagator for those operators is written as [7]

$$\langle\langle \mathcal{A}; \mathcal{B} \rangle\rangle_E = \sum_{n \neq 0} \left[\frac{\langle 0|\mathcal{A}|n\rangle\langle n|\mathcal{B}|0\rangle}{E - E_n + E_0} - \frac{\langle 0|\mathcal{B}|n\rangle\langle n|\mathcal{A}|0\rangle}{E + E_n - E_0} \right] \tag{29}$$

where $|0\rangle$ is the state out of which excitation occurs, and the sum is over all possible excitations. The poles of the propagator correspond to the excitation

energies of the system ($E_{0n} = E_n - E_0$) and the residues are the transition matrix elements. If the operators are chosen such that

$$\mathcal{A}^\dagger = \mathcal{B} = \mathrm{e}^{\mathrm{i}\mathbf{q}\cdot\mathbf{r}} \tag{30}$$

then the transition energies and transition moments will be those necessary to calculate the GOSs from equation (9). We note that if we choose $\mathcal{A} = \mathcal{B} = \mathbf{r}$ then the poles and residues of the propagator give the optical transition energies and transition moments, which lead to the optical (dipole) oscillator strengths and distributions (DOSD) in the dipole length formulation:

$$f_{0n}^{L} = \frac{2m_\mathrm{e}E_{0n}}{3\hbar^2}\langle 0|\mathbf{r}|n\rangle\langle n|\mathbf{r}|0\rangle \tag{31}$$

Similarly, choice of $\mathcal{A} = \mathcal{B} = \mathbf{p}$ or $\mathcal{A} = \mathbf{r}$, $\mathcal{B} = \mathbf{p}$ lead to the DOSDs in the velocity and mixed formulations, respectively. Note that in a complete basis set, these formulations are equivalent in the sense that they give identical oscillator strengths. These quantities are those necessary for calculation of the mean excitation energies needed for evaluation of the Bethe formulation of stopping power theory [4].

The method described here is a basis set based method. It means that a finite, discrete, computational basis is chosen, and an orbital space of the same dimension as the basis is generated. Note that there are no continuum orbitals in this treatment. The consequence of using a finite basis is that we clearly cannot span the full excitation space, as there are only a finite number of particle–hole excitations which can be constructed from the basis. The consequence of not including continuum states is that we clearly cannot represent ionization states properly; they are represented by a finite number of discrete, positive-energy pseudostates which, in some average way, represent the continuum. We expect that the first few transitions calculated will correspond to physical transitions in the system, but the higher lying ones will not correspond to physically extant transitions. Although sums over all the states give results which are correct, in the sense of obeying the sum rules other than for some of the lowest lying excited states, no physical significance can be attached to the (pseudo)states.

Solution of the equation of motion for the polarization propagator at various levels of sophistication leads to a hierarchy of approximations to the exact solution which one classifies according to the order in perturbation theory through which the energy differences are correct. The perturbation is the fluctuation potential, which is the electronic repulsion minus the Fock average potential [7]. The zeroth order solution is generally considered to be the Hartree–Fock (HF) solution, where ground and excited states are made up of single determinants of unrelaxed, ground state HF orbitals. In the context of this work, we will consider this to be the uncorrelated solution [37]. Some excited state correlation is included at the Mono-Excited

Configuration Interaction (MECI) level of approximation, and both ground and excited states are correlated in the Random Phase Approximation (RPA), which is the consistent first-order approximation to the polarization propagator [38]. The second-order polarization propagator approximation (SOPPA) [39] adds more correlation in both ground and excited states, as do higher order approximations [40].

Experience has shown [41] that in order to calculate oscillator strength related properties reliably, correlation must be included at least to the level of RPA. Indeed, the degree to which the relevant sum rules (*vide infra*) are fulfilled changes greatly as one increases correlation from HF to MECI to RPA, but does not change significantly by further increasing the level of correlation.

4.2. Sum rules and basis sets

There are decades of experience behind the art of choosing basis sets for ground state electronic structure calculations, and the variational principle guides one while choosing a computational basis. Clearly such bases are not complete, but the variational principle guides one in their choice: in terms of energy, lower is better. However, when dealing with response properties, such as oscillator strengths associated with electronic transitions, a good energy optimized basis is only necessary, but it is not sufficient for a good result. This is obvious, as a good energy based basis optimizes only the occupied, but not the virtual, orbitals. Thus, for response properties, other criteria for quality of the bases must be found.

4.2.1. GOS: the Bethe sum rule

When dealing with computed oscillator strength distributions, sum rules are of considerable use, as they provide simple checks on the accuracy of the computation, and thus provide the criteria mentioned above. Although much has been written concerning various sum rules, the article by Hirschfelder *et al.* [42] continues to be the most useful.

For the GOS, the appropriate sum rule is the Bethe sum rule [4], usually written as

$$\sum_n F_{0n}^i(\mathbf{q}) = N_i \tag{32}$$

and which is valid for all kinematically allowed values of the momentum transfer. Here i normally refers to the target with excitations $|n_0\rangle \rightarrow |n\rangle$, when the projectile is considered a point charge. In the case where the projectile is dressed, such as described in Section 3.4.2, the sum rule must be applied to the projectile and target individually. If capture and loss between projectile and target is allowed – not the usual case – all excitations in

the supermolecule must be considered. (It should be noted that energy deposition is an intrinsically dynamic process: a projectile with its own electronic structure and with a velocity with respect to a target molecule comes from a large distance from the target, moves through an interaction zone, and moves off again. During this process, the electronic structure of the projectile/target supermolecule changes, and especially so in the interaction zone. On the other hand, the GOS is calculated for a static situation and describes excitation from one static state to another. Thus a logical inconsistency arises.)

In equation (32), the sum is over all allowed excitations; so the equality only holds for the complete, exact, theoretical oscillator strength distribution. Since no computational basis is complete, and no calculation provides exact transitions, one expects that the BSR cannot be fulfilled exactly in any calculation. However, it has been shown [43] that the BSR is fulfilled at the RPA level of approximation to the polarization propagator, again for a complete basis. Thus, if one restricts to RPA the approach of the sum to N should serve as a criterion of increasing basis set quality.

The problem is that the calculations of the Bethe sum (the LHS of equation (32)) typically only give good values, i.e., values close to N, for small values of the transferred momentum [43,44]. This can be seen for He in Fig. 1 (after Fig. 4 in Ref. [43]). Although there is some improvement from the extended [13s, 11p, 4d, 3f] HF basis, even with the best basis that we could construct [13s, 5p, 5d, 5f, 5g], the BSR is only satisfied for a few (Hartree) atomic units of momentum exchange. Some criteria have been developed to optimize such a basis set [43], but the results are not encouraging.

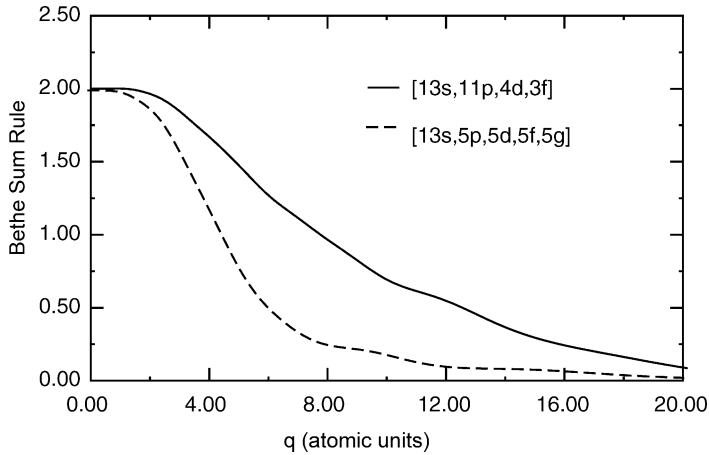

Fig. 1. Bethe sum rule for He generated with a Hartree–Fock basis [45] and a basis optimized according to Ref. [43].

The diminution of the Bethe sum with increasing momentum change can be understood in a qualitative way by expanding the exponential in equation (9) in powers of $\mathbf{q}$ about $\mathbf{q} = 0$. In the simple case of $\mathbf{q} = (0, 0, q)$ one obtains

$$F_{0n}(\mathbf{q}, E) = \frac{2m_e E_{0n}}{\hbar^2 q^2}\left\{|\langle 0|z|n\rangle|^2 + q^2\left(\frac{1}{4}|\langle 0|z|n\rangle|^2 - \frac{2}{3}|\langle 0|z|n\rangle\langle n|z^3|0\rangle|\right) + \cdots\right\} \tag{33}$$

As q increases, the basis needs to be able to describe correctly the increasing multipole transition moments, and thus basis functions with ever increasing l-quantum numbers are required in the basis. Clearly increasing the basis for large momentum transfer is bound to fail eventually, and thus purely basis set based methods will not solve the problem.

(NB. This is *not* the way that we have calculated the BSR, but rather we display the expansion on heuristic grounds. The calculation is done using the polarization propagator directly.)

Another possible approach is to calculate the Bethe sum for low momentum transfer and then graft an analytical tail onto it at some pre-chosen momentum transfer. We proposed [44] to use the polarization propagator to compute the GOSs for transitions less than some critical value, $E_{n0} < E_L$, and use a hydrogenic expansion [46] for larger excitation energies. Thus the Bethe sum rule (equation (32)) becomes

$$\sum_{n\neq 0}^{E_L} F_{0n}(q) + \int_{E_L}^{\infty} \frac{\mathrm{d}F(q, E)}{\mathrm{d}E}\mathrm{d}E = N \tag{34}$$

where $\mathrm{d}F(q, E)/\mathrm{d}E$ is the density of GOS per unit energy in the hydrogenic approximation. The scheme contains several parameters describing the target atom [44] as well as the cut-off energy E_L.

Although this approach seems to work well for He [44], it fails seriously for Be [47], where a dip in the Bethe sum to nearly $N/2$ cannot be eliminated.

Although GOSs and the GOSD is most frequently discussed for the non-relativistic case, it is possible to formulate the Bethe sum rule for the relativistic case as well. Although the formulation has been made [48], we are unaware of any calculations on the relativistic sum rule.

4.2.2. DOS: the Thomas–Reiche–Kuhn sum rule

If, consistent with Bethe's development [4] of stopping theory, we take the limit of zero momentum transfer from the projectile to the target, the DOSD becomes the quantity of interest, as it leads to the mean excitation energy (see equation (13)), and the appropriate sum rule is

the Thomas–Reiche–Kuhn, or TRK, sum rule [49,50]

$$S(0) = \sum_n f_{0n} = N \tag{35}$$

where the f_{0n} are the DOSs (equation (14)) and the sum is over the complete set of excitations $|0\rangle \rightarrow |n\rangle$. The comments in Section 4.2.1 apply, and for reasonable basis sets, excellent results are obtained. For example, the sum rule calculated for a variety of small molecules and ions [32] yields the results in Table 1.

In all cases, the calculations were carried out the in RPA and the length representation. Basis sets were generally of the size [5s4p1d] for hydrogen and [9s9p5d2f] for first row heavy atoms. Details can be found in the original paper [32]. It should be noted that the TRK sum $S(0)$ should be the same whether calculated in the length, velocity, or mixed representations. Namely, one would expect $S^L(0) = S^V(0) = S^M(0) = N$ but, again, this is only true for a complete basis. This is another criterion that can be used for comparing bases. We find that $S^L(0)$ normally approaches N more quickly than do the other two; so it is the nearness of $S^L(0)$ to N that we normally use as a criterion of an adequate basis set.

If one examines the DOSD, it appears that the individual transition moments for high-lying transitions are small. Thus it might be tempting to cut-off the sum at some sufficiently high excitation energy in order to save computational resources. However, the DOS also contains the transition energy so that even excitations with small transition moments may contribute significantly to the sum and thus to the mean excitation energy. This is illustrated for H_2O using a basis of 101 Gaussian functions in Fig. 2 (after Fig. 1 of Ref. [51]), where we show the partial sum $S^N(0) = \sum_n^N f_{0n}$ carried out over all excitations with excitation energy less than E_N.

Table 1. Calculated molecular TRK sums at the RPA level of approximation

Molecule	N	TRK sum	Molecule	N	TRK sum
BH_3	8	8.024	SiH^+	14	13.928
CH_4	10	10.016	GeH^+	32	29.957
NH_3	10	10.006	C_2H_2	14	14.006
H_2O	10	10.007	CH_2O	16	16.020
HF	10	10.013	CO	14	14.008
BH	6	6.001	CN^-	14	14.008
AlH	14	13.916	HCN	14	13.991
BeH^-	6	6.002	N_2	14	14.009
MgH^-	14	13.728	BF	14	14.009
CH^+	6	6.001	F_2	18	18.016

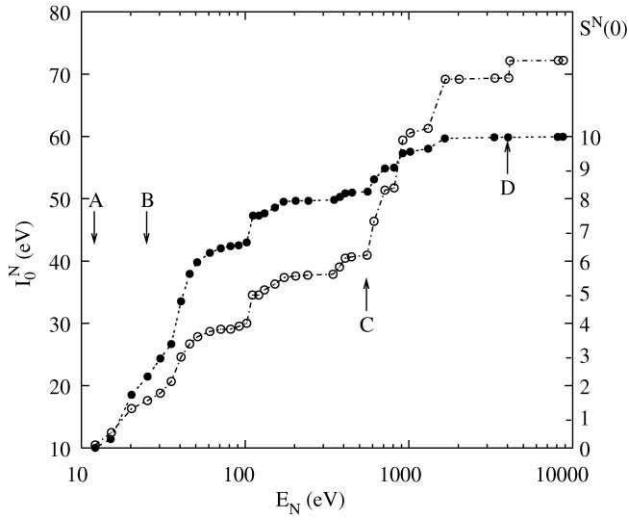

Fig. 2. Partial Thomas–Reiche–Kuhn sum, $S^N(0)$ (filled circles) and associated mean excitation energy I_0^N (open circles) for H_2O.

Here 'A' denotes the first ionization energy of H_2O, 'B' indicates the energy where excitations from the O:2s orbital begin, 'C' is where excitations from O:1s begin, and 'D' indicates where excitations out of O:1s and into the Rydberg levels begin. Note that there are significant contributions to both the TRK sum rule and to the mean excitation energy from transitions throughout the spectrum, even up to several thousand electron volts.

The question of electron correlation needs to be addressed. In most of our work, we have calculated oscillator strength distributions at the RPA level of approximation. As the sum rules are exact in RPA for a complete basis, the sum rules are a good indicator of basis set quality. It is fortuitous that most smaller molecules are easily calculable in RPA as well. The TRK sum rule, however, addresses the basis set, not the level of the calculation in the sense of an approximate solution to the Schrödinger equation. RPA seems to work remarkably well in most instances. An investigation of the effect of correlation on the DOSD of Be [41] leads to the conclusion that although the lower orbitals are most affected by correlation, there is not a great effect on the mean excitation energy. As an example, values of the TRK sum rule for Be, calculated in both the length ($S^L(0)$) and velocity ($S^V(0)$) formulations, and with at various levels of correlation are shown in Table 2. Comparing the mean excitation energy of Be calculated in RPA to that calculated using the coupled cluster singles and doubles polarization propagator approximation (CCSDPPA) [41], a method generally recognized as providing a good level of correlation, one sees a difference of only

Table 2. TRK sum rule for Be at various levels of correlation

Method	$S^L(0)$	$S^V(0)$
HF	5.386	3.201
MECI	4.876	3.378
RPA	4.008	3.954
SOPPA	4.038	4.017
CCSDPPA	4.102	4.079

a few percent. On the other hand, the HF value is more than 30% too low. Thus correlation at the level of RPA is a minimum necessity for calculating the DOSD and associated mean excitation energies for use in energy deposition calculations. The basis used for these calculations is a [9s, 9p, 5d] contracted set with 66 functions.

As an aside, we note that the effect of an external magnetic field on the Bethe and TRK sum rules has also been considered [52].

5. SOME EXAMPLES

In illustration of the points made above, we offer a few specific examples from our own work dealing with the calculation of oscillator strength distributions and their effects on energy deposition properties.

5.1. Comparison of GOS and DOS results

As an example and a comparison, we consider the calculation of the stopping cross-section of He for protons in both the first Born approximation, dependent on the GOSD [43,44], and in the Bethe approximation to the first Born approximation, which depends on the DOSD, using a mean excitation energy of 42.69 eV. The results are shown in Fig. 3 for projectile energies both less than and greater than the maximum in the stopping cross-section. In addition, in the same figure, we show results calculated using the kinetic theory of stopping [29] also using a mean excitation energy of 42.69 eV [53]. We note that although the kinetic theory formulation includes shell corrections, it is still not possible to reproduce the first Born calculation exactly. Best fit experimental results can be found in the tables of Andersen and Ziegler [54] for comparison.

5.1.1. Stopping power of He using the GOSD

As has been discussed above in Section 4.2.1, it is difficult to calculate the GOSD so that the Bethe sum rule is satisfied for large momentum transfer.

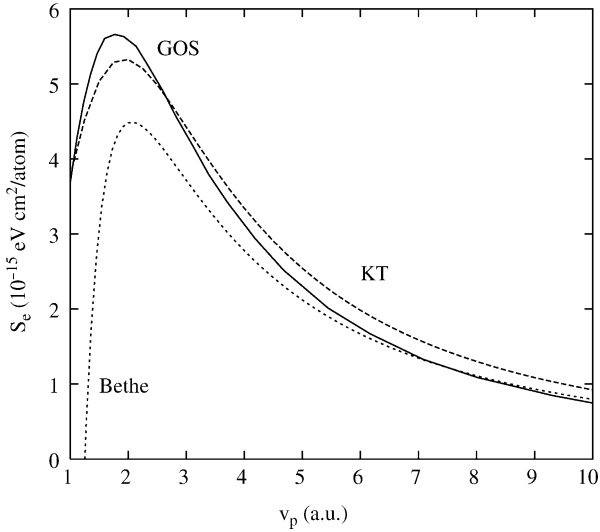

Fig. 3. Stopping cross-section for swift protons colliding with He calculated in the first Born approximation (solid line, labeled GOS), calculated using the kinetic theory (dashed line, labeled KT), and in the pure Bethe approximation (dotted line, labeled Bethe).

The basis used is the [13s, 5p, 5d, 5f, 5g] basis mentioned above, and from Fig. 1, it is clear that the basis only satisfies the BSR out to a momentum transfer of something less than $q = 4$ a.u. In spite of that, a look at the Bethe surface [5] soon convinces one that the lower momentum transfer regime makes the largest contribution to the stopping, and it is this region that is clearly best represented in this formulation. It is also clear that increasing the basis with ever higher angular momentum functions will make the BSR satisfied to larger momentum transfer, and thus increase the accuracy of the calculated stopping power. However, this route does not provide a general feasible solution to the problem due to the high computational costs associated with it.

5.1.2. Stopping power of He using the DOSD

The stopping in the Bethe approximation is considerably easier to calculate, and the curve presented in Fig. 3 is calculated from the Bethe formula of equation (12) using a mean excitation energy of $I_0 = 42.69$ eV calculated in the RPA using a contracted [13s11p4d] basis [53]. In the region where the Bethe theory is expected to do well, namely, when the projectile velocity is large, the results are fine. However, at lower energies, the results begin to deviate from the GOS-based calculations as well as from experimental results. This behavior is expected, as equation (12) diverges for small

projectile velocity where the assumption that the projectile velocity is greater than that of the target valence electrons no longer holds.

The Bethe theory can be greatly improved by adding shell corrections to equation (12) to mimic the deviations from the first Born approximation caused by the fast projectile assumption not being fulfilled

$$S_0(v) = \frac{4\pi e^4 Z_1^2 Z_2}{m_e v^2}\left[\ln\frac{2m_e v^2}{I_0} + \frac{C(v)}{Z_2}\right] \tag{36}$$

In addition, it is unaesthetic that the shell corrections are generally not generated using the same theoretical framework as that used to obtain the mean excitation energy, but there are several sets readily available (cf. e.g., Refs. [26–28]). To illustrate the effect of adding shell corrections to the Bethe logarithmic term, we have also included a stopping curve calculated using the kinetic theory [29] in Fig. 3. Here, the mean excitation energy used was again $I_0 = I_0^{1s} = 42.69$ eV. The agreement is somewhat better than the case without added shell corrections, and the divergence at low projectile velocity is avoided, but the stopping cross-section goes negative when $2m_e v_2 < I_0$, which is not physical.

5.2. Directional differences

5.2.1. GOS

The bulk of work done on directional differences in the GOSD of molecules has been done on individual transitions (CO [55]; H_2 [56]), as individual transitions are much more easily dealt with than is the entire distribution. This is due to the multipole nature of the operator $e^{i\mathbf{q}\cdot\mathbf{r}}$ which allows many transitions between states of different polarizations to contribute to the GOS. As described in Section 3.3.1, the GOSs depend on the orientation of the target molecule with respect to the beam, but here, the contributions will differ in size, rather being simply allowed or not. As an example, in Fig. 4 (after Fig. 5 of Ref. [55]) we show the directional components of the GOS for the $F^1\Sigma^+ \leftarrow X^1\Sigma^+$ transition in CO. The bond is aligned along the z-axis, which is parallel to the beam direction. Such differences will result in differences in the stopping cross-section dependent on the orientation of the target molecule with respect to the beam.

5.2.2. DOS

The case for the DOS, and thus the mean excitation energy and stopping power is more clear. The DOS matrix elements are of the sort $\langle 0|r_i|n\rangle$, where r_i is a Cartesian direction. The only non-zero matrix elements will thus be states that have polarization perpendicular to the beam direction [31,32].

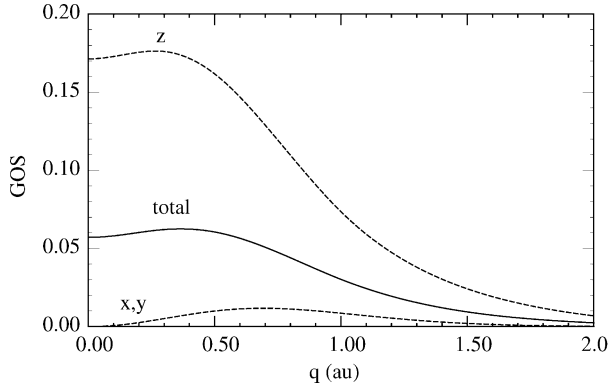

Fig. 4. Generalized oscillator strength for the $F^1\Sigma^+ \leftarrow X^1\Sigma^+$ transition in CO with polarization parallel and perpendicular to the bond axis.

The logarithm of the mean excitation energy, and thus the stopping power, can then be shown to be linear in $\sin^2\theta$, where θ is the angle between the beam and the principle molecular axis [32]. To illustrate, in Fig. 5 (after Fig. 2 of Ref. [57]) we show the calculated directional mean excitation energies of H_2O as a function of OH bond length.

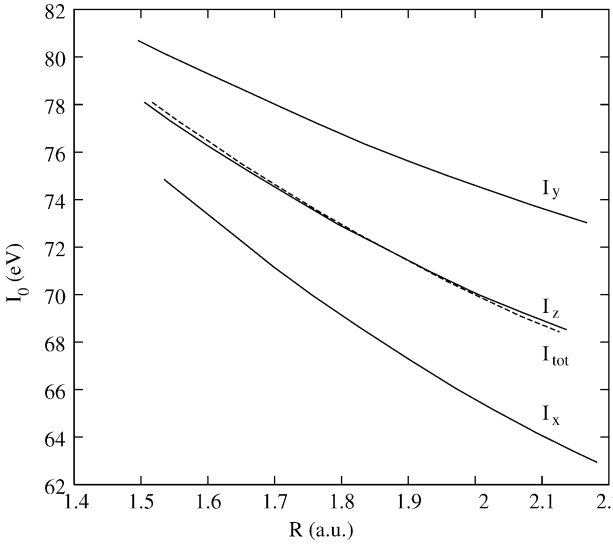

Fig. 5. Mean excitation energy of H_2O and its directional components as a function of R_{OH} for $\theta = 104.45°$.

The mean excitation energy along the molecular C_2 symmetry axis at the equilibrium geometry ($R_{OH} = 1.811$ a.u.; $\theta = 1.182$ rad) is $I_z = 72.89$ eV, very nearly the isotropic value of $I_0 = 72.91$ eV. On the other hand, the mean excitation energies aligned along the two orthogonal axes are $I_x = 69.21$ eV and $I_y = 76.76$ eV, a difference of about 10%. The change in electronic structure of the molecule with bond length is also clear from Fig. 5, and the change is again about 10% over the range shown. The conclusion is clearly that both geometry and direction will influence energy deposition.

5.3. Dressed projectiles

The effect of dressed projectiles has been addressed earlier [19], in the sense that the effect of the projectile electronic structure was included in the treatment. However, since that work was reported, Porter [58] has made a more systematic study of the mean excitation energies, which should be energy independent and characteristic only of the target electronic structure in the simple Bethe description, of various projectiles impinging on a common target. He noticed a general trend that the mean excitation energy of a target decreased with increasing projectile atomic number when determined by fitting experimental data to a modified Bethe–Bloch formula [59]. However, the stopping cross-section curves per unit projectile atomic number decreased with increasing projectile atomic number, inconsistent with simple Bethe theory. One should note, however, that as well as a change in mean excitation energy, an explanation involving projectile effective charge could be formulated.

The observations can also be looked upon as the result of the interaction of electronic structure of the projectile with that of the target. When that is done [60], the trends become reasonable, and, using standard mean excitation energies, a decrease in stopping curves per unit projectile atomic number with increasing projectile atomic number is found.

By way of an example, in Fig. 6 (after Fig. 5 of Ref. [60]) we show the results obtained for projectiles from H to C on a C target, along with some experimental results from Trzaska [61]. Note that the experimental numbers also decrease with increasing atomic number.

As only differences among the various projectiles are rooted in the projectile electronic structure, in this case the DOSD, it must be the root of the different stopping cross-sections for several projectiles on a single target. If the projectile electronic structure is taken into account explicitly, as it is in the extended Bethe theory described in Section 3.4, the correct behavior, namely, decreasing stopping cross-section per unit charge with increasing projectile atomic number, is obtained. The explanation clearly lies in the electronic structure of the projectile, which, as can be seen from the extended Bethe theory calculations, is critical. Fitting the experiments to a Bethe-like theory forces all the electronic effects of both target and projectile

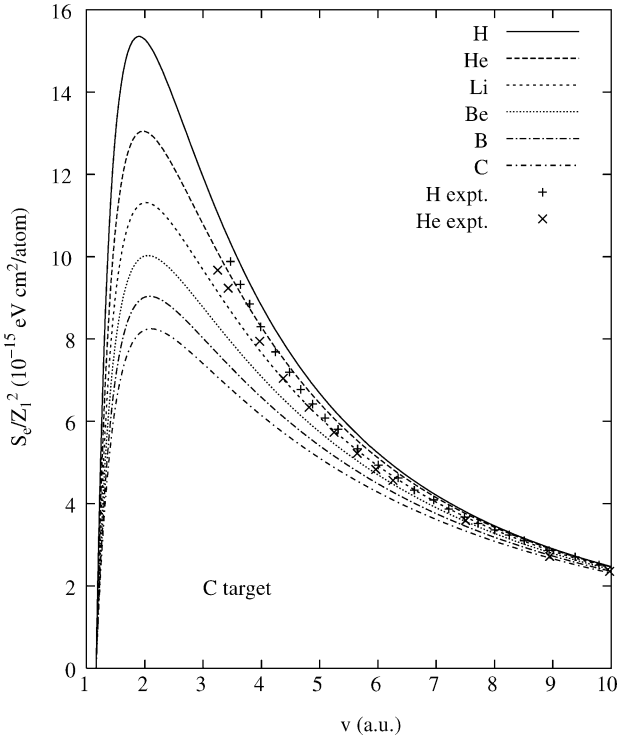

Fig. 6. Carbon stopping cross-section per unit projectile nuclear charge as a function of velocity. Experimental points from Ref. [61].

into the free parameters of the fit, namely, the target mean excitation energy and the much less important Barkas parameter. Consequently, the mean excitation energy obtained from the fitting procedure should be viewed as a parameter of the fit that does not correspond directly to theoretical mean excitation energies determined from calculated DOSDs. Neither should their decrease with increasing projectile atomic number be of concern.

Previous concerns with the accuracy of stopping power parameters extracted from experimental measurements by fitting to Bethe-like formulas have led us to conclude that accuracy and consistency of better than a few percent for these parameters cannot be expected [62].

5.4. Aggregation effects

It has long been known that the mean excitation energies of aggregated systems differ from those of the single atom constituents [63]. The two main

sorts of aggregation effects result from atoms associating into condensed phases, the so-called phase effect, and the formation of molecules. In each case, the aggregation affects the electronic excitation spectrum of the target enough to change the oscillator strength distribution enough to give a change of several percent in the calculated or measured stopping cross-sections [63–65].

Although we are aware of no work on the effects of aggregation through the GOSD on the stopping cross-section, there has been considerable attention paid to the effects of aggregation on the mean excitation energy and thus the DOSD.

5.4.1. Aggregation in the Bethe theory

In the case of solid targets, the effects of aggregation are generally absorbed by moving from an atomic to band-like description of the target. Clearly, the most atomic-like solids, for example rare gas solids, will suffer the least deviation from their atomic counterparts in the stopping cross-section, while the most delocalized band systems, the metals, will see the largest. The general method of dealing with band-like systems in the Bethe theory has been to adopt the so-called local plasma approximation of Lindhard and Scharff [66]. Here, the part of the mean excitation energy is played by the plasma frequency ω_p which is evaluated locally and integrated:

$$\ln I = \frac{1}{Z_2} \int \mathrm{d}^3 r \rho(\mathbf{r}) \ln(\chi \hbar \omega_p(\mathbf{r})) \tag{37}$$

Here, $\rho(\mathbf{r})$ is the local electron density at point $\mathbf{r}$, and χ is an *ad hoc* scaling parameter that Lindhard originally set to $\sqrt{2}$. The local plasma frequency is related to the density by $\omega_p = (4\pi e^2 \rho / m_e)^{1/2}$, as usual. An orbital version of this scheme has also been developed [67].

In these schemes, changes in the electron excitation spectrum are reflected in the plasma frequency and thence in the stopping cross-section.

In the case of molecules, the effects of aggregation are embodied in the Bragg rule [68]. In its simplest form, the Bragg rule states that the stopping cross-section for a molecule is simply the atom weighted sum of the stopping cross-sections of the constituents. Thus

$$S_{\text{molecule}}(v) = \sum_i n_i S_i(v) \tag{38}$$

where the molecule consists of n_i atoms of type i. In the context of the Bethe approximation, the Bragg rule can be written in terms of the mean excitation energies of the constituents I_0^i as

$$\ln I_0^{\text{molecule}} = \frac{1}{Z_2} \sum_i n_i \ln I_0^i \tag{39}$$

The Bragg rule, is especially attractive in terms of predicting the stopping cross-sections of organic molecules, as there are millions of known molecules, and it would be attractive to be able to predict their stopping cross-sections from a few atomic values. The Bragg rule is accurate to *ca.* 10% in most cases [63–65], but the deviations occasionally can be several times more. As in the case of solid targets, deviations from the Bragg rule for molecules arise from changes in the excitation spectrum of the constituents when a molecule is formed. As in the case with solids, the greatest deviations from atomic-like electronic structure lead to the greatest deviations from fulfillment of the Bragg rule.

An alternative formulation is to divide a molecule into the constituent chemical bonds and atomic cores (non-valence electrons) [69] rather than into atoms. Since each bond is associated with a bond mean excitation energy, the effects of chemical bonding can be included to some extent. There are certainly more possible bonds than there are atoms, but many fewer than molecules.

In the *cores-and-bonds* approach, the Bragg rules become

$$S_{\text{molecule}}(v) = \sum_{i}^{\text{cores}} n_i S_i^{\text{cores}}(v) + \sum_{j}^{\text{bonds}} m_j S_j^{\text{bonds}}(v) \tag{40}$$

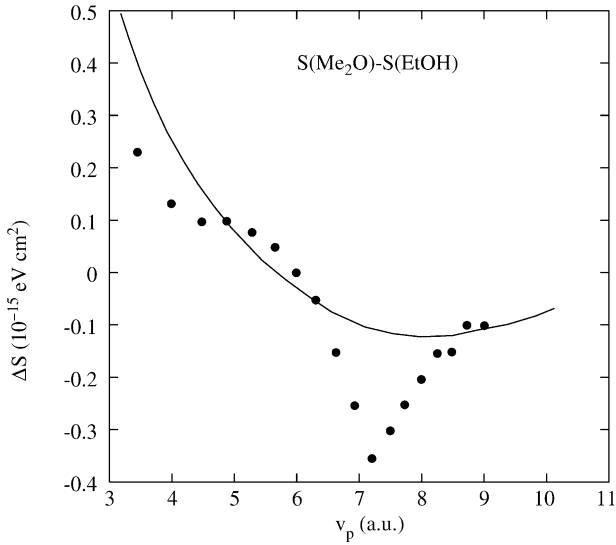

Fig. 7. Difference in stopping cross-section for two isomers of C_2H_6O as a function of proton velocity.

and

$$\ln I_0^{\text{molecule}} = \frac{1}{N}\left[\sum_i^{\text{cores}} \omega_i \ln I_{0,i}^{\text{cores}} + \sum_j^{\text{bonds}} \omega_j \ln I_{0,j}^{\text{bonds}}\right] \tag{41}$$

where there are n_i cores of type i, m_j bonds of type j, ω_i electrons in core type i, and ω_j electrons in core type j. Clearly

$$\sum_i^{\text{cores+bonds}} \omega_i = N \tag{42}$$

As expected, the cores-and-bonds approach gives somewhat better fulfillment of the Bragg rule, than does the atom formulation.

As an example, in Fig. 7 (after Fig. 1 in Ref. [70]) we show the difference in stopping power between the two isomers of C_2H_6O: dimethyl ether (Me_2O) and ethyl alcohol (EtOH). The solid line is calculated using the cores-and-bonds method discussed above, and the points are from the experimental work of Chau *et al.* [71]. Although the agreement is far from perfect, the main features of the experiment are reproduced. As the two compounds are isomers, the atom form of the Bragg rule will predict $\Delta S = 0$ at all projectile velocities.

References to other work on cores-and-bonds formulations of molecular stopping can be found in Refs. [69,72].

6. REMARKS AND CONCLUSIONS

It is clear that energy deposition by swift ions colliding with the orbital electrons in target atoms, molecules, and solids will be governed by the electronic structure of both the projectile and the target. As, within the first Born approximation, the excitation properties of the target are completely determined by the GOSD, it is understandable that the GOSD is the quantity of interest when studying energy deposition. However, the GOSD is difficult to calculate at present and, as discussed above, cannot clearly represent large momentum transfer collisions in any conceivable computational basis.

The Bethe approximation to the first Born approximation, i.e., adding the additional assumption that the projectile is fast with respect to the orbital electrons, or equivalently, that the collision time is short, leads to a much more computationally tractable scheme. The problem in this case is that the results from simple Bethe theory (equation (12)) are unphysical except at large collision energies, where almost all theories give nearly equivalently good results. The Bethe formulation is, however, very useful in that it may

include changes in molecular structure, targets aligned in a specific way with respect to the beam, projectile electronic structure, all of which have been discussed above, as well as other specific concerns.

The Bethe theory is generally corrected by the addition of shell corrections to compensate for the restriction that the collision time be small, and such corrections are normally useful. The problem here is that shell corrections are neither derived from the GOSD nor from the DOSD, so there is some mixing of theoretical bases when such things are done.

As the projectile charge appears explicitly in the Bethe formula, and it is clear that there can be capture and loss of electrons by the projectile when traversing a target, sometimes the concept of effective charge [73], normally written as Z^*, is introduced into the Bethe formula replacing Z_1, and is intended to represent, in some way, the average charge of the projectile as it penetrates the target. In fact, there seems to be little physics in this and it is, rather, an attempt to make the experiments fit a Bethe stopping formula. Z^* becomes, in essence, a fitting parameter. In fact we also need plead guilty to the same failing. In Section 3.4, we introduced the Bohr adiabatic criterion for determining the number of electrons associated with a projectile into a purely Bethe type development.

At this level, the accuracy of the full first Born approximation is clearly better than that of the Bethe theory, but the first Born approximation is much more difficult to implement.

Further corrections can also be made. One need not stop with the first term in the Born series (equation (2)), but one can rather include terms proportional to higher powers of Z_1, such as the Barkas ($\propto Z_1^3$) [74,75] and Bloch ($\propto Z_p^4$) [76] terms. Again, these terms must be determined by methods not related to the oscillator strength distributions, and thus leave something to be desired in terms of theoretical consistency.

If one is interested in producing stopping curves that agree with experiment and, perhaps, provide extrapolations and predictions for experiments not yet done, it is possible to start with the Bethe formulation and add all, or many of, the various above-mentioned, differently based corrections to it to produce a scheme which will calculate stopping powers that agree well with experiments. Some do this, and with considerable success [58,59,77,78]. It is our opinion, however, that this approach does not add significantly to our understanding of the physics involved. We would rather utilize methods based on first principles which are grounded in quantum mechanics, to describe the problem of energy deposition, as we believe that this approach is more likely to contribute to our intuitive understanding of the energy deposition process.

Clearly, oscillator strength distribution based methods can provide the basis for explanations of the more gross aspects of the physics of energy deposition, and more sophisticated methods are necessary for understanding the details. Other contributions in this volume happily offer other, and more

sophisticated, and more theoretically enlightening methods for studying energy deposition.

ACKNOWLEDGEMENTS

This work has been supported in part by ONR grant No. N0014-96-1-0707 to JRS, and by IBM SUR grant to the Quantum Theory Project. This support is gratefully acknowledged.

REFERENCES

[1] For an excellent summary of the basics of energy deposition theory, see E. Bonderup, *Penetration of Charged Particles through Matter*, 2nd edn., Aarhus University, Aarhus, Denmark, 1981.
[2] N. Bohr, *Phil. Mag.*, 1913, **25**, 10.
[3] J. Lindhard, *Mat. Fys. Medd. Dan. Vidensk. Selsk.*, 1954, **28** (8).
[4] H. Bethe, *Ann. Phys. (Leipzig)*, 1930, **5**, 325.
[5] M. Inokuti, *Rev. Mod. Phys.*, 1971, **43**, 297.
[6] M. Inokuti, Y. Itakawa and J. E. Turner, *Rev. Mod. Phys.*, 1978, **50**, 23.
[7] J. Oddershede, *Adv. Chem. Phys.*, 1987, **69**, 201.
[8] See J. R. Sabin and J. Oddershede, *Pol. J. Chem.*, 1998, **72**, 1376, and references therein for a bibliography.
[9] T. J. Gannon, M. Tassotto and P. R. Watson, *Chem. Phys. Lett.*, 1999, **300**, 163.
[10] M. Machholm and N. E. Hendriksen, *Phys. Rev. Lett.*, 2001, **87**, 19301.
[11] B. Friedrich and D. R. Herschbach, *J. Phys. Chem.*, 1991, **95**, 8118.
[12] B. Friedrich and D. R. Herschbach, *Phys. Rev. Lett.*, 1995, **74**, 4623.
[13] B. Siegmann, U. Werner, R. Mann, Z. Kaliman, N. M. Kabachnik and H. O. Lutz, *Phys. Rev. A*, 2001, **65**, 010704.
[14] For a review of techniques of orienting molecules, see H. J. Loesch, J. Bulthius, S. Stolte, A. Durand, J. C. Loison and J. Vigué, *Europhys. News*, 1996, **27**, 12.
[15] U. Fano and R. D. Deslattes, *Comments At. Mol. Phys.*, 1972, **3**, 187.
[16] H. Klar, *Phys. Rev. Lett.*, 1987, **59**, 1656.
[17] N. Bohr, *Mat. Fys. Medd. Dan. Vidensk. Selsk.*, 1948, **18** (8).
[18] Y. K. Kim and K. T. Cheng, *Phys. Rev. A*, 1980, **22**, 61.
[19] R. Cabrera-Trujillo, S. Cruz, J. Oddershede and J. R. Sabin, *Phys. Rev. A*, 1997, **55**, 2864.
[20] R. Cabrera-Trujillo, J. R. Sabin, Y. Öhrn and E. Deumens, *Int. J. Quantum Chem.*, 2003, **94**, 215.
[21] S. P. Ahlen, *Rev. Mod. Phys.*, 1980, **52**, 121.
[22] cf. e.g., E. N. Lassettre and S. A. Francis, *J. Chem. Phys.*, 1964, **40**, 1208.
[23] U. Fano and J. W. Cooper, *Rev. Mod. Phys.*, 1968, **40**, 441.
[24] J. D. Jackson, *Classical Electrodynamics*, Wiley, New York, 1962.
[25] U. Fano, *Annu. Rev. Nucl. Sci.*, 1963, **13**, 1.
[26] M. C. Walske, *Phys. Rev.*, 1952, **88**, 1283.
[27] M. C. Walske, *Phys. Rev.*, 1956, **101**, 940.
[28] E. Bonderup, *Mat. Fys. Medd. Dan. Vidensk. Selsk.*, 1967, **35** (17).
[29] J. R. Sabin and J. Oddershede, *Phys. Rev. A*, 1982, **26**, 3209.
[30] J. Oddershede and J. R. Sabin, *At. Data Nucl. Data Tables*, 1984, **31**, 275.

[31] H. H. Mikkelsen, J. Oddershede, J. R. Sabin and E. Bonderup, *Nucl. Instrum. Methods B*, 1995, **100**, 451.
[32] S. P. A. Sauer, J. R. Sabin and J. Oddershede, *Nucl. Instrum. Methods B*, 1995, **100**, 458.
[33] P. Sigmund and L. G. Glazov, *Eur. Phys. J. D*, 2003, **23**, 211.
[34] U. Fano and A. R. P. Rao, *Atomic Collisions and Spectra*, Academic Press, New York, 1986.
[35] N. Bohr, *Phys. Rev.*, 1940, **58**, 654.
[36] N. Bohr, *Phys. Rev.*, 1941, **59**, 271.
[37] W. A. Parkinson, J. R. Sabin and J. Oddershede, *Theor. Chim. Acta*, 1993, **86**, 167.
[38] J. Oddershede and P. Jørgensen, *J. Chem. Phys.*, 1977, **66**, 1541.
[39] E. S. Nielsen, J. Oddershede and P. Jørgensen, *J. Chem. Phys.*, 1980, **73**, 6238.
[40] J. Oddershede, *Adv. Quantum Chem.*, 1978, **11**, 275; J. Oddershede, P. Jørgensen and D. Yeager, *Comp. Phys. Rep.*, 1984, **2**, 33; J. Geertsen, S. Eriksen and J. Oddershede, *Adv. Quantum Chem.*, 1991, **22**, 167.
[41] c.f., e.g., J. Oddershede and J. R. Sabin, *Phys. Rev. A*, 1989, **39**, 5565.
[42] J. O. Hirschfelder, W. B. Brown and S. T. Epstein, *Adv. Quantum Chem.*, 1964, **1**, 255.
[43] R. Cabrera-Trujillo, J. R. Sabin, J. Oddershede and S. P. A. Sauer, *Adv. Quantum Chem.*, 1999, **35**, 175.
[44] E. H. Mortensen, J. Oddershede and J. R. Sabin, *Nucl. Instrum. Methods B*, 1992, **69**, 24.
[45] F. B. van Duijneveldt, *Technical Report RJ945*, IBM Research Laboratory, San Jose, 1971.
[46] S. N. Ketkar and R. A. Bonham, *J. Chem. Phys.*, 1986, **84**, 6091, NB: This paper contains misprints.
[47] R. Cabrera-Trujillo, S. B. Trickey, J. R. Sabin and J. Oddershede, unpublished work.
[48] See G. A. Aucar, J. Oddershede and J. R. Sabin, *Phys. Rev. A*, 1995, **52**, 1054, for further references.
[49] F. Reiche and F. Thomas, *Z. Phys.*, 1925, **34**, 510.
[50] W. Kuhn, *Z. Phys.*, 1925, **33**, 408.
[51] J. Geertsen, J. Oddershede and J. R. Sabin, *Phys. Rev. A*, 1986, **34**, 1104.
[52] R. Cabrera-Trujillo, J. R. Sabin, Y. Öhrn and J. Oddershede, *Phys. Rev. A*, 1998, **57**, 3115.
[53] J. R. Sabin, J. Oddershede and G. H. F. Diercksen, *Phys. Rev. A*, 1990, **42**, 1302.
[54] H. H. Andersen and J. F. Ziegler, *Hydrogen: Stopping Powers and Ranges in all Elements*, Pergamon Press, New York, 1977.
[55] J. R. Sabin and J. Oddershede, *Pol. J. Chem.*, 1998, **72**, 1376.
[56] J. R. Sabin and J. Oddershede, *Nucl. Instrum. Methods B*, 1996, **115**, 79.
[57] S. P. A. Sauer, J. R. Sabin and J. Oddershede, *Phys. Rev. A*, 1993, **47**, 1123.
[58] L. E. Porter, *Int. J. Quantum Chem.*, 2002, **90**, 682.
[59] L. E. Porter, *Int. J. Quantum Chem.*, 1999, **75**, 943.
[60] R. Cabrera-Trujillo, J. R. Sabin and J. Oddershede, *Phys. Rev. A*, 2003, **68**, 042902.
[61] W. H. Trzaska, V. Lyapin, A. Alanko, M. Mutterer, J. Räisänen, G. Tjurin and M. Wojdyr, *Nucl. Instrum. Methods B*, 2002, **195**, 147.
[62] J. R. Sabin and J. Oddershede, *Nucl. Instrum. Methods B*, 1990, **44**, 253.
[63] c.f. e.g., D. Thwaites, *Nucl. Instrum. Methods B*, 1987, **27**, 293, and references cited therein.
[64] J. Oddershede, J. R. Sabin and P. Sigmund, *Phys. Rev. Lett.*, 1983, **51**, 1332.
[65] J. R. Sabin, J. Oddershede and P. Sigmund, *Nucl. Instrum. Methods B*, 1985, **12**, 80.
[66] J. Lindhard and M. Scharff, *Kgl. Dan. Vidensk. Selsk. Mat.-Fys. Medd.*, 1953, **27** (15).
[67] cf. e.g., D. E. Meltzer, J. R. Sabin and S. B. Trickey, *Phys. Rev. A*, 1990, **41**, 220.
[68] W. H. Bragg and R. Kleeman, *Phil. Mag.*, 1905, **10**, 318.
[69] See J. Oddershede and J. R. Sabin, *Nucl. Instrum. Methods B*, 1989, **42**, 7, for details and references.

[70] J. R. Sabin and J. Oddershede, *Nucl. Instrum. Methods B*, 1992, **64**, 678.
[71] E. K. L. Chau, R. B. Brown, A. S. Lodhi, D. Powers, S. Matteson and S. R. Eisenbarth, *Phys. Rev. A*, 1977, **16**, 1407.
[72] R. Trujillo-Cabrera, S. A. Cruz and J. Soullard, *Nucl. Instrum. Methods B*, 1994, **93**, 166.
[73] cf. e.g., W. Brandt and M. Kitagawa, *Phys. Rev. B*, 1982, **25**, 5631.
[74] W. H. Barkas, J. N. Dyer and H. H. Heckman, *Phys. Rev. Lett.*, 1963, **11**, 26;
[75] cf. e.g., J. Lindhard, *Nucl. Instrum. Methods*, 1976, **132**, 1; G. Basbas, *Nucl. Instrum. Methods B*, 1984, **4**, 227, for comments.
[76] F. Bloch, *Ann. Phys.*, 1933, **16**, 285.
[77] P. Sigmund and A. Schinner, *Nucl. Instrum. Methods B*, 2002, **193**, 49.
[78] P. Sigmund and A. Schinner, *Nucl. Instrum. Methods B*, 2002, **195**, 64.

This Page Intentionally Left Blank

Chemical and Physical State Effects in Electronic Stopping

Peter Bauer and Dieter Semrad

Institut fuer Experimental Physik, Johannes Kepler Universitaet Linz, A-4040 Linz, Austria

Abstract

Present knowledge on electronic stopping of protons in gases and solids is summarized with special emphasis on the question of how stopping is influenced when the target element changes its state of aggregation (physical state effect, PSE) or when it is incorporated into a compound (chemical state effect, CSE). Bragg's rule assumes that for a compound the stopping cross-section is simply the weighted sum of stopping cross-sections of its constituents (additivity rule). To overcome the oversimplification of Bragg's rule, a phenomenological description is presented on how the two state effects may cause deviations from Bragg's rule. Then theoretical and semi-empirical models are summarized that are able to describe PSE and CSE at high, intermediate and low velocities.

Contents

1. INTRODUCTION

In ion beam analysis or ion beam modification, one often deals with compound materials or materials in different states of aggregation, so that one arrives at a huge number of projectile–target combinations of possible interest. It is obvious that not all of these measurements can be done. And even when experimental data are available, it may be questionable whether the uncertainties of the stopping cross-section data meet the requirements of accuracy in the application. So one is in the dilemma that on the one hand stopping data of innumerable target materials are needed for a variety of projectiles at a high level of accuracy, while on the other hand the difficulties to obtain these data are sometimes insurmountable.

ADVANCES IN QUANTUM CHEMISTRY, VOLUME 46
ISSN: 0065-3276 DOI 10.1016/S0065-3276(04)46006-7

Let us illustrate in an example what is the subject of physical state effects (PSE) and chemical state effects (CSE). We focus on a simple case, i.e., the slowing down process of protons in H_2O, with special emphasis on the regime of the stopping maximum (Fig. 1, from Ref. [1]). The energy loss information is given in terms of the stopping cross-section, ε, which refers to the interaction of the projectile with one H_2O molecule, being independent of the density of the material.

It is obvious that in this energy range there are no energy loss data for protons in liquid water, since it is impossible to think of such an experiment at low-energy ions (for high-energy experiments, see Refs. [2,3]). Thus, experimental data are just available for the same chemical item, H_2O, but in different states of aggregation, namely in the solid (ice), or in the gas phase (water vapor). The difference between the electronic stopping in vapor and in ice due to the different states of aggregation is called PSE. For water vapor, larger values are obtained than for ice; the differences between these data sets being largest in the regime of the stopping maximum which occurs at proton energies of 50–100 keV. Of course, one has to expect also a difference between stopping in water and in ice, due to the differences in the electronic states in these two phases. Intuitively one may expect that the data for ice may be closest to the information wanted for water. This expectation has been confirmed by theory; due to its high relevance for medical applications, there is an ongoing theoretical interest on this subject [4–6].

One also could think of using the data available for proton stopping in H_2 and in O_2 gas and thus describe water by an equivalent mixture of gases, i.e.,

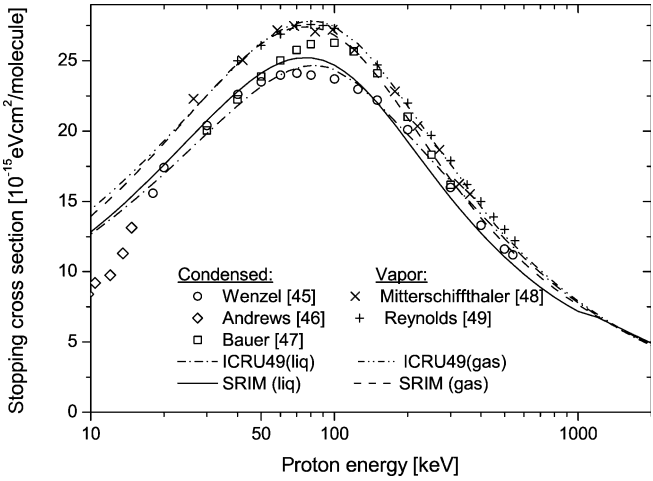

Fig. 1. Stopping cross-section of H_2O for protons in two different states of aggregation (ice, vapor). Experimental results and data from tabulations are presented.

water $\equiv H_2 + \frac{1}{2}O_2$. Here, one has to deal with two different types of effects: first, one would try to describe a liquid as H_2O by a mixture of gases and will have to be aware of the PSE, and second, even if one would compare water vapor to the mixture $H_2 + \frac{1}{2}O_2$, one would have to expect CSE, leading to a larger stopping cross-section in the gas mixture than in the vapor [7].

2. BRAGG'S RULE

It is almost unbelievable that the beginning of the stopping theory dates back to the time well before Bohr's model of the atom. Thus, at the time when pioneers like Thomson, Bragg and Kleeman started to think about stopping powers, there was no understanding of atomic structure or of atomic collisions. At that time no chemical effect had been found in the range of high-energy particles, and the power of stopping of a target element was assumed to depend on the square root of its atomic mass [8]. As the atomic mass is subject neither to PSE nor to CSE, a simple additivity rule was assumed for chemical compounds. From today's point of view, Bragg's findings are not surprising since chemical effects become apparent mainly in modifying the shape of the stopping maximum. Hence, no significant effect on the ion range is expected, in analogy to the Barkas effect where a 4% difference in the range of π^+ and π^- mesons is observed as a result of an almost 50% difference in the stopping power around the stopping maximum. Already Bragg and Kleeman expressed their additivity rule in terms of a microscopic quantity (we would say, in terms of stopping cross-sections). In our language, Bragg's rule states that the stopping cross-section of a compound A_mB_n, $\varepsilon_{A_mB_n}$, is the weighted sum of the stopping cross-sections of its constituents, ε_A and ε_B

$$\varepsilon_{A_mB_n} = m\varepsilon_A + n\varepsilon_B \tag{1}$$

where m and n are the relative abundances of the atom species A and B, respectively. From the above discussion it follows that Bragg's rule cannot hold good, except for stripped projectiles in a mixture of non-reacting components. For slow H ions, in a mixture of non-interacting gases (H_2 and He) deviations of up to 50% from Bragg's rule have been found [9] due to synergetic effects in charge exchange processes; H^+ captures easily and H^0 loses inefficiently an electron in a collision with a H_2 molecule. The opposite is true for collisions of these projectiles with He atoms. Thus, the presence of *both* the atomic species in the target enhances the probability for charge exchange in the mixture. This discussion of processes in gas mixtures leads us to the conclusion that, strictly speaking, Bragg's rule is not rigorously valid, it is just a model which in many cases permits an estimate of the stopping behavior of a compound in case of lacking experimental data.

3. DEFINITION OF PSE AND CSE

To obtain absolute measures of PSE and CSE, we define

$$\Delta\varepsilon_P = \varepsilon_{gas} - \varepsilon_{solid} \tag{2}$$

$$\Delta\varepsilon_C = \varepsilon_{mixture} - \varepsilon_{compound} \tag{3}$$

Note that $\Delta\varepsilon_C$ is exactly the deviation from Bragg's additivity rule (see equations (2) and (3)) and that $\Delta\varepsilon_P$ is defined analogously. The sign of this definition is chosen so that the result obtained is positive for point charge projectiles. Note that it is an inherent problem of experimental investigations of CSE and PSE that the interesting quantity is obtained as a difference of two measurements, and therefore, scatter much more than the stopping cross-section measurements themselves.

4. PHENOMENOLOGICAL DESCRIPTION OF PSE AND CSE

Within the charge state approach, for partly dressed projectiles the following effects contribute to stopping:

(i) excitation and ionization of target atoms by the projectiles in their specific charge state ('partial stopping cross-section'),
(ii) average charge state of the projectile ('charge state fractions'),
(iii) excitation of the projectile (without changing the charge state), and
(iv) capture and loss of electrons by the projectile (which also defines the average charge state, see (ii)).

Note that the average charge state (ii) depends only on the ratio of charge changing cross-sections and is, therefore, unaffected by changes in the cross-sections themselves, as long as all the relevant cross-sections increase or decrease by the same constant factor. The absolute value of the charge changing cross-sections is, however, of crucial importance for the calculation of the energy loss due to charge exchange (iv). At low velocities, i.e., below the stopping maximum, the contribution of charge exchange collisions may be a major contribution to the total stopping, see, e.g., Ref. [6]. For completely stripped projectiles at $v \gg Z_1^{2/3} v_0$, the charge state is $Z_1 e$, and there are no contributions from (ii), (iii) and (iv), therefore, bare ions are the simplest projectiles to be handled (e.g., protons at energies above ≈ 100 keV). In the following, the physical foundation of the contributions (i)–(iv) listed above is analyzed in a simplified manner

- Changes of the total stripping and capture cross-sections have been observed even in a mixture of non-reacting components. One should,

therefore, expect that changes in the physical or chemical state generally have an influence on the dynamic charge state of the projectile and hence on charge changing processes (iv).

- Changes in the configuration of the target valence electrons evidently influence excitation and ionization of target atoms (i); a smaller influence might be expected on the average charge state of the projectile (ii), and on the excitation of the projectile (iii). However, a change in the distribution of the valence electrons may seriously alter the capture and lose cross-sections and hence influence (iv) and, to a lesser extent, also (ii) and (iii) (see below).
- Changes in the target density have an influence on the charge exchange processes of the projectile – hence on (iv), and therefore, also on (ii) and (iii) – when the collision frequency times the life time of the excited state exceeds unity, and to a lesser extent on target excitation (i). These arguments are based on local density approximation considerations [10] and lead to the observation that while for point charges like protons the gas phase is the medium with larger stopping cross-section, the opposite is true for heavy ions [11].

5. VELOCITY DEPENDENCE OF CSE AND PSE

Whenever the physical or chemical state of an atom is changed, one expects noticeable changes only in the configuration of the outermost (slowest) electrons (the valence electrons, which are mostly s- and p-electrons, and to a lesser extent d-electrons). In the following we describe, on the basis of the influences discussed above, how PSE and CSE develop in the different velocity regimes. It is well known that the maximum stopping power of a sub-shell is observed when the projectile velocity roughly equals the mean velocity of the electrons in this sub-shell [12]. Since the valence electrons have characteristic velocities in the order of the Bohr velocity, they are ionized with highest probability by ions of the same speed, which for protons is equivalent to an energy of about 25 keV. Since core electrons are more strongly bound, their corresponding sub-shell stopping maximum will appear at higher ion velocities, with a lower maximum value. At very low velocities the contribution from valence electrons dominates; here, however, the stopping cross-section is small. With increasing projectile energy this contribution increases but it will only become dominant in the region of the stopping maximum if all core electrons are so tightly bound that they do not contribute considerably to ε at the stopping maximum. These arguments apply best for light elements (lighter than Ar) where the atomic core is formed by tightly bound closed shells (K- or L-shell). An instructive example is carbon, which is a material that exists in various allotropic forms as diamond, graphite, amorphous carbon, fullerenes, etc. The K shell

represents the atomic core, and the L electrons the valence electrons, whose band structure differs significantly in the various modifications of carbon, as indicated by the different values of the band gap (e.g., 0.5 eV for graphite and 5.5 eV for diamond). Therefore, large PSE may be expected in this case. In the following we summarize briefly the theoretical models that might be relevant for the description of PSE and CSE, in the different velocity regimes.

High velocities. Light ions (with atomic number $Z_1 < 3$, i.e., H and He) at sufficiently high velocity ($v \gg v_0 Z_2^{2/3}$, where $v_0 = c/137$ denotes the Bohr velocity and Z_2 is the atomic number of the target) are point charges, i.e., they do not carry bound electrons. Here, the Bethe–Bloch theory including some corrections and higher order Z_1 terms yields quite accurate results for the stopping cross-section ε:

$$\varepsilon = \frac{4\pi Z_1^2 e^4}{mv^2} Z_2 \left[\ln\left(\frac{2mv^2}{I(1-\beta^2)} \right) - \beta^2 - \frac{C}{Z_2} - \frac{\delta}{2} + Z_1 L_1 + Z_2^2 L_2 \right] \quad (4)$$

Here, e and m denote charge and mass of an electron, respectively, and I the mean ionization potential of the target atom. As usual, $\beta = v/c$. There are various approaches to calculate the different terms in equation (4). The density effect $\delta/2$ is discussed in Ref. [13] but contributes to stopping only in the far relativistic region where PSE and CSE are irrelevant. Shell corrections, C/Z_2, may be taken from Ref. [14], where available calculations of the Barkas correction term $Z_1 L_1$ are also discussed; however, the influence of PSE and CSE on the Barkas term is not yet well understood. The term L_2 is exclusively determined by projectile properties; it has been calculated (without shell corrections) by Bloch [15,16]. Since in this regime the ions are point charges, only target effects will contribute to PSE and CSE. This means that here the only contribution to PSE and CSE comes from changes of the binding of the valence electrons (see above). In the case of a light atom where the number of electrons is small, this also leads to a noticeable change in the I value. This explains qualitatively, why largest effects are observed for elements with $Z_2 < 17$ (Cl). Calculating the absolute PSE in terms of $\Delta\varepsilon_P$ according to the definition in equation (2), we obtain from equation (4)

$$\Delta\varepsilon_P = \frac{4\pi Z_1^2 e^4}{mv^2} Z_2 \ln\left(\frac{I_{solid}}{I_{gas}} \right) \quad (5)$$

and analogously for the CSE

$$\Delta\varepsilon_C = \frac{4\pi Z_1^2 e^4}{mv^2} Z_2 \ln\left(\frac{I_{solid}}{I_{gas}} \right) \quad (6)$$

In equations (5) and (6) we have omitted the correction terms to the Bethe equation discussed above. Note that in this velocity regime both $\Delta\varepsilon_P$ and $\Delta\varepsilon_C$

follow a $1/E$ dependence. Strictly speaking, this approximation holds only for point charges at velocities $v \gg v_0 Z_2^{2/3}$, but according to Lindhard [17] the range of applicability extends down to lower velocities since the inner shell contributions to I cancel each other in equations (5) and (6). As a consequence, equations (5) and (6) may, for protons, become applicable down to the region of the stopping maximum. It may be worth discussing the ratios $I_{\text{solid}}/I_{\text{gas}}$ and $I_{\text{compound}}/I_{\text{mixture}}$ in some detail: one may divide the Z_2 electrons of the target into N_{core} core electrons (with a mean excitation energy I_{core}) and N_{val} valence electrons (with a mean excitation energy I_{val}). Then, these quantities are related [18] as

$$Z_2 \ln I = N_{\text{core}} \ln I_{\text{core}} + N_{\text{val}} \ln I_{\text{val}} \tag{7}$$

Since the core electrons may be assumed to be unaffected by the state of aggregation, the PSE is exclusively due to changes in the valence states, which leads to

$$\begin{aligned} Z_2(\ln I_{\text{gas}} - \ln I_{\text{solid}}) &= Z_2 \ln\left(\frac{I_{\text{gas}}}{I_{\text{solid}}}\right) = N_{\text{val}} \ln\left(\frac{I_{\text{val,gas}}}{I_{\text{val,solid}}}\right) \\ &= N_{\text{val}}(\ln I_{\text{val,gas}} - \ln I_{\text{val,solid}}) \end{aligned} \tag{8}$$

For elements with known I for a certain state of aggregation, e.g., the solid phase (either from theory or deduced from experimental data), equation (8) may be used to calculate the I value of another phase, e.g., the gas phase, as follows: for $I_{\text{val,gas}}$ only theoretical values are available, e.g., from Ref. [19]; for $I_{\text{val,solid}}$, the (measured or calculated) plasmon energy $\hbar\omega_{\text{p}}$ may be taken, which is correct [20] in the asymptotic velocity limit $v \gg v_{\text{F}}$.

Looking for a simple way to quantitatively estimate CSE, in Ref. [21] a correlation between $I_{\text{mixt}} - I_{\text{comp}}$ and the binding enthalpy of the compound ΔH [22] was found

$$I_{\text{comp}} \approx I_{\text{mixt}} + \Delta H, \tag{9}$$

where ΔH is the energy needed to decompose the compound into its constituents in their standard state of aggregation; e.g., Al_2O_3 is decomposed into Al metal and O_2 gas.

Along these lines, one is able to estimate PSE and CSE in the high velocity limit by the use of equations (7) and (8).

At *intermediate velocities*, $v \approx v_0 Z_1^{2/3}$, the projectiles are 'dressed', i.e., able to carry bound electrons when traversing matter. As a consequence, the Bethe–Bloch equation as it stands is no longer applicable, since the dynamic screening of the point charge (by the electrons bound to the projectile *and* by the valence electrons of the target) must be taken into account. In addition, the energy loss of the ions becomes more complex since numerous charge states of the projectile may contribute and since projectile ionization opens new energy loss channels, i.e., capture and loss of electrons. All these

different processes are included in the charge state approach of stopping [23–25]. This model is in principle applicable in the whole range of velocities, but it is beneficial only at intermediate velocities when several energy loss mechanisms contribute to the stopping cross-section. The charge state model reads

$$\varepsilon = \sum_{ij} \Phi_i(\varepsilon_i + \sigma_{ij} T_{ij}) \tag{10}$$

Here, Φ_i denotes the probability to find the ion in charge state i, ε_i is the corresponding stopping cross-section of a frozen charge i, σ_{ij} is the cross-section for the transition from charge state i to state j (by capture or loss of an electron) and T_{ij} is the energy transferred to the target in this process. This formalism is applicable to gas targets as well as to solid targets. The different mechanisms of ion screening and of capture and loss processes can be described by appropriate approximations [25,26]. Due to the detailed treatment of input channels the model proved to reproduce the stopping behavior of a certain target material quite realistically, but for the same reason it is too elaborate for general application.

Concerning PSE and CSE, the regime of intermediate velocities is, on the one hand, the most complex one, since the number of possible influences of PSE and CSE is large. On the other hand, for that same reason one can gain a lot of insight from investigations in this regime. An instructive example is the explanation of the phase effect for proton stopping in a metal vapor like zinc or magnesium, where theory predicts a stopping cross-section of the vapor that is larger than that of the metal by almost one order of magnitude for protons moving at $v = v_0$ [27]. The main reason for this huge effect is that while in a metal the proton is very efficiently screened by the conduction band electrons and thus does not interact very efficiently, it ionizes very efficiently the weakly bound valence electrons of the atoms in the gas phase. In the experiment, however, this large PSE is not observed, since the fraction of protons in the gas phase is $\ll 1$ at $v = v_0$. As a consequence, the measured stopping cross-section of the vapor is much lower than the prediction for protons since for H^0 the ionization cross-section of the valence electrons is reduced very efficiently due to screening by the projectile electron [28]. In spite of these insights, it is not easy to gain knowledge that would allow one to derive a general rule to estimate the size of PSE and CSE in any target material at intermediate ion velocities.

At *low velocities*, $v < v_0$, scattering theory predicts that the stopping power S of a point charge in an electron gas is proportional to velocity:

$$S = Qv \tag{11}$$

where the 'friction coefficient' Q depends on the electron gas density and on the charge of the projectile. The density functional theory (DFT) in

the Kohn–Sham representation permits a nonlinear calculation of screening in an electron gas [29,30] and has been successfully applied to describe the stopping of slow ions ($1 \leq Z_1 \leq 60$) in metals. Qualitatively speaking, the success of the DFT is based on the following facts: (i) it includes Z_1 effects to all orders, (ii) in this velocity regime the contribution of the core electrons to the stopping process is negligible and (iii) the stopping cross-section does not depend on the details of the band structure of the metal. However, since most compounds are insulators with a band gap, the question of whether the picture of free electrons with $v = v_F$, which are scattered by the screened ion charge, is justified. This is especially true for large band-gap insulators [28,31].

Therefore, in principle the question of how PSE and CSE influence the stopping power at low velocities is quite complex; both the magnitude of the stopping cross-section and its velocity dependence might be changed. When we think about changes of the velocity dependence, we should expect larger effects in a gas (especially with large binding energy [32] or in an insulator (especially with a large band gap). The experimental information available, however, points into a different direction: in gases, the influence of the non-zero minimum excitation energy ('threshold effect') is usually masked by efficient energy loss due to charge changing collisions [33]. In insulators, the stopping cross-section for protons is proportional to velocity, showing no influence of the gap. This is even true for LiF, which is the insulator with the largest gap so far observed (14 eV). This is probably due to ionization *via* electron promotion processes, which – similarly as for heavy ions – provide an efficient mechanism of energy loss. These electron promotion processes are very efficient since the band structure of the insulators is strongly perturbed by the presence of the proton, so that as a consequence the actual energy gap is much smaller than in the static case ('metallization' of the insulator [31,34]).

Thus, when estimating the stopping behavior of a gas or an insulating compound for slow projectiles, we may neglect changes in the velocity dependence and assume velocity proportional stopping for velocities $v < v_0$ as a general rule.

With the definitions of equations (2) and (3), we conclude that in the low-velocity regime, PSE and CSE lead to changes of the friction coefficients only:

$$\Delta\varepsilon_P = (Q_{gas} - Q_{solid})v \tag{12}$$

$$\Delta\varepsilon_C = (Q_{mixture} - Q_{compound})v \tag{13}$$

If we could assume that the interaction of ions with insulators and atoms is similar to that with metals we might dare to apply the free electron gas picture and just characterize the compounds and atoms by effective electron gas densities [31]. Doing so will allow us to calculate PSE and CSE from equations (11) and (12). However, since the energy loss processes in the compounds are more complex than in an electron gas, this description is not

justified, and the successful application to large band gap insulators [31] may have just been fortuitous.

Recently, strong efforts have been undertaken to describe the stopping of heavy ions in elemental targets [35] on the basis of the classical Bohr theory [36] but abandoning the high velocity approximation of the original theory and including static screening and projectile excitation. Up to now, results have been presented only for elemental targets, and no applications for compound systems have been published.

REFERENCES

[1] H. Paul, Stopping power for light ions, Available from http://www.exphys.uni-linz.ac.at/stopping/.
[2] H. Bichsel and T. Hiraoka, *Nucl. Instrum. Methods B*, 1992, **66**, 345.
[3] H. Bichsel, T. Hiraoka and K. Omata, *Radiat. Res.*, 2000, **153**, 208.
[4] S. Uehara, L. H. Toburen, W. E. Wilson, D. T. Goodhead and H. Nikjoo, *Radiat. Phys. Chem.*, 2000, **59**, 1.
[5] M. Dingfelder, M. Inokuti and H. G. Paretzke, *Radiat. Phys. Chem.*, 2000, **59**, 255.
[6] S. Endo, E. Yoshida, H. Nikjoo, S. Uehara, M. Hoshi, M. Ishikawa and K. Shizuma, *Nucl. Instrum. Methods B*, 2002, **194**, 123.
[7] C. Mitterschiffthaler and P. Bauer, *Nucl. Instrum. Methods B*, 1990, **48**, 58.
[8] W. H. Bragg and R. Kleeman, *Phil. Mag.*, 1905, **10**, 318.
[9] R. Golser, D. Semrad and F. Aumayr, *Phys. Rev. Lett.*, 1996, **76**, 3104.
[10] G. Both, R. Krotz, K. Lohmer and W. Neuwirth, *Phys. Rev. A*, 1983, **28**, 3212.
[11] H. Geissel, Y. Laichter, W. F. W. Schneider and P. Armbruster, *Phys. Lett.*, 1983, **99A**, 77.
[12] C.-M. Romo-Kroeger, *Nucl. Instrum. Methods B*, 1998, **136–138**, 196, and references therein.
[13] Stopping Powers for Electrons and Positrons, ICRU Report No. 37, International Commission on Radiation Units and Measurements, Bethesda, MD, 1984.
[14] H. Bichsel, *Phys. Rev. A*, 2002, **65**, 52709-1-11.
[15] F. Bloch, *Z. Phys.*, 1933, **81**, 363.
[16] J. Lindhard and A. Sörensen, *Phys. Rev. A*, 1996, **53**.
[17] J. Lindhard, private communication, 1991.
[18] J. Oddershede and J. R. Sabin, *At. Data and Nucl. Data Tables*, 1984, **31**, 275.
[19] D. E. Meltzer, J. R. Sabin and S. B. Trickey, *Phys. Rev. A*, 1990, **41**, 220.
[20] P. M. Echenique, F. Flores and R. H. Ritchie, *Solid State Phys.*, 1990, **43**, 229.
[21] P. Bauer and D. Semrad, *Nucl. Instrum. Methods B*, 2001, **182**, 62.
[22] E. Lax, *Taschenbuch für Chemiker und Physiker, Band I*, 3rd edn, Springer, Berlin, 1967.
[23] D. R. Bates and G. W. Griffing, *Proc. Phys. Soc. London, Sect. A*, 1953, **66**, 961.
[24] S. K. Allison and S. D. Warshaw, *Rev. Mod. Phys.*, 1953, **25**, 779.
[25] A. Arnau, M. Pealba, P. M. Echenique and F. Flores, *Nucl. Instrum. Methods B*, 1992, **69**, 102.
[26] A. Arnau, P. Bauer, F. Kastner, A. Salin, V. H. Ponce, P. D. Fainstein and P. M. Echenique, *Phys. Rev. B*, 1994, **49**, 6470.
[27] M. Bergsmann, W. Raab, G. Schrenk, F. Kastner, R. Dez Muio, A. Arnau, A. Salin, P. Bauer and P. M. Echenique, *Phys. Rev. B*, 2000, **62**, 3153.
[28] P. Bauer, W. Rssler and P. Mertens, *Nucl. Instrum. Methods B*, 1992, **69**, 46.

[29] P. M. Echenique, R. Nieminen and R. H. Ritchie, *Solid State Commun.*, 1981, **37**, 779.
[30] P. M. Echenique, R. M. Nieminen, J. C. Ashley and R. H. Ritchie, *Phys. Rev. A*, 1986, **33**, 897.
[31] J. I. Juaristi, C. Auth, H. Winter, A. Arnau, K. Eder, D. Semrad, F. Aumayr, P. Bauer and P. M. Echenique, *Phys. Rev. Lett.*, 2000, **84**, 2124.
[32] R. Golser and D. Semrad, *Phys. Rev. Lett.*, 1991, **66**, 1831.
[33] A. Schiefermueller, R. Golser, R. Stohl and D. Semrad, *Phys. Rev. A*, 1993, **48**, 4467.
[34] K. Eder, D. Semrad, P. Bauer, R. Golser, P. Maier-Komor, F. Aumayr, M. Peñalba, A. Arnau and P. M. Echenique, *Phys. Rev. Lett.*, 1997, **79**, 4112.
[35] P. Sigmund and A. Schinner, *Nucl. Instrum. Methods*, 2002, **B195**, 64.
[36] N. Bohr, *Phil. Mag.*, 1913, **25**, 10; N. Bohr, *Phil. Mag.*, 1915, **30**, 581.

This Page Intentionally Left Blank

Calculation of Cross-Sections for Proton and Antiproton Stopping in Molecules

Lukáš Pichl,[1] Robert J. Buenker[2] and Mineo Kimura[3]

[1] *Foundation of Computer Science Laboratory, University of Aizu, Tsuruga, Ikki, Aizuwakamatsu, Fukushima 965-8580, Japan*
[2] *Bergische Universitaet Wuppertal, Fachbereich C, Theoretische Chemie Gaussstr. 20, D-42119 Wuppertal, Germany*
[3] *Graduate School of Science and Engineering, Yamaguchi University, Ube, Yamaguchi 755-8611, Japan*

Abstract

Various characteristic phenomena and consequences arising from electron capture and ionization in proton interactions with molecules at low-keV to high-eV collision energy region are discussed. A theoretical treatment to properly handle these problems is provided from quantum-chemical structure calculations of colliding systems to scattering dynamical calculations based on an electronic-state close-coupling scheme. For better understanding of the interaction mechanisms, a comparative investigation between antiproton and proton impact on atoms and molecules is also given. Particular emphasis is placed on the clear illustration of fragmentation mechanism and kinds of fragmented species of molecules by both antiproton and proton impacts. In addition, the collision effects representative for molecular targets such as the isotope effect, the steric effect and the vibrational effect are illustrated here.

Contents

ADVANCES IN QUANTUM CHEMISTRY, VOLUME 46
ISSN: 0065-3276 DOI 10.1016/S0065-3276(04)46007-9

1. INTRODUCTION

When energetic high-MeV particles impinged on matter lose their energy through various collision processes with constituent atoms and molecules and reach low-MeV to high-keV, the magnitude of total cross-sections becomes appreciable, and various inelastic processes begin to simultaneously contribute causing a variety of unique physical phenomena. A collision process or energy-loss process in this energy domain appears unique and important for application. In medical applications, heavy ions are used for cancer treatment (hadron therapy). This is because they are known to produce a characteristic dependence of the dose as a function of depth, in particular a sharp peak in the dose at a certain depth of a human tissue, which is referred to as the Bragg peak. Beyond this peak, all penetrating particles completely stop. In the Bragg peak region the strongest energy loss takes place throughout penetration, and the most effective cell killings are experimentally confirmed to occur, although very little of the relevant physics and chemistry is known. In the area from the peak to the tail of the Bragg peak, transverse impact ions carry energy in the low-keV to high-eV region, and hence, ionization and electronic excitation of constituent atoms and molecules should be most dominant and frequent there. Once these atoms and molecules are ionized, or electronically excited, they often become unstable, and dissociate to smaller fragments after a short period of lifetime of the parent species. Therefore, in the Bragg peak, ion–atom/molecule, ion–radical, and radical–radical reactions are expected to occur and these radicals and ions may participate in breaking DNA bonds to cause severe damage leading to cell cycle termination and ultimately cell death. This is referred to as the indirect process. However, as we described, very little detail of what is going on inside the Bragg peak is actually known.

In nano-scale material manufacturing and fabrication based on ion-beam technologies, the beam energies are usually restricted and controlled below a few tens of keV region so that the most efficient etching or sputtering, and particle implantation or deposition on/from surface, for instance, can be achieved. The ion-beam energy and ionic species under normal operations used in industries is an issue of economical efficiencies, which is optimized to be well below a few tens of keV. Again, in this energy domain, various inelastic processes between target surface including ionization, electronic and rovibrational or phonon excitation dominate. Therefore, for various applications, the understanding for spectroscopy and dynamics of ions below low-to-intermediate keV would be very significant. Providing

a concrete foundation of knowledge on scattering dynamics under multiple scattering conditions when particles traverse in condensed matter is essential for manipulating and controlling reactions in/on matter at the atomic and molecular levels.

From a theoretical point of view, it is challenging to investigate ion impact in this energy domain since many different channels strongly couple each other resulting in a variety of new phenomena in ion–molecule/surface complex systems such as new form of resonance through multi-channel couplings or providing different perspectives on particle scattering. This in turn may lead to the opening of new research fields. In this work, we attempt to shed some light on unique features in scattering dynamics in collisions of heavy ions with molecules observed in the low-keV to high-eV region. We also discuss, on a comparative basis, proton and antiproton impacts on molecules where a limited theoretical study was conducted in our group. This comparison is important for providing the underlying physics of the interaction scheme more clearly. Antiproton is an anti-matter of proton, with the same mass, but opposite charge. Thus, when antiproton approaches matter, electrons in the material are repelled whereas for proton they are attracted, thus reducing interactions for antiproton and causing smaller cross-sections and stopping powers. Therefore, by observing the difference and similarity between proton and antiproton, a finer and more detailed picture of dynamics emerges which will be expected to greatly enhance our level of understanding. Therefore, wherever possible, we try to follow this direction.

High-energy collisions of protons and antiprotons with atomic and molecular targets generally lead to a wide variety of products. In order to adequately describe the various reaction channels, it is important to compute not only the associated potential surfaces but also various types of coupling matrix elements that connect them. These include transition moments for radiative processes and various non-adiabatic couplings: radial, rotational and spin–orbit. Multireference configuration interaction (CI) techniques are especially well suited for this purpose because they allow one to obtain a balanced treatment of all types of electronic states over a very large range of internuclear geometrical arrangements. The only major disadvantage for this technique is the steep dependence of its computational times on the number of active electrons in theoretical treatment. Configuration selection techniques and a combined variational-perturbation theory approach to the calculation of total electronic energies at least help to minimize difficulties of this nature. At the same time, such methods produce many-electron wave functions which can be used to evaluate the various types of coupling elements needed for the requisite scattering cross-section calculations in the next stage of the theoretical treatment.

Throughout the text, the atomic units are used unless otherwise stated ($e = m = \hbar = 1$, where e is the electronic charge, m the electronic mass and $\hbar$ the Planck constant/2π).

2. THEORETICAL MODEL

As indicated in Section 1, two types of expertise are required to achieve the overall goal of describing the dynamics of collision processes. We will begin with the general approach employed in the first area, electronic structure calculation, followed by the second area, heavy particle scattering.

2.1. From the first principles

2.1.1. The multireference single- and double-excitation CI method

The great breakthrough in systematizing many-electron quantum-mechanical calculations was made in the late 1920s by Hartree, Slater and Fock [1–3]. The main idea was to define a single electronic configuration to describe a particular state of an atom or molecule (within the Born–Oppenheimer Approximation in the latter case) and solve a differential equation to obtain the optimum one-electron functions (orbitals) that minimize the energy for it. At first the calculations were done numerically without computers, but this changed in the late 1940s with Roothaan's realization [4] of the LCAO-MO method of Hund and Mulliken [5,6]. There remained one great problem. As flexible as the resulting method is, it fails to produce realistic potential energy curves for a system as simple as the hydrogen molecule. The problem was easily traced back to the single-configuration approximation itself, so researchers such as Hylleraas [7], Kotani *et al.* [8], and Boys *et al.* [9] began experimenting with multiconfigurational wave functions. Today we know that there are other ways to go beyond the Hartree–Fock level of treatment that are far simpler computationally [10] and therefore have a much broader range of applicability than does CI. Nonetheless, there is evidence that a method such as density functional theory [11] is notably more reliable for the treatment of the ground states of atomic and molecular systems than it is for excited states. Many authors feel that there are good theoretical grounds for believing that this state of affairs will continue indefinitely.

Only time will tell whether this assessment is correct, but at least for the present the only sure way to obtain a reasonably quantitative description of the potential energy surfaces and non-adiabatic coupling elements for large groups of electronic states is the CI method. In order to make significant progress with the CI method in general, it is necessary to severely restrict the class of configurations that are actually treated explicitly in the calculations. If one employs an orthonormal set of one-electron functions to describe the molecular orbitals (MOs) to be included in the electronic configurations, there is a simple prescription for reducing the amount of computational expense without significantly lowering the accuracy level of the overall theoretical treatment. This is because Hamiltonian matrix elements between

configurations differing by more than two such orbitals must vanish under these circumstances. At the same time, one has to be careful to not just restrict one's attention to configurations that are only related by single and double excitations to a single-reference configuration such as the Hartree–Fock solution. Especially when interest turns to excited states of molecular systems that are in geometrical arrangements which are far removed from the corresponding equilibrium structures, as is the norm in scattering cross-section calculations, it becomes necessary to consider many different electronic configurations as generators for the final CI space. The conclusion is that one should use a multireference single- and double-excitation CI method, as introduced in the 1970s by Buenker and Peyerimhoff (MRD-CI method [12,13]). For large atomic orbital (AO) basis sets and many electrons in a given application, however, even the restriction to a moderately large number of reference configurations from which all such excitations are permitted turns out to produce CI spaces which are too large. This is still true today, despite the great advances in computer science that have been made in the past half a century.

The approach that has been taken in the present work to deal with this problem is to use perturbation theory to simplify the computations. This is used to select configurations from the original MRD-CI space to be excluded from a strictly variational treatment, and also to obtain reliable estimations of their contributions to a given state's total energy [13]. In addition, one can reduce the number of active electrons, i.e., those allowed to participate in the excitation process at the configuration-generation stage by defining a core of relatively stable orbitals [14,15]. The selected MRD-CI spaces produce truncated quantum-mechanical wave functions which are suitable for the evaluation of various other key properties such as transition moments and radial, rotational and spin–orbit coupling matrix elements. As mentioned above, these types of quantities are indispensable in scattering cross-section calculations. In the case of radial coupling elements, which involve the derivative operator $\mathrm{d}/\mathrm{d}R$ for various vibrational degrees of freedom, a finite-difference approach has been employed to carry out the evaluations. In practice, these results are employed to effect a suitable diabatic transformation [16] of the original adiabatic (CI) electronic wave functions, so that all subsequent calculations are carried out in this basis. The rotation-coupling matrix elements are computed analytically. They are just expectation values of the angular momentum operator's components.

The treatment of the spin–orbit interaction requires an additional development. To avoid variational collapse because of the short-range nature of the corresponding operator, it is helpful to employ effective core (or pseudo-) potentials [17,18] for the constituent atoms. The calculations are then reduced to the evaluation of one-electron matrix elements which greatly simplifies the overall computational procedure, especially when heavy atoms

are involved. This type of coupling mixes states of different multiplicity, whereas the rotational (Coriolis) coupling is important for pairs of states of different spatial symmetry but equal spin multiplicity. For most of the applications considered below, however, the main coupling mechanism involves the radial $\mathrm{d}/\mathrm{d}R$ operators which are fully symmetric and therefore can only cause mixing between electronic states of the same spatial symmetry.

The computer program package that has been employed for the great majority of calculations to be described below makes use of the Table-Direct CI algorithm [19–21]. It is capable of dealing with more than 10^8 generated configurations from a series of reference states. The actual secular equations which are diagonalized in the variational portion of the theoretical treatment comprise as many as 2×10^6 spin-adapted functions (SAFs). As many as 20 different roots of a given spatial symmetry and spin multiplicity can be treated simultaneously in a given secular problem. Relativistic terms in the Hamiltonian, including the spin–orbit interaction, are treated in essentially two different ways [22]. In a relatively simple procedure [23] adequate for lighter atoms ($Z < 70$), small secular equations are solved in a contracted basis of S^2 eigenfunctions (Λ–S states) obtained employing the programs already discussed. This procedure is also quite attractive from a purely qualitative point of view since it affords a direct analysis of the final spin-perturbed wave functions in terms of its pure-spin components. The other standard technique is of the Direct SO-CI variety, i.e., a large secular equation is solved employing a basis of Λ–S SAFs. One can think of this as a large CI with 'small' basis functions, whereas the technique discussed first is a small CI employing 'large' basis functions. They give results very close to those in the intermediate range of nuclear charge for the constituent atoms, but the Direct SO-CI procedure begins to have a noticeable advantage when one comes to the Au–Pb portion of the periodic table.

2.1.2. Formulation of scattering dynamics

Below high-keV energies, electrons in the projectile and target can follow the movement of nuclei so that one can regard the colliding system as forming a quasi-molecule during collision, i.e., in a molecular picture. Further, in this energy region, it is known that various inelastic processes simultaneously occur with nearly the same magnitude of cross-sections for ionization, electronic excitation, etc. Hence, traditionally, for collisions in this energy region, the basis set to describe electronic motion for the collision system is expanded in terms of molecular states. Also, adaptation of some kind of close coupling technique to treat many channels occurred on an equal footing is essential for the correct description of collision dynamics. For this purpose, electronic-state close-coupling (ESCC)

approaches both within a fully quantal and semiclassical formalism have been developed over the years, and been successfully applied to provide a firm basis for our better understanding of collisions dynamics for various systems below high-keV domain and also accurate cross-section data for applications. Here we provide a brief account of the ESCC method we primarily employ. For simplicity, let us consider the proton–hydrogen molecule collision system in the collision energy region from several eV/u to several keV/u as an illustration of the theoretical framework. In the following, we also assume the Born–Oppenheimer approximation to separate electronic and nuclear motions. In addition, the so-called Franck–Condon principle is also assumed to be valid for describing the nuclear transition of the target molecule. We shall come back to this assumption in more detail below. The coordinates are $\vec{R}$, $\vec{r}$, $\vec{r}'$ and $\vec{\rho}$ for the distance between proton (p) and hydrogen molecule, electron (e) and projectile proton, electron and target protons, and two nuclei within the target molecule, respectively. The additional collision parameters are $\vec{b}$ – the impact parameter and $\vec{v}_0$ – the initial velocity.

Here we adopt several crucial approximations which allow simpler numerical computations, and these are: (i) Because of the large disparity between the nuclear and electron masses, the approximation to describe the relative motion of the nuclei classically is reasonable above a few tens of eV – semiclassical treatment. (ii) Since the collision time is much shorter (of the order of 10^{-15} s) than the nuclear motion of a target molecule (10^{-13} s) in this energy domain, it should be a good assumption to treat the nuclear motion of a target molecule as frozen during the collision. (iii) Since the transition for nuclear motion of the target molecule is much slower than that of electrons, the Franck–Condon principle generally holds. Hence, the vertical nuclear transition of the target molecule before and after collision is assumed for fragmentation analysis.

Therefore, from (i) above, we can adopt the semiclassical approach, i.e., the relative motion of projectile nuclei is described classically, while the motion of electrons is treated quantum-mechanically. The relative coordinate $\vec{R}(t)$ is given by the Newtonian equation

$$M\frac{\mathrm{d}^2\vec{R}(t)}{\mathrm{d}t^2} = -\nabla V(\vec{R}), \tag{1}$$

where M is the reduced mass of the projectile and target. The time dependence of the relative coordinate can be determined by solving the equation of motion (equation (1)) for the given impact parameter $\vec{b}$ and initial velocity $\vec{v}_0$. The electron motion satisfies the Schrödinger equation

$$\mathrm{i}\frac{\partial}{\partial t}\Psi(\vec{r},t;\vec{R}(t)) = H_{\mathrm{el}}\Psi(\vec{r},t;\vec{R}(t)), \tag{2}$$

where H_{el} is the electronic Hamiltonian and $\Psi(\vec{r}, t; \vec{R}(t))$ is the total scattering wave function.

The Hamiltonian is then given by

$$H_{\mathrm{el}} = -\frac{1}{2}\sum_i \nabla_i^2 - \sum_i \frac{1}{r_i} - \sum_{ij} \frac{Z_j}{r'_{ij}} + \sum_{i<i'} \frac{1}{|\vec{r}_i - \vec{r}_{i'}|} + \eta, \qquad (3)$$

where j labels the nuclei of the target molecule and η is the electrostatic energy of all target nuclei and the projectile.

2.2. Electronic-state close-coupling method

In the ESCC [24], the total wave function Ψ is expanded in terms of electronic states $\{\Psi_j\}$ of known functions as

$$\Psi(\vec{r}, \vec{\rho}, t; \vec{R}(t)) = \sum_j c_j(t)\,\Psi_j(\vec{r}; \vec{R}(t))\chi_j(\vec{\rho})\exp\left[-\mathrm{i}\frac{1}{2}\frac{\mathrm{d}\vec{R}(t)}{\mathrm{d}t}\vec{r}\right] \times \exp\left[-\mathrm{i}\int E_j(R(t))\mathrm{d}t\right]. \qquad (4)$$

Here, $\chi_j(\vec{\rho})$ describes the nuclear wave function of a target molecule, and

$$\exp\left[-\mathrm{i}\frac{1}{2}\frac{\mathrm{d}\vec{R}(t)}{\mathrm{d}t}\vec{r}\right]$$

represents the so-called electron translation factor (ETF). The ETF is introduced to take into account an effect that the electron is moving together with moving nuclei, and ensures that the correct boundary conditions for the scattering process are satisfied.

At the low- to intermediate-energy region, choosing the eigenfunctions Ψ_j of the electronic Hamiltonian as the basis of the expansion is considered to be appropriate as described above, and thus

$$H_{\mathrm{el}}\,\Psi_j(\vec{r}; \vec{R}) = E_j(R)\,\Psi_j(\vec{r}; \vec{R}), \qquad (5)$$

where Ψ_j satisfies an orthonormal condition

$$\int \Psi_i^*(\vec{r}; \vec{R})\,\Psi_j(\vec{r}; \vec{R})\mathrm{d}\vec{r} = \delta_{ij}. \qquad (6)$$

Substituting expansion (4) into Schrödinger equation (2), we can derive a set of coupled equations in terms of the expansion coefficient $c_j(t)$ as follows

$$\mathrm{i}\dot{c}_i = \frac{\dot{\vec{R}}^2}{8}c_i - \mathrm{i}\sum_j c_j \dot{\vec{R}}\left\langle \Psi_i\chi_i\middle|\nabla_R - \frac{1}{2}\nabla_r\middle|\Psi_j\chi_j\right\rangle \exp\left[-\mathrm{i}\int(E_j - E_i)\mathrm{d}t\right]$$

$$-\sum_j \frac{1}{2}c_j \ddot{\vec{R}}\langle \Psi_i\chi_i|\vec{r}|\Psi_j\chi_j\rangle \exp\left[-\mathrm{i}\int(E_j - E_i)\mathrm{d}t\right]. \quad (7)$$

We solve these coupled equations under the appropriate set of initial conditions $\{c_j(-\infty)\}$ for each particular process.

From equation (7), it is clear that if the relative speed $\dot{\vec{R}}$ is non-zero, then the transition becomes possible between different states. Because we are concerned only with slow-to-intermediate collisions, terms beyond the square of the relative speed are ignored, and hence, only up to the second term needs to be evaluated.

Generally, it is convenient to represent the coupled equation in terms of the molecular coordinates. Let us denote the basic unit vectors by $\vec{i}, \vec{j}, \vec{k}$, and label the molecular coordinates with the subscript 'M'. Using such a coordinate system and the Franck–Condon approximation, we can rewrite the second term in the coupled equation (7) as

$$\dot{\vec{R}}\left\langle \Psi_i\chi_i\middle|\nabla_R - \frac{1}{2}\nabla_r\middle|\Psi_j\chi_j\right\rangle = \dot{R}\left\langle \Psi_i\middle|\frac{\partial}{\partial R} - \frac{1}{2}\frac{\partial}{\partial z_{\mathrm{M}}}\middle|\Psi_j\right\rangle\langle\chi_i|\chi_j\rangle$$

$$-\dot{\Theta}\left\langle \Psi_i\middle|\mathrm{i}l_{y_{\mathrm{M}}} + \frac{1}{2}R\frac{\partial}{\partial x_{\mathrm{M}}}\middle|\Psi_j\right\rangle\langle\chi_i|\chi_j\rangle. \quad (8)$$

In this equation, the first term is called a radial coupling term due to the radial motion of the nuclei, while the second term is a rotational coupling which arises from the rotation of the molecular axis. The nuclear wave function overlap integral is also included in both the coupling terms. From now on, we will omit the subscript M from the notation since all discussions concerned with are based on the molecular coordinate framework. Then we derive the new form of the coupled equation:

$$\mathrm{i}\dot{c}_i = -\mathrm{i}\sum_j c_j\left\{\dot{R}\left\langle \Psi_i\middle|\frac{\partial}{\partial R} - \frac{1}{2}\frac{\partial}{\partial z}\middle|\Psi_j\right\rangle\langle\chi_i|\chi_j\rangle\right.$$

$$\left.-\dot{\Theta}\left\langle \Psi_i\middle|\mathrm{i}l_y + \frac{1}{2}R\frac{\partial}{\partial x}\middle|\Psi_j\right\rangle\langle\chi_i|\chi_j\rangle\right\}\exp\left[-\mathrm{i}\int(E_j - E_i)\mathrm{d}t\right]. \quad (9)$$

This coupled equation can be solved numerically to determine the scattering amplitudes c_j, absolute square of which gives the particular transition probabilities. As the conventional procedure, the integration of the

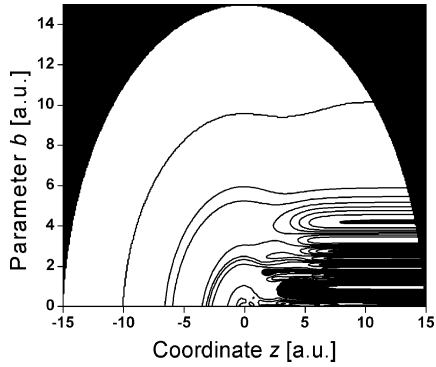

Fig. 1. Typical behavior of the probability landscape in the initial collision channel as a function of the impact parameter b and collision coordinate $z = vt$ for a fixed energy.

probability over the impact parameter yields the cross-section. Typical dependence of the transition probabilities on impact parameters and the collision time is shown in Fig. 1.

In the diatomic target case, by using the infinite-order sudden approximation [25], the total cross-section can be obtained by summation of partial wave contributions

$$\sigma_{nn'} = \frac{2\pi}{k_n^2} \int_0^{\pi} \mathrm{d}\gamma \sin\gamma \sum_{\bar{l}} (l + 1/2)|\delta_{nn'} - S^l_{nn'}|^2. \tag{10}$$

Here $S^l_{nn'}$ is the lth partial wave scattering matrix element, γ is the fixed collision angle and k_n the wave vector for channel n. The cross-section formula simplifies by using the semiclassical approach outlined above,

$$\sigma_{nn'} = 2\pi \int_0^{\pi} \mathrm{d}\gamma \sin\gamma \int_0^{\infty} b|\delta_{nn'} - S^b_{nn'}|^2 \mathrm{d}b. \tag{11}$$

3. RESULTS AND DISCUSSIONS

In the following we present our results for the He atom and the molecular targets of CH_4, C_2H_2, C_2H_4, H_2, D_2, H_2O, and CO. A comparative study for the proton–antiproton impact, and effects arising from the polyatomic target structure are discussed.

3.1. Protonation of molecular targets

In order to give a typical example of proton-collision cross-section calculations, let us consider one of the simpler hydrocarbon molecules,

ethylene C_2H_4 [26], as the target system. Conformation changes and stability of this planar molecule during protonation from various directions have large practical importance, e.g., carbon nanostructures can be grown by using the catalytic decomposition of C_2H_4. It is also possible to detect neutral molecules in experiments by means of chemical ionization with ethylene, i.e., the charge transfer reaction $C_2H_5^+ + M \rightarrow MH^+ + C_2H_4$, in which the protonated molecule $C_2H_5^+$ creates ions with moderate internal energy and therefore causes less fragmentation. Last but not the least, the proton ethylene charge transfer collisions have been well studied experimentally using the time-of-flight method in the low-energy region [27]. Both the antisymmetric vibration nodes (due to ion-induced dipole mechanism) and symmetric vibration modes (due to vibronic coupling) could be observed in the angular-resolved charge transfer measurements.

In order to describe the constituent atoms, a fairly large Gaussian AO basis has been employed: a (10s5p2d1f) primitive basis for carbon, contracted to [4s3p2d1f], and a (5s2p1d) primitive basis for hydrogen. Because some of the low-lying excited states of C_2H_4 are so-called Rydberg states, with diffuse charge distributions, additional functions were added with small exponents placed at the midpoint of the C−C double bond. Altogether, the resulting AO basis consists of 159 contracted Gaussian functions.

The proton is brought in along each of three perpendicular directions, whereby the C−C bond is placed along the x-direction and the latter's midpoint is chosen as the origin of the cartesian coordinate system. The energy level of the system in these space configurations are shown in Fig. 2. Ethylene is a planar molecule, and the z-axis is taken to be perpendicular to this plane. The target system is placed in its experimental equilibrium geometry, similarly as in the previous work [28] with other hydrocarbons such as methane CH_4 [29] and acetylene C_2H_2 [30]. Since the main interest in this work lies in relatively high-energy collisions, attention will be restricted to proton approaches in which the C_2H_4 molecule is fixed in this geometry, although it is not critical that this be done.

The first step in the treatment for a given location of the external proton is to carry out an SCF calculation. The main purpose of this procedure is to generate the orthonormal one-electron basis for the subsequent CI treatment. Theoretically, it should not matter what electronic state is chosen for this purpose. This is an important issue because the ultimate goal of the calculations is to deal with a large number of electronic states simultaneously in a balanced manner, i.e., one that allows each of the states of interest to be treated at about the same level of accuracy. A potentially more difficult aspect of the calculations is the choice of states to be considered. The SCF calculations can also help with this problem, however, by producing one-electron solutions that can be used to order the possible electronic states according to their (approximate) energy. Normally, one already knows from spectroscopic investigations what states lie in a particular energy range.

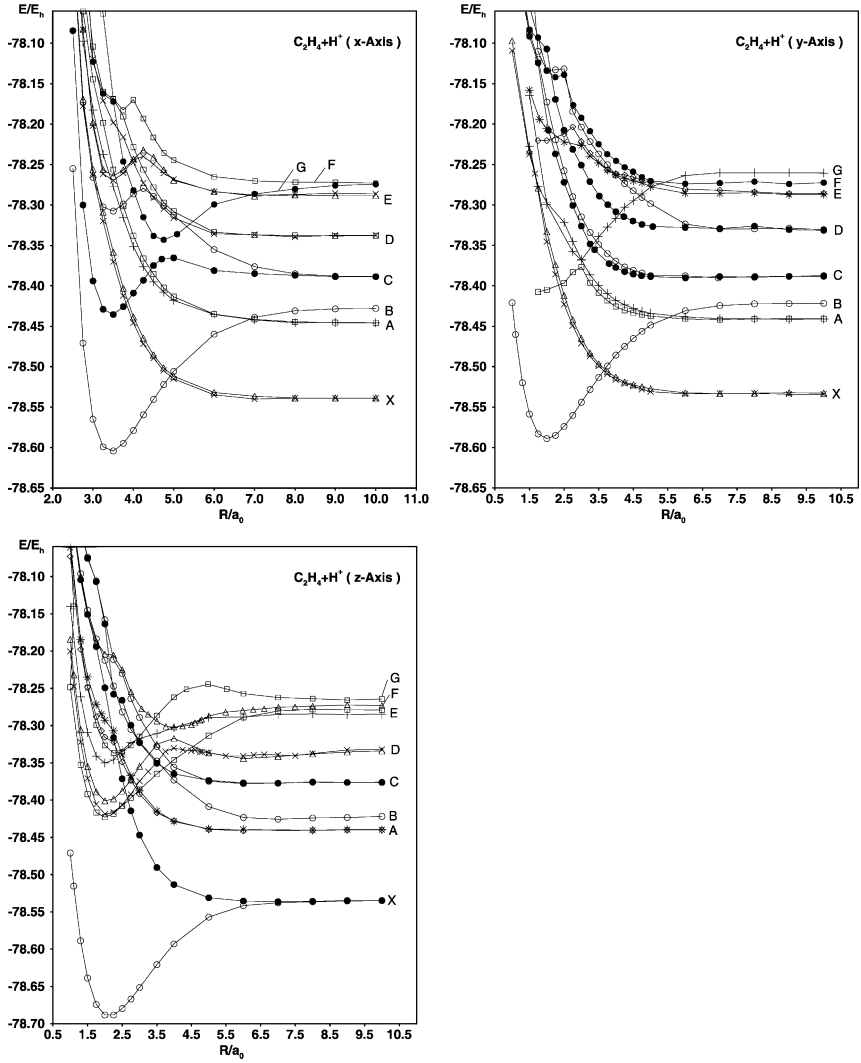

Fig. 2. Energy levels of the $\{H^+|C_2H_4\}$ system ($\vec{r}_x \subset$ C–C-axis, $\vec{r}_y \subset H_2C{=}CH_2$ plane, and $\vec{r}_z$ is perpendicular).

Such information is not really necessary, however, as it can be obtained in a straightforward fashion by scanning the singly and doubly excited states that can be formed from the highest occupied and lowest unoccupied orbitals (MOs) of the system.

Once one has a tentative list of such states, the next step is to carry out an MRD-CI calculation in which the reference set of configurations consists of all these states. In most cases the resulting CI wave functions will contain

new configurations with relatively large coefficients in one or more roots. In a subsequent run all such configurations, i.e., with squared coefficients above a threshold value (typically set to 0.002) are included in the reference space and the corresponding CI eigenvalues are computed. Rarely does one have to repeat this procedure to include still more reference configurations. Exceptions can usually be avoided by being more careful in one's choice of states (roots of the secular equation) to be treated. Finally, it is important to scan the range of internuclear geometries of interest in the overall treatment to see whether the set of reference configurations changes from short- to long-range interactions. In general, one tries to use a 'common denominator' of reference configurations throughout to ensure maximum continuity for the resulting potential energy surfaces and coupling elements.

The potential curves obtained for the proton approach along the z-axis (perpendicular to the molecular plane) are given in Fig. 2. The lowest energy asymptote is for the $C_2H_4^+$ molecular ion and an H atom X channel. The initial channel ($C_2H_4 + H^+$) is labeled B in Fig. 2. The X channel consists of a triplet and a singlet electronic state, and their potential curves are seen to be strikingly different. The reason for this difference is that the B channel consists only of a singlet state, and it possesses the same spatial symmetry (A_1) as the X singlet. There is a strong interaction between these two states, which causes the X singlet's potential to be pushed downward at short proton separations. The X triplet state is repulsive, which is the true character of this channel. One can see this most clearly by comparing with the analogous potentials for the y approach of the proton (Fig. 2). In this case the B channel no longer has the same spatial symmetry as the X singlet and thus cannot interact with it. Thus, both the X triplet and singlet are repulsive for this approach, whereas the B state shows a definite minimum in its potential. From this comparison it is evident that the X singlet in Fig. 2 changes its character as the proton approaches, and the B state does so as well in a complementary fashion. There is another channel (A) that lies just below the B at the asymptotic limit. It also corresponds to a $C_2H_4^+$ ionic state, but in this case the electron is absent from the MO which is the antibonding combination of p_y AOs on carbon. As such it has a different spatial symmetry than X and B for both the H^+ approaches along the z- and y-directions, and its potentials do not show any interaction with these two channels. The radial couplings among the B, C and X states are shown in Fig. 3.

3.2. Isotope effect of the target molecule

The isotope effect has been systematically neglected in the keV region of collision energies for decades. For instance, it has long been customarily assumed that in $H^+ + H_2$ and $H^+ + D_2$ collisions, vibrationally excited target molecules do not play any significant role in keV/u collision energies,

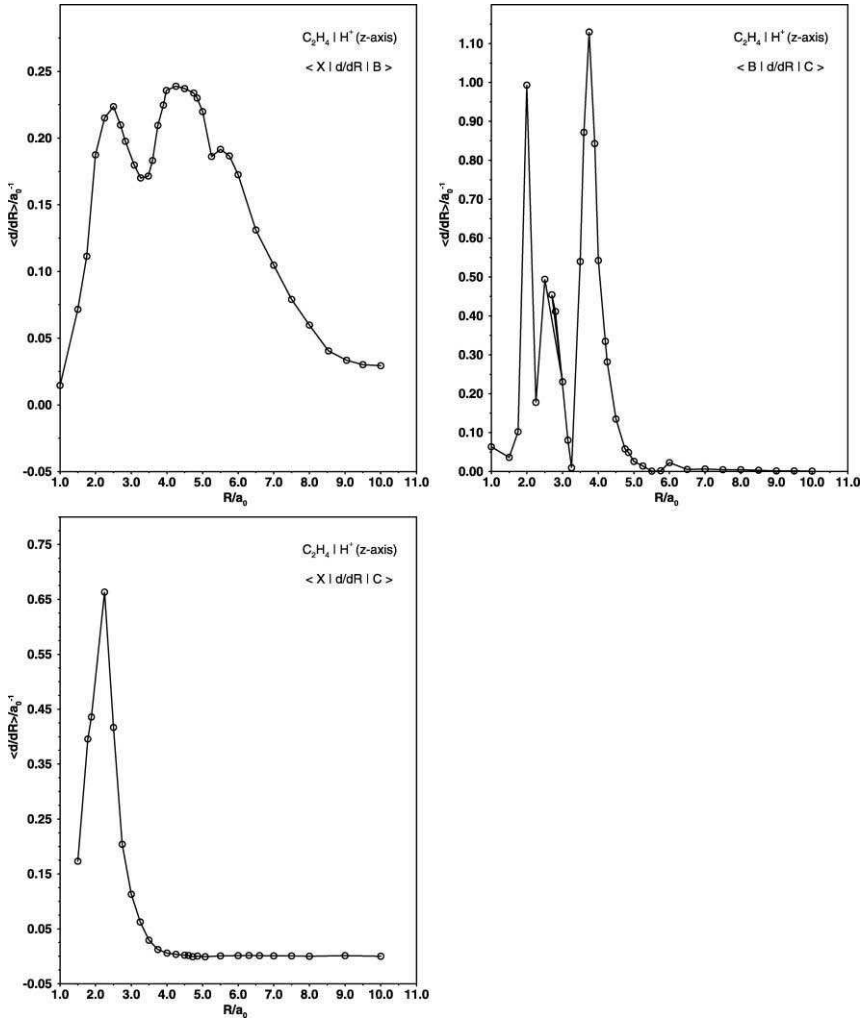

Fig. 3. Radial coupling terms among the three states of the $\{H^+|C_2H_4\}$ system (for proton approaching in the z-direction, i.e., perpendicular to the $H_2C{=}CH_2$ plane).

because the vibrational energy levels are much smaller (0.546 eV for H_2 and 0.386 eV for D_2, respectively), compared to the relative collision energy of keV, and also because statistically only a small fraction of the vibrationally excited species are present at thermal-temperature collision processes. Thus, practically no differences in the cross-sections were expected to appear in the charge transfer cross-sections. There also exists a small difference between the electron binding energy between H_2 and D_2 molecules ($\sim$41 meV),

which is also termed as the 'isotope effect', but has not been thoroughly explored yet.

We have, therefore, studied these phenomena recently [31]. Furthermore, as we will discuss in Section 3.3, there exists an important vibrational effect of target molecules on charge transfer in general ion–molecule collisions by which the charge transfer cross-sections can be enhanced by orders of magnitude. This is often possible even if only the first vibrationally excited state of the target molecule is involved in dynamics in the low-collision energy. Thus, even the presence of only a small fraction of vibrationally excited species is known to cause a huge difference in charge transfer measurements [32–35]. In order to explore the isotope effect explicitly, the specific processes we are concerned with are charge transfer from the ground electronic and vibrational states, viz.,

$$H^+ + H_2(D_2), (X^1\Sigma_g; v_i = 0) \rightarrow H(nl) + H_2(D_2)^+ (ns\sigma, np\sigma, np\pi,\ n = 1,2; v_f),$$

where v_i and v_f are the quantum number for the initial and final vibrational states, respectively, and nl describe the final principal and angular quantum numbers of H atom. For the dynamical calculation, states included are $[H^+ + H_2, D_2(X^1\Sigma_g; v_i = 0)]$ for the initial channel, and $[H(1s, 2s, 2p) + H_2^+, D_2^+(1s\sigma_g, 2p\sigma_u, 2p\pi_u; v_f)]$ for charge transfer channels, in addition to excitation channels $[H^+ + H_2, D_2(A^1\Sigma_g; v_f)]$. Vibrational levels for the final products are explicitly considered up to $v_f = 5$ for excitation and $v_f = 10$ for charge transfer. This collision process is endothermic if the initial vibrational level $v_i < 4$ for H_2, and $v_i < 6$ for D_2, respectively, and this apparent difference, viz., the isotope effect, is certainly expected to cause the difference in dynamics, but the question is which energy and how it emerges or diminishes.

If the initial vibrational level of the target is in the excited state, then it makes the collision more near-resonant and therefore favorable. One example of potential surfaces, which illustrates the above points, is shown in Fig. 4, including the Franck–Condon regions for the vibrational ground state of H_2 and D_2.

In Fig. 5, the present results of the cross-section ratio of the charge transfer by H^+ ions with D_2 and H_2, i.e., $\sigma(D_2)/\sigma(H_2)$, are shown together with the earlier measurements of Cramer and Marcus [36] and Cramer [37]. As apparent, the ratio continues to decrease smaller than a unity below 1 keV/u, and reaches a value of 0.59 at the collision energy 0.18 keV/u. The ratio of Cramer's measurements appears to agree well with the present result at around 0.2 keV/u, but then flattens out in the energy region from 0.2 to 0.1 keV/u followed by the slight increase at much lower energies up to 0.05 keV/u. Nevertheless, a clear evidence of the isotope effect on charge transfer emerges in the energy domain from high-eV to low-keV. Our theoretical results are also included in the figure, and are in good accord

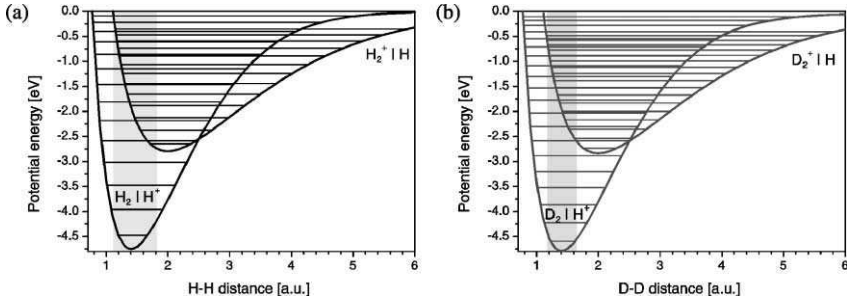

Fig. 4. The calculated potential curves and vibrational levels for H_2 (a) and D_2 (b) molecules. Franck–Condon regions are shown for the $v_i = 0$ ground states.

with the present measured results in the entire energy region, but do not agree with those of Cramer particularly below 0.08 keV. Such an isotope effect can be explained as follows: it is easily noted (as seen in Fig. 4) that there are two small differences in the energy involved in the charge transfer for H_2 and D_2 molecules.

First, although the electron binding energy for D_2 is larger merely by 41 meV than that of H_2 molecules, nevertheless we have found that this difference is non-negligible for particles to surmount for collisions below 1 keV/u. Secondly, the potential energy curves for the initial and final channels show a larger energy defect by the amount of the vibrational energy for the $[H^+ + D_2]$ collision than that of the $[H^+ + H_2]$. The energy defect between the $v_i = 0$ level in the initial $X^1\Sigma_g$ state and $v_f = 0$ in the $1s\sigma_g$ state

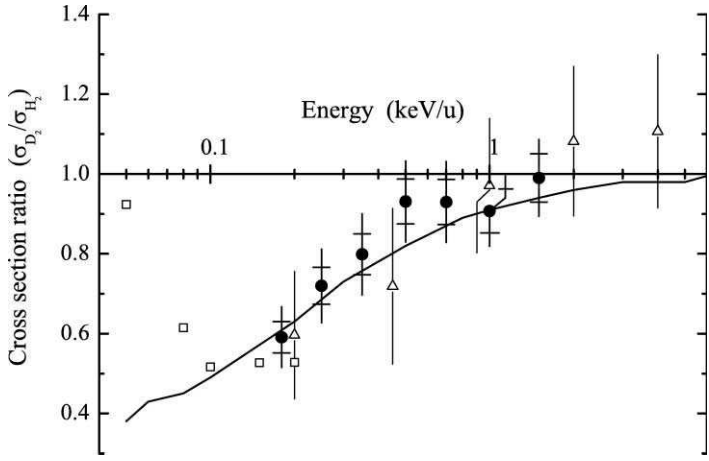

Fig. 5. Relative ratio of electron capture cross-sections by H_2 and D_2.

(see Fig. 4) is roughly 37 meV more endothermic for the D_2 molecules than that for the H_2 molecules. In addition, the vibrational spacing is denser for the D_2 molecules, and hence, the nuclear wave functions are more contracted within a smaller spatial region, thus giving rise to a smaller Franck–Condon factor than that for the H_2 case for the transition between the two potential curves.

As for indirect processes and/or when the target is first vibrationally excited, subsequent transitions are favored to the nearest vibrational levels of the molecular ion. Since the target nuclear wave functions in case of D_2 molecules are more oscillatory within a narrower space in the same energy region as compared to H_2, the overlap integrals for such a mechanism were also found to be smaller. These combined effects become influential to the collision dynamics and tend to make the charge transfer less favorable for D_2 molecules, particularly below keV-energies. Therefore, the ratio is expected to continue to fall as the collision energy decreases before other processes such as reactive scattering become dominant below low-eV. Since the present theory does not include this process, our cross-section monotonically decreases with decreasing energy within the energy region studied.

Another molecular target of enormous importance in proton–molecular collisions is the water molecule. The main collision orientations we have considered so far are (1) an in-plane impact along the axis of the H–O–H angle (from both directions) and (2) the impact trajectory on the oxygen atom perpendicular to the H–O–H plane. The strong geometry effect for different collision orientations are illustrated in Fig. 6. Table 1 shows the energy defects computed in the equilibrium geometries of neutral parent molecules that correspond to the fast-collision encounters. Potential energy curves for the H_2O^+ ion were obtained previously [38].

3.3. The vibrational effect in $H^+ + CH_4$ and $H^+ + C_2H_2$ collisions

Contribution from vibrationally excited states of a target molecule to charge transfer and ionization has been considered to be negligibly small, again, due to the same reason above, i.e., a small energy involved for vibrational states. However, as we will show below, explicit and accurate inclusion of vibrational state in the theoretical framework, both for the initial molecular target as well as the final molecular ionic state after charge transfer in particular, is essential for correct description of dynamics and assessment of measured data. As an representative example, we start with the CH_4 molecule [29,39].

The cross-sections for CH_4 molecules are as shown in Fig. 7 together with those previously published [29,39]. Though there are some discrepancies among them, the experimental data seem to be in a reasonable accord. As the collision energy increases, the charge transfer cross-sections decrease monotonically. The energy defect of $H^+ + CH_4$ collisions is 0.618 eV.

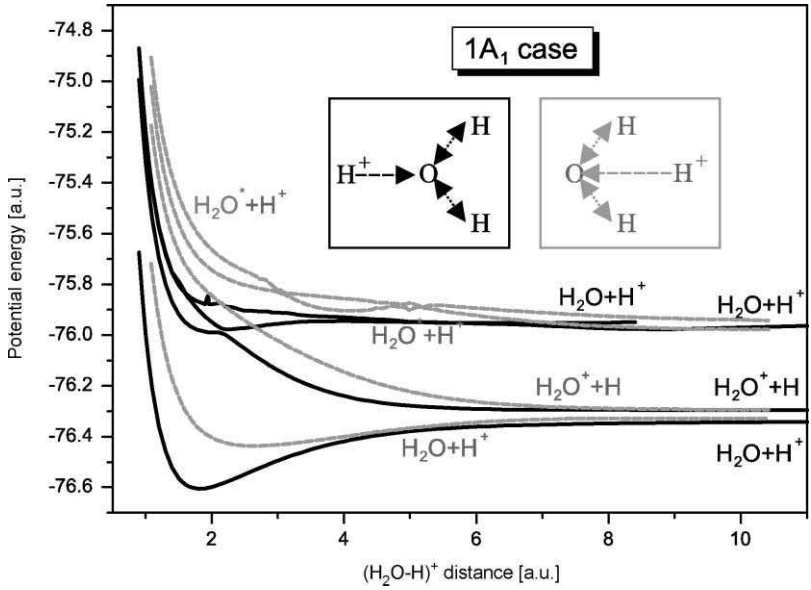

Fig. 6. $^1A_1$ electronic states of proton–water collision system in two different geometries.

Table 1. Fragment particle energies for the proton–water system

Fragment	Symmetry	Energy, E (a.u.)	$\Delta(E)$ (eV)
OH_2	$^1a_1$	−76.333465	−23.049
OH_2^*	$^1b_1$	−76.048270	−15.288
OH_2^+	$^2a_1$	−75.797037	−8.452
OH	$^2b_2$	−75.644296	−4.295
OH^*	$^2a_1$	−75.490944	−0.122
OH^+	$^1a_1$	−75.091712	10.741
H_2	$^1a_1$	−1.173609	−18.330
H_2^+	$^2a_1$	−0.569849	−1.901
$H_2/O^+(^4S)$	$^4a_2$	−75.666750	−4.906
$H_2^+/O(^3P)$	$^4a_2$	−75.556295	−1.901
$H_2/O^+(^2D)^*$	$^2a_1$	−75.539987	−1.457
$H_2/O^+(^2P)^*$	$^2a_1$	−75.477487	0.244
$H_2^+/O(^1D)^*$	$^2a_1$	−75.478833	0.207
$H_2^+/O(^1S)^*$	$^2a_1$	−75.396614	2.444

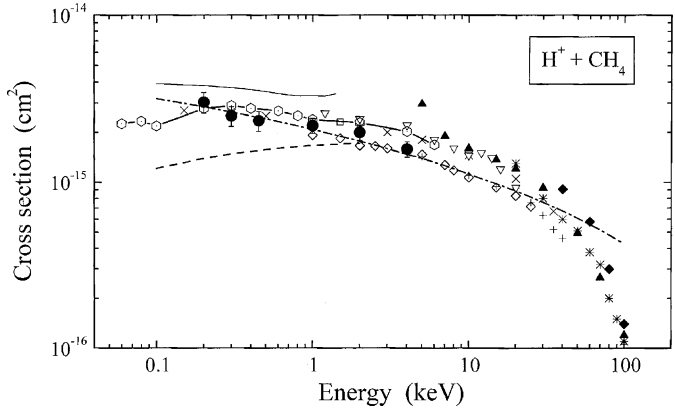

Fig. 7. Charge transfer cross-section for the $\{H^+|CH_4\}$ collision.

The present theoretical results based on the molecular representation, which took two different molecular configurations, i.e., the C_{2v} and C_{3v} symmetries into account, were obtained in Ref. [29]. In the present treatment, the energy defect was adjusted in order to match vibrational excited states of the target molecular ion. The present results, which account for vibrational excited states show good agreement with most of the experimental data except for the low-energy region. The results have a broad peak around 0.3 keV, and on both sides of this energy they gradually decrease. The cross-section values based on the Olson formula under the assumption that the target molecule results in the ground state after the collision are consistently smaller than all measurements and show a rapid increase with smaller amplitude as the collision energy increases up to about 2 keV.

If vibrational excited states in the product molecular ions are taken into account properly, then this extra internal energy helps produce an accidental resonant condition, and hence, brings the magnitude of the cross-section closer to the experimental value. Therefore, it is essential to take the vibrational state of the target molecule correctly into account before and after the collision for accurate description of collision dynamics. This observation has been completely ignored in earlier studies of molecular targets, but is very significant to assess the dynamics and corresponding cross-sections correctly.

As another example of the vibrational effect, we illustrate in Fig. 8 cross-sections for charge transfer of H^+ ions from C_2H_2 molecules [30,39]. We had calculated the charge transfer processes in $H^+ + C_2H_2$ collisions for C_{2v} and $C_{\infty v}$ symmetries assuming that the vibrationally ground states of products, in which the cross-sections showed rapid increase as the collision energy increases with much smaller magnitude.

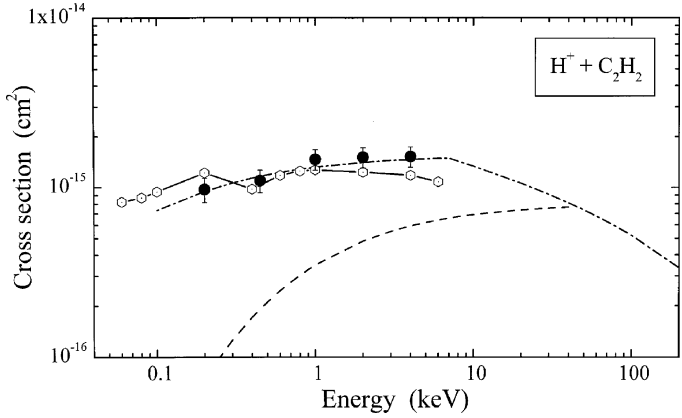

Fig. 8. Charge transfer cross-section for the $\{H^+|C_2H_2\}$ collision.

An extra calculation was carried out by taking the correct energy defect for the vibrationally excited initial and final states ($v_i = 0-3$ and $v_f = 1-3$) of the target molecule and molecular ion into account. The effect of vibrationally excited states is found to be more significant for the $H^+ + C_2H_2$ measured data than for the $H^+ + CH_4$ system. The new theoretical results are now closer to the present measurement. The vibrational excited state of the target molecular ions of this system is more favorable energetically for the resonant conditions, hence increasing rather drastically the cross-sections. As another check on the present experimental data, the Olson formula was employed to calculate the cross-sections for the vibrational ground state as well as the excited states of target molecule ions. Similar to the MO results mentioned above, the cross-sections for the vibrational ground state target significantly underestimates the magnitude, while if the vibrationally excited state is taken into account (the energy defect is chosen to be approximately 0.8 eV), the results are found to be in good agreement with the experimental data. These predictions are very indicative of the temperature effect importance for charge transfer involving molecular targets.

3.4. The steric effect H^+/CO

The effect of molecular orientation, or steric effect, for various inelastic processes in atomic collisions at low-eV to high-meV collisions has been known to be extremely crucial for effective chemical reactions and rovibrational excitation, but has been widely paid little attention for those of above-eV collision energies because of the same reason as in Section 3.2. Here, we stress its importance even at keV-collisions.

Our study of electron capture resulting from proton collisions with CO molecules for collision energies less than 10 keV has been specifically intended to examine the steric effect on capture dynamics [40]. The process is important in various applications such as modeling the interaction of the solar wind with comets, fusion research, plasma chemistry, and medical physics for cancer research. The CO molecule is expected to show an enhanced steric effect due to its heteronuclear structure, and hence can provide much detailed information on collision dynamics. The processes we are concerned with are

$$H^+ + CO \rightarrow H + CO^+(X^2\Sigma^+) \qquad -3357\ \text{cm}^{-1}\ \text{electron capture}, \tag{12a}$$

$$H^+ + CO \rightarrow H + CO^{+*}(X^2\Sigma^+) \quad -24\,090\ \text{cm}^{-1}\ \text{capture excitation}, \tag{12b}$$

$$H^+ + CO \rightarrow H^+ + CO^*(A^2\Pi) \qquad -48\,687\ \text{cm}^{-1}\ \text{target excitation}. \tag{12c}$$

Because of the small energy defect, process (12a) is expected to dominate in the energy region considered, while processes (12b) and (12c) are weaker channels with an energy defect larger than 3 eV. Note that the energy defects in equations (12a)–(12c) are determined based on the assumption that the C–O distance is fixed at the equilibrium distance. As for the orientation, we have considered three molecular configurations: (i) the H^+ approaches the center of mass of CO (CO perpendicular to the incoming H^+); (ii) H^+ approaches the C atom, in which CO lies along the collision trajectory (collinear case); and (iii) the H^+ approaches the O atom (also collinear case). The collision orientations are shown in Fig. 9 for cases I–III.

Total electron capture cross-sections averaged over the three molecular orientations, calculated within the quantum-mechanical molecular representation, are shown in Fig. 10. Included in the figure are earlier experimental results by Browning and Gilbody [41], Rudd *et al*. [42], Shah and Gilbody [43], and Gao *et al*. [44]. Generally, the overall agreement with the present

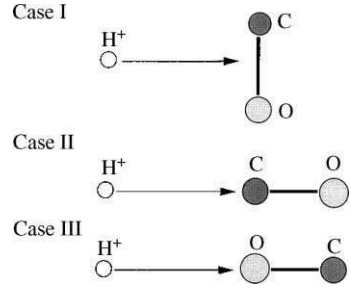

Fig. 9. The three collision arrangements for the $\{H^+|CO\}$ collision considered in the calculation.

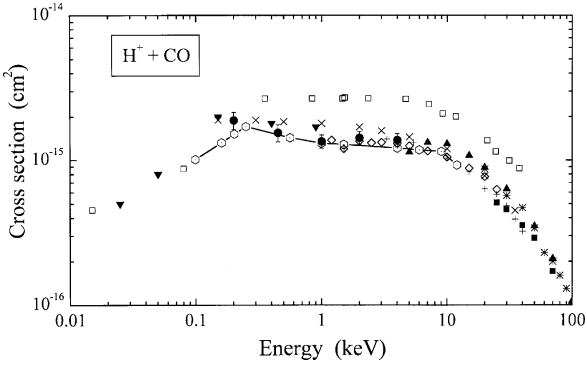

Fig. 10. Charge transfer cross-section for the $\{H^+|CO\}$ collision.

results and the four measurements is found to be very good. The maximum of the cross-section is found to occur around 250 eV/u with a value of 1.71×10^{-15} cm^2. The electron capture cross-section is found to decrease slowly for higher energies, and is consistent with all of the measurements. At 1.5 keV/u, our result reaches a value of 1.3×10^{-15} cm^2, which compares favorably with that of Gao *et al*. who reported the value of 1.48×10^{-15} cm^2. Shah and Gilbody reported the slightly smaller cross-section with 1.0×10^{-15} cm^2 at 10 keV/u, but the present result lies well within their error bars. In their measurement, Browning and Gilbody found that CO^+ ion formation is dominant for energies less than 10 keV/u. However, gradually, C^+ and O^+ ion formations increase with increasing collision energy.

In the present calculation, the orientation for which the proton approaches the C atom in the collinear configuration (Case I) is found to give the largest electron capture cross-section among the three configurations. The second largest contribution comes from Case III, while Case II is only the secondary effect. This is because Case I coupling peak is located at the largest internuclear distance among the three cases where the energy defect between the two channels becomes much smaller, and hence, they couple more effectively, making this case more ideal for electron capture. Furthermore, electron capture to the $[H + CO^+(X^2\Sigma^+)]$ channel is dominant for all energies studied, which is obvious from the energy defect between the relevant adiabatic potentials. Electron capture to the $[H + CO^+(^2\Pi)]$ channel is very weak in all three configurations, and in particular, at the lower end of the energy range their magnitudes are less than 10^{-18} cm^2. They become comparable, however, with capture through the $[H + CO^+(X^2\Sigma^+)]$ channel at the highest energy in the present study. This finding is also obvious from the behavior of the adiabatic potentials and the endoergic nature of the reaction. As stated, even in the total cross-section, the steric effect is remarkably conspicuous at 10 keV/u, although it begins to

diminish at much higher collision energy. It is apparent from the above-discussion that electron capture is very sensitive to the molecular orientation, i.e., the steric effect.

In Fig. 11, we present the scattering *S*-matrix elements for all three molecular configurations at the collision energy of 0.5 keV/u, and some features can be summarized: (i) the magnitude for Case III is the smallest of all, while that for Case II is the largest; (ii) the number of oscillations is different for the three cases; and (iii) for Case II, the last tail of the *S*-matrix element stretches out for the largest l value. All these characteristics are the reflection of those of the dominant radial coupling matrix elements coupled with the features of the adiabatic potentials, and are clear manifestations of the steric effect due to the molecular charge distribution. As the collision energy increases to 10 keV/u, the highest energy we studied, this feature of the steric effect is found to still persist. From the present study, it may be possible that the geometrical structure of the target molecule can be analyzed based on the perturbative procedure similar to an electron scattering study.

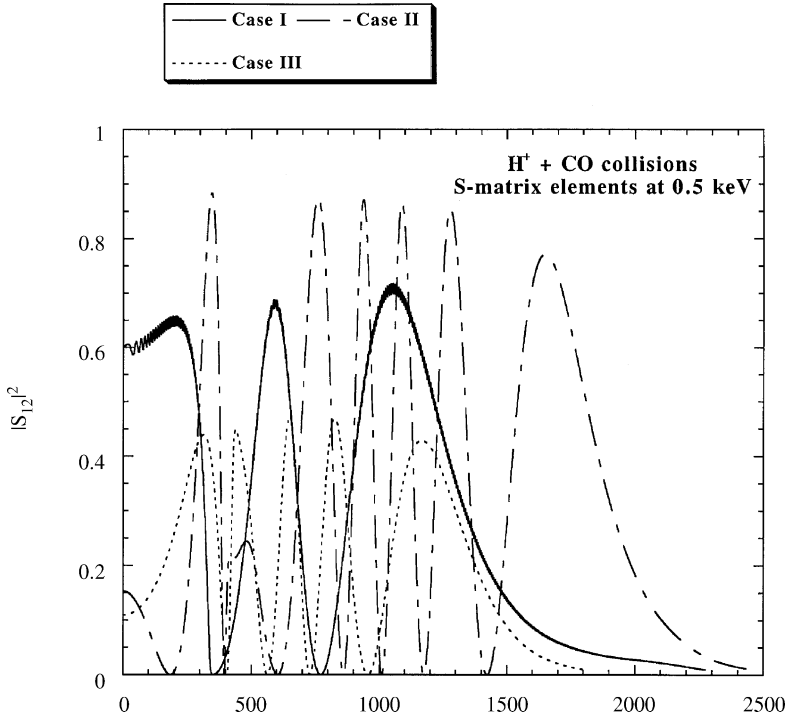

Fig. 11. Comparison of electron-capture probabilities for the three principle orientations in the $\{H^+|CO\}$ collision (energy of 0.5 keV).

3.5. Comparative study of antiproton vs. proton

3.5.1. Atomic case

It is known from the stopping-power study that at sufficiently high-energy collisions where the Born approximation is valid, inelastic cross-sections should be identical for proton and antiproton impact since the cross-section depends solely on the nature of the target wave function. However, as the energy decreases, the higher order terms of the Born series come to play a role, and the third-order term which has the Z^3-dependence, where Z is the projectile charge, causes the deviation between proton and antiproton, the so-called Barkas effect. Therefore, for atomic targets, it raises an important and practically interesting issue as to how mechanisms for ionization and electronic excitation and corresponding cross-section values differ between proton and antiproton in low-keV to high-eV energy region. As an illustration partly to respond to these questions, proton and antiproton impacts on He were investigated. The theoretical method is described in Ref. [45] and references therein.

The p and $\bar{p}$ + He collisions. Adiabatic potentials for antiproton, or proton and He systems clearly show that the electronic binding energy of every state decreases as the internuclear separation decreases and vanishes at a particular value of the internuclear separation except for the ground state. At the united atom limit, the ground-state electronic energy for the antiproton–He system approaches that of H^- ion and remains bound. This feature was originally pointed out by Fermi and Teller for antiproton–H system, and is termed as the Fermi–Teller effect. These characteristics of adiabatic potentials for the antiproton–He system is the manifestation that only the ground electronic state of H^- ion forms a stable bound state, while all other excited states are just finite-lived resonance states. All electronic energies for the proton–He system, by contrast, are bound at any internuclear separation and go to those of Li atom at the united atom limit. The Fermi–Teller effect may significantly contribute to dynamical aspects of these collision systems. Single and double ionization by proton and antiproton impacts have been studied theoretically and experimentally in the low-keV region.

As shown in Fig. 12, the ratio of double to single ionization for antiproton impact continues to increase as the collision energy decreases down to a few keV, while that for proton impact falls rather sharply below 30–40 keV. A more detailed investigation for each collision parameter suggests that (i) antiproton impact is found to produce larger ionization probability than that for proton in distant collisions, i.e., the Fermi–Teller mechanism; (ii) antiproton impact is also found to produce larger ionization probability than that for proton impact at close collisions, again, the consequence of the Fermi–Teller mechanism; (iii) the flux that goes to charge transfer in proton

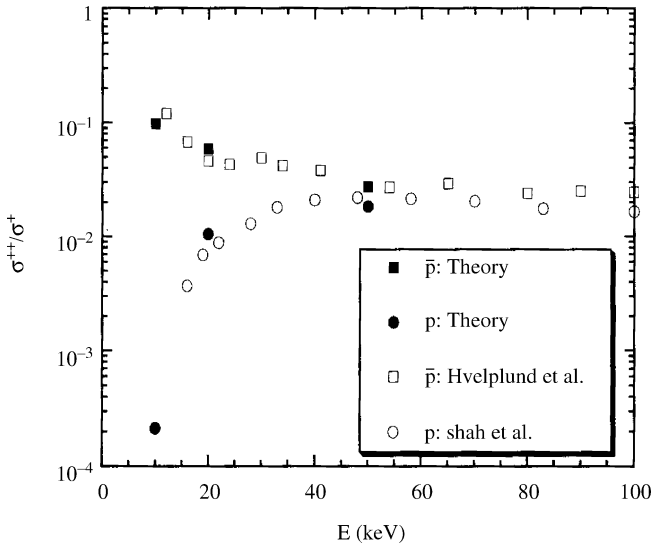

Fig. 12. Comparison of the proton and antiproton ionization cross-sections for He.

impact is found to end up in ionization for the antiproton impact; and (iv) others including more effective electron–electron interaction for double ionization for the antiproton impact.

For proton impact, after one electron is removed, the second electron moves in the field created by two bare nuclei. This situation leads to a drastic decrease of the double-ionization compared to the single-ionization with decreasing energy and hence, the ratio for the proton decreases. For antiproton impact, as the energy decreases, the increase of the effective interaction time of electron–electron coupling leads to an increase of double ionization and hence, the ratio increases. These observations provide a rationale for the larger ratio for antiproton impact than that for proton impact.

3.5.2. Molecular case

For molecular targets, on top of those interests described above for atomic cases, there are interesting questions regarding how nuclear motions are affected by an approaching proton or antiproton, and as its extreme, how dissociation may occur. Therefore, precise knowledge of the coupling between electronic and nuclear motions, dissociation dynamics and resulting fragmented species by comparing proton and antiproton impacts will aid in the essential and systematic understanding of the underlying physics at much deeper sense.

Vibrational excitation has been examined in collisions of proton and antiproton with CO molecules above a few tens of eV. At the impact energy

of 20 eV, the vibrational excitation to CO ($v_f = 1$). from the vibrational ground state CO ($v_i = 0$) by antiproton impact reaches close to 10^{-13} cm^2 and is larger by nearly two orders of magnitude than that of proton impact. The vibrational excitation cross-section for antiproton slowly decreases with the increasing v_f value, while that for proton decreases much faster. Thus, the difference becomes wider as the v_f increases with the difference being of three orders of magnitude at $v_f = 10$. This is because an antiproton can penetrate much more deeply than its proton counterpart, in which nuclear repulsion prohibits coming closer to nuclei of the molecule, hence causing vigorous perturbation to the nuclear motion and resulting in the larger and different energy-dependent vibrational excitation cross-sections. On the other hand, rotational excitation is driven by a torque from the incoming particle to the molecule, thus causing similar consequences for proton and antiproton impacts. In reality, however, rotational excitation always associates with vibrational excitation simultaneously. This yields the different distribution of rotational excitation when compared with the more idealistic pure rotational excitation only.

3.6. Dissociation and fragmentation

We provide some results and insight into the fragmentation process when a methane target or its positive ion undergoes subsequent relaxation and dissociation after electron capture or target excitation. In the low-keV proton impact [46], single-electron capture is the dominant process, and ionization and double-electron capture processes are considered to be of negligible importance. As the present result shows, the CH_4^+ ion produced is mostly in its ground electronic state, which is a degenerate Jahn–Teller state that forms a stable molecular ion of a distorted geometry. The $[CH_4 + H^+]$ asymptote lies below that of $[H + CH_4^+]$. Relaxation of the CH_4 geometry reverses this situation, and the H atom asymptote lies 0.6 eV below that of H^+ at equilibrium. Because in the energy region considered, the collision time is about 10^{-15} s, whereas more than 10^{-13} s would be required for a vibrational period; such nuclear relaxation processes do not have sufficient time to occur. The combination of lowest energy fragments involving two hydrogen atoms and/or ions is found to be $[CH_3^+ + H + H]$, with an energy that is 1.2 eV above that of the $[CH_4^+ + H]$ limit. In other words, the dissociation energy of CH_4^+ is significantly smaller (1.2 eV) than that of neutral methane (4.4 eV). Thermodynamically, the distinction arises because the ionization potential of methane (12.99 eV) is 3.2 eV larger than that for CH_3 (9.843 eV).

The next most stable set of fragments is $[CH_3^+ + H + H^+]$, whose energy is 5.0 eV above the lowest $[CH_4^+ + H]$ limit. This limit can be reached from the second most stable set of fragments, $[CH_4 + H^+]$, by removal of an H atom from the methane system. The dominant breakup pathway for the CH_4^+

ion is known to be $CH_4^+ \rightarrow CH_3^+ + H$, leading to a CH_3^+ ion and a neutral H atom. This CH_3^+ ion is unstable and likely to break into smaller fragments through predissociation. If the CH_4^+ ion produced is in one of electronic excited states with a rovibrationally excited level, then a large number of breakup pathways become available for producing a variety of fragments of neutral and ionic species like $[CH_3 + H^+]$ and $[CH_2^+ + H^+ + H]$, which are rovibrationally excited, thus often unstable, and may undergo a further breakup. In high-density-gaseous or condensed media, these species can also be involved in a series of chemical chain reactions.

For the low-keV antiproton impact, there is no charge transfer channel. Instead, all charge transfer channels correspond to ionization, and there are also target excitation channels. The excitation cross-section below 10 keV gives a slowly increasing trend with a maximum value of 6×10^{-17} cm^2 at 5 keV, but this value is larger by a factor of 3–4 than that of proton impact. The small-scale calculation for ionization gives a tentative result with a value of 1×10^{-16} cm^2 at 5 keV that appears to nicely tie in the experimental data by the Aarhus group, which show a magnitude of 2.5×10^{-16} cm^2 at 35 keV. Hence, for antiproton impact, the dissociation of CH_4^+ ions may be dominant, followed by fragmentation from excited CH_4^* species. Once a collision is over, the mechanism of fragmentation from these species should be the same as that of proton case. However, the distribution of excited states and their yields are expected to be significantly different from those of proton impact, leading to a difference in fragmented production yields. Although the present result discussed is still too rough to lead to any conclusive remarks, it is nevertheless interesting to carry out a comparative study on molecular fragmentation between proton and antiproton so that a new research area of physical chemistry and application may become possible.

4. CONCLUSION

The building blocks for the theoretical description of dynamics in collisions of bare nuclei with molecules reviewed in this chapter are the multireference single- and double-excitation CI method and the electronic-state close-coupling method. Both methods in a unified framework have been successfully applied to the variety of molecular targets: CH_4, C_2H_2, C_2H_4, H_2, D_2, H_2O, CO, and others. The importance of the steric effect, isotope effect, and vibrational effects of the target molecule was discussed here. Better understanding of the phenomena that occur in proton/antiproton collisions with molecular matter brings an important impact on the fields of radiation medicine, microbeam lithography or growth of nanostructures.

In general terms, by studying the proton–molecule systems in the *ab initio* framework, we explore the mechanisms that couple intramolecular transfer of light electrons with the transport of heavy ions. Such mechanisms are

important in biochemistry, for instance, in the studies of cytochrome c oxidase enzyme which functions as an electron-current driven proton pump. Protonation, electron transfer, or the tight coupling between proton motion and electron transfer rank among the most frequent terms in this area. In this context, the interactions of protons with aminoacids or protein assemblies are also very important. As another example, let us note that multi-dimensional charge transfer in dissipative environment appears to be an important mechanism for conformation changes of DNA base pairs.

In the high-energy range, on the other hand, a complete description of proton–molecule collision encounters is necessary to improve the instrumentation for hadron therapy of brain cancer. As a first step, trajectory deflection angles and real-dose distributions are needed for proton–H_2O collisions in the liquid phase. Since water accounts only for about 70% of the tissue matter, the cross-sections for high-energy proton collisions with other common biological molecules are also of interest. This account is inevitably incomplete and new research areas and further developments are expected to emerge in near future.

REFERENCES

[1] D. R. Hartree, *Proc. Cambridge Phil. Soc.*, 1928, **24**, 89, see also p. 111 and 426.
[2] J. C. Slater, *Phys. Rev.*, 1930, **35**, 210.
[3] V. Fock, *Z. Physik*, 1930, **61**, 126; V. Fock, *Z. Physik*, 1930, **62**, 795.
[4] C. C. J. Roothaan, *Rev. Mod. Phys.*, 1951, **23**, 69.
[5] F. Hund, *Z. Physik*, 1928, **51**, 759; F. Hund, *Z. Physik*, 1931, **73**, 1.
[6] R. S. Mulliken, *Rev. Mod. Phys.*, 1932, **4**, 1.
[7] E. A. Hylleraas, *Z. Physik*, 1928, **48**, 469.
[8] M. Kotani, Y. Mizuno, K. Kayama and E. Ishiguro, *J. Phys. Soc. Jpn*, 1957, **12**, 707; M. Kotani, Y. Mizuno, K. Kayama and E. Ishiguro, *Rev. Mod. Phys.*, 1960, **32**, 266.
[9] S. F. Boys, G. B. Cook, C. M. Reeves and I. Shavitt, *Nature*, 1956, **178**, 1207.
[10] W. Kohn and L. J. Sham, *Phys. Rev.*, 1965, **140**, A1133.
[11] R. G. Parr and W. Yang, *Density Functional Theory of Atoms and Molecules*, Oxford University Press, Oxford, 1989.
[12] R. J. Buenker and S. D. Peyerimhoff, *Theor. Chim. Acta*, 1974, **35**, 33.
[13] R. J. Buenker and S. D. Peyerimhoff, *Theor. Chim. Acta*, 1975, **39**, 217.
[14] G. Hirsch, P. J. Bruna, R. J. Buenker and S. D. Peyerimhoff, *Chem. Phys.*, 1980, **45**, 335.
[15] R. J. Buenker, G. Hirsch, S. D. Peyerimhoff, P. J. Bruna, J. Roemelt, M. Bettendorff and C. Petrongolo, in *Studies in Physical and Theoretical Chemistry* (ed. R. Carbo), Current Aspects of Quantum Chemistry 1981, Elsevier, Amsterdam, 1982, Vol. 21, p. 81.
[16] T. G. Heil, S. E. Butler and A. Dalgarno, *Phys. Rev. A.*, 1981, **23**, 1100.
[17] L. R. Kahn, P. Baybutt and D. G. Truhlar, *J. Chem. Phys.*, 1976, **65**, 3826.
[18] Y. S. Lee, W. C. Ermler and K. S. Pitzer, *J. Chem. Phys.*, 1977, **67**, 5861.
[19] R. J. Buenkerin, in *Proceedings of Workshop on Quantum Chemistry and Molecular Physics in Wollongong, Australia* (ed. P. Burton), Studies in Physical and Theoretical Chemistry, Vol. 21: Current Aspects of Quantum Chemistry 1981, University Press, Wollongong, 1982, p. 17; R. J. Buenker and R. A. Philips, *J. Mol. Struct. (THEOCHEM)*, 1985, **123**, pp. 291.

[20] S. Krebs and R. J. Buenker, *J. Chem. Phys.*, 1995, **103**, 5613.
[21] R. J. Buenker and S. Krebs, The configuration-driven approach for multireference configuration interaction calculations. in *Recent Advances in Multireference Methods* (ed. K. Hirao), World Scientific, Singapore, 1999, p. 1.
[22] A. B. Alekseyev, H.-P. Liebermann and R. J. Buenker, Spin–orbit multireference configuration interaction method and applications to systems containing heavy atoms. in *Relativistic Molecular Calculations* (eds K. Hirao and M. Ishikawa), World Scientific, Singapore, 2004, in press.
[23] R. J. Buenker, A. B. Alekseyev, H.-P. Liebermann, R. Lingott and G. Hirsch, *J. Chem. Phys.*, 1998, **108**, 3400.
[24] M. Kimura and N. F. Lane, *Adv. At. Mol. Opt. Phys.*, 1989, **26**, 79.
[25] V. Sidis, *Adv. At. Mol. Phys.*, 1989, **26**, 161.
[26] S. N. Rai, H.-P. Liebermann, R. J. Buenker and M. Kimura, *Int. J. Quantum Chem.*, 2003, **95**, 866.
[27] N. Aristov, W. Maring, G. Niedner-Schatteburg, J. P. Toennies, Y.-N. Chiu and H. Kuppel, *J. Chem. Phys.*, 1993, **99**, 2682.
[28] R. J. Buenker, Y. Li, G. Hirsch and M. Kimura, *J. Phys. Chem. A*, 1998, **102**, 7127.
[29] M. Kimura, Y. Li, G. Hirsch and R. J. Buenker, *Phys. Rev. A*, 1995, **52**, 1196.
[30] M. Kimura, Y. Li, G. Hirsch and R. J. Buenker, *Phys. Rev. A*, 1996, **54**, 5019.
[31] T. Kusakabe, M. Kimura, L. Pichl, R. J. Buenker and H. Tawara, *Phys. Rev. A*, 2003, **68**, 050701.
[32] T. Kusakabe, K. Asahina, J. P. Gu, G. Hirsch, R. J. Buenker, M. Kimura, H. Tawara and Y. Nakai, *Phys. Rev. A*, 2000, **62**, 062714.
[33] T. Kusakabe, S. Satoh, H. Tawara and M. Kimura, *Phys. Rev. Lett.*, 2001, **87**, 243201.
[34] T. Kusakabe, K. Asahina, A. Iida, Y. Tanaka, Y. Li, G. Hirsch, R. J. Buenker, M. Kimura, H. Tawara and Y. Nakai, *Phys. Rev. A*, 2000, **62**, 062715.
[35] A. Ichihara, O. Iwamoto and R. K. Janev, *J. Phys. B: At. Mol. Opt. Phys.*, 2000, **33**, 4747.
[36] W. H. Cramer and A. B. Marcus, *J. Chem. Phys.*, 1960, **32**, 186.
[37] W. H. Cramer, *J. Chem. Phys.*, 1961, **35**, 836.
[38] L. Pichl, Y. Li, H.-P. Liebermann, R. J. Buenker and M. Kimura, *J. Chem. Phys.*, 2003, **118**, 4872.
[39] T. Kusakabe, K. Hosomi, H. Nakanishi, H. Tawara, M. Sasao, Y. Nakai and M. Kimura, *Phys. Rev. A*, 2000, **62**, 062715.
[40] M. Kimura, J. P. Gu, G. Hirsch, R. J. Buenker and P. C. Stancil, *Phys. Rev. A*, 2000, **61**, 0327081.
[41] R. Browning and H. B. Gilbody, *J. Phys. B*, 1968, **1**, 1149.
[42] M. E. Rudd, R. D. DuBois, L. H. Toburen, C. A. Ratcliffe and T. V. Goffe, *Phys. Rev. A*, 1983, **28**, 3244.
[43] M. B. Shah and H. B. Gilbody, *J. Phys. B*, 1990, **23**, 1491.
[44] R. S. Gao, L. K. Johnson, C. L. Hakes, K. A. Smith and R. F. Stebbings, *Phys. Rev. A*, 1990, **41**, 5929.
[45] T. W. Imai, M. Kimura, J. P. Gu, G. Hirsh, R. J. Buenker, J. G. Wang, P. C. Stancil and L. Pichl, *Phys. Rev. A*, 2003, **68**, 01276.
[46] T. Kusakabe, K. Asahina, A. Iida, Y. Tanaka, Y. Li, G. Hirsch, R. J. Buenker, M. Kimura, H. Tawara and Y. Nakai, *Phys. Rev. A*, 2000, **62**, 062715.

This Page Intentionally Left Blank

Advances in the Core-and-Bond Formalism for Proton Stopping in Molecular Targets

Salvador A. Cruz[1] and Jacques Soullard[2]

[1] *Departamento de Física, Universidad Autónoma Metropolitana-Iztapalapa, Apartado Postal 55 534, 09340 México, D.F., Mexico*
[2] *Instituto de Física, Universidad Nacional Autónoma de México, Apartado Postal 20 364, 01000 México, D.F., Mexico*

Abstract

An account is presented of the main efforts leading to the development of the Core-and-Bond (CAB) treatment of chemical binding and phase state effects in the stopping of ions in molecular target materials. The relevance of molecular structure and properties in the stopping process is highlighted through revision of theoretical schemes developed to distinguish between the different contributions from inner-shell (core) and valence molecular orbitals. New results are presented for a CAB model of molecular confinement advanced to study the stopping of protons in dense matter.

Contents

1. INTRODUCTION

The quantum many-body character of ion penetration phenomena in matter constitutes the main difficulty in developing a theory that fully accounts for the mechanisms through which an ion loses energy while traversing a given

ADVANCES IN QUANTUM CHEMISTRY, VOLUME 46
ISSN: 0065-3276 DOI 10.1016/S0065-3276(04)46008-0

target material. However, a perceptive physical insight into the dominating processes taking place, in a binary collision, as the projectile slows down made the Bethe theory the first successful application of quantum mechanics to the problem [1–3]. Since its development, the Bethe theory of stopping has constituted a cornerstone in the study of swift-ion penetration and has given confidence in the adequacy of physically well-founded approximations to deal with such a complex problem. On the other hand, the pioneering work of Bohr [4–6] and Lindhard [7–9] on the role of the collective response of the target medium has been seminal for the development of modern approaches to account for non-local effects in ion–solid interactions [10–13]. The basis of these successful theories for understanding the energy loss process rests on the paramount role played by experiment, which has unequivocally guided the necessary refinements and the development of suitable models. In this connection, the outcome of more accurate experimental techniques to measure stopping power cross-sections in compound target materials has revealed important deviations from Bragg's additivity rule [14–21]. Indeed, during the last two decades, target density effects on the electronic stopping cross-section (S_e) of ions have been confirmed by experimentally observed differences in S_e of light projectiles traversing the same target material but in a different physical phase state. It has also been experimentally established that the target molecular composition has an important influence on S_e and the effect has been attributed to chemical binding. These so-called chemical binding and physical phase state effects have imposed necessary refinements on the theory, whereby the state of aggregation of matter and chemical structure and composition have to be accounted for. An account of the present knowledge of chemical and physical phase effects is given by Bauer and Semrad in this volume; hence in the foregoing we shall concentrate on the partition scheme of cores-and-bonds (CAB) and its implementation for the study of chemical- and physical state effects.

In this work, a review of the main ideas leading to the CAB formalism, its theoretical foundation as well as its further development is presented. This approach has been of particular relevance to the understanding of chemical binding effects on the molecular contribution to ion stopping and has deep roots from experimental origin. It is noteworthy that the pioneering work by the Köln [19] and Baylor [20] groups on systematization of, respectively, Li and He ion stopping measurements in organic targets in the gas (Baylor) and liquid (Köln) phase led to important ideas on the partial contribution of specific functional groups as well as spatial molecule limitation effects in the condensed phase [68]. These ideas were geminal for the empirical partition rule of CAB later proposed by Ziegler and Manoyan [30] to account for the stopping contribution from the different molecule constituents. In this connection, the theoretical footing for the CAB approach was first stated by Sabin and Oddershede [23–28], whereby the molecular electronic excitation

energy is cast in terms of the molecular orbital contributions. In this development, the Local Plasma Approximation (LPA) [7–9] has constituted a fundamental piece in a simplified, yet powerful, development of this formalism to represent the mean molecular excitation energy in terms of orbital contributions. With regard to the physical phase state effects on stopping, the Köln idea of spatial confinement was also explored by Xu *et al.* [69] using a renormalized electronic density of a water molecule caged inside a spherical box to explain observed changes in proton stopping in the condensed phase as compared to the gas phase. In this paper, an account of the abovementioned developments will be discussed. Surprisingly, besides these pioneering studies based on the CAB formalism, the theoretical efforts to further explore its capabilities are scarce and have been mainly limited to the work reported by the present authors. Our work in this direction is also revisited and recent preliminary results are presented for the first time.

The paper is organized as follows. In Section 2, an appraisal of the CAB formalism is given. Section 3 deals with some fundamental ideas and implementations of the LPA to the CAB scheme. In Section 4, the main contributions from the present authors are presented, together with the recent results. Finally, in Section 5 conclusions regarding the assessment of the CAB formalism are given.

2. THE CORES-AND-BOND FORMALISM

The origin of the CAB approach lies in a series of systematic experimental stopping power measurements in organic compounds carried out independently by the Köln [19] and Baylor [20] groups. While the former group analyzed the stopping of (14–114 keV/amu) Li^+ projectiles in solid and liquid organic compounds, the latter group measured stopping powers of He^+ (100–500 keV/amu) in gaseous organic compounds. In both cases, significant deviations from Bragg's additivity rule were observed and the influence of bonds on the stopping cross-section (Baylor and Köln) as well as that due to the state of aggregation (Köln) were clearly demonstrated. A major breakthrough to rationalize the role of the molecular constituents in the evaluation of the stopping power was given by both groups after comparing the relative contributions from specific functional entities within different hydrocarbons. Accordingly, a decomposition of the molecular stopping cross-section was proposed as [22]

$$S_e(\text{molecule}) = \sum_i S_i(\text{group}), \tag{1}$$

where S_i(group) is the contribution to S_e(molecule) from a characteristic functional group. Although this partitioning rule had practical advantages in

constructing the stopping cross-section for other molecules, it could only be defined for symmetric bonding partners between two different groups. In the same seminal paper where the above analysis was presented, the Köln group recognized the different contributions from CAB electrons to the total electronic stopping power by assuming the independent role of electrons from core and valence orbitals. Thus, for a molecule with M types of different bonds and N types of atoms the molecular electronic stopping cross-section becomes [22]

$$S_{\mathrm{e}}(\text{molecule}) = \sum_{i=1}^{M} m_i \sigma_i + \sum_{j=1}^{N} n_j \rho_j, \tag{2}$$

where ρ_i and σ_i are the contributions from CAB electrons, respectively; m_i is the number of times a bond of type i occurs and n_j the number of times an atom (core) j is present. Equations (1) and (2) were originally labeled by the Köln group as the *independent groups* and *independent bonds* approximations, respectively.

The first fundamental theoretical study to account for the role of different bond types according to equation (2) was given by Oddershede and Sabin [23–28], who successfully applied Sigmund's kinetic theory (KT) of stopping [29] to evaluate the CAB contribution to S_{e} for proton stopping in small organic molecules in the gas phase. A key characteristic of Sigmund's KT of stopping is that it is based on the binary encounter approximation whereby the energy loss problem is treated through individual scattering events between projectile and target electrons. Furthermore, the KT accounts for the velocity distribution of scatterers in the target material (electrons), which is an important aspect to consider. Within the shellwise implementation of the KT for atoms by Sabin and Oddershede [28], the stopping cross-section is expressed as

$$S_{\mathrm{e}}(v) = \sum_{\mathrm{k}}^{\text{shells}} S_{\mathrm{k}}(v), \tag{3}$$

with $S_{\mathrm{k}}(v)$ the shell contribution to $S_{\mathrm{e}}(v)$ for a projectile moving with velocity v, i.e.,

$$S_{\mathrm{k}}(v) = \frac{4\pi^2 e^4 Z_1^2 Z_2}{m v^2} \int_0^{\infty} \rho_{\mathrm{k}}(v_2) v_2 \, \mathrm{d}v_2 \int_{|v-v_2|}^{v+v_2} \frac{\omega_{\mathrm{k}}}{Z_2} \ln\left(\frac{2mv'^2}{I_{\mathrm{k}}}\right) \left[1 + \frac{v^2}{v'^2} - \frac{v_2^2}{v'^2}\right] \mathrm{d}v', \tag{4}$$

where Z_1 and Z_2 are the projectile and target atomic numbers, respectively, and $\rho_k(v_2)$ is the target electron velocity distribution in orbital k such that:

$$4\pi \int_0^\infty \rho_k(v_2) v_2^2 \, dv_2 = 1. \tag{5}$$

In this case (atomic systems), the orbital mean excitation energies I_k given in equation (4) were defined by requiring that the total mean excitation energy could be written as

$$\ln I = \frac{1}{Z_2} \sum_k \omega_k \ln I_k, \tag{6}$$

with ω_k the orbital weights $\omega_k = (n_k + n_k f_k)/2$ given in terms of the orbital occupation numbers n_k and total oscillator strengths $n_k f_k$ of all optical transitions from level k into the unoccupied states (both discrete and in the continuum) [23].

Following a parallel reasoning as with atoms, the total molecular mean ionization energy was split up into the corresponding CAB mean excitation energies as [27]

$$\ln I_{\text{molecule}} = \frac{1}{N} \left[\sum_i^{\text{cores}} \omega_i \ln I_i^{\text{core}} + \sum_j^{\text{bonds}} \omega_j \ln I_j^{\text{bond}} \right], \tag{7}$$

where N is the total number of electrons and ω_k the corresponding orbital weight factors which satisfy the sum rule:

$$\sum_\lambda^{\text{cores+bonds}} \omega_\lambda = N. \tag{8}$$

According to this description, the total molecular stopping cross-section may be cast as

$$S_e^{\text{molecule}}(v) = \sum_i^{\text{cores}} S_i^{\text{core}}(v) + \sum_j^{\text{bonds}} S_j^{\text{bond}}(v), \tag{9}$$

which constitutes the formal theoretical confirmation of the expression proposed by the Köln group (equation (2)) after their experimental analysis.

According to Sabin and Oddershede [25], the mean excitation energy for bonds (I^{bond}) is obtained from equation (7) after calculating the atomic core mean excitation energy (I^{core}) and using available (either theoretical or experimental) accurate estimates for the total molecular mean excitation energy. On the other hand, the electron velocity distribution $\rho_k(v_2)$ required in equation (4) may be obtained from the use of isotropic Compton profiles (ICP) derived either from *ab initio* molecular calculations or experimentally

and with recourse to the known relation between the isotropic momentum distribution ($\rho(q)$) and the ICP ($J_0(q)$):

$$\rho(q) = -\frac{1}{2q}\frac{\mathrm{d}J_0}{\mathrm{d}q}. \tag{10}$$

Sabin and Oddershede applied their theory to calculate proton stopping cross-sections and mean excitation energies of the C–H, C–C, C=C, O–H, C–O, C=O and N–H bonds after using accurate estimates for I_{molecule} and $J_0(q)$ [26,27]. These values are displayed in Table 1. Excellent agreement was obtained with experimental measurement in various molecular targets for which bond ICP and I_{molecule} were available. Figure 1 shows the comparison between their theoretical predictions and experiment for the velocity dependence of proton stopping cross-sections in CH_4 and N_2.

Soon after the advent of the formal theoretical footing by Sabin and Oddershede for the *independent bonds approximation* originally proposed by the Köln group, Ziegler and Manoyan [30] gave a further step in the derivation of a semi-empirical method to account for the stopping of ions in compounds based on the above ideas and using the extensive compilation of experimental results of the Baylor and Köln groups. The natural partition of the molecular stopping into contributions due to core and valence electrons was first labeled by Ziegler and Manoyan as the CAB approach.

The motivation and relevance of the contribution by Ziegler and Manoyan was to broaden the applicability of the CAB method to as many ion/compound combinations as possible so that the stopping of all ions in compound materials could be assessed through a single method. The well-documented results of the Baylor and Köln groups for He and Li stopping in

Table 1. Bond stopping cross-sections for protons calculated by Oddershede and Sabin using their accurate treatment of the kinetic theory of stopping

u (a.u.)	C–H	C–C	C=C	O–H	N–H	C–O	C=O	C	O	N
0.5	5.007	3.197	7.453	4.015	4.403	3.535	7.414	0.053	0.024	0.035
1.0	8.363	5.251	12.522	7.272	7.663	6.374	13.310	0.106	0.049	0.069
1.5	9.406	6.666	14.888	9.320	9.286	8.266	17.124	0.160	0.073	0.104
2.0	8.592	6.502	14.500	9.989	9.233	9.136	18.748	0.213	0.097	0.138
2.5	7.181	5.848	12.650	9.510	8.238	8.960	18.346	0.264	0.121	0.172
3.0	5.871	4.976	10.612	8.535	7.046	8.183	16.780	0.314	0.144	0.205
3.5	4.839	4.186	8.887	7.496	5.968	7.225	14.382	0.358	0.167	0.236
4.0	4.035	3.548	7.528	6.556	5.075	6.303	12.917	0.396	0.188	0.264
8.0	1.578	1.451	2.979	2.686	1.893	2.441	4.895	0.454	0.274	0.350
10.0	1.129	1.026	2.142	1.910	1.331	1.736	3.518	0.396	0.265	0.323

Units in 10^{-15} eV cm^2/bond. Reproduced from Ref. [27].

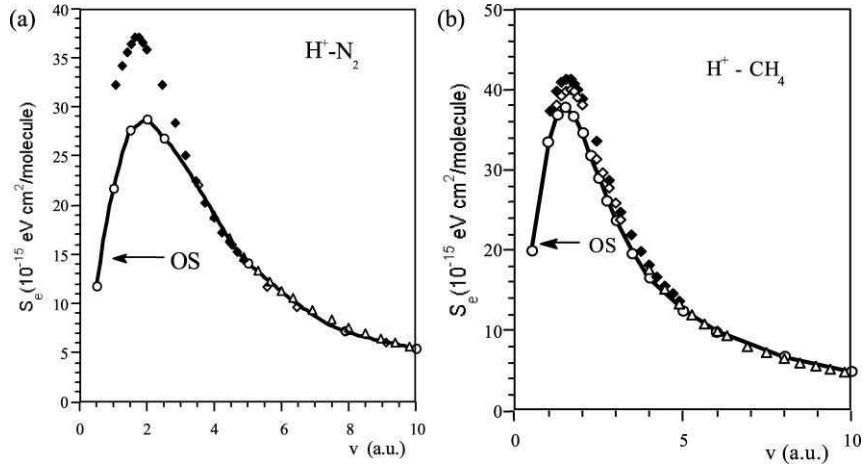

Fig. 1. Theoretical predictions by Sabin and Oddershede [26] (–○–) for the proton stopping cross-section in (a) N_2 and (b) CH_4. Experimental values: ◆ [88]; ◇ [89]; △ [92].

compounds constituted the main working source for the project, although perhaps also considering Thwaites' recommendation [17] that the experimental uncertainties in relative stopping measurements from one compound to another are strongly reduced when those measurements are carried up in the same laboratory. The first task addressed by Ziegler and Manoyan was to use effective charge theory to scale the heavy-ion stopping cross-section (S_{HI}) to that of protons (S_{p}) moving at the same velocity as

$$S_{\mathrm{HI}}(v) = S_{\mathrm{p}}(v)(\gamma Z_{\mathrm{HI}})^2, \tag{11}$$

where Z_{HI} is the ion nuclear charge, γ the fractional effective charge and assuming that the proton charge within the medium is $Z_{\mathrm{p}} = 1$. Moreover, the fractional effective charge is estimated through use of the Brandt–Kitagawa theory [31] adapted as [32]

$$\gamma = q + \frac{1}{2}(1-q)\left(\frac{v_0}{v_{\mathrm{F}}}\right)^2 \ln\left[1 + \left(2.084\frac{\Lambda}{a_0}\frac{v_{\mathrm{F}}}{v_0}\right)^2\right], \tag{12}$$

where q is the fractional charge state of the ion, v_0 the Bohr velocity ($v_0 = 2.1883 \times 10^6$ m/s), a_0 the Bohr radius ($a_0 = 0.5292 \times 10^{-10}$ m) and v_{F} the Fermi velocity of the medium, which was assumed as $v_{\mathrm{F}} = v_0$ in the case of hydrocarbons. Λ in equation (12) is the dynamical screening length

defined in the Brandt–Kitagawa theory in terms of the ion nuclear charge Z as

$$\Lambda = 0.686 a_0 \frac{(1-q)^{2/3} Z^{-1/3}}{1 - \frac{1}{7}(1-q)}. \tag{13}$$

In their analysis, Ziegler and Manoyan use their previously derived simple expansion to estimate the fractional charge state of an ion [32]

$$q = 1 - \exp[-(-0.803 y_r^{0.3} + 1.3167 y_r^{0.6} + 0.38157 y_r + 0.008983 y_r^2)], \tag{14}$$

with $y_r = Z^{-2/3} v_r / v_0$, v_r being the relative velocity of the ion's electrons to the Fermi velocity of the medium approximated in this case (for $v > v_0$) as $v_r \approx v(1 + 1/5 v_F^2/v^2)$, recalling that $v_F = v_0$ was assumed for hydrocarbons.

Using the effective charge formalism described above, these authors first scaled the He (125 keV/amu) and Li (25 keV/amu) stopping cross-sections into an equivalent data set for proton (125 keV) stopping cross-sections. Hence, using equation (11) together with the definitions in equations (12)–(14), these authors could scale to a proton stopping database the experimentally measured S_e(molecule) (left-hand side in equation (2)) for about 114 compounds and generate a set of simultaneous algebraic equations – each one of the type given by equation (2) – where the quantities to be determined were the *proton-stopping equivalent* bonds σ_i and cores ρ_i contributions. This procedure allowed to estimate the stopping of any ion in a compound through the effective charge scaling relation:

$$S_e^{HI}(\text{molecule}) = (\gamma Z_{HI})^2 \left[\sum_i^{\text{cores}} S_i^{\text{core}} + \sum_j^{\text{bonds}} S_j^{\text{bond}} \right]_p. \tag{15}$$

Although Ziegler and Manoyan applied equation (15) only to ions with a fixed energy (125 keV/amu) corresponding to the region where the proton stopping cross-section approximately yields its maximum for hydrocarbon targets (and, hence, where the greatest deviations from Bragg's rule are expected), the task of calculating any energy dependence on the term in square brackets in equation (15) and obtaining the corresponding heavy ion stopping was not pursued. Alternatively, they proposed an empirical rule to account for the energy dependence of heavy ion stopping in compounds [31,32], which is more phenomenological than justifiable on physical grounds; hence, we shall not discuss it here. It suffices to say that their method as applied to the Baylor and Köln data yielded highly accurate molecular stopping cross-sections for He (125 keV/amu) and Li (25 keV/amu) incident on a wide set of compounds after obtaining the associated CAB stopping values for protons (125 keV) reproduced in Table 2. Since its development, the CAB method of Ziegler and Manoyan for heavy ions at different energies was implemented in the well-known TRIM [32,33] and SRIM [34] computer algorithms widely used for simulations of ion penetration in matter.

Table 2. Core and bond stopping values obtained by Ziegler and Manoyan [30] for protons at 125 keV

H	C	N	O	F	S	Cl		
0.0	6.145	5.859	5.446	5.431	32.735	28.795		
H–H	H–C	H–N	H–O	C–C	C=C	C≡C	C–N	
9.590	7.224	8.244	8.758	3.938	9.790	15.022	5.080	
C–O	C=O	C–F	C–Cl	N≡N	N–O	O=O	S–H	S–C
6.168	13.926	10.998	3.713	20.380	15.796	21.290	4.844	1.617

Units in 10^{-15} eV cm^2/bond.

3. MEAN EXCITATION ENERGY AND THE LPA

In dealing with the inelastic energy loss process between a bare charged projectile and a target atom or molecule, the energy transfer to the internal degrees of freedom of the target material must be accounted for through an excitation function. For a swift bare ion of charge Z_1 and velocity v greater than that of any of the Z_2 electrons composing a target scatterer (atom or molecule), Bethe has shown that the corresponding stopping cross-section becomes [1–3]

$$S_e(v) = \frac{4\pi Z_1^2 Z_2 e^4}{mv^2} \ln\left(\frac{2mv^2}{I_0}\right), \tag{16}$$

where I_0 is the logarithmic mean excitation energy defined as

$$Z_2 \ln I_0 = \sum_n f_{n0} \ln(E_n - E_0), \tag{17}$$

and f_{n0} is the dipole oscillator strength (DOS) for the transition from the ground state energy E_0 to a state of energy E_n, the sum involving all discrete and continuum states. Clearly, a fundamental quantity to account for the inelastic energy loss is the target mean excitation energy for stopping, I_0, which in general is given in terms of the DOS sums S_0 and L_0 as [35–38]

$$I_0 = (e^2/a_0)\exp[S_0/L_0], \tag{18}$$

where

$$S_0 = \int (df/dE) \ln E \, dE, \tag{19}$$

$$L_0 = \int (df/dE) dE, \tag{20}$$

with df/dE the differential DOS corresponding to the atomic (molecular) target excitation energy E (in units of $e^2/a_0 = 27.2$ eV $= 1$ hartree) and the integration is understood as including all excitations with energy E and oscillator strength f. The formal evaluation of I_0 for atoms and molecules through equations (18)–(20) has proven to yield accurate predictions as compared to experiment. However, the actual theoretical computation of reliable dipole oscillator strength distributions (DOSD) – (df/dE) *vs.* E – requires a difficult and complicated process involving well-defined *ab initio* methods to construct accurate atomic and molecular wavefunctions from which the DOSD may be evaluated. Although a number of *ab initio* DOSD calculations are available for atomic systems [15,39], for molecules the frequency of this type of calculation is scarce and mainly for small systems [40, 41]. Hence, most of the I_0 values for elemental and compound target materials have been extracted experimentally from accurate fittings to a Bethe–Bloch–Born–Barkas equation including shell corrections [42,43] or from photo-absorption spectra and fast-electron inelastic scattering cross-sections from which the DOSD are constructed [35,44].

The LPA, first proposed by Lindhard and Scharff [7–9], constitutes a useful alternative means to evaluate the mean ionization energy. Within this approximation, the dynamical response of an atom in the stopping medium is characterized by the plasma oscillation of the electronic cloud, viewing the atom as an inhomogeneous electron gas with a local plasma frequency $\omega_p(\mathbf{r})$ given as

$$\omega_p(\mathbf{r}) = [4\pi e^2 \rho(\mathbf{r})/m]^{1/2}, \tag{21}$$

with $\rho(\mathbf{r})$ the local electron density, which is treated as locally uniform so that absorption spectra result from independent absorption frequencies given by equation (21) from each atomic volume element. Using dielectric response theory, the mean excitation energy, I_0, for an atom with Z electrons was cast in the form

$$Z \ln I_0 = \int \rho(\mathbf{r}) \ln[\gamma \hbar \omega_p(\mathbf{r})] d^3\mathbf{r}, \tag{22}$$

with $\omega_p(\mathbf{r})$ given by equation (21) and where γ is an empirical parameter introduced to account for differences in single-particle excitations between light atoms ($\gamma = 1$), where polarization effects are not so important, and heavier atoms ($\gamma = \sqrt{2}$).

Since its development, the LPA has proved to have reasonable success in estimates of the mean ionization energy of atoms and molecules [40,45–48]. However, according to Johnson and Inokuti [49] a major drawback of the LPA seems to be its failure to describe the shell structure of the oscillator strength spectra and the apparent inability to derive it from the spectral distribution of oscillator strengths. In spite of this, according to these authors,

the LPA "seems to allow one to calculate I_0 with some confidence" provided accurate wavefunctions are used. Indeed, it has been shown that the use of accurate atomic wavefunctions with $\gamma = \sqrt{2}$ in equation (20) yields reasonable estimates for I_0 as compared to the oscillator strength approach for low-Z atoms [40,46,50] and other suggested values for the parameter γ have been proposed after using different electronic wavefunctions for atoms of various elements [40,45,47]. With regard to the empirical character of the parameter γ, using a shellwise decomposition of the dielectric response function, Tung *et al*. [47] have discussed the origin of γ in terms of a plasma-damping effect neglected in the original derivation of the LPA, although concluding that it is more practical to consider it as a parameter. More recently, an interesting link between the LPA and the Shannon information entropy has been reported [51].

One of the major advantages of the LPA in the context of stopping theory is its representation in terms of the electronic distribution alone. This characteristic makes the LPA very attractive for a density-functional theory (DFT) treatment of mean excitation energies as shown by Meltzer *et al.* [48] in their study of atomic orbital mean excitation energies through the shellwise decomposition of the LPA, labeled by these authors as the Orbital Local Plasma Approximation (OLPA). Incidentally, the LPA orbital decomposition had also been previously suggested by Tung *et al*. [47] in their analysis of the plasma damping effect, although apparently the former authors were not aware of that work.

The OLPA proposed by Meltzer, Sabin and Trickey (MST) follows a parallel definition of total atomic mean ionization, I, to that given by equation (6) where the weight factors $\{\omega_k\}$ are substituted by the orbital occupation numbers $\{n_k\}$ and the mean orbital excitation energies I_k are defined as

$$\ln I_k = \frac{1}{n_k} \int \rho_k(\mathbf{r}) \ln \left[\hbar \gamma_k \left(\frac{4\pi e^2 \rho_k(\mathbf{r})}{m} \right)^{1/2} \right] \mathrm{d}^3\mathbf{r}, \tag{23}$$

where $\rho_k(\mathbf{r})$ is the local electronic density of orbital k and γ_k the corresponding scaling parameter as proposed in the Lindhard–Scharff LPA theory. This parameter, which was related to a subshell plasma damping coefficient by Tung *et al*. [47], is seldom available and hence remains treated as an empirical quantity. Since no specific criterion exists to assign a value to γ_k for each orbital, its value was chosen as unity by MST in order to avoid dependence of the theoretical predictions upon an *ad hoc* parameter. According to these authors, the OLPA scheme provides, in general, a good agreement with experimental stopping curves and with calculations by Oddershede and Sabin [52] using equations (3)–(6). Even though some discrepancies in orbital mean ionization energies appear when compared

to oscillator-strength based ones [48], the conclusion is that the OLPA is a useful method to calculate stopping cross-sections in systems where more formal methods are difficult to implement.

In a more recent analysis on density decomposition options in the OLPA, Meltzer *et al.* [53] have refined their original OLPA treatment making a physically more consistent consideration of the plasma frequency as determined by the total electron density at the point of consideration. Accordingly, instead of equation (23), the recommended expression for the OLPA treatment of I_k is

$$\ln I_k = \frac{1}{n_k} \int \rho_k(\mathbf{r}) \ln \left[\hbar \gamma_k \left(\frac{4\pi e^2 \rho(r)}{m} \right)^{1/2} \right] d^3\mathbf{r}, \tag{24}$$

where $\rho(r)$ is the local total electron density obtained after taking the angular average of each orbital charge density.

The OLPA scheme provides a natural footing for the calculation of molecular orbital mean excitation energies in the CAB approach. This can be done by combining equations (7) and (24) where the I_k now correspond to the CAB contributions to the molecular mean ionization energy. A decade ago, Sabin and Oddershede [54] pointed out the need to perform more systematic theoretical work on the stopping power of molecules both for protons and heavier ion projectiles in order to gain a better understanding of chemical binding effects and phase effects. The work carried out since then by the present authors seems to be the only one pursued to account for chemical binding effects and phase effects using the CAB within the OLPA. In the following sections we give an account of our efforts in this direction.

4. ADVANCES IN CAB STUDIES OF MOLECULAR STOPPING

4.1. The floating spherical Gaussian orbital model

The Floating Spherical Gaussian orbital (FSGO) model was first introduced by Frost [55] in the *ab initio* study of the electronic and geometric structure of ground state closed-shell molecules using localized orbitals. Within this model, each localized orbital, associated to an electron pair of opposite spin is represented by a normalized spherical Gaussian function

$$\Psi_i(\mathbf{r}) = \left(\frac{2\alpha_i}{\pi} \right)^{3/4} \exp[-\alpha_i(\mathbf{r} - \mathbf{R}_i)^2], \tag{25}$$

where α_i is the square of the inverse of the orbital radius σ_i and $\mathbf{R}_i$ is the position vector of the orbital center. The FSGO are classified as inner-shell (core), bond and lone-pair orbitals; hence, this orbital representation is quite

adequate for the CAB study of chemical binding effects on the electronic stopping cross-section. In Frost's model, the total wavefunction is taken as a single Slater determinant of non-orthogonal orbitals and the electronic energy of the molecule is cast as

$$E_{\mathrm{el}} = 2\sum_{j,k}\langle j|k\rangle T_{jk} + \sum_{k,l,p,q}\langle kl|pq\rangle[2T_{kl}T_{pq} - T_{kq}T_{lp}], \tag{26}$$

where $\mathbf{T} = \mathbf{S}^{-1}$ is the inverse overlap matrix and where

$$\langle j|k\rangle = \int \Psi_j h \Psi_{\mathrm{k}}\, \mathrm{d}\tau, \tag{27}$$

and

$$\langle kl|pq\rangle = \int \Psi_{\mathrm{k}}(1)\Psi_l^*(1) r_{12}^{-1} \Psi_{\mathrm{p}}^*(2)\Psi_q(2)\mathrm{d}\tau_1\, \mathrm{d}\tau_2, \tag{28}$$

are the one-electron integrals and the two-electron Coulomb and exchange integrals, respectively. The one-electron Hamiltonian operator h is

$$h = -\frac{1}{2}\nabla^2 - \sum_{\nu}^{N}\frac{Z_\nu}{r_\nu}, \tag{29}$$

Z_ν being the atomic number of the nucleus ν and r_ν the distance of the electron from that nucleus. The total energy, obtained by adding the electronic energy E_{el} to the internuclear repulsion energy, becomes

$$W = E_{\mathrm{el}} + \sum_{\lambda<\nu}\frac{Z_\lambda Z_\nu}{|\mathbf{R}_\lambda - \mathbf{R}_\nu|}, \tag{30}$$

with $\mathbf{R}_\mu$ the vector position of nucleus μ. Energy minimization relative to all quantities $(\alpha_i, \mathbf{R}_i, \mathbf{R}_\mu)$ provides the parameters defining the corresponding molecular configuration. According to Frost, the use of a single Gaussian orbital per electron pair constitutes a subminimal basis and hence the molecular energies are typically about 80% of the corresponding Hartree–Fock value. However, the electron density and molecular geometry are reasonably well described, especially in the case of hydrocarbons where the average error with respect to experiments is around 1.7 and 1.0% for bond length and bond angle, respectively. For other systems the quantitative agreement is generally less satisfactory although reasonable. Using this procedure, Frost and co-workers reported molecular parameters for a wide number of systems [55] with encouraging results in spite of the simplicity of the model, which is strictly *ab initio*. Another feature of this model consists in a description of large molecules in terms of molecular fragments [56,57]. They are defined as molecular entities acting as functional groups which correspond to regions centered on a heavy atom of the molecule where other

orbitals pack together. When two molecular fragments share a bonding orbital, the latter is partitioned according to its relative distance to the fragment centers. An example of the definition of molecular fragment in the case of the propylene molecule is shown in Fig. 2. This description of the molecule in terms of fragments has proved to be very useful in the CAB calculation of the stopping cross-section of heavy ions of low energy, as we shall discuss further below.

In Section 2, it was noted that the formal application of the CAB parti tioning scheme to molecular stopping requires a sophisticated procedure to estimate theoretically the partial contributions due to inner shell and valence molecular orbitals, as carried out by Sabin and Oddershede. Alternatively, a large database of experimental measurements is required to generate a semiempirical rule valid for heavy ions, as carried out by Ziegler and Manoyan. As an effort to explore chemical binding effects in the stopping of heavy ions within the CAB approach, Cruz, Soullard and Cabrera-Trujillo [58–61] adapted the FSGO idea of molecular fragments to the Firsov model [62] as follows.

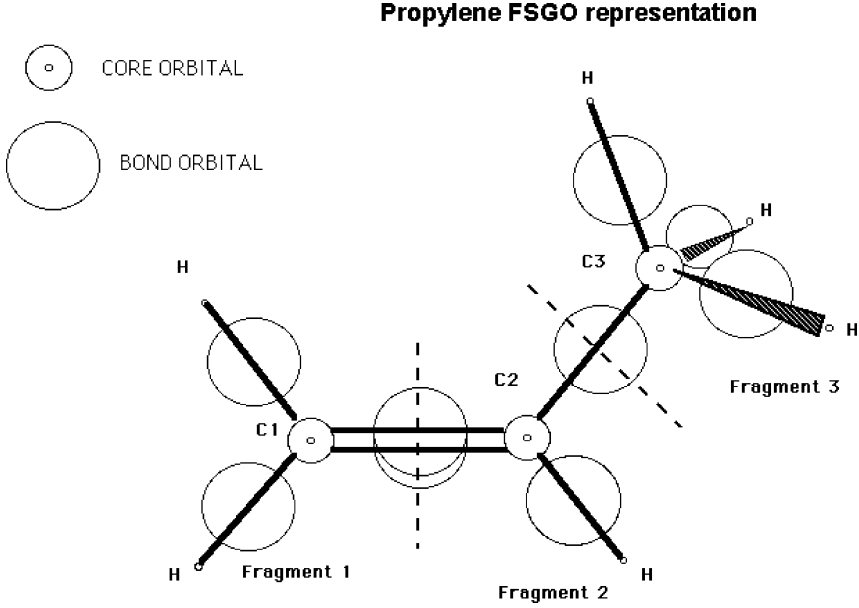

Fig. 2. Doubly occupied core and bond localized molecular orbitals in the FSGO representation of the propylene molecule and the corresponding molecular fragments.

4.2. The CAB–FSGO Firsov model for low-energy heavy ion molecular stopping

Within the Firsov model, the energy loss in a collision between two atomic systems takes place due to a drag force resulting from a momentum exchange involving both target electrons and projectile electrons. In the light of this scheme, the electronic stopping cross-section is written as [62]

$$S_{\mathrm{e}} = mu \int\int\int \varphi(x', y', z')\mathrm{d}x'\,\mathrm{d}y'\,\mathrm{d}z', \tag{31}$$

which is split into two contributions, one relative to the projectile $S_{\mathrm{e,p}}$, the other one to the target $S_{\mathrm{e,t}}$ thus

$$S_{\mathrm{e}} = S_{\mathrm{e,t}} + S_{\mathrm{e,p}}. \tag{32}$$

In equation (31) m is the electron mass, u the projectile velocity and φ the electron flux across a hypothetical plane (the Firsov plane) located between the projectile and the target. The spatial coordinates of the projectile relative to the target atom are denoted x', y', z'.

The momentum flux evaluation for both projectile and target was carried out through a previously generalized expression of equation (31) [63], adapted for the study of molecular targets considering the FSGO representation, whereby the orbital *one-electron* contribution to S_{e} becomes

$$S_{\mathrm{e}}^{i} = \pi\hbar u\beta_i^{-3} \int_{-\infty}^{\infty} \mathrm{d}k_x \int_{-\infty}^{\infty} \mathrm{d}k_y \int_{0}^{\infty} k_z |\partial\phi_i/\partial k_z|^2 \mathrm{d}k_z, \tag{33}$$

where ϕ_i is the Fourier transform of orbital Ψ_i (equation (25)) and β_i the fractional position between the projectile and the orbital center $\mathbf{R}_i$ at which a local Firsov plane is located [64]. This position is defined as the point where the electrostatic potentials of each partner of the binary encounter are equal, as shown schematically in Fig. 3.

Since the structure of each FSGO (equation (25)) has an implicit orientational dependence, for the molecular target the orbital contributions were cast after Fourier transforming equation (25) and averaging equation (31) over all orientations with the result [58]

$$\langle S_{\mathrm{e}}^{i} \rangle = 2(\pi/8)^{1/2}\hbar u\beta_i^{-3}\alpha_i^{-1/2}\left[1 + \tfrac{2}{3}\alpha_i R_i^2\right], \tag{34}$$

where the factor 2 accounts for the double occupancy of each FSGO. Equation (33) applies equally for the projectile atomic orbitals. Hence, for the projectile electrons, these authors used Hartree–Fock–Slater (HFS)

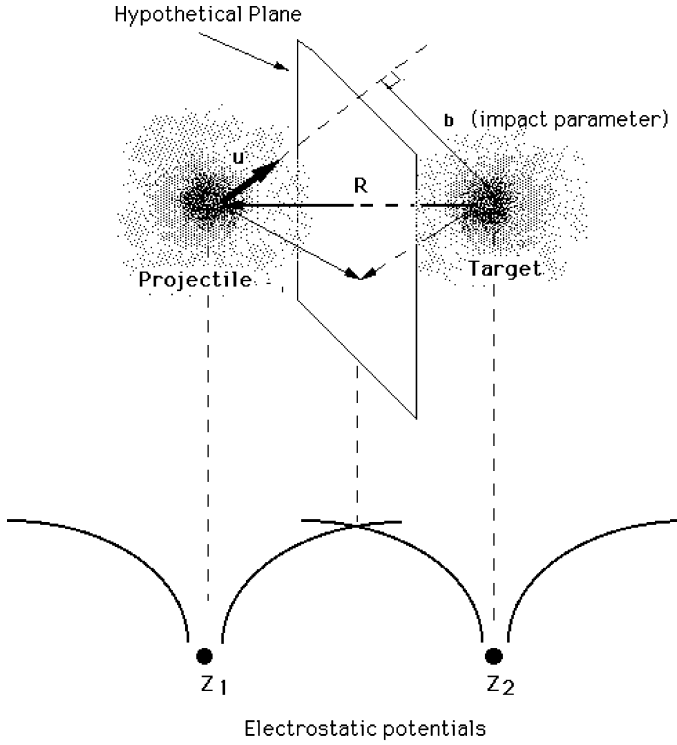

Fig. 3. Schematic diagram showing the location of the hypothetical Firsov plane between projectile and target at the point where the electrostatic potentials are equal.

orbitals [65] in equation (33). The projectile and target contributions to S_e given in equation (32) were calculated as follows. For the projectile,

$$S_{e,p} = \sum_f \left[\sum_\lambda n_\lambda S_e^\lambda \right]_f , \tag{35}$$

where the quantity in square brackets is the sum of one-electron atomic orbital contributions S_e^λ weighted by the orbital population n_λ. The exterior summation is performed over all the molecular fragments identified in the target molecule. For each molecular fragment–projectile combination, a given hypothetical surface was set at a position dictated by the matching of the corresponding electrostatic potentials [61] and S_e^λ calculated as prescribed by equation (33) using the HFS atomic orbitals. As an example, Figure 4 shows schematically this situation for an atomic projectile colliding with a propylene molecule.

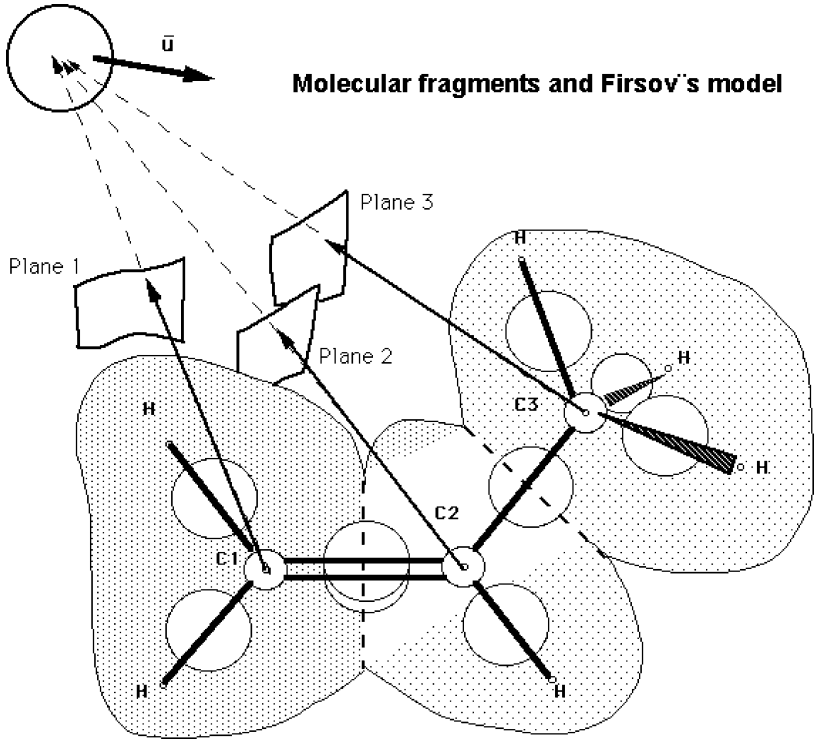

Fig. 4. Schematic representation of the use of molecular fragments to locate the corresponding Firsov planes relative to the projectile in the calculation of molecular stopping.

Analogously, for the target molecule,

$$S_{\mathrm{e,t}} = \sum_f \left[\sum_i \langle S_{\mathrm{e}}^i \rangle \right]_f = S_{\mathrm{e}}^{\mathrm{cores}} + S_{\mathrm{e}}^{\mathrm{bonds}} + S_{\mathrm{e}}^{\mathrm{lone\text{-}pairs}}, \tag{36}$$

which represents the sum over fragments f of the stopping contribution (equation (34)) from the molecular orbitals constituting each fragment. Partition criteria to consider the actual contribution from bonding orbitals between two molecular fragments were also given in these studies [59,60].

The above calculations were carried out for all hydrocarbon, alcohol and amine target molecules for which the FSGO parameters were known [55] and for several projectiles [59–61]. Tables 3 and 4 show the corresponding CAB contributions obtained after taking their average over different molecular environments for some selected projectiles with velocity $v = v_0$ as an example. It was also noted that for second-row atoms the K and L shells need a special treatment within the FSGO approach so that sp^3 hybridization

Table 3. Core contributions to the stopping cross-section for some low-energy ($v = v_0$) heavy projectiles in simple molecular targets calculated with the FSGO–Firsov model

Z_p	O	N	C	$S_{K\ shell}$	$S_{L\ shell}$
2	0.377	0.471	0.607	0.147	2.428
3	0.430	0.556	0.735	0.162	2.701
7	0.622	0.879	1.183	0.210	3.585
8	0.646	0.914	1.201	0.219	3.736

All units in 10^{-15} eV cm^2/bond (Reproduced from Ref. [61]).

is taken into account [66]. In this case, the K- and L-shell contributions ($S_{K\ shell}, S_{L\ shell}$) to stopping must be calculated in place of that for core electrons [61].

Table 5 displays the predictions (compared with experiment) of the model described here for He and Li projectiles incident with a velocity $v = v_0$ on several organic molecular targets of varying structural complexity. For helium projectiles, the data of the Baylor group [20] were extrapolated to low energy ($v = v_0$) assuming a linear variation for S_e below 300 keV; for Li projectiles comparison was made with the experimental results from the Köln group [19] (see Refs. [58–61] for details). The general agreement found with experiment is reasonable, in spite of the simplicity of the model employed.

Table 4. Bond and lone-pair contributions to the stopping cross-section for some low-energy ($v = v_0$) heavy projectiles in simple molecular targets using the FSGO–Firsov model

Z_p	C–H	C–C	C=C	C≡C	O–H (H_2O)	O=O (O_2)	N–H (NH_3)
2	7.385	7.772	15.690	22.734	3.945	9.976	5.231
3	8.732	9.504	19.672	28.248	6.379	15.963	9.379
7	12.013	13.584	26.812	36.388	8.262	22.381	9.025
8	11.517	12.964	24.838	35.614	8.181	22.182	11.920
	N≡N (N_2)	S–H (H_2S)	C≡O (CO)	L_p (O)	L_p (N)	L_p (C)	L_p (S)
2	17.739	6.588	11.876	3.739	4.751	4.888	6.086
3	20.805	12.041	19.329	6.225	5.836	6.023	11.607
7	30.786	16.347	26.993	8.394	8.275	8.239	9.773
8	30.310	15.876	26.699	8.281	8.144	8.153	9.580

All units in 10^{-15} eV cm ^{2}/bond (Reproduced from Ref. [61]).

Table 5. Comparison between experiment and the FSGO–Firsov theory for the electronic stopping cross-section of He and Li ions incident on various selected organic targets at $v = v_0$

Molecule	Formula	Helium		Lithium	
		Theory	Exp.[a]	Theory	Exp.[a]
Alkanes[b]					
Methane	CH_4	42.3	50.9, 50.0, 46.3	57.2	–
Ethane	C_2H_6	76.9	85.0	124.6	124.8
Propane	C_3H_8	111.5	76.6, 121.9, 122.4	182.0	163.7
n-Butane	C_4H_{10}	146.1	158.1	239.4	209.0
Isooctane	C_8H_{18}	253.8	–	416.4	407.0
Cyclooctane	C_8H_{16}	276.7	285.8	458.9	386.7
Alkenes[b]					
Ethylene	C_2H_4	69.3	72.2, 73.9, 65.3	115.4	102.4
Propylene	C_3H_6	103.9	108.7, 109.8	172.7	150.0
Pentene	C_5H_{10}	173.1	–	287.4	246.9
Cyclohexene	C_6H_{10}	192.2	202.6	325.4	273.9
1,3-Butadiene	C_4H_6	130.8	133.4	220.7	–
Alkynes[b]					
Acetylene	C_2H_2	60.8	63.0, 63.7, 57.3	104.4	–
Aromates[b]					
Benzene	C_6H_6	184.5	181.3	316.1	239.1
Toluene	C_7H_8	219.0	215.9	373.2	285.4
Phenylacetylene	C_8H_6	237.4	229.8	410.2	–
Alcohols[c]					
Methanol	CH_3OH	62.9	71.8	–	–
Propanol	C_3H_7OH	132.0	143.2	–	–
Diethylether	$C_4H_{10}O$	166.7	177.7	–	–
Amines[c]					
Dimethlylamine	$(CH_3)_2NH$	101.3	119.5	–	–
Ethylamine	$CH_3CH_2NH_2$	101.7	117.9	–	–
Other[b]					
Nitrogen	N_2	50.2	49.7	–	–
Oxygen	O_2	47.7	47.3	–	–
Water (vapor)	H_2O	32.1	36.5	–	–
Water (liquid)	H_2O	–	–	58.0	46.8
Ammonia	NH_3	33.0	44.3	–	–
Hydrogen sulfide	H_2S	48.5	62.1	–	–

All units in 10^{-15} eV cm^2/molecule. (Reproduced from Refs. [60,61].

[a] See the corresponding reference for details.

[b] Ref. [61].

[c] Ref. [60].

It is also important to note that no adjustable parameters were used throughout the calculation.

Another consistent result was observed by these authors with regard to phase effects. The S_e values for Li projectiles (Table 5) are systematically about 20% above the experimental data, in contrast with the case of He particles. A possible explanation for this behavior is that the Li measurements were done in the liquid phase whereas the model was developed for targets in the gas phase; hence, the better agreement with experiments with targets in the gaseous phase. Indeed, a condensed phase is characterized by a reciprocal influence of neighboring molecules and this fact was not included in the model. A CAB model which attempts to account for the condensed phase will be discussed in a subsequent section.

In spite of the serious limitations of the Firsov model (no Barkas and Bloch corrections nor projectile/target electron promotion mechanisms are considered), its CAB implementation in terms of molecular fragments yielded reasonable agreement with experiment for a wide class of hydrocarbon molecules and for simpler molecular systems bombarded with low-energy He or Li ions. This gave further support to the ideas put forward by the Baylor and Köln groups regarding the decomposition of the stopping cross-section of *n*-alkanes and *n*-alkenes in terms of characteristic molecular groups. Thus, in agreement with the other studies discussed before, the CAB approach seems to be a useful means to understand the stopping of slow heavy ions in materials presenting a covalent bonding.

4.3. OLPA/FSGO implementation of the kinetic theory of stopping

The success of the orbital implementation of Sigmund's KT by Sabin and Oddershede to distinguish the characteristic contribution to S_e (protons) from valence and core electrons in a molecular target and the scaling possibilities to heavy ion projectiles deemed by Ziegler and Manoyan in the CAB approach through effective charge theory stimulated further studies of proton stopping in molecular targets based on the FSGO representation of molecular orbitals. Following the ideas put forward by Oddershede and Sabin, Cabrera-Trujillo, Cruz and Soullard [64] applied the KT by performing their calculations in the frame of reference moving with the projectile leading to a simpler mathematical treatment. Accordingly, S_e was cast as

$$S_e(v_1) = -\int f(v_1 - v')\frac{\mathbf{v}_1\cdot\mathbf{v}'}{v_1 v'} S_0(v')\mathrm{d}^3\mathbf{v}', \tag{37}$$

where $\mathbf{v}'$ is the velocity of target electrons relative to the projectile, $f(v_1 - v')$ is the target electron velocity distribution *in the laboratory frame* and $S_0(v')$ is the value for S_e when the scatterers are at rest [29]. A natural option for

$S_0(v')$ is the expression given by equation (16) obtained in the Bethe/Born regime, which involves the logarithm of the target mean excitation energy.

Using equation (37) and assuming isotropic orbital velocity distributions $f_k(|\mathbf{v}_1 - \mathbf{v}'|)$, the corresponding expression to equation (4) for the orbital contribution to the molecular stopping was obtained as

$$S_k(v_1) = \frac{4\pi e^4 Z_1^2 v_1^2 \omega_k}{m} \int_{\beta_k}^{\infty} \ln\left[\frac{2mv^2}{I_k}\right] dv' \times \int_0^{\pi} f_k\left(\sqrt{v_1^2 + v'^2 - 2v_1 v' \cos\theta}\right) d(\sin^2\theta), \tag{38}$$

where I_k is the orbital mean excitation energy, ω_k the orbital population and $\beta_k = \sqrt{I_k/2m}$.

The mean orbital excitation energy I_k was obtained using the OLPA approach through equation (23) with the scaling parameter $\gamma_k = 1$ and the FSGO defined by equation (25) yielding a simple expression in terms of the orbital parameters

$$I_k = 2^{11/4}\pi^{-1/4}(e^2/2a_0)\omega_k^{1/2} e^{-3/4}\alpha_k^{3/4}. \tag{39}$$

Finally, equation (38) was evaluated after taking the Fourier transform of the FSGO (equation (25)) in order to obtain the velocity distribution f_k with the result

$$S_k(u) = 2^{5/2}\pi^{1/2}\hbar a_0 v_0 Z_1^2 \omega_k \alpha_k^{-3/2} e^{-u^2/2\alpha_k} G_k(\alpha_k, I_k, u), \tag{40}$$

with

$$G_k(\alpha_k, I_k, u) = \int_{\beta_k}^{\infty} \exp\left(-\frac{x^2}{2\alpha_k}\right) \ln\left[\frac{2e^2x^2}{a_0 I_k}\right] \times \left[\frac{\alpha_k \cosh(xu/\alpha_k)}{xu} - \frac{\alpha_k^2 \sinh(xu/\alpha_k)}{x^2u^2}\right] dx, \tag{41}$$

where $u = v_1/v_0$ and $x = v'/v_0$.

This scheme, called the OLPA/FSGO approach to the KT, allows to make a CAB decomposition of the molecular stopping as prescribed by equation (9) and is a natural extension of the ideas proposed by Sabin and Oddershede [23–27] together with the orbital local plasma definition by Meltzer *et al.* [48,53]. A particular feature of the OLPA/FSGO treatment is that all quantities related to the evaluation of CAB stopping contributions are obtained consistently through the properties of the molecular orbitals (i.e., electronic density and velocity distribution) with no input from external sources. Of course, the approximate character of the FSGO as compared

to accurate Hartree–Fock wavefunctions would seem to limit the confidence in the OLPA/FSGO quantitative predictions. However, the quantitative and qualitative behavior of the relevant quantities such as orbital mean ionization energies I_k and orbital stopping contributions S_k, for proton stopping are generally satisfactory when compared with more accurate treatments as shown in Tables 6–8.

Table 6 displays the OLPA/FSGO orbital mean ionization energies ($I_k^{OLPA/FSGO}$) [67] as compared with those obtained by the accurate treatment by Sabin and Oddershede [27] for various organic molecules (I_k^{OS}). In the case of hydrocarbons, a good agreement is observed for the mean excitation energies of the C–H bond and the C=C bond. However, the surprisingly strong difference for the C–C bond remains unexplained. In the case of diatomic molecules and the two hydrides, the FSGO model treats the lone-pair orbitals (indexed as LP) as molecular entities distinct from the bond orbitals, in contrast with the treatment by Sabin and Oddershede where the lone-pair electrons are included in the bonds; this situation precludes any meaningful comparison. Notice also the predicted effect of the different chemical environment on the mean ionization energy for the same type of bond in isomers with different structure like cyclopropane and propylene. On the other hand, when comparing with experimental recommended total mean ionization energies, the corresponding OLPA/FSGO predictions – calculated through equation (7) – lie systematically below between 18 and 30%.

The OLPA/FSGO calculation of mean excitation energies for inner-shell orbitals of some first- and second-row atoms is shown in Table 7 [67] together with the accurate estimates of Meltzer *et al.* (I_k^{MST}) [48] and Sabin and Oddershede (I_k^{OS}) [52]. Inspection of this table indicates that the $I_k^{OLPA/FSGO}$ values are systematically greater than the I_k^{MST} values but lower than I_k^{OS}, remaining closer to the former values. This behavior is explained in terms of electronic density distribution which is found to be more compact in the FSGO representation than in the more accurate calculations with more realistic atomic wavefunctions. The discrepancies between the I_k^{MST} and I_k^{OS} have been discussed in Ref. [48], the main conclusion being that the implications of these differences on total stopping values are negligible in view of the dominating contribution from outer orbitals in the proton energy range $0.1\ \text{MeV} \leq E \leq 10\ \text{MeV}$. Hence, the same conclusion applies to the predicted $I_k^{OLPA/FSGO}$ values.

Once the orbital mean excitation energies were obtained as discussed above, the CAB contributions S_k to the total molecular stopping $S_e^{molecule}$ were calculated through equations (40) and (41). Table 8 shows the velocity dependence of the various CAB stopping contributions for various parent molecules calculated within the OLPA/FSGO approach ($S_k^{OLPA/FSGO}$) [67], which can be compared with the corresponding values reported by Sabin and Oddershede S_k^{OS} [27] given in Table 1. Since the I_k^{OS} bond excitation energies

Table 6. Orbital ($I_k^{OLPA/FSGO}$) and total ($I^{OLPA/FSGO}$) molecular mean excitation energies calculated in Ref. [67] for different bonds and lone pairs appearing in the indicated parent molecules

Molecule	Molecular constituent	$\alpha_k^{-1/2}$ (a_0)	ω_k	$I_k^{OLPA/FSGO}$	I_k^{OS}	$I^{OLPA/FSGO}$	$I_{molecule}$
CH_4	C–H	1.694	2	20.83	21.20	34.09	41.70
C_2H_4	C–H	1.642	2	21.83		42.12	49.93
	C=C	1.794	4	27.03	27.93		
C_2H_2	C–H	1.581	2	23.10		53.13	–
	C≡C	1.781	6	33.47			
C_2H_6	C–H	1.695	2	20.81		36.16	45.40
	C–C	1.646	2	21.75	33.63		
C_3H_6 (cyclopropane)	C–H	1.683	2	21.04		38.12	–
	C–C	1.770	2	19.50			
C_3H_6 (propylene)	C_1–H	1.649	2	21.69		40.96	50.05
	C_2–H	1.645	2	21.77			
	C_3–H	1.688	2	20.94			
	C_1=C_2	1.796	4	26.99			
	C_2–C_3	1.620	2	22.27			

(*continued*)

Table 6. Continued

Molecule	Molecular constituent	$\alpha_k^{-1/2}$ (a_0)	ω_k	$I_k^{\mathrm{OLPA/FSGO}}$	I_k^{OS}	$I^{\mathrm{OLPA/FSGO}}$	I_{molecule}
H_2O	O–H	1.308	2	30.70	40.68	50.53	72.46
	O_{LP}	1.331	2	29.91			
NH_3	N–H	1.554	2	23.71	29.49	39.23	53.69
	N_{LP}	1.627	2	22.13			
O_2	O=O	1.264	4	45.71		65.44	95.02
	O_{LP}	1.271	2	32.05			
N_2	N≡N	1.449	6	45.61		66.93	81.84
	N_{LP}	1.489	2	25.28			
H_2	H–H	1.772	2	19.47		19.47	19.26

In addition, the corresponding theoretical calculations (I_k^{OS}) from Oddershede and Sabin [27] and accepted values for I_{molecule} are shown (see text). All energies are given in eV. See Ref. [67] for details.

Table 7. Orbital mean excitation energies ($I_k^{\mathrm{OLPA/FSGO}}$) for the K and L shells of selected atomic systems

Atom[a]	Orbital	$1/\alpha_k^{1/2}$ (a_o)	ω_k	$I_k^{\mathrm{OLPA/FSGO}}$	I_k^{MST} [b]	I_k^{OS} [c]
He	1s	1.142	2	37.63	33.66	38.83
C	1s	0.328	2	244.49	220.78	451.34
N	1s	0.277	2	315.03	283.07	590.00
O	1s	0.240	2	390.62	349.72	729.41
Na	1s	0.171	2	649.49	577.82	1110.36
	2s	0.799	2	64.31	47.12	119.24
	2p	0.799	6	111.38	93.51	124.41
Mg	1s	0.156	2	745.39	661.87	1243.15
	2s	0.697	2	78.93	56.77	151.05
	2p	0.697	6	136.70	118.75	169.86
Al	1s	0.143	2	849.31	749.74	1373.04
	2s	0.618	2	94.53	66.87	187.14
	2p	0.618	6	163.74	145.18	221.15

In addition, the corresponding OLPA (I_k^{MST}) and Hartree–Slater calculations (I_k^{OS}) are shown. Excitation energies are given in eV. (Reproduced from Ref. [67]).
[a] See Ref. [67] for details.
[b] Ref. [48].
[c] Ref. [54].

are systematically higher than the $I_k^{\mathrm{OLPA/FSGO}}$ values (see Table 6), the S_k^{OS} values are systematically smaller than the $S_k^{\mathrm{OLPA/FSGO}}$ ones. In spite of this, the agreement between both calculations in predicting proton stopping cross-sections in various molecular targets is rewarding, as may be verified from Figs 5 and 6, where the CAB approach is used within the OLPA/FSGO scheme in Ref. [67] to calculate the proton stopping cross-section for various molecular gases and compared with available experimental data and the corresponding predictions by Sabin and Oddershede [26]. A fair overall agreement with experiment is observed for all cases. Note, however, that Barkas and Bloch terms were not accounted for; hence, care must be taken in making proper comparison with experiment in the velocity region below and around the maximum of the stopping curve. Thus, under the same Bethe/Born conditions, the OLPA/FSGO curves were found to lie above those obtained by Sabin and Oddershede around the maximum and merge at high energies.

So far, a brief review of the main theoretical developments based on the CAB concept to account for chemical binding effects on molecular stopping has been discussed. Since the formal settlement of the CAB approach was advanced by Sabin and Oddershede on firm theoretical grounds using the KT of stopping, its adequacy has been shown in reproducing with reasonable

Table 8. Core, bond and lone-pair contribution to the molecular electronic stopping cross-section for protons incident on selected molecular targets in the gas phase

u (a.u.)	C–H (CH_4)	C–C (C_2H_6)	C=C (C_2H_4)	C≡C (C_2H_2)	O–H (H_2O)	O=O (O_2)	N–H (NH_3)	N≡N (N_2)
0.5	5.916	5.527	8.998	10.001	3.189	3.992	4.822	6.265
1.0	9.889	9.314	16.175	19.173	5.658	7.472	8.246	12.105
1.5	10.835	10.349	18.763	23.727	6.905	9.778	9.411	16.044
2.0	9.666	9.366	17.285	22.911	6.952	10.553	8.760	17.099
2.5	7.946	7.772	14.454	19.697	6.276	10.087	7.414	15.962
3.0	6.440	6.329	11.838	16.383	5.385	9.010	6.104	13.966
3.5	5.272	5.195	9.764	13.638	4.551	7.818	5.039	11.963
4.0	4.384	4.327	8.163	11.474	3.856	6.737	4.212	10.238
8.0	1.526	1.513	2.898	4.155	1.407	2.574	1.487	3.870
10.0	1.064	1.055	2.027	2.918	0.988	1.823	1.038	2.738
	LP1 (H_2O)	LP2 (O_2)	LP3 (NH_3)	LP4 (N_2)	C	O	N	H–H (H_2)
0.5	3.326	2.975	5.377	4.354	0.096	0.042	0.061	6.578
1.0	5.882	5.306	9.089	7.523	0.189	0.083	0.122	10.850
1.5	7.136	6.536	10.157	8.745	0.278	0.123	0.179	11.613
2.0	7.131	6.659	9.244	8.307	0.360	0.162	0.234	10.132
2.5	6.395	6.079	7.701	7.140	0.434	0.198	0.285	8.214
3.0	5.461	5.258	6.284	5.932	0.498	0.232	0.331	6.610
3.5	4.603	4.466	5.164	4.922	0.553	0.263	0.372	5.391
4.0	3.894	3.795	4.304	4.156	0.596	0.290	0.407	4.472
8.0	1.415	1.393	1.508	1.467	0.616	0.386	0.487	1.547
10.0	0.993	0.979	1.052	1.026	0.522	0.368	0.441	1.076

These values were obtained through the OLPA/FSGO implementation of the KT. Units in 10^{-15} eV^2/bond. (Reproduced from Ref. [67]). Compounds in parentheses are parent molecules.

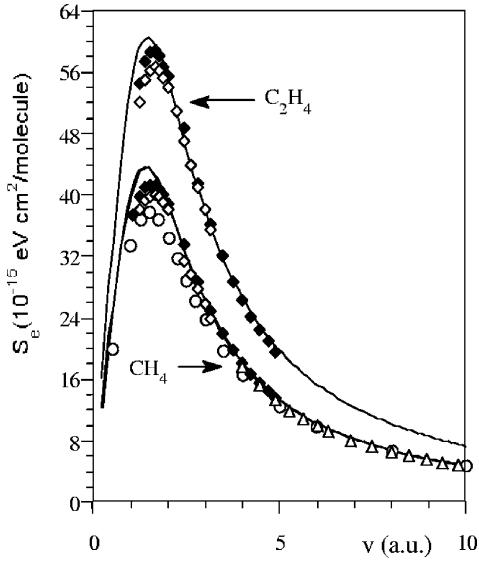

Fig. 5. Molecular stopping cross-section for protons incident on CH_4 and C_2H_4 predicted by the OLPA/FSGO method (solid line); ○ Sabin–Oddershede [26]. Experiment: ◆ [88]; △ [92]; ◇ [89]. Reproduced from Ref. [67].

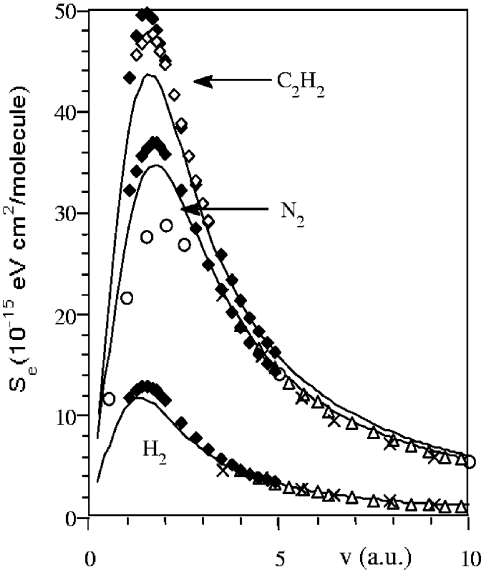

Fig. 6. Same as Fig. 5 for H_2, N_2 and C_2H_2, plus experimental data (×) from Ref. [91]. Reproduced from Ref. [67].

success the experimentally observed proton electronic stopping curves for various molecular targets in the gaseous phase. Furthermore, it has been shown that the use of approximate molecular wavefunctions such as the FSGO, together with the OLPA, provide a useful means to extend the predictions of the CAB approach-based theory to other molecular systems. Two questions remain in assessing the scope of the theory, namely, to deal with physical phase state effects and with heavy ion stopping. In Section 4.4, we discuss the main efforts carried out on the first of these issues.

4.4. CAB treatment of phase effects

The CAB theoretical models analyzed so far are based on the free-molecule properties and thus are adequate for the treatment of molecular targets in the gas phase. However, for a molecular liquid or solid, the intermolecular distances are short enough so that the electronic distribution of a given molecule in the medium is perturbed by the neighboring molecules, giving rise to changes in its electronic and structural properties. Indeed, it has been largely recognized experimentally that the mean ionization energy of a given molecule is lower than the corresponding value for the same molecule in its condensed phase [15–18,35]. This observation has been consistent with measurements of electronic stopping cross-sections S_e of ions traversing the same material in different physical phase states with the relative outcome $S_e^{gas} > S_e^{solid} > S_e^{liquid}$ [17,18,21]. Clearly, physical phase state and chemical binding effects on the ion stopping power appear concomitantly. Hence, any theoretical model aimed to assess the issue of molecular stopping in a condensed medium should take this into account. The first ideas to model this situation were put forward by the Köln group [68] and Xu *et al*. [69]. The former authors studied the target density effect on the stopping power of Li ions incident on liquid ethane while the latter devoted their analysis to explain the observed differences between proton stopping measurements in water in the gas phase and in the solid phase. Both groups considered the state of aggregation of the medium in terms of the spatial limitation imposed on a given molecule by other molecules in the surrounding medium. The model used in these approaches is that of a molecule confined by a box with hard walls such that the redistribution of the total molecular electronic density is obtained from the renormalization of the free-molecule density within the cage volume. The molecular density was considered as the direct overlap of the atomic constituent densities, i.e.,

$$\rho_{mol}(\mathbf{r}) \approx \sum_i \rho_i(\mathbf{r} - \mathbf{R}_i), \tag{42}$$

where $\rho_i(\mathbf{r} - \mathbf{R}_i)$ is the local electron density due to an atom located at position $\mathbf{R}_i$ and the overlap between charge distributions of neighboring centers forming a bond is neglected. Bonding effects were incorporated by

invoking Pauling's definition [70] of the partial ionic character of bonds, which were finally expressed in terms of scaled free-atom densities. In the case of ethane, the Köln group used a spherically averaged sp^3-hybridized wavefunction for the carbon atoms [71], whereas Xu *et al*. used Hartree–Fock–Slater wavefunctions [65] for the oxygen atom. Accordingly, the electronic stopping cross-section was then calculated within the original LPA [53] by introducing the renormalized molecular densities and performing all the required calculations within the confinement volume. For Li projectiles, an effective charge was used by the Köln group. The results obtained by the latter authors for the stopping cross-section S_e of Li projectiles with $v = v_0$ on liquid ethane for two different densities (0.525 and 0.362 g/cm^3) yielded predicted differences of about 2% in the corresponding S_e values in agreement with experiment. With regard to the calculations of Xu *et al*., Figure 7 shows their predicted proton stopping cross-section for water in its vapor, and condensed phase as compared with available experimental data.

The quantitative and qualitative agreement with experiment is readily apparent from this curve, in spite of the approximations introduced. Moreover, the predicted S_e values for the gas and liquid phase follow the order $S_e^{gas} > S_e^{liquid}$, as expected. Xu *et al*. explain the reason for the differences in terms of the difficulty to remove or excite an electron from

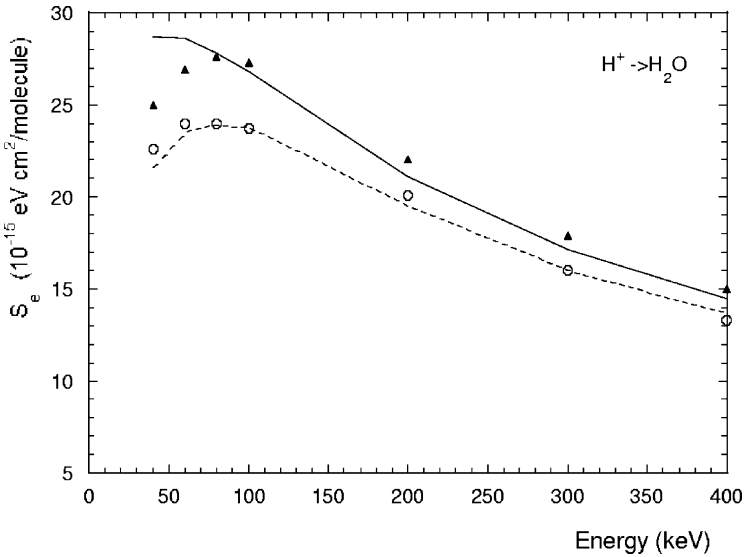

Fig. 7. Proton stopping cross-section of water in the gaseous and condensed phase. Gas: solid line, theoretical prediction from Xu *et al.* [69]; (▲) experimental results from Reynolds *et al.* [88]. Condensed phase: dashed line, theoretical prediction from Xu *et al.* [69] for liquid water; (○) experimental results from Wenzel and Whaling [90] for D_2O ice.

the water molecule due to the confinement effect of the surrounding molecules, which creates a barrier potential, thus increasing the binding energy of the electrons. This effect was then rationalized through the LPA as an increase in the mean excitation energy due to a corresponding increase in the local electronic density. Since water molecules in ice are less compacted than in the liquid phase, the expected mean excitation energies should follow an order $I_{\text{solid}} < I_{\text{liquid}}$, yielding the observed trend in the S_e values for each phase.

Unfortunately, to the present authors' knowledge, the physical plausibility of the above-discussed models, as well as their feasibility to account for phase effects in view of the reasonable agreement with experimental observation, was not pursued further until recently – with regard to the CAB treatment of stopping – as we discuss below.

4.5. The CAB approach and molecular confinement

The perturbation approach represented by equation (42) for the molecular electronic density was proven by Gordon and Kim [72] to be adequate for the analysis of interatomic and intermolecular forces when realistic atomic wavefunctions are used within the uniform electron gas approximation. However, in the case of confined atoms or molecules, the linear superposition of free atomic densities may not be completely justified, since the redistribution of the electron density is accompanied by nuclear position relaxation with corresponding changes in the total molecular energy, as shown by studies on small confined molecules [73] and more recently for larger molecules [74]. Hence, proper modeling of target density effects based on spatial confinement should consider, self-consistently, both the changes in electronic density and in molecular conformation.

As a continuing effort along these ideas to study phase effects on S_e within the CAB approach, the present authors have recently applied the OLPA/FSGO implementation of the KT to the case of proton stopping in molecular hydrogen at various densities [75]. Also, further below, new results will be presented here for the case of proton stopping on CH_4, H_2O and NH_3 within the same approach, although a more elaborate treatment is required.

4.5.1. Proton stopping in dense hydrogen

In the case of H_2, the electron pair is represented by a single FSGO as given by equation (25) for the free molecule. For a condensed phase, the confinement model was used considering the molecule as enclosed within a spherical box limited by a finite barrier height potential V_B such that the

potential function entering the molecular Hamiltonian becomes

$$V(\mathbf{r}) = \begin{cases} 0, & \mathbf{r} \in \Gamma \\ V_{\mathrm{B}}, & \mathbf{r} \notin \Gamma, \end{cases} \tag{43}$$

where Γ denotes the confinement volume and $\mathbf{r}$ the electron position relative to the origin located at the center of the box.

Equation (43) demands an interior and exterior representation of a localized orbital such that fulfillment of the logarithmic derivative at the boundary is satisfied as well as normalization over all space. Since $\mathbf{R}_i = 0$ in equation (25) for the H_2 molecule, the following modified FSGO representations of the interior and exterior region were proposed, respectively [75]

$$\Psi^{\mathrm{i}}(r) = N^{\mathrm{i}}(\mathrm{e}^{-ar^2} - \mathrm{e}^{-bR_{\mathrm{c}}^2}), \qquad r < R_{\mathrm{c}}, \tag{44}$$

$$\Psi^{\mathrm{e}}(r) = N^{\mathrm{e}}\,\mathrm{e}^{-gr^2}, \qquad r \geq R_{\mathrm{c}}, \tag{45}$$

with R_{c} the radius of the confining sphere, N^{i} and N^{e} normalizing factors for the interior and exterior wavefunctions, respectively, and a, b, and g the corresponding orbital parameters. Both the normalizing factors and the orbital parameters are then related through the normalization and boundary conditions; hence, only two independent orbital parameters remain.

For a given box radius R_{c} and barrier height V_{B}, the total molecular energy given by equations (26)–(30) were then optimized relative to the independent orbital parameters and nuclear positions. Hence, the FSGO energy, electronic density as well as changes in the internuclear distance could be constructed for different sizes of the confining box and barrier heights. For the purposes of our discussion here, we turn our attention to the relevant quantities involved in the calculation of S_{e} according to equations (3) and (38). Figure 8 shows the behavior of the mean excitation energy I_0 as a function of confinement radius R obtained for two extreme cases ($V_{\mathrm{B}} = 0$ and ∞) of the confinement barrier height. These values were obtained using the recommended expression (equation (24)) for the mean excitation energy together with the optimized FSGO. From this figure, the monotonic increase in I_0 as density increases is evidenced in both cases, in qualitative agreement with the conclusions by Xu *et al*. However, an important feature to observe is the exaggerated rapid increase in the I_0 values for the infinitely hard wall ($V_{\mathrm{B}} = \infty$) case as compared with the 'transparent' ($V_{\mathrm{B}} = 0$) case.

Since the value of I_{k} ($= I_0$ in this case) enters in the lower limit in the integral expressed by equation (38), it is anticipated that the predicted S_{e} values using an impenetrable confining box will exaggerate target density effects for all but the lowest densities. In spite of this, hard-wall confining boxes have been used to explore the trend of pressure effects on atomic and

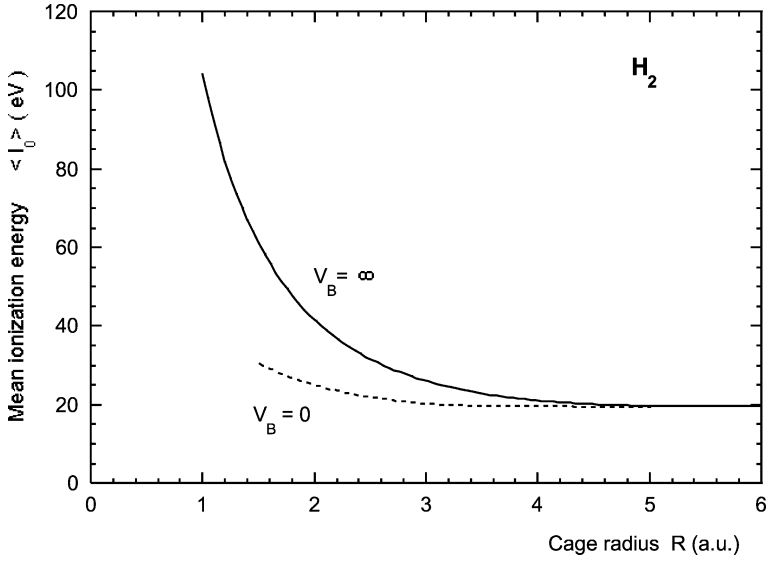

Fig. 8. Mean excitation energy of the hydrogen molecule as a function of confinement radius for two extreme potential barrier heights.

molecular properties [76,77] since it is not always possible to simulate the effect of a finite barrier height.

The different density conditions, were related to the volume $\Gamma (= 4\pi R_c^3/3)$ of the confining cage as

$$\rho = \frac{\Omega}{N_0 \Gamma}, \tag{46}$$

with Ω the molecular weight and N_0 the Avogadro number. However, as we shall show further below, this assignment is not correct, since pressure and density must be related through an equation of state. Since only the evolution of the ground-state energy was studied, the cold pressure associated to the different confinement volumes was estimated as $P = -\partial W/\partial \Gamma$, where W is the total molecular energy (equation (30)). Figure 9 shows the ($V_B = 0$) behavior of S_e calculated by Cruz *et al.* [75] for protons incident on molecular hydrogen as a function of proton velocity for different pressures starting from the gas phase (dashed curve).

The conclusion drawn from this study was that, as pressure (density) increases, the S_e curve diminishes in amplitude with a slight shift of its maximum towards higher proton velocities. However, almost negligible (about 0.5%) differences in S_e were predicted between the gas phase and the low-density liquid phase (0.036 mol/cm^3) of hydrogen. This was the first application of the confinement model within the OLPA/FSGO approach

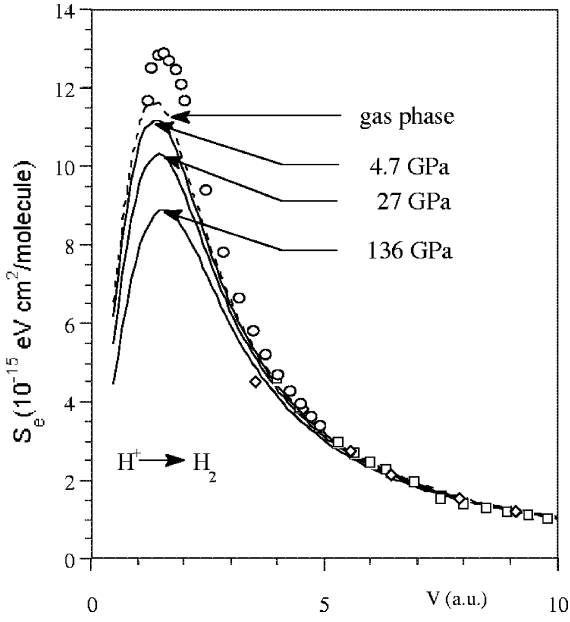

Fig. 9. Electronic stopping cross-section of protons incident on dense molecular hydrogen under different pressures as a function of projectile velocity. Dashed line, theoretical results for $P = 0$. Experiments: ○ [88]; ◇ [91]; □ [92]. Reproduced from Ref. [75].

where chemical binding effects as well as target density effects were self-consistently treated. Although no experimental information is available for proton stopping cross-sections in any condensed phase of hydrogen, the model showed an interesting feature regarding its apparent ability to predict stopping effects on dense matter.

4.5.2. Proton stopping in dense water, ammonia and methane

The treatment of molecular systems larger than H_2 under confinement has not yet been reported in the literature. In the following, we present for the first time some preliminary results on predicted target density effects on proton stopping cross-sections for the CH_4, H_2O and NH_3 molecular systems using the CAB approach and the OLPA/FSGO scheme as above. Our study is based on recent results of confinement effects on the ground state, electronic structure and molecular conformation of the above molecules [74] obtained by resorting to a previously modified FSGO treatment of multicenter integrals for molecules confined within spherical hard boxes [78]. Although it is clear that hard-wall confinement models tend to exaggerate the quantitative prediction of the stopping cross-section, we can get some insight

into the relative participation in the stopping process from different molecular constituents as density increases.

Within the modified FSGO approach, the localized molecular orbitals (equation (25)) are modified as

$$\Psi_i(\mathbf{r}-\mathbf{R}_i) = N_i\, \mathrm{e}^{-\alpha_i(\mathbf{r}-\mathbf{R}_i)^2}(1 - r^2/R_\mathrm{c}^2), \tag{47}$$

where all quantities have the same meaning as before and the factor in parentheses is introduced so that the boundary condition $\Psi_i(r = R_\mathrm{c}) = 0$ is satisfied. Clearly, normalization and the evaluation of one- and two-electron integrals implied by equations (26)–(29) are restricted to the confinement volume Γ. Taking into account the off-center character of the various FSGO and the spherical symmetry of the confining box [78], for a given confinement radius R_c, the total molecular energy (equation (30)) is then optimized relative to all orbital parameters α_i, orbital centers $\mathbf{R}_i$ and nuclear positions $\mathbf{R}_\mu$, thus yielding all the necessary input quantities for evaluating the stopping cross-section as follows.

According to the OLPA, the orbital mean ionization energy is calculated by use of equation (24), where the local orbital electron density is now obtained from equation (47) as

$$\rho_\mathrm{k}(\mathbf{r}) = N_\mathrm{k}^2\omega_\mathrm{k}\, \mathrm{e}^{-2\alpha_\mathrm{k}(\mathbf{r}-\mathbf{R}_k)^2}(1 - r^2/R_\mathrm{c}^2)^2, \tag{48}$$

and the angularly averaged total local electron density given as

$$\rho(r) = 2\left\langle \sum_{j,k} \Psi_j^*(\mathbf{r},\mathbf{R}_j)\Psi_\mathrm{k}(\mathbf{r},\mathbf{R}_k)T_{jk} \right\rangle_\Omega, \tag{49}$$

with Ψ_λ given by equation (47) and T_{jk} the elements of the inverse overlap matrix. Using the Rayleigh expansion [79]

$$\mathrm{e}^{\lambda\mathbf{r}\cdot\mathbf{R}} = 4\pi \sum_{l,m} i_l(\lambda r R) Y_l^m(\hat{\mathbf{r}}) Y_l^{m*}(\hat{\mathbf{R}}), \tag{50}$$

where $i_l(z)$ is the modified Bessel function of the first kind and $Y_l^m(\hat{\mathbf{u}})$ the spherical harmonics, it may be shown that equation (49) becomes, after integrating over the angular variable

$$\begin{aligned}\rho(r) = {} & 2(1 - r^2/R_\mathrm{c}^2)^2 \sum_{j,k} N_j N_\mathrm{k}\, \mathrm{e}^{-A_{jk}R_{jk}^2 - \alpha_{jk}\Lambda_{jk}^2} \\ & \times\, \mathrm{e}^{-\alpha_{jk}r^2} i_0(2\alpha_{jk}\Lambda_{jk}) T_{jk},\end{aligned} \tag{51}$$

with the following definitions

$$\begin{aligned} \alpha_{jk} &= \alpha_j + \alpha_{\mathrm{k}}, \\ A_{jk} &= \alpha_j \alpha_{\mathrm{k}} / \alpha_{jk}, \\ R_{jk} &= |\mathbf{R}_j - \mathbf{R}_k|, \\ \Lambda_{jk} &= |\alpha_j \mathbf{R}_j + \alpha_{\mathrm{k}} \mathbf{R}_k| / \alpha_{jk}. \end{aligned} \tag{52}$$

Accordingly, the logarithmic orbital mean ionization energy (equation (24)) becomes after some manipulation

$$\begin{aligned} \ln I_{\mathrm{k}} = 2\pi N_{\mathrm{k}}^2 \, \mathrm{e}^{-2\alpha_{\mathrm{k}} R_{\mathrm{k}}^2} \int_0^{R_{\mathrm{c}}} \mathrm{e}^{-2\alpha_{\mathrm{k}} r^2} (1 - r^2/R_{\mathrm{c}}^2)^2 i_0(4\alpha_{\mathrm{k}} R_{\mathrm{k}} r) \\ \times \ln[4\pi e^2 \hbar^2 \rho(r)/m] r^2 \, \mathrm{d}r, \end{aligned} \tag{53}$$

where $\rho(r)$ is given by equation (51).

Table 9 shows, as an example, the calculated mean excitation energy for CAB orbitals of the H_2O molecule as a function of confinement radius. Figure 10(a–c) displays the behavior of the various orbital I_{k} values for all three molecules as the confinement radius varies. Note that, since each FSGO is doubly occupied, for small confinement radii ($R_{\mathrm{c}} \leq 2$ a.u.) the bond and lone-pair I_{k} values merge towards a single curve indicating a uniform behavior which would characterize an electron gas, while the core values require a smaller confinement radius to show this trend. This may be better realized from Fig. 11 for the corresponding total molecular mean ionization

Table 9. Core, bond, lone pair and total mean excitation energies for the confined H_2O molecule obtained from the OLPA/FSGO approach for different confinement radii

R (a.u.)	I_{core}	$I_{\mathrm{lone\ pair}}$	I_{bond}	I_{molecule}
0.75	529.6	302.1	301.1	357.5
1.0	484.0	227.3	225.7	263.2
1.25	447.3	159.8	157.8	195.3
1.5	430.4	127.3	125.0	161.2
2.0	411.9	88.8	85.9	119.6
2.5	404.1	71.2	67.7	98.8
3.0	400.8	63.1	58.9	88.9
4.0	399.3	58.6	53.7	83.1
6.0	399.1	57.7	52.6	81.8
8.0	399.0	57.6	52.4	81.7
∞	399.0	57.6	52.4	81.6

All energies are given in eV.

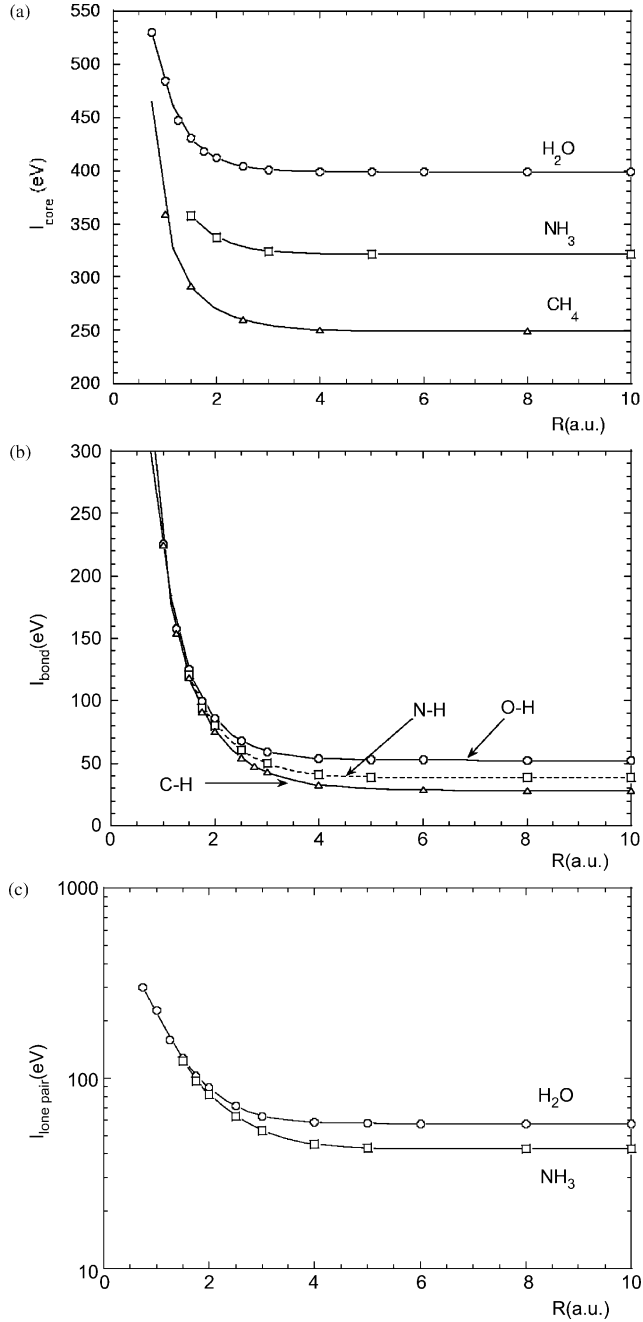

Fig. 10. Core (a), bond (b) and lone-pair (c) mean excitation energies as a function of the confinement radius for CH_4, H_2O and NH_3 (see text).

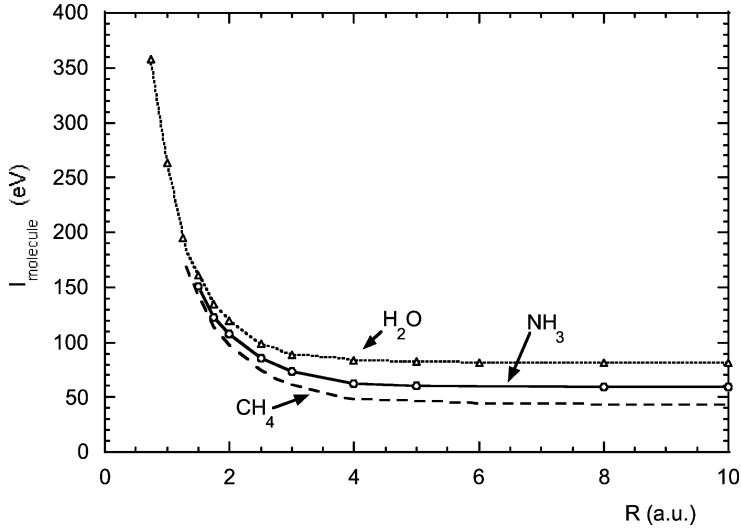

Fig. 11. Total molecular mean excitation energy for the systems CH_4, NH_3 and H_2O as function of confinement radius.

energy calculated through equation (7), noting that the three systems are isoelectronic.

Looking at molecules in a condensed phase as spatially limited by their neighbors, it is clear that the actual target-density dependence of orbital mean excitation energies brings as a consequence an interplay between chemical binding and physical phase state effects on ion stopping. We now proceed to evaluate the CAB contributions to S_e through use of equation (38). To this end, we require to calculate the isotropic momentum distribution function

$$f_k(|\mathbf{k}|) = \frac{1}{4\pi} \int \varphi_k(\mathbf{k}) \varphi_k^*(\mathbf{k}) d\Omega_k, \tag{54}$$

where $\varphi(\mathbf{k})$is the Fourier transform of equation (47)

$$\varphi_k(\mathbf{k}) = (2\pi)^{-3/2} N_k \int_{\Gamma} e^{-\alpha_k(\mathbf{r}-\mathbf{R}_k)^2} (1 - r^2/R_c^2) e^{-i\mathbf{k}\cdot\mathbf{r}} \, d^3\mathbf{r}, \tag{55}$$

and Γ indicates integration within the confinement volume. Using equation (50) and the plane-wave expansion [79]

$$e^{-i\mathbf{k}\cdot\mathbf{r}} = 4\pi \sum_{\lambda,\mu} (-1)^{\lambda} j_{\lambda}(kr) Y_{\lambda}^{\mu}(\hat{\mathbf{r}}) Y_{\lambda}^{\mu *}(\hat{\mathbf{k}}), \tag{56}$$

with $j_\lambda(z)$ the spherical Bessel function of order λ, equation (54) may be shown to become

$$f_k(k) = \left(\frac{2}{\pi}\right) N_k^2 \, e^{-2\alpha_k R_k^2} \sum_l (21+1)$$

$$\times \left[\int_0^{R_c} e^{-\alpha_k r^2} i_l(2\alpha_k R_k r) j_l(kr)(1 - r^2/R_c^2) r^2 \, dr \right]^2, \qquad (57)$$

with $k = (m/\hbar)\sqrt{v_1^2 + u^2 - 2v_1 u \cos\theta}$, (see equation (38)).

Using the I_k values obtained for each confinement radius, and inserting equation (57) into equation (38), the orbital stopping contributions may be obtained after numerical integration. The sum appearing in equation (57) converges fairly rapidly within 10^{-5} accuracy for $l \approx 10$. All necessary integrations were performed with a 96-point mesh in a Gauss–Legendre procedure.

Table 10 displays the velocity dependent core, bond and lone-pair contributions to the total molecular stopping cross-section for protons incident on H_2O at $P = 0$ (water vapor; $R_c = \infty$) and at $P \approx 4.9$ GPa ($R_c = 5$ a.u.) estimated from the energy *vs.* volume values shown in Table 11. Figure 12 shows the total molecular contribution to the proton electronic stopping cross-section as a function of proton velocity for the two pressure values cases indicated above, as compared with experimental data on the vapor and solid phase.

While a good agreement is observed with experiment for the gas phase, from the results shown in this figure it is clear that the lower stopping curve calculated for a confinement radius of 5 a.u. cannot be associated to a target

Table 10. Contribution of cores, bonds and lone pairs to the total molecular electronic stopping cross-section for protons incident on water at $P = 0$ and 4.9 GPa

v (a.u.)	S_e (core)	S_e (O–H)	S_e (LP)	S_e (4.9 GPa)	S_e (free)
0.5	0.041 (0.042)	1.668 (3.189)	1.462 (2975)	6.301	13.072
1.0	0.082 (0.083)	3.217 (5.658)	2.889 (5.306)	12.294	22.011
1.5	0.128 (0.123)	4.347 (6.905)	4.001 (6.536)	16.824	27.005
2	0.160 (0.162)	4.815 (6.952)	4.527 (6.659)	18.844	27.384
2.5	0.196 (0.198)	4.685 (6.276)	4.461 (6.079)	18.488	24.908
3	0.229 (0.232)	4.232 (5.385)	4.061 (5.258)	16.815	21.518
3.5	0.259 (0.263)	3.698 (4.551)	3.586 (4.466)	14.827	18.297
4	0.286 (0.290)	3.203 (3.856)	3.099 (3.795)	12.890	15.592
8	0.381 (0.386)	1.243 (1.407)	1.216 (1.393)	5.299	5.986

Values in parentheses correspond to the free-CAB contributions (Units: 10^{-15} eV cm^2/bond). Total S_e in units of 10^{-15} eV cm^2/molecule.

Table 11. Ground-state energy of the confined H_2O molecule as a function of cavity radius (volume) calculated through the FSGO method adapted for confined systems

R (a.u.)	V (a.u.^{3})	Total energy (hartree)
0.85	2.572	1.98276
1.0	4.189	−22.62842
1.25	8.181	−43.39037
1.5	14.137	−53.11896
1.75	22.449	−58.09729
2	33.510	−60.78203
2.5	65.450	−63.11407
3	113.097	−63.86156
4	268.083	−64.19976
5	523.598	−64.25812
6	904.778	−64.27481
10	4188.790	−64.28623
∞	∞	−64.28719

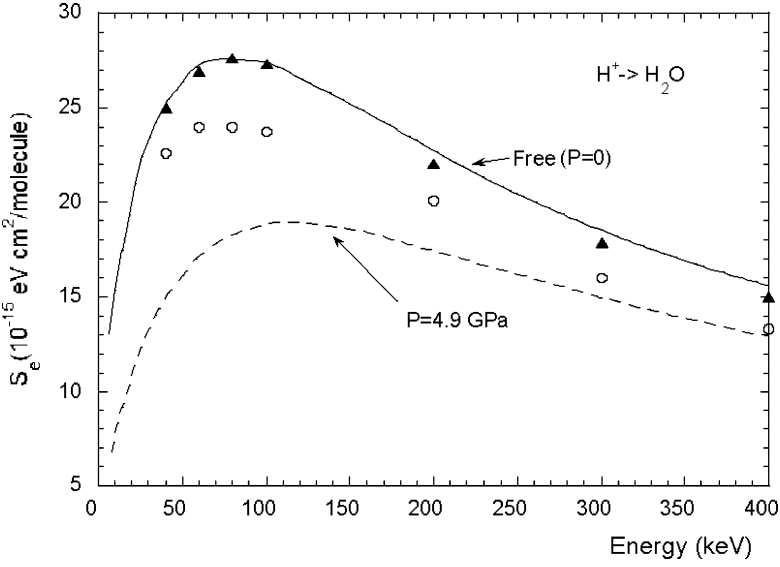

Fig. 12. Total molecular stopping cross-section of protons incident on H_2O as a function of their velocity. The solid line and the dotted line correspond to our results for the gaseous phase and the confined case, respectively. (▲) gas phase experimental results [88]. (○) Experimental results for D_2O ice [90].

density extracted from the simple relation given in equation (46). For instance, if $R_c = 5$ a.u., according to equation (46) the density would be $\rho = 0.385$ g/cm^3, almost one third of the density of liquid water at $T = 0$ °C, which is contradictory to the high pressure estimated from the energy values given in Table 11. Since pressure incorporates the dynamic change of the total molecular energy as the molecular volume is changed, we conclude with some confidence that the stopping curves obtained through the confinement model discussed so far correspond more closely to that of a target subject to high pressure. This is deemed to be true even for soft confining wall models. Indeed, the corresponding target density should then be obtained through a proper equation of state (EOS) of the medium [80]. Nonetheless, since density increases with pressure, by analyzing pressure effects on S_e we may deem qualitatively the associated effects by increasing density.

An important consequence of this analysis is that the results obtained by Xu *et al*. [69] may be fortuitous since the same system has been treated here under a more robust approach using the same cage model. For instance, for a cage size $R_c \approx 3.64$ a.u. which, according to equation (46), would correspond to a density $\rho = 0.998$ g/cm^3 of liquid water at $T = 20$ °C, the

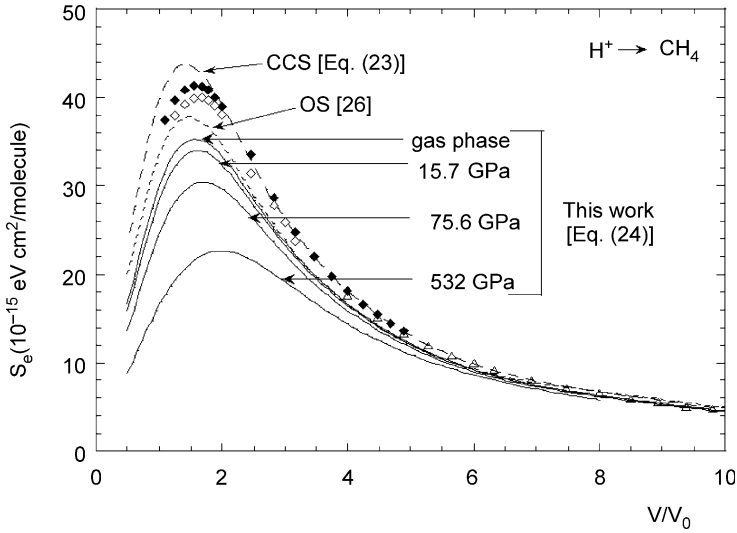

Fig. 13. Stopping cross-section of protons incident on CH_4 as a function of their velocity and for several pressures. The short dashed curve represents the theoretical predictions from Sabin and Oddershede (OS) [26]. The long dashed curve corresponds to results from Ref. [67] (Fig. 5) using equation (23) for the OLPA. Note that using the recommended equation (24) [53] for the OLPA, the result for the gas phase ($P = 0$) is now lower than the experimental data and the theoretical values of (OS). Experiment: ▲ [88]; ◇ [89]; △ [92].

energy change would lead to an associated pressure of about 200 GPa. The same conclusion may also apply to the model developed by the Köln group [68]. This aspect is of concern and deserves particular attention to draw definite conclusions on the feasibility of cage models to describe physical phase state effects on S_e.

If we consider pressure effects on the basis of the previous discussion, in Figs 13 and 14 the predicted proton stopping cross-sections for CH_4 and NH_3 are shown, respectively, as a function of proton velocity and for a set of estimated pressures [74]. The general trend of the stopping curves as pressure increases is to become lower in amplitude and to shift their maximum towards higher projectile velocities.

From this set of preliminary studies we conclude that the CAB approach together with the OLPA/FSGO scheme adapted to molecular confinement may be a useful means to study target density effects on S_e, provided an associated EOS for the medium is used to relate pressure and density. Also, since hard-wall models overestimate the energy changes as the molecular volume is reduced, it is desirable to develop more realistic confining potentials to make definitive assessments on the ability of these models to study ion stopping in condensed matter. These questions are still open and deserve special attention to explore possible extensions of the CAB model to the study of chemical binding and pressure effects in stopping power.

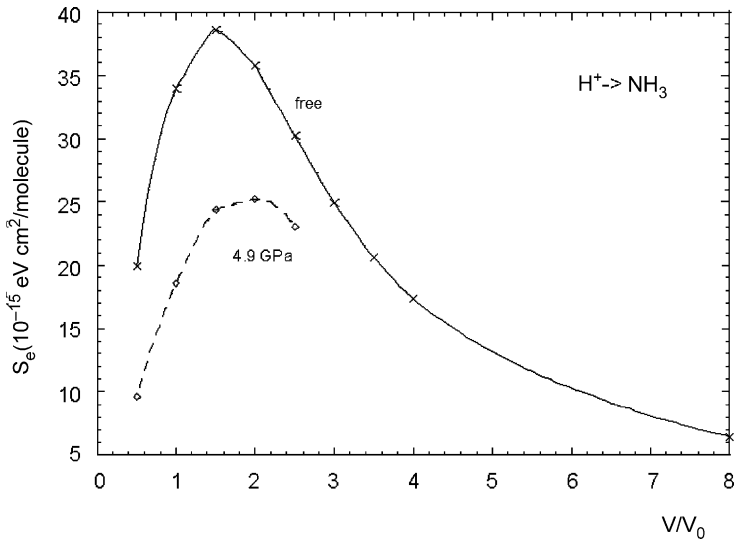

Fig. 14. Partial results for the stopping cross-section of protons incident on NH_3 as a function of their velocity and for two pressures, $P = 0$ (free) and $P = 4.9$ GPa.

5. CONCLUSIONS

The CAB approach was initially designed to calculate the electronic stopping cross-section of particles slowing down in compound materials when the Bragg's additivity rule fails. This approach is based on the analysis of a set of experimental results relative to the stopping of heavy particles (He^+ and Li^+) in organic compounds in the gaseous or in the liquid state, which leads to consider the stopping either as the sum of the stopping of characteristic groups of the molecule or as the sum of the contributions of core and valence electrons.

Even though other approaches have been developed to study phase and chemical binding effects [21,81,82], in this contribution we have focused our interest on the assessment of theoretical models which retain the features of the initial CAB approach. The Sabin–Oddershede shell-wise stopping formalism constitutes a theoretical cornerstone for the CAB approach whereby the stopping cross-section is cast as the sum of CAB orbital contributions. On the other hand, the CAB–FSGO–FIRSOV model – designed for low-energy heavy ion stopping – combines the role of characteristic groups (molecular fragments) to that of core, lone-pair and bond orbitals. Finally, the OLPA/FSGO implementation of the KT takes advantage of the natural FSGO assignment to core, bond and lone-pair orbitals and allows to extend the predictions of the original OS theory to a wider set of molecular targets. The three models seem to account reasonably well for the effect of the chemical binding on the stopping cross-section of gaseous molecular targets. However, they have severe limitations, e.g., higher order effects such as Barkas and shell corrections are not included, nor are dynamic charge states, etc. In this respect, more elaborate treatments are being considered by use of modern time-dependent quantum molecular treatments [83–86].

With regard to target density effects within the CAB approach, molecular confinement models seem attractive since they present a natural combination of both chemical binding and physical phase state effect in terms of increasing density. However, the results discussed on the assessment of these models indicate that the mere assignment of a cavity radius to enclose a molecule does not mean a specific density. In fact, the role of the cage is to induce changes in the total molecular energy – due to the actual spatial confinement – and hence estimate the pressure on the wall due to the modified electronic distribution. Accordingly, cage models provide the pressure-dependent changes in molecular properties. The corresponding density should be obtained from an EOS for the medium, if available. In spite of this difficulty, we deem that cage models may be a valuable means to explore, for instance, the influence of pressure on fission fragment track length registration and annealing in apatite, which is useful for thermochronology studies [87a–c].

REFERENCES

[1] H. Bethe, *Ann. Phys. (Leipzig)*, 1930, **5**, 325.
[2] H. Bethe, *Z. Physik*, 1932, **76**, 293.
[3] H. A. Bethe and R. Jackiw, *Intermediate Quantum Mechanics*, 3rd edn., Addison-Wesley, Massachusetts, 1997, Chapter 17.
[4] N. Bohr, *Phil. Mag.*, 1913, **25**, 10.
[5] N. Bohr, *Phil. Mag.*, 1915, **30**, 581.
[6] N. Bohr, *K. Dan Vidensk. Selsk. Mat.-Fys. Medd.*, 1948, **18** (8).
[7] J. Lindhard and M. Scharff, *K. Dan Vidensk. Selsk. Mat-Fys. Medd.*, 1953, **27** (15).
[8] J. Lindhard, *K. Dan Vidensk. Selsk. Mat.-Fys. Medd.*, 1954, **28** (8).
[9] J. Lindhard and M. Scharff, *Phys. Rev.*, 1961, **124**, 128.
[10] P. M. Echenique, R. M. Nieminen and R. H. Ritchie, *Solid State Commun.*, 1981, **37**, 79.
[11] C. C. Montanari, J. E. Miraglia and N. Arista, *Phys. Rev. A*, 2002, **66**, 042902.
[12] N. P. Wang, I. Nagy and P. M. Echenique, *Phys. Rev. B*, 1998, **58**, 2357.
[13] J. E. Miraglia and M. S. Gravielle, *Phys. Rev. A*, 2003, **67**, 062901.
[14] W. H. Bragg and R. Kleeman, *Phil. Mag.*, 1905, **10**, 318.
[15] D. I. Thwaites, *Radiat. Res.*, 1983, **95**, 495.
[16] D. I. Thwaites, *Nucl. Instrum. Methods B*, 1985, **12**, 84.
[17] D. I. Thwaites, *Nucl. Instrum. Methods B*, 1987, **27**, 293.
[18] D. I. Thwaites, *Nucl. Instrum. Methods B*, 1992, **69**, 53.
[19] W. Neuwirth and G. Both, *Nucl. Instrum. Methods B*, 1985, **12**, 67.
[20] D. Powers, *Acc. Chem. Res.*, 1980, **13**, 433.
[21] P. Bauer and D. Semrad, *Nucl. Instrum. Methods B*, 2001, **182**, 62.
[22] R. Kreutz, W. Neuwirth and W. Pietsch, *Phys. Rev. A*, 1980, **22**, 2606.
[23] J. R. Sabin and J. Oddershede, *Phys. Rev. A*, 1982, **26**, 3209.
[24] J. R. Sabin and J. Oddershede, *Phys. Rev. A*, 1984, **29**, 1757.
[25] J. Oddershede and J. R. Sabin, *Phys. Rev. A*, 1987, **35**, 3283.
[26] J. R. Sabin and J. Oddershede, *Nucl. Instrum. Methods B*, 1987, **27**, 280.
[27] J. Oddershede and J. R. Sabin, *Nucl. Instrum. Methods B*, 1989, **42**, 7.
[28] J. Oddershede and J. R. Sabin, *Int. J. Quantum Chem.: Quantum Chem. Symp.*, 1989, **23**, 557.
[29] P. Sigmund, *Phys. Rev. A*, 1982, **26**, 2497.
[30] J. F. Ziegler and J. M. Manoyan, *Nucl. Instrum. Methods B*, 1988, **35**, 215.
[31] W. Brandt and M. Kitagawa, *Phys. Rev. B*, 1982, **25**, 5631.
[32] J. F. Ziegler, J. P. Biersack, U. Littmark, *The Stopping and Range of Ions in Solids*, Pergamon Press, New York, 1985, Vol. 1.
[33] J. P. Biersack and L. G. Haggmark, *Nucl. Instrum. Methods B*, 1980, **174**, 257.
[34] H. Paul and A. Schinner, *Nucl. Instrum. Methods B*, 2003, **209**, 252.
[35] B. J. Jhanwar, W. J. Meath and J. C. F. MacDonald, *Radiat. Res.*, 1986, **106**, 288.
[36] J. L. Dehmer, M. Inokuti and R. P. Saxon, *Phys. Rev. A*, 1975, **12**, 102.
[37] M. Inokuti, T. Baer and J. L. Dehmer, *Phys. Rev. A*, 1978, **17**, 1229.
[38] M. Inokuti, J. L. Dehmer, T. Baer and J. D. Hanson, *Phys. Rev. A*, 1981, **23**, 95.
[39] See e.g., S. P. Ahlen, *Rev. Mod. Phys.*, 1980, **52**, 121.
[40] For a review, see E. Kamaratos, *Chem. Rev.*, 1984, **84**, 561.
[41] J. Geertsen, J. Oddershede and J. R. Sabin, *Phys. Rev. A*, 1986, **34**, 1104, and references therein.
[42] L. E. Porter, *Nucl. Instrum. Methods B*, 2000, **170**, 35.
[43] H. Bichsel, *Phys. Rev. A*, 2003, **65**, 052709-1 and references therein.
[44] G. D. Zeiss, W. J. Meath, J. C. F. MacDonald and D. J. Dawson, *Radiat. Res.*, 1977, **70**, 284.
[45] E. Kamaratos, *Phys. Lett.*, 1984, **104**, 419.

[46] J. W. Wilson and Y. J. Xu, *Phys. Lett.*, 1982, **90A**, 253.
[47] C. J. Tung, R. L. Shyu and C. M. Kwei, *J. Phys. D: Appl. Phys.*, 1988, **21**, 1125.
[48] D. E. Meltzer, J. R. Sabin and S. B. Trickey, *Phys. Rev. A*, 1990, **1**, 220; D. E. Meltzer, J. R. Sabin and S. B. Trickey, *Phys. Rev. A*, 1990, **42**, 666(E).
[49] R. E. Johnson and M. Inokuti, *Comments At. Mol. Phys.*, 1983, **14**, 19.
[50] W. K. Chu and D. Powers, *Phys. Lett.*, 1972, **40A**, 23.
[51] M. Ho, D. F. Weaver, V. H. Smith, R. P. Sagar and R. O. Esquivel, *Phys. Rev. A*, 1998, **57**, 4512.
[52] J. Oddershede and J. R. Sabin, *At. Data Nucl. Data Tables*, 1984, **31**, 275.
[53] D. E. Meltzer, J. R. Sabin, S. B. Trickey and J. Z. Wu, *Nucl. Instrum. Methods B*, 1993, **82**, 493.
[54] J. R. Sabin and J. Oddershede, *Nucl. Instrum. Methods B*, 1992, **64**, 678.
[55] A. A. Frost, *Theor. Chim. Acta*, 1970, **18**, 156, and references therein.
[56] R. E. Christoffersen, D. Spangler, G. G. Hall and G. M. Maggiora, *J. Am. Chem. Soc.*, 1973, **95**, 8526.
[57] P. H. Blustin, *Chem. Phys. Lett.*, 1975, **35**, 1.
[58] S. A. Cruz and J. Soullard, *Nucl. Instrum. Methods B*, 1991, **61**, 433.
[59] S. A. Cruz and J. Soullard, *Nucl. Instrum. Methods B*, 1992, **71**, 387.
[60] J. Soullard, S. A. Cruz and R. Cabrera-Trujillo, *Nucl. Instrum. Methods B*, 1993, **80/81**, 20.
[61] S. A. Cruz, J. Soullard and R. Cabrera-Trujillo, *Nucl. Instrum. Methods B*, 1993, **83**, 5.
[62] O. B. Firsov, *ZH Eksp. Teor. Fiz.*, 1959, **36**, 1517, *Sov. Phys. JETP* 1959, **9**, 1076.
[63] D. K. Brice and S. A. Cruz, *Radiat. Effects Lett.*, 1979, **43**, 143.
[64] cf. e.g., S. A. Cruz, C. Vargas-Aburto, D. K. Brice, E. V. Alonso and D. G. Armour, *Phys. Rev. A*, 1983, **27**, 2403.
[65] E. Clementi and C. Roetti, *At. Data Nucl. Data Tables*, 1974, **14**, 177.
[66] S. Y. Chu and A. A. Frost, *J. Chem. Phys.*, 1971, **54**, 760.
[67] R. Cabrera-Trujillo, S. A. Cruz and J. Soullard, *Nucl. Instrum. Methods B*, 1994, **93**, 166.
[68] G. Both, R. Krotz, K. Lohmer and W. Neuwirth, *Phys. Rev. A*, 1983, **28**, 3212.
[69] Y. J. Xu, G. S. Khandewal and J. W. Wilson, *Phys. Rev. A*, 1985, **32**, 629.
[70] L. Pauling, *The Nature of the Chemical Bond*, 3rd edn., Cornell University Press, Ithaca, NY, 1960.
[71] W. L. Luken and O. Sinanoglu, *At. Data Nucl. Data Tables*, 1976, **18**, 525.
[72] R. G. Gordon and Y. S. Kim, *J. Chem. Phys.*, 1972, **56**, 3122.
[73] S. Mateos-Cortes, E. Ley-Koo and S. A. Cruz, *Int. J. Quantum Chem.*, 2002, **86**, 376, and references therein.
[74] S. A. Cruz, J. Soullard, in preparation.
[75] S. A. Cruz, J. Soullard and E. G. Gamaly, *Phys. Rev. A*, 1999, **60**, 2207.
[76] N. H. March and M. P. Tosi, *Nuovo Cimento D*, 1996, **18**, 106.
[77] cf. e.g., W. Jaskolski, *Phys. Rep.*, 1996, **271**, 1.
[78] S. A. Cruz and J. Soullard, *Int. J. Quantum Chem.*, 2001, **83**, 271.
[79] M. Abramowitz and I. Stegun, *Handbook of Mathematical Functions*, Dover, New York, 1972.
[80] cf., e.g., R. J. Hemley, *Annu. Rev. Phys. Chem.*, 2003, **51**, 763.
[81] M. Dingfelder, M. Inokuti and H. G. Paretzke, *Radiat. Phys. Chem.*, 2000, **59**, 255.
[82] M. Bergsmann, W. Raab, G. Schrenk, F. Kastner, R. D. Muino, A. Arnau, A. Salin, P. Bauer and P. M. Echenique, *Phys. Rev. B*, 2000, **62**, 3153.
[83] J. R. Sabin, *Adv. Quantum Chem.*, 1997, **28**, 107.
[84] R. Cabrera-Trujillo, Y. Ohrn, E. Deumens and J. R. Sabin, *J. Chem. Phys.*, 2002, **116**, 2783.
[85] R. Cabrera-Trujillo, Y. Ohrn, J. R. Sabin and E. Deumens, *Phys. Rev. A*, 2002, **65**, 024901.
[86] R. Cabrera-Trujillo, J. R. Sabin, Y. Ohrn and E. Deumens, *J. Electr. Spectrosc. Relat. Phenom.*, 2003, **129**, 303.

[87] A. S. Wendt, O. Vidal and L. T. Chadderton, *Earth Planet Sci. Lett.*, 2002, **201**, 593; B. P. Kohn, D. X. Belton, R. W. Brown, A. J. W. Geadow, P. F. Green and J. F. Lovering, *Earth Planet Sci. Lett.*, 2003, **215**, 299; O. Vidal, A. S. Wendt and L. T. Chadderton, *Earth Planet Sci. Lett.*, 2003, **215**, 307.
[88] H. K. Reynolds, D. N. F. Dunbar, W. A. Wentzel and W. Whaling, *Phys. Rev.*, 1953, **92**, 742.
[89] J. T. Park and E. J. Zimmerman, *Phys. Rev.*, 1963, **131**, 1611.
[90] W. A. Wenzel and W. Whaling, *Phys. Rev.*, 1952, **87**, 499.
[91] R. A. Langley, *Phys. Rev. B*, 1975, **12**, 3575.
[92] H. Bichsel and L. E. Porter, *Phys. Rev. A*, 1982, **25**, 2499.

This Page Intentionally Left Blank

Aspects of Relativistic Sum Rules

Scott M. Cohen

Department of Physics, Duquesne University, Pittsburgh, PA 15282-0321, USA

Abstract

The status of our understanding of relativistic sum rules is reviewed. The recent development of new theoretical methods for the evaluation of these sum rules offers hope for further advances in this challenging field. These new techniques are described, along with a discussion of the source of difficulties inherent in such relativistic calculations. A connection is pointed out between certain sum rules for atomic interactions with charged particles and those for interactions with photons.

Contents

1. INTRODUCTION

In the theory of energy deposition from fast, charged particles and from photons, sums of quantum mechanical matrix elements weighted by a power of energy can play an important role [1–3]. While the matrix elements involved depend explicitly on the excited states of the system under consideration, these sums can often be shown to depend solely on properties of that system's ground state. Such a demonstration involves the use of closure, and the resulting expressions are known as 'sum rules'. In this article, I review work on these sum rules for the case of a relativistic target.

ADVANCES IN QUANTUM CHEMISTRY, VOLUME 46
ISSN: 0065-3276 DOI 10.1016/S0065-3276(04)46009-2

As an illustration of such weighted sums of matrix elements, calculations of the average energy transfer in descriptions of scattering processes lead to sums of the form

$$S = \sum_n E_{ni} |\langle n|A|i\rangle|^2, \tag{1}$$

where the sum is over all eigenstates, $|n\rangle$ with energy E_n, of the Hamiltonian describing the target system, A is an operator representing an interaction between incident particle and target, and $E_{ni} = E_n - E_i$, with E_i the energy of the target's initial state $|i\rangle$. For a dipole interaction, $A = z$, equation (1) becomes the well-known Thomas–Reiche–Kuhn (TRK) sum, whereas with $A = e^{i\vec{q}\cdot\vec{r}/\hbar}$ it is the Bethe sum, with $\vec{q}$ the momentum transferred to the target, and z and $\vec{r}$ the position operators. A non-relativistic (NR) theory of photon absorption involves the interaction $A = \vec{\varepsilon}\cdot\vec{p}\, e^{i\vec{k}\cdot\vec{r}}$, where $\vec{\varepsilon}$ and $\hbar\vec{k}$ are, respectively, the polarization and momentum of the absorbed photon, the magnitude of the latter being related to the energy transfer by $\hbar k = E_{ni}/c$. A relativistic theory for photoabsorption has a similar form, but the momentum operator $\vec{p}$ is replaced by the Dirac matrix, $\vec{\alpha}$.

In NR theories, evaluation of these sums is often quite simple. One need only remember the Schrödinger equation, $H|n\rangle = E_n|n\rangle$, and the closure relation, $\sum_n |n\rangle\langle n| = \mathcal{I}$ with $\mathcal{I}$ the identity operator, where the sum extends over the complete set of states of the Hamiltonian. For a single particle bound in a static potential, we have the Schrödinger Hamiltonian

$$H_S = \frac{p^2}{2m} + V. \tag{2}$$

Then, using $A = z$, the TRK sum rule is

$$\begin{aligned} S_1 &\equiv \frac{2m}{\hbar^2} \sum_n E_{ni} \langle i|z|n\rangle\langle n|z|i\rangle \\ &= \frac{m}{\hbar^2} \sum_n \left(\langle i|z|n\rangle\langle n|[H_S, z]|i\rangle + \langle i|[z, H_S]|n\rangle\langle n|z|i\rangle\right) \\ &= \frac{m}{\hbar^2} \langle i|[z, [H_S, z]]|i\rangle = 1. \end{aligned} \tag{3}$$

In this chapter, I will discuss the effects of relativity on this and other sum rules. Unlike their NR counterparts, calculations of relativistic sum rules are fraught with difficulties. These difficulties can generally be traced to the presence of negative energy states, or from another point of view, the existence of positrons. Let us see what happens if we simply replace H_S in equation (3) by the Dirac Hamiltonian

$$H_D = (\beta mc^2 + c\vec{\alpha}\cdot\vec{p} + V). \tag{4}$$

Then,

$$S_1 = \frac{m}{\hbar^2}\langle i|[z,[H_{\mathrm{D}},z]]|i\rangle = 0, \tag{5}$$

a result of the fact that H_{D} is linear in the momentum operator. There is obviously no way that this result can reduce to that obtained in the NR calculation, indicating that there is something seriously wrong. It is not difficult to show that transitions into final states $|n\rangle$ of negative energy have precisely canceled transitions into those with energies that are positive [4]. In a relativistic theory and assuming the system is initially in its ground state, the negative energy states are all filled ('Dirac sea'), so that transitions into these states are specifically forbidden by Pauli's exclusion principle. Of course, our naive approach utilizing closure in the Dirac representation automatically includes these forbidden transitions. To obtain sensible results for relativistic sum rules, a method must be found to impose the exclusion principle by projecting out the negative energy states.

The case of photoabsorption has additional difficulties, since the operator A appearing in the matrix elements then includes an exponential of E_{ni}. One might again try eliminating the explicit dependence on E_n in favor of H, by

$$\mathrm{e}^{\mathrm{i}E_{ni}z/\hbar c}|n\rangle = \mathrm{e}^{\mathrm{i}(H-E_i)z/\hbar c}|n\rangle, \tag{6}$$

but because of the fact that H and z do not commute, this relation is not even correct. Therefore, as will be discussed below, calculations of photoabsorption sum rules have resorted to expansions of the exponential in powers of $E_{ni}z$, under the assumption of long-wavelengths, and keeping only the first few terms in the expansion.

The outline of the chapter is as follows: in Section 2, I discuss how studies of interactions between atoms and charged particles or photons lead to a consideration of sum rules. In Section 3, I review early efforts to evaluate these sum rules using a relativistic model of the target. Following this in Section 4, I present the results of my own work on this subject, studying the relativistic Bethe sum rule in the context of stopping power or mean energy loss from charged projectiles. I also demonstrate a close relationship between other sums that arise in the context of charged particle scattering and those related to studies of photon absorption. In Section 5, I consider relativistic sum rules from the perspective of Dirac's hole theory, and offer some thoughts on how the infinities present in this theory – of energy and of the number of electrons – lead to difficulties similar to those described above in the context of a single-particle theory. Finally, a conclusion is given in Section 6.

2. ORIGIN OF SUM RULES

In this section, I review basic ideas concerning interactions between atoms and either charged particles or photons, and show how sum rules arise in such contexts. I begin in Section 2.1 with a discussion of the interaction of fast, charged particles with matter, and then in Section 2.2 describe the case of photoabsorption.

2.1. Scattering of fast, charged particles

In the first-Born approximation, the differential scattering cross-section (DCS) for an excitation of the target to a state of energy E_n by a fast, charged projectile may be written in the Coulomb gauge as [5]

$$\mathrm{d}\sigma_n = \frac{2\pi z^2\,\mathrm{e}^4}{mv^2}\left\{\frac{|F_n|^2}{Q^2(1+Q/2mc^2)^2} + \frac{|\vec{\beta}_t\cdot\vec{G}_n|^2}{[Q(1+Q/2mc^2) - E_{ni}^2/2mc^2]^2}\right\} \times\left(1+\frac{Q}{mc^2}\right)\mathrm{d}Q. \tag{7}$$

Here, $\vec{v}$ is the initial velocity, and z the atomic number, of the projectile, and $Q = \sqrt{m^2c^4 + q^2c^2} - mc^2$ is known as the recoil energy. The component of $\vec{\beta} = \vec{v}/c$ perpendicular to $\vec{q}$ is denoted by $\vec{\beta}_t$. The quantities, F_n and $\vec{G}_n$ in equation (7), are defined by

$$F_n = \sum_{j=1}^{Z}\langle n|\mathrm{e}^{\mathrm{i}\vec{q}\cdot\vec{r}_j/\hbar}|i\rangle \tag{8}$$

$$\vec{G}_n = \sum_{j=1}^{Z}\langle n|\mathrm{e}^{\mathrm{i}\vec{q}\cdot\vec{r}_j/\hbar}\vec{\alpha}_j|i\rangle, \tag{9}$$

where Z is the atomic number of the target atoms. The first term in equation (7) is referred to as the longitudinal interaction and may readily be derived using the static, unretarded Coulomb interaction. The other term, containing $\vec{G}_n$, corresponds to the exchange of a single, transverse photon and is referred to as the transverse interaction.

Use of equation (7) leads to consideration of sums in various contexts. An important example is the calculation of the stopping power, or mean energy loss per unit pathlength from the projectile [6,7]. This is found from $\mathrm{d}\sigma_n$ as

$$-\frac{\mathrm{d}E}{\mathrm{d}x} = {\sum_n}' E_{ni}\int \mathrm{d}\sigma_n, \tag{10}$$

and the prime on the summation symbol means the sum is restricted by energy conservation, such that there is a maximum energy transfer,

$E_{ni} < E_{\max}$. From equation (7), it is seen that the above equation involves an integral over the recoil energy. It turns out from kinematic considerations that the range of this integration is $Q_m < Q < Q_{\max}$, where the minimum is related to the energy transfer as $Q_m = E_{ni}^2/2mv^2$, and $Q_{\max} = 2mv^2(M/m)^2$, with M the projectile mass [1,5]. Since the sum does not include a complete set of states of the target system, closure may not immediately be used to perform the summation. Nonetheless, it has been argued [5] that it is a good approximation to extend this sum to include all energies, $\sum' \to \sum_n$, as long as one also replaces the upper limit of the Q-integral with $Q_{\mathrm{M}} = 2mv^2/(1 - v^2/c^2)$. The errors incurred by this replacement are part of the much studied shell corrections [8–11].

When $v \ll c$, only the longitudinal interaction is important, and then

$$-\frac{\mathrm{d}E}{\mathrm{d}x} = \sum_n E_{ni} \int_{Q_m}^{Q_{\mathrm{M}}} \frac{|F_n(\vec{q})|^2}{Q^2(1 + Q/2mc^2)^2}(1 + Q/mc^2)\mathrm{d}Q. \qquad (11)$$

It is advantageous to perform the summation before the integration, but one must first account for the fact that the lower limit of integration depends explicitly on E_n. A common approach is to split the Q-integral into two parts: the low- and high-Q regimes, separated by a cut-off, Q_{c}. Then the integration limits for the high-Q regime do not depend on the energy of the excited state, and the order of summation and integration may be interchanged in the expressions for these integrated quantities. Thus, we are led to the consideration of the Bethe sum [12]

$$S_1(Q) = \sum_n E_{ni}|F_n(\vec{q})|^2 = \sum_{j=1}^{Z} \sum_n E_{ni}|\langle n|\mathrm{e}^{\mathrm{i}\vec{q}\cdot\vec{r}_j/\hbar}|i\rangle|^2, \qquad (12)$$

where I have followed Bethe in neglecting the small correlation terms involving two different electrons.

For the low-Q region, the integration must be done first. To accomplish this, a long-wavelength approximation is introduced by expanding the exponential in $F_n(\vec{q})$ as $\mathrm{e}^{\mathrm{i}\vec{q}\cdot\vec{r}_j} \approx 1 + \mathrm{i}\vec{q}\cdot\vec{r}_j$. Then, neglecting terms $\mathcal{O}(Q/mc^2)$ gives $F_n(\vec{q}) \approx Qf_n/E_{ni}$, with the optical dipole oscillator strength defined as

$$f_n = \frac{2mE_{ni}}{\hbar^2}\left|\sum_j \langle n|z_j|i\rangle\right|^2. \qquad (13)$$

This leads to the TRK sum rule, which for a system of Z electrons is

$$S_1 = \sum_n f_n = \lim_{q\to 0} \frac{2m}{q^2} S_1(Q) = Z. \qquad (14)$$

For a relativistic projectile, the transverse part of the DCS must also be included. The appearance of E_{ni} in the denominator of this term complicates

its treatment in terms of sum rules. I have recently shown how to treat the high-Q case by expanding the denominator in powers of the small quantity $(Q - E_{ni})/Q$ [13], leading to sums of the form

$$\mathcal{T}^{(\nu)}(Q) = \sum_{j=1}^{Z} \sum_{n} (Q - E_{ni})^{\nu} |\langle n|e^{i\vec{q}\cdot\vec{r}_j/\hbar} \vec{\beta}_t \cdot \vec{\alpha}_j |i\rangle|^2. \tag{15}$$

For the low-Q case, expansion of the denominator is not appropriate, since $Q - E_{ni}$ and Q may be comparable in magnitude. When the target system is non-relativistic, Fano showed that the transverse contribution is proportional to S_1 for small Q. In the case of a relativistic target, I have also shown [13] that Fano's approach must be generalized, as will be discussed in Section 4.2.

2.2. Photon interactions

The study of sum rules for photon–matter interactions grew out of a conjecture by Gell-Mann, Goldberger, and Thirring (GGT) [14]. In the course of investigating the implications of causality on quantum theory and, in particular, on scattering amplitudes derived from field theory, these authors arrived at a dispersion relation between the dispersive and absorptive parts of the photon forward scattering amplitude. Let us now look at how this leads to sums that are quite similar to those discussed in Section 2.1.

In their paper, GGT considered the matrix element of the S matrix, $S = 1 - iR$, for scattering of a photon of four-momentum k'' and polarization σ into one of four-momentum k' and polarization λ, by a matter system which is ultimately left with its energy unchanged. They wrote

$$\begin{aligned} \langle \lambda k' f|R|i\sigma k''\rangle &= -i \int_{-\infty}^{\infty} d^4x' \int_{-\infty}^{\infty} d^4x'' \langle \lambda k' f|V(x')V(x'')|i\sigma k''\rangle \eta(t' - t'') \\ &\equiv F^{fi}_{\lambda\sigma}(k', k''), \end{aligned} \tag{16}$$

with the step function $\eta(t' - t'')$ vanishing unless $t' > t''$, in which case it is unity. The interaction potential is

$$V(x) = -\vec{j}(x)\cdot\vec{A}(x), \tag{17}$$

where the current operator $\vec{j}$ and the transverse vector potential,

$$\vec{A}(x) = \int d^3k \sum_{s=1}^{2} \left[a_{\vec{k}s} \vec{\varepsilon}_s \, e^{i(\vec{k}\cdot\vec{x} - \omega t)} + a^{\dagger}_{\vec{k}s} \vec{\varepsilon}_s \, e^{-i(\vec{k}\cdot\vec{x} - \omega t)} \right], \tag{18}$$

are operators in the interaction representation. The operator $a^{\dagger}_{\vec{k}s}$ ($a_{\vec{k}s}$) creates (annihilates) a photon with momentum $\hbar\vec{k}$, frequency $\omega = kc$, and polarization $\vec{\varepsilon}_s$ perpendicular to $\vec{k}$.

Since the initial and final states each have a single photon present and V creates or annihilates one photon, it is clear that in equation (16), there are two possible ways for the system to pass from the initial to the final state. Either a photon is first emitted and then one is later absorbed, or *vice versa*. This yields two separate terms in equation (16), from which the scattering amplitude becomes [14]

$$F^{fi}_{\lambda\sigma}(k',k) = \sum_n \int \mathrm{d}^3x' \int \mathrm{d}^3x'' \left[\frac{\langle f|j_\lambda(\vec{x}')|n\rangle\langle n|j_\sigma(\vec{x}'')|i\rangle}{E_i + \hbar\omega - E_n + \mathrm{i}\varepsilon} \mathrm{e}^{-\mathrm{i}\vec{k}\cdot\vec{x}' + \mathrm{i}\vec{k}'\cdot\vec{x}''} + \frac{\langle f|j_\sigma(\vec{x}')|n\rangle\langle n|j_\lambda(\vec{x}'')|i\rangle}{E_i - \hbar\omega - E_n + \mathrm{i}\varepsilon} \mathrm{e}^{\mathrm{i}\vec{k}\cdot\vec{x}' - \mathrm{i}\vec{k}'\cdot\vec{x}''} \right]. \tag{19}$$

By considering the analytic properties of this quantity, GGT derived the following dispersion relation between the real (Re) or dispersive and the imaginary (Im) or absorptive parts of the forward scattering amplitude for photons of frequency ω:

$$\begin{aligned} \mathrm{Re}\, f(\omega) - \mathrm{Re}\, f(0) &= \frac{2\omega^2}{\pi} P \int_0^\infty \mathrm{d}\omega' \frac{\mathrm{Im}\, f(\omega')}{\omega'(\omega'^2 - \omega^2)} \\ &= \frac{\omega^2}{2\pi^2} P \int_0^\infty \mathrm{d}\omega' \frac{\sigma_{\mathrm{abs}}(\omega')}{\omega'^2 - \omega^2}, \end{aligned} \tag{20}$$

where $f(\omega) = F^{ii}_{\lambda\lambda}(k,k)$, P denotes the principal value of the integral, and use has been made of the optical theorem, $\mathrm{Im}\, f(\omega) = \omega\sigma_{\mathrm{abs}}(\omega)/4\pi$, with $\sigma_{\mathrm{abs}}(\omega)$ the total absorption cross-section for a photon of frequency, ω. For scattering from bound electrons, $\mathrm{Re}\, f(0) = 0$ (Rayleigh scattering). Then, with the conjecture that for $\omega \to \infty$, $f(\omega)$ approaches its free electron value

$$\mathrm{Re}\, f(\infty) = -e^2/m, \tag{21}$$

GGT obtain the sum rule

$$\int_0^\infty \mathrm{d}\omega\, \sigma_{\mathrm{abs}}(\omega) = \frac{2\pi^2 e^2}{m}. \tag{22}$$

As I will now demonstrate, this is closely related to the TRK sum rule, equation (3). For a single NR electron, we have

$$\vec{j}(\vec{x}) = \frac{e}{2m} \{\vec{p}, \delta(\vec{x} - \vec{r})\} \tag{23}$$

Then the total photoabsorption cross-section may be found directly from equation (19) and the optical theorem, and is given by

$$\sigma_{\mathrm{abs}}(\omega) = \frac{4\pi^2 e^2}{m^2\omega} \sum_n |\langle n|p_x\, \mathrm{e}^{\mathrm{i}kz}|i\rangle|^2 [\delta(\hbar\omega - E_{ni}) + \delta(\hbar\omega + E_{ni})], \tag{24}$$

where I have taken the polarization λ along the x-direction and the momentum $\vec{k}$ along z. If the system is initially in its ground state, $E_{ni} > 0$, and the second delta function will not contribute for positive frequencies. Then, expanding the exponential, we obtain

$$\int_0^\infty d\omega\, \sigma_{\text{abs}}(\omega) = \frac{4\pi^2 e^2 \hbar}{m^2} \sum_n \frac{1}{E_{ni}} \left(|\langle n|p_x|i\rangle|^2 + \frac{E_{ni}^2}{\hbar^2 c^2} |\langle n|p_x z|i\rangle|^2 - \frac{E_{ni}^2}{2\hbar^2 c^2} \left[\langle n|p_x|i\rangle\langle n|p_x z^2|i\rangle + \text{H.c.} \right] \right), \tag{25}$$

with H.c., the hermitian conjugate. The first term in parentheses is the dipole term $E1$, the next is the quadrupole $E2$, and the remaining terms represent retardation effects on the dipole interaction, denoted as $E1^{\text{ret}}$.

In the dipole approximation only the first term is kept, and using the identity $p_x = im[H, x]/\hbar$, we see that the GGT sum rule, equation (22), becomes

$$\frac{2m}{\hbar^2} \sum_n E_{ni} |\langle n|x|i\rangle|^2 = 1, \tag{26}$$

which is just the dipole oscillator strength sum rule of TRK, as claimed. The important point is that equation (22) is much more general in that it has been derived without the assumptions of long wavelengths, a dipole interaction, and a NR matter system. Unfortunately, as we will discuss in the following section, the conjecture equation (21) is incorrect and so is the GGT sum rule.

3. REVIEW OF EARLY WORK

The conjecture of GGT was based on the notion that for very high-energy photons, one might reasonably suppose that the binding energy of the electron will have little import, and can, therefore, be neglected. Nonetheless, GGT expressed concern about the correctness of this conjecture. In particular, they pointed out that the photoelectric cross-section was then believed to have a $1/\omega$ dependence at high frequencies, leading to a logarithmic ω-dependence on the right-hand side of equation (20).

The apparent divergence of $\text{Re}\, f(\omega)$ at large ω can be circumvented by introducing a procedure that was originally suggested by Brown [15]. This procedure involves defining the relevant cross-section as the difference between the photoelectric cross-section and σ_{pps}, the cross-section for pair production in which the electron of the pair is produced in the occupied 1s

state. As was later discussed in detail by Erber [16], this definition of the cross-section corresponds to scattering by the bound electron, alone. That is, it is in fact the difference between the cross-section for a one-electron atom and that for an isolated proton [16]. Erber then argues that the logarithmic dependence of the dispersive amplitude that was mentioned above is exactly canceled by this subtraction procedure. It should be noted that along with this subtraction of cross-sections, one must include a corresponding subtraction of forward scattering amplitudes, which has also been carefully discussed by Erber [16]. As is shown in his equation (3.1), the correct amplitude is not then obtained directly from the scattering amplitude of GGT (equation (19)). Rather, by carefully considering the various processes involved in scattering from the atom and also from the free proton, and in particular, the processes involving creation and annihilation of electron–positron pairs, Erber has argued that the correct amplitude requires the replacement of $i\varepsilon$ by $-i\varepsilon$ in the second term of our equation (19) (compare Erber's equation (3.1)).

Shortly after publication of the paper by GGT, Levinger and co-workers, using the Brown/Erber procedure, showed that the conjecture, equation (21), still turns out to be incorrect [4,17,18]. These authors began [17,18] with numerical studies of the dipole oscillator strengths for a single electron in the field of a Pb nucleus undergoing transitions from the 1s into higher discrete states. They found that the retarded, relativistic oscillator strengths for these discrete transitions were only about 80% of their NR values [17]. For transitions to the continuum states, they obtained values from the work of Brown [19,20] and Hulme [21]. Including Jacobsohn's NR calculations of the electric quadrupole transitions ($E2$) [22], they found a summed oscillator strength of approximately 0.86, in stark contrast to the value of unity predicted by GGT (inclusion of retardation in $E2$ changes this value to 0.87 [4]). They argued that this result should be accurate to within a few percent, even considering the neglect of higher multipoles.

The following year, Levinger *et al.* addressed this question through the evaluation of sum rules [4]. To overcome the difficulties arising from the existence of negative energy states, these authors used a semi-relativistic Hamiltonian, which does not have the negative energy eigenstates of the original Dirac Hamiltonian. The important difference between their Hamiltonian and H_S is the inclusion of the mass-variation term, $H_m = -p^4/8m^3c^2$ (other correction terms in their Hamiltonian are at most linear in the momentum operator, and therefore, do not contribute to the sum rule). Since the negative energy states have already been removed, the Brown/Erber subtraction procedure discussed above is not appropriate here (nor is it needed in the related sum rule calculations discussed below), since that procedure is specifically related to pair production, which is not included in this approach.

For the unretarded $E1$ term, H_{m} adds a relativistic correction of (see equation (3))

$$E1^{\mathrm{rel}} = -\frac{1}{8m^2c^2\hbar^2}\langle i|[z,[p^4,z]]|i\rangle = -\frac{5}{3mc^2}T_0 \tag{27}$$

for an isotropic initial state, with $T_0 = \langle i|p^2/2m|i\rangle$. Using this same Hamiltonian, the $E2$ contribution was calculated relativistically, as were the retardation effects, $E1^{\mathrm{ret}}$, on the dipole transitions. They found

$$E2 = \frac{2}{3mc^2}T_0 + \frac{1}{15mc^2}\left\langle i\left|\left(r^2\frac{\mathrm{d}^2V}{\mathrm{d}r^2} + 4r\frac{\mathrm{d}V}{\mathrm{d}r}\right)\right|i\right\rangle, \tag{28}$$

and

$$E1^{\mathrm{ret}} = -\frac{1}{15mc^2}\left\langle i\left|\left(r^2\frac{\mathrm{d}^2V}{\mathrm{d}r^2} + 4r\frac{\mathrm{d}V}{\mathrm{d}r}\right)\right|i\right\rangle. \tag{29}$$

The terms involving V in $E2$ are exactly canceled by $E1^{\mathrm{ret}}$. This is one illustration of the well-known fact that higher multipoles and retardation each contribute at the same order of magnitude as relativistic effects, and that it is inconsistent to include one without the others [23,24].

Combining results, these authors obtained

$$f(\infty) = -\frac{e^2}{m}\left(1 - \frac{T_0}{mc^2}\right) \approx -\frac{e^2}{(m + T_0/c^2)} \tag{30}$$

for the GGT sum rule. They pointed out that the presence of T_0 in the denominator represents the increase of mass due to the electron's kinetic energy, consistent with the fact that its presence results directly from inclusion of H_{m} in the Hamiltonian. To obtain a numerical result, they used the value, $T_0/mc^2 = Z^2\alpha^2/2 = 0.18$ for Pb, with α the fine structure constant. This yields a summed oscillator strength of 0.82, in satisfactory agreement with their earlier result of 0.87 [18]. They observed that exact agreement should not be expected, due to the approximate nature of their numerical calculations [17,18], as well as the neglect of contributions $\mathcal{O}(Z^4\alpha^4)$ in the sum rule calculations.

The above result was confirmed a decade later by Goldberger and Low [25], who calculated the forward scattering amplitude in the limit of very high photon energies. They obtained the result

$$f(\infty) = -\frac{e^2}{m}\left(1 - \frac{Z^2\alpha^2}{2} + \frac{5Z^4\alpha^4}{24} + \cdots\right), \tag{31}$$

which is in agreement with equation (30) to lowest order. An exact expression for $f(\infty)$ in terms of quadratures was also derived [25].

Over the next several years, a number of papers considered the integrated photoabsorption cross-section [26–30], using analytical methods based on closure and generalizing the sum rules by (a) including a world-scalar potential and utilizing the Foldy–Wouthuysen transformation (FWT) [31] to obtain a semi-relativistic Hamiltonian [27], and (b) studying a many-electron system with interactions [28]. In spite of Levinger's work [4,17,18], Gerasimov concluded that the GGT sum rule, equation (22), was in fact correct [29]. By studying specific models, Matsuura [28] obtained results in agreement with Levinger's [4], and pointed out that Gerasimov had incorrectly assumed that $f(\omega)$ is analytic everywhere except on the real ω-axis, invalidating his conclusions.

In 1985, Schmitt and Arenhövel [32] studied the GGT sum, using both analytical and numerical techniques. For the analytical efforts, they studied the leading relativistic corrections to the sum rule in three different models of the target particle: (a) NR or Schrödinger, (b) Foldy–Wouthuysen (FW) using the FWT [31] to obtain a semi-relativistic model, and (c) Dirac using H_{D} and introducing projection operators to exclude contributions from the negative energy states. In the latter case, they used an expansion of the projection operators in powers of H_{D}/mc^2, so those results are also semi-relativistic. Their use of the FWT to transform the multipole operators for the FW model represented a technical improvement over previous efforts [4,27], wherein only the Hamiltonian and states had been transformed. Nonetheless, all their results were in agreement with that of the earlier work.

These authors also numerically calculated $f(\infty)$, using the exact (fully relativistic) expression of Goldberger and Low (see equation (4.1) of Ref. [25]) for a particle in a square well. Their results were such that $f(\infty)$ and the FW calculation of the GGT sum differed by an insignificant amount (less than 0.1%). The implications of this result for our understanding of relativistic effects is not completely clear, however, since their chosen binding energies are rather small, being at most about 5% of the particle's rest energy. Nonetheless, they did find a small, but significant, contribution to the GGT sum from the pair production term, σ_{pps}.

Shortly thereafter, Leung *et al.* [33] considered relativistic corrections to the Bethe sum rule. In a NR theory, this sum can be readily evaluated exactly including all multipoles:

$$S_1(Q) = \sum_n E_{ni} |\langle n | \mathrm{e}^{\mathrm{i}\vec{q}\cdot\vec{r}/\hbar} | i \rangle|^2 = \langle i | \mathrm{e}^{-\mathrm{i}\vec{q}\cdot\vec{r}/\hbar} [H_{\mathrm{S}}, \mathrm{e}^{\mathrm{i}\vec{q}\cdot\vec{r}/\hbar}] | i \rangle = Q, \quad (32)$$

where I have again assumed an isotropic initial state. To obtain the relativistic corrections, Leung *et al.* [33] used an approach similar to that of Ref. [27], performing the FWT on H_{D} for a one-electron system, obtaining

$$S_1(Q) = Q\left(1 - \frac{5}{6m^2c^2} \langle \tilde{\imath} | p^2 | \tilde{\imath} \rangle\right), \quad (33)$$

where $|\tilde{\imath}\rangle$ is the transformed initial state, and terms $\mathcal{O}(Q^3)$ and $\mathcal{O}(Q^2p^2)$ were neglected. Leung later used this result [34] to obtain the leading relativistic corrections to the Bethe stopping power. Note that this result is obtained by transforming the Hamiltonian and states, alone, while leaving the operator $e^{i\vec{q}\cdot\vec{r}/\hbar}$ unchanged. Thus, this procedure is inconsistent in its treatment of the various operators. We can also see that the result is incorrect by comparing to that for a relativistic free particle at rest [5]

$$S_1^0(Q) = \frac{Q(1 + Q/2mc^2)}{(1 + Q/mc^2)} \approx Q(1 - Q/2mc^2). \tag{34}$$

The result of equation (33) should reduce to this expression if the expectation value of p^2 is set to zero, and is thus seen to be missing the term proportional to Q^2. A proper treatment using the FWT and transforming all operators was later formulated [35], obtaining

$$S_1(Q) = Q\left(1 - \frac{5}{6m^2c^2}\langle\tilde{\imath}|p^2|\tilde{\imath}\rangle - Q/2mc^2\right), \tag{35}$$

in agreement with equation (34). Other sums, involving various moments of the energy transfer, were also evaluated [35].

It was suggested in Ref. [33] that the use of a no-pair Hamiltonian [36] and/or field-theoretic techniques might be useful for the consideration of many-electron atoms. Such techniques were later used by Aucar *et al.* [37] in their work on the relativistic corrections to the Bethe sum. They introduced a second-quantized no-pair Hamiltonian and projected the operator $e^{i\vec{q}\cdot\vec{r}_j/\hbar}$ onto the space of positive energy states, thereby excluding transitions into the negative energy states. These authors mention that it is straightforward to use their approach for the case of a many-electron atom, but they explicitly consider only the one-electron case. Unfortunately, although the techniques used in this approach are formidable, it does not appear to the present author that there is any simple way to obtain detailed results from their expressions, which are still in the form of a sum over a complete set of eigenstates of the Hamiltonian.

4. RECENT ADVANCES

4.1. Relativistic Bethe sum rule

In this section, I describe the work I have recently done on the relativistic Bethe sum rule. I will discuss the FWT [31], derive a formally exact expression for the sum rule, and then explain why the results of Refs. [33,35] are only valid when q is small. I will also show how to obtain an exact treatment of the q-dependence of the Bethe sum rule, using an FWT-type

transformation introduced by Douglas and Kroll [38]. When combined with the evaluation of sum rules for the transverse part of the DCS, these results permit the calculation of relativistic corrections to the stopping power that are valid for a fully relativistic projectile [13]. At the end of this section, I outline a method that appears to give highly accurate expressions for the TRK and Bethe sums even for very strongly bound systems.

To implement the FWT, one inserts the identity operator in the form of $e^{-iU}\, e^{iU}$, with U chosen to be Hermitian so that e^{iU} is unitary. For this preliminary discussion, I will assume that U is the exact FWT operator for a general many-electron Hamiltonian H. Then, for example,

$$\langle n|H\, e^{i\vec{q}\cdot\vec{r}_j/\hbar}|i\rangle = \langle n|e^{-iU}\, e^{iU} H\, e^{-iU}\, e^{iU}\, e^{i\vec{q}\cdot\vec{r}_j/\hbar}\, e^{-iU}\, e^{iU}|i\rangle. \tag{36}$$

Thus, e^{iU} induces a canonical transformation of the states and operators, with the identification, $|\tilde{n}\rangle = e^{iU}|n\rangle$ and $\tilde{H} = e^{iU} H\, e^{-iU}$. Then, defining $\vec{q}$-dependent operators through the replacement of $\vec{p}_j$ by $\vec{p}_j + \vec{q}$ due to a transformation of the form, $\mathcal{M} \rightarrow \mathcal{M}(\vec{q}) = e^{-i\vec{q}\cdot\vec{r}_j/\hbar}\mathcal{M}\, e^{i\vec{q}\cdot\vec{r}_j/\hbar}$, we have

$$\langle n|H\, e^{i\vec{q}\cdot\vec{r}_j/\hbar}|i\rangle = \langle\tilde{n}|e^{i\vec{q}\cdot\vec{r}_j/\hbar}\tilde{H}(\vec{q})(e^{iU(\vec{q})}\, e^{-iU})|\tilde{\imath}\rangle. \tag{37}$$

The FWT operator, e^{iU}, is chosen so as to bring the Hamiltonian into a 'block diagonal' form, explicitly separating the positive and negative energy subspaces. Now these positive energy states are still four-component spinors, but their third and fourth components vanish. Therefore, though $e^{iU(\vec{q})}e^{-iU}$ is a 4×4 operator, only its upper-left 2×2 block will contribute to the matrix elements in our sum. Defining this block to be R_j, we then have

$$\langle n|[H, e^{i\vec{q}\cdot\vec{r}_j/\hbar}]|i\rangle = \langle\tilde{n}|e^{i\vec{q}\cdot\vec{r}_j/\hbar}(\tilde{H}(\vec{q})R_j - R_j\tilde{H})|\tilde{\imath}\rangle, \tag{38}$$

and

$$\langle i|e^{-i\vec{q}\cdot\vec{r}_j/\hbar}|n\rangle = \langle\tilde{\imath}|R_j^{\dagger}\, e^{-i\vec{q}\cdot\vec{r}_j/\hbar}|\tilde{n}\rangle, \tag{39}$$

which when combined and summed, yield a formally exact expression [13] for the Bethe sum, equation (12)

$$S_1(Q) = \sum_{j=1}^{Z}\langle\tilde{\imath}|R_j^{\dagger}(\tilde{H}(\vec{q})R_j - R_j\tilde{H})|\tilde{\imath}\rangle. \tag{40}$$

To this point, I have assumed that U is the exact FWT operator. However, given that this operator is not known for the case of bound electrons, it will eventually be necessary to introduce approximations for e^{iU}. Nonetheless, the fact that equation (40) is an exact result for the sum rule implies that the excited states have been treated exactly, and an approximate treatment of the operators appearing in the resultant expectation value does not alter this conclusion. In particular, this expression remains valid even when a semi-relativistic approximation to the FWT is used under circumstances for

which the original summation includes significant contributions from highly relativistic states $|n\rangle$, such as with very large values of Q.

Let us now see why the approximations used in Refs. [33,35] for a single electron yield results that are only valid when q is small. These authors used the approximation of Ref. [31]

$$e^{iU} = \cdots e^{iU_3}\, e^{iU_2}\, e^{iU_1}, \tag{41}$$

which involves an expansion in powers of the small quantities p/mc and V/mc^2, with $U_N \sim \mathcal{O}(1/m^N)$. The calculation of the FW Hamiltonian [31] then proceeds by an expansion in powers of the U_N. For example, the first step of the FWT gives

$$H_1 \equiv e^{iU_1} H\, e^{-iU_1} = H + i[U_1, H] - \tfrac{1}{2}[U_1, [U_1, H]] + \cdots, \tag{42}$$

which is an expansion in powers of p/mc, since $U_1 = -i\beta\vec{\alpha}\cdot\vec{p}/2mc$. Higher order corrections to the Hamiltonian are obtained from U_2 and U_3 in a similar fashion [31]. Now, $H_1(\vec{q})$ is obtained from H_1 by the replacement of $\vec{p}$ by $\vec{p} + \vec{q}$. This means that the above expansion in powers of p/mc leads directly to an expansion in powers of q/mc. Since this approach has started out with a p-expansion, it ends up with a q-expansion and is, therefore, incapable of handling large values of q. Therefore, unlike the NR Bethe sum rule, the relativistic corrections of Refs. [33,35] do not include contributions from all multipoles. In fact, the difference between the free and bound particle results, given in equations (34) and (35), arises only from the dipole contributions. Therefore, the latter equation gives us little more information than the corrections to the TRK sum rule.

An expansion in powers of the potential energy V does not lead to the difficulty described in the previous paragraph, at least as long as V commutes with $e^{i\vec{q}\cdot\vec{r}/\hbar}$ so that $e^{-i\vec{q}\cdot\vec{r}/\hbar} V\, e^{i\vec{q}\cdot\vec{r}/\hbar} = V$. This indicates that the way to circumvent the restriction to low q is to avoid, or at least delay, the expansion in powers of p. Douglas and Kroll [38], have introduced a modified FWT that only expands in powers of V [38–40] and is, therefore, suitable for this purpose. This transformation (DKT), which is still of the form of equation (41), takes $U_1 = U_f$ for a many-electron system, where

$$e^{iU_f} = \prod_{k=1}^{Z} e^{iU_k}, \tag{43}$$

and the free particle FW operator for the kth electron is given by

$$e^{\pm iU_k} = \frac{1}{\sqrt{2\varepsilon_k(\varepsilon_k + mc^2)}}(\varepsilon_k + mc^2 \pm \beta_k\vec{\alpha}_k\cdot\vec{p}_k), \tag{44}$$

with $\varepsilon_k = \sqrt{p_k^2c^2 + m^2c^4}$.

For H, I have used [13] a no-pair many-electron Hamiltonian [36]

$$H = \sum_{k=1}^{Z} H_{\mathrm{D}}^{k} + \mathcal{L}_{+}\left(\sum_{k>l}^{Z} V_{kl}\right)\mathcal{L}_{+}, \tag{45}$$

where H_{D}^{k} is the single-electron Dirac Hamiltonian for electron k, V_{kl} is the interaction (Coulomb–Breit, for example) between electrons k and l, and $\mathcal{L}_{+} = \prod_{k=1}^{Z} \mathcal{L}_{+}(k)$ with $\mathcal{L}_{+}(k)$ the projection operator onto the space of positive energy states of H_{D}^{k}. It is true that the V_{kl} part of the potential energy does not commute with $\mathrm{e}^{\mathrm{i}\vec{q}\cdot\vec{r}_j/\hbar}$, so it is not precisely correct to claim that a V-expansion will yield the exact q-dependence for this Hamiltonian. Nevertheless, the contributions to the sum rule from V_{kl} (apart from its effect on the eigenstate $|\tilde{i}\rangle$, which will not depend on q) turn out to be quite small [13,41], so the error incurred by omitting this q-dependence should be negligible.

The first step of the DKT transforms H into

$$\tilde{H} = \sum_{k=1}^{Z} \varepsilon_k + \tilde{V} \tag{46}$$

where I have written $\tilde{V} = \mathrm{e}^{\mathrm{i}U_f}(\sum_{k=1}^{Z} V_k + \mathcal{L}_{+}\sum_{k>l}^{Z} V_{kl}\mathcal{L}_{+})\mathrm{e}^{-\mathrm{i}U_f}$ to represent the potential energy terms. As I will discuss below, these terms appear to lead to very small corrections, so will not be further considered in any explicit manner. Using this as our transformed Hamiltonian, we have

$$\tilde{H}(\vec{q}) = \sum_{k\neq j}^{Z} \varepsilon_k + \varepsilon_j(\vec{q}) + \tilde{V}. \tag{47}$$

Furthermore,

$$\mathrm{e}^{\mathrm{i}U_f(\vec{q})} = \mathrm{e}^{\mathrm{i}U_j(\vec{q})} \prod_{k\neq j}^{Z} \mathrm{e}^{\mathrm{i}U_k}, \tag{48}$$

and

$$\mathrm{e}^{\mathrm{i}U_j(\vec{q})} = \frac{1}{\sqrt{2\varepsilon_j(\vec{q})(\varepsilon_j(\vec{q}) + mc^2)}}(\varepsilon_j(\vec{q}) + mc^2 \pm \beta_j\vec{\alpha}_j\cdot(\vec{p}_j + \vec{q})). \tag{49}$$

All these expressions may now be incorporated into equation (40) and expanded in powers of p_j, while keeping the exact dependence on q. When this is done, one finds the relativistic Bethe sum rule to be [41]

$$S_1(Q) = ZS_1^0(Q)(1 - \Delta_f(Q) - \Delta_V(Q)), \tag{50}$$

with

$$\Delta_f(Q) = \frac{1}{3m^2c^2Z(1+Q/mc^2)^2}\left(1+\frac{3}{2(1+Q/mc^2)^2}\right)\sum_{j=1}^{Z}\langle\tilde{\imath}|p_j^2|\tilde{\imath}\rangle - \frac{7}{8m^4c^4Z(1+Q/mc^2)^8}\sum_{j=1}^{Z}\langle\tilde{\imath}|p_j^4|\tilde{\imath}\rangle, \tag{51}$$

and

$$\Delta_V(Q) = -\frac{\hbar(1+Q/3mc^2)}{2m^3c^4Z(1+Q/mc^2)^4(1+Q/2mc^2)} \times \sum_{j=1}^{Z}\langle\tilde{\imath}|\vec{\sigma}_j\cdot(\nabla_j V_j \times \vec{p}_j)|\tilde{\imath}\rangle, \tag{52}$$

Note that in $\Delta_V(Q)$, the coefficient of $\nabla_j^2 V_j$ vanishes identically. This is somewhat surprising, given the complicated nature of the calculations leading to this result. Expectation values of the remaining spin–orbit operator are usually smaller than some of the two-body terms that arise from V_{kl}, and which I have omitted [13,41] because they are known to be quite small [42–44]. Therefore, to a high level of accuracy we have

$$\Delta_V(Q) = 0, \tag{53}$$

and the potential energy of the electrons does not appear explicitly in the result, entering only through its effects on the ground-state wavefunction of the target system. These results give the relativistic corrections to $\mathcal{O}(p^4/m^4c^4)$ and $\mathcal{O}(p^2V/m^3c^4)$. Since they are valid to all orders in Q/mc^2, they include contributions from all multipoles, unlike earlier studies [33,35]. It should also be remembered that the Bethe sum arises from the longitudinal part of the DCS and as such, does not involve retardation, in contrast to the photoabsorption sum of GGT.

The TRK sum rule may be obtained directly from the above results as $S_1 = Z(1-\Delta_f)$, with [41]

$$\Delta_f = \frac{5}{6m^2c^2Z}\sum_{j=1}^{Z}\langle\tilde{\imath}|p_j^2|\tilde{\imath}\rangle - \frac{7}{8m^4c^4Z}\sum_{j=1}^{Z}\langle\tilde{\imath}|p_j^4|\tilde{\imath}\rangle. \tag{54}$$

The first term is just that found by numerous others [4,26–28,32], but the second term had not previously been known. The reader may recall that the TRK sum rule for a single electron in the field of a Pb nucleus was evaluated (along with electric quadrupole and retardation contributions) using perturbative methods in Ref. [4]. It is consistent with these methods to evaluate the p^4 term using an NR wavefunction. For the one-electron case and a Pb nucleus, this gives a contribution of $-35(Z\alpha)^4/8 \approx -0.53$, whereas the first-order term is 0.30. Thus, it is quite clear that this approach

fails badly for such strongly bound systems. For neutral atoms, on the other hand, we may expect that the average over electrons will diminish the errors and allow the perturbative approach to give a reasonably close approximation. This notion is supported by the results I obtained in Ref. [41]. Nonetheless, it needs to be checked with the more accurate approach described below, using DKT wavefunctions.

Numerical studies of equations (51) and (54) indicate that perturbative calculations of these sum rules for neutral atomic systems yield accurate results over a wide range of Z [41]. Further work is needed, however, when $Z > 70$ and Q is small, if one wishes to achieve an accuracy of 0.5% or better [41]. To obtain this greater accuracy for high Z, it is possible to use the methods already described, but to forego completely the expansion in powers of p_j. That is, we may insert equations (44), (46), (47), and (49), directly into equation (40), and evaluate the expectation value using the accurate DKT ground state of $\tilde{H}$. Expectation values using these states, and carefully including the effects of V_{kl}, have been used extensively by Hess and coworkers [39,45,46]. The success these authors have had with such calculations, keeping only low-order terms in V, makes it quite likely that this approach will also yield highly accurate results for the sum rules.

For the $\mathcal{O}(V)$ terms calculated without the p-expansion, numerical evaluation of the Bethe sum for nonzero Q appears to offer quite a significant challenge [47]. Therefore, I have begun with consideration of the TRK sum, $S_1 = Z(1 - \Delta_f - \Delta_V)$, keeping only $\mathcal{O}(V)$ in Δ_V. Now, Δ_f has the relatively simple form

$$\Delta_f = \frac{mc^2}{3Z} \sum_{k=1}^{Z} \left\langle \tilde{i} \middle| \left(\frac{2}{\varepsilon_k} + \frac{m^2c^4}{\varepsilon_k^3} \right) \middle| \tilde{i} \right\rangle, \tag{55}$$

but the expression for Δ_V is quite complicated, so will not be written out here. Though accurate numerical calculations of Δ_f and Δ_V are yet to be completed, I have obtained order-of-magnitude estimates of these quantities for a single-electron system by using NR hydrogenic wavefunctions. The results are intriguing, and they will be the basis of the discussion in the remainder of this section, which will mainly be speculative in nature pending the outcome of work in progress.

For all values of Z, these rough estimates indicate that Δ_V is much smaller than Δ_f. Considering once again a single electron in the field of a Pb nucleus, I find $\Delta_f = 0.17$, while $\Delta_V = 0.002$. If instead we have a nucleus with $Z = 120$, then $\Delta_f = 0.27$ and $\Delta_V = 0.008$. We see that even for such extreme conditions, $\Delta_V/\Delta_f \approx 0.03$, and Δ_V itself is only about 1% of the total sum. For most physical systems, only a small fraction of the electrons will have binding energies approaching those just considered. For neutral atoms, I have found Δ_f to be no more than about 0.03 in the perturbative approach [13,41]. If the relative size of the two terms remains even

approximately the same, then we will be justified in neglecting Δ_V. If this is confirmed by the more accurate numerical methods using many-electron DKT wavefunctions, then equation (55) will give us the effectively exact relativistic corrections, E_1^{rel}, to the TRK sum rule. Since this expression does not involve the potential energy V and is rather simple in form, it should be relatively easy to evaluate even with realistic wavefunctions.

We may hope for more. In studies of the Bethe sum, it was found that the relativistic corrections were never much larger than their value at $Q = 0$ [41]. Therefore, given the relationship between the TRK sum and the $Q \rightarrow 0$ limit of the Bethe sum (see equation (14)), it seems probable that $\Delta_V(Q)$ will be negligible over the whole range of Q. If this can be demonstrated, then the corrections to the Bethe sum rule will be given to high accuracy by setting $V = 0$ in the operators appearing in the expectation value of equation (40). This reduces to the simple expression [13,35]

$$S_1(Q) = \frac{c^2}{2} \sum_{j=1}^{Z} \left\langle \tilde{\imath} \middle| \left(\frac{q^2 + \vec{q}\cdot\vec{p}_j}{\varepsilon_j(\vec{q})} + \frac{\vec{q}\cdot\vec{p}_j}{\varepsilon_j} \right) \middle| \tilde{\imath} \right\rangle. \tag{56}$$

Then this approach, using the DKT without expanding in powers of p, could be used to obtain accurate stopping powers for targets consisting of even the heaviest elements.

4.2. Photoabsorption sum rules for scattering of charged particles

In this section, I will discuss the summations that arise from considerations of the transverse part of the DCS, given in equation (7), and show they are closely related to the GGT sum. In Ref. [13], I have evaluated sum rules for these contributions to the stopping power using both low- and high-Q approximations. In the high-Q region, the recoil energy and energy transfer cannot differ significantly [1,5], so it is a good approximation to make an expansion in powers of $(Q - E_{ni})/Q$, which leads to sums of the form given in equation (15). Although these sums involve the Dirac operators $\vec{\alpha}_j$, they can be handled with the same techniques described in Section 4.1 for treatment of the longitudinal contributions. Details of this approach, along with corresponding results for the stopping power, are given in Ref. [13].

The low-Q transverse contributions to the stopping power are given by

$$B_{\mathrm{t}} = \frac{1}{2} \sum_n E_{ni} \int_{Q_m}^{Q_{\mathrm{c}}} \left[\frac{|\vec{\beta}_t \cdot \vec{G}_n|^2}{[Q(1 + Q/2mc^2) - E_{ni}^2/2mc^2]^2} \right] (1 + Q/mc^2) \mathrm{d}Q. \tag{57}$$

Fano's treatment of B_{t} began with the change of variables [5]

$$\cos^2\psi = \frac{Q_m(Q_m + 2mc^2)}{Q(Q + 2mc^2)}, \tag{58}$$

giving $q = E_{ni}/v\cos\psi$ and

$$B_{\mathrm{t}} = \sum_n \frac{mc^2\beta^4}{ZE_{ni}} \int_{\cos^2\psi_{\mathrm{c}}}^1 \frac{\sin^2\psi}{[1-\beta^2\cos^2\psi]^2} \left| \sum_{j=1}^{Z} \langle n|\mathrm{e}^{\mathrm{i}qz_j/\hbar}\alpha_{jx}|i\rangle \right|^2 \mathrm{d}(\cos^2\psi). \quad (59)$$

Here, ψ is the angle between $\vec{\beta}$ and $\vec{q}$ so that $\beta_{\mathrm{t}} = \beta\sin\psi$, and ψ_{c} is the value of ψ when $Q = Q_{\mathrm{c}}$. Fano then set $q = 0$ in the exponential and related the matrix element of α_x to that of x, reducing this expression to one proportional to the dipole oscillator strength, f_n [5].

In obtaining the relativistic corrections to the stopping power, I found it necessary to keep terms $\mathcal{O}(q^2)$ from the exponential in equation (59) in order that the results for the stopping power were independent of the choice of cut-off, Q_{c} [13]. Rewriting q in terms of E_{ni} and expanding the exponential allows the ψ-integral to be done, and yields an expression for B_t involving the two sums,

$$\sum_n \frac{1}{E_{ni}} \left| \sum_{j=1}^{Z} \langle n|\alpha_{jx}|i\rangle \right|^2 \quad (60)$$

and

$$\sum_n E_{ni} \left[\left| \sum_{j=1}^{Z} \langle n|z_j\alpha_{jx}|i\rangle \right|^2 - \frac{1}{2} \left(\sum_{j,k=1}^{Z} \langle i|\alpha_{kx}|n\rangle\langle n|z_j^2\alpha_{jx}|i\rangle + \mathrm{H.c.} \right) \right], \quad (61)$$

where the terms linear in z_j vanish due to conservation of parity. Since $[H, x_j] = -\mathrm{i}\hbar c\alpha_{jx}$ (apart from small two-body terms), equation (60) is just the relativistic TRK sum, representing the unretarded dipole contributions $E1$. Comparison to equation (25) reveals that equation (61) is just the relativistic form of the combination, $E2 + E1^{\mathrm{ret}}$, considered in the work on photoabsorption sum rules. It is thus seen to have been no accident that for a relativistic treatment of the target, I needed to keep higher order terms in the expansion of the exponential of equation (59). As has been pointed out previously, the effects of higher multipoles, retardation, and relativity all lead to contributions of the same order of magnitude. Keeping only the leading term in the expansion excludes the $E2$ and $E1^{\mathrm{ret}}$ contributions, and cannot yield a consistent relativistic formulation. We also see here a direct relationship between the GGT sum, which arose out of studies of photoabsorption, and the sums related to the transverse contributions to the stopping power.

Though we have arrived at this conclusion from consideration of the lowest order multipoles, it can be shown that this relationship holds for all multipoles. If the lower limit of the integral in equation (59) is avoided, then

we may directly extract from equation (59) the sum

$$\sum_n \frac{1}{E_{ni}} \left| \sum_{j=1}^{Z} \langle n | e^{iqz_j/\hbar} \alpha_{jx} | i \rangle \right|^2, \tag{62}$$

which is just the relativistic generalization ($\vec{p} \to \vec{\alpha}$) of the integrated photoabsorption cross-section in equation (24). Thus, the sums for the transverse contributions to the stopping power have contributions that are exactly the same as those appearing in the photoabsorption dispersion relation of GGT.

We may understand the appearance of the photoabsorption sum in the context of charged particle scattering in the following way: First, note that this contribution to the stopping power represents the exchange of transverse photons between projectile and target. If the target is initially in its ground state, it cannot emit, and can only absorb. Then, observe that in equation (59), the projectile states have already been integrated out, leaving a description in terms of the target states alone. Thus, this equation describes the absorption of photons by the target, and it is completely reasonable that it contains the photoabsorption sum.

Nonetheless, the reader may note two important differences between equations (24) and (59). First, for the charged particle case, the energy-momentum relation given after equation (58) is not that usually seen for photons. This is because these are virtual photons, for which energy and momentum can take on any value, and each may do so independently of the other. One may imagine that both projectile and target are constantly emitting and reabsorbing virtual photons, and occasionally one of these photons gets exchanged between the two. The photons that are exchanged must be ones that lead to conservation of both energy and momentum in the overall interaction between projectile and target, since that is a real process. This requirement leads to the relation, $q = E_{ni}/v \cos\psi$ (except at extremely high incident energies, approaching the Tev range for protons) instead of E_{ni}/c.

The second difference has to do with the presence of the ψ-integration in equation (59). This integral simply reflects the fact that contributions from all possible final states of the projectile have already been summed. Therefore, unlike in the photoabsorption case where there is only one possible momentum transfer for each E_{ni}, here there is a range of momentum transfer, or equivalently ψ, that is possible. One may also note that the upper limit, $\cos^2\psi_c$, of the ψ-integral depends on E_{ni}. Therefore, there are additional terms that differ in form from those resembling the photoabsorption sum.

5. THE TROUBLE WITH RELATIVITY

We have seen that significant challenges arise in the evaluation of sum rules for relativistic systems. Unlike their NR counterparts, the use of

closure for relativistic sum rules requires the introduction of special techniques, such as the FWT or projection operators [32], to exclude contributions from negative energy states. Direct use of closure without such techniques in a single-particle theory of a hydrogenic system includes contributions from transitions of the electron into negative energy states. As previously stated, these contributions precisely cancel those from transitions into positive energy states [4], yielding unphysical vanishing results for the sum rules.

If one views these sums from the many-electron perspective of Dirac's hole theory, on the other hand, the negative energy states are filled (Dirac sea) and transitions into these states are automatically excluded. Then one might expect an absence of such difficulties when using the closure relation, $\sum_n |n\rangle\langle n| = \mathcal{I}$, with $|n\rangle$ now a many-electron state including the filled Dirac sea. However, one still obtains a vanishing result when an average over the direction of $\vec{q}$ is taken (the mathematics is essentially the same as for single-electron theory). The explanation of this result is no longer straightforward, but as I will now describe, it is related to the appearance of infinities from the participation of electrons in the Dirac sea. For the following discussion let us consider the Bethe sum

$$S_1(Q) = \sum_j \sum_n E_{ni} |\langle n | e^{i\vec{q}\cdot\vec{r}_j/\hbar} | i \rangle|^2, \tag{63}$$

and now $\sum_j$ includes all negative energy electrons, as well as those with positive energy. For simplicity, I will restrict the discussion to a single, free electron at rest in the presence of the Dirac sea. Then with $|i\rangle$ and $|n\rangle$ given by suitably symmetrized sets of momentum states, the matrix elements for a given $\vec{q}$ are proportional to $\delta(\vec{p}_j' - \vec{p}_j - \vec{q})$, and only one final state contributes to the sum over states for each j. For bound electrons, this probability distribution will be broadened, as has been discussed in reference to the Bethe surface [1,5,48], but the basic arguments presented below still hold. Therefore, the conclusions should be quite general.

In consideration of this system, we may identify two possible sources of infinity. The first is the infinite energy, E_{D}, of the Dirac sea contained in each of E_n and E_i. The other is the fact that $\sum_j$ runs over an infinite number of electrons. Let us consider each of these in turn.

For a given j, we have a sum over states $|n\rangle$ and a subtraction of the energies, $E_{ni} = E_n - E_i$. If the subtraction is taken first, explicitly calculating each individual term prior to the summation over states, there is a precise cancellation of the infinite E_{D} between E_n and E_i. Then a finite result is obtained, which is proportional to q^2 for small q (this calculation is straightforward for the free particle states presently under consideration).

On the other hand, when the sum over states is done first using closure, we obtain a very different result

$$S_1(Q) = \sum_j \langle i|\mathrm{e}^{-\mathrm{i}\vec{q}\cdot\vec{r}_j/\hbar}[H, \mathrm{e}^{\mathrm{i}\vec{q}\cdot\vec{r}_j/\hbar}]|i\rangle = c\sum_j \langle i|\vec{\alpha}_j\cdot\vec{q}|i\rangle. \tag{64}$$

For each j, the result is again finite, but here it is linear in $\vec{q}$, and therefore, upon averaging over the direction of $\vec{q}$, we obtain the vanishing result referred to above. What has happened is that we have reformulated the sum into a difference of two terms

$$\sum_n E_n|\langle n|\mathrm{e}^{\mathrm{i}\vec{q}\cdot\vec{r}_j/\hbar}|i\rangle|^2 - \sum_n E_i|\langle n|\mathrm{e}^{\mathrm{i}\vec{q}\cdot\vec{r}_j/\hbar}|i\rangle|^2 = \langle i|H(\vec{q})|i\rangle - \langle i|H|i\rangle, \tag{65}$$

each of which is infinite. While the infinities still cancel, the resulting finite result is of a very different form as that found by explicit calculation of each individual term, followed by the summation. Because of the presence of infinities, it is incorrect to interchange the order of these mathematical operations, the subtraction and summation being considered here.

One may ask, which method is the correct one? We will argue that it is the first one, where the subtraction is taken before the summation, even though, as we shall see, this yields an infinite result.

To begin with, I remind the reader that the Bethe sum arose in a calculation of the mean energy loss from fast charged particles to matter. The definition of this sum thus involves terms, each of which has a factor of the energy transfer, E_{ni}. Each term to be summed is proportional to this energy difference; that is, according to the original derivation of the sum, the difference should be taken before the summation over states. As further evidence, note that our result should reduce to the NR result in the appropriate limit. The NR result is also proportional to q^2 and does not vanish upon averaging over the direction of $\vec{q}$. Therefore, we conclude that the correct result is that obtained when the summation over states comes after the subtraction of energies. The alternative, where closure is used directly to obtain a sum rule, is seen to be faulty, as a result of the interchange of mathematical operations in the presence of infinities.

Next let us consider the sum over electrons. As I have said, for any given free electron only a single transition contributes to the sum, that for which $\vec{p}_j' = \vec{p}_j + \vec{q}$. For a positive energy electron initially at rest, the energy difference between these states is just $Q \leq Q_{\mathrm{M}}$. Transitions involving energies greater than Q_{M} cannot occur. In this sense, though energy conservation has been discarded by including all eigenstates of the Hamiltonian in the summation, it has been effectively reinstated by the upper limit of the Q-integration.

With the Dirac sea of electrons, we are not so lucky. For each negative energy state of momentum $\vec{p}_j$, there is a corresponding positive energy state

of momentum $\vec{p}_j + \vec{q}$, and the energy difference between these states can be as large as $2|E_i|$ or larger. Since summation over the entire Dirac sea includes the limit $|E_i| \rightarrow \infty$, transitions involving the production of arbitrarily high-energy electron–positron pairs make significant contributions to the sum. Although the corresponding matrix elements decrease with increasing $|E_i|$, they do not decrease fast enough to keep the sum over electrons from diverging. An explicit calculation, readily done for the free-electron model, shows that the resulting sum is infinite.

Though these arguments have specifically considered a free-electron model, the basic ideas hold for bound electrons, as well. The transition probability will in this case be broadened by the binding energy, but pairs of arbitrarily high energy will still be produced for any given recoil energy Q. Therefore, the conclusions of the previous paragraphs should be valid generally. The same conclusions also apply to the TRK sum, since it may be obtained directly from the Bethe sum, as shown in equation (14). In the photoabsorption sum of GGT the momentum transfer is fixed by the relationship, $q = E_{ni}/c$. While this differs from that in the free-electron model for charged particle scattering, the above arguments do not depend on the precise relationship between these quantities. Therefore, the arguments are applicable to all sum rules considered in this article.

I wish to stress that it is completely 'reasonable' that the result is infinite. The use of closure has removed any limits on the energy transfer, and the model no longer obeys conservation of energy, at least not with respect to the finite energy of any realistic physical system. This point is of some interest, since it seems to imply that the presence of infinities is an unavoidable consequence of the use of closure along with inclusion of pair production processes in these sums. The sums include contributions from creation of arbitrarily high-energy electron–positron pairs. Furthermore, these are real, as opposed to virtual, pairs. It is not, for example, a matter of an electron being surrounded by a sea of virtual pairs, leading to polarization of the vacuum and altering observable quantities, such as the electron's charge and mass. Rather, these are real pairs being produced by collision with a projectile, which in this treatment is effectively being considered to have infinite energy. Since there is infinite energy available, real pairs of unlimited energy can be produced, and the infinite result for the mean energy transfer is in this sense quite reasonable. Though one might have hoped that an approach utilizing the full power of quantum electrodynamics, including the removal of infinities by the methods of renormalization, would allow the effects of pair production to be incorporated along with the usual excitation of positive energy electrons, these observations seem to indicate that any such efforts will prove unsuccessful if they also utilize closure to obtain sum rules. It appears that calculations of the pair production contributions to these sums will require an approach with explicit limits on the amount of energy exchanged between projectile and target.

6. CONCLUSION

In this article, I have discussed relativistic effects on sum rules appearing in the description of scattering of charged particles and photons from atoms. Having begun with considerations of how sum rules arise in these contexts, I then reviewed the early work on this challenging subject. Following this, I discussed my own recent contributions utilizing the Foldy–Wouthuysen and Douglas–Kroll transformations, and conjectured the latter has the capability of producing relatively simple expressions that give highly accurate results for these sums for even the heaviest of elements. I also demonstrated the equivalence of sums for the transverse interaction in the charged particle case and those, which describe photoabsorption. Finally, I have discussed the difficulties that arise in evaluating these sum rules from the perspective of Dirac's hole theory, and shown that the understanding of these difficulties is much less straightforward than when considered from a single-particle point of view. In hole theory, the difficulties were traced to infinities that arise due to the presence of the filled Dirac sea. These considerations suggest that it will not be possible to obtain physically reasonable sum rules using closure if pair production processes are also included in the treatment.

I have recently succeeded in confirming the speculations put forth near the end of Section 4.1. Using Dirac wave functions for hydrogenic systems, I have found that Δ_v/Δ_f is always quite small, and is only as large as 1% for extreme cases, such as for a single electron bound in the field of a nucleus with atomic number $Z = 120$. It is also possible to generalize these results to the case of many-electron systems. Therefore, it is indeed a good approximation to neglect Δ_v under almost all circumstances. Details of these calculations will be published elsewhere.

ACKNOWLEDGEMENTS

I would like to offer my thanks to the members of the Physics Department at Lewis and Clark College for their gracious hospitality during my summer stay in Portland where this paper was written. Acknowledgment is also made to the donors of The Petroleum Research Fund, administered by the American Chemical Society, for support of this research.

REFERENCES

[1] M. Inokuti, *Rev. Mod. Phys.*, 1971, **43**, 297.
[2] A. Dalgarno, *Rev. Mod. Phys.*, 1963, **35**, 522.
[3] R. Jackiw, *Phys. Rev.*, 1967, **157**, 1220.
[4] J. S. Levinger, M. L. Rustgi and K. Okamoto, *Phys. Rev.*, 1957, **106**, 1191.
[5] U. Fano, *Annu. Rev. Nucl. Sci.*, 1963, **13**, 1.
[6] H. Bethe, *Ann. Physik*, 1930, **5**, 325.

[7] H. Bethe, Handbuch der Physik, Springer, Berlin, 1933, Vol. 24/1, p. 273.
[8] M. Walske, *Phys. Rev.*, 1952, **88**, 1283.
[9] M. Walske, *Phys. Rev.*, 1956, **101**, 940.
[10] H. Bichsel, *Phys. Rev. A*, 2002, **65**, 052709.
[11] M. Livingston and H. Bethe, *Rev. Mod. Phys.*, 1937, **9**, 245.
[12] H. Bethe and R. Jackiw, *Intermediate Quantum Mechanics*, 2nd edn, Benjamin, New York, 1968, Chapter 11.
[13] S. M. Cohen, *Phys. Rev. A*, 2003, **68**, 012720.
[14] M. Gell-Mann, M. L. Goldberger and W. E. Thirring, *Phys. Rev.*, 1954, **95**, 1612.
[15] G. E. Brown, private communication referenced in [17,18].
[16] T. Erber, *Ann. Phys.*, 1959, **6**, 319.
[17] W. B. Payne and J. S. Levinger, *Phys. Rev.*, 1956, **101**, 1021.
[18] J. S. Levinger and M. L. Rustgi, *Phys. Rev.*, 1956, **103**, 439.
[19] S. Brenner, G. E. Brown and J. B. Woodward, *Proc. R. Soc. London Ser. A*, 1954, **227**, 59.
[20] G. E. Brown and D. F. Mayers, *Proc. R. Soc. London Ser. A*, 1956, **234**, 387.
[21] Hulme, McDougall, Buckingham and Fowler, *Proc. R. Soc. London Ser. A*, 1935, **149**, 131.
[22] B. Jacobsohn, PhD Dissertation, University of Chicago, 1947, unpublished.
[23] R. H. Pratt and Y. S. Kim, *Rom. J. Phys.*, 1993, **38**, 353.
[24] A. Ron, I. Goldberg, J. Stein, S. Manson, R. Pratt and R. Yin, *Phys. Rev. A*, 1994, **50**, 1312.
[25] M. L. Goldberger and F. E. Low, *Phys. Rev.*, 1968, **176**, 1778.
[26] H. O. Dogliani and W. F. Bailey, *J. Quantum Spectrosc. Radiat. Transfer*, 1969, **9**, 1643.
[27] J. L. Friar and S. Fallieros, *Phys. Rev. C*, 1975, **11**, 274.
[28] T. Matsuura and K. Yazaki, *Phys. Lett.*, 1973, **46B**, 17.
[29] S. B. Gerasimov, *Phys. Lett.*, 1964, **13**, 240.
[30] S. Goldman and G. Drake, *Phys. Rev. A*, 1982, **25**, 2877.
[31] L. L. Foldy and S. A. Wouthuysen, *Phys. Rev.*, 1950, **78**, 29.
[32] K.-M. Schmitt and H. Arenhövel, *Z. Phys. A*, 1985, **320**, 311.
[33] P. T. Leung, M. L. Rustgi and S. A. T. Long, *Phys. Rev. A*, 1986, **33**, 2827.
[34] P. T. Leung, *Phys. Rev. A*, 1989, **40**, 5417.
[35] S. M. Cohen and P. T. Leung, *Phys. Rev. A*, 1998, **57**, 4994.
[36] J. Sucher, *Phys. Rev. A*, 1980, **22**, 348.
[37] G. A. Aucar, J. Oddershede and J. R. Sabin, *Phys. Rev. A*, 1995, **52**, 1054.
[38] M. Douglas and N. Kroll, *Ann. Phys. (NY)*, 1974, **82**, 89, see pp. 110–113 and Appendix III beginning on p. 151.
[39] B. Hess, *Phys. Rev. A*, 1986, **33**, 3742.
[40] G. Jansen and B. Hess, *Phys. Rev. A*, 1989, **39**, 6016.
[41] S. M. Cohen, *Phys. Rev. A*, October, 2003, **68**, 042704.
[42] B. Lo, K. Saxena and S. Fraga, *Theor. Chim. Acta (Berl.)*, 1972, **25**, 97.
[43] K. Saxena, B. Lo and S. Fraga, *J. Phys. B*, 1972, **5**, 768.
[44] B. Lo, K. Saxena and S. Fraga, *Theor. Chim. Acta (Berl.)*, 1972, **24**, 300.
[45] A. Wolf, M. Reiher and B. A. Hess, *J. Chem. Phys.*, 2002, **117**, 9215.
[46] A. Wolf, M. Reiher and B. A. Hess, in *Relativistic Quantum Chemistry* (ed. P. Schwerdtfeger), Elsevier, Amsterdam, 2002, Vol. 24/1, pp. 622–663.
[47] B. A. Hess, private communication.
[48] A. Rau and U. Fano, *Phys. Rev.*, 1967, **162**, 68.

This Page Intentionally Left Blank

Stopping Power of an Electron Gas for Heavy Unit Charges: Models in the Kinetic Approximation

István Nagy and Barnabás Apagyi

Department of Theoretical Physics, Institute of Physics, Technical University of Budapest, H-1521 Budapest, Hungary

Abstract

The energy loss per unit path length of heavy unit-charge intruders, moving with constant velocity in a degenerate electron gas, is calculated using the kinetic theory framework. This framework is implemented by quantum scattering description of binary electron–projectile collisions and model potentials based on different approximations for screening. The comparative study performed results in a detailed theoretical understanding of the key ingredients of an important observable of particle–matter interactions.

Contents

ADVANCES IN QUANTUM CHEMISTRY, VOLUME 46
ISSN: 0065-3276 DOI 10.1016/S0065-3276(04)46010-9

1. INTRODUCTION AND MOTIVATIONS

The use of moving external charges as probes of the static and dynamical properties of matter dates back to the earliest days of modern physics. Particularly, unit-charge intruders such as proton (p) and antiproton ($\bar{p}$), and heavy leptons, i.e., muons ($\mu^{\pm}$) are routinely used in various experimental studies. Their applications in slowing down [1,2], implantation profile [3], Knight shift and quantum diffusion [4], and muon-catalyzed fusion [5] result in useful information. A *key* observable in these studies exploring the interaction of heavy charges with a target is the stopping power $\mathrm{d}E/\mathrm{d}x$ [6,7].

In the present theoretical study, the target is modeled by a degenerate, three-dimensional (3D) homogeneous electron gas: the prototype of metals. The projectile is characterized by its simultaneously known position and velocity $\mathbf{v}$. It is considered as a classical object in the *proper* slowing down process. Thus, the stopping power is expressed by the retarding force $\mathbf{F}$, the momentum ($\mathbf{P} = M\mathbf{v}$) relaxation rate of the projectile, projected on the direction of the straight-line motion:

$$\frac{\mathrm{d}E}{\mathrm{d}x} = \frac{\mathbf{v}}{v}\mathbf{F} = \frac{\mathbf{v}}{v}\frac{\mathrm{d}}{\mathrm{d}t}\mathbf{P}. \tag{1}$$

In order to implement this classical interpretation, first we discuss our assumptions, inherent in theoretical modeling, for the target without the presence of the external probe. Then we shall return to the applied *microscopic* description of $\mathbf{F}$. After a short description of this microscopic approach, its basic problem, i.e., the proper construction of shielded effective potentials will be outlined. Among others, the density functional method is employed by comparing both the implicit and explicit functional versions, in iterative treatments of screening.

The detailed results are presented in a comparative way which allows a physical understanding of the key elements of the underlying kinetic approximation for an observable quantity, the stopping power. This work is pedagogical in nature and contains, therefore, more technical details than a usual research paper. On the other hand, its survey of the vast literature is limited to the applied theoretical method.

2. THE TARGET MODEL

We use an independent electron model for the *motion* of electrons in the field of a rigid neutralizing background. In this model the motion of a given electron is assumed to be independent of the motions of all other electrons. The *effect* of other electrons on this electron is then either entirely neglected (ideal quantum-gas model) or represented by a common smeared out potential, the exchange-correlation potential (auxiliary model). In this,

formally external, constant field the one-electron momentum states are still plane waves. The states are populated according to the ideal Fermi–Dirac occupation function $f^0(p)$, as prescribed *solely* by the Pauli exclusion principle for fermions.

The auxiliary model gives, by construction, the exact ground-state density n_0, and its charge polarizability is described by the standard Lindhard function $\chi_0(q, \omega)$. The smeared out potential is an *input* in the auxiliary model. The phase relations between the various electron wave functions which produce correlation and exchange effect (pair correlations) in the overall distribution of charge, are 'reintroduced' by this input. The value of the common potential, at a given density of the gas, is taken from the *output* of many-body treatments for the correlated ground-state energy of the unperturbed system. Such treatments are: dielectric formulation [8] with coupling-constant integration, field theoretical diagrammatic attempts [9], and accurate quantum Monte Carlo simulations [10]. It is important to note that one can define the common, constant potential in different ways. A frequently applied way, motivated by the self-energy effect [11] for one-particle states, is the so-called screened exchange plus remaining correlation approximation, in addition to the original *definition* (unscreened exchange plus correlation) of Wigner.

In the model just fixed, and termed as Kohn–Sham model of jellium [12], one cannot, of course, make a frontal attack to further details of the many-body problem. A system of identical quantum particles not localized in space *and* strong interaction with one another, represents a genuinely important problem. The auxiliary model allows (using the central field approximation) a natural description of nonlinear modulations in the density, and nonperturbative treatments of elastic binary scatterings in the presence of ions. It provides practical and controllable estimations for the stopping power in targets characterized by mobile charges. This is a remarkable fact, but a term is omitted in the central field approximation: the difference between the actual electrostatic interaction between electrons and the average interaction that is included in the central field.

3. THE MICROSCOPIC MODEL OF STOPPING

In the above-outlined purely kinetic picture for electrons the retarding force is derived as a result of independent, binary electron–projectile collisions. This force is calculated as the total momentum transferred per unit time to the heavy particle by successive electron scattering off it. Let us take coordinates moving with the projectile. In *this* frame of reference an electron is characterized by its kinematical variable **p** (atomic units are used throughout this work). The momentum distribution (F^0) function in

a moving gas differs from the original only by a Galilean transformation; $F^0 = [2/(2\pi)^3] f^0(\mathbf{p} + \mathbf{v})$ in these coordinates.

The electron carries momentum $\mathbf{p}$ and $\mathbf{p}'$ before and after an elastic ($p = p'$) collision with a heavy (no recoil effect) intruder. The momentum transferred to the rest particle in such a collision is $\mathbf{p} - \mathbf{p}'$. We multiply this by the product of $F^0\, \mathrm{d}^3\mathbf{p}\, \mathrm{d}\Omega'$ and $p\, \mathrm{d}\sigma$, where $\mathrm{d}\sigma(\mathbf{p}, \mathbf{p}') = \mathrm{d}\sigma(\mathbf{p}', \mathbf{p})$ is the differential cross-section. Using this *rate* and averaging, we obtain the total force; the defining expression, equation (1), thus becomes [13]

$$\frac{\mathrm{d}E}{\mathrm{d}x} = \frac{2}{(2\pi)^3} \int \mathrm{d}^3\mathbf{p} f^0(\mathbf{p} + \mathbf{v}) p \frac{\mathbf{v}}{v} \int \mathrm{d}\Omega'(\mathbf{p} - \mathbf{p}') \mathrm{d}\sigma(\mathbf{p}, \mathbf{p}'). \tag{2}$$

It is remarkable that an adiabatic quantum mechanical treatment, in which one calculates the force matrix elements between stationary scattering states of the total (noninteracting electrons plus moving potential) Hamiltonian, gives [14] a complete agreement with equation (2). In this treatment the necessarily statistical aspect (ensemble averaging) of the problem is considered by the Fermi–Dirac occupation numbers for single-particle states. For completeness, in first-order Born approximation $\mathrm{d}\sigma(\mathbf{p}, \mathbf{p}') = \mathrm{d}\sigma(\mathbf{p} - \mathbf{p}') = \mathrm{d}\sigma(\mathbf{q})$, and $\mathbf{vq} = \omega$ is the energy transfer in elastic binary collision.

For *spherical* potentials, where $\mathrm{d}\sigma(\mathbf{p}, \mathbf{p}') = \mathrm{d}\sigma(p, \theta)$ and $\mathbf{p}' = \mathbf{p} \cos\theta$, the stopping power appears in a more simple form

$$\frac{\mathrm{d}E}{\mathrm{d}x} = \frac{2}{(2\pi)^3} \int \mathrm{d}^3\mathbf{p} f^0(\mathbf{p} + \mathbf{v}) \frac{\mathbf{v}}{v} p\mathbf{p} \sigma_{\mathrm{tr}}(p), \tag{3}$$

in which the standard notation

$$\sigma_{\mathrm{tr}}(p) = 2\pi \int_0^{\pi} \mathrm{d}\theta \sin\theta (1 - \cos\theta) \mathrm{d}\sigma(p, \theta), \tag{4}$$

for the transport cross-section is introduced. Finally, the simple transformation $\mathbf{p} + \mathbf{v} \rightarrow \mathbf{p}$, and the notation $\mathbf{v_r} = \mathbf{p} - \mathbf{v}$ with $v_{\mathrm{r}}^2 = v^2 + p^2 - 2vp \times \cos\phi$, results in the following expression

$$\frac{\mathrm{d}E}{\mathrm{d}x} = \frac{2}{(2\pi)^3} \int \mathrm{d}^3\mathbf{p} f^0(p) v_{\mathrm{r}} \frac{\mathbf{v}\mathbf{v_r}}{v} \sigma_{\mathrm{tr}}(v_{\mathrm{r}}), \tag{5}$$

with $\mathrm{d}^3\mathbf{p} = 2\pi p^2\, \mathrm{d}p \sin\phi\, \mathrm{d}\phi$ for convenience [15]; $\phi \in [0, \pi]$.

Notice that the Pauli principle does not introduce any restriction, in the case of a heavy particle without recoil, for the evaluation of the retarding force [16]. The absence of the Pauli blocking term, $f^0(\mathbf{p} + \mathbf{v}) f^0(\mathbf{p}' + \mathbf{v})$, in equations (2) and (3) is due to the implicit assumption that all electrons are scattered by the *same* (mean field) potential. Thus, the stationary states (orbitals) are orthogonal. The Galilean transformation will not change the original orthogonality. The stopping power is linear [14] in the distribution

function; a nice similarity with the well-known [17] one-electron description of the resistivity is established.

Sections 3.1 and 3.2 are devoted to physically motivated selected examples. Their goal is mainly pedagogical and the results presented may allow a phenomenological understanding of few important facts in stopping.

3.1. Velocity dependence of d*E*/d*x*

We shall illustrate kinematical trends in $\mathrm{d}E/\mathrm{d}x$ by using the $\sigma_{\mathrm{tr}}^{\mathrm{a}}(v_{\mathrm{r}}) = 4\pi A/v_{\mathrm{r}}^2$ and $\sigma_{\mathrm{tr}}^{\mathrm{b}}(v_{\mathrm{r}}) = 4\pi B/v_{\mathrm{r}}^4$ models in equation (5). One obtains

$$\frac{\mathrm{d}E}{\mathrm{d}x}(v \le p_{\mathrm{F}}) = n_0 v p_{\mathrm{F}} \frac{4\pi A}{v_{\mathrm{F}}^2}\left[1 - \frac{1}{5}\left(\frac{v}{p_{\mathrm{F}}}\right)^2\right], \tag{6}$$

$$\frac{\mathrm{d}E}{\mathrm{d}x}(v > p_{\mathrm{F}}) = n_0 v^2 \frac{4\pi A}{v^2}\left[1 - \frac{1}{5}\left(\frac{p_{\mathrm{F}}}{v}\right)^2\right], \tag{7}$$

for the first (a) case, while the other option (b) results in even simpler forms

$$\frac{\mathrm{d}E}{\mathrm{d}x}(v \le p_{\mathrm{F}}) = n_0 v p_{\mathrm{F}} \frac{4\pi B}{v_{\mathrm{F}}^4} \tag{8}$$

$$\frac{\mathrm{d}E}{\mathrm{d}x}(v > p_{\mathrm{F}}) = n_0 v^2 \frac{4\pi B}{v^4}. \tag{9}$$

Generally, for well-behaved interactions the asymptotic limits from equation (5) are

$$\frac{\mathrm{d}E}{\mathrm{d}x}(v \ll p_{\mathrm{F}}) = n_0 v p_{\mathrm{F}} \sigma_{\mathrm{tr}}(p_{\mathrm{F}}), \tag{10}$$

$$\frac{\mathrm{d}E}{\mathrm{d}x}(v \gg p_{\mathrm{F}}) = n_0 v^2 \sigma_{\mathrm{tr}}(v), \tag{11}$$

for very low and very high velocities, respectively. The illustrative, quite different, examples in equations (6) and (8) signal that a linear velocity dependence may remain practically up to the Fermi velocity. This linearity is in accord with experimental predictions [1] for the stopping power. Equation (11) *completely* describes the case of an ideal boson-gas target, as well.

The calculation of stopping for *charged* intruders requires shielded interaction between the electrons and the incoming ion. For spherical potentials the general form of the transport cross-section, based on partial wave representation of the scattering amplitudes, is as follows

$$\sigma_{\mathrm{tr}}(v_{\mathrm{r}}) = \frac{4\pi}{v_{\mathrm{r}}^2} \sum_{l=1}^{\infty} (l+1)\sin^2[\delta_l(v_{\mathrm{r}}) - \delta_{l+1}(v_{\mathrm{r}})], \tag{12}$$

where the phase shifts are denoted by δ_l. A bare Coulomb interaction $V(r) = -Z/r$ would give, using equation (12) and $\delta_l(v_r) - \delta_{l+1}(v_r) = \arctan(Z/[v_r(l+1)])$, a logarithmically divergent cross-section, as the well-known

$$\sigma_{tr}^{c}(v_r) = \frac{4\pi}{v_r^2} \sum_{l=1}^{\infty} (l+1) \frac{u^2}{1+u^2}, \tag{13}$$

expression, with the corresponding $u = Z/[v_r(l+1)]$ notation, clearly shows. One can consider the mentioned, selected examples as an energy-independent phase-shift approximation (case a) to equation (12), and a *first*-order Born approximation (case b) to equation (13) *with* a certain l_{max} to avoid the logarithmic divergence.

3.2. Charge-sign effect in d*E*/d*x*

It is well known that for a bare Coulomb interaction the differential cross-section, the famous Rutherford cross-section, scales as Z^2. This is the result from first-order Born, exact, and classical treatments in three dimension. Therefore, in a scattering interpretation of stopping the charge-sign dependence originates from the screening and higher order effects. We illustrate this statement by an exactly solvable *classical* collision problem using a physically motivated model potential.

Let us use the following potential of strictly finite range

$$V(r) = -\frac{Z}{r}\left(1 - \frac{r}{R}\right), \tag{14}$$

for $r \le R$, with $V(r) = 0$ for $r > R$. Solving [18] the classical equation for the scattering angle θ, in terms of the impact parameter b, at a given velocity v_r, one gets

$$\tan^2\left(\frac{\theta}{2}\right) = \left(\frac{Z}{bv_r^2}\right)^2 \frac{1-(b/R)^2}{[1-Z/(Rv_r^2)]^2}, \tag{15}$$

for $b \le R$. The Rutherford expression corresponds to $R = \infty$. The differential cross-section is given by $d\sigma = 2\pi|b\,db|$; thus the total cross-section is simply $\sigma_t = \pi R^2$. But the transport cross-section

$$\sigma_{tr} = \int_0^{\pi} d\sigma(1 - \cos\theta), \tag{16}$$

behaves differently. A straightforward calculation results in

$$\sigma_{tr} = \pi R^2 \frac{2}{(A-1)^2}[A \ln A - (A-1)], \tag{17}$$

for any value of $A = (Rv_r^2/Z)^2[1 - Z/(Rv_r^2)]^2$. This equation shows, by taking for simplicity the $(|Z/R|/v_r^2) \to 0$ high-energy limit, that the classical charge-sign effect appears as

$$\sigma_{tr} = \frac{4\pi Z^2}{v_r^4}\left[1 + \frac{(Z/R)}{(v_r^2/2)}\right]\ln\frac{Rv_r^2}{|Z|}, \tag{18}$$

and clearly gives a difference in stopping for $Z = \pm 1$. This result, with an $R \sim (v_r/\omega_0)$ choice, *resembles* the classic result of Bohr [19] obtained for stopping of a medium of N 'atoms' with harmonically bound (ω_0) electrons, if we use $(dE/dx) = Nv_r^2\sigma_{tr}$ at $v_r = v$. We stress the point that in 3D Coulomb scattering the differential cross-section does not contain $\hbar$. In the 2D Coulomb case, Planck's constant *appears*, giving the possibility to 'tune' to the classical ($\hbar \to 0$) limit [15].

4. SCREENING

Screening is a fundamental property of an electron gas. When one considers the energy transfer in successive binary collisions between the projectile and electrons it is essential to include the shielding of the Coulomb potential, as the mathematical result in equation (13) already heralds. One should use an appropriate effective ion–electron interaction which, however, needs careful determination.

The target charge density is modulated by the intruder; the average field produced by the new charge distribution can be treated *as part* of the potential energy for each separate electron. The applied purely kinetic approximation suggests, therefore, the use of the mean-field concept. Thus, in an orbital representation of this concept one obviously defines a self-consistency problem. This representation, as our auxiliary model for the target itself, rests on the *a priori* assumption of the kinetic-energy dominance. A mathematically self-consistent result based on iterated solutions of an effective one-electron treatment depends, of course, on the exchange-correlation input as well.

Clearly, *any* theory which provides an expression for 'the energy of a single electron' as a function (Poisson equation) or functional (exchange-correlation) of the distribution of total electron density might be used as a basis for the *definition* of a self-consistent field. Yet, one ought to remember that the many-body problem is a topic in its own right, with its own characteristic methods (see Section 2). The density is the simplest *physical* parameter; it is the diagonal element of the one-particle density matrix. The proper normalization of the induced density is a particularly important constraint in reliable stopping calculations for bare-charged intruders moving in an 3D electron gas.

4.1. Impurity screening

A *static* electric charge becomes neutralized (screened) in an extended free electron gas by an excess of electrons within a finite distance [20]. Let us consider a spherically symmetric local potential $V_{\rm eff}(r)$ embedded in our system. With this potential at the center there are phase-shifted *stationary-state* solutions of the one-particle Schrödinger equation compared with the corresponding solutions when $V_{\rm eff}(r) = 0$. The existence of this type of solutions is at the heart of the partial wave method of solving the problem of *scattering* from such a potential; the solutions are 'automatically useful' to calculate quantum-mechanical cross-sections in the low-velocity limit. One can consider the displaced electronic charge as an average (see Section 4.3) of delayed electron motions due to scattering.

In order to characterize this density modulation we can use the stationary one-particle solutions as the basic eigenstates of the *whole* system and fill them up to the Fermi wave-vector $p_{\rm F}$ (defined from the density as $n_0 = p_{\rm F}^3/3\pi^2$) just as for the plane-wave states. For the charged impurity case the number of excess electrons is expressed [21] as follows:

$$Z = \frac{2}{\pi}\sum_{l=0}^{\infty}(2l+1)\delta_l(p_{\rm F}) - \frac{2}{\pi}\sum_{l=0}^{\infty}(2l+1)\delta_l(0) + N_{\rm b}. \qquad (19)$$

In a ground-state situation the last two terms cancel due to the Levinson theorem. Equation (19) is the Friedel sum rule which *fixes* a number for occupied bound states $N_{\rm b}$.

Notice that in *any* orbital treatment which is defined as a self-consistent field treatment for screening in the auxiliary model system, one should find that the calculated phase shifts 'automatically' satisfy equation (19). Clearly, the way of designing an expression for 'the energy of a single electron' needs physical motivations. Furthermore, considering *only* the density as a basic variable, other methods are also applicable to the screening problem. The alternative methods are based [22] on the single-particle Green's function (one-sided boundary value problem and does not require the determination of eigenvalues or phase shifts), an Euler–Lagrange equation expressed solely [23] in terms of the density, or on an inhomogeneous integral equation [24] with linear-response input.

4.2. Backflow around slowly moving ions

In Section 4.1 we have studied the screening of a fixed charged impurity using the self-consistent field concept. For slowly moving massive impurity the dynamical screening produces a velocity-proportional current flow (backflow) around it. This backflow concept is based on the particle conservation equation for the charge and current induced in the electron gas.

Within *linear* (l) response theory the backflow is proportional to the density response function and purely dipolar in character [8]. The dipolar flow represents the electron current far from the intruder and, in the case of an ion, its amplitude (h_l) is given by the charge Z. This is the result of perfect screening which requires that the backflow identically cancels the longitudinal part of the charged impurity current.

In the *scattering* (sc) description of the induced current, generated by a spherical potential, the dipolar part is only the next-to-leading term which has zero divergence (stationary flow) and zero curl (the perturbation is longitudinal). Its amplitude (h_{sc}) is expressed [25] by the following sums of phase shifts:

$$h_{sc} = \frac{1}{\pi}\sum_{l=0}^{\infty}(2l+1)\sin 2\delta_l + \frac{4}{\pi}\sum_{l=0}^{\infty}(l+1)^2 \sin\delta_l \sin\delta_{l+1} \sin(\delta_l - \delta_{l+1}). \tag{20}$$

This perfect screening condition implies $h_{sc} = Z$, for a point-like ion. Note that the derivation of this expression needed [25] proper scattering amplitudes *solely* at the Fermi level [$\delta_l(p_F)$]. For small phase shifts, equations (19) and (20) represent the same condition.

For not-point-like moving ions (ions with bound states) the problem of screening is not trivial. In the above picture there is a steady current of electrons towards the intruder, and a steady current of scattered electrons away from it. If one includes higher order effects, active electrons can, by mutual collision, jump between various states of excitation constrained by the many-body spectral function of energetically allowed (mediating bosons) transitions. Equation (19) could describe, by forcing a nonpopulation (putting holes) in N_b, excited state-like configurations. Equation (20), based on a total balance concept, could model ionic states by fixing $h_{sc} = Z - N_B$, where N_B is the number of intact bound electrons around a moving ion. Thus, a total balance in the stationary flow ($n_0\mathbf{v}$) can replace [26] the often-used concept of competing capture and loss processes for active electrons in bound states.

4.3. Screening of fast ions in the kinetic model

The polarization or kinetic attempts, in which the system is considered as a dielectric or as an ensemble of independent electrons, respectively, are complementary to each other. In stopping calculations a continuum treatment should describe the particles in the excitation spectrum, while the collision-based treatment should involve a screened two-body potential. Let us motivate an adiabatic, but velocity-dependent screening of intruders to be used in equation (11), with the corresponding limit (Bethe limit) of

the dielectric [6,7] description

$$\frac{\mathrm{d}E}{\mathrm{d}x} = Z^2 \frac{4\pi n_0}{v^2} \log \frac{2v^2}{\omega_\mathrm{p}}, \tag{21}$$

in which $\omega_\mathrm{p}^2 = 4\pi n_0$ is the classical plasma frequency. We model the effective screened interaction by a standard Yukawa form: $V(r) = (Z/r)\exp(-\lambda r)$. The first-order Born treatment of equation (12) gives, in this case, the following transport cross-section

$$\sigma_\mathrm{tr}(v_\mathrm{r}) = Z^2 \frac{4\pi}{v_\mathrm{r}^4} \left[\frac{1}{2} \log(1+a) - \frac{1}{2} \frac{a}{1+a} \right], \tag{22}$$

where the abbreviation $a = (2v_\mathrm{r}/\lambda)^2$ is introduced. For high velocities equation (11) with equation (22) gives, after a comparison with equation (21), the $\lambda = \omega_\mathrm{p}/v$ form at prescribed equivalence.

Next, we describe an averaging method which could provide support to this, apparently phenomenological, statement for dynamical screening length obtained here from an averaged *observable*, the stopping. We use a picture in which an axial screened potential is replaced by its spherical average. For such a potential one can [27] calculate the

$$A(v_\mathrm{r}) = \lim_{R\to\infty} \int_0^R \mathrm{d}^3 r [|\psi_{v_\mathrm{r}}(r)|^2 - |\psi_{v_\mathrm{r}}^0(r)|^2] \tag{23}$$

quantity, where ψ_{v_r} is the *scattering* solution (with relative velocity v_r, introduced already at equation (5)) while $\psi_{v_\mathrm{r}}^0$ the incident plane wave. One obtains [28] the following expressions

$$A(v_\mathrm{r}) = \frac{2\pi}{v_\mathrm{r}^2} \sum_{l=0}^{\infty} (2l+1) \frac{\mathrm{d}\delta_l(v_\mathrm{r})}{\mathrm{d}v_\mathrm{r}}, \tag{24}$$

$$A^\mathrm{B}(v_\mathrm{r}) = -\frac{2\pi}{v_\mathrm{r}^2} \frac{\mathrm{d}}{\mathrm{d}v_\mathrm{r}} \left[\frac{v_\mathrm{r}}{2\pi} V_\mathrm{eff}(q=0) \right], \tag{25}$$

by using standard partial wave representation in exact, equation (24), and first-order Born, equation (25), descriptions. Here $V_\mathrm{eff}(q)$ is the Fourier transform of the effective potential, and the $q = 0$ limit refers to the forward direction.

The induced charge (Q) is calculated, similarly to the static case outlined at equation (19) with $v_\mathrm{r} = p$, from

$$Q = \frac{2}{(2\pi)^3} \int \mathrm{d}^3 p f^0(p) A(v_\mathrm{r}), \tag{26}$$

which gives, by using equation (25) the simple analytical [28,29] expression

$$Q = V_{\text{eff}}(q=0)\frac{p_{\text{F}}}{\pi^2}\left[\frac{1}{2} + \frac{p_{\text{F}}^2 - v^2}{4p_{\text{F}}v}\log\left|\frac{v+p_{\text{F}}}{v-p_{\text{F}}}\right|\right]. \tag{27}$$

For any one-parametric potential with finite forward limit, this expression gives the velocity dependence of the screening length by taking $Q = Z - N_{\text{B}}$. Particularly, for the Yukawa case such a treatment gives the same limit value as the stopping-based prediction for $\lambda(v)$.

5. RESULTS

In order to get insight into the important role of applied scattering approximation we have performed numerical calculations for the phase-shifts (and thus to equation (12)) at v_{F}, using a simple Yukawa-like potential with $\lambda_{\text{TF}}^2 = 4p_{\text{F}}/\pi$ screening parameter. This form of the effective interaction refers to the Thomas–Fermi direct approach in density-functional theory (DFT), and linearization of the resulting Euler–Lagrange (see Section 5.2) equation.

In Fig. 1 we exhibit the ratios (R_p and $R_{\bar{p}}$) of these results and equation (22), for cases of $Z = \pm 1$ and $r_s \in [1, 4]$ where the density parameter is defined as $r_s = [3/(4\pi n_0)]^{1/3}$. The figure shows that for a commonly applied potential the deviations from the perturbative first-order Born treatment (equation (22) with $v_{\text{r}} = v_{\text{F}}$) are notable. The calculations, with an *a priori*

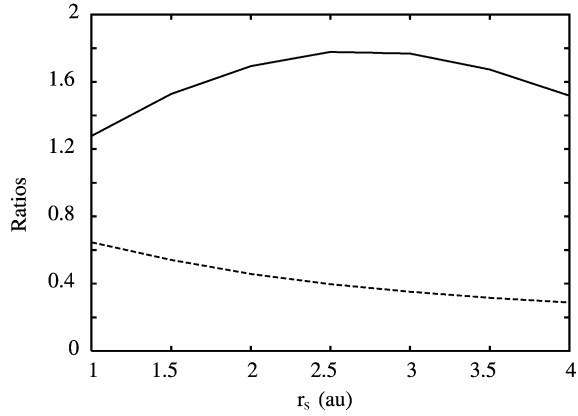

Fig. 1. The transport cross-section ratios, defined by dividing the numerically calculated ones with the first-order Born result (equation (22) with $v_{\text{r}} = p_{\text{F}}$), for the proton ($R_p$, solid curve) and antiproton ($R_{\bar{p}}$, dashed curve) cases. A Yukawa-type potential with $\lambda_{\text{TF}}^2 = 4p_{\text{F}}/\pi$ screening parameter is used.

fixed model potential, result in a quite big charge-sign effect in stopping powers for proton and antiproton; the $R_p/R_{\bar{p}}$ factor is roughly four (c.f., Section 5.1). Next, we investigate a self-consistent quadratic description for the same ratios.

This attempt is based on linear and quadratic polarizabilities of the electron gas and the Hartree self-consistent field concept [30]. By taking the long-wavelength limit in such a treatment one can write [31] for the effective potential, the following transparent form in Fourier momentum space

$$V(q) = -\frac{4\pi Z}{q^2+\lambda_{\rm TF}^2} + \frac{4\pi Z^2 \lambda_{\rm TF}}{(q^2+\lambda_{\rm TF}^2)(4p_{\rm F}^2+\lambda_{\rm TF}^2)}, \tag{28}$$

and the corresponding first-order scattering amplitude is simply $f^{(1)}(q) = (1/2\pi)V(q)$. Of course, the correct characterization of the charge-sign dependent Z^3-term in the low-velocity stopping requires the second-order amplitude for the linearly screened potential, as well. For a Yukawa potential this is well known [32], and has the form

$$f^{(2)}(q) = -\frac{2Z^2\lambda_{\rm TF}}{\lambda_{\rm TF}^4 + 4p_{\rm F}^2\lambda_{\rm TF}^2 + p_{\rm F}^2 q^2}. \tag{29}$$

Note the intact nature of the forward limit: $f^{(1)}(q=0) + f^{(2)}(q=0) = 2/\lambda_{\rm TF}^2$. The linearly screened potential already includes the properly normalized screening charge; therefore, in such an attempt the quadratic charge contribution has a zero norm.

Using the sum of the above amplitudes, and taking the square of the sum, we obtain the differential cross-section. Substituting into equation (4), the perturbative transport cross-section will consist of two terms

$$\sigma_{\rm tr}(v_{\rm F}) = Z^2 \frac{4\pi}{v_{\rm F}^4} F_1(b) + Z^2 \frac{4\pi}{v_{\rm F}^4}\frac{Z}{v_{\rm F}} F_2(b), \tag{30}$$

in which F_1 and F_2 depend on the density parameter, as the variable $b = (\lambda_{\rm TF}/2v_{\rm F})^2$ clearly shows ($b = 0.166 r_s$). They are given by

$$F_1(b) = \frac{1}{2}\left[\log\left(1+\frac{1}{b}\right) - \frac{1}{1+b}\right] \tag{31}$$

$$F_2(b) = \sqrt{b}\,\frac{3+4b}{1+b}\int_0^1 {\rm d}u \frac{u^5}{(b+u^2)^2(4b^2+4b+u^2)}. \tag{32}$$

After performing numerical integrations in equation (32), we define the perturbative ratios R_p and $R_{\bar{p}}$ by dividing equation (30) with its first term. The obtained results are plotted in Fig. 2. The symmetric deviations are not small and, somewhat surprisingly, are similar in magnitude to those in Fig. 1 which were based on a different attempt. From these figures one can conclude that

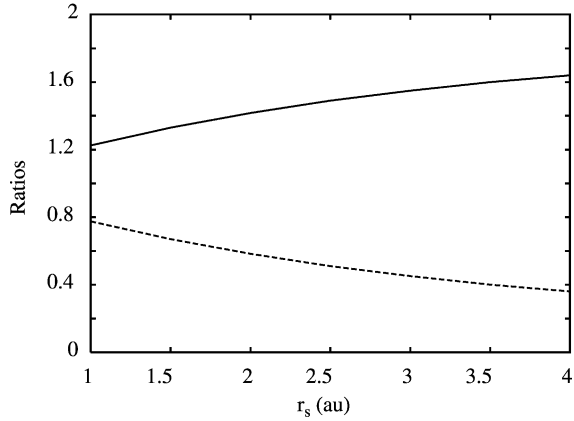

Fig. 2. The transport cross-section ratios, defined by dividing equation (30) by its first term, for proton (R_p, solid curve) and antiproton ($R_{\bar{p}}$, dashed curve) cases.

the physical $Z = \pm 1$ intruders represent strong perturbation at the experimentally important metallic density range.

5.1. Consistent models based on sum rules

The above illustrative results show that the applied scattering approximation is an essential constituent in reliable estimations for the observable quantity, the stopping power. In this section, we summarize numerical results based on consistent models, i.e., *forcing* the phase-shifts to satisfy the first term of equation (19) or the complete equation (20). We use a one-parametric effective potential

$$V(r) = -Z\frac{\Lambda}{\mathrm{e}^{\Lambda r} - 1}, \tag{33}$$

in the scattering Schrödinger equation with $Z = \pm 1$. Tables 1 and 2 contain the transport cross-sections calculated in such a way at p_{F} scattering momenta, together with the corresponding consistent screening parameters $\Lambda(r_s)$.

The results for the cross-sections, determined by using equation (20) with $h_{\mathrm{sc}} = Z$ as constraint, are only moderately higher than those based on equation (19). This fact is very interesting in the case of protons, where the application of the Friedel sum rule results in a very compact and rigid screening, while backflow-based constraint gives a more extended effective potential (see Section 4.2 also). The results for antiprotons are practically insensitive to the applied constraints. Finally, the stopping powers for proton and antiproton give a factor of about two for their ratio. This shows an

Table 1. Screening parameters and transport cross-section computed at several values of r_s

r_s	Λ^{Fr}	$\sigma_{\mathrm{tr}}^{\mathrm{Fr}}(v_{\mathrm{F}})$	Λ^{Zw}	$\sigma_{\mathrm{tr}}^{\mathrm{Zw}}(v_{\mathrm{F}})$
2	1.98	8.23	1.71	9.43
3	1.81	26.61	1.23	33.13
4	1.80	52.53	0.97	63.82
5	1.81	84.69	0.82	95.31
6	1.87	122.11	0.73	126.28

Upper indices Fr and Zw refer to the underlying constraints, equation (19) and equation (20), respectively. The model potential, equation (33) with $Z = 1$, is used for a screened proton.

essential charge-sign effect at metallic densities, although the ratio is smaller than the fixed potential calculations would suggest.

Notice, that independent of the charge-sign, the screening parameters are similar to each other in the backflow-mediated approach, suggesting a collective *system* behavior. The screening parameter shows, in this case, a quite similar r_s-dependence as the one $[\lambda_{\mathrm{ee}}(r_s)]$ established for electron–electron interactions in an optimized potential treatment of the many-body problem. By a rescaling [33] between the Hulthen and Yukawa potentials we have $\Lambda(r_s) = 1.6\lambda_{\mathrm{ee}}(r_s)$, in which $\lambda_{\mathrm{ee}}(r_s) = \lambda_{\mathrm{TF}}(r_s)(1 + 0.166r_s)^{-1/2}$ [34].

In positive ($Z = 1$) muon spin resonance (μSR) experiments [3,4] an important observable is the Knight shift in metals. The magnetic resonance frequency is shifted by a ΔH value from the externally applied (H) magnetic field

$$\frac{\Delta H}{H} = \frac{8\pi}{3}\chi_{\mathrm{P}}E(p_{\mathrm{F}}), \tag{34}$$

in which χ_{P} is the Pauli's spin susceptibility and $E(p)$ the scattering-wave enhancement at the Fermi level $p = p_{\mathrm{F}}$. For our model potential

Table 2. The same data as in Table 1, for the antiproton ($Z = -1$) case

r_s	Λ^{Fr}	$\sigma_{\mathrm{tr}}^{\mathrm{Fr}}(v_{\mathrm{F}})$	Λ^{Zw}	$\sigma_{\mathrm{tr}}^{\mathrm{Zw}}(v_{\mathrm{F}})$
2	1.53	6.32	1.50	6.53
3	1.18	16.21	1.15	17.26
4	0.98	30.78	0.95	32.97
5	0.84	50.86	0.81	55.59
6	0.75	73.45	0.72	81.14

this factor is given by

$$E(p) = Z\frac{2\pi}{p}\,\frac{\sinh(\alpha)}{\cosh(\alpha) - \cos(\alpha\beta)}, \tag{35}$$

where $\alpha = (2\pi p/\Lambda)$ and $\beta^2 = (2Z\Lambda/p^2) - 1$. If β^2 becomes negative the cos-term has to be replaced by the $\cosh(\alpha\sqrt{1 - (2Z\Lambda/p^2)})$ term. Detailed calculation [35] shows that the $\Lambda = \Lambda_{\mathrm{Zw}}(r_s)$ choice results in good agreement with Knight-shift data, obtained for different metals. As *muonium* is not detected [3] in metals, one can consider the applied model as a consistent one.

5.2. Model potentials based on iterative treatments

The *a priori* fixed and the consistent models of screening are physically motivated and allow relatively straightforward calculations for different observables, like the stopping power discussed in this work. The key elements, as the effective range of screening and the role of applied scattering approximations, are transparent. On the other hand, a comparison of results obtained in such a way with those based on more sophisticated, self-consistent, calculations may support the real capability of models, at least under the same kinematical conditions. An established capability, and understanding of key elements, could give a well-motivated starting point in modeling under *different* physical conditions.

For charged impurities one can use the DFT and apply the obtained results for slow intruders. Particularly, in any orbital-based implementation of the theory a charge state of positive ions can be fixed by the method itself (see Section 4.1). The DFT is a formally exact theory which states that the ground-state properties of the whole system (electron gas plus impurity) may be obtained by minimizing a functional $E[n(\mathbf{r})]$ of the electron number density $n(\mathbf{r})$. The minimum value of the functional is the exact ground-state energy, and this minimum is obtained when $n(\mathbf{r})$ is the exact ground-state density [36].

When a direct minimization is carried out in our problem by varying the *density* with the constraint that the total number of electrons is fixed, one gets the corresponding Euler–Lagrange equation:

$$\frac{\delta T[n]}{\delta n(\mathbf{r})} - \frac{Z}{r} + \int \mathrm{d}\mathbf{r}'\,\frac{\Delta n(\mathbf{r}')}{|\mathbf{r} - \mathbf{r}'|} + \bar{v}_{\mathrm{xc}}[n] = \mu[n_0]. \tag{36}$$

Here μ is the exact chemical potential prescribed by the unperturbed extended system and $T[n(\mathbf{r})]$ is the exact kinetic energy functional. The induced density to the Hartree-part is defined as $\Delta n(\mathbf{r}) = n(\mathbf{r}) - n_0$ and $\bar{v}_{\mathrm{xc}}[n(\mathbf{r})]$ is an exchange-correlation potential. Clearly, far from the impurity

$\bar{v}_{\rm xc}[n_0] = \mu_{\rm xc}[n_0]$; it is determined as a functional derivative of the expectation value of the exact potential energy of an interacting electron gas.

For the auxiliary system introduced in Section 2, one can start with a trial density $n(\mathbf{r})$ constructed out of some fictitious one-particle orbitals

$$n(\mathbf{r}) = 2 \sum_{i \in \text{occ.}} |\psi_i(\mathbf{r})|^2, \tag{37}$$

over the lowest occupied (occ.) states. In this representation $T[n]$ is given by the single-particle kinetic energy $T_{\rm s}[n]$; this is an *implicit* functional. The energy variation is carried out with respect to the orbitals $\psi_i^*(\mathbf{r})$ as in the Hartree approximation and the procedure results in the standard Kohn–Sham set of equations

$$\left(-\frac{1}{2}\nabla^2 - \frac{Z}{r} + \int \mathrm{d}\mathbf{r}' \frac{\Delta n(\mathbf{r}')}{|\mathbf{r} - \mathbf{r}'|} + \Delta v_{\rm xc}[n]\right)\psi_i(\mathbf{r}) = \varepsilon_i \psi_i(\mathbf{r}). \tag{38}$$

Here, in the usual local-density approximation (LDA), the many-body effect is accounted for by $\Delta v_{\rm xc}[n(\mathbf{r})] = \mu_{\rm xc}(n) - \mu_{\rm xc}(n_0)$ in order to have [21,37] a vanishing effective potential at infinity. The ε_i quantities appear as Lagrange multipliers for each orbital. Due to the definition of the auxiliary system, the Fermi energy is the same as for an ideal system: $\varepsilon_{\rm F} = p_{\rm F}^2/2$. Equations (37) and (38) define a self-consistent field problem. The results obtained depend on the input exchange-correlation term, but the calculated phase-shifts always have to satisfy equation (19) by construction (see Section 4.1).

The principal advantage of equation (36), in comparison with a set of Hartree-like equations, is that one has to solve only one equation, which is an integro-differential equation. But the Coulomb singularity heralds the special role of the kinetic term in order to satisfy the nuclear-cusp condition for the induced density. Clearly, this term is better described in a single-particle representation, like in equation (38). Of course, motivated by the original enticing idea of DFT, approximate treatments on $T[n]$ solely in terms of the density (*explicit* functional) are available. Now, we outline the models based on these treatments.

The oldest attempt is the Thomas–Fermi (TF) approximation. It uses a local kinetic energy functional of the ideal electron gas $T_{\rm TF}[n]$, and neglects exchange-correlation. In a perturbative description, i.e., *linearizing* the corresponding equation (36), one gets the well-known Yukawa-type effective screened potential used previously in this work for simple phase-shift calculations. On the other hand, the Poisson's equation gives a divergent induced density at the Coulomb singularity. This is the most unphysical behavior of the TF approximation; the induced density should be finite everywhere.

A more sophisticated treatment, still based on the direct variational method, rests on using the *sum* [38] of the mentioned Thomas–Fermi

functional $T_{TF}[n]$ and the von Weizsäcker kinetic expression (the $T_W[n]$-only case would refer to an ideal boson system)

$$T_W[n] = \frac{\lambda}{8} \int d\mathbf{r} \frac{[\nabla n(\mathbf{r})]^2}{n(\mathbf{r})}, \tag{39}$$

in equation (36) for $T[n]$. It is reasonable to suppose [38] that $T_s[n] < T_W[n] + T_{TF}[n]$; therefore, we neglect residual exchange-correlation contributions and take $\mu^0[n_0] = p_F^2/2$. After a partial linearization, solely in the Thomas–Fermi term, one gets [23] the following equation

$$\left(-\frac{\lambda}{2}\nabla^2 + b\right)w(r) + \left(-\frac{Z}{r} + \int d\mathbf{r}' \frac{\Delta n(\mathbf{r}')}{|\mathbf{r} - \mathbf{r}'|}\right)[w(r) + w_0] = 0, \tag{40}$$

in which $w(r) = n^{1/2} - n_0^{1/2}$, $w_0 = n_0^{1/2}$ and $b = 2p_F^2/3$ is the Pauli's potential.

The iterative solution of equation (38) is usually carried out with the following expression, obtained [39] from a self-energy treatment for the homogeneous system

$$\mu_{xc}(r_s) = -\frac{0.6108}{r_s} - 0.0333 \log\left(1 + \frac{11.4}{r_s}\right), \tag{41}$$

and in our case (LDA) the parameter $r_s(r)$ is defined from $n(r) = 3/[4\pi r_s^3(r)]$. It is well established, based on practice [21,37], that this input gives in KS–DFT very reasonable results for various physical quantities related to ion embedding.

The numerical results [40–42] for the $Q_{tr}(v_F) = n_0 v_F \sigma_{tr}(v_F)$ transport collision frequency, needed in the low-velocity stopping, equation (10), are given in Table 3 for protons and antiprotons. The results are based on equations (38) and (40) with $\lambda = 1$, and show a remarkable theoretical agreement for the observable quantities (see Table 2, for a comparison). The agreement is a notable fact, since the phase-shifts based on equation (38) are, from a rigorous point of view, auxiliary quantities in the fictitious one-particle orbitals. Of course, the calculation based on equation (40) was implemented by the scattering Schrödinger equation using the output-iterated potentials. Interestingly, these potentials result in almost perfect agreement [42] with the sum rules of equations (19) and (20) for the antiproton case.

Note that an iterative treatment, using [43] an inhomogeneous (linear) integral equation for the induced density, also gives a perfect agreement with the above antiproton stopping power values if the resulting density is used, *via* Poisson's equation, in potential construction and thus in phase-shifts

Table 3. Transport collision frequency $Q_{\rm tr}$ computed at several values of the density parameter r_s

r_s	$Q_{\rm tr}^{\rm (TFW)}(p)$	$Q_{\rm tr}^{\rm (KS)}(p)$	$Q_{\rm tr}^{\rm (TFW)}(\bar{p})$	$Q_{\rm tr}^{\rm (KS)}(\bar{p})$
0.5	0.451	0.459	0.364	0.355
1.0	0.363	0.377	0.227	0.220
1.5	0.305	0.310	0.155	0.154
2.0	0.254	0.259	0.113	0.114
2.5	0.205	0.210	0.086	0.088
3.0	0.162	0.163	0.067	0.070
3.5	0.126	0.126	0.052	0.055
4.0	0.098	0.098	0.044	0.048

Upper indices TFW and KS indicate, respectively, the Thomas–Fermi–Weizsäcker (equation (40)) and Kohn–Sham (equation (38)) approximations in DFT. The arguments, p and $\bar{p}$, in $Q_{\rm tr}$ refer to the proton and antiproton cases.

calculation. The basic equation [24] is the following

$$\Delta n(q) = \Delta n_{\rm L}(q)\left[1 + \frac{1}{\pi\omega_{\rm p}^2}\int_0^\infty {\rm d}k\, k^2 f(k,q)\Delta n(k)\right], \tag{42}$$

in which $\Delta n_{\rm L}(q)$ is the linear-response input, and the function $f(q,k)$ has the form

$$f(q,k) = 1 + \frac{q^2-k^2}{2qk}\log\left|\frac{q+k}{q-k}\right|. \tag{43}$$

Finally, this method allows a rigorous convergence-investigation for the Neumann series expansion up to infinite order. The mathematical result [44] found, namely the restricted range of applicability of an expansion in terms of a linear input, is in accord with the more physical statements outlined in Fig. 2 and Tables 1 and 2.

5.3. Adiabatic model potentials for swift ions

In the impurity limit there are convincing theoretical results for the stopping power of an electron gas for heavy unit-charge intruders. The applied kinetic approximation clearly shows the importance of correct quantum scattering description in binary collisions. Thus, there is a nontrivial challenge for higher velocities. The illustrative results in equations (6)–(9), already give a kinematics- and potential-dependent explanation for the experimentally verified velocity proportionality in stopping, practically up to the Fermi velocity.

At present, the most sophisticated theoretical model, within the kinetic approximation, is based on equation (2) with cylindrically symmetric potential obtained from a set of Kohn–Sham auxiliary equations. In this extended model the single-particle orbitals are populated according to the velocity-shifted [45] zero-temperature Fermi–Dirac occupation function. The cross-section, needed in equation (2), is calculated by an expansion method [46] developed for nonspherical, fixed potentials. This remarkable theoretical attempt, implemented for velocities close (from below) to the Fermi velocity, heralds that the above-mentioned, straight velocity proportionality is the result of an interplay between kinematics and screening.

The quite essential role of kinematics suggests the possibility of other model calculations, based on physically motivated velocity-dependent (still adiabatic) screening descriptions. On the other hand, a comparison of Fig. 1 with Table 2 and the observed strong dependence on potential forms shows that one-parametric models need care, especially for antiprotons. This is related to the repulsive nature of the shielded interaction. The induced density obviously has a natural bound $|\Delta n(r)| \leq n_0$, in this case. Therefore, we use the model derivable formally from equation (40) by a complete linearization. This corresponds to $\Delta n(r) \Rightarrow 2w_0 w(r)$ and $w(r) + w_0 \Rightarrow w_0$ at relevant places of the equation.

The resulting equation is now analytically solvable by Fourier transformation method and one obtains the following transparent expression

$$\Delta n(q) = Z \frac{16\pi n_0}{\lambda q^4 + 2bq^2 + 16\pi n_0}, \tag{44}$$

for the induced density. The screened potential is obtained by Poisson's equation, and has the $V(q=0) = Zb/(2n_0)$ value in the forward limit. Using equation (27) with the $Q = Z$ constraint, we obtain a velocity-dependent form for the b-factor

$$b(v, p_{\mathrm{F}}) = \frac{2}{3} p_{\mathrm{F}}^2 \left[\frac{1}{2} + \frac{p_{\mathrm{F}}^2 - v^2}{4 p_{\mathrm{F}} v} \log \left| \frac{v + p_{\mathrm{F}}}{v - p_{\mathrm{F}}} \right| \right]^{-1}, \tag{45}$$

representing *now*, as pseudopotential [$b(v \gg p_{\mathrm{F}}) \sim v^2$], an average kinetic energy. The effective potential $V(r)$, with $\lambda = 1$ as in the previous iterative case, is as follows

$$V(r, b) = -\frac{Z}{r} \mathrm{e}^{-\alpha r} \left[\frac{\mathrm{e}^{\gamma r} + \mathrm{e}^{-\gamma r}}{2} + \frac{b}{4\alpha\gamma} (\mathrm{e}^{\gamma r} - \mathrm{e}^{-\gamma r}) \right], \tag{46}$$

in which $\alpha^2 = (b/2) + \omega_{\mathrm{p}}$ and $\gamma^2 = (b/2) - \omega_{\mathrm{p}}$. Note that $V(r)$ may have an oscillatory behavior as a function of the model parameters b and n_0.

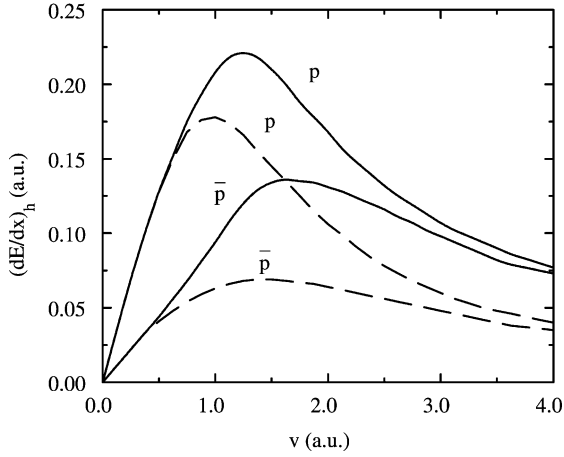

Fig. 3. The stopping power of a homogeneous electron gas with $r_s = 2.07$, as a function of the projectile velocity v, for protons (p) and antiprotons ($\bar{p}$). The solid curves are based on consistent velocity-dependent potentials, while the dashed ones are based on the corresponding static potentials.

Illustrative numerical results obtained for proton and antiproton stopping powers, using this velocity-dependent spherical model potential in the scattering Schrödinger equation to calculate transport cross-sections needed in equation (5), are exhibited in Fig. 3, at a typical density parameter $r_s = 2.07$.

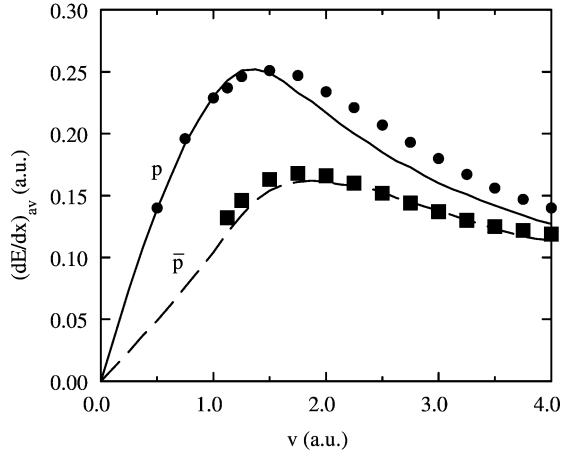

Fig. 4. The average stopping power (see equation (47)) of an Al target for proton (p) and antiproton ($\bar{p}$) as a function of the projectile velocity v. The data are denoted by ● for proton [48] and by ■ for antiproton [2].

The comparison of solid and dashed curves, based on velocity-dependent and static potentials, respectively, clearly shows the important role of screening-modeling in addition to the kinematics in binary collisions [47].

In order to compare with experimental data [2,48] derived for real metallic (Al) target, a volume average of theoretical results, obtained above for an homogeneous (h) electron gas, is performed over the solid state atomic electron density

$$\left(\frac{\mathrm{d}E}{\mathrm{d}x}\right)_{\mathrm{av}} = \frac{3}{R_{\mathrm{W}}^3}\int_0^{R_{\mathrm{W}}} \mathrm{d}r\, r^2 \left(\frac{\mathrm{d}E}{\mathrm{d}x}\right)_h [r_s(r)], \tag{47}$$

at fixed v values ($R_{\mathrm{W}} = 3$ for Al). The comparison of theoretical and measured data is given in Fig. 4, which shows [47] a very reasonable agreement.

5.4. A sudden approximation for the charge-sign effect

All the above calculations are based on the *adiabatic* assumption in screening descriptions. When the results obtained for a homogeneous electron system are employed (using the local-plasma approximation, LPA) for atomistic targets, the time-scale associated with the atomic period becomes an important question. This question was discussed by Bohr [49] and the role of the atomic binding force (a central-field concept), as regards the energy transfer, was considered as a kind of screening of dynamical origin. On the other hand, as we mentioned in Section 2, the actual interaction between electrons needs a careful, separate consideration.

These *two* aspects, namely, the short interaction time for fast intruders and the effective interaction of atomic electrons, were considered in a calculation [50] for the charge-sign effect. The electronic correlation is described locally by a screened potential and the scattering of a bare intruder ($Z_1 = \pm 1$) off this static potential by second-order Born approximation. Thus the LPA is implemented *via* a *sudden* approximation in the kinetic theory. The obtained result is [50] as follows

$$\frac{\mathrm{d}E}{\mathrm{d}x} = N\frac{4\pi Z_1^2 Z_2}{v^2}\left[\ln\frac{2v^2}{I_{\mathrm{eff}}} + Z_1\frac{1.7\lambda_{\mathrm{eff}}}{v^2}\ln\frac{2v}{\lambda_{\mathrm{eff}}}\right], \tag{48}$$

in which $I_{\mathrm{eff}} = 0.35Z_2$ and $\lambda_{\mathrm{eff}} = 0.72Z_2^{1/3}$ are, respectively, the effective (averaged) excitation energy and electronic screening associated with the target atom (Z_2). N is, as in Section 3.2, the target density. The $(1/v^2)$ and

weak Z_2 dependences of the Barkas term (second term) are in agreement with experimental [2,51] predictions.

6. SUMMARY AND REMARKS

Models of different sophistications are used in this work in order to calculate an important observable of heavy ion interaction with matter, the stopping power. The theoretical study presented follows a comparative way to understand the key ingredients and thus establish a clear phenomenology to explanations.

The results obtained herald that for a metallic electron gas even the simplest $Z = \pm 1$ intruders represent strong perturbations. This fact requires a nonperturbative description of binary electron–ion collisions in terms of phase-shifts. The charge-sign effect in stopping is notable in a broad range of the bombarding-ion velocity. Combined theoretical attempts, proper scattering description and consideration of the inhomogeneity in the electron density, are needed to achieve a quantitative agreement with experimental predictions.

For low-velocity antiprotons *three* nonperturbative treatments give an excellent agreement for the stopping power. This case is, therefore, well described and can provide a transferable knowledge. There is a nice agreement between *two* iterative methods based on DFT for the proton stopping. Here, there are remaining questions. In the KS–DFT one should populate an auxiliary weakly bound state, while in the applied TFW–DFT attempt one does not divide the induced density into bound and scattering components.

In Hartree-like, single-particle description of the static screening in a paramagnetic electron gas, one satisfies the Pauli principle in an *ad hoc* way by giving double occupancy to any bound state. On the other hand, it follows from the fundamental theorem of Kohn and Majumdar [52] that, in a ground-state situation, *this* occupancy is the proper one. The basic physical variable, the density, should change in an analytic (smooth) fashion where a new bound state appears.

We illustrate this statement *via* our Hulthen-type potential with $Z = 1$. Without loss of mathematical rigor we take $p_F \ll 1$ and $\Lambda = 2(1 \pm \Delta)$, with the $\Delta \ll 1$ *but* $(p_F/\Delta) \gg 1$ constraints. The total induced density at the proton position is $n(0) = n_{sc}(0) + n_b(0)$ if there is a bound (b) state in addition of scattering (sc) states. Under the *above* conditions the enhancement (see equation (35)) factor $E(p)$, where $p \in [0, p_F]$, is given by

$$E(p) = \frac{2}{(\sqrt{\Lambda} - \sqrt{2})^2 + p^2/2}. \tag{49}$$

Thus the scattering-mediated part, $n_{sc}(0)$, has the following form

$$n_{sc}(0) = 2\frac{4\pi}{(2\pi)^3}\int_0^{p_F} dp\, p^2 E(p) \approx \left(\frac{2}{\pi}\right)^2 p_F - \frac{2}{\pi}\sqrt{2}|\sqrt{\Lambda} - \sqrt{2}|, \quad (50)$$

showing a peaked (and *symmetric*) kink-type behavior at $\Lambda = 2(1 \pm \Delta)$, i.e., around the critical ($\Lambda = 2$) screening parameter. A bound state [$\Lambda = 2(1 - \Delta)$] contribution comes from the 1s-type normalized wave-function [33] as

$$n_{1s}(0) = |\psi_0(0)|^2 = \frac{1}{\pi}\left[1 - \left(\frac{\Lambda}{2}\right)^2\right] \approx \frac{2}{\pi}\Delta. \quad (51)$$

Therefore, the smooth nature of $n(0)$ prescribes a $n_b(0) = 2n_{1s}(0)$ contribution (double occupancy) in order to get an analytic behavior.

The possible capture-loss processes for moving positive ions are considered, usually, within a different, perturbative theoretical framework [53,54] based on a self-energy treatment. In such a treatment the role of the proper form of a weakly bound state in capture-loss rates and associated energy loss contributions is a special problem [54], as the above exact treatment on the bound state clearly heralds.

As we already remarked in Section 4.2, a *unified* description would need further works in this field, i.e., using certain total balance [26] and continuity concepts to treat nontrivial, higher order processes. The nonperturbative (static ground state) and perturbative (capture loss) descriptions are, in a certain sense, artificially separated without a dynamical (current conservation) constraint between them.

The applied kinetic model is strongly tied to an essentially Sommerfeld picture for the electron gas. In this model all many-body complications are 'embedded' in an effective one-body screened potential. Dynamical exchange-correlation, i.e., multiparticle processes [55,56] require, beyond the one-particle attempt, a different theoretical framework [57,58]. The probing of such processes is better designed with excited electrons; they are more natural probes for the *details* of dynamical correlations [59,60] in an electron gas.

ACKNOWLEDGEMENTS

This work has been supported by the Hungarian OTKA (Grant Nos. T034363, T038162, and T038191). Many useful discussions, during years, with A. Arnau, P. M. Echenique, K. Ladányi†, A. Salin, and E. Zaremba are gratefully acknowledged.

†Deceased

REFERENCES

[1] S. P. Moller, A. Csete, T. Ichioka, H. Knudsen, U. I. Uggerhoj and H. H. Andersen, *Phys. Rev. Lett.*, 2002, **88**, 193201.
[2] S. P. Moller, E. Uggerhoj, H. Blume, H. Knudsen, U. Mikkelsen, K. Paludan and E. Morenzoni, *Phys. Rev. A*, 1997, **56**, 2930.
[3] E. Morenzoni, H. Glückler, T. Prokscha, R. Khasanov, H. Luetkens, M. Birke, E. M. Forgan, Ch. Niedermayer and M. Pleines, *Nucl. Instrum. Methods B*, 2002, **192**, 254.
[4] V. G. Storchak and N. V. Prokof'ev, *Rev. Mod. Phys.*, 1998, **70**, 929.
[5] H. E. Rafelski and B. Müller, in *Muon-Catalyzed Fusion* (eds S. E. Jones, J. Rafelski and H. J. Monkhorst), AIP, New York, 1989, p. 335.
[6] M. A. Kumakhov and F. F. Komarov, *Energy Loss and Ion Ranges in Solids*, Gordon & Breach, New York, 1981.
[7] P. M. Echenique, F. Flores and R. H. Ritchie (eds E. H. Ehrenreich and D. Turnbull), *Solid State Physics*, Academic Press, New York, 1990, Vol. 43, p. 229.
[8] D. Pines and P. Nozieres, *The Theory of Quantum Liquids*, Benjamin, New York, 1966.
[9] G. D. Mahan, *Many-Particle Physics*, Plenum Press, New York, 1981.
[10] W. M. C. Foulkes, I. Mitas, R. J. Needs and G. Rajagopal, *Rev. Mod. Phys.*, 2001, **73**, 33.
[11] G. E. Engel, *Phys. Rev. Lett.*, 1997, **78**, 3515.
[12] B. Farid, V. Heine, G. E. Engel and I. J. Robertson, *Phys. Rev. B*, 1993, **48**, 11602.
[13] G. Zwicknagel, Ch. Toepffer and P. G. Reinhard, *Phys. Rep.*, 1999, **309**, 117, and references therein.
[14] L. Bonig and K. Schönhammer, *Phys. Rev. B*, 1989, **39**, 7413; R. Diez Muiño and A. Salin, *Phys. Rev. B*, 2000, **62**, 5207.
[15] I. Nagy, *Phys. Rev. B*, 1995, **51**, 77.
[16] P. Sigmund, *Phys. Rev. A*, 1982, **26**, 2497.
[17] J. M. Luttinger and W. Kohn, *Phys. Rev.*, 1958, **109**, 1892.
[18] I. Nagy, *Nucl. Instrum. Methods B*, 1994, **94**, 377.
[19] N. Bohr, *Phil. Mag.*, 1913, **25**, 10; N. Bohr, *Phil. Mag.*, 1915, **30**, 581.
[20] J. S. Langer and S. H. Vosko, *J. Phys. Chem. Solids*, 1959, **12**, 196.
[21] C. O. Almbladh, U. von Barth, Z. D. Popovic and M. J. Stott, *Phys. Rev. B*, 1976, **14**, 2250.
[22] M. J. Watrous, L. Wilets and J. J. Rehr, *Phys. Rev. E*, 1999, **59**, 3554.
[23] K. Ladányi, I. Nagy and B. Apagyi, *Phys. Rev. A*, 1993, **45**, 9203.
[24] S. Sjölander and M. J. Stott, *Phys. Rev. B*, 1972, **5**, 2109.
[25] W. Zwerger, *Phys. Rev. Lett.*, 1997, **79**, 5270.
[26] J. Lindhard and A. Winter, *Nucl. Phys. A*, 1971, **166**, 413; P. F. Meier, *Helv. Phys. Acta*, 1975, **48**, 227.
[27] S. Servadio, *Phys. Rev. A*, 1971, **4**, 1256.
[28] I. Nagy and A. Bergara, *Nucl. Instrum. Methods B*, 1996, **115**, 58.
[29] A. F. Lifschitz and N. R. Arista, *Phys. Rev. A*, 1998, **57**, 200.
[30] C. D. Hu and E. Zaremba, *Phys. Rev. B*, 1988, **37**, 9268.
[31] G. Paasch and P. Rennert, *Phys. Status Solidi (b)*, 1977, **83**, 501.
[32] R. G. Newton, *Scattering Theory of Waves and Particles*, Springer, New York, 1982.
[33] R. Dutt, K. Chowdhury and Y. P. Varshni, *J. Phys. A: Math. Gen.*, 1985, **18**, 1379.
[34] H. Yasuhara and Y. Takada, *Phys. Rev. B*, 1991, **43**, 7200.
[35] I. Nagy, B. Apagyi, J. I. Juaristi and P. M. Echenique, *Phys. Rev. B*, 1999, **60**, R12546.
[36] W. Kohn, *Rev. Mod. Phys.*, 1999, **71**, 1253.
[37] E. Zaremba, L. M. Sander, H. B. Shore and J. H. Rose, *J. Phys. F: Metal Phys.*, 1977, **7**, 1763.
[38] R. M. Dreizler and E. K. U. Gross, *Density Functional Theory*, Springer, Berlin, 1990.
[39] O. Gunnarsson and B. I. Lundquist, *Phys. Rev. B*, 1976, **13**, 4274.

[40] P. M. Echenique, R. M. Nieminen and R. H. Ritchie, *Solid State Commun.*, 1981, **37**, 779; M. J. Puska and R. M. Nieminen, *Phys. Rev. B*, 1983, **27**, 6121; P. M. Echenique, R. M. Nieminen, J. C. Ashley and R. H. Ritchie, *Phys. Rev. A*, 1986, **33**, 897.
[41] I. Nagy, A. Arnau, P. M. Echenique and E. Zaremba, *Phys. Rev. B*, 1989, **40**, R11983.
[42] I. Nagy and B. Apagyi, *J. Mol. Struct. (Theochem)*, 2000, **501/502**, 495.
[43] A. Krakovsky and J. K. Percus, *Phys. Rev. B*, 1995, **52**, R2305.
[44] I. Nagy and A. Bergara, *J. Phys.: Condens. Matter*, 1999, **11**, 3943.
[45] A. Salin, A. Arnau, P. M. Echenique and E. Zaremba, *Phys. Rev. B*, 1999, **59**, 2537.
[46] A. D. Boardman, A. D. Hill and S. Sampanthar, *Phys. Rev.*, 1967, **160**, 472.
[47] I. Nagy and B. Apagyi, *Phys. Rev. A*, 1998, **58**, R1653.
[48] Ch. Eppacher and D. Semrad, *Nucl. Instrum. Methods B*, 1992, **69**, 33.
[49] N. Bohr, *K. Dan Vidensk. Selsk. Mat. Fys. Medd.*, 1948, **18** (8).
[50] I. Nagy, *Phys. Rev. A*, 2001, **65**, 014901.
[51] L. H. Andersen, H. Hvelpund, H. Knudsen, S. P. Moller, J. O. P. Pedersen, E. Uggerhoj, K. Elsener and E. Morenzoni, *Phys. Rev. Lett.*, 1989, **62**, 1731.
[52] W. Kohn and C. Majumdar, *Phys. Rev.*, 1965, **138**, A1617.
[53] F. Guinea, F. Flores and P. M. Echenique, *Phys. Rev. Lett.*, 1981, **47**, 604.
[54] M. Alducin, A. Arnau and I. Nagy, *Phys. Rev. A*, 2003, **68**, 014701.
[55] A. A. Kugler, *J. Stat. Phys.*, 1975, **12**, 35.
[56] E. K. U. Gross and W. Kohn, *Phys. Rev. Lett.*, 1985, **55**, 2850.
[57] I. Nagy, J. László and J. Giber, *Z. Phys. A*, 1985, **321**, 221.
[58] J. Ortner and I. M. Tkachenko, *Phys. Rev. E*, 2001, **63**, 026403.
[59] P. M. Echenique, J. M. Pitarke, E. V. Chulkov and A. Rubio, *Chem. Phys.*, 2000, **252**, 1.
[60] M. Alducin, J. I. Juaristi and I. Nagy, *J. Electron Spectrosc.*, 2003, **129**, 117.

This Page Intentionally Left Blank

High Z Ions in Hot, Dense Matter

James W. Dufty,[1] Bernard Talin[2] and Annette Calisti[2]

[1] *Department of Physics, University of Florida, Gainesville, FL 32611, USA*
[2] *UMR6633, Université de Provence, Centre Saint Jérôme, 13397 Marseille Cedex 20, France*

Abstract

Current and proposed experiments on high-energy density matter include conditions for high Z ions in fully ionized plasmas. A semi-classical description is proposed whereby the classical Coulomb interactions are 'regularized' at short distances to account for quantum diffraction effects. One motivation for this approach is to allow application of classical molecular dynamics (MD) simulation methods. Here, attention is focused on energy transfer between a heavy-impurity ion at low velocities and an electron gas. The relationship between the mobility, diffusion, and stopping power is noted and clarified. Some examples of MD simulation to explore the dependence on charge number of the impurity are given for an impurity in an electron gas.

Contents

1. INTRODUCTION

In recent years there has been growing interest in the properties of hot, dense matter due to the accessibility of such conditions through new laboratory devices. For example, the new National Ignition Facility being built at Lawrence Livermore Laboratories will provide experimental state conditions at higher temperatures and densities than those of the interior of the sun. It is expected that in many cases there will be fully ionized matter consisting of electrons and ions with some of the latter having large charge number, Z. In some cases these ions will be inserted as spectroscopic probes. Equally important will be their role in transport and exchange of energy

ADVANCES IN QUANTUM CHEMISTRY, VOLUME 46
ISSN: 0065-3276 DOI 10.1016/S0065-3276(04)46011-0

among different degrees of freedom. An understanding of the energetics of such high Z ions in hot, dense matter is clearly important for the interpretation of these experiments and an understanding of matter at extreme conditions.

The interaction among ions is largely semi-classical due to the repulsive Coulomb forces that enforce average distances larger than their thermal de Broglie wavelength. In contrast, the electron thermal de Broglie wavelength is much larger due to its smaller mass and quantum effects can be important even at high temperatures. In particular, the ion–electron interaction always requires quantum theory to avoid the un-physical classical collapse due to the attractive Coulomb force. In fact, there is no well-defined classical statistical mechanics for ions and electrons interacting *via* pure Coulomb forces due to this collapse. However, in recent years a great deal of attention has been given to the idea of using modified Coulomb interactions that regularize the short-range divergence. The original proposal was to define a classical pair potential in terms of the quantum two-particle density matrix [1–3]. This assures that a class of two-particle expectation values is given exactly through a corresponding classical calculation. More phenomenologically, it is assumed that this regularized pair potential can be used in classical many-body calculations to account for the relevant quantum many-body effects. This assumption has been justified in some limiting cases (weak coupling) and has been supported by a number of comparisons between semi-classical and quantum predictions for many applications [4]. Generally speaking, the approach is limited to conditions for which independent pair interactions dominate.

The objective here is to describe a semi-classical treatment of the energetics for high Z ions in a fully ionized plasma, based on the assumption of regularized Coulomb interactions among the charges. A primary motivation for this approach is the potential to use a wide range of well-developed many-body methods, both theoretical and numerical. Of particular interest is the possibility to apply classical molecular dynamics (MD) simulation methods [5] to this problem. MD simulation accounts for all possible semi-classical correlations induced by the regularized potentials and therefore accounts for effects that necessarily are missing in any approximate theoretical treatment. Its success in the description of classical fluids, plasmas, and solids [6] has been extended in recent years to high-temperature semi-classical systems by the methods proposed here. From the theoretical side an accurate description exists for a positive impurity charge among positive ions [7], where both collisional and collective effects are properly accounted for. An accurate theoretical description of the interaction of the impurity charge with the electrons remains a difficult unsolved problem [8].

It has been noted elsewhere that there is a close exact relationship between stopping power at low velocity, impurity diffusion, and mobility [9].

The experimental conditions for these three properties are quite different; so their common characterization by the same material constant is somewhat surprising. The connection to the coefficient of stopping power at low velocities is more complex. Still, all are interesting and important properties for which MD simulation methods are appropriate in this semi-classical formulation. The generality of the simulation gives access to effects (charge–charge correlations) that are difficult to treat theoretically in a controlled fashion.

The regularized Coulomb potentials are described in Section 2 along with a brief overview of the MD simulation method. Next the Green–Kubo relations for diffusion, mobility, and the stopping power coefficient are recalled and their relationship is discussed. In Section 4, the simple case of a heavy impurity ion in an electron gas is considered [10]. In this case all coefficients are simply related. The stopping power is calculated from MD simulation in terms of the equilibrium electron electric field autocorrelation function [11]. The properties of this function are illustrated as a function of the electron-impurity coupling, showing strong deviations from the usual Born approximation. The result is interpreted by a simple theoretical model that reproduces well the qualitative features of the simulation. Finally, these results are summarized and the outlook for future MD simulation is indicated.

2. SEMI-CLASSICAL STATISTICAL MECHANICS

The system considered is two-component plasma with N_e electrons with charge $-e$, and N_i ions with charge Ze at equilibrium. Charge neutrality implies the condition $N_i Z = N_e$. In addition, an impurity ion of charge $Z_0 e$ is included. The Hamiltonian for the system is therefore

$$H = \sum_{\alpha=1}^{N_e} \frac{p_\alpha^2}{2m_e} + \frac{1}{2} \sum_{\alpha \neq \nu}^{N_e} \sum^{N_e} \frac{e^2}{|\mathbf{r}_\alpha - \mathbf{r}_\nu|} + \sum_{\alpha=1}^{N_i} \frac{p_\alpha^2}{2m_i} + \frac{1}{2} \sum_{\alpha \neq \nu}^{N_i} \sum^{N_i} \frac{Z^2 e^2}{|\mathbf{r}_\alpha - \mathbf{r}_\nu|}$$
$$- \sum_{\alpha \neq \nu}^{N_e} \sum^{N_i} \frac{Ze^2}{|\mathbf{r}_\alpha - \mathbf{r}_\nu|} + \frac{p_0^2}{2m_0} + \sum_{\alpha=1}^{N_i} \frac{ZZ_0 e^2}{|\mathbf{r}_\alpha - \mathbf{r}_0|} - \sum_{\alpha=1}^{N_e} \frac{Z_0 e^2}{|\mathbf{r}_\alpha - \mathbf{r}_0|}. \quad (1)$$

The first five terms represent the Hamiltonian for an isolated two-component plasma; the last three terms represent the Hamiltonian for the impurity interacting with the constituents of this plasma. In all of the following, the properties of the impurity are denoted by a subscript 0.

The equilibrium statistical mechanics for this system is well defined for quantum mechanics but not for classical mechanics. The reason for the failure in the latter case is the unbounded attractive Coulomb interactions of

ions and electrons. The quantum theory tempers these divergencies in all expectation values of physical properties through diffraction effects arising from the non-commutation of kinetic energy and potential energy terms. Effectively, the interaction becomes finite inside a sphere of the radius of the thermal de Broglie wavelength, $\lambda = (h^2/2\pi\mu_{12}k_{\mathrm{B}}T)^{1/2}$, where μ_{12} is the reduced mass of the interacting pair. This property can be made explicit by defining a semi-classical pair potential with the two-particle Slater sum (diagonal matrix element of the two-particle electron–ion density matrix) according to

$$V(|\mathbf{r}_1 - \mathbf{r}_2|) \equiv -kT \ln\langle r_1, r_2|\lambda^{-3} \times \exp\left(-\frac{1}{kT}\left(\frac{p_1^2}{2m_1} + \frac{p_2^2}{2m_2} + \frac{q_1 q_2}{|\mathbf{r}_1 - \mathbf{r}_2|}\right)\right)|r_1, r_2\rangle. \quad (2)$$

A more explicit analytic form is obtained in the high-temperature limit, known as the Kelbg potential [1]

$$V(r) = \frac{q_1 q_2}{r}\left(1 - \mathrm{e}^{-r^2/\lambda^2} + \sqrt{\pi}\frac{r}{\lambda}\left(1 - \mathrm{erf}\left(\frac{r}{\lambda}\right)\right)\right). \quad (3)$$

Recently, it has been found that the Kelbg potential can be reparameterized ($\lambda \rightarrow \lambda'$) to yield good agreement with the exact form (equation (2)) at much lower temperatures [4]. Extensions to include spin are also possible. Application of this new form to hydrogen shows good results for the energy including formation of atomic hydrogen in partially ionized plasmas. In summary, there is growing evidence in support of a semi-classical statistical mechanics based on these regularized potentials as a satisfactory representation of the underlying quantum system [12]. In all of the following, we assume this semi-classical picture for our discussion.

For the simulations presented below, a simpler semi-quantitative representation of the Kelbg potential [13] is used

$$V(r) = \frac{q_1 q_2}{r}(1 - \mathrm{e}^{-r/\lambda}). \quad (4)$$

The maximum coupling between an impurity ion of charge number Z and an electron is given by dimensionless number $\sigma = V(0)/k_{\mathrm{B}}T = Ze^2/k_{\mathrm{B}}T\lambda = Z\Gamma/\delta$. Here, $\Gamma = e^2/k_{\mathrm{B}}Tr_0$ is the electron coupling constant (r_0 is the average inter-particle distance $4\pi n r_0^3/3 = 1$) and $\delta = \lambda/r_0$ is the thermal de Broglie wavelength relative to this distance. In Section 4 we consider conditions such that $\Gamma < 1$ but a range of values for $\sigma > 1$.

The assumption of a classical statistical mechanics allows the use of sophisticated classical many-body tools. Foremost among these is MD simulation. In principle, MD accounts for all correlations and many-body effects for both static and dynamic properties of classical systems. It has been exceptionally useful for predicting new properties and testing theoretical

methods for such diverse systems as gases, liquids, solids, plasmas, and glasses. In this classical context the only limitations are due to the finite system size (particle number) in relation to the force range, and to the time interval required for accurate statistics. For its application here, however, new difficulties are encountered due to the attractive ion–electron force at strong coupling. Electron trapping by the ion in metastable states with large life times can occur, requiring very long simulation times to obtain good statistics for properties such as electric fields. To allow the most efficient MD simulations, periodic boundary conditions are used and the potential is screened at distances of the order of the system size. This screening is always much larger than the correlation length; so the results are essentially the same as would be obtained with an Ewald sum to correct for small finite system size.

Standard MD techniques have been used here, but for unusual conditions. First, the accretion of the electrons around the ion has to be compensated by a large number of particles in the simulation volume in order to minimize the depletion that might result at large distances, particularly in the case of large Z. Second, the size of the simulation volume has to be large enough to ensure that the numerical model is a relevant representation for the long-range Coulomb potential, and to minimize interaction with other ions duplicated through the periodic boundary conditions. Third, equilibrium conditions have to be reached in the presence of the attractive central force. These equilibrium conditions are fulfilled provided a careful set-up for the particles in the simulation volume is carried out before sampling the system. Practically, times representing several crossing times of an average electron over the simulation volume are considered. During this time fluctuations in the total energy of the system must be negligible. Limitations related to strong electron–ion attraction are imposed for this protocol. For small de Broglie wavelength, an electron with a low kinetic energy can stay trapped in the attractive central potential for times comparable to the simulation time. Such an event is interpreted as a failure of the simulation model, and do not occur for the results reported below. Nevertheless, the charge density structure near the ion, represented by the density correlation function at small r, generally shows a noticeable noise representative of a more difficult sampling in this domain. Still, the quality is quite good as illustrated in Fig. 1 for a two-component plasma simulation of the ion–ion and ion–electron pair correlation functions.

3. GREEN–KUBO RELATIONS AT SMALL VELOCITIES

Consider an impurity ion in a complex medium at local equilibrium, a typical experimental condition. The condition of local equilibrium means that within each cell the properties are the same as those for an equilibrium

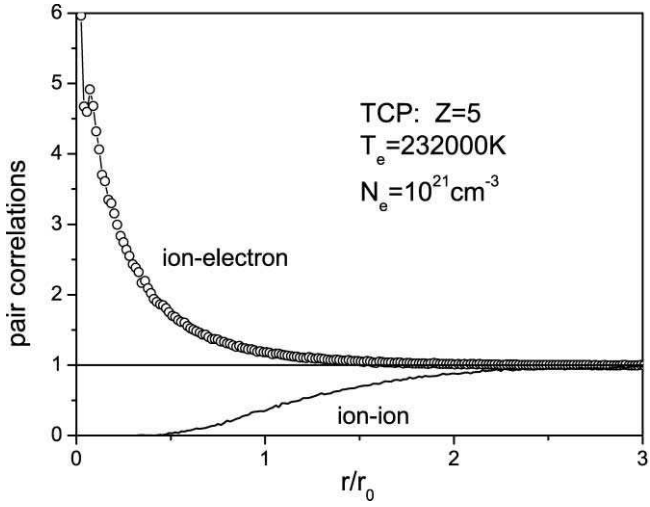

Fig. 1. Ion and electron charge density around an ion in a two-component plasma.

system at the local state conditions. It is well known from linear response theory that the mobility μ (characterizing the average velocity under an external force) and the diffusion coefficient D are given by [14]

$$k_B T\mu = D = \frac{1}{6}\int_{-\infty}^{\infty} dt\langle \mathbf{v}_0(t)\cdot\mathbf{v}_0\rangle. \tag{5}$$

The first equality is known as an Einstein relation. The second equality is a Green–Kubo expression resulting from two quite different but exact calculations of linear response. The brackets denote an equilibrium ensemble average and $\mathbf{v}_0(t)$ is the velocity of the impurity ion at time t. This result is valid for a complex mixture of electrons and ions, and applies to both quantum and classical limits. In particular, there are no restrictions on the impurity ion charge or mass.

A seemingly quite different Green–Kubo relation has been obtained in a more restrictive context. Consider an impurity ion injected in an idealized electron fluid (electrons plus a uniform neutralizing positive background) with an initial speed u. Then in two limits of small electron impurity mass ratio followed by small u the stopping power is given exactly by [9]

$$S(u) \equiv \frac{dK}{dt}\frac{dt}{dl} \to u\frac{Z^2e^2}{m_0}\int_{-\infty}^{\infty} dt\langle \mathbf{E}_e(t)\cdot\mathbf{E}_e\rangle. \tag{6}$$

Here K is the average kinetic energy of the impurity and l is its path length. The Green–Kubo expression is now given as a time integral of

the autocorrelation function for the total electric field at the impurity due to the electrons, $\mathbf{E}_e$. While this result is interesting on its own, there is a surprising relationship to μ and D in this same limit. Quite generally, the velocity autocorrelation function can be expressed in terms of a 'memory' function $M(t)$ by

$$\partial_t \langle \mathbf{v}_0(t)\cdot\mathbf{v}_0\rangle + \int_0^t \mathrm{d}t' M(t-t')\langle \mathbf{v}_0(t')\cdot\mathbf{v}_0\rangle = 0. \tag{7}$$

An alternative form for equation (5) is therefore

$$(k_B T\mu)^{-1} = D^{-1} = \frac{1}{6}\int_{-\infty}^{\infty} \mathrm{d}t\, M(t). \tag{8}$$

In general, the form of $M(t)$ is quite complex and not related in any simple way to the correlation function of equation (6). However, when specialized to the electron fluid and the small mass ratio limit above $M(t)$ becomes proportional to this field autocorrelation function. In this case there is the exact relationship [15]

$$S(u)/u = \mu^{-1} = k_B T D^{-1} = \frac{Z^2 e^2}{m_0}\int_{-\infty}^{\infty} \mathrm{d}t \langle \mathbf{E}_e(t)\cdot\mathbf{E}_e\rangle. \tag{9}$$

Since $Ze\mathbf{E}_e$ is the force on the ion, the Green–Kubo expression is the time integral of the force autocorrelation function. This is familiar from the classical theory of Brownian motion where the friction constant in the Fokker–Planck equation is given by the force autocorrelation function. For this reason, the stopping coefficient $S(u)/u$ at small u is frequently referred to as the 'friction coefficient'. Also from the Fokker–Planck equation it is easy to derive the relationships given in equation (5). However, it should be noted that the Fokker–Planck limit does not exist for quantum mechanics, yet equation (9) remains valid. More importantly, a real medium consists of both electrons and ions so that the mass ratio limit is not applicable for all species. Consequently, a result like equation (9) does not apply and it is misleading to associate the stopping coefficient, in general, with a friction coefficient empirically defined by Stokes law. To our knowledge a formally exact Green–Kubo expression for the stopping coefficient outside this small mass ratio limit does not seem to have been given.

4. IMPURITY ION IN AN ELECTRON GAS

In spite of the warning of these last remarks, it is useful to consider the idealized electron gas to illustrate the utility and power of MD simulation in the semi-classical representation. The problem is to evaluate the electron electric field autocorrelation function at an impurity ion of charge Z. In this

infinite mass limit the ion can be taken at rest at the origin. What is the qualitative behavior of this correlation function? At $Z = 0$ it can be expressed in terms of the electron gas dielectric function for which there are many good approximations. At $Z > 0$ there is neither well-developed theory nor phenomenology for guidance. How does it behave as a function of Z, or more accurately, as a function of the maximum coupling between the ion and the electrons $\sigma = Z\Gamma/\delta$? MD simulation provides the necessary guidance and control (benchmark) for theoretical interpretations. In this section the qualitative features of the correlation function are identified by MD simulation and later interpreted by a theoretical model reproducing those results [8].

All of the cases considered in this section correspond to weakly coupled electrons, $\Gamma < 1$. However, the electron–ion coupling can be strong.

First, Fig. 2 shows the dimensionless field autocorrelation function $C(t)$

$$C(t) = \frac{r_0^4}{e^2}\langle \mathbf{E}_e(t)\cdot\mathbf{E}_e\rangle, \tag{10}$$

for $\Gamma = 0.1$, $\delta = 0.4$, and $\sigma = 0.25Z$, with $0 \le Z \le 30$ $(1 \le \sigma \le 7.5)$. The corresponding density and temperature are $n_e = 2.5 \times 10^{22}\ \mathrm{cm}^{-3}$ and $T = 7.9 \times 10^5$ K. Recall that the familiar Born approximation is $\sigma = 0$ and is similar to the $\sigma = 1$ result shown. At stronger coupling three

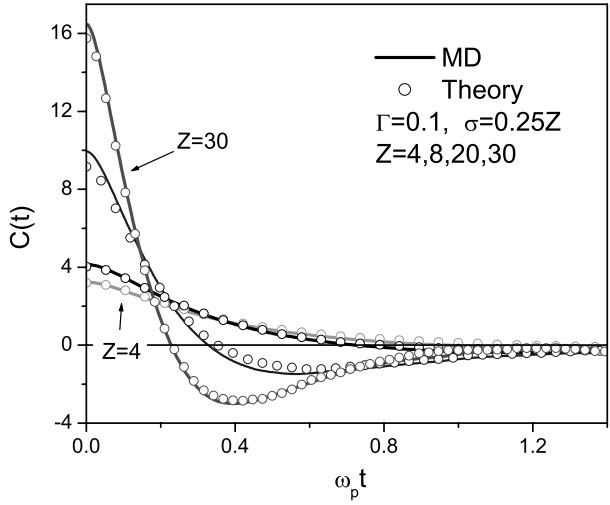

Fig. 2. Field autocorrelation function *vs.* time for several different coupling strengths.

qualitative features are observed. First, there is a significant increase in the initial correlations due to the enhanced electron population near the ion with increasing σ. Second, the initial decay time decreases with increasing σ. Finally, there is the development of an anti-correlation at stronger coupling.

Figure 3 shows the time integral behavior of $C(t)$ ('area') resulting from the competition between the initial increase in correlation and the dynamical decrease due to shorter correlation time and the anti-correlation domain. Three different conditions are represented on this graph, that of Fig. 2, the extreme electron–ion coupling conditions of $\Gamma = 0.5$, $\delta = 0.2$, and $\sigma = 2.5Z$, with $0 \leq Z \leq 5$ ($n = 3.2 \times 10^{18}$ cm^{-3}, $T = 7.9 \times 10^3$ K), and the experimentally relevant conditions of $\Gamma = 0.029$, $\delta = 0.059$, and $\sigma = 0.5Z$, with $0 \leq Z \leq 8$ ($n = 1 \times 10^{19}$ cm^{-3}, $T = 2 \times 10^5$ K). All show a decrease in the time integral of $C(t)$ with stronger coupling, indicating a dominance of the decreasing correlation time and increasing anti-correlation over the enhanced initial value.

The σ (or equivalently the Z) dependence of Fig. 3 implies a decrease in the stopping power relative to that of the Born approximation. This is illustrated for the weak coupling conditions ($\Gamma = 0.029$, $\delta = 0.059$, $\sigma = 0.5Z$) in Fig. 4.

The Born approximation is obtained by fitting the first two points to a Z^2 dependence. Deviations are seen for $\sigma > 2$. This is more evident for

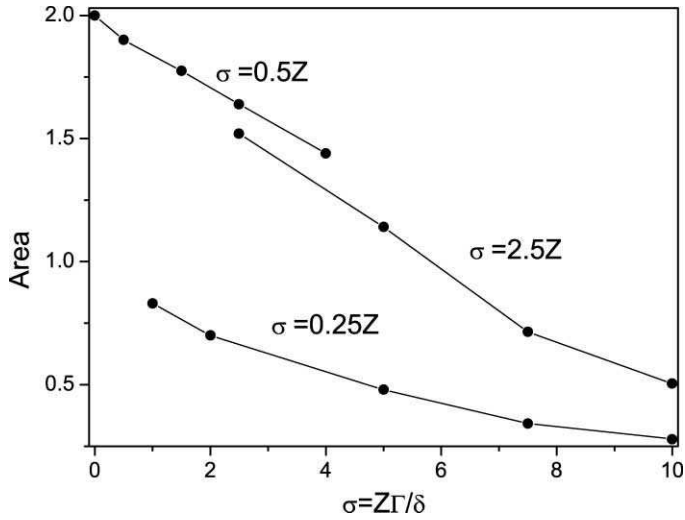

Fig. 3. Time integral of the field autocorrelation function (area) *vs.* coupling strength for three different electron state conditions.

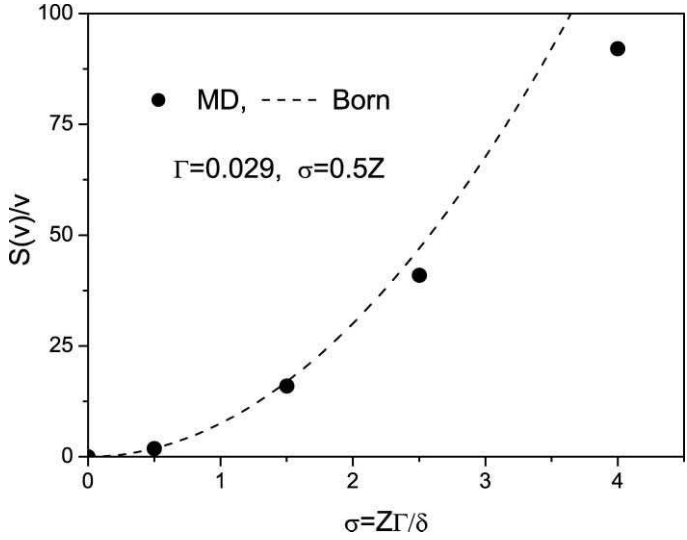

Fig. 4. Stopping power *vs*. coupling for moderate coupling conditions.

the stronger coupling conditions ($\Gamma = 0.1,\ \delta = 0.4,\ \sigma = 0.25Z$) shown in Fig. 5. Again the deviations are significant for $\sigma > 2$.

A key role of MD simulation is to provide benchmarks for guidance to a correct theory. The theory then provides a more complete explanation of

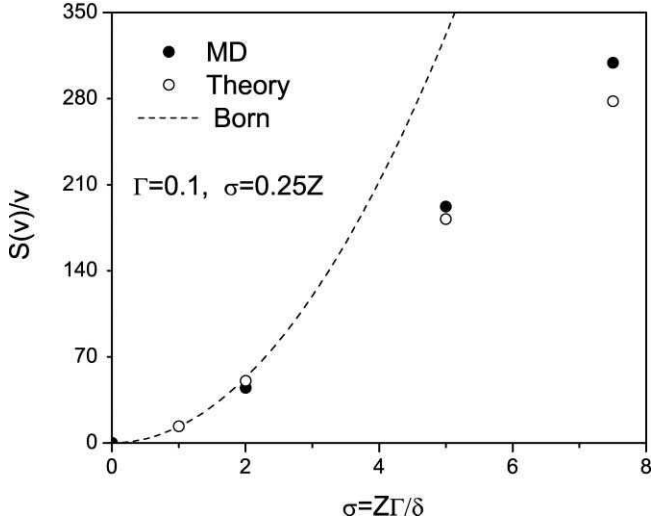

Fig. 5. Stopping power *vs*. coupling for strong coupling conditions.

the simulation results. In the present cases, the electron–electron coupling is weak and an appropriate kinetic theory for the electron distribution function $f(\mathbf{r}, \mathbf{v}, t)$ is provided by the Vlasov equation in the presence of the impurity ion potential at the origin. The solution allows conditions of strong electron-impurity coupling including those above. The details of the calculation of the field autocorrelation function are described elsewhere [8]. The result is that the correlation function is determined by single particle dynamics around the impurity ion *via* an effective potential that determines the initial correlations exactly. In addition, this motion is dynamically screened by the other electrons. The theory is particularly simple if the dynamic screening is neglected, so that the entire dynamics is given by the effective single-particle dynamics. The results are shown in Fig. 2. The corresponding results for the stopping power are shown in Fig. 5. The agreement in both cases is quite reasonable.

The mean field dynamics is that of a single electron in the same effective potential as for the initial correlations; so this simple theoretical model provides a means to interpret the MD simulation data for the beginning of a phenomenological understanding of electron dynamics near a positive ion. The initial correlation for the electric field $C(0)$ increases with Z as the equilibrium distribution of electrons is enhanced near the ion with configurations corresponding to larger fields. The latter is well described by the equilibrium solution to the non-linear Vlasov equation. The initial decay of $C(t)$ is essentially the decorrelation time for a 'most probable' electron near the ion. This most probable distance can be estimated from the maximum of the electron density distribution, r_0. The decorrelation time is approximately the time needed to accelerate this electron to the position of the ion. A rough estimate gives $t_c \sim \sqrt{1/Z}$. The anti-correlation can be understood to occur at later times because as the electron continues past the ion its acceleration changes sign as it is attracted to the ion with a field opposite to that of the original field. Thus, the qualitative features of the MD simulation are understood from this effective single-particle motion. The self-diffusion coefficient, stopping power, friction coefficient, and width of spectral lines are proportional to the integral of $C(t)$. At $Z = 0$ this is the field autocorrelation function at a neutral point and is independent of Z, depending only on the electron–electron coupling. As Z increases the electron distribution becomes non-uniform about the ion and $C(0)$ increases. At the same time t_c decreases. For small Z these two effects become negligible. As Z increases these effects increase and eventually lead to the decrease in the integral of $C(t)$. This analysis provides a new picture for the puzzling decrease of stopping power with increasing Z, relative to the Born approximation. The stopping power is proportional to Z^2 times the time integral of $C(t)$ which is essentially the total cross-section for all the electrons and the ion. The decrease towards a $Z^{3/2}$ dependence at strong coupling observed earlier in both simulations [11] and experiments [16] is seen to be

due to the effects just described. However, the precise dependence on Z may be more complicated as the coupling increases.

5. SUMMARY AND DISCUSSION

Interesting new experimental conditions involving high Z ions in hot and dense plasmas are expected to continue to provide challenges and opportunities to explore new physical phenomena. Although the electron–ion interaction is inherently quantum mechanical, even at high temperatures there is growing evidence that a semi-classical representation in terms of 'regularized' Coulomb interactions may be applicable. An important consequence is the possibility to apply MD simulation methods to these problems. Here, this approach has been illustrated by the evaluation of the field autocorrelation function relevant for the self-diffusion, mobility, and stopping of heavy ions in an electron gas. Extensions of this study to two-component plasmas and other properties (e.g., spectroscopy [17]) are in progress.

The practical limitations of the semi-classical approach are not well understood as yet. There are two different types of potential difficulties. The first is the definition of the effective pair potential, as in equation (2), and its approximate evaluation, as in equation (3). Definition (2) is appropriate for equilibrium problems but may not be the best choice for non-equilibrium states. As noted above, the approximate evaluation leading to the Kelbg potential can be improved significantly so that the original limitation to very high temperatures has been removed. A quite different problem with the semi-classical approach is the description of many-body quantum effects through the regularized pair potential. This limitation is much less clear, although many successful applications are beginning to demonstrate a large domain of applicability. Certainly, such low-temperature effects as three-body bound states are excluded from such a treatment.

In summary, MD simulation has been proposed as a powerful tool to address electron–ion systems under conditions of strong coupling where other many-body methods are compromised. Hot, dense plasmas provide an interesting example.

ACKNOWLEDGEMENTS

This research was supported by the Department of Energy Grants DE-FG03-98DP00218 and DE-FG02ER54677. JWD is grateful to the University of Provence and the University of Seville where parts of this work were performed.

REFERENCES

[1] G. Kelbg, *Ann. Physik*, 1963, **12**, 219; G. Kelbg, *Ann. Physik*, 1964, **13**, 354; G. Kelbg, *Ann. Physik*, 1964, **14**, 394.

[2] W. Ebeling, *Ann. Physik*, 1967, **19**, 104; W. Ebeling, B. Miltzer and F. Schautz, *Contrib. Plasma Phys.*, 1997, **37**, 137.

[3] F. J. Rogers, *J. Chem. Phys.*, 1980, **73**, 6272; F. J. Rogers, *Phys. Rev. A*, 1984, **29**, 868.

[4] A. Filinov, M. Bonitz and W. Ebeling, *J. Phys. A*, 2003, **36**, 5957; A. Filinov, V. Golubnychiy, M. Bonitz, W. Ebeling and J. W. Dufty, *Improved Quantum Pair Potentials for Correlated Coulomb Systems*, preprint, cond-mat/0310665.

[5] M. P. Allen and D. J. Tildesley, *Computer Simulation of Liquids*, Clarendon Press, Oxford, 1987; D. C. Rapaport, *The Art of Molecular Dynamics Simulation*, Cambridge University Press, New York, 1995.

[6] J.-P. Hansen and I. MacDonald, *Theory of Simple Liquids*, Academic Press, San Diego, 1990.

[7] M. Berkovsky, J. W. Dufty, A. Calisti, R. Stamm and B. Talin, *Phys. Rev. E*, 1996, **54**, 4087.

[8] J. W. Dufty, I. Pogorelov, A. Calisti and B. Talin, *J. Phys. A*, 2003, **36**, 6067; J. W. Dufty, I. Pogorelov, A. Calisti and B. Talin, *Electron Dynamics at a Positive Ion*, preprint.

[9] J. W. Dufty and M. Berkovsky, *Nucl. Instrum. Methods B*, 1995, **96**, 626; J. W. Dufty and M. Berkovsky, in *Physics of Strongly Coupled Plasmas* (eds W. Kraeft, M. Schlanges, H. Haberland and T. Bornath), World Scientific, River Edge, NJ, 1996.

[10] B. Talin, A. Calisti and J. W. Dufty, *Phys. Rev. E*, 2002, **65**, 056406; B. Talin and J. W. Dufty, *Contrib. Plasma Phys.*, 2001, **41**, 195; B. Talin, A. Calisti and J. W. Dufty, *Contrib. Plasma Phys.*, 2001, **41**, 195.

[11] For a more complete description of stopping power based on non-equilibrium MD simulation see G. Zwicknagel, C. Toepffer and P-G. Reinhard, *Phys. Rep.*, 1999, **309**, 118.

[12] Some recent applications to hydrogen plasmas with references are, T. Pschiwul and G. Zwicknagel, *J. Phys. A*, 2003, **36**, 6251; T. Pschiwul and G. Zwicknagel, *Contrib. Plasma Phys.*, 2001, **41**, 271; G. Norman, A. Valuev and I. Valuev, *J. Phys. IV France*, 2000, **10**, Pr5-255; W. Ebeling, G. Norman, A. Valuev and I. Valuev, *Contrib. Plasma Phys.*, 1999, **39**, 61; J. Ortner, I. Valuev and W. Ebeling, *Contrib. Plasma Phys.*, 1999, **39**, 311.

[13] H. Minoo, M. Gombert and C. Deutsch, *Phys. Rev. A*, 1981, **23**, 924.

[14] J. A. McLennan, *Introduction to Nonequilibrium Statistical Mechanics*, Prentice-Hall, Englewood Cliffs, NJ, 1989.

[15] J. Dufty, unpublished; for the classical analysis see, D. Forster, *Hydrodynamic Fluctuations, Broken Symmetry, and Correlation Functions* (ed. W. Benjamin) Reading, MA, 1975.

[16] Th. Winkler, *et al.*, *Nucl. Instrum. Methods A*, 1997, **391**, 12.

[17] B. Talin, E. Dufour, A. Calisti, M. A. Gigosos, M. A. González, T. del Río Gaztelurrutia and J. W. Dufty, *J. Phys. A*, 2003, **36**, 6049.

This Page Intentionally Left Blank

Interferences in Electron Emission from H_2 Induced by Fast Ion Impact

N. Stolterfoht[1] and B. Sulik[2]

[1] *Hahn-Meitner-Institut Berlin, Glienickerstr. 100, D-14109 Berlin, Germany*
[2] *Institute of Nuclear Research (ATOMKI), H-4001 Debrecen, Hungary*

Abstract

Interferences in electron spectra produced by coherent emission from the two atomic centers of the H_2 molecule are analyzed. Theoretical treatments in first and second order are presented for collisions of H_2 with fast ions. To describe the basic features of the interferences, methods known from wave optics are used. Moreover, a full quantum treatment is given to determine in detail the amplitudes responsible for the interference effects. The theory is compared with recent experiments revealing interferences in first and second order.

Contents

1. INTRODUCTION

During the last decades, the process of single ionization of atoms and molecules by fast ions has received a great deal of attention. Particular effort has been devoted to the molecular target H_2, which is the simplest molecule composed of two atoms. While the overall ionization is well understood [1–5], little is known about the phenomena associated with the indistinguishability of the atomic H centers. As outlined in Fig. 1, ionization of H_2 resembles Young's two-slit experiment where the atomic H centers

ADVANCES IN QUANTUM CHEMISTRY, VOLUME 46
ISSN: 0065-3276 DOI 10.1016/S0065-3276(04)46012-2

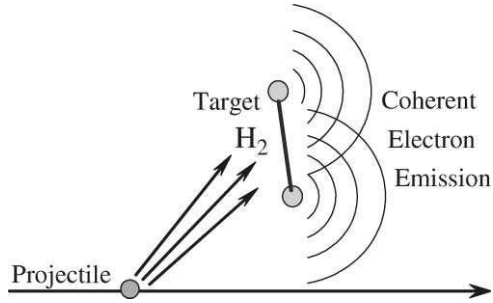

Fig. 1. Electron emission from two identical centers similar to Young's two-slit experiment.

(or slits) simultaneously emit radial waves. The coherent electron emission from the two centers may produce interference effects in the ionization spectra. Such interferences, which reveal the wave aspect of electrons, played an essential role in the early development of quantum mechanics.

Considerable effort has been devoted to reveal interference effects in atomic collisions with H_2. Early studies of collisionally induced interferences from H_2 centered on the processes of electron capture [6] and photoionization [7]. These studies were followed by additional theoretical work ([8,9] and references therein). Experimentally, ion-induced interference effects in ionization spectra were observed only recently. In these experiments electron emission spectra from H_2 were measured using fast Kr projectiles [10]. Moreover, data for 3 and 5 MeV H^+ impact show similar interference effects in electron emission from H_2 [11].

The scenario depicted in Fig. 1 refers to a projectile passing H_2 at large impact parameter. We consider fast projectiles whose velocity is much larger than that of the electron to be ionized. This case involves small momentum transfer resembling dipole transitions similar to those induced by photons [12]. In contrast to dipole transitions, binary collisions at small impact parameters result in large momentum transfer. Dipole transitions and binary encounter processes have been recognized to play fundamentally different roles in the ionization process leading to interferences [10]. Interference effects are favored by dipole transitions which are dominant at forward angles, especially for fast projectiles. Indeed, the spectra obtained at forward observation angles 20° and 30° exhibit oscillatory structures in good agreement with model calculations [10]. Near $\theta = 90°$, binary-encounter collisions are strongly enhanced [13] and, hence, first-order interferences are expected to diminish in importance [14].

Recent theoretical studies [15–19] revealed additional properties of the interference effects in H_2. Calculations [17] based on the semiclassical approximation showed explicitly that the frequency of the oscillation

decreases as the emission angle increases up to 90°. This prediction was essentially confirmed by further measurements of electron emission from H_2 by fast Kr impact [14], where good agreement was also found with calculations using the Born approximation. However, certain structures in the spectra remained unexplained.

Specifically, superimposed on the main interference structure, the electron spectra show an interference pattern with an oscillation frequency that is about double that of the first-order oscillation [20]. This structure suggests second-order effects as indicated schematically in Fig. 2. The electron wave emitted at one center interferes with this same wave after it is rescattered at the other center. It is evident that the rescattering phenomenon differs from Young's experiment, where both slits simultaneously emit radial waves. The frequency doubling for the second-order rescattering observed in the H_2 electron spectra was found to be consistent with model calculations [20]. Related investigations, performed using synchrotron radiation [21,22], focused on heavier molecules where one atomic center is photoionized in an inner shell. The different scattering processes resulting in first- and second-order interferences are summarized by Messiah [23] for electron impact.

The present work is devoted to the theoretical analysis of first- and second-order interferences observed in H_2 electron spectra using fast ions. First, the Born approximation is introduced in conjunction with the treatment by Bethe allowing for a separation into dipole transitions and binary collisions. Then, the interference effects in electron spectra are elucidated using methods known from wave optics. Finally, detailed quantum-mechanical treatments of the interferences are given in first and second order. The theoretical results are compared with experimental data available from the literature.

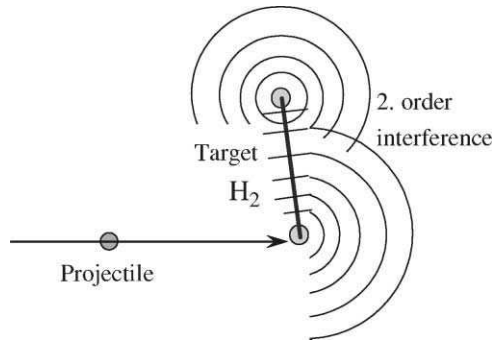

Fig. 2. Electron emission from the lower center with rescattering from the upper center. The overlay of the primary wave with the rescattered wave leads to second-order interferences.

2. BETHE–BORN APPROXIMATION

For fast projectiles the cross-section for electron emission from an atom or a molecule can be described within the first Born approximation [4,24]

$$\frac{\mathrm{d}\sigma}{\mathrm{d}q\,\mathrm{d}\Omega_q\,\mathrm{d}\varepsilon\,\mathrm{d}\Omega} = \frac{4kZ_\mathrm{p}^2}{v_\mathrm{p}^2 q^3}|F_{if}(\mathbf{q})|^2 \tag{1}$$

where v_p and Z_p are the velocity and charge of the projectile. The energy ε and the solid angle Ω refer to the ionized electron of outgoing momentum $\mathbf{k} = (k, \Omega)$. The Born cross-section is governed by the momentum transfer vector $\mathbf{q} = (q, \Omega_q)$ whose direction is given by the solid angle Ω_q. The form factor is equal to the matrix element

$$F_{if}(\mathbf{q}) = \langle \varphi_\mathbf{k} | \mathrm{e}^{\mathrm{i}\mathbf{q}\cdot\mathbf{r}} | \phi_0 \rangle \tag{2}$$

where ϕ_0 and $\varphi_\mathbf{k}$ are, respectively, the initial and final wave function of the active electron. The Born operator $\mathrm{e}^{\mathrm{i}\mathbf{q}\cdot\mathbf{r}}$ is obtained from the Fourier transform of the projectile–electron interaction $V_\mathrm{p} = Z_\mathrm{p}/|\mathbf{R} - \mathbf{r}|$.

It should be emphasized that for the ionization processes studied here, the form factor (2) depends on the direction of the momentum transfer. To compare with experiments, in which the momentum transfer is not observed, the cross-section in equation (1) is to be integrated over the direction and modulus of the momentum transfer:

$$\frac{\mathrm{d}\sigma}{\mathrm{d}q\,\mathrm{d}\varepsilon\,\mathrm{d}\Omega} = \int_0^{2\pi} \frac{\mathrm{d}\sigma}{\mathrm{d}q\,\mathrm{d}\Omega_q\,\mathrm{d}\varepsilon\,\mathrm{d}\Omega}\mathrm{d}\phi_q \tag{3}$$

and

$$\frac{\mathrm{d}\sigma}{\mathrm{d}\varepsilon\,\mathrm{d}\Omega} = \int_{q_\mathrm{min}}^{\infty} \frac{\mathrm{d}\sigma}{\mathrm{d}q\,\mathrm{d}\varepsilon\,\mathrm{d}\Omega}\mathrm{d}q \tag{4}$$

where $q_\mathrm{min} = \Delta E/v_\mathrm{p}$ is the minimum momentum transfer obtained from the energy transfer ΔE and the projectile velocity v_p. In equation (3) the angular integration over the solid angle $\Omega_q = (\theta_q, \phi_q)$ is reduced to the integration over the azimuthal angle ϕ_q, since the polar angle is fixed due to the relation $\cos\theta_q = q_\mathrm{min}/q$.

In 1930 Bethe [25] pointed out that the integration over the momentum transfer can be performed in two parts associated with the processes of dipole ionization and binary collisions between the incident projectile and the active electron. With the introduction of an intermediate momentum q_x the integration can be split into two parts

$$\frac{\mathrm{d}\sigma}{\mathrm{d}\varepsilon\,\mathrm{d}\Omega} = \int_{q_\mathrm{min}}^{q_x} \frac{\mathrm{d}\sigma}{\mathrm{d}q\,\mathrm{d}\varepsilon\,\mathrm{d}\Omega}\mathrm{d}q + \int_{q_x}^{\infty} \frac{\mathrm{d}\sigma}{\mathrm{d}q\,\mathrm{d}\varepsilon\,\mathrm{d}\Omega}\mathrm{d}q \tag{5}$$

The momentum q_x is to be chosen within $q_{\min} < q_x < k$, where k is the momentum of the outgoing electron.

The principle of Bethe's method is demonstrated in Fig. 3, where the cross-section $\mathrm{d}\sigma_H/\mathrm{d}q\,\mathrm{d}\varepsilon\,\mathrm{d}\Omega$ for electron emission from atomic hydrogen by 60 MeV Kr^{34+} impact is given as a function of the momentum transfer. The results are obtained using a well-known analytic expression reported in the current literature [4,5]. The outgoing electron energy is 200 eV, corresponding to a momentum of $k = 3.83$ a.u. The observation angles are 20 and 90° as indicated.

The figure shows two regions, denoted *dipole* and *binary*, which are separated by the vertical arrow placed at $q_x \approx 1.5$ a.u. For 20° this separation is reasonable, but it appears arbitrary for 90°. It is noted, however, that the separation into dipole and binary region can more reliably be performed using a multipole expansion of the cross-section. As shown previously [13] for an initial S state, dipole transitions lead to the final angular momentum $l = 1$, whereas binary collisions are dominated by the angular momenta $l \neq 1$. The separation by different angular momenta provides the main justification for division into dipole and binary regions.

The denominator q^3 in equation (1) produces a singularity in the cross-section curve at $q \rightarrow 0$. Hence, in the dipole region the cross-section curve maximizes at the minimum momentum transfer $q_{\min}$, which is equal to the smallest momentum transfer possible in a collision. In contrast, the binary region shows a broad maximum, which peaks at the momentum $q_{\mathrm{bin}} = |\mathbf{k} - \mathbf{q}_i| \approx k$, where $\mathbf{q}_i$ is the initial momentum of the bound electron. It is

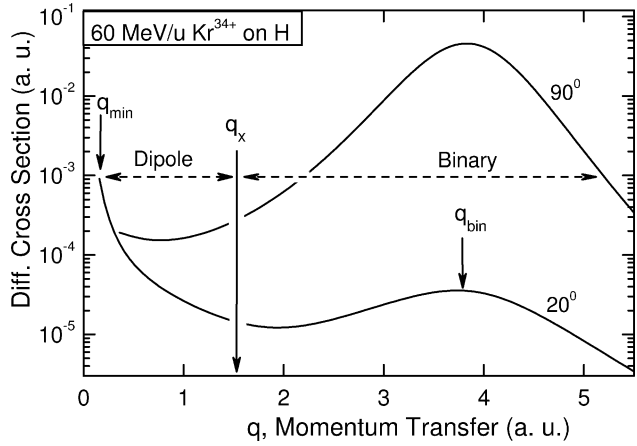

Fig. 3. Triply differential cross-section $\mathrm{d}\sigma_H/\mathrm{d}q\,\mathrm{d}\varepsilon\,\mathrm{d}\Omega$ for emission of 200 eV electrons from atomic H by 60 MeV Kr^{34+} impact as a function of the momentum transfer q. Electron observation angles are 20 and 90°. The separation point between the dipole and binary region is located at $q_x \approx 1.5$ a.u.

seen from Fig. 3 that at 20° the dipole part is larger than the binary part, whereas for 90° the binary part dominates. Hence, by changing the observation angle the influence of different ionization mechanisms can be strongly altered.

It should be noted that the characteristic properties of the emission cross-sections are primarily a consequence of the high velocity considered for the projectile. For instance, the strong variation of the binary contribution with the observation angle is a result of such high velocity. In binary collisions, fast particles produce slow recoil electrons predominantly at 90°. Thus, at forward and backward angles, the dipole transitions (involving three-body interactions) dominate [13]. Furthermore, dipole transitions are enhanced by the fact that $q_{\min}$ decreases with increasing projectile velocity. Hence, the dipole region is enlarged when fast projectiles are used. The enhancement of dipole transitions has important consequences for the observation of interference effects as will be discussed in Sections 3–5.

3. WAVE OPTICAL TREATMENT

For the basic understanding of the interferences in first and second order, methods known from wave optics will be used. The analysis is based on phase differences of the incoming and outgoing waves revealing the fundamental properties of the interference effects. The important aspect of the analysis is that the Born operator $e^{i\mathbf{q}\cdot\mathbf{r}}$ in equation (2) is considered as an electromagnetic wave interacting with the centers of the H_2 molecule.

3.1. Emission from identical centers

The case of electron emission from two identical centers is depicted in Fig. 4. The particle wave $e^{i\mathbf{q}\cdot\mathbf{r}}$ with momentum $\mathbf{q}$ (of arbitrary mass) is incident on two centers a and b, where a plane wave $\varphi_{\mathbf{k}} \sim e^{i\mathbf{k}\cdot\mathbf{r}}$ of momentum $\mathbf{k}$ is emitted. Since the mass is arbitrary it can be equal to zero too, so that the incident wave represents photons (see the formalism by Cohen and Fano [7]). In the present case of ion impact, the incident wave $e^{i\mathbf{q}\cdot\mathbf{r}}$ may represent virtual photons similar to those considered in the early work by Williams [26]. Moreover, the scenario in Fig. 4 also includes elastic scattering of electrons treated in Messiah's textbook [23]. Hence, the following analysis equally apply for photoionization, electron scattering, and ionization by electrons and heavy particle impact.

In first order, it follows that the intensity of the emitted particles at large distances is equal to the coherent sum $I_1 = |A_a + A_b|^2$. For identical centers $|A| = |A_a| = |A_b|$ one obtains $I_1 = 2|A|^2(1 + \cos\delta)$, where δ is the relative phase between the amplitudes. The latter quantity is obtained as $\delta = \delta_k - \delta_q + \delta_a - \delta_b$, where δ_a and δ_b are phase delays occurring close to

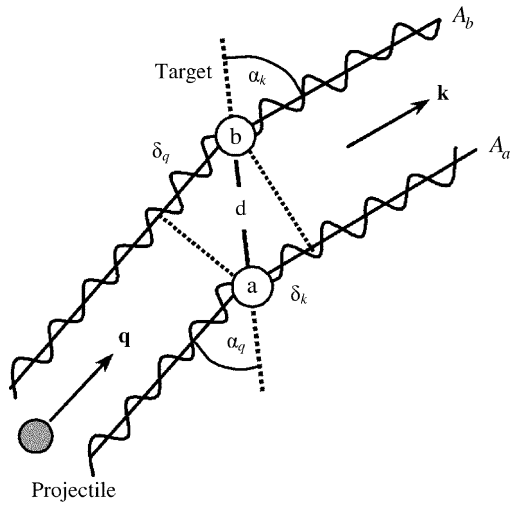

Fig. 4. Young's two-slit experiment for a particle incident as a plane wave with momentum **q** emitting a particle wave with momentum **k**.

the centers a and b, respectively, between the incident **q** wave and the emitted **k** wave. Since the centers are identical, these phases are equal so that $\delta_a - \delta_b = 0$. The additional phases δ_q and δ_k are created along the paths crossing the centers a and b, respectively (Fig. 4). Thus, one obtains

$$I_1 = 2|A|^2[1 + \cos(\delta_k - \delta_q)] \tag{6}$$

The phases δ_q and δ_k can be determined from methods using wave optics. The wavelengths of the incident and emitted waves are given by $\lambda_q = 2\pi/q$ and $\lambda_k = 2\pi/k$, respectively. Then, it is readily shown that $\delta_q = qd \cos \alpha_q = \mathbf{q}\cdot\mathbf{d}$ and $\delta_k = kd \cos \alpha = \mathbf{k}\cdot\mathbf{d}$. Hence, it follows that

$$I_1 = 2|A|^2[1 + \cos((\mathbf{k} - \mathbf{q})\cdot\mathbf{d})] \tag{7}$$

With the definition $\mathbf{p} = \mathbf{k} - \mathbf{q}$ one obtains

$$I_1 = 2|A|^2[1 + \cos(\mathbf{p}\cdot\mathbf{d})] \tag{8}$$

It is recalled that this equation is valid for the description of interference effects occurring in different scattering and ionization mechanisms. Indeed, analogous expressions have been derived for elastic electron scattering [23], ionization by photons [7], electrons [19], and heavy ions [15,16]. In first order, these theories yield the same term $1 + \cos(\mathbf{p}\cdot\mathbf{d})$ representing the interference effects. (This term has also been obtained for the stopping power of H_2 moving in condensed matter [27].) On the other hand, the non-oscillating term $2|A|^2$ describes the specific scattering and ionization

mechanisms at non-interfering centers. Although $2|A|^2$ may be influenced by interactions between the centers, it is free of interference effects.

For the case of elastic electron scattering the quantity **p** in equation (8) can be interpreted as the momentum loss by the incident electron [23]. In addition, for electron and ion impact, equation (8) shows that the interference is governed not only by the momentum **k** of the ejected electron but also by the momentum transfer **q**. Figure 4 displays that the **q** wave incident at the angle α_q ionizes the two centers with a phase shift of δ_q. Obviously, this phase shift affects the interference in the same way as the phase shift δ_k for the outgoing wave.

Expression (8) can be further developed by averaging over the orientation of the molecular vector **d** (i.e., by integration over the orientation and division by 4π). It should be noted that $|A|$ does not depend on the orientation of the molecule. Hence it follows that

$$\frac{\mathrm{d}\sigma_{\mathrm{H_2}}}{\mathrm{d}q\ \mathrm{d}\Omega_q\ \mathrm{d}\varepsilon\ \mathrm{d}\Omega} = 2|A|^2\left(1 + \frac{\sin(pd)}{pd}\right) \tag{9}$$

It is recalled that the quantity $p = |\mathbf{k} - \mathbf{q}|$ depends on the direction of the momentum transfer and the momentum of the outgoing electron.

3.2. One-center emission with rescattering

The ionization of one center with rescattering at the second center is shown in Fig. 5. For instance, the restriction to one center applies to inner-shell

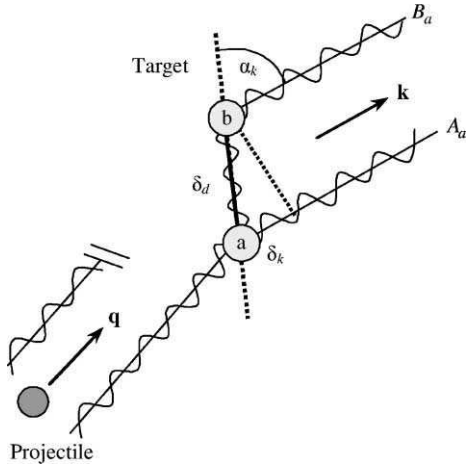

Fig. 5. Interference in second order. The incident beam is split at center *a* into a direct wave of momentum **k** and a wave propagated along **d** and scattered at center *b*.

ionization of a heteronuclear molecule [21,22]. Here, we consider ionization of H_2 dominated by binary collisions. For two-body interactions the momentum difference $\mathbf{p} = \mathbf{k} - \mathbf{q}$ is equal to the initial momentum $\mathbf{p}_i$ of the bound electron. Violent binary collisions involve momentum transfer $|\mathbf{q}| \gg |\mathbf{p}_i| \approx 1$ a.u. so that $\mathbf{q} \approx \mathbf{k}$. Here, two aspects are important. If $\mathbf{q} \approx \mathbf{k}$ we expect that the phases δ_q and δ_k are nearly equal and the interferences are constant. Furthermore, if $|\mathbf{q}| \gg 1$ the wavelength λ_q of the incident wave is much smaller than the internuclear distance $d = 1.4$ a.u. and coherences are expected to diminish. In this case, the incident particle essentially passes through one center only, i.e., the other center appears to be 'closed'. Hence, the incident $\mathbf{q}$ wave is assumed to interact only with one center (a) and we do not expect a significant interference pattern of first order. Indeed, this is confirmed in the quantum-mechanical treatment presented below.

However, an interference pattern may be produced in second order as shown in Fig. 5. The incident wave of momentum $\mathbf{q}$ emits at center a the first-order wave with amplitude A_a which is rescattered at center b to produce a second-order wave of amplitude B_a and the outgoing momentum $\mathbf{k}$. In the latter case, the phase $\delta_d = kd$ is acquired as the wave propagates from one center to the other. A further phase $\delta_{ab} = \delta_a^d + \delta_b' - \delta_a$ is obtained from phases created close to the centers a and b. The phase δ_a (already introduced) is due to the delay that occurs at center a between the incident $\mathbf{q}$ wave and the emitted $\mathbf{k}$ wave and δ_a^d is a similar phase delay for the wave emitted along the internuclear axis. The phase delay δ_b' is created as this latter wave is rescattered at center b. Hence, the interference is governed by the difference $\delta = \delta_k - \delta_d - \delta_{ab}$. The intensity in second order, restricted to the branch a, is given by $I_2^a = |A_a + B_a|^2$, which yields the expression

$$I_2^a = |A_a|^2 + 2|A_a B_a| \cos(\delta_k - \delta_d - \delta_{ab}) \tag{10}$$

It should be noted that the square modulus of the second-order amplitude $|B_a|^2$ is much smaller than $|A_a|^2$ so that $|B_a|^2$ is neglected. Recalling that $\delta_k = kd \cos\alpha = \mathbf{k}\cdot\mathbf{d}$ and $\delta_d = kd$ it follows that

$$I_2^a = |A_a|^2 + 2|A_a B_a| \cos(\mathbf{k}\cdot\mathbf{d} - kd - \delta_{ab}) \tag{11}$$

This expression cannot readily be integrated over the direction of $\mathbf{d}$, since the rescattering amplitude B_a depends on the orientation of the H_2 molecule. Thus, the average of I_2^a over the molecular orientation cannot be carried out in closed form, as was done to arrive at equation (9). To obtain a rough idea about the interference effects produced in second order, we focus our attention on the oscillatory part $\cos(\mathbf{k}\cdot\mathbf{d} - kd + \delta_{ab}) = \cos(kd\cos\alpha - kd + \delta_{ab})$, where α is the angle between $\mathbf{k}$ and $\mathbf{d}$. Let $\Omega_d = (\alpha, \varphi)$ be the solid angle specifying the direction of $\mathbf{d}$. When B_a and δ_{ab} are assumed to be constant, the integration over Ω_d (and division by 4π) can be performed in

closed form

$$\bar{I}_2^a = |A_a|^2 + 2|A_a B_a| \frac{\sin(2kd + \delta_{ab}) - \sin(\delta_{ab})}{kd} \tag{12}$$

Apart from a phase shift this expression predicts a doubling of the oscillation frequency in comparison with the results of equation (8). The frequency doubling is essentially produced by the additional phase $\delta_d = kd$ acquired in second order as the electron wave propagates along the internuclear axis from one center to the other.

3.3. Two-center emission with rescattering

Finally, the formalisms of Sections 3.1 and 3.2 are combined, i.e., the primary emission from the second center b is included. Then, two additional waves with amplitudes A_b and B_b are created and the intensity in second order is deduced from $I_2 = |A_a + A_b + B_a + B_b|^2$. Keeping in mind that $|A| = |A_a| = |A_b|$ and $\delta_a = \delta_b$ one obtains with an analogous notation as in Section 3.2

$$\begin{aligned} I_2 = {} & 2|A|^2[1 + \cos((\mathbf{k} - \mathbf{q})\cdot\mathbf{d})] \\ & + 2|AB_a|[\cos(\mathbf{k}\cdot\mathbf{d} - kd - \delta_{ab}) + \cos(\mathbf{q}\cdot\mathbf{d} - kd - \delta_{ab})] \\ & + 2|AB_b|[\cos(\mathbf{k}\cdot\mathbf{d} + kd + \delta_{ba}) + \cos(\mathbf{q}\cdot\mathbf{d} + kd + \delta_{ba})] \end{aligned} \tag{13}$$

where small terms involving products of B_a and B_b are neglected. Assuming again that B_a, B_b, $\delta_{ab} \approx \delta_{ba}$ are constant, the integration over the molecular orientation can be carried out in closed form

$$\begin{aligned} \bar{I}_2 = {} & \bar{I}_1 + 2|A|(|B_a| + |B_b|) \\ & \times \left[\frac{\sin(2kd + \delta_{ab}) - \sin(\delta_{ab})}{kd} + 2\frac{\cos(kd + \delta_{ab})\sin(qd)}{qd} \right] \end{aligned} \tag{14}$$

where $\bar{I}_1$ is the first-order interference given by equation (8).

Thus, the sum of the terms inside the square brackets appears as an oscillatory structure superimposed on the first-order structure described by $\bar{I}_1$. The first term in parenthesis indicates that the frequency of the second-order structure is doubled as in equation (12). The second term is more complicated. For forward angles, dipole transitions with $q \approx 0$ dominate so this latter term has the same frequency as the first-order term. For binary encounter collisions with $q \approx k$, the second term may also be doubled in the oscillation frequency. It should be emphasized, however, that the expressions for the integrated quantities $\bar{I}_2^a$ and $\bar{I}_2$ should be taken with

care since they neglect the dependence of the rescattering amplitude on the molecular alignment.

4. QUANTUM-MECHANICAL TREATMENT

In this section, quantum-mechanical methods are used to analyze interference effects in first and second order. The results of Section 3 will be recovered and unspecified amplitudes will be identified as matrix elements for ionization and electron scattering. The first-order formalism has been given before [10,15–17]. The second-order treatment of ion impact ionization is introduced here in analogy with formalism for electron scattering given by Messiah [23].

4.1. Interference in first order

In the first-order treatment, the origin is located at the center of mass of the H_2 molecule. The interference effects in the electron emission from H_2 originate from the initial two-center wave function, which can be approximated by a linear combination of two atomic wave functions (see for instance, Refs. [15,16]):

$$\phi_0 = \frac{1}{\sqrt{2N}}(\varphi_{1s}(\mathbf{r} + \mathbf{d}/2) + \varphi_{1s}(\mathbf{r} - \mathbf{d}/2)) \tag{15}$$

where φ_{1s} is the atomic 1s wave function centered at the two H atoms and $N \lesssim 1$ is an appropriate normalization factor. The final state $\varphi_{\mathbf{k}}$ is approximated by a plane wave or a Coulomb wave centered at the origin.

These initial and final wave functions are inserted into the form factor from equation (2). For further development the substitutions $\mathbf{r} \pm \mathbf{d}/2 \rightarrow \mathbf{r}$ of the integration variables and the translational transformation $\varphi_{\mathbf{k}}(\mathbf{r} \pm \mathbf{d}/2) = \varphi_{\mathbf{k}}(\mathbf{r})e^{\pm \mathbf{k}\cdot\mathbf{d}/2}$ are used. This latter transformation can readily be verified for a plane wave (or a Coulomb wave). After some algebra it follows that

$$F_{if} = \int \varphi^*_{\mathbf{k}}(\mathbf{r})e^{i\mathbf{q}\cdot\mathbf{r}}\varphi_{1s}(\mathbf{r})d\mathbf{r}\,\frac{1}{\sqrt{2N}}(e^{i\mathbf{p}\cdot\mathbf{d}/2} + e^{-i\mathbf{p}\cdot\mathbf{d}/2}) \tag{16}$$

where $\mathbf{p} = \mathbf{k} - \mathbf{q}$ as before. After inserting F_{if} in equation (1) one obtains the cross-section for electron emission from H_2

$$\frac{d\sigma_{H_2}}{dq\,d\Omega_q\,d\varepsilon\,d\Omega} = \frac{8kZ_p^2}{Nv_p^2q^3}|\langle\varphi_{\mathbf{k}}|e^{i\mathbf{q}\cdot\mathbf{r}}|\varphi_{1s}\rangle|^2(1 + \cos(\mathbf{p}\cdot\mathbf{d})) \tag{17}$$

It is useful to introduce the cross-section for two non-interfering H atoms

$$\frac{\mathrm{d}\sigma_{2\mathrm{H}}}{\mathrm{d}q\,\mathrm{d}\Omega_q\,\mathrm{d}\varepsilon\,\mathrm{d}\Omega} = \frac{8kZ_\mathrm{p}^2}{Nv_\mathrm{p}^2q^3}|\langle\varphi_\mathbf{k}|\mathrm{e}^{\mathrm{i}\mathbf{q}\cdot\mathbf{r}}|\varphi_{1\mathrm{s}}\rangle|^2 \tag{18}$$

which may include molecular effects (e.g., increase of the effective nuclear charge and screening by the passive electron [16,28]) but is free of the interferences due to the indistinguishability of the atomic centers. Thus, it follows that

$$\frac{\mathrm{d}\sigma_{\mathrm{H}_2}}{\mathrm{d}q\,\mathrm{d}\Omega_q\,\mathrm{d}\varepsilon\,\mathrm{d}\Omega} = \frac{\mathrm{d}\sigma_{2\mathrm{H}}}{\mathrm{d}q\,\mathrm{d}\Omega_q\,\mathrm{d}\varepsilon\,\mathrm{d}\Omega}(1+\cos(\mathbf{p}\cdot\mathbf{d})) \tag{19}$$

This expression can be compared with equation (7) showing that these equations are identical when setting $2|A|^2 = \mathrm{d}\sigma_{2\mathrm{H}}/\mathrm{d}q\,\mathrm{d}\Omega_q\,\mathrm{d}\Omega\,\mathrm{d}\varepsilon$. Thus, the present analysis allows for the determination of the unknown quantity A in equation (7). It should be added that the interference term $1+\cos(\mathbf{p}\cdot\mathbf{d})$ can be derived under more general conditions [16,19] than implied in the Born approximation.

Similar as for equation (9) an averaging over the orientation of the molecular vector $\mathbf{d}$ can be carried out yielding

$$\frac{\mathrm{d}\sigma_{\mathrm{H}_2}}{\mathrm{d}q\,\mathrm{d}\Omega_q\,\mathrm{d}\varepsilon\,\mathrm{d}\Omega} = \frac{\mathrm{d}\sigma_{2\mathrm{H}}}{\mathrm{d}q\,\mathrm{d}\Omega_q\,\mathrm{d}\varepsilon\,\mathrm{d}\Omega}\left(1+\frac{\sin(pd)}{pd}\right) \tag{20}$$

For comparison with experiment, a further integration is required with respect to the momentum transfer $\mathbf{q}$

$$\frac{\mathrm{d}\sigma_{\mathrm{H}_2}}{\mathrm{d}\varepsilon\,\mathrm{d}\Omega} = \int_{q_{\min}}^{\infty}\int_0^{2\pi}\frac{\mathrm{d}\sigma_{2\mathrm{H}}}{\mathrm{d}q\,\mathrm{d}\Omega_q\,\mathrm{d}\varepsilon\,\mathrm{d}\Omega}\left(1+\frac{\sin(pd)}{pd}\right)\mathrm{d}\phi_q\,\mathrm{d}q \tag{21}$$

Details of the integration are given in conjunction with equations (3) and (4).

Following Bethe's method, described above, the cross-sections can be split into a dipole and binary term. Then, these terms can be integrated using 'peaking' approximations [10] by setting

$$\begin{aligned} &\mathbf{q}\approx 0, && \text{for dipole transitions}\\ &\mathbf{q}=\mathbf{k}-\mathbf{p}_\mathrm{i}\approx\mathbf{k}, && \text{for binary encounters}\end{aligned} \tag{22}$$

where $\mathbf{p}_\mathrm{i}$ is recalled to be the initial momentum of the bound electron. Thus, the integrated cross-section is obtained as

$$\frac{\mathrm{d}\sigma_{\mathrm{H}_2}}{\mathrm{d}\varepsilon\,\mathrm{d}\Omega} = \frac{\mathrm{d}\sigma_{2\mathrm{H}}^{\mathrm{dip}}}{\mathrm{d}\Omega\,\mathrm{d}\varepsilon}\left[1+\frac{\sin(kd)}{kd}\right]+\frac{\mathrm{d}\sigma_{2\mathrm{H}}^{\mathrm{bin}}}{\mathrm{d}\Omega\,\mathrm{d}\varepsilon}s \tag{23}$$

where $\mathrm{d}\sigma_{2\mathrm{H}}^{\mathrm{dip}}/\mathrm{d}\Omega\,\mathrm{d}\varepsilon$ and $\mathrm{d}\sigma_{2\mathrm{H}}^{\mathrm{bin}}/\mathrm{d}\Omega\,\mathrm{d}\varepsilon$ are integrated cross-sections referring to the dipole and binary components, respectively. The quantity $s = 1+\sin(p_\mathrm{i}d)/(p_\mathrm{i}d)\approx 1.6$ is nearly constant for $p_\mathrm{i}\approx 1$ a.u. Thus, equation (23)

suggests that the oscillatory structure in the cross-section is produced predominantly by the dipole component.

Unlike the interference term, the cross-section associated with the independent H atoms is strongly dependent on the electron emission energy and angle. These cross-sections may vary with energy by several orders of magnitude [4,5], whereas the variation due to interference effects is limited to a factor of two as can be seen from equation (23). Therefore, to observe the interference effects, it is necessary to remove the strong energy and angle variations of the cross-sections. This is done by normalizing (dividing) the cross-section for H_2 by the corresponding quantity $\mathrm{d}\sigma_{2\mathrm{H}}/\mathrm{d}\Omega\,\mathrm{d}\varepsilon$ for the independent H atoms

$$\left(\frac{\mathrm{d}\sigma_{\mathrm{H}_2}}{\mathrm{d}\Omega\,\mathrm{d}\varepsilon}\right)_{\mathrm{nor}} = D\left[1 + \frac{\sin(kd)}{kd}\right] + Bs \tag{24}$$

where the subscript 'nor' denotes the cross-section normalization. The quantities D and B (with $D + B = 1$) are used as abbreviations for, respectively, the normalized dipole and binary cross-sections, which are slowly varying with k. For simplicity D and B are assumed to be constant.

In Fig. 6 the theoretical results are plotted as a function of the electron velocity v (in atomic units used here, v is equal to the electron momentum k). It is seen that the model calculation of equation (24) compares well with the experimental data observed at 20 and 30° [10]. Similar good agreements were obtained between the experiment and subsequent calculations using different theoretical approaches [16–18].

For angles approaching 90° electron emission is increasingly affected by binary collisions. In this case, equation (24) fails in its simplest form with constant parameters D, B, and s. An advanced analysis was performed by Nagy *et al.* [17] using a semiclassical approximation. The theory yields an expression similar to equation (24), however, with the important difference that the oscillation frequency varies with the electron observation angle. Hence, to compare with the experiment, a frequency parameter c was introduced [14]

$$\left(\frac{\mathrm{d}\sigma_{\mathrm{H}_2}}{\mathrm{d}\Omega\,\mathrm{d}\varepsilon}\right)_{\mathrm{nor}} = F\left[1 + \frac{\sin(kcd)}{kcd}\right] + G \tag{25}$$

where F and G (with $F + G = 1$) are interfering and non-interfering cross-section fractions. Within the model by Nagy *et al.* [17], the oscillatory term is governed by the electron momentum component parallel to the beam direction $k_{\|} = k\cos\theta = kc$. Thus, the frequency parameter c is equal to $\cos\theta$, obtained from the electron observation angle θ.

In Fig. 7 theoretical and experimental results are compared [14]. Since c may differ from the predicted value $\cos\theta$, the quantity c was used as an adjustable parameter. The functions fitted to the experimental data are shown

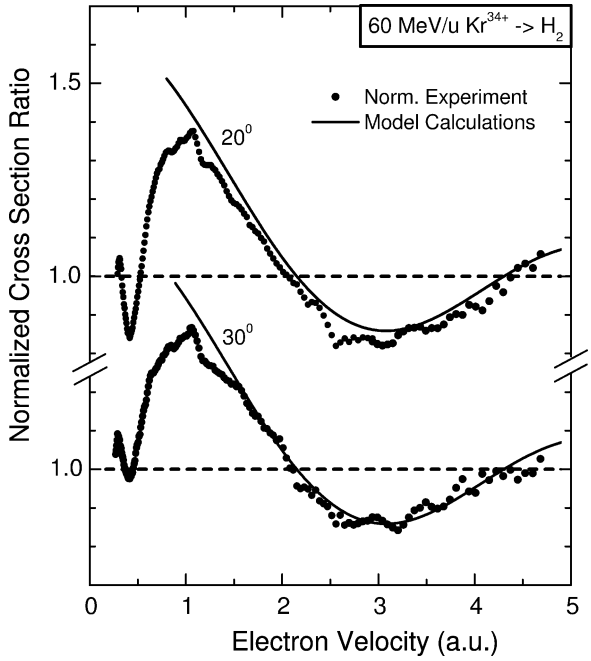

Fig. 6. Experimental H_2 to theoretical 2H cross-sections for electron emission by 60 keV Kr^{34+} impact plotted as a function of the electron velocity. The theoretical cross-sections were obtained using the continuum distorted wave-Eikonal initial state (CDW-EIS) approximation [29]. The electron observation angles are 20 and 30° as indicated. The solid lines represent model calculations using equation (24) (from Ref. [10]).

as dash-dotted lines in Fig. 7. To obtain more details from theoretical predictions, numerical calculations were performed using equation (21) in conjunction with analytical Born cross-sections for atomic hydrogen [5]. These calculations are plotted as solid lines in Fig. 7.

It is seen that the results from the Born approximation are in good agreement with experiment for 30 and 60°. Also, the Born results are found to agree well with the model calculations by Nagy *et al.* [17]. Accordingly the fit values of c agree well with $\cos\theta$ for 30 and 60° confirming the prediction of an angular dependent oscillation frequency. However, discrepancies between the Born results and experiment occur for 90° and 150°. In particular, for 150°, the oscillation frequency is observed to be enhanced in comparison with the Born calculations. This finding, which is not fully understood at present, may indicate effects leading beyond the Born approximation [18].

In addition, it is noted that in Figs 6 and 7 below $v \approx 1$ a.u. the experimental results strongly decrease with decreasing velocity in contrast to

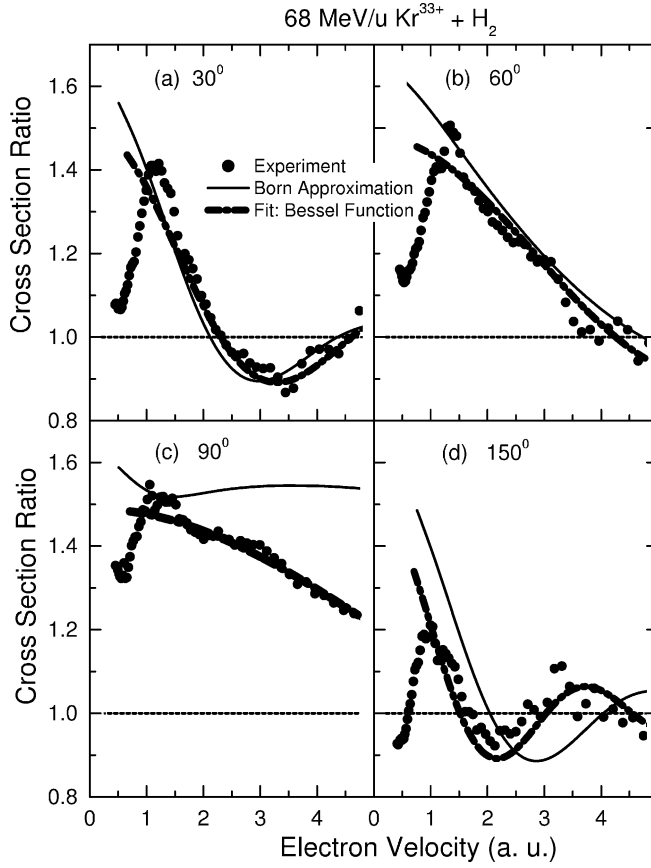

Fig. 7. Ratios of experimental to theoretical CDW-EIS cross-sections for electron emission in 68 MeV/u $Kr^{33+} + H_2$ collisions plotted as a function of the ejected electron velocity. From (a) to (d) the electron observation angles are 30, 60, 90, and 150° as indicated. The solid lines represent Born calculations from equation (21) and the dash-dotted lines are obtained from fits using the analytic function of equation (25) (from Ref. [14]).

the calculations. This decrease might indicate that a two-center wave function is necessary for the final state. It should be realized that for slow electrons the corresponding wavelength may become much larger than the distance between the two atomic H centers. In this case, one would expect that interferences diminish (i.e., the ratio of cross-sections approaches unity). Indeed, the experimental data show this tendency. However, the present model results approach values as high as two. This may be due to the use of an approximate one-center wave function for the final state.

4.2. Interference in second order

The second-order case involving binary-encounter processes is depicted in Fig. 5. To recall, the projectile emits an electron in a binary collision from center *a*. Part of the ejected spherical wave hits center *b* and produces a new spherical wave, which may interfere with the original one in a second-order process.

Hence, the interference is produced by the superposition of two paths associated with the amplitudes A_{if} and B_{if} of first and second order:

$$\frac{\mathrm{d}\sigma_{\mathrm{H}_2}}{\mathrm{d}q\,\mathrm{d}\Omega_q\,\mathrm{d}\varepsilon\,\mathrm{d}\Omega} = \frac{4kZ_{\mathrm{p}}^2}{v_{\mathrm{p}}^2 q^3}|A_{if} + B_{if}|^2 \tag{26}$$

For further evaluation of the matrix element it is useful to locate the origin at one H center. The first-order amplitude, introduced in Section 4.1, is obtained as

$$A_{if}(\mathbf{q}) = \langle \varphi_{\mathbf{k}} | \mathrm{e}^{\mathrm{i}\mathbf{q}\cdot\mathbf{r}} | \varphi_0 \rangle \tag{27}$$

where for the H_2 molecules the atomic wave function φ_0 is replaced by the hydrogenic wave function $\varphi_{1\mathrm{s}}$ located at the H center *a*.

The second-order treatment is similar to that given by Messiah [23] for elastic electron scattering:

$$B_{if} = \int F_b(\mathbf{r}'') G(\mathbf{r}'', \mathbf{r}') F_a(\mathbf{r}') \mathrm{d}\mathbf{r}''\,\mathrm{d}\mathbf{r}' \tag{28}$$

This amplitude consists of three components representing the interaction with the first H center (label *a*), the propagation along the internuclear axis, and the final scattering at the second H center (label *b*). Two of the components are given as Fourier transforms

$$F_a(\mathbf{r}') = \int \mathrm{e}^{\mathrm{i}\mathbf{k}'\cdot\mathbf{r}'} \langle \varphi_{\mathbf{k}'} | \mathrm{e}^{\mathrm{i}\mathbf{q}\cdot\mathbf{r}} | \varphi_0 \rangle \mathrm{d}\mathbf{k}' \tag{29}$$

$$F_b(\mathbf{r}'') = \int \mathrm{e}^{\mathrm{i}\mathbf{k}''\cdot\mathbf{r}''} \langle \varphi_{\mathbf{k}} | V_{\mathrm{e}} | \varphi_{\mathbf{k}''} \rangle \mathrm{d}\mathbf{k}'' \tag{30}$$

where V_{e} is the elastic interaction of an electron with an H atom. Thus, the matrix element $\langle \varphi_{\mathbf{k}} | V_{\mathrm{e}} | \varphi_{\mathbf{k}''} \rangle$ represents the (elastic) scattering (i.e., $|\mathbf{k}''| = |\mathbf{k}|$) of an electron at the second H center. The wave propagation between the two centers is governed by the free Greens function

$$G(\mathbf{r}', \mathbf{r}'') = \frac{1}{2\pi} \frac{\mathrm{e}^{\mathrm{i}k|\mathbf{r}' - \mathbf{r}''|}}{|\mathbf{r}' - \mathbf{r}''|} \tag{31}$$

which may be approximated as

$$G(\mathbf{r}', \mathbf{r}'') \approx \frac{1}{2\pi} \frac{e^{i\mathbf{k}_d(\mathbf{r}'-\mathbf{r}'')}}{d} \tag{32}$$

where $\mathbf{k}_d = k\mathbf{d}/d$ and the expansion $|\mathbf{r}' - \mathbf{r}''| \approx d + \mathbf{d}(\mathbf{r}'' - \mathbf{d} - \mathbf{r}'')/d + \cdots$ is used. Thus, in equation (28) the integrations over $\mathbf{r}'$ and $\mathbf{r}''$ may be carried out in closed form yielding

$$B_{if} = \frac{1}{2\pi d} \langle \varphi_{\mathbf{k}} | V_e | \varphi_{\mathbf{k}_d} \rangle \langle \varphi_{\mathbf{k}_d} | e^{i\mathbf{q}\cdot\mathbf{r}} | \varphi_0 \rangle \tag{33}$$

We recall that for H_2 the initial state φ_0 is equal to a hydrogenic wave function φ_{1s} centered at the origin. Then, the matrix element describing the elastic scattering of the electron at center b is given by

$$\langle \varphi_{\mathbf{k}} | V_e | \varphi_{\mathbf{k}_d} \rangle = \int \varphi^*_{\mathbf{k}}(\mathbf{r}) V_e(\mathbf{r} - \mathbf{d}) \varphi_{\mathbf{k}_d}(\mathbf{r}) d\mathbf{r} \tag{34}$$

where $V_e(\mathbf{r} - \mathbf{d})$ represents the interaction with center b shifted from the origin by the internuclear distance $\mathbf{d}$. Similar as for equation (16) we substitute the integration variable $\mathbf{r} - \mathbf{d} \rightarrow \mathbf{r}$ and apply the translational transformation $\varphi_{\mathbf{k}}(\mathbf{r} + \mathbf{d}) = \varphi_{\mathbf{k}}(\mathbf{r}) e^{\mathbf{k}\cdot\mathbf{d}}$. With the initial state plane wave $\varphi_{\mathbf{k}_d} = (2\pi)^{-3/2} e^{i\mathbf{k}_d\cdot\mathbf{r}}$ one obtains

$$\langle \varphi_{\mathbf{k}} | V_e | \varphi_{\mathbf{k}_d} \rangle = e^{i(\mathbf{k}_d - \mathbf{k})\mathbf{d}} \int \varphi^*_{\mathbf{k}}(\mathbf{r}) V_e(\mathbf{r}) \varphi_{\mathbf{k}_d}(\mathbf{r}) d\mathbf{r} = e^{i(kd - \mathbf{k}\cdot\mathbf{d})} \langle \varphi_{\mathbf{k}} | \tilde{V}_e | \varphi_{\mathbf{k}_d} \rangle \tag{35}$$

where $\tilde{V}_e(\mathbf{r})$ represents the 'unshifted' center for elastic scattering. We recall that $\mathbf{k}_d$ is parallel to $\mathbf{d}$ and $|\mathbf{k}_d| = |\mathbf{k}|$ so that $\mathbf{k}_d \cdot \mathbf{d} = kd$. Hence, from equation (33) it follows for the second-order amplitude that

$$B_{if} = \frac{e^{i(kd - \mathbf{k}\cdot\mathbf{d})}}{2\pi d} \langle \varphi_{\mathbf{k}} | \tilde{V}_e | \varphi_{\mathbf{k}_d} \rangle \langle \varphi_{\mathbf{k}_d} | e^{i\mathbf{q}\cdot\mathbf{r}} | \varphi_0 \rangle \tag{36}$$

From equation (26) the cross-section is obtained as

$$\frac{d\sigma_{H_2}}{dq\, d\Omega_q\, d\varepsilon\, d\Omega} = \frac{4kZ_p^2}{v_p^2 q^3} [|A_{if}|^2 + |B_{if}|^2 + 2\,\mathrm{Re}(B^*_{if} A_{if})] \tag{37}$$

where the third term describes the interference of the first- and second-order amplitude, which is governed by

$$A^*_{if} B_{if} = \frac{e^{i(kd - \mathbf{k}\cdot\mathbf{d})}}{2\pi d} \langle \varphi_{\mathbf{k}} | \tilde{V}_e | \varphi_{\mathbf{k}_d} \rangle^* \langle \varphi_{\mathbf{k}_d} | e^{i\mathbf{q}\cdot\mathbf{r}} | \varphi_0 \rangle^* \langle \varphi_{\mathbf{k}} | e^{i\mathbf{q}\cdot\mathbf{r}} | \varphi_0 \rangle \tag{38}$$

It should be realized that the matrix elements are complex and depend on the orientation of the molecule.

To obtain the modulus of the matrix elements, their phases are extracted. The phase difference $\delta_{ab} = \delta_a^d + \delta_b' - \delta_a$, already used in Section 4.1, can be obtained from

$$\langle \varphi_{\mathbf{k}} | \tilde{V}_e | \varphi_{\mathbf{k}_d} \rangle = e^{-i\delta_b'} | \langle \varphi_{\mathbf{k}} | \tilde{V}_e | \varphi_{\mathbf{k}_d} \rangle | \tag{39}$$

and similar expressions for the Born matrix elements $\langle \varphi_{\mathbf{k}_d} | e^{i\mathbf{q}\cdot\mathbf{r}} | \varphi_0 \rangle$ and $\langle \varphi_{\mathbf{k}} | e^{i\mathbf{q}\cdot\mathbf{r}} | \varphi_0 \rangle$ identifying the phases δ_a^d and δ_a, respectively. Thus, it follows that

$$2\,\mathrm{Re}(A_{if}^* B_{if}) = \frac{1}{\pi d} | \langle \varphi_{\mathbf{k}} | \tilde{V}_e | \varphi_{\mathbf{k}_d} \rangle^* \langle \varphi_{\mathbf{k}_d} | e^{i\mathbf{q}\cdot\mathbf{r}} | \varphi_0 \rangle^* \langle \varphi_{\mathbf{k}} | e^{i\mathbf{q}\cdot\mathbf{r}} | \varphi_0 \rangle | \cos(\mathbf{k}\cdot\mathbf{d} - kd - \delta_{ab}) \tag{40}$$

Hence, equation (11) is recovered and the unknown quantities A, B_a, and B_b can be identified by means of a comparison with expressions (37)–(40).

The evaluation of the matrix elements has not been carried out yet. Therefore, only specific features of the present formalism will be used. The integration over the molecular orientation and the extension to the case of two-center emission with rescattering are performed in Section 4.1 using wave optics methods. Hence, these tasks shall not be repeated here. Although the integration over the molecular orientation was done only approximately, it reveals that the frequency of the oscillations was doubled.

Second-order oscillations with an enhanced frequency were observed in the experiments [20] as shown in Fig. 8. In the upper diagrams, the measured cross-section ratios are again shown together with improved fits to the analytic function given by equation (25). Careful inspection of the cross-section ratios shows evidence for higher frequency oscillations superimposed on the main oscillatory structure for each of the angles displayed. After division of the cross-section ratios by the fit curves these secondary oscillations are clearly revealed as seen in the lower part of Fig. 8. In addition to a higher frequency, these secondary oscillations appear to have nearly equal frequencies for the electron emission angles considered here.

An attempt was made to reproduce the secondary oscillations by using the fit function from equation (25) [20]. In accordance with equation (12) the phase δ_{ab} was added by replacing kcd by $kcd + \delta_{ab}$. The resulting fit curves are given as solid lines in the lower diagrams of Fig. 8. The fit parameters were set to the same values for all angles, yielding $c = 2.5$ and $\delta_{ab} = \pi$. This confirms that the oscillation frequency is at least doubled. Also, it is noted that the oscillation in equation (14) is governed by the momentum k, instead of $p = |\mathbf{k} - \mathbf{q}|$, so that the oscillatory structure is expected to be independent of the electron emission angle. Indeed, the experimental results appear to confirm this result.

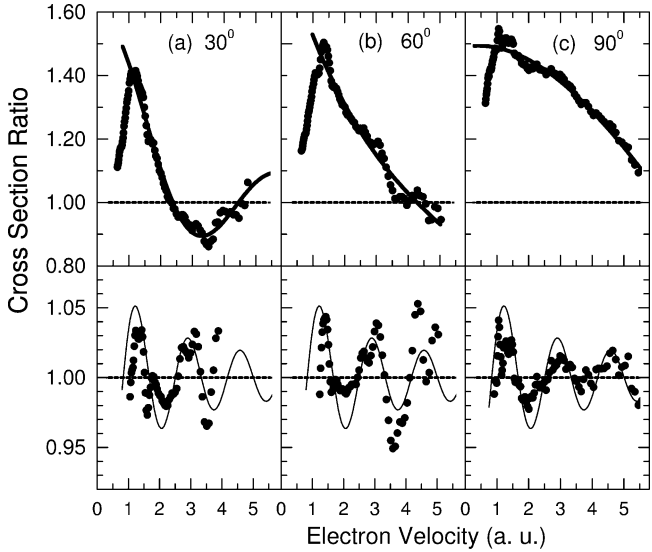

Fig. 8. Ratios of experimental to theoretical CDW-EIS cross-sections for electron emission by 68 MeV/u Kr^{33+} impact on H_2 for different electron observation angles. In the upper diagrams the ratios are shown together with fits to an analytic function (see text). The ratios are divided by the corresponding fit functions and plotted in the lower diagrams together with a second-order fit (from Ref. [20]).

5. FINAL REMARKS AND CONCLUSIONS

The present analysis treats interference effects in electron emission from molecular hydrogen colliding with fast projectiles. Two cases are considered referred to as interferences in first and second order. Using methods of wave optics a unified picture is given for the interference effects combining the processes of photoionization, electron scattering, and ionization by charged particles, in particular, heavy ions. In the latter case the incident wave is attributed to virtual photons with a wavelength equal to the momentum transfer.

In first order, the electron emission from two centers is similar to Young's two-slit experiment. The interference pattern observed in the experiments has been confirmed by several theoretical approaches. In the present analysis, results from the Born approximation are used to compare with the experimental data. The oscillation frequency of the interference pattern is found to depend on the observation angle in agreement with a previous theoretical prediction. At the observation angle of 150° the oscillation frequency is found to be enhanced in comparison with the theoretical results. Significant discrepancies at electron velocities lower than $\sim$1 a.u. are

likely to be due to the use of an approximate one-center wave function in the final state. In this case, further work is needed to apply an appropriate two-center wave function for the outgoing continuum electron.

The second-order treatment is performed analogous to electron scattering as given in Messiah's textbook. While the development of the formalism is finalized, no numerical results are extracted yet from the present theory. Rather, the formalism is applied for the identification of unknown quantities introduced in the analysis using methods of wave optics. In particular, the formalism predicts the doubling of the oscillation frequency in agreement with the experimental results.

The analysis indicates that the most pronounced oscillation of the double frequency is likely to occur at 90°, where electron emission by binary encounter processes dominates. A similar result is obtained for 60°, where binary-encounter collisions retain importance. Also at smaller angles, e.g., 30°, we expect a secondary oscillatory contribution with a frequency doubling and this result is seen in the experimental data. However, effort is needed to improve the statistical error for the experimental data at forward angles. The frequency doubling is found to involve a phase shift of about π. This finding shows that further work is required to examine additional phase shifts produced during the secondary scattering at the centers.

ACKNOWLEDGEMENTS

The authors are indebted to the team participating in the previous experiments at GANIL. In particular, we thank John Tanis and Jean Yves Chesnel for a long-standing motivating collaboration. We are indebted to John Briggs, Uwe Becker, Roberto Rivarola, Ladislau Nagy, Laszlo Sarkadi for fruitful discussions concerning theoretical aspects and the communication of results prior to publication. Support by the Hungarian–German Intergovernmental S&T Collaboration (Project # D-17/99) is acknowledged.

REFERENCES

[1] C. E. Kuyatt and T. Jorgensen, *Phys. Rev.*, 1963, **130**, 1444.
[2] W. E. Wilson and L. H. Toburen, *Phys. Rev. A*, 1973, **7**, 1535.
[3] A. Köver, S. Ricz, D. Szabó, D. Berényi, E. Koltay and J. Vegh, *Phys. Lett.*, 1980, **79A**, 305.
[4] M. E. Rudd, Y. K. Kim, D. H. Madison and T. J. Gay, *Rev. Mod. Phys.*, 1992, **64**, 441.
[5] N. Stolterfoht, R. D. Dubois and R. D. Rivarola, *Electron Emission in Heavy Ion–Atom Collisions*, Springer Series on Atoms and Plasmas, Springer, Heidelberg, 1997.
[6] T. F. Tuan and E. Gerjuoy, *Phys. Rev.*, 1960, **117**, 756.
[7] H. D. Cohen and U. Fano, *Phys. Rev.*, 1966, **150**, 30.
[8] S. E. Corchs, H. F. Busnengo and R. D. Rivarola, *Nucl. Instrum. Methods Phys. Res. B*, 1999, **149**, 247.

[9] M. Walter and J. S. Briggs, *J. Phys. B*, 1999, **32**, 2487.
[10] N. Stolterfoht, B. Sulik, V. Hoffman, B. Skogvall, J. Y. Chesnel, J. Rangama, F. Frémont, D. Hennecart, A. Cassimi, X. Husson, A. L. Landers, J. A. Tanis, M. E. Galassi and R. D. Rivarola, *Phys. Rev. Lett.*, 2001, **87**, 023201.
[11] S. Hossain, A. Alnaser, A. L. Landers, D. J. Pole, H. Knutson, A. Robison, B. Stamper, N. Stolterfoht and J. A. Tanis, *Nucl. Instrum. Methods Phys. Res. Sect. B*, 2003, **205**, 484.
[12] M. Inokuti, *Rev. Mod. Phys.* 1971, **43**, 297.
[13] N. Stolterfoht, J. Y. Chesnel, M. Grether, B. Skogvall, F. Frémont, D. Leder, D. Hennecart, X. Husson, P. Grandin, B. Sulik, L. Gulyás and J. A. Tanis, *Phys. Rev. Lett.*, 1998, **80**, 4649.
[14] N. Stolterfoht, B. Sulik, L. Gulyás, B. Skogvall, J. Y. Chesnel, F. Frémont, D. Hennecart, A. Cassimi, L. Adovi, S. Hossain and J. A. Tanis, *Phys. Rev. A*, 2003, **67**, 030702.
[15] J. S. Briggs, W. Ihra and N. Stolterfoht, in *XXII International Conference on Photonic, Electronic, and Atomic Collisions, Abstracts of Papers* (eds S. Datz, J. Burgdörfer, J. S. Cohen and C. R. Vane), Rinton Press, Princeton, NJ, 2001, p. 565.
[16] M. E. Galassi, R. D. Rivarola, P. D. Fainstein and N. Stolterfoht, *Phys. Rev. A*, 2002, **66**, 052705.
[17] L. Nagy, L. Kocbach, K. Pora and J. Hansen, *J. Phys. B*, 2002, **35**, L453.
[18] L. Sarkadi, *J. Phys. B*, 2003, **36**, 2153.
[19] C. R. Stia, O. A. Fojón, P. F. Weck, J. Hanssen and R. D. Rivarola, *J. Phys. B*, 2003, **36**.
[20] N. Stolterfoht, B. Sulik, L. Gulyás, B. Skogvall, J. Y. Chesnel, F. Frémont, D. Hennecart, A. Cassimi, L. Adov, S. Hossain and J. A. Tanis, *Phys. Rev. A*, 2004, **69**, 012701.
[21] F. Heiser, O. Geßner, J. Vichauf, K. Wieliczek, R. Hentges and U. Becher, *Phys. Rev. Lett.*, 1997, **79**, 2435.
[22] J. D. Mills, J. A. Sheeby, T. A. Ferret, S. H. Southworth, R. Mayer, D. W. Lindle and P. W. Langhoff, *Phys. Rev. Lett.*, 1997, **79**, 383.
[23] A. Messiah, *Quantum Mechanics*, North Holland, Amsterdam, 1970, Vol. II, p. 854.
[24] N. Stolterfoht, J. W. Chesnel, M. Grether, J. A. Tanis, B. Skogvall, F. Frémont, D. Lecler, D. Hennecart, X. Husson, P. Grandin, Cs. Koncz, L. Gulyás and B. Sulik, *Phys. Rev. A*, 1999, **59**, 1262.
[25] H. A. Bethe, *Ann. Phys. (Leipzig)*, 1930, **5**, 325.
[26] E. J. Williams, *Phys. Rev.*, 1934, **45**, 325.
[27] N. R. Arista, *Nucl. Instrum. Methods Phys. Res. B*, 2000, **164/165**, 108.
[28] P. D. Fainstein, V. H. Ponce and R. D. Rivarola, *J. Phys. B*, 1991, **24**, 3091.
[29] L. Gulyás, P. D. Fainstein and A. Salin, *J. Phys. B*, 1995, **28**, 245.

This Page Intentionally Left Blank

Thoughts About Nanodosimetry

Hans Bichsel

Nuclear Physics Laboratory 354290, University of Washington, Seattle, WA 98195-4290, USA

Abstract

The measurement of energy deposition in very small volumes has been called *nanodosimetry*. The concept has appeared in the scientific literature for some time. In this study it is shown that very little knowledge can be gained from nanodosimetry.

Contents

1. INTRODUCTION

The observation of the energy loss, energy deposition and radiation effects of fast charged particles in *small volumes* is of interest in fields such as microdosimetry, radiation biology, materials science and high energy particle physics. I want to use the expression *signal* to describe the effect observed in a detector. In most measurements the signal is produced by the energy deposition rather than the energy loss. Here I want to consider volumes in which the particles make fewer than 10 collisions on the average. Then the classical Landau [1] and Bethe–Bloch ideas [2] are not applicable. Concepts such as mean energy loss and absorbed dose are not suitable to relate energy loss and radiation effects in small volumes because energy loss or energy deposition spectra show a very large spread and consequently radiation effects will show large variations, too. As a corollary we note that it may not be necessary to obtain fine detail of the collision cross-sections used in the simulation of energy loss.

For detectors of high energy radiation attention must be paid to selecting a proper size of the detector. In superconducting wires with diameters of less

ADVANCES IN QUANTUM CHEMISTRY, VOLUME 46
ISSN: 0065-3276 DOI 10.1016/S0065-3276(04)46013-4

than 1 μm, or in Ar gas of thickness less than 1 mm, no interactions will occur for some traversing particles, or the radiation signal is too small to be observed, and the particles will not be detected, even though the mean energy loss may exceed 300 eV.

Radiation effects in small volumes have been described for over 30 years in the symposia on microdosimetry, most recently in Ref. [3]. The problems I want to consider here occur in the investigations for *very small volumes*, as for example, that of a DNA structure. Many effects encountered in radiation biology are discussed by Lea [4]. This book should be studied in detail by all researchers in this field.

2. INTERACTIONS OF CHARGED PARTICLES WITH MATTER

The interactions of charged particles with matter are inherently stochastic in nature: collisions take place at random intervals and in each collision a random energy loss occurs. The probability of collisions in traversing a length x of material by particles with charge ze and speed $v = \beta c$ is given by the Poisson distribution[1]

$$P_n = \frac{m_c^n}{n!} e^{-m_c} \tag{1}$$

where n is the number of collisions *one* particle experiences, $m_c = x/\lambda$ is the average number of collisions particles suffer and λ (which depends on v) is the mean free path between collisions. The probability for an energy loss E is given by the differential collision cross-section $\sigma(E)$ and its integral

$$\Sigma(E) = \int_0^E \sigma(E')dE' \Big/ \int_0^\infty \sigma(E')dE' \tag{2}$$

which is used for Monte Carlo simulations. Examples of $\sigma(E)$ and $\Sigma(E)$ for P10 gas are shown in Fig. 1. The moments of $\sigma(E)$ are

$$M_\nu = \int_0^\infty E^\nu \sigma(E)dE, \qquad \nu = 0, 1, 2, \ldots \tag{3}$$

Note that λ in equation (1) is equal to $1/M_0$. The 'Bethe–Bloch equation' [2] is an evaluation of M_1. For singly charged particles with $\beta\gamma = 3.5$, near minimum specific ionization, traversing P10 gas, the total collision cross-section is $M_0 = 30$ collisions/cm and the stopping power is $M_1 = 2.56$ keV/cm. For Si, $M_0 = 4$ collisions/μm, $M_1 = 0.4$ keV/μm, and for liquid water $M_0 \sim 2.5$ collisions/μm, $M_1 \sim 0.2$ keV/μm.

[1] The dependence on v will not be indicated explicitly in the expressions for m_c, λ, $\sigma(E)$, $f(\Delta; x)$, etc.

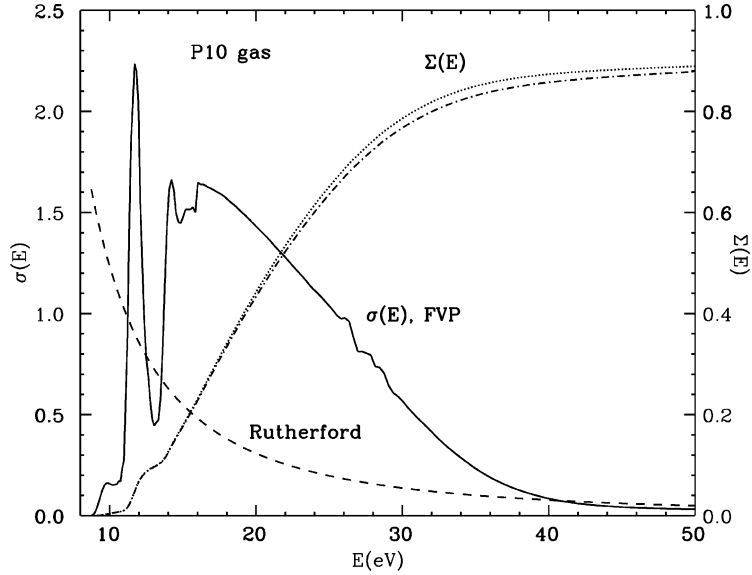

Fig. 1. Differential collision cross-section $\sigma(E)$ for single collisions of charged particles with speed $\beta\gamma = 3.6$ in P10 gas, as calculated with the Fermi-virtual-photon method (FVP) [8,11]: solid line. The function extends to a value $E_{\max} \sim 12$ MeV. For present purposes only the part shown here is relevant. Except for the scale of the ordinate, the function depends very little on particle speed. The Rutherford cross-section which is used for the Vavilov–Landau calculation is given by the dashed line. It is normalized to give the same stopping power as $\sigma(E)$. The integral function $\Sigma(E)$, equation (2) for $\beta\gamma = 3.6$, is shown by the dotted line, that for $\beta\gamma = 0.1$ by the dash-dotted line. Note the small difference in $\Sigma(E)$ for a large change in $\beta\gamma$. For only 12% of the collisions an energy loss exceeding 50 eV will happen, also see Fig. 3 in Ref. [6] or Fig. 5 in Ref. [9].

P10 gas (90% Ar and 10% methane) is used in high energy particle ionization chambers. The structure of this spectrum is similar to that of ice [5], except for the spike of excitation to the first excited state at 12 eV. Spectra for Si can be found in Refs. [6–8], for water in Ref. [9].

The collision cross-section $\sigma(E)$ is different for each material, but the general features are similar: there is a pronounced peak between 12 and 25 eV which, for solids, is ascribed to a collective- or plasmon- excitation, there are further peaks at higher energies, usually broader and related to excitations of M-, N-, O-shells, and further well defined peaks related to excitations of inner-shell electrons [10]. It is one of the purposes of this study to show that for the descriptions of radiation effects considered here the *detailed structure of the collision spectrum is not important.*

The *total* energy loss spectrum $f(\Delta)$ in an absorber of thickness x is derived in Section 3.

3. CALCULATED ENERGY LOSS SPECTRA ('STRAGGLING FUNCTIONS') $f(\Delta; x)$

Straggling functions can be calculated with computer-analytic methods [7,12]

$$f(\Delta; v, x) = \sum_{n=0}^{\infty} \frac{m_c^n \, e^{-m_c}}{n!} \sigma(\Delta; v)^{*n} \tag{4}$$

where

$$\sigma(\Delta)^{*n} = \int_0^{\Delta} \sigma(E)\sigma^{*(n-1)}(\Delta - E)\mathrm{d}E \tag{5}$$

is the n-fold convolution of the single collision spectrum $\sigma(E)$. The particle speed v is implicit as a parameter. The convolution spectra of equation (5) for P10 are given in Fig. 2. Note the large reduction of the 12 eV spike for $n = 2$, and its complete disappearance for $n = 3$. The spectra for Si are given in Fig. 3.

The energy loss spectrum $f(\Delta; v, x)$, equation (4), for particles with $\beta\gamma = 3.6$ passing through $x = 1$ mm in P10 is given by the solid line in Fig. 4, its integral, $F(\Delta) = \int_0^E f(\Delta')\mathrm{d}\Delta' / \int_0^{\infty} f(\Delta')\mathrm{d}\Delta'$, by the dashed line. Here, $m_c = 3$,

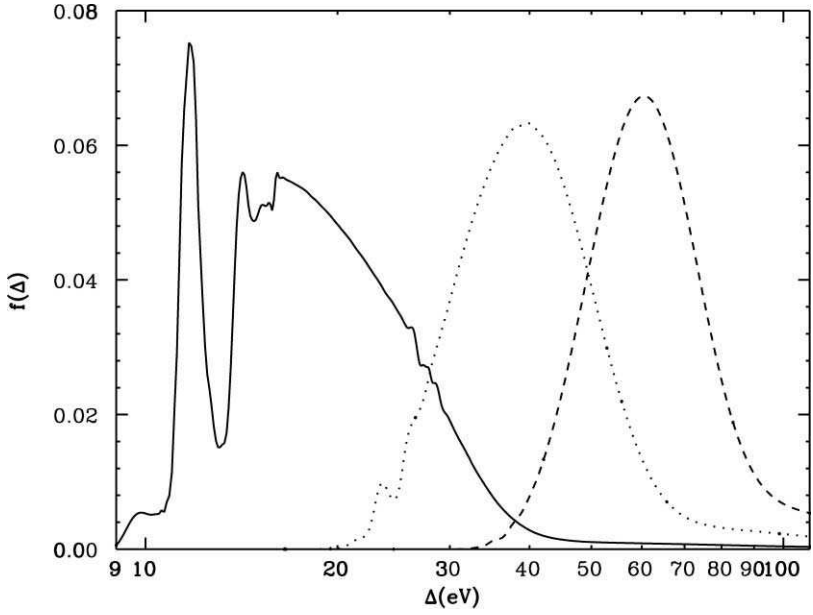

Fig. 2. The convolution spectra $\sigma(E)^{*n}$ defined in equation (5) for P10 gas are given. Solid line: single collisions, dotted line: two collisions, dashed line: three collisions.

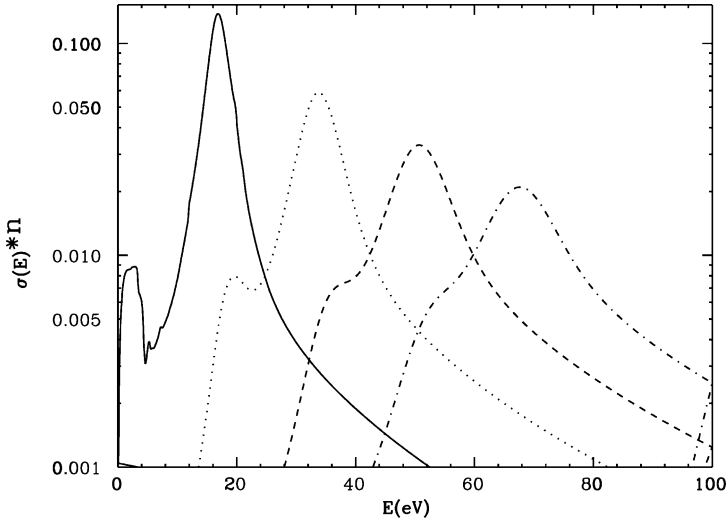

Fig. 3. Same as Fig. 2 for solid Si, but $\sigma(E)^{*4}$ is also shown. The 'plasmon peak' at 17 eV appears again at $17n$ eV, and its FWHM is proportional to n. The structure at ~ 2 eV also appears at $2 + 17(n - 1)$ eV, but diminishes with increasing n.

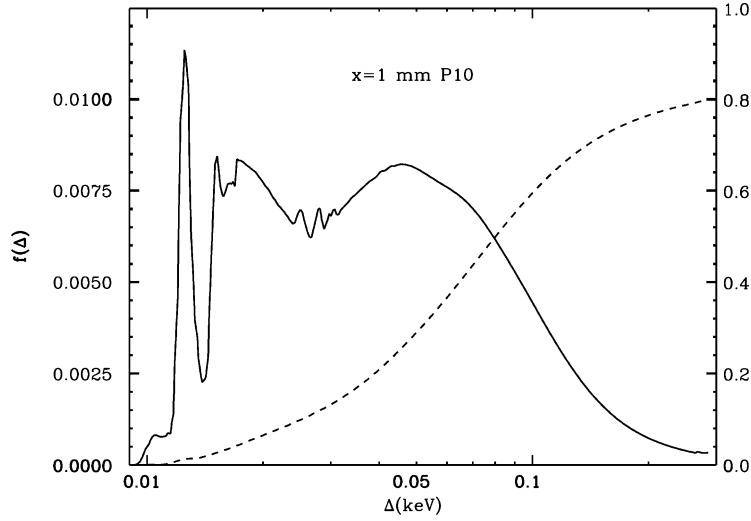

Fig. 4. The energy loss spectrum for minimum ionizing particles passing through $x = 1$ mm of P10 gas is given by the solid line. No collisions will occur for 5% of the particles. Single collisions occur between 10 and 20 eV, and a small structure remains at 25 eV, but 2 and 3 collision spectra (as shown in Fig. 2) are merged at 50 eV. The integral spectrum $F(\Delta)$ shows that only 20% of the particles lose more than the mean energy loss $\langle\Delta\rangle = 250$ eV.

$P_0 = 0.05,\ P_1 = 0.15,\ P_2 = 0.22,\ P_3 = 0.22,\ P_4 = 0.17,\ P_5 = 0.10,$ and $P_6 = 0.05$. Thus, 5% of all particles will make no collisions at all, and the single collision spectrum is clearly seen, while most of the structure of $\sigma(E)$ has disappeared for multiple collisions.[2] The mean energy loss for the full spectrum is 260 eV, while for 60% of the collisions the energy deposition Δ is less than 100 eV.

Energy loss spectra for thin absorbers can be measured with electron microscopy or related methods [5,13].

4. A SIMULATED ENERGY DEPOSITION SPECTRUM $g(\Delta, x)$

In this section, I want to demonstrate fundamental problems encountered in *measuring* radiation signals or effects. In order to show that these problems cannot be avoided even with a very good detector, the example of a 'measurement' is made with a Monte Carlo simulation on a computer, using the following assumptions:

(a) energy deposition and energy loss are the same;
(b) the energy loss spectrum $F(\Delta)$ shown in Fig. 4 is binned into 0.1 eV intervals;
(c) values of the energy loss Δ are obtained with random numbers from $F(\Delta)$;
(d) the hypothetical detector inside the absorber produces *signals s* which are binned into 1 eV intervals, resulting in a distribution function $g(s)$ which can be represented by a histogram;
(e) the passage of 100,000 particles is simulated.

Two examples, calculated with a different initial value for the random number generator are shown in Fig. 5 by crosses and circles. As we must expect, the two 'measured' spectra differ. I have made calculations with 1,000,000 particles, resulting in a similar aspect, but with smaller variations. The important observation we can make is that *the detailed features of the energy loss spectrum are smeared out in the 'observed' spectrum.* The most important reason for this is the random uncertainty due to the finite number of signals for each bin. A secondary reason is the loss of resolution due to the larger bins for the 'measurement'.

For realistic detectors, this smearing will be more pronounced.

[2] This is different for materials with a narrow plasmon peak, e.g., Al or Si [8,12].

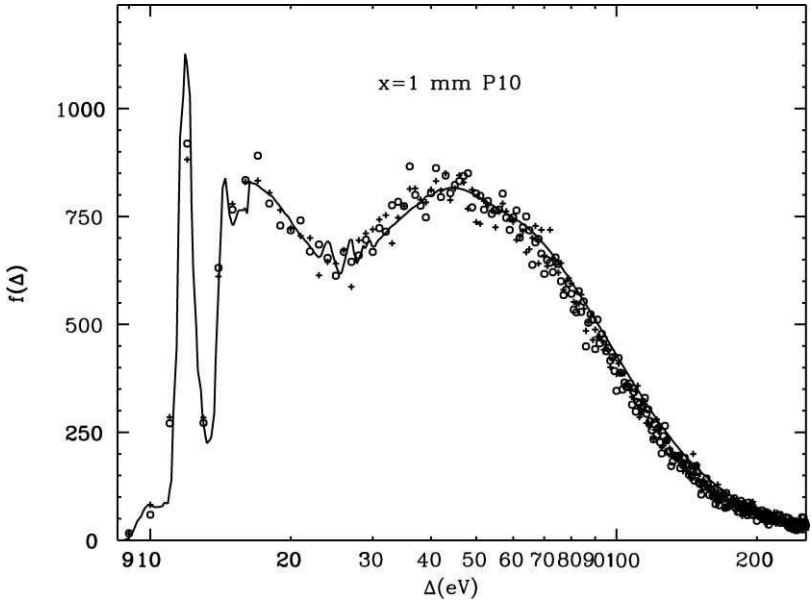

Fig. 5. 'Measured spectra' for a hypothetical detector described in the text are shown by circles and crosses. The energy loss spectrum of Fig. 4 is shown by the solid line. The 'measurement' is simulated with a Monte Carlo calculation. Instead of showing the histogram $g(s)$, the central point for each bar is given.

5. REALISTIC RELATION OF ENERGY LOSS TO RADIATION EFFECT

In order to derive the radiation-signal or -effect from energy deposition spectra we must consider the nature of the detector. A fundamental problem for all detectors is the escape of secondary radiation, such as delta-rays or fluorescence photons from the volume under observation [14–16]. It is neglected here.

Let us consider two detectors schematically.

(A) *Ionization devices*. For both solid state and gaseous detectors, a minimum energy is needed to produce a signal, i.e., an ion-pair or an electron–hole pair. For the energy deposition spectrum in P10 (for which the energy needed to produce one ion pair is $w = 25$ eV [17]), postulated in Fig. 5, this means, schematically, that all energy losses between 12 and 25 eV are represented by *one* ion pair, energy losses between 25 and 50 eV are represented by *two* ion pairs, etc., i.e., the spectrum of ion pairs will be represented by δ functions at 22, 40, 65, 90 eV, etc. and no other energy deposition effects can be measured. This 'observable spectrum' is shown in Fig. 6. The exact process of the ionization by a given energy deposition is

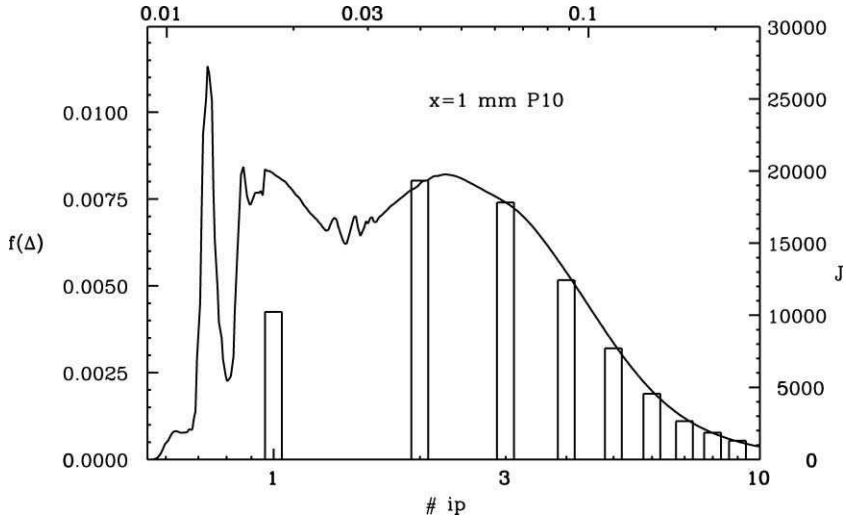

Fig. 6. The 'observable spectrum' for an ionization detector described in the text is shown by the bars representing the frequency (right hand scale) of signals from #ip ion pairs. The energy loss spectrum of Fig. 4 is shown by the solid line. The 'observation' is derived from the Monte Carlo spectrum shown in Fig. 5. Clearly, very little about the energy loss spectrum could be derived from the observation. In a real world detector, several sources of 'noise' would cause a spread in the bar give here, resulting in a Polya distribution for $n = 1$, approaching a Gaussian for large n [18].

not relevant: while an energy deposition of 125 eV might produce as many as 10 ion-pairs (on the average five), signals will always occur at integral numbers of ion-pairs; alternatively, a signal of five ion-pairs could be caused by any energy deposition between 70 and 140 eV. Clearly, any fine structure of the *energy loss* spectrum cannot be seen.[3]

For a Si detector (where $w = 3.6$ eV), the fact that the most probable energy loss is 17 eV means, schematically, that a single collision on the average produces five electron–hole pairs so that the δ functions will be located at multiples of 17 eV [16]. The complication that the processing of each signal additionally is smeared by amplifier noise [18] will disguise the discrete nature of the radiation effect.

(B) *DNA structures*. If DNA is considered as a detector, the situation is much more complex because the absorber is inherently highly inhomogeneous and the location of the collisions relative to the DNA will influence the probability of finding a break in a strand, as will the spatial extent of

[3] In principle, M_0 or λ can be calculated precisely for a given $\sigma(E)$, thus will change even with small changes in $\sigma(E)$, but no differences in energy deposition will be discernible because of the random nature of their distribution.

the collective excitations and their magnitude. These problems are considered in a study by Chatterjee and Holley [19]. A second problem is caused by the particle fluence, the energy loss spectrum will have random numbers of losses in any given interval $[\Delta, \Delta + \delta\Delta]$ and in any given volume. While it appears that energy transfers of the order of 2 or 3 eV are sufficient to produce a single-strand break, the most probable energy losses in water [9] and organic molecules [20] are the collective excitations at about 20 eV, enough to cause several DNA breaks in the neighborhood of the location of the collisions. Clearly, it will be difficult to correlate the collective excitations in water with any specific DNA break. Furthermore, radiation effects on DNA will also be caused by the free radicals produced as a by-product of the energy depositions. Thus at the level of single collisions, the radiation effect will essentially be completely random.

6. CONCLUSIONS

The experimental measurement of radiation effects in physical detectors with very small volumes will not produce any meaningful results for the determination of biological effects. In particular the attempt to correlate physical measurements with biological effects does not make sense because the effect mechanisms are different. It allows only very coarse conclusions about the nature of the energy loss process. In particular very little can be derived about the structure of the differential collision cross-section. Nanodosimetry in the meaning of measuring spectra of radiation signals in small volumes is a futile exercise.

REFERENCES

[1] L. Landau, *J. Phys.*, 1944, **VIII**, 201.
[2] K. Hagiwara *et al*., Review of Particle Physics, *Phys. Rev. D*, 2002, **66**, 01001-1.
[3] R. Cherubini, D. T. Goodhead, H. G. Menzel and A. Ottolenghi (Eds.), Microdosimetry, Proceedings of the 13th Symposium on Microdosimetry, Stresa, Italy, May 27–June 1, 2001, *Radiat. Protect. Dosimetry*, 2002, **99**(1–4).
[4] D. E. Lea, *Actions of Radiations on Living Cells*, 2nd edn, Cambridge University Press, Cambridge, 1955.
[5] C. D. Wilson, C. A. Dukes and R. A. Baragiola, Search for the plasmon in condensed water, *Phys. Rev. B*, 2001, **63**, 121101(R).
[6] H. Bichsel, *Nucl. Instrum. Methods B*, 1990, **52**, 136–139.
[7] H. Bichsel, *Rev. Mod. Phys.*, 1988, **60**, 663.
[8] H. Bichsel, Section 87 in *Atomic, Molecular And Optical Physics Handbook* (ed. G. Drake), American Institute of Physics (1996), 2nd edn, in preparation.
[9] M. Dingfelder, D. Hantke, M. Inokuti and H. G. Paretzke, *Radiat. Phys. Chem.*, 1998, **53**, 1–18.
[10] EELS atlas, C. C. Ahn and O. L. Krivanek, Gatan, Inc. Warrendale, PA, Center for Solid State Science, Arizona State University, Tempe, AZ, 1983.

[11] H. Bichsel, STAR Note SN 0439 (3.3.2002).
[12] H. Bichsel and R. P. Saxon, *Phys. Rev. A*, 1975, **11**, 1286.
[13] J. Ph. Perez, J. Sevely and B. Jouffrey, *Phys. Rev. A*, 1977, **16**, 1061.
[14] N. S. Laulainen and H. Bichsel, *Nucl. Instrum. Methods*, 1972, **104**, 531.
[15] H. Bichsel, Proceedings of the Ninth Symposium on Microdosimetry, *Radiat. Protect. Dosimetry*, 1985, **13**, 91.
[16] F. Scholze, *J. Appl. Phys. Rev.*, 1998, **84**, 2926–2938.
[17] *Average energy required to produce an ion pair*, ICRU report 31, International Communcation on Radiation Units, 7910 Woodmont Ave., Washington, DC, 20014, 1979.
[18] G. F. Knoll, *Radiation Detection and Measurement*, 3rd edn, Wiley, New York, 1999.
[19] A. Chatterjee and W. R. Holley, *Adv. Radiat. Biol.*, 1993, **17**, 181–226.
[20] M. Isaacson, *J. Chem. Phys.*, 1972, **56**, 1803.

Index

T

V

W

Y